ADA 278 512

UNITED STATES AIR FORCE

SUMMER RESEARCH PROGRAM -- 1993

SUMMER RESEARCH PROGRAM FINAL REPORTS

VOLUME 10

WRIGHT LABORATORY

RESEARCH & DEVELOPMENT LABORATORIES
5800 Uplander Way
Culver City, CA 90230-6608

Program Director, RDL
Gary Moore

Program Manager, AFOSR
Col. Hal Rhoades

Program Manager, RDL
Scott Licoscos

Program Administrator, RDL
Gwendolyn Smith

Program Administrator, RDL
Johnetta Thompson

Submitted to:

AIR FORCE OFFICE OF SCIENTIFIC RESEARCH
Bolling Air Force Base
Washington, D.C.
December 1993

DTIC QUALITY INSPECTED 3

94-12294

94 4 21 078

Master Index For Graduate Students

Ahmad, Imad
BS
Electrical Engineering
Portland State University
Portland, OR 97207-0000

Field: Electrical Engineering
Laboratory: PL/WS

Vol-Page No: 8-19

Anselmo, Andrew
MS
Mechanical Engineering
Columbia University
New York, NY 10027-0000

Field: Mechanical Engineering
Laboratory: RL/ER

Vol-Page No: 9- 3

Bapty, Theodore
MS
Box 1649 Station B
Vanderbilt University
Nashville, TN 37235-0000

Field: Electrical Engineering
Laboratory: AEDC/

Vol-Page No: 11- 1

Barber, Brian
BS
Electrical Engineering
Washington University
St. Louis, MO 63130-0000

Field: Electrical Engineering
Laboratory: RL/OC

Vol-Page No: 9-10

Bard, David
MS
Mechanical Engineering
Columbia University
New York, NY 10027-0000

Field: Applied Mechanics
Laboratory: PL/SX

Vol-Page No: 8-14

Barnett, William
BS
CLOUD & Aerosol Science L
University of Missouri
Rolla, MO 65401-0000

Field: Chemistry
Laboratory: PL/LI

Vol-Page No: 8- 6

Bartell, Craig
BS
Chemistry
Wright State University
Fairborn, OH 45435-0000

Field: Chemistry
Laboratory: WL/PO

Vol-Page No: 10-26

Bartelt, Timothy
MS
Physics
Clarkson University
Potsdam, NY 13676-0000

Field: Physics
Laboratory: RL/ER

Vol-Page No: 9- 4

Accesion For
NTIS CRA&I ☑
DTIC TAB ☐
Unannounced ☐
Justification
By
Distribution /
Availability Codes
Dist | Avail and / or Special
A-1

GSRP Participant Data

Brocklehurst, William
BS
Aerospace Engineering
University of Cinc nati
Cincinnati, OH 45221-0000

Field: Aerospace Engineering
Laboratory: PL/RK

Vol-Page No: 8-10

Burns, Paul
BS
Electrical Engineering
Auburn University
Auburn, AL 36849-0000

Field: Electrical Engineering
Laboratory: WL/MN

Vol-Page No: 10-21

Carlen, Edwin
BS
Electrical Engineering
Oakland University
Rochester, MI 48309-4401

Field: Electrical Engineering
Laboratory: WL/AA

Vol-Page No: 10- 1

Carter, Charity
MS
Electrical Engineering
Stevens Institute of Tech.
Hoboken, NJ 7030-0000

Field: Interdisciplinary Engr.
Laboratory: RL/IR

Vol-Page No: 9- 8

Caslin, Barry
BS
Computer Science/Engineer
Wright State University
Dayton, OH 45435-0000

Field: Computer Science
Laboratory: WL/ML

Vol-Page No: 10-14

Charley, David
BS
Electrical Engineering
University of Cincinnati
Cincinnati, OH 45221-0030

Field: Computer Science
Laboratory: WL/AA

Vol-Page No: 10- 2

Cisneros, John
BS
Psychology
California State University
Los Angeles, CA 90032-0000

Field: Psychology
Laboratory: RL/XP

Vol-Page No: 7- 8

Craig, Ralph
BS
Mathematics
North Carolina State Univ.
Raleigh, NC 27695-8205

Field: Mathematics
Laboratory: PL/VT

Vol-Page No: 8-15

GSRP Participant Data

Curtis, Joseph
MS
Zoology
University of California
Davis, CA 95616-0000

Field: Biomedicine
Laboratory: AL/OE

Vol-Page No: 7-25

Darnell, Julie
BS
Mechanical Engineering
University of Tennessee
Tullahoma, TN 37388-0000

Field: Mechanical Engineering
Laboratory: AEDC/

Vol-Page No: 11- 2

Davis, Wyatt
BS
Mechanical Engineering
Washington State University
Pullman, WA 99164-2920

Field: Mechanical Engineering
Laboratory: FJSRL/

Vol-Page No: 11-10

DeWilbiss, Alan
BS
Physics
University of Colorado
Colorado Springs, CO 80901-7150

Field: Physics
Laboratory: FJSRL/

Vol-Page No: 11-11

Detwiler, Duane
BS
Aeronautical Engineering
Ohio State University
Columbus, OH 43235-0000

Field: Aerospace Engineering
Laboratory: WL/FI

Vol-Page No: 10- 7

DiPietro, Jr., Anthony
BS
Aerospace Engineering
Virginia Polytechnic Institute
Blacksburg, VA 24060-0000

Field: Aerospace Engineering
Laboratory: AEDC/

Vol-Page No: 11- 3

Dobransky, Mary
MS
Systems Science
Binghamton University
Binghamton, NY 13902-6000

Field: Advanced Technology
Laboratory: RL/XP

Vol-Page No: 9-15

Doss, Ellen
BS
Biophysics
University of Scranton
Scranton, PA 18505-0898

Field: Biophysics
Laboratory: AL/AO

Vol-Page No: 7- 1

Best Available Copy

GSRP Participant Data

DuBois, Travis
BS
Mechanical Engineering
Old Dominion University
Norfolk, VA 23529-0247

Field: Mechanical Engineering
Laboratory: FJSRL/

Vol-Page No: 11-12

Farquhar, John
MS
Instructional Technology
University of Georgia
Athens, GA 30602-0000

Field: Instructional Technology
Laboratory: AL/HR

Vol-Page No: 7-17

Fischer, Verlyn
BS
Materials Science & Engr.
University of Florida
Gainesville, FL 32611-0000

Field: Physics
Laboratory: WL/ML

Vol-Page No: 10-15

Foster, Robert
BS
Mechanical Engineering
University of Iowa
Iowa City, IA 52240-0000

Field: Mechanical Engineering
Laboratory: WL/PO

Vol-Page No: 10-27

Frank, Jonathan
MS
Mechanical Engineering
Yale University
New Haven, CT 6520-0000

Field: Mechanical Engineering
Laboratory: WL/PO

Vol-Page No: 10-28

Fuller, Joan
BS
Chemistry
University of Alabama
Tuscaloosa, AL - 0

Field: Chemistry
Laboratory: FJSRL/

Vol-Page No: 11-13

Gavora, Mark
MS
Instructional Systems
Florida State University
Tallahassee, FL 32304-3551

Field: Instructional Systems
Laboratory: AL/HR

Vol-Page No: 7-18

Geierman, Robert
BS
Mechanical Engineering
University of Tennessee
Tullahoma, TN 37388-0000

Field: Mechanical Engineering
Laboratory: AEDC/

Vol-Page No: 11- 4

Best Available Copy

GSRP Participant Data

Gluck, Kevin BS Psychology Trinity University San Antonio, TX 78212-0000	Field: Psychology Laboratory: AL/HR Vol-Page No: 7-19
Gottlob, Lawrence MS Psychology Arizona State University Tempe, AZ 85287-0000	Field: Psychology Laboratory: AL/HR Vol-Page No: 7-20
Griffin, Steven BS Engineering University of Texas San Antonio, TX 78249-0665	Field: Mechanical Engineering Laboratory: PL/VT Vol-Page No: 8-16
Grosskopf, Kevin BS FAC 101 University of Florida Gainesville, FL 32611-0000	Field: School of Bldg. Construct Laboratory: WL/FI Vol-Page No: 10- 8
Harn, Patricia BS Technical Communication University of Washington Seattle, WA 98195-0000	Field: Communications Laboratory: AL/HR Vol-Page No: 7-21
Hickman, Mary BS Physics and Astronomy University of Wyoming Laramie, WY 82071-0000	Field: Astrophysics Laboratory: PL/LI Vol-Page No: 8- 7
Hovey III, Leland BS Computer Science SUNY Institute of Technology Utica, NY 13504-3050	Field: Mathematics Laboratory: RL/XP Vol-Page No: 9-16
Jain, Sanjay BS Northeastern Ohio University Rootstown, OH 44272-0000	Field: Natural Sciences Laboratory: WHMC/ Vol-Page No: 11-16

GSRP Participant Data

Jefferson, Ellen
BS
Biology
Trinity University
San Antonio, TX 78212-0000

Field: Biology
Laboratory: AL/OE

Vol-Page No: 7-26

Jenny, Jason
BS
Materials Science
Carnegie-Mellon University
Pittsburgh, PA 15213-0000

Field: Materials Science
Laboratory: WL/ML

Vol-Page No: 10-16

Jolly, Mohanjit
BS
Aeronautics/Astronautics
MIT
Cambridge, MA 2139-0000

Field: Aeronautics/Astronautics
Laboratory: PL/RK

Vol-Page No: 8-11

Jones, Claud
BS
Electrical & Computer Eng
University of SW Louisiana
Lafayette, LA 70504-3890

Field: Petroleum Engineering
Laboratory: RL/C3

Vol-Page No: 9- 1

Kelly, John
BS
Electrical Engineering
University of Florida
Gainesville, FL 32601-0000

Field: Electrical Engineering
Laboratory: PL/LI

Vol-Page No: 8- 8

Kimball, Lucia
MS
Mathematics
Worcester Polytechnic Inst.
Worcester, MA 1609-0000

Field: Applied Mathematics
Laboratory: PL/GP

Vol-Page No: 8- 1

Kundich, Robert
MS
899 Madison Ave., Ste 801
Univ. Tennessee-Memphis
Memphis, TN 38163-0000

Field: Biomedical Engineering
Laboratory: AL/CF

Vol-Page No: 7- 9

Kvasnak, William
MS
Mechanical Engineering
Clarkson University
Potsdam, NY 13699-5725

Field: Mechanical Engineering
Laboratory: AEDC/

Vol-Page No: 11- 5

GSRP Participant Data

Lair, John
BS
Civil Engineering
University of New Orleans
New Orleans, LA 70148-0000

Field: Industrial Design
Laboratory: WL/FI

Vol-Page No: 10- 9

Lee, Daniel
BS
Electrical Engineering
Southern Illinois University
Carbondale, IL 62901-0000

Field: Electrical Engineering
Laboratory: RL/ER

Vol-Page No: 9- 5

Leiweke, Robert
BS
Aeronautical Engineering
Ohio State University
Columbus, OH 43210-0000

Field: Aerospace Engineering
Laboratory: PL/WS

Vol-Page No: 8-20

Litvin, Kerry
MS
Electrical Engineering
Cornell University
Ithaca, NY 14853-0000

Field: Electrical Engineering
Laboratory: RL/OC

Vol-Page No: 9-11

Luker, Stephen
MS
Biological Science
University of Alabama
Tuscaloosa, AL 35487-0344

Field: Marine Science
Laboratory: PL/GP

Vol-Page No: 8- 2

Masterson, Gina
BS
Industrial Engineering
Auburn University
Auburn, AL - 0

Field: Industrial Engineering
Laboratory: AL/OE

Vol-Page No: 7-27

McMurtry, J.
MS
Mechanical Engineering
Louisiana Tech University
Ruston, LA 71272-0046

Field: Mechanical Engineering
Laboratory: WL/MN

Vol-Page No: 10-22

Menendez-Barreto, Melani
MS
Physics
University of Puerto Rico
Mayaguez, PR 681-0000

Field: Physics
Laboratory: PL/GP

Vol-Page No: 8- 3

GSRP Participant Data

Messerschmitt, Jane
MS
Electrical Engineering
Polytechnic University
Farmingdale, NY 11735-0000

Field:
Laboratory: PL/WS

Vol-Page No: 8-21

Mills, Jeffrey
MS
Cheistry
Indiana University
Bloomington, IN 47405-0000

Field: Chemistry
Laboratory: PL/RK

Vol-Page No: 8-12

Monka, Gary
BS
Chemistry
University of Scranton
Scranton, PA 18510-0000

Field: Chemistry
Laboratory: AL/OE

Vol-Page No: 7-28

Moore, Michael
MS
Electrical Engineering
Vanderbilt University
Nashville, TN 37235-0000

Field: Electrical Engineering
Laboratory: AEDC/

Vol-Page No: 11- 6

Moriarty, Daniel
MS
Nuclear Engineering
MIT
Cambridge, MA 2139-0000

Field: Nuclear Engineering
Laboratory: PL/GP

Vol-Page No: 8- 4

Nagaraja, Chandra
BS
Mechanical Engineering
University of Dayton
Dayton, OH 45469-0000

Field: Mechanical Engineering
Laboratory: WL/PO

Vol-Page No: 10-29

Naghski, David
MS
Electrical Engineering
University of Cincinnati
Cincinnati, OH 45221-0000

Field: Electrical Engineering
Laboratory: WL/ML

Vol-Page No: 10-17

Neaffer, Ronald
BS
Polymer Science
University of Akron
Akron, OH 44325-3909

Field: Physics
Laboratory: WL/ML

Vol-Page No: 10-18

GSRP Participant Data

Newell, Tim MS Physics University of North Texas Denton, TX 76203-0000	Field: Physics Laboratory: PL/LI Vol-Page No: 8- 9
Nguyen, Sonny BS Electrical Engineering Wright University Dayton, OH 45401-0000	Field: Electrical Engineering Laboratory: WL/PO Vol-Page No: 10-30
Nuteson, Todd BS Electrical Engineering Wright State University Dayton, OH 45435-0000	Field: Electrical Engineering Laboratory: WL/EL Vol-Page No: 10- 4
Olson, Michael BS Electrical Engineering Florida State University Tallahassee, FL 32316-0000	Field: Electrical Engineering Laboratory: WL/MN Vol-Page No: 10-23
Panek, Heather MS Biology University of Scranton Scranton, PA 18510-0000	Field: Biochemistry Laboratory: AL/AO Vol-Page No: 7- 3
Petroziello, Joseph BS Biology University of Scranton Scranton, PA 18510-0000	Field: Biology Laboratory: AL/AO Vol-Page No: 7- 4
Pobst, Jeffrey BS Aerospace Engineering University of Southern Calif. Los Angeles, CA 90089-1191	Field: Aerospace Engineering Laboratory: PL/RK Vol-Page No: 8-13
Povich, Clinton BS Aerospace Engineering University of Kansas Lawrence, KS 66045-0000	Field: Aerospace Engineering Laboratory: FJSRL/ Vol-Page No: 11-14

GSRP Participant Data

Radomsky, Leon
MS
Chemical Engineering
Columbia Univeristy
New York, NY 10027-0000

Field: Materials Science
Laboratory: WL/EL

Vol-Page No: 10- 5

Reed, Jason
BS
Electrical Engineering
Cornell University
Ithaca, NY 14853-0000

Field: Physics
Laboratory: RL/OC

Vol-Page No: 9-12

Reichmeyer, Francis
MS
Electlrical Engineering
Syracuse University
Syracuse, NY 13244-1240

Field: Electrical Engineering
Laboratory: RL/C3

Vol-Page No: 9- 2

Reiley, Daniel
MS
Physics
University of Alabama
Huntsville, AL 35899-0000

Field: Physics
Laboratory: WL/MN

Vol-Page No: 10-24

Reister, Craig
BS
Electrical Engineering
North Dakota State University
Fargo, ND 58105-0000

Field: Electrical Engineering
Laboratory: AL/AO

Vol-Page No: 7- 5

Reuster, Daniel
MS
Electrical Engineering
University of Dayton
Dayton, OH 45469-0000

Field: Electrical Engineering
Laboratory: WL/AA

Vol-Page No: 10- 3

Riesinger, Joyce
BS
Ecology/Evolutionary Biol
University of West Florida
Pensacola, FL 32514-0000

Field: Marine Biology
Laboratory: AL/EQ

Vol-Page No: 7-14

Ryan, Arthur
BS
Psychology
Wright State University
Dayton, OH 45435-0001

Field: Psychology
Laboratory: AL/CF

Vol-Page No: 7-10

GSRP Participant Data

Samad, Mohammed BS Mechanical Engineering University of New Orleans New Orleans, LA 70148-0000	Field: Mechanical Engineering Laboratory: WL/FI Vol-Page No: 10-10
Schroeder, Mark BS Electrical Engineering North Dakota State University Fargo, ND 58105-0000	Field: Electrical Engineering Laboratory: AL/AO Vol-Page No: 7- 6
Schwing, Ronald BS Mechanical Engineering University of Iowa Iowa City, IA 52242-0000	Field: Mechanical Engineering Laboratory: WL/PO Vol-Page No: 10-31
Seifert, Jason BS Psychology University of Dayton Dayton, OH 45410-0000	Field: Psychology Laboratory: AL/HR Vol-Page No: 7-22
Seydel III, Robert BS Aerospace Engineering University of Missouri Rolla, MO 65401-0000	Field: Aerospace Engineering Laboratory: WL/FI Vol-Page No: 10-11
Shahidi, Anoosh MS Intelligent Systems Studi University of Pittsburgh Pittsburgh, PA 15260-0000	Field: Intelligent Systems Laboratory: AL/HR Vol-Page No: 7-23
Shahrokhi, Kimball BS Mechanical Engineering Vanderbilt University Nashville, TN 37232-0000	Field: Mechanical Engineering Laboratory: AEDC/ Vol-Page No: 11- 7
Slater III, Robert MS Mechanical Engineering University of Cincinnati Cincinnati, OH 45221-0000	Field: Engineering Laboratory: WL/FI Vol-Page No: 10-12

Socci, Ed
MS
Materials Science & Engr
University of Virginia
Charlottesville, VA 22903-2442

Field:
Laboratory: WL/ML

Vol-Page N 10-19

Sodoy, Maureen
BS
Biology
Trinity University
San Antonio, TX 78212-0000

Field: Biology
Laboratory: AL/OE

Vol-Page No: 7-29

Sorensen, Bryant
MS
Electrical Engineering
University of Tennessee
Tullahoma, TN 37388-0000

Field: Mathematics
Laboratory: AEDC/

Vol-Page No: 11- 8

Spencer, Robert
BS
Electrical Engineering
Cornell University
Ithaca, NY 14853-0000

Field: Electrical Engineering
Laboratory: RL/OC

Vol-Page No: 9-13

Stadler, Bethanie
BS
Materials Science
Massachusetts Inst. of Tech.
Cambridge, MA 2139-0000

Field: Materials Science
Laboratory: RL/ER

Vol-Page No: 9- 6

Stansbery, Donald
BS
Aerospace Engineering
University of Missouri
Rolla, MO 65401-0000

Field: Aerospace
Laboratory: WL/MN

Vol-Page No: 10-25

Starchville, Jr., Thomas
MS
Aerospace Engineering
Pennsylvania State University
University Park, PA 16802-0000

Field: Aerospace Engineering
Laboratory: WL/FI

Vol-Page No: 10-13

Starks, Michael
BS
Electrical Engineering
Boston University
Boston, MA 2215-0000

Field: Electrical Engineering
Laboratory: PL/GP

Vol-Page No: 8- 5

GSRP Participant Data

Stauffer, Joseph
MS
Management
University of Iowa
Iowa City, IA 52242-1323

Field: Management
Laboratory: AL/HR

Vol-Page No: 7-24

Stenger, Vincent
BS
Electrical Engineering
University of Cincinnati
Cincinnati, OH 45221-0030

Field: Electrical Engineering
Laboratory: WL/EL

Vol-Page No: 10- 6

Stohs, Jonathan
BS
Physics
University of New Mexico
Albuquerque, NM 87131-0000

Field: Math
Laboratory: PL/VT

Vol-Page No: 8-17

Stroman, Ronald
BS
Pharmacy
University of South Carolina
Columbia, SC 29208-0000

Field: Pharmacy
Laboratory: AL/AO

Vol-Page No: 7- 7

Sullins, Tashia
BS
Chemistry
University of Georgia
Athens, GA 30605-0000

Field: Chemistry
Laboratory: AL/EQ

Vol-Page No: 7-15

Sutcliffe, Ronald
BS
Chemistry
Southwest Texas State
San Marcos, TX 78666-0000

Field: Chemistry
Laboratory: AL/OE

Vol-Page No: 7-30

Sweeney, Walter
MS
Electrical Engineering
University of Maine
Orono, ME 4469-0000

Field: Electrical Engineering
Laboratory: RL/IR

Vol-Page No: 9- 9

Swindal, J.
MS
Applied Physice
Yale University
New Haven, CT 6520-0000

Field: Applied Physics
Laboratory: WL/PO

Vol-Page No: 10-32

GSRP Participant Data

Tascillo, Mark
MS
Electrical Engineering
Binghamton University
Binghamton, NY 13902-0000

Field: Electrical Engineering
Laboratory: RL/OC

Vol-Page No: 9-14

Thomas, Stuart
BS
Chemical Engineering
North Carolina State Univ.
Raleigh, NC 27695-0000

Field: Chemical Engineering
Laboratory: AL/EQ

Vol-Page No: 7-16

Tipton, Kevin
MS
Nutrition and Food Scienc
Auburn University
Auburn, AL 36849-5605

Field: Zoology
Laboratory: AL/CF

Vol-Page No: 7-11

Tornow, Carina
BS
Quantitive Psychology
Ohio State University
Columbus, OH 43210-0000

Field: Psychology
Laboratory: AL/CF

Vol-Page No: 7-12

Trick, Kimberly
MS
Chemical Engineering
University of Dayton
Dayton, OH 45401-0240

Field: Chemical Engineering
Laboratory: WL/ML

Vol-Page No: 10-20

Weaver, Michael
MS
Aerospace Engineering
Georgia Institute of Technolog
Atlanta, GA 30332-0150

Field: Aerospace Engineering
Laboratory: AEDC/

Vol-Page No: 11- 9

Weitzman, Peter
MS
Thayer School of Engineer
Dartmouth College
Hanover, NH 3755-0000

Field: Electrical Engineering
Laboratory: FJSRL/

Vol-Page No: 11-15

Whitmore, Christine
BS
Mechanical Engineering
Washington University
St. Louis, MO - 0

Field: Mechanical Engineering
Laboratory: AL/CF

Vol-Page No: 7-13

GSRP Participant Data

Widener, Charles
MS
Electrical Engineering
Syracuse University
Syracuse, NY 13244-0000

Field: Electrical Engineering
Laboratory: PL/VT

Vol-Page No: 8-18

Wierman, Mark
MA
Systems Science
Binghamton University
Binghamton, NY 13902-6000

Field: Mathematics
Laboratory: RL/XP

Vol-Page No: 9-17

Willemsen, Balam
MS
Physics
Northeastern University
Boston, MA 2115-0000

Field: Physics
Laboratory: RL/ER

Vol-Page No: 9- 7

Wolfe, Randall
MS
Biopsychology
University of Georgia
Athens, GA 30612-0000

Field: General Psychology
Laboratory: AL/OE

Vol-Page No: 7-31

Worthy, Mark
BS
Environmental Engineering
University of Alabama
Huntsville, AL 35899-1750

Field: Electrical Engineering
Laboratory: PL/WS

Vol-Page No: 8-22

SIGNAL PROCESSING METHODS FOR SPECTRAL ESTIMATION USING SIGNAL SUBSPACE METHODS, AND ANGLE OF ARRIVAL ESTIMATION

Edwin Carlen
Graduate Student
Department of Electrical and Systems Engineering

Oakland University
Dodge Hall of Engineering
Rochester, MI 48309-4401

Final Report for:
Graduate Student Research Program
Wright Laboratory

Sponsored by:
Air Force Office of Scientific Research
Bolling Air Force Base, Washington, D.C.

December 1993

SIGNAL PROCESSING METHODS FOR SPECTRAL ESTIMATION USING SIGNAL SUBSPACE METHODS, AND ANGLE OF ARRIVAL ESTIMATION

Edwin Carlen
Graduate Student
Department of Electrical and Systems Engineering
Oakland University

Abstract

The paper outlines two main tasks assigned during my employment as a graduate student research associate at the Wright Laboratory, Wright Paterson Air Force Base. Upon arrival at the Wright Laboratories, I was to investigate a method of signal processing, different from the common Fourier transform, in that inherent mathematical properties of the signal space are exploited in retrieving the spectrum of the signal. The two alternative signal processing methods investigated are the MUSIC and Minimum-Norm procedures for high resolution signal processing. The results of the investigation are included with a general comment section regarding the performance of the algorithms. The second main task assigned was the investigation of angle of arrival (AOA) calculation. Traditionally, methods such as beamforming have been used to estimate the AOA using arrays of sensors and sophisticated signal processing algorithms. We are curious as to whether the AOA can be measured using only two sensors and FFT processing measuring the phase difference of the signal at two adjacent sensors. Results of this study are presented with general comments as to the validity of the measuring paradigm.

ASSIGNMENT ONE

Introduction

The analysis of signals and properties of such has been done primarily using "classical" methods of data processing. these classical methods have been dominated by the DFT (Discrete Fourier Transform) and more specifically the FFT (Fast Fourier Transform), because of implementation simplicity. These methods lack the precision sometimes necessary to perform detailed spectrum analysis due to the inherent structure of the mathematics involved, in other words are too computation extensive for high resolution signal processing. Since the early 1980's an alternative method of spectrum analysis surfaced using a more complex, yet far more precise, method of spectrum analysis based on the properties of the signal and noise subspaces[1]. The traditional FFT analysis does not take into account the signal and noise it is analyzing, rather performs the processing algorithm on any data that is presented to it, then the precision depends on the number of points used in calculation of the FFT. The subspace method of spectral estimation does processing on the characteristics of each signal that is presented to it, whereby creating a much more detailed approximation of the respective signal and noise vectors presented to it. There are many subspace analysis methods available[2]:

- Pisarenko Harmonic Decomposition.
- Multiple Signal Classification (MUSIC).
- Principal Components Linear Prediction.
- ESPRIT: Son of MUSIC.
- Maximum Likelihood and weighted Subspace Fitting.
- Computation of Subspace-Based Estimates.
- Minimum-Norm Procedure.

This paper deals with an in-depth analysis of the MUSIC and Minimum-Norm procedure with simulations and recommendations for preferable data sets and a matlab program for quick and easy spectral analysis of any particular data set.

Mathematical Theory

The MUSIC and Minimum-Norm spectral estimation methods are based heavily on eigenanalysis. Essentially, the eigenvectors and eigenvalues are approximated from the estimated correlation matrix of the input sequence. These eigenvectors are then manipulated based on the eigenvalues, which are used to discriminate between the signal and noise subspaces. Figure 1 depicts how this procedure would work.

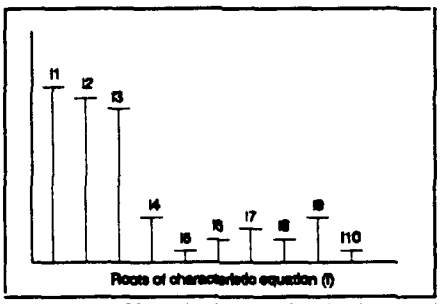

Figure 1: Hypothetical distribution of eigenvalues. Large values belong to signal space, while small belong to noise space

The eigenvalues l1, l2 and l3 correspond to the signal subspace (assuming a large SNR (Signal-to-Noise-Ratio)) because of their values. The eigenvalues l4, l5, l6, l7, l8, l9 and l10 correspond to the noise subspace. The number of eigenvalues in the signal space is directly proportional to the number of sources in the input sequence. This characteristic is critical for correct operation of these estimation methods. If the number of sources is incorrectly identified, then generally speaking the remaining estimations will also be incorrect.

The purpose for calculating the correlation matrix is that it inherently possesses the fundamental harmonic spectral frequencies of the input sequence[3]. The correlation matrix is of course an approximation and not an exact calculation, because the input sequence is finite. The estimated correlation matrix is computed using forward and forward-backward calculations, as depicted in equations (1) and (2) respectively.

$$\hat{R}_{xx} = \frac{1}{K}\sum_{k=0}^{K-1} x_k x_k^h \qquad (1)$$

Where, K is the number of data vectors, and h corresponds to the conjugate transpose operation. Where

$$\hat{R}_{xx} = \frac{1}{K}\sum_{k=0}^{K-1} (x_k x_k^h + \bar{x}_k \bar{x}_k^h) \qquad (2)$$

the term $\bar{x}_k = (x^*[k+L-1], \ldots, x^*[k+1], x^*[k])^T$ and * corresponds to the complex conjugate operation and T is the transpose operation. Also, K = N - L + 1. The forward-backward estimation usually yields better resolution than the forward estimation procedure.

Once the estimated correlation matrix has been computed, the eigenvectors and eigenvalues are computed. The estimation of the eigenvalues was done with the eig function provided with the Matlab simulation environment[4]. Essentially, the relationship between the correlation matrix and the eigenvectors is

$$R_{xx} u_i = \lambda_i u_i \qquad \|u_i\| = 1 \qquad (4)$$

defined by observing the defining equation (4).

$$\lambda_i u_i \approx \frac{1}{K}\sum_{k=0}^{K-1} (x_k^h u_i)\, x_k \qquad (5)$$

Therefore, the following relationship can be formed in equation (5)[5]. Therefore the eigenvalues are some linear combination of the input sequence. It is assumed that all sources are incoherent from one another.

MUSIC Simulation Results

The eigenvalues and eigenvectors have been formed from the input sequence, now the calculation of the pseudospectrum is performed. The MUSIC and Min-Norm procedures differ in method in the approximation of the spectral components of the signal. The main idea is that the signal space and noise space are embedded in a some final space. The final space is the space which is received by the receiver equipment, whatever that may be. The formula for the calculation of the MUSIC pseudospectrum, $P_{MU}(e^{j\omega})$, calculation method is listed in (6).

$$P_{MU}(e^{j\omega}) = \frac{1}{w^{*T} E_{noise} E_{noise}^{*T} w} \tag{6}$$

Where the matrix $\mathbf{E}_{noise}$ is the noise space of the estimated correlation matrix of the input sequence. The procedure for determining the noise and signal space is simply based upon analysis of the eigenvalues and eigenvectors. The estimated correlation matrix is partitioned into two portions representing the signal and noise spaces. The columns of the estimated correlation matrix are chosen based on the eigenvalues. For example, refer to Figure 1 and the estimated correlation matrix would be partitioned such that columns 1, 2 and 3 would be the signal space and columns 4, 5, 6, 7, 8, 9 and 10 the noise space. The **w** matrix is called the frequency vector which simply contains components for each of the frequencies components, also determining the resolution of the pseudospectrum. The frequency vector is depicted in equation (7).

$$\begin{matrix} 1 \\ e^{j\omega} \\ e^{2j\omega} \\ e^{3j\omega} \\ \vdots \end{matrix} \tag{7}$$

Where ω is the frequency, which is of course variable. From equation (6), The pseudospectrum will be a maximum when the quantity in the denominator is at a minimum. The denominator is minimum when the noise space $\mathbf{E}_{noise}$ and frequency vector, **w**, are perpendicular to each other. Theoretically, the noise subspace is perpendicular to the frequency vector when the variable ω is equal to the frequency of the source(s) in the signal space. Therefore, when the variable frequency, ω, equals the frequency of the sources of the input sequence, then the pseudospectrum will have a peak. The Matlab simulation program of the MUSIC method is located in Appendix A. The results of the simulation for three different signal environments. The first of these environments is the following real data: $x(n) = \cos(\omega_1 n + .1) + 2\cos(\omega_2 n) + 1.9\cos(\omega_3 n)$; where $\omega_1 = 1.32$ rad/sec, $\omega_2 = 2.26$ rad/sec, $\omega_3 = 2.39$ rad/sec and $n = 1, 2, 3, \ldots, 32$. The resolution capability of the simulated algorithm is 0.004 rad/sec with 256 frequency components in the frequency vector **w**. The results are depicted in Figure 2. The main difference between the processing of real data verses complex data is the fact that twice as many

eigenvalues represent the signal subspace, than that of the complex data.

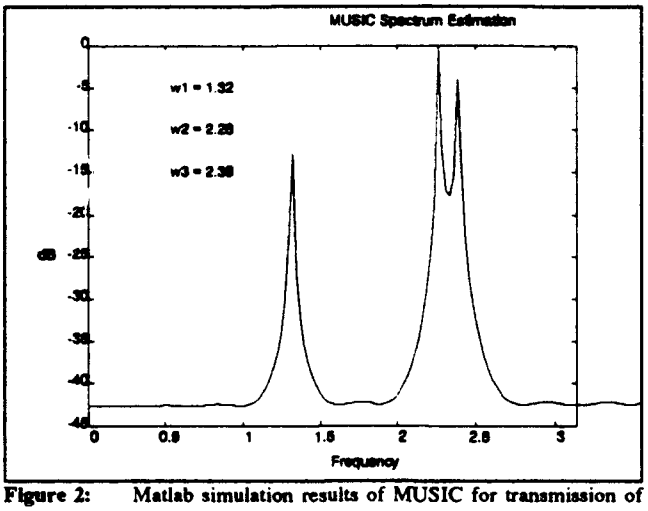

Figure 2: Matlab simulation results of MUSIC for transmission of three sources

The second data set is similar to the previous simulation with the exception of using complex representation. The data is represented with the following equation: $x(n) = \exp(j\omega_1 n + .1) + 2\exp(j\omega_2 n) + 1.9\exp(j\omega_3 n)$.

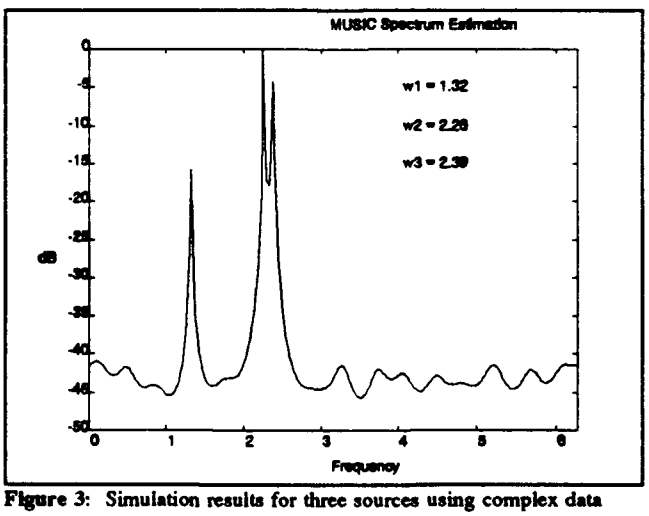

Figure 3: Simulation results for three sources using complex data

Figure 3 depicts the Matlab simulation results for the second data set. Notice in Figure 3, when complex data is used there seems to be spurious noise, however, no noise is included in the signal. The third data set is taken

from[1] as comparison to results received previously. The data sequence is formed with the following expression: $x(n) = A_1\exp(j\omega_1 n + \Phi_{1n})) + A_2\exp(j\omega_2 n + \Phi_{2n})) + \varpi(n)$; where Φ_{in} is the uniformly distributed phase angle on the interval $(-\pi,\pi)$, $\varpi(n)$ is a Gaussian noise source with variance: $\sigma^2 = 0.5$ and mean: $\mu = 0$. Figure 4 depicts the simulation results for $A_1=A_2=A_3=3.162$; $\omega_1 = 1.8019$ rad/sec. $\omega_2 = 2.0194$ rad/sec.

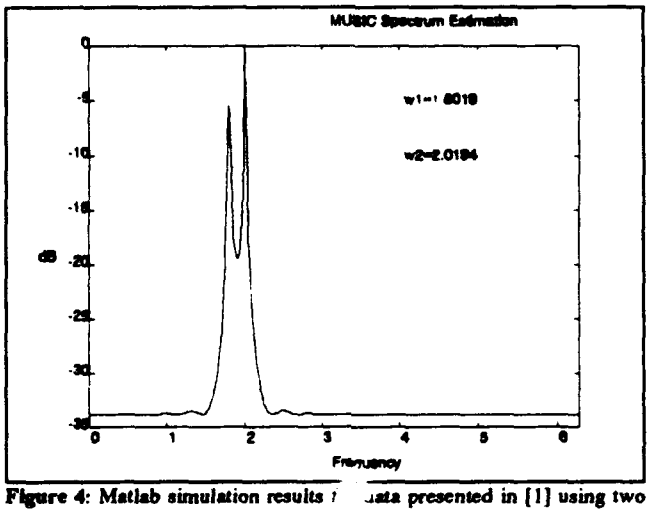

Figure 4: Matlab simulation results for data presented in [1] using two sources and Gaussian noise

Minimum-Norm Simulation Results

The Minimum-Norm (Min-Norm) procedure is similar, but different from the MUSIC method. After estimating the eigenvectors and eigenvalues, the Min-Norm procedure begins with choosing an appropriate vector, **d** to compute the pseudospectrum, $P_{MN}(e^{j\omega})$ listed in equation (8).

$$P_{MN}(e^{j\omega}) = \frac{1}{w^{*T}dd^{*T}w} \tag{8}$$

Since **w** is a known quantity, the frequency vector, then the vector **d** is the only calculation to be performed. The vector d is defined as shown in (9).

$$d = \frac{1}{c^{*T}c}E_{noise}c \tag{9}$$

Where the matrix c^{*T} is the top row of the noise space matrix E_{noise}, which is estimated from the previously calculated eigenvalues and eigenvectors. Once **d** is calculated the pseudospectrum P_{MU} can be calculated using

equation (8). However, equation (8) can be written as in equation (10). Where D is expressed in equation (11).

$$P_{MN}(e^{j\omega}) = \frac{1}{|D(e^{j\omega})|^2} \tag{10}$$

$$D(z) = \sum_{k=0}^{N-1} d[k]z^{-k} \tag{11}$$

Where d is denoted as d[0], d[1], d[2], ... , d[N-1]. Then , the general formula can be derived[2]. The equation $D(z) = D_1(z)D_2(z)...$, where D(z), $D_1(z)$ and $D_2(z)$ are comonic polynomials in z^{-1}[2]. Upon solving for roots of D(z) yields the frequency of the input sequence(s). It is obvious that the Min-Norm procedure would eliminate to a great extent computation time to determine the frequency of the input sequence(s), however, if the results are displayed graphically there would be no significant improvement. The Min-Norm is simulated with the Matlab environment using the exact input data used for the MUSIC simulations. The Matlab program for the Min-Norm simulation is listed in Appendix B. The first of these signal spaces is: $x(n) = \cos(\omega_1 n + .1) + 2\cos(\omega_2 n) + 1.9\cos(\omega_3 n)$; where $\omega_1 = 1.32$ rad/sec, $\omega_2 = 2.26$ rad/sec and $\omega_3 = 2.39$ rad/sec. The resolution capability of the simulated algorithm is 0.007 rad/sec with 256 frequency components in the frequency vector w. The results are depicted in Figure 5.

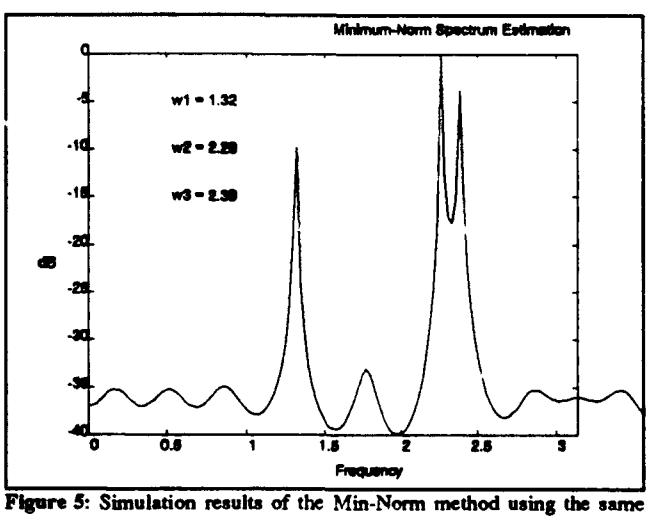

Figure 5: Simulation results of the Min-Norm method using the same data used in Figure 2.

The main difference between the processing of real data verses complex data is the fact that twice as many eigenvalues represent the signal subspace, than that of the complex data. The second data set is of the same as the previous simulation with the exception of using complex data. The data is represented with the following equation: $x(n) = \exp(j\omega_1 n + .1) + 2\exp(j\omega_2 n) + 1.9\exp(j\omega_3 n)$.

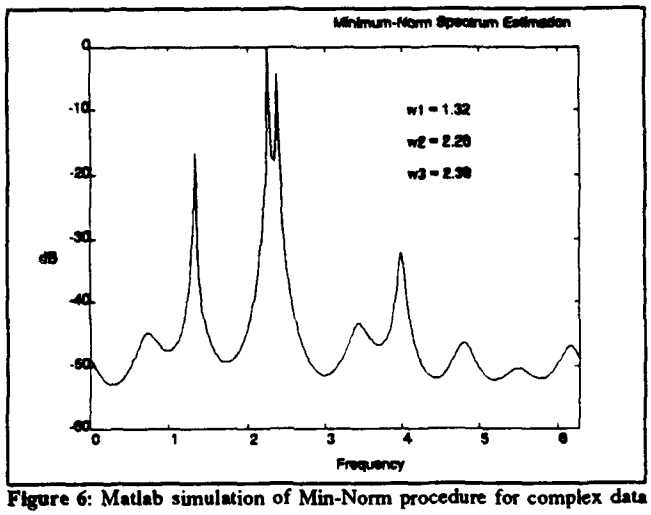

Figure 6: Matlab simulation of Min-Norm procedure for complex data with three sources.

Figure 6 depicts the Matlab simulation results for the second data set. Take note of the large levels of apparent noise in the spectrum despite the input sequence being void of any noise sources. The third data set is taken from[1] as comparison to results received previously. The data sequence is formed with the following expression: $x(n) = A_1\exp(j\omega_1 n + \Phi_{1n})) + A_2\exp(j\omega_2 n + \Phi_{2n})) + \varpi(n)$; where Φ_{in} is the uniformly distributed phase angle on the interval $(-\pi,\pi)$, $\varpi(n)$ is a Gaussian noise source with variance: $\sigma^2 = 0.5$ and mean: $\mu = 0$. Figure 7 depicts the simulation results for $A_1=A_2=A_3=3.162$; $\omega_1 = 1.8019$ rad/sec; $\omega_2 = 2.0194$ rad/sec.

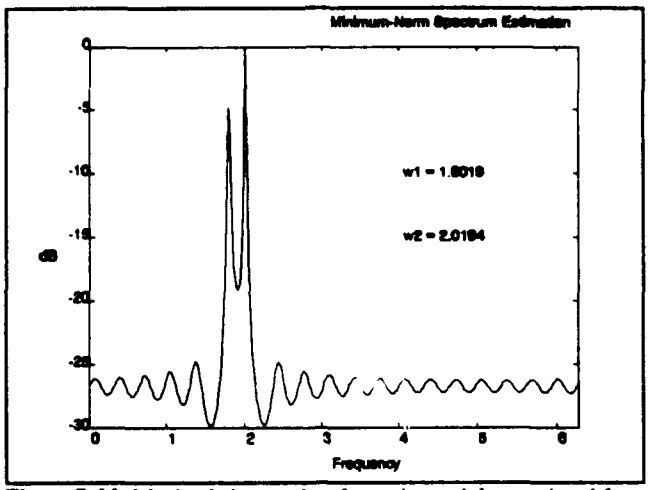

Figure 7: Matlab simulation results of experimental data retrieved from [1] with 2 sources.

Conclusions

The performance of the two signal processing methods is similar, however, the MUSIC method continually performed better in terms of rejecting noise than that of the Min-Norm method. In fact the Min-Norm method behaved very peculiar when large filter sizes were used to produce the estimated correlation function, even when there was no induced noise in the system. This peculiarity was not determined because all data sets and correlation matrix estimation techniques were identical between MUSIC and Min-Norm. The largest problem with using these spectral estimation techniques, is the fact that the number of sources must be known *a priori*, which is not always possible in electronic warfare (EW) equipment. There have been attempts to construct source estimators for detecting the number of signals in a multichannel time series. These are the AIC and MDL methods, which show a glimmer of promise, but are not reliable enough to warrant the use in practical systems.

ASSIGNMENT TWO

Introduction

Traditionally the AOA measurement has been performed using techniques such as beamforming[2] or interferometry[9]. This assignment involves the construction of a Matlab program to illustrate the performance of a more general method of AOA measurement. The measurement of the AOA parameter is performed using only two sensors for two signals, and pairs of sensors are used to resolve the ambiguity of the distance between sensors and varying signal frequencies[10]. Simulation results conclude assignment two.

Mathematical Theory

Figure 8 depicts the arrangement where each of the three sensors are separated by a distance **d**. The incoming signal is depicted with the wide arrow line. The AOA is depicted as θ.

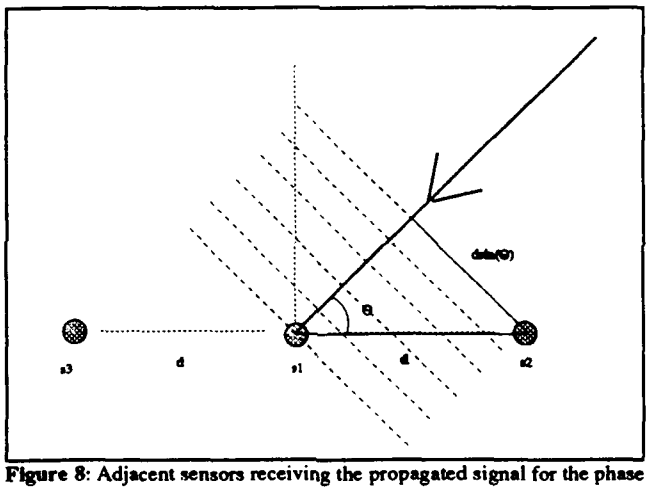

Figure 8: Adjacent sensors receiving the propagated signal for the phase and time delay estimations.

Wave propagation theory states that there will exist a time delay between sensors s_1 and s_2. This delay is

$$x = d\sin(\theta) \tag{13}$$

calculated by assigning the distance **x** the quantity in equation (13). Then the relative time delay is formulated in equation (14).

$$\tau = \frac{x}{c} \tag{14}$$

Where c is the wave propagation speed in a particular medium (speed of light). Combining equations (13) and (14) the time delay expression can be formulated.

$$\tau = \frac{d\sin(\theta)}{c} \tag{15}$$

The time delay figure is related to the phase delay of the system by simply multiplying the delay with the frequency of the incoming wave. Therefore this phase delay can be formulated using $c=f\lambda$ and $\omega=2\pi f$.

$$\varphi = 2\pi\frac{d\sin(\theta)}{\lambda} \tag{16}$$

The estimation of the AOA parameter is done using only two of the three sensors, s_1 and s_2, shown in Figure 8. The phase is measured for the incoming signals and the frequency component of that frequency is extracted whichever method is most appropriate for the application. The method used for this simulation is the Fourier transform, more specifically the fast Fourier transform (FFT). Other methods, such as MUSIC or Autoregression, can be used for higher resolution applications. Once the estimated phase delay has been measured, then the AOA parameter is found by rearranging equation (16).

$$\theta = \arcsin\left(\frac{\varphi 2\pi d}{\lambda}\right) \tag{17}$$

The assumptions for the wave propagation estimations are that $d < \lambda/2$, and that $c = 3.0\text{x}10^8$m/s.

AOA Estimation Simulation Results

The Matlab computation package is used to determine the performance and validity of the AOA estimation method discussed previously. The Matlab program is listed in Appendix C. The simulation environment consists of two incoming signals (used only as a test here), two pair of adjacent sensors separated by a distance d that depends on the incoming frequency. For simulation purposes the two frequencies f_1 and f_2 are variable, therefore, so are the distances between adjacent sensors, d_1 and d_2. The signal, CW modulated, is received by sensor s_1, and sensor s_2 is used as the reference. Each frequency component is to be extracted from the composite signal. A standard FFT algorithm is used to determine the spectrum of the incoming signal. The location of the peak(s) of the FFT output should correspond to the phase angle ψ of equation (16). Once the peak is determined, the complex component at this peak position is extracted and processed to determine the phase angle ψ. Then equation (17) is used to calculate the AOA for each signal with the assumption that $d=0.95(\lambda/2)$. The input signal sequences are real and have the $\cos(\omega n - \phi)$ form, where ω is the signal frequency and ϕ is the phase delay from an adjacent sensor. The noise space for the input sequence is Gaussian. Figure 9 depicts the incoming signal where ω_1=1GHz and ω_2=2GHz (G=10^9) with the SNR=20. Time jitter and pulse rise and fall times are also incorporated into the composite signal. For all simulation the time jitter factor is 1 ps

($p=10^{-12}$) and rise and fall times of 1ns ($n=10^{-9}$). Figure 9 also depicts the FFT output sequence in the lower plot.

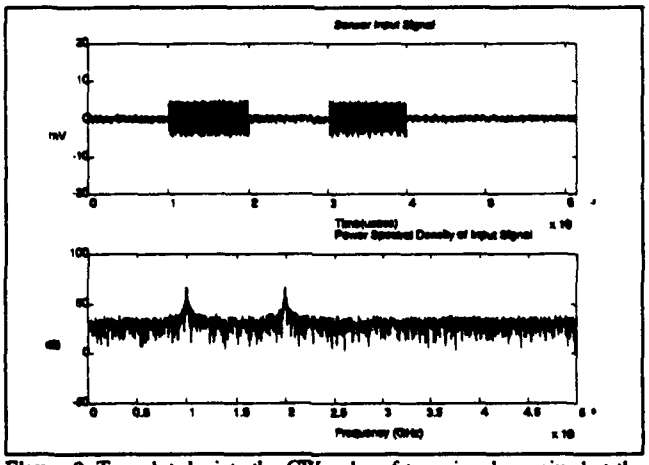

Figure 9: Top plot depicts the CW pulse of two signals received at the sensor. Bottom plot depicts the FFT output.

The method for extracting the AOA information form the FFT output sequence performed reliably, however, is extremely sensitive to noise. Table 1 lists several simulations for different values of ϕ and different SNR levels.

***Table 1**: Accuracy analysis of estimating the phase delay parameter for several values of ϕ.*

SNR	ϕ_1 (rad)	ϕ_{1E} (rad)	Error (%)	ϕ_2 (rad)	ϕ_{2E} (rad)	Error (%)
10	0.3000	0.3460	15	0.4000	0.4270	6.75
10	1.5708	1.5627	0.52	1.0472	1.0646	1.66
20	0.3000	0.3081	2.7	0.4000	0.3886	2.85
20	1.5708	1.5785	0.49	1.0472	1.0375	0.93
30	0.3000	0.3058	1.9	0.4000	0.3942	1.4
30	1.5708	1.5686	0.14	1.0472	1.0460	0.11

From Table 1 it is obvious that if the phase delay component is small, it is difficult to retrieve an accurate estimate if the SNR is too low. Figures 10 and 11 depict the final output of the AOA detection program using the method described earlier for phase delays chosen randomly. In both Figures 10 and 11, the assumption is that sensor s_1 is at the coordinate (0,0) and the sensor s_2 is located to the right of s_1 on the horizontal axis at a

distance of d as discussed earlier. Figure 11 depicts the measurement of two angles, the first measurement is in the first quadrant of the cartesian plane with an AOA measurement of approximately $\theta_1 \approx 6°$. The second approximately $\theta_2 \approx 24°$.

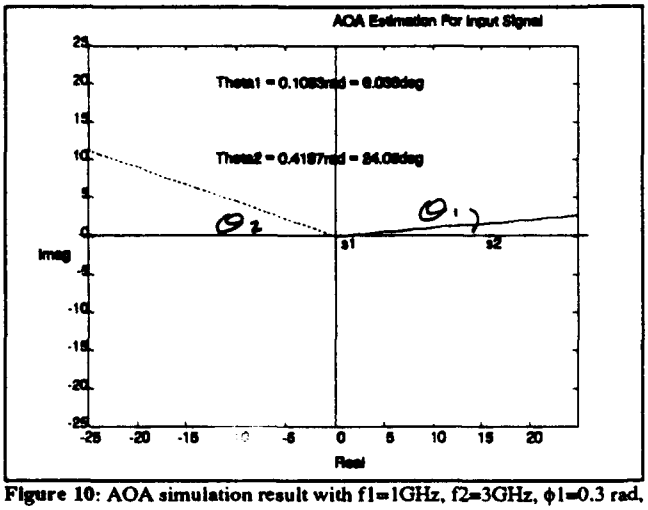

Figure 10: AOA simulation result with f1=1GHz, f2=3GHz, ϕ1=0.3 rad, ϕ2=0.5 rad.

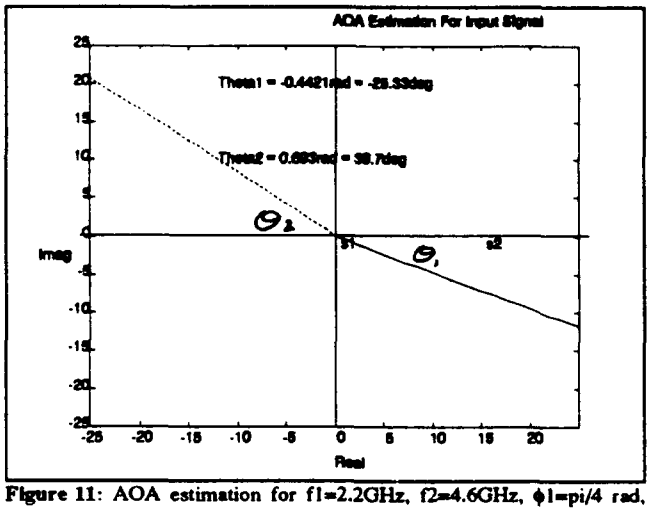

Figure 11: AOA estimation for f1=2.2GHz, f2=4.6GHz, ϕ1=pi/4 rad, ϕ2=pi/3 rad.

Both measurements are displayed correctly as approaching sensor s_1. Figure 10 depicts similar simulation results except that the first signal has a negative AOA due to the difference in the signal frequency f_1 and the phase delay ϕ_1. The AOA estimation values for the simulation depicted in Figure 10 are $\theta_1 \approx -25°$ for signal one and $\theta_2 \approx 40°$ for signal two. All simulations were performed with the SNR=30.

Conclusion of AOA estimation

The presented method for estimating the AOA parameter worked very well for SNR values that are large, and also if the frequency and phase delay are large, then the signal is not as easily susceptible to external noise. This direct method of AOA estimation was not detailed anywhere in literature that could be found. The idea of processing two signals using only two sensors and directly extracting information from the spectrum of the signal is new and was originated by Dr. B.Y. Tsui[11].

ACKNOWLEDGEMENTS

Thanks are extended to Dr. Tsui of the Wright Laboratory for making this summer research project enjoyable and intellectually stimulating. Thanks are also extended to Dr. Arnab Shaw and W. Xia at Wright State University for discussions about assignment one. Thanks finally to Dr. Prasala from the University of Dayton for discussion about assignment two.

APPENDIX A

```
%%%%%%%%%%%%%%%%%%%%%%%%%%%%%%
% This progam computes the MUSIC algorithm          %
% for spectral estimation using the subspace method.
% 9 August 1993
%
% If creating a data file the final signal variable
% must be ''X''. this is the vector variable name
%
%
%%%%%%%%%%%%%%%%%%%%%%%%%%%%%%
% Input the input vector size and load input data
%%%%%%%%%%%%%%%%%%%%%%%%%%%%%%
clear
%%%%%%%%%%%%%%%%%%%%%%%%%%%%%%
Q = menu('ENTER FILE TYPE','Prespecified Variables','Raw
Data');
if Q == 1,
  m = input('Enter Name Of Data File: ','s');
  eval(['load ',m]);
  sig = X;
else,
  m = input('Enter Name Of Data File: ','s');
  eval(['load ',m]);
  sig = x;
end
%%%%%%%%%%%%%%%%%%%%%%%%%%%%%%
% Input Data
%%%%%%%%%%%%%%%%%%%%%%%%%%%%%%
mf  = input('Enter Desired Filter Order: ');
numpts = input('Enter Number of Output Data Points: ');
Ns = input('Enter Number of Sources: ');
real = input('Enter the Type of Data: 1 - Real; 2 - Complex: ');
[a,b] = size(sig);
K = b;   % Number of snapshots
%%%%%%%%%%%%%%%%%%%%%%%%%%%%%%
% Compute the correlation matrix using the covariance method
%%%%%%%%%%%%%%%%%%%%%%%%%%%%%%
C2 = [];
for k = 1:mf,
  C1 = sig(k:K-mf+k);
  C1 = C1(:);
  C2 = [C2 C1];
end
Ca = fliplr(C2);
C3 = C2';
Cb = flipud(C3);
rmat = Cb*Ca*1/(K);
%%%%%%%%%%%%%%%%%%%%%%%%%%%%%%
% Find eigenvalues
%%%%%%%%%%%%%%%%%%%%%%%%%%%%%%
[v d] = eig(rmat);
   [lambda,k1]=sort(diag(d));
   E=v(:,k1);
   if real == 1,
     nspace = E(:,1:(mf-2*Ns));
   elseif real ==2,
     nspace = E(:,1:(mf-Ns));
   end
   for k2 = 1:numpts+1,
      w(k2) = (2*pi*(k2-1))/(numpts);
      l = 1:mf;
      ss = exp(j*w(k2)*(l-1));
      s = ss(:);
      pmu(k2) = 1.0/(s'*nspace*nspace'*s);
   end
   pmu = pmu(:);
   pmu = 10.0*log10(pmu/max(pmu));
%%%%%%%%%%%%%%%%%%%%%%%%%%%%%%
% Plotting
%%%%%%%%%%%%%%%%%%%%%%%%%%%%%%
plot(w,pmu);
grid;
title('MUSIC Spectrum Estimation');
xlabel('Frequency');
ylabel('dB');
```

APPENDIX B

```
%%%%%%%%%%%%%%%%%%%%%%%%%%%%%%%%
% This program computes the minimum normal algorithm
% for spectral estimation using the subspace method.
%
% 9 August 1993
%
% If creating a data file the final signal variable
% must be ''X''.  this is the vector variable name
%
%%%%%%%%%%%%%%%%%%%%%%%%%%%%%%%%
% Input the input vector size and load input data
%%%%%%%%%%%%%%%%%%%%%%%%%%%%%%%%
clear
Q = menu('ENTER FILE TYPE','Prespecified Variables','Raw
Data');
if Q == 1,
  m = input('Enter Name of Data File: ','s');
  eval(['load ',m]);
else,
  m = input('Enter Name of Data File: ','s');
  eval(['load ',m]);
  X = x;
end
Fs = input('Enter Desired Filter Size: ');
real = input('Enter the Type of Data: 1 - Real; 2 - Complex: ');
points = input('Enter Number of Output Data Points: ');
Ns = input('Enter the Number of Sources: ');
[a,b] = size(X);
K = b;   % Number of snapshots
%%%%%%%%%%%%%%%%%%%%%%%%%%%%%%%%
% Compute the correlation matrix using covariance method
%%%%%%%%%%%%%%%%%%%%%%%%%%%%%%%%
C2 = [];
for k = 1:Fs,
  C1 = X(k:K-Fs+k);
  C1 = C1(:);
  C2 = [C2 C1];
end
Ca = fliplr(C2);
C3 = C2';
Cb = flipud(C3);
Rx = Cb*Ca*1/(K);
%%%%%%%%%%%%%%%%%%%%%%%%%%%%%%%%
% Compute the eigenvalues and eigenvectors of Rx
%%%%%%%%%%%%%%%%%%%%%%%%%%%%%%%%[
Ea,L] = eig(Rx);
EL = length(Ea);
[lambda,k1]=sort(diag(L));
E=Ea(:,k1);
if real == 1,
  En = E(:,1:(Fs-2*Ns));
elseif real ==2,
  En = E(:,1:(Fs-Ns));
end
Enp = En(2:EL,:);
c = En(1,:);
%%%%%%%%%%%%%%%%%%%%%%%%%%%%%%%%
% Compute the vector d.
%%%%%%%%%%%%%%%%%%%%%%%%%%%%%%%%
d = 1/(c*c')*(En*c');
%%%%%%%%%%%%%%%%%%%%%%%%%%%%%%%%
% Compute Pseudospectrum
%%%%%%%%%%%%%%%%%%%%%%%%%%%%%%%%f
or k=1:points + 1,
  w(k) = 2*pi*(k-1)/(points); % 2pi coverage
  [v,t]=size(d);
  l=1:v;
  B1 = exp(j*w(k)*(l-1));
  B = B1(:);
  Pmn(k) = 1.0/(B'*d*d'*B);
end
Pmn = Pmn(:);
Pmn = 10*log10(Pmn/max(Pmn));
%%%%%%%%%%%%%%%%%%%%%%%%%%%%%%%%
% Plotting
%%%%%%%%%%%%%%%%%%%%%%%%%%%%%%%%
plot(w,Pmn)
xlabel('Frequency')
ylabel('dB')
title('Minimum-Norm Spectrum Estimation')
```

APPENDIX C

```
%%%%%%%%%%%%%%%%%%%%%%%%%%%%%%%%%%
% AOA.M
%
% Program for calculating the AOA primarily from phase
% of propagated waves captured at adjacent sensor in the array.
%%%%%%%%%%%%%%%%%%%%%%%%%%%%%%%%%%
clear
format long
l1=1; %normalized wavelength
d1=0.95*(l1/2); %distance between sensor 1 and sensor 2
c1 = (2*pi*d1)/l1;
l2=1; %normalized wavelength
d2=0.95*(l2/2); %distance between sensor 1 and sensor 3
c2 = (2*pi*d2)/l2;

%%%%%%%%%%%%%%%%%%%%%%%%%%%%%%%%%%
%  Initialize signal parameters.
%%%%%%%%%%%%%%%%%%%%%%%%%%%%%%%%%%
num_signals=2; num_samples=6144; samples=num_samples;
fre1 = input('Enter the first frequency (GHz): ');
ph1 = input('Enter the first phase delay in radians: ');
fre2 = input('Enter the second frequency (GHz): ');
ph2 = input('Enter the second phase delay in radians: ');
freq(1)=fre1*1e9; freq(2)=fre2*1e9;
phase_init(1) = ph1; phase_init(2) = ph2;
s_freq=10e9; rf_bw=1.5e9; noise_fig=3;
rf_gain_db=25; jitter=1e-12;
pw(1)=1e-7; pw(2)=1e-7;
snrdb(1)=20; snrdb(2)=20;
pulse_offset(1)=0.1e-6; pulse_offset(2)=0.3e-6;
rise_fall(1)=1e-9; rise_fall(2)=1e-9;

%%%%%%%%%%%%%%%%%%%%%%%%%%%%%%%%%%
%  Create matrices for time and frequency.
%%%%%%%%%%%%%%%%%%%%%%%%%%%%%%%%%%
sample_num = (0:num_samples-1);
time = sample_num/s_freq;

%%%%%%%%%%%%%%%%%%%%%%%%%%%%%%%%%%
%  Create noise jitter.
%%%%%%%%%%%%%%%%%%%%%%%%%%%%%%%%%%j
itter_noise = randn(size(time)) * jitter;
time_jittered = time + jitter_noise;

%%%%%%%%%%%%%%%%%%%%%%%%%%%%%%%%%%
%  Calculate pw and pulse offset in samples.
%%%%%%%%%%%%%%%%%%%%%%%%%%%%%%%%%%r
ise_samples = round( rise_fall * s_freq);
if rise_samples == 0,
   rise_samples = 1;
end
pw_samples = round(pw * s_freq) ;
pulse_offset_s = round(pulse_offset * s_freq) + 1;
pulse_end = pulse_offset_s + pw_samples;

%%%%%%%%%%%%%%%%%%%%%%%%%%%%%%%%%%
% Check to see if the end of the pulse is longer than the number
% samples. If it is limit, the pulse width to the last sample.
%%%%%%%%%%%%%%%%%%%%%%%%%%%%%%%%%%f
or a = 1:num_signals,
  if (pulse_end(a) > num_samples)
      pulse_end(a) = num_samples;
      pw_samples(a)=num_samples - pulse_offset_s(a);
  end
end

%%%%%%%%%%%%%%%%%%%%%%%%%%%%%%%%%%
% Initialize some matrices for use later.
%%%%%%%%%%%%%%%%%%%%%%%%%%%%%%%%%%
pw_matrix = zeros(2,num_samples);

%%%%%%%%%%%%%%%%%%%%%%%%%%%%%%%%%%
%  Create the pulse width matrix.
%%%%%%%%%%%%%%%%%%%%%%%%%%%%%%%%%%
for p = 1:num_signals
  pw_matrix(p,:) = sample_num >= pulse_offset_s(p) &
sample_num < pulse_end(p);
  p_rise =  0:1/rise_samples(p):1-1/rise_samples(p);
  p_fall = 1-1/rise_samples(p):-1/rise_samples(p):0;

pw_matrix(p,pulse_offset_s(p):pulse_offset_s(p)+rise_samples(p)-
1) = p_rise(1:rise_samples(p));
  pw_matrix(p,pulse_end(p)-rise_samples(p)+1:pulse_end(p)) =
p_fall(1:rise_samples(p));
end

%%%%%%%%%%%%%%%%%%%%%%%%%%%%%%%%%%
%  Calculate the signal with phase shift.
%%%%%%%%%%%%%%%%%%%%%%%%%%%%%%%%%%
signal1 = cos((2*pi*freq(1)*time_jittered) - phase_init(1));
signal2 = cos((2*pi*freq(2)*time_jittered) + phase_init(2));
signal = [signal1; signal2];

%%%%%%%%%%%%%%%%%%%%%%%%%%%%%%%%%%
%  Multipy signal with pulse width matrix.
%%%%%%%%%%%%%%%%%%%%%%%%%%%%%%%%%%
signal = signal .* pw_matrix;

%%%%%%%%%%%%%%%%%%%%%%%%%%%%%%%%%%
%  Create noise. Noise power = kTBGF where kT = -174 dbm
%  or -204 dbW  at room temperature. Calculate noise power at
% input of RF amplifier  chain.
%%%%%%%%%%%%%%%%%%%%%%%%%%%%%%%%%%
noise_pwr_in = -204 + 10*log10(rf_bw);

%%%%%%%%%%%%%%%%%%%%%%%%%%%%%%%%%%
%  Add RF gain and amplifier noise figure to get noise ouput
power.
%%%%%%%%%%%%%%%%%%%%%%%%%%%%%%%%%%
noise_pwr_out=noise_pwr_in + rf_gain_db + noise_fig;
noise_pwr_m=[noise_pwr_out noise_pwr_out];
noise_fig_m=[noise_fig noise_fig];

%%%%%%%%%%%%%%%%%%%%%%%%%%%%%%%%%%
%  SNR at output of RF amplifiers.
%%%%%%%%%%%%%%%%%%%%%%%%%%%%%%%%%%
snr_out = snrdb - noise_fig_m;

%%%%%%%%%%%%%%%%%%%%%%%%%%%%%%%%%%
```

```
% Signal power at output of RF amplifier.
%%%%%%%%%%%%%%%%%%%%%%%%%%%%%%
signal_ref = snr_out + noise_pwr_m;

%%%%%%%%%%%%%%%%%%%%%%%%%%%%%%
% Assume 50 ohm impedances for noise calculation.
%%%%%%%%%%%%%%%%%%%%%%%%%%%%%%%%i
mpedance_db = 10 * log10(50);
db_2 = 10 * log10(2);
noise_amp=1000 * 10^((noise_pwr_out + impedance_db)/20);

%%%%%%%%%%%%%%%%%%%%%%%%%%%%%%
% Create the Gaussaian noise signal.
%%%%%%%%%%%%%%%%%%%%%%%%%%%%%%
noise = noise_amp * randn(size(time));

%%%%%%%%%%%%%%%%%%%%%%%%%%%%%%
% Scale signal level to get the desired SNR.
%%%%%%%%%%%%%%%%%%%%%%%%%%%%%%
signal_amp = zeros(1,2);
for l=1:num_signals
  signal_amp(l) = 1000 * 10^((signal_ref(l) + impedance_db +
db_2)/20);
end
sig_amp_matrix = [(signal_amp(1)*ones(1,num_samples))
          (signal_amp(2)*ones(1,num_samples))];
signal = sig_amp_matrix .* signal;
sig = sig_amp_matrix .* sig;

%%%%%%%%%%%%%%%%%%%%%%%%%%%%%%
% Add the signals together to create one signal.
%%%%%%%%%%%%%%%%%%%%%%%%%%%%%%
signal_summed = zeros(1,num_samples);
for k = 1:num_signals
  signal_summed = signal_summed + signal(k,:);
end

%%%%%%%%%%%%%%%%%%%%%%%%%%%%%%
% Add the noise to the signal.
%%%%%%%%%%%%%%%%%%%%%%%%%%%%%%
signal_summed = signal_summed + noise;

%%%%%%%%%%%%%%%%%%%%%%%%%%%%%%
% Perform the FFT operation of the composite signal
%%%%%%%%%%%%%%%%%%%%%%%%%%%%%%
fft_signal = fft(signal_summed);
power_db = 10*log10(fft_signal.*conj(fft_signal));
freq_res=(s_freq/num_samples);
freq_fft=(0:samples-1)*freq_res;


%%%%%%%%%%%%%%%%%%%%%%%%%%%%%%
% Find the maximum value coordinates
%%%%%%%%%%%%%%%%%%%%%%%%%%%%%%
power=power_db;
[x1,y1]=max(power(1:samples/2));
power(y1:y1+3)=[0 0 0 0];
power(y1-3:y1)=[0 0 0 0];
[x2,y2]=max(power(1:samples/2));
power(y2:y2+3)=[0 0 0 0];
power(y2-3:y2)=[0 0 0 0];

%%%%%%%%%%%%%%%%%%%%%%%%%%%%%%
% Check if y1 < y2
%%%%%%%%%%%%%%%%%%%%%%%%%%%%%%
if y1 > y2,
 temp1=y1;  temp2=y2; y1=temp2; y2=temp1;
elseif y1a > y2a,
  temp1=y1a; temp2=y2a;  y1a=temp2; y2a=temp1;
end;

%%%%%%%%%%%%%%%%%%%%%%%%%%%%%%
% Calculate the first phase angle and first AOA
%%%%%%%%%%%%%%%%%%%%%%%%%%%%%%
x11=fft_signal(y1); a1=angle(x11);

%%%%%%%%%%%%%%%%%%%%%%%%%%%%%%
% Calculate the second phase angle and second AOA
%%%%%%%%%%%%%%%%%%%%%%%%%%%%%%
x22=fft_signal(y2); a2=angle(x22);

%%%%%%%%%%%%%%%%%%%%%%%%%%%%%%
% Calculate Phase angle
%%%%%%%%%%%%%%%%%%%%%%%%%%%%%%t
theta1 = asin(a1/c1); theta1d=theta1*(180/pi);
theta2 = asin(a2/c2); theta2d=theta2*(180/pi);
for k=1:26,
  k1(k) = k; p1 = k-1;
  b1(k) = p1*tan(theta1); b2(k) = p1*tan(theta2);
  tst1(k) = p1 + i*b1(k); tst2(k) = -p1 + i*b2(k);
  abcissa1(k) = 0 + i*(k-1); abcissa2(k) = 0 - i*(k-1);
   abcissa = [abcissa1 abcissa2];
  ordinate1(k) = (k + i*0.000001);
   ordinate2(k) = (-k + i*0.000001);
  ordinate = [ordinate1 ordinate2];
 end

%%%%%%%%%%%%%%%%%%%%%%%%%%%%%%
% Plot results
%%%%%%%%%%%%%%%%%%%%%%%%%%%%%%f
format short
subplot(2,1,2), plot(tst1,'r:')
hold on
plot(tst2,'g:') plot(abcissa,'w-') plot(ordinate,'w-')
hold off
axis([-25 25 -25 25]);
title('AOA Estimation For Input Signal');
text(-15,20,['Theta1 = ', num2str(theta1),'rad',' =
',num2str(theta1d),'deg']);
text(-15,10,['Theta2 = ', num2str(theta2),'rad',' =
',num2str(theta2d),'deg']);
xlabel('Real');
ylabel('Imag');
```

REFERENCES

[1] Ramdas Kumaresan, Donald Tufts, "Estimating the Angles of Arrival of Multiple Plane Waves," IEEE Transactions on Aerospace and Electronic Systems, Vol. AES-19, No. 1, January 1983.

[2] Charles W. Therrien, *Discrete Random Signals and Statistical Signal Processing*, Prentice Hall, 1992.

[3] V.F. Pisarenko, "The Retrieval of Harmonics from a Covariance Function," Geophys. J. Roy. Astron. Soc., 33, 1973.

[4] Matlab, *MATLAB for MS-DOS Personal Computers - User's Guide*, The MathWorks, Inc.

[5] Juha T. Karhunen, Jyrki Joutsensalo, "Sinusoidal Frequency Estimation by Signal Subspace Approximation," IEEE Transactions on Signal Processing, Vol. 40,No. 12, December 1992.

[6] S.W. Lang, J.H. McClellan, "Spectral Estimation for Sensor Arrays," IEEE Transactions on Acoustics, Speech and Signal Processing, Vol. ,April 1983.

[7] Mati wax, Thomas Kailath, "Detection of Signals by Information Theoretic Criteria," IEEE Transactions on ASSP, Vol. ASSP-33, No. 2, April 1985.

[8] Lavon B. Page, *Probability for Engineering; with Applications to reliability*, Comput· Science Press, 1989.

[9] Ernest Jacobs, Elizabeth W. Ralston, "Ambiguity Resolution in Interferometry," IEEE Transactions on Aerospace and Electronic Systems, Vol. AES-17, No. 6, November 1981.

[10] Dr. Prasala, Personal communication, September 20, 1993.

[11] James B.Y. Tsui, Personal communication, September 17, 1993.

Communication via Shared Memory

David A. Charley
Graduate Student
Department of Electrical & Computer Engineering

University of Cincinnati
Cincinnati, Oh. 45221-0030

Final Report for:
Graduate Student Research Program
Wright Laboratory

Sponsored by:
Air Force Office of Scientific Research
Bolling Air Force Base, Washington, D.C.

September, 1993

Communication via Shared Memory

David A. Charley
Graduate Student
Department of Electrical & Computer Engineering
University of Cincinnati

Abstract

Interprocess communication has received much attention in recent years. Communication kernels have been developed to enable communication for many types of applications as well as generic systems. This paper provides a generic classification scheme for shared memory communication systems. Existing systems are discussed in the context of their classifications. The conclusion of this paper is that the scientific exploration of shared memory communication needs to be continued to further develop the classification scheme and eventually establish a design methodology.

Communication via Shared Memory

David A. Charley

1 Introduction

This report describes the activities undertaken by the author as a participant in the Air Force Office of Scientific Research (AFOSR) Graduate Student Research Program (GSRP) during the summer of 1993.

Interprocess communication (IPC) has received much attention in recent years because many applications take advantage of multiple process designs (Example: Parallel Discrete Event Simulation [8]). Other researchers [1, 6] have found that shared memory can be used to improve the speed of IPC between processes residing on the same machine.

This report concentrates on the use of shared memory for InterProcess Communication. The components of a shared memory communication system and performance indicators are identified. Multiple partitioning strategies are presented to illustrate trade-offs and the characteristics of some existing systems are discussed. Finally, an alternative for a second generation communication facility to support the Parallel Discrete Event Simulation (PDES) of Very high speed integrated circuits Hardware Description Language (VHDL) descriptions is considered.

2 Shared Memory

Shared memory refers to a single physical memory area that is accessed bv multiple processes.

In a virtual memory environment, processes typically map a common physical memory area into their virtual address spaces. In single address space environments (such as [4]), shared areas are typically accessed by giving multiple processes the appropriate access rights to an address.

In this study, we are concerned with management policies to guide the efficient use of shared memory. One of the simplest uses is to share a variable between multiple processes. Any process can update or read a shared variable as long as it obeys the management policies. Examples of management policies are 1) Any process can write or read a variable at any time, or 2) Any process can read, but only one process can update a variable at any given time.

While there are many policies, the purpose of this study is to evaluate shared memory as a tool for reliable communication between processes. Policies that allow simultaneous updates to a single shared location work well for applications that only need estimates of a variables value. However, such policies are not appropriate for communication systems where corrupted messages can cause unpredictable results. We therefore limit the scope of this study to non-destructive communication policies using shared memory as the .nderlying medium for data transfer.

3 The Components of a Shared Memory Communication System

The basic components of any communication system are: **Messages** (data to be transferred), **Senders** (message composers), **Receivers** (message interpreters), and the **Transmission** of messages from senders to receivers.

Messages are sequences of bytes to be transferred. **Message Blocks** are physical shared memory locations where messages are placed. Message blocks may be statically or dynamically allocated,

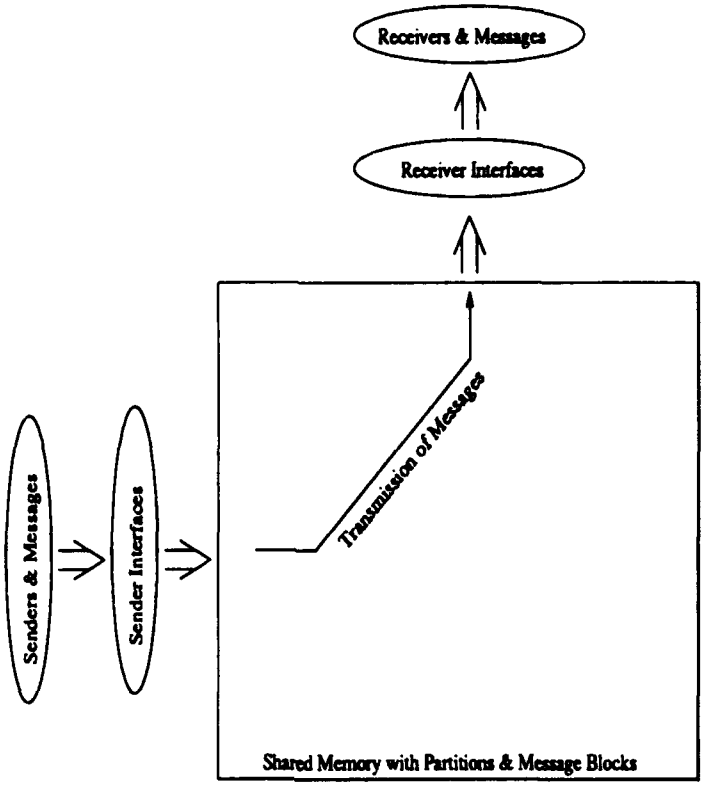

Figure 1: Components of a Communication System.

but at any given instant, each message block is either accessible or not accessible by each sender and each receiver. Shared memory can be split into message blocks by a pre-defined data structure or left in its most raw form (bytes). If memory is treated as a set of raw bytes, then policies and methods are relied upon to allocate these bytes to senders. These areas (either defined by a policy and raw byte management mechanism, or a pre-defined data structure) are viewed as message blocks.

The term **Partition** is used to refer to a set of message blocks. An example of a partition is a free list containing available message blocks for senders. A partition could also be a queue of messages ready to be interpreted by receivers. The intersection of any two partitions is empty and the union of all partitions is the entire set of message blocks.

In order to transmit messages, shared memory resources must be managed so that senders can access partitions in a mutually exclusive manner. In addition, receivers must be able to access the appropriate partitions to get messages. **Sender Interfaces** and **Receiver Interfaces** are introduced as components of a communication system for the purpose of accessing partitions according to existing policies.

Sets of senders and receivers can overlap each other. A single process can be both a sender and a receiver at the same time. To be generic, a single process could comprise all of the senders and all of the receivers if such a design were desired.

Figure 1 shows the components of a communication system.

3.1 Observations

A few observations are made that provide basic concepts about the the design of a communication system. We assume there are n senders and n receivers in this study.

Each sender interface must access one or more partitions because if a sender is not associated with

any partition, then the sender cannot access message blocks and therefore cannot send messages.

Each receiver interface must access one or more partitions because if a receiver is not associated with any partition, then the receiver cannot access message blocks and therefore cannot receive messages.

Each partition will have between 0 and n senders and between 0 and n receivers associated with it.

4 Communication System Indicators

Many indicators exist that point to how a communication system will perform. **Contention** is a factor that measures conflict and can be represented by two sub-factors: **Sender Contention** and **Receiver Contention**. Senders place messages in the communication system and receivers take messages out. Senders conflict with each other if they attempt to use a common area for message placement. Receivers typically read messages addressed to themselves and do not contend because each message is associated with only one receiver. On the other hand, multicast and broadcast systems allow single messages to be addressed to multiple destinations. In systems of this type, receivers contend if they access a single resource (such as decrementing a counter) to represent the reception of a message. Communication systems vary from those that avoid contention to those that allow maximal contention. Usually, some mechanism, such as a mutual exclusion (**mutex**) [5] device is used to guarantee that contention is non destructive.

Allocation refers to the overhead associated with allocating message blocks to senders. Static allocation is the easiest technique to implement and requires little management overhead. However, this approach provides little ability to adjust to dynamic communication needs (such as changing bandwidth requirements). Dynamic allocation provides more flexibility than static allocation, but at an increased overhead cost. Another aspect of allocation is whether the algorithm is decentralized (each individual sender handles allocation of blocks) or centralized (a single entity handles allocation for all senders).

Delivery refers to the overhead of delivering messages from sender interfaces to receiver interfaces. Delivery overhead exists if receiver interfaces do not overlap sender interfaces. This situation requires a mechanism to move messages from sender interfaces to receiver interfaces.

Location refers to the overhead required for receivers to locate messages delivered to their address. If receivers must scan large areas for messages, then much time can be wasted. On the other hand, if each receiver has exactly one location where all messages are delivered, then the overhead associated with finding messages can be minimized.

Finally, **Reclamation** is the overhead of reclaiming message blocks for future allocation. If dynamic block allocation is used, message blocks can be placed in a buffer space (for future allocation) or immediately allocated to waiting senders. If static block allocation is used, reclaimable blocks simply need be given a usable status.

5 Partitioning

The number of partitions used in a communication system and the associations each partition has with both senders and receivers can vary widely. Four partitioning strategies are discussed below. The scenarios all assume a decentralized (or distributed) approach for contention, allocation, delivery, location, and reclamation management. They also assume that multicasting and broadcasting are not used.

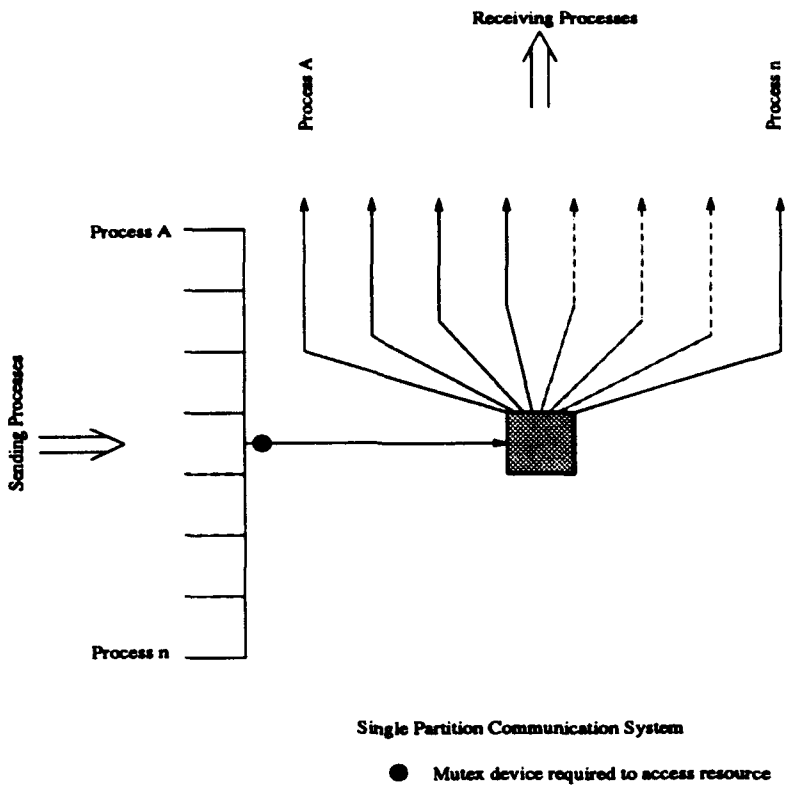

Figure 2: Single Partition, Decentralized Control Communication System

5.1 The single partition

This point in the design space requires each sender and receiver to contend for access to a single shared resource. In a decentralized approach, as shown in figure 2, each sender finds a spot to place messages in. Since all senders write in a common partition, a mutex device is required to guarantee senders do not interfere with each other. Receivers read information and do not contend with one another.

While requiring only one mutex device and little partitioning overhead, this approach serializes the action of sending messages. It also groups delivered messages in a single bin that receivers must search. This situation corresponds to an alternative postal service that would require every person who sends a letter to deposit it into one large (very large) bin, and each recipient would be responsible for searching the bin to find their own mail. The only costs are the overhead of a large bin (split between all participants), the time for each sender to wait in line to access the slot for the bin and the time for each recipient to search through the set of delivered messages. While the shared cost is low, the individual costs are high.

5.2 Sender Partitions

Another approach to solving the communication problem is to associate a partition with each sender as shown in figure 3.

A sender orientation removes the contention that was present in the single partition model as well as the need for a mutex device. Receivers must still search all message blocks to find those that have been delivered to their address. The difference for receivers is that they must search n partitions instead of 1.

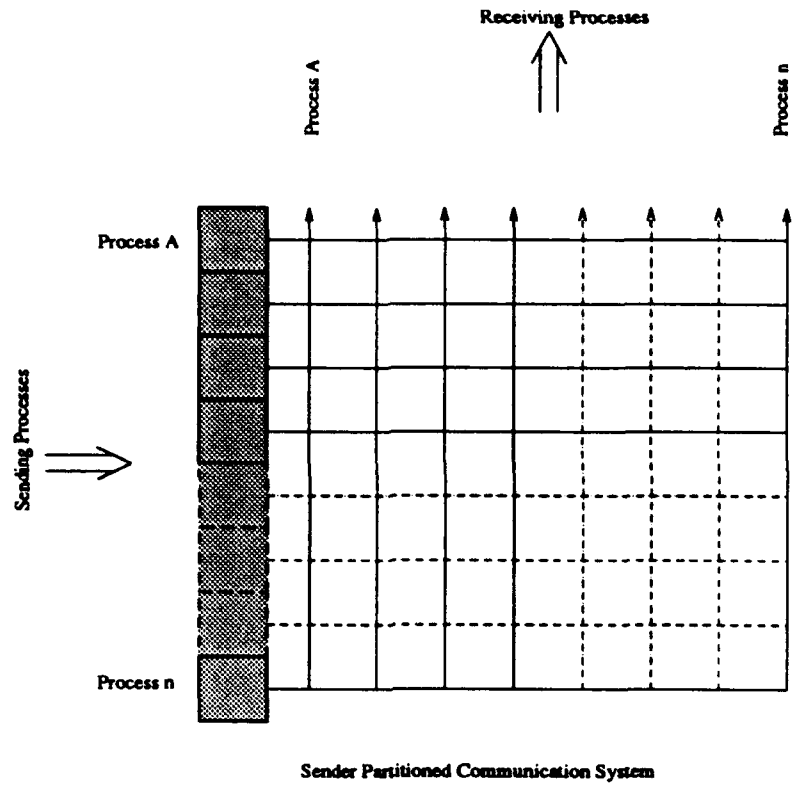

Figure 3: Sender Partitions, Decentralized Control Communication System

Extending the postal service analogy, each person who might send a letter would purchase a mail bin for their own use. Each recipient would have to search each of the bins independently to find their mail. In total, the senders fixed cost (cost of the bin) would be higher than the single bin solution, but then they would not have to wait in line to mail their letters. Recipients still have to search through all of the mail, with the exception of the slots that can be classified as irrelevant (such as a junk mail slot, or the slot associated with a friend who never writes).

This approach requires $O(n)$ partitioning overhead and no mutex devices. It allows senders to work in parallel, but has the drawback that receivers must search all messages. This style of partitioning may be appropriate for systems where messages are delivered relatively often so that receivers do not have to waste a lot of time looking for messages.

5.3 Receiver Partitions

A third point in the communication design paradigm is to associate a partition with each receiver. Figure 4 depicts how this design would look.

This approach requires that senders place messages directly in the appropriate receivers partition. Since multiple senders may try to send messages to the same destination, mutex devices are needed to ensure that only one sender accesses a receivers partition at any given time. While this approach serializes access to each partition, it allows many senders to work at the same time, provided they send messages to different destinations. Receivers need only look at one place to determine if a message has been delivered or not.

The postal analogy in this case requires each possible mail recipient to purchase a bin. When a person has the desire to mail a letter, he or she must find the recipients bin, wait in line until the slot is available, and then deposit mail into the bin. Recipients need only pull delivered mail out of

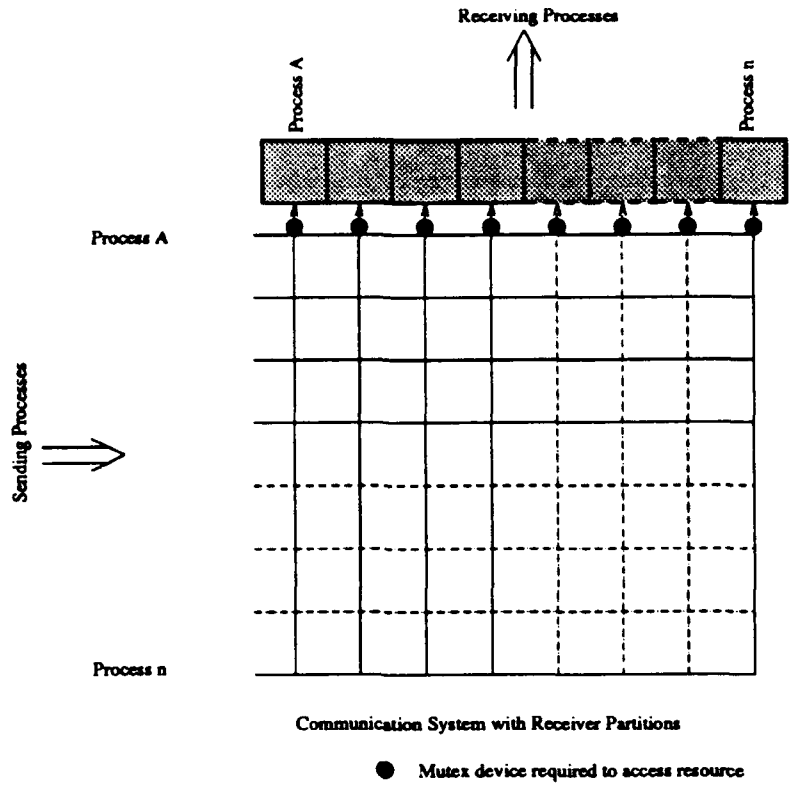

Figure 4: Receiver Partitions, Decentralized Control Communication System

their bin. While recipients must pay a price to have their own bin, they need not search everyones mail to find their own. On the other hand, individual senders may spend a lot of time delivering letters.

Like the previous approach (section 5.2), this strategy requires $O(n)$ partitioning overhead. However, it also requires $O(n)$ mutex devices. Receiver partitions may work well for low-turnaround systems. The overhead of message location can be minimized as receivers do not need to search multiple partitions. On the other hand, the cost of using a mutex device for each message delivered can be extensive.

5.4 Sender X Receiver Partitions

A fourth design requires one partition between each sender and receiver pair. Figure 5 depicts this approach.

The n^2 partition solution removes the problem of using mutex devices as shown in section 5.3. This approach also places each receivers set of messages in a known set of locations. The major drawback to this approach is that receivers must search a set of locations (a column in Figure 5) to find messages.

The postal analogy in this case requires that each sender and receiver pair purchase one bin. When people want to send mail, they determine where the mail should be placed (which bin) and then deposit it. There is never a line associated with any bin. Recipients need to look in n bins, but any messages they find are guaranteed to be addressed to themselves. This approach has a high fixed cost ($n/2$ bins per sender and $n/2$ bins per receiver) but avoids the need for senders to wait in line and for receivers to search mail addressed to other people.

The sender X receiver approach requires no mutex devices and $O(n^2)$ partitioning overhead.

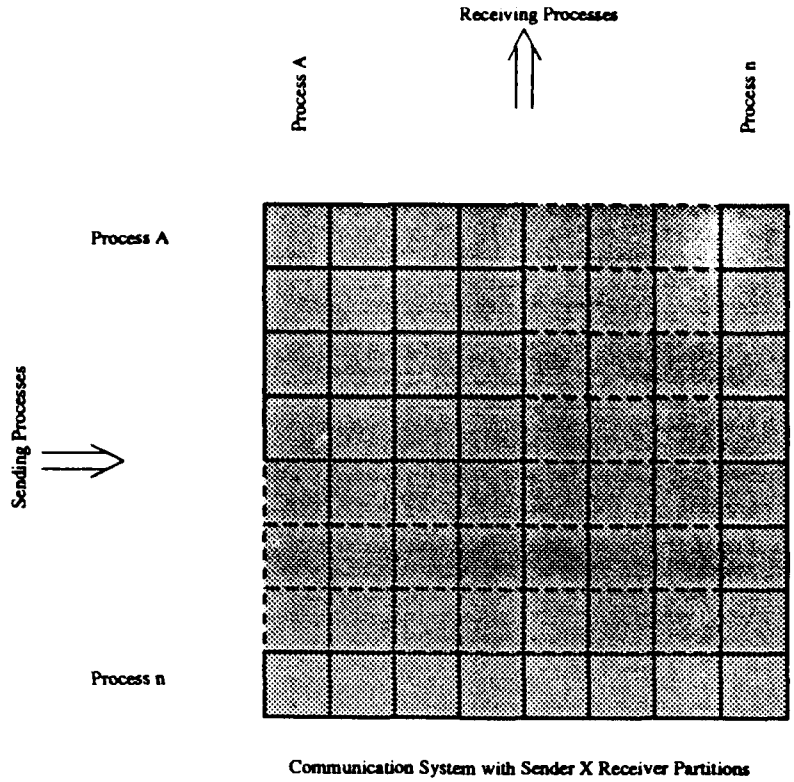

Figure 5: Sender X Receiver Partitions, Decentralized Control Communication System

While taking advantage of characteristics from both sender and receiver partitioning, this approach is not necessarily better than either of the sender or receiver partition approaches (depending upon the application).

5.5 Other approaches

Another approach would be to allow messages to be delivered in stages. This idea parallels the concepts of multistage networks [9, Chapter 5]. Partitions can be allocated to mimic the connections of a multistage network. Messages would travel through intermediate steps before arriving at their destinations. Figure 6 shows how the partitions might be set up for eight senders and receivers to mimic a multistage cube network. From any point in the cube, three points are reachable in one step, three points are reachable in two steps and a single point is reachable in three steps.

A centralized routing model could be used to remove contention among senders and provide a single access partition for each receiver. Such a model is shown in figure 7. The central router allows senders to avoid contention and run in parallel. This approach also provides a single partition for each receiver so that messages are easy to find. A major drawback of this approach is that a single threaded router will serialize the delivery of messages, even though senders work in parallel. The router must also continuously search the senders partitions (performing the decentralized location service on behalf of all receiving processes). One option is to create multiple threads in the router to transfer messages from sender partitions to receiver partitions. The drawback of this approach is that the multiple threads must then contend for access to the receiver partitions, thus losing the benefit gained by avoiding contention in the first place.

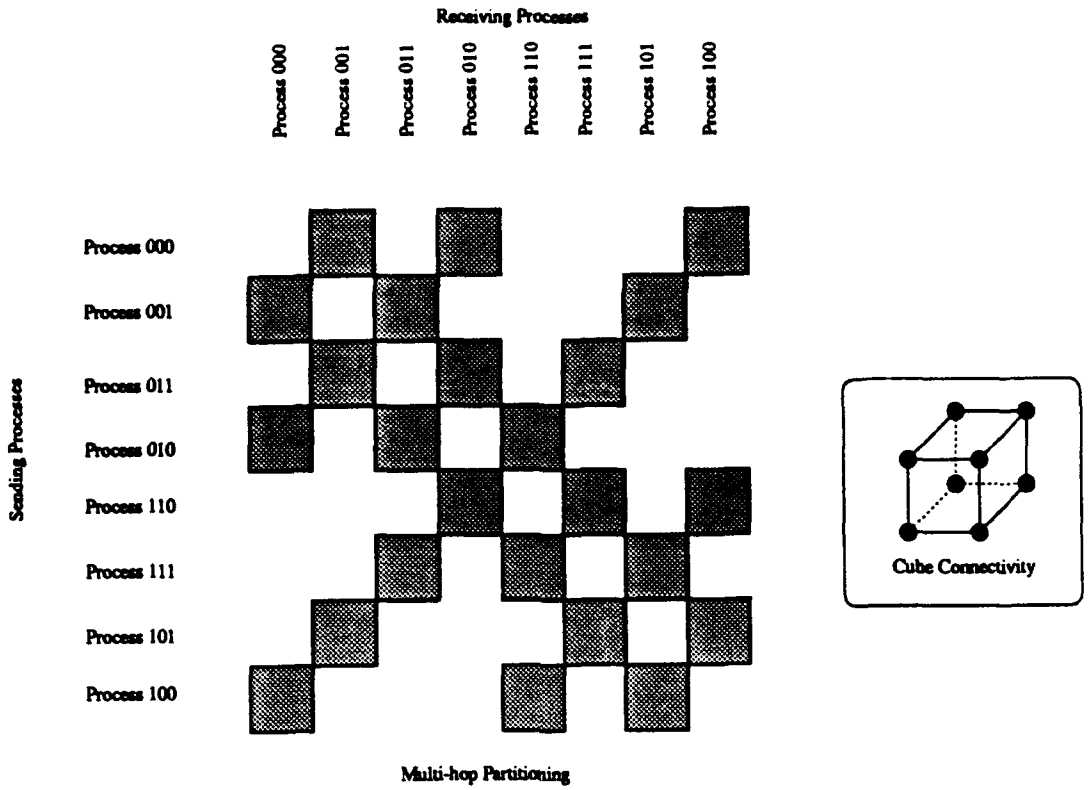

Figure 6: Multi Stage Partitioning, Decentralized Control Communication System

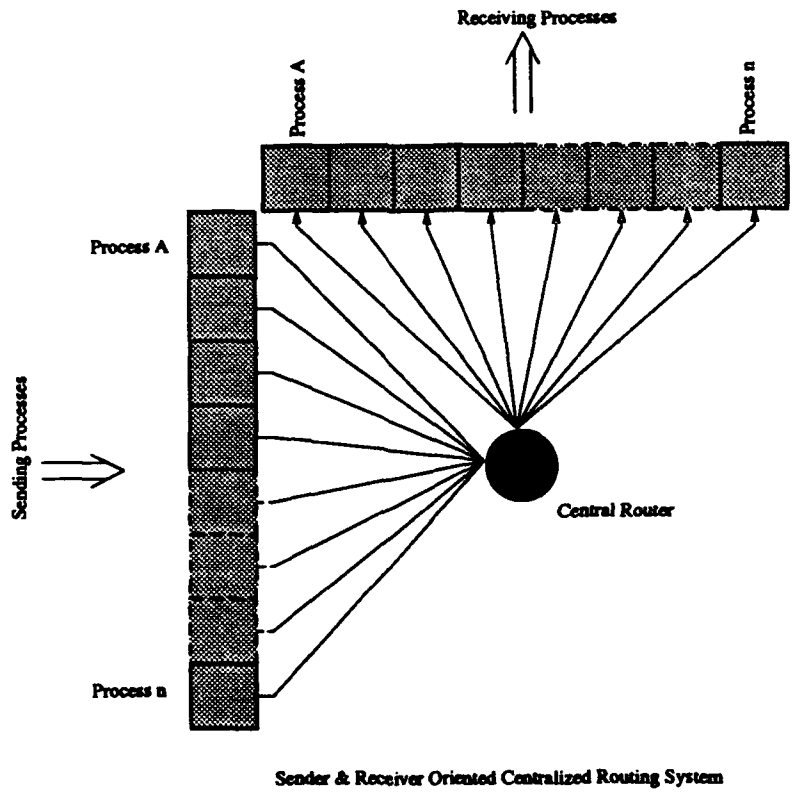

Figure 7: Sender & Receiver Partitions, Centralized Communication System

6 Underlying Memory Implementation Issues

Shared memory implementations can impact the design of a communication system. Until now, shared memory has been treated as a black box where underlying details are ignored. Distributed Shared Memory (DSM) systems such as SCRAMNet [1] do not guarantee consistency. Instead, users avoid non-consistent states (if undesired) with software and design techniques.

A mutual exclusion algorithm (for a semaphore) in SCRAMNet memory is expensive for larger sets of users (the details of this algorithm are not presented). For this reason, when designing a communication system using a similar type of distributed shared memory, designs that avoid mutual exclusion devices might be favored. The partitioning strategies shown in figures 3 and 5 would most likely be more effective than the strategies shown in figures 2 and 4 due to the excessive mutual exclusion overhead inherent in the SCRAMNet distributed shared memory design.

7 Classifications

This section describes some existing communication systems according to the factors mentioned in previous sections.

7.1 Current University of Cincinnati Communication System

A communication system has been developed at the University of Cincinnati [3] to support a distributed VHDL PDES simulator. The system enables communication between processes on a single machine through local shared memory, and processes on differing machines via SCRAMNet distributed memory (described in section 6) or Unix Sockets (via Ethernet). The design is shown in figure 8.

The environment consists of multiple workstations connected via Ethernet and SCRAMNet resources. All machines are accessible over Ethernet, and subsets of the machines are interconnected via SCRAMNet (Distributed Shared Memory).

Each process uses an interface that provides two unidirectional links between the user and the router. One link is for sending messages and the other for receiving messages. All communication (by all users on a machine) is handled by a single, centralized router.

The transfer of information between processes on the same machine is accomplished by a sender filling in a shared memory block and forwarding the message to the centralized router. The centralized router eventually finds the message and places it on the receivers input queue.

Communication to processes on other machines is established by either a SCRAMNet link or Ethernet link. If SCRAMNet is available, messages are routed from the local machine router to a process that moves the message into the distributed shared memory. From there the message is transferred by the distributed shared memory router to a process that can move the message into shared memory on the destination machine. Finally, the router on the destination machine delivers the message to the appropriate process.

[1] SCRAMNet [11] is a distributed set of memory boards (one per workstation). The boards are connected in a ring structure with fiber optic cables. The function of SCRAMNet is to emulate shared memory between physically distinct workstations. Upon writing to a SCRAMNet location from a workstation, a message is passed around the ring and the appropriate location on each memory board is updated to the new value. A memory location may not be consistent (across all SCRAMNet boards) if two or more workstations attempt to write different values to the same location simultaneously.

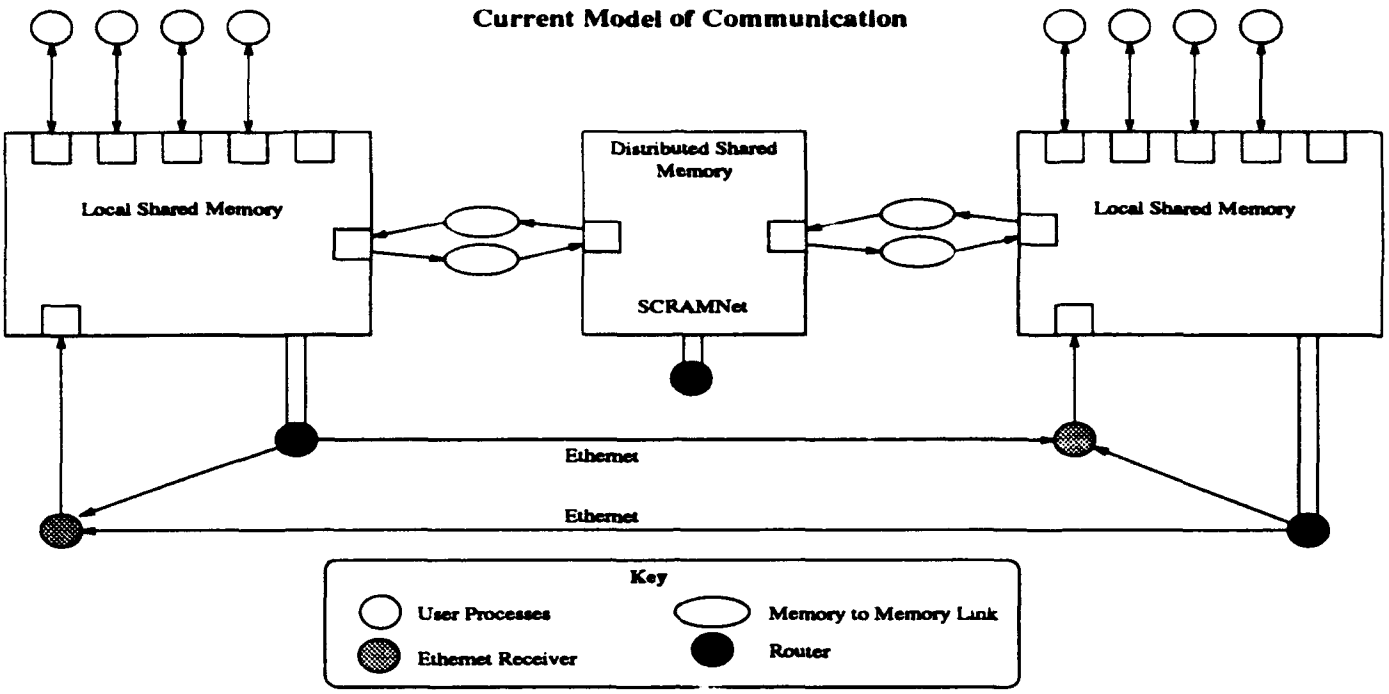

Figure 8: Centralized Routing Communication System

If SCRAMNet is not available, then messages are sent via Ethernet to a receiver process on the destination machine where they are placed in local shared memory for subsequent delivery by the destination machine router.

Each of the shared memory areas are managed by the centralized approach shown in figure 7 which is discussed in section 5.5.

The benefits of this approach are as follows:

- Use of Shared memory avoids the need to copy data.
- A one to one relationship between each sender and the router.
- A one to one relationship between the router and each receiver.
- Destructive contention is avoided.
- The partitioning and management policies apply to both physical mediums (local and distributed shared memory), requiring development of only one communication system.
- Each user of the system has dynamic bandwidth available. This is due to dynamic block management strategies employed in the design. Any block may be used as the router (centralized manager) finds appropriate.

We learned the following from the centralized routing system:

- The router serializes the delivery of messages, even though the senders can work in parallel.
- The central router does not know when blocks have been sent and must continuously scan for work.

- Messages pass through multiple interfaces. Locally, each message must pass through two interfaces (sender to router and router to receiver). In addition, messages pass through an additional interface if sent over Ethernet or an additional four interfaces if sent over the hierarchical oriented distributed shared memory.

- Dynamic block management is costly as the router must continuously update lists of blocks.

7.2 YACKOS

YACKOS [6] (Yet Another Communication Kernel Operating System) was developed by Finkel and Hensgen to provide high bandwidth, low latency communication. The design consists of users and a kernel. Each user of YACKOS gets an interface area that is in shared memory. An interface is comprised of two message buffer pools (circular queues), one for incoming messages and one for outgoing messages. Message buffers come in two sizes: large (1024 bytes) or small (32 bytes).

The interface also contains access methods for sending and receiving messages. Upon sending a large message, the kernel removes an empty message buffer from the receivers input queue (of large size), removes the senders message block from its outgoing queue and exchanges the message buffers by placing them on the appropriate queues. Small messages are copied to avoid the overhead of swapping pointers. This strategy maintains a balance between the amount of space allocated to each user. Contention is avoided as a result of the one to one relationship between each sender/kernel, and kernel/receiver.

YACKOS also takes advantage of a hint queue that allows the kernel to find sent messages quickly.

The centralized system shown in figure 7 is the appropriate characterization of the partitioning scheme used in YACKOS. The set of outgoing queues for each user represent the partitions associated with senders. The kernel represents the centralized entity that transfers messages from senders to receivers. The set of incoming queues for each user represent the partitions associated with receivers. The allocation strategy is a combination of static and dynamic algorithms. The bandwidth allocated to each partition remains constant via the swapping of large message blocks and copying of small message blocks. However, large message blocks can dynamically move around the system. Delivery is serialized as the router is single threaded. Location does not require much overhead, as receivable messages are accessible through a single queue. Finally, reclamation is handled inherently by the allocation and delivery strategies.

7.3 LRPC & URPC

User-Level Remote Procedure Call (URPC) and Lightweight Remote Procedure Call (LRPC) [1, 2] are systems designed by Bershad to improve the efficiency of Remote Procedure Calls (RPC). Scheduling and communication are considered as a complementary pair of factors where the existence of a communication can be considered as a trigger for scheduling action.

The designs use pair-wise shared memory. Each server registers its methods that are available to be called with a clerk. Each method has the following information associated with it: an entry address (method identifier), number of simultaneous calls initially permitted by a client, and the size of the argument stack (A-stack) where arguments and return values are placed. When a client binds to a servers interface (set of methods), a set of A-stacks are allocated for each method (the number of A-stacks is equal to the number of simultaneous calls permitted). These A-stacks are placed in a shared memory area.

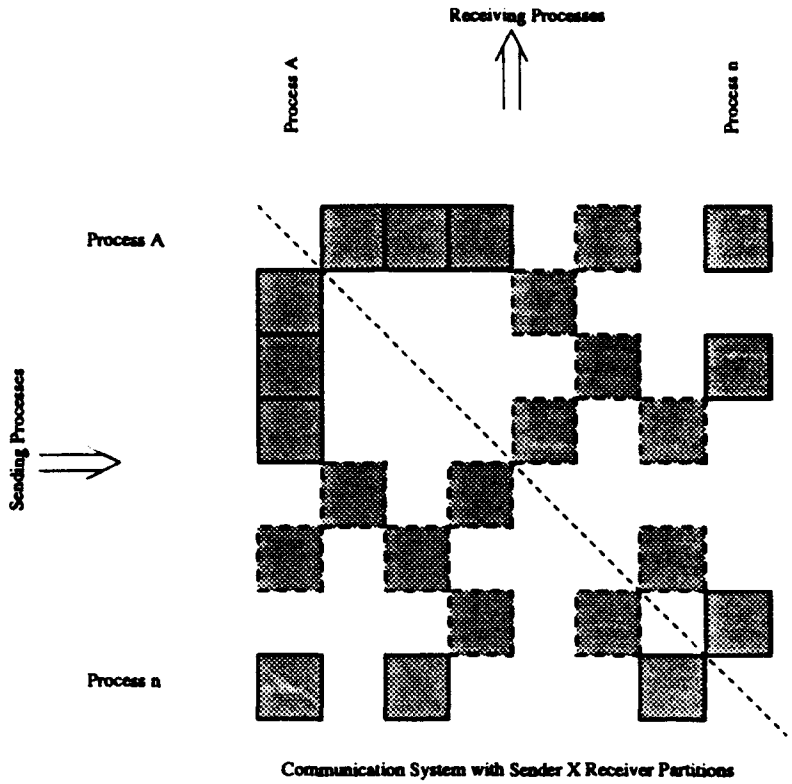

Figure 9: Sender X Receiver Partitions, Decentralized Control Communication System

Once a set of A-stacks is set up in shared memory, a client can fill in an A-stack, and a server can immediately begin processing the RPC. Further details about the exchange can be found in [2].

Figure 9 shows the partitioning strategy used in URPC and LRPC. The design is similar to the Sender X Receiver design (figure 5) except selected partitions are established and others are ignored. The partitions are symmetrically arranged about the dashed line representing RPC semantics: if a client (sender of requests) communicates with a server (receiver of requests), then the server (sender of results) is expected to return results to the client (receiver of results). Each symmetrically oriented pair of partitions resides in its own shared memory space [2] (as opposed to a subdivided monospace for all pairs). A benefit of creating separate shared areas is that only the appropriate sender and receiver can access them. A drawback is the overhead associated with creation of the shared areas.

Since clients and servers may be multithreaded, contention for A-stacks within a partition may exist. Test-and-set locks are used to ensure that contention is handled appropriately.

Allocation in Bershad's approach is static in that each A-frame (the equivalent of a message block) has a set size. Delivery is automatic as A-frames move between the individual segments of each partition pair (arguments from client to server and results from server to client).

Polling is analogous to the location overhead of finding messages. Bershad states that "URPC can scale to include large numbers of clients and servers before the overhead of polling message channels causes URPC's performance to degrade to that of a conventional, kernel based approach." While polling can be overwhelming for even small numbers of users in typical systems, URPC impacts the scheduling system, resulting in a more efficient selection of processes to run (avoiding excessive polling).

Finally, reclamation is handled automatically in URPC and LRPC by servers returning results

[2]Due to the Firefly operating system, which does not support pair-wise shared memory, Bershad's implementation actually resides in a globally shared virtual memory.

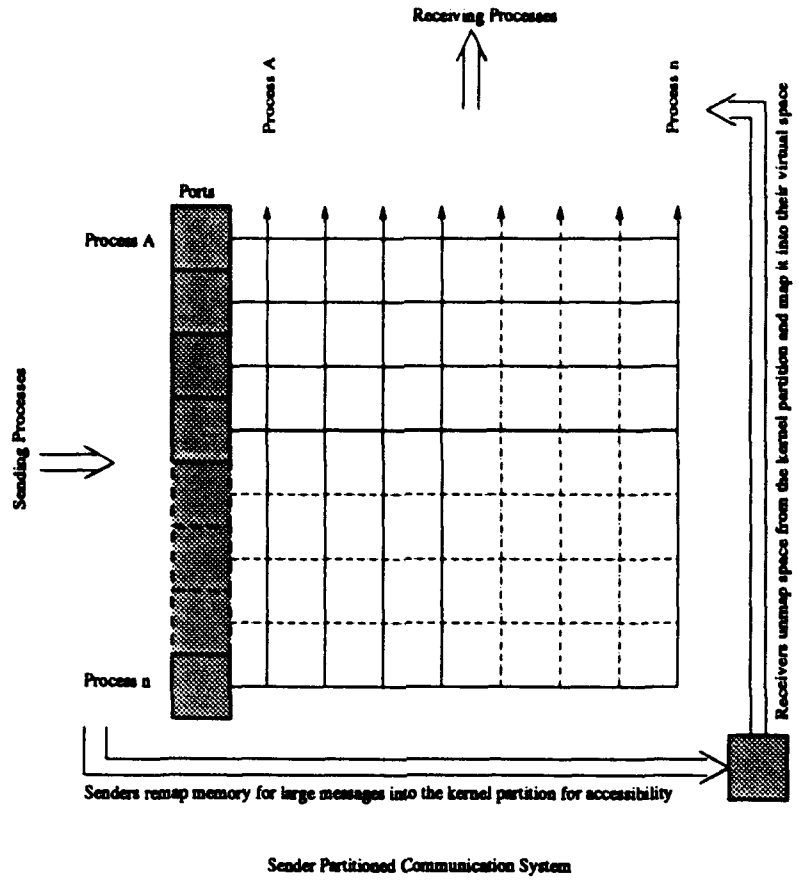

Figure 10: Accent Partitioning, Decentralized Control Communication System

to clients using the same A-frame that the original arguments were passed in.

8 Accent

Accent [7] is a communication-oriented operating system kernel that uses memory remapping techniques for large interprocess data transfers and messages for small interprocess data transfers (such as pointers).

A port is a kernel protected queue for messages. Each port has three port capabilities associated with it: send access, receive access, and ownership. A port is created by the kernel for each process. The state of a process and its virtual memory can be manipulated by sending messages to the port.

The kernel primitive *MoveWords* maps a contiguous area, existing in the virtual address space of a source process, to the virtual address space of a destination process. The area can be unmapped from the source address space, or left intact. If the area is left intact (shared by both the source and destination processes), then the pages are marked as *copy on write*. The result of this action is that, even though the memory exists in only one physical location, both processes appear to have their own copy of the data.

MoveWords is used to remap messages from a sender process to the kernel process when sending, and to remap messages from the kernel process to a receiving process when receiving (memory is unmapped from the kernel process during the receive process).

This approach allows any segment of memory to be shared by all pairs of senders and receivers (as long as the appropriate capabilities have been established). The partitioning strategy as it

relates to the work presented in this paper is shown in figure 10. Each sender has a port associated with it that the kernel and receivers can access. For this reason, the partitioning is similar to the sender partitions shown in figure 3.

Contention in Accent is not easily identifiable from the information presented in [7]. Accent is designed for uniprocessor systems, and so only one point of control can be active at any time. This design inherently avoids most contention. However, it is not clear whether users can be stalled in the middle of a critical section or not. Contention is avoided when accessing ports because each sender has their own port. However, when large messages are remapped into the kernel space, there exists the potential for contention as multiple users may attempt to remap portions of the kernel space simultaneously.

Allocation is done statically. Each port is given a fixed amount of space (it is possible to change the size of the space). Small messages and pointers to large messages are placed in messages blocks within a port. Large messages do not require message block allocation because memory is allocated in a processes virtual address space. The allocation and reallocation strategies for message blocks within a port are not addressed here.

Delivery overhead for small messages does not exist. Delivery overhead for large messages requires each message to be mapped into the kernels address space when sent and mapped from the kernels address space into the receivers address space when received. While paralleling the ideas of a centralized system (requiring messages to interact with a central entity), the remapping scheme is decentralized and does not result in serial message delivery. The remapping strategy provides the idea of copying data but avoids the copying overhead in reality by accessing physical pages from multiple virtual address spaces. If any process attempts to write to a shared page marked as *copy on write*, then the underlying system will create a copy for that process.

Location overhead could be extensive. If receivers continually poll many ports, then much time could be wasted. If indications are given to receivers when messages are sent (thus allowing receivers to avoid searching), then the model shown in figure 10 is incorrect. A set of receiver partitions would need to be added in this case.

9 A Recommendation for VHDL PDES

The theory of designing a shared memory communication system, while addressed in this paper, has not been fully developed. We will consider a design alternative for the University of Cincinnati VHDL PDES Communication system in this section, but this alternative is based solely on our experience to date. There is much work to be done in the scientific exploration of shared memory communication before we will be able to determine the best design approach for a given application.

The communication bandwidth requirements and connectivity vary from simulation to simulation with VHDL designs. For this reason, selecting a communication system for a VHDL PDES simulator is very complicated.

Based on the experience from our first design (figure 7) a decentralized control system will most likely provide an improvement in efficiency. The reasons for this are that messages can be delivered immediately and in parallel by senders instead of being serially managed by the central router. The designs shown in figures 3, 4 and 5 all allow senders to work in parallel to some extent.

Each sender in a VHDL PDES simulation is associated with a limited set of receivers. The idea that PDES communication paths are known at compile time supports the idea of using a static block allocation strategy. This would save on allocation overhead.

Figure 11 shows a slightly modified version of the Sender X Receiver partitioning strategy shown in figure 5. $O(n^2)$ partitions exist in this scheme, however some of the partitions are empty (those

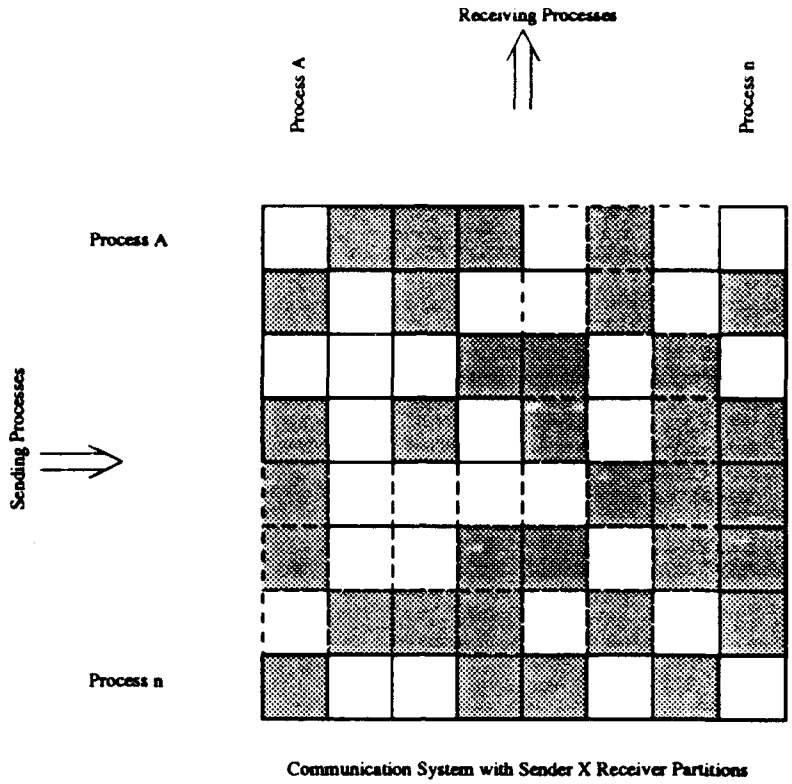

Figure 11: Sender X Receiver Partitions, Decentralized Control Communication System

that have no shading). Such a design may be appropriate for the PDES communication system at UC. Each sender could be given a statically defined set of message blocks. The sender could then further partition the blocks according to its relationships with receivers. This approach can handle many different types of discrete event simulations as each sender can determine how to allocate its set of message blocks. A drawback to this approach is that receivers must search multiple partitions to find messages.

A communication system alternative using the empty partitioning mentioned above is shown in figure 12. In contrast to the centralized system (figure 7), no central routing process exists. Instead, a routing table (not shown) would be stored in shared memory so that each process could perform the delivery function.

To avoid contention for Ethernet resources, a single Ethernet Router can be placed on each machine (processes labeled with an R) and messages that must travel over Ethernet are sent to the Ethernet router.

The distributed shared memory is also directly accessible by each user process. Messages can be pulled out of the appropriate partitions at any time. Messages can also be sent to remote processes directly through the distributed shared memory. Mutex devices are shown to emphasize that explicit mutual exclusion is used in this particular design. In order to keep the number of distributed shared memory users low , each machine is considered as a single user. The mutex oval represents an array of mutex's, one for each column. Senders that wish to access a common partition must first gain access to the appropriate mutex. Since senders on different machines do not conflict (senders on a workstation only compete for partitions in a common row), the mutex devices can be placed on the local workstations. This design avoids use of the costly distributed shared memory mutex devices.

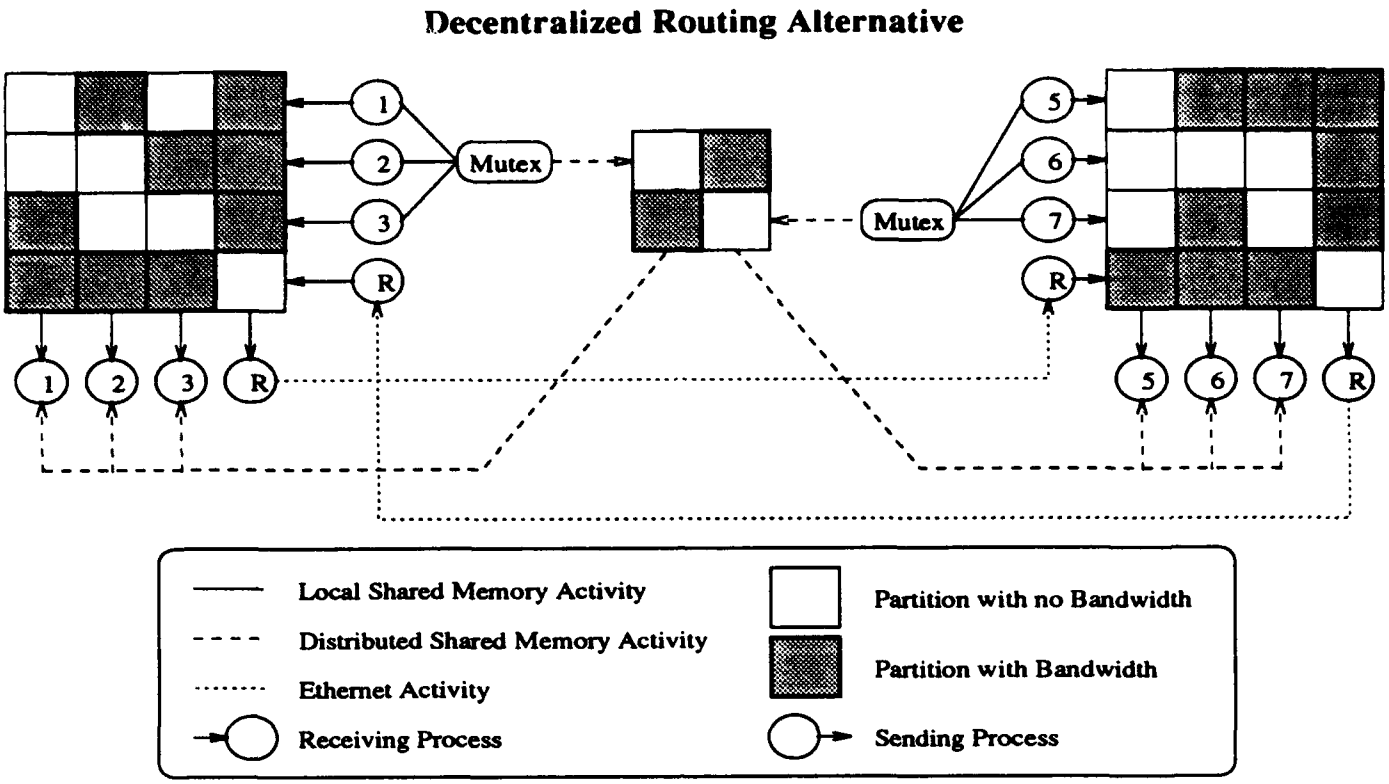

Figure 12: Decentralized Routing Communication System

10 Summary & Future Work

The components of a generic shared memory communication system and indicators of how such a system might perform were identified. The existing University of Cincinnati communication system was analyzed from the characterizations. The benefits and drawbacks of the centralized approach were discussed. A second generation communication system alternative was presented based on the research conducted this summer.

The key contribution of this work is that a generic classification scheme for shared memory communication systems has been identified. The ability to analyze communication systems from a generic viewpoint allows designers to choose better alternatives. While the classification mechanism has not been developed to the point of solving the world's communication design problems, it has been used to reason about why one communication system might be better than another.

The scientific exploration of shared memory communication needs to be continued to further develop the classification scheme and eventually establish a design methodology. Such a methodology will provide input to the design phases of new computer systems and software development.

References

[1] Brian N. Bershad, T. E. Anderson, E. D. Lazowska, and H. M. Levy *"User-Level Interprocess Communication for Shared Memory Multiprocessors"*, ACM Transactions on Computer Systems, Vol. 9 No. 2, May 1991, Pages 175-198.

[2] Brian N. Bershad *"High Performance Cross-Address Space Communication"*, Dissertation, University of Washington, Technical Report 90-06-02, June 1990.

[3] D. Charley, T. McBrayer, D. Hensgen, P. Wilsey and M. Ankola, *"Distributed Simulation on a Reconfigurable Network using Non-Uniform Message Passing"*, Proceedings of the ISMM International Conference on Parallel and Distributed Computing, Pittsburgh, PA., October 1992.

[4] J. S. Chase, H. M. Levy, M. J. Feeley, and E. D. Lazowska, *Sharing and Protection in a Single Address Space Operating System*, Department of Computer Science and Engineering, FR-35, University of Washington, Technical Report 93-04-02

[5] R. A. Finkel, An Operating Systems Vade Mecum, Copyright 1986, Prentice Hall, Englewood Cliffs, New Jersey 07632

[6] R. Finkel and D. Hensgen, *"YACKOS on a shared memory multiprocessor"*, Special Issue of Computer Architecture News on Architectural Support for Operating Systems, Vol. 16, No. 4, September 1988.

[7] Robert Fitzgerald and Richard F. Rashid, *"The Integration of Virtual Memory Management and Interprocess Communication in Accent"*, ACM Transactions on Computer Systems, Vol. 4, No. 2, May 1986, pages 147-177.

[8] R. M. Fujimoto, *"Parallel Discrete Event Simulation"*, Communications of the ACM, Vol. 30, No. 10, October 1990.

[9] Ki Hwang and Faye A. Briggs Computer Architecture and Parallel Processing, Copyright 1984, McGraw-Hill Publishing Company, New York, New York, ISBN 0-07-031556-6.

[10] Lauer, H.C. and Needham, R.M., *"On the Duality of Operating System Structures"* in Proc. Second International Symposium on Operating Systems, IRIA, Oct. 1978, reprinted in Operating Systems Review, 13,2 April 1979, pp.3-19.

[11] *SCRAMNet(tm) Network Reference manual for VME-BUS Hardware Interface Node*, Document No. A-T-MR-VME#####-A-O-C1, SYSTRAN Corporation, 1989.

AN ITERATIVE METHOD FOR COMPUTING THE SCATTERED ELECTRIC FIELDS AT THE APERTURES OF LARGE PERFECTLY CONDUCTING CAVITIES

Daniel D Reuster

Department of Electrical Engineering

University of Dayton

300 College Park

Dayton, OH 45469-0227

Final Report for:

AFOSR Summer Research Program

Wright-Paterson Air Force Base

Sponsored by:

Air Force Office of Scientific Research

Wright-Paterson Air Force Base, Dayton, OH

August 1993

AN ITERATIVE METHOD FOR COMPUTING THE SCATTERED ELECTRIC FIELDS AT THE APERTURES OF LARGE PERFECTLY CONDUCTING CAVITIES

Daniel D Reuster
Department of Electrical Engineering
University of Dayton

Abstract

An iterative method is developed for computing the scattered electric fields at the apertures of large perfectly conducting cavities. The technique uses Kirckhoff's approximation to initiate a two stage iterative process, involving both the magnetic field integral equation (MFIE) and the electric field integral equation (EFIE), to calculate the electric currents on the internal cavity walls and the electric fields across the aperture of the cavity. The technique combines the flexibility of the boundary-integral method with the speed necessary to efficiently analyze large scale cavity problems. The following paper presents the general theory, and applies the technique to the problem of TE scattering from 2-dimensional perfectly conducting cavities.

1 Introduction

The problem of electromagnetic scattering from large open-ended cavities (see figure 1) has received much attention in research areas such as automatic target recognition and low-observable vehicle design. The cavity problem presents many interesting challenges from the standpoint of computational electromagnetics. The cavity's large electrical size makes it a prime candidate for ray based or asymptotic techniques, while the cavity's geometrical complexities require more exact techniques such as the method of moments or the boundary integral approach. As a result of these diverse requirements, many hybrid techniques have been developed, in an effort to meet these computational challenges. Techniques, such as shooting and bouncing rays (SBR) [1] and the generalized ray expansion (GRE) [2], were created in an effort to enhance asymptotic based methods in order to analyze the complex geometries associated with the cavity problem. Likewise, approaches such as the hybrid boundary-integral/modal method [3] were developed in hopes of increasing the electrical size limitations of moment method based techniques. While both of these approaches to the cavity problem show promise in the small to mid-size cavity range, their ability to effectively analyze large scale cavity problems is still a matter of debate, and the need for new approaches is evident.

The cavity problem, such as the electromagnetic scattering from a jet engine, may be visualized as consisting of three unique phenomenon: 1) an aperture field is established from the external region sources; 2) the electric and magnetic fields propagate down the cavity, "guided" by the cavity walls; 3) a reflection occurs at the termination. After reflection, the fields propagate back towards the aperture where they maybe integrated to give the scattered field (i.e., the RCS). The purpose of this short paper is to propose an efficient and accurate way of propagating the field from the aperture to the termination (i.e., item 2 above) and back to the aperture. In the examples that follow, the termination will be approximated as a short circuit. In an actual engine, the termination is very complex and must be accounted for by other methods such as the finite element method. In this paper we bypass the termination problem by employing the simplest of all possible terminations, the short circuit, since our objective here is to focus on the duct propagation problem.

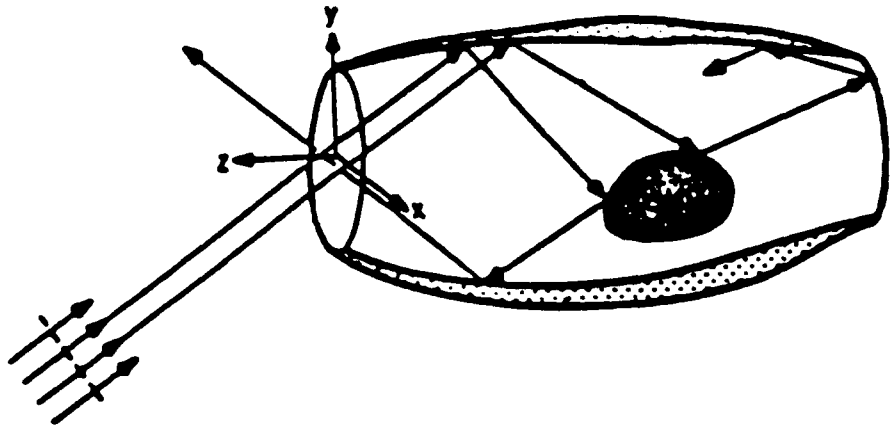

Figure 1 Common Cavity Scattering Problem

2 Methodology

In the theory which follows, the equivalence principle is used to divide the cavity problem into an internal scattering problem and an external scattering problem. Because of the cavity's assumed large electrical size, the electromagnetic coupling between the internal and external problems is assumed negligible. While this approximation breaks down when the cavity size is small compared to the wavelength of interest, the approximation provides valid results for cavities of large electrical size. Since the external scattering problem's geometry is usually much less complex than the internal scattering problem, it will be assumed that standard asymptotic analysis may be applied directly to the external problem; and thus, analysis of the external problem will not be considered in the following discussion. The internal scattering problem, which normally requires a much more rigorous solution is solved using the newly developed iterative method. The scattered fields from the internal and external scattering problems may then be combined to produce the total field scattered by the cavity. For comparison purposes, the calculated scattered electric fields at the aperture of the cavity are integrated to produce a prediction of the radar cross section (RCS) for the cavity. The RCS prediction is only approximate in the sense that the external scattering from the cavity is not included; however, the RCS prediction is expected to produce accurate results in those regions where the internal scattering phenomenon is dominate.

The iterative technique presented in this paper, for the internal propagation problem, is an extension of the previous work [4-8] performed on the external scattering problem. In [4], Kim and Thiele developed a hybrid asymptotic-moment method technique to find the induced currents on the surface of scatters in the intermediate frequency region. Kaye, Murthy, and Thiele [6] significantly improved on that work by eliminating the moment method regions, thereby making the method potentially applicable to large scatters as well as ones of modest size. In the work of Kaye, Murthy, and Thiele, the magnetic field integral equation was reduced to a sequence of integral equations for both the "optics" currents and the "correction" currents, each of which is solved by iteration. On the other hand, in Kim and Thiele [4] the "correction" currents were solved by the moment method. In Murthy, Hill, and Thiele [7], the purely iterative technique formulated in [6] was further improved by reducing the amount of computation required. Later, the iterative approach was applied to a 3-dimensional object, the cube [8].

3a Formulation of the Internal Scattering Problem

Consider the perfectly conducting cavity shown in figure 2a. The cavity scattering problem may be separated into an internal scattering and an external scattering problem by sealing the aperture of the cavity with a perfectly conducting plate and impressing a magnetic current, equivalent to the total electric field at the aperture, on both sides of the plate (see figure 2b) [10]. Then, by assuming that the electromagnetic coupling between the internal and external scattering problems is negligible, the internal scattering and external scattering problems may be solved independently. Since the internal scattering problem now consists solely of calculating the electric and magnetic fields on a simple closed surface, the MFIE can be applied directly to the problem. The MFIE for a simple closed surface is given as [9]:

$$\overline{H}_{total}(r) = \frac{1}{4\pi}\oint_s \overline{J}(r') \times \nabla' G(r,r')\, ds' \tag{1}$$

$$- \frac{j\omega\epsilon}{4\pi}\oint_s \overline{M}(r')\, G(r,r')\, ds' - \frac{j}{4\pi\omega\epsilon}\nabla\,\nabla\cdot\oint_s \overline{M}(r')\, G(r,r')\, ds'$$

where $\overline{J} = \hat{n} \times \overline{H}_{total}$

and $\overline{M} = (\overline{E}_{inc} + \overline{E}_{scat}) \times \hat{n} = \overline{E}_{total} \times \hat{n}$ along the closed cavity surface S.

Since $\overline{M}$ equals zero along the perfectly conducting walls of the cavity, equation (1) is rewritten as:

$$\overline{H}_{total}(r) = \frac{1}{4\pi}\int_{s_1+s_2} \overline{J}(r') \times \nabla' G(r,r')\, ds' \tag{2}$$

$$- \frac{j\omega\epsilon}{4\pi}\int_{s_1} \overline{M}(r')\, G(r,r')\, ds' - \frac{j}{4\pi\omega\epsilon}\nabla\,\nabla\cdot\int_{s_1} \overline{M}(r')\, G(r,r')\, ds'$$

where $S_1 + S_2 = S$ (see figure 2c).

By use of image theory, equation (2) may be further simplified to its final working form given by equation (3) (see figure 2d).

$$\overline{H}_{total}(r) = \frac{1}{4\pi}\int_{s_2} \overline{J}(r') \times G(r,r')\, ds' \tag{3}$$

$$- \frac{j\omega\epsilon}{4\pi}\int_{s_1} 2\overline{M}(r')\, G(r,r')\, ds' - \frac{j}{4\pi\omega\epsilon}\nabla\,\nabla\cdot\int_{s_1} 2\overline{M}(r')\, G(r,r')\, ds'$$

Likewise, the EFIE for the cavity problem may be stated as:

$$\overline{E}_{scat}(r) = -j\frac{\eta}{\beta}\left[\beta^2\int_{s_2} \overline{J}(r')\, G(r,r')\, ds' + \nabla\int_{s_2} \nabla'\cdot\overline{J}(r')\, G(r,r')\, ds'\right]. \tag{4}$$

Equations (3) and (4), along with the knowledge of the incident electric field at the aperture of the cavity, provides a complete description of the electric and magnetic fields inside the perfectly conducting cavity.

3b Computer Implementation

Equations (3) and (4) may be implemented numerically on a digital computer by approximating the integral operators by matrix operators. Using a pulse-basis, point-matching

approximation technique, equations (3) and (4) may be approximated by the following matrix equations

$$\begin{bmatrix} H_t \end{bmatrix} = \begin{bmatrix} U \end{bmatrix} \begin{bmatrix} H_t \end{bmatrix} + \begin{bmatrix} V \end{bmatrix} \begin{bmatrix} E_t \end{bmatrix} \tag{5}$$

$$\begin{bmatrix} E_s \end{bmatrix} = \begin{bmatrix} W \end{bmatrix} \begin{bmatrix} H_t \end{bmatrix} \tag{6}$$

$$\begin{bmatrix} E_t \end{bmatrix} = \begin{bmatrix} E_i \end{bmatrix} + \begin{bmatrix} E_s \end{bmatrix} \tag{7}$$

where the matrices U, V and W represent the corresponding integral operators and the lengths of the vectors E_{total} and H_{total} depend on the electrical size of the surfaces S_1 and S_2 respectively. Due to the basis functions selected, the elements of each matrix may be calculated in closed form. For the 2-dimensional TE case, the matrix elements are as follows, a similar set of equations may be developed for the TM case.

$$u_{m,n} = \frac{-j\beta\Delta_n}{4} H_1^{(2)}(\beta r) \frac{(x_m - x_n) Nx_n + (y_m - y_n) Ny_n}{r} \tag{8}$$

$$v_{m,n} = \frac{-\beta\Delta_n}{2\eta} H_0^{(2)}(\beta r) \tag{9}$$

$$w_{m,n} = \frac{-\beta\eta\Delta_n}{8}\left[Nx_n H_0^{(2)}(\beta r) + H_2^{(2)}(\beta r)\left(\frac{2(y_m-y_n)^2}{r_{m,n}^2} - 1\right)\right.$$

$$\left. -Ny_n H_2^{(2)}(\beta r)\frac{2(x_m-x_n)(y_m-y_n)}{r_{m,n}^2}\right] \tag{10}$$

where Δ_n is the length of the nth facet

$$r_{m,n} = \sqrt{(x_m-x_n)^2 + (y_m-y_n)^2}$$

and Nx_n, Ny_n are the components of the inward pointing normal of the nth facet.

Equations (8) through (10) can be combined to produce one matrix equation expressing the total field at the cavity aperture in terms of the incident electric field. In theory, this equation may be solved directly by matrix inversion; however, for electrically large cavities, the matrix requiring inversion would consist of several hundred thousand elements making practical matrix inversion all but impossible. Thus, an iterative solution to equations (8) through (10) is implemented as a practical, high speed, method of obtaining a solution.

3c The Iteration Procedure

The iteration process is initiated by assuming that the total electric field at the aperture is equal to the electric field incident upon the aperture. Substituting this approximation into equation (5) provides the initial magnetic field along the cavity walls, S_2. The initial magnetic field along S_2 is then substituted into equation (6) to obtain the scattered electric field at the

mouth of the aperture of the cavity, S_1. Next, the scattered electric field is added to the incident electric field to obtain an updated version of the total electric field along S_2. The updated version of the total electric field is then substituted back into equation (5) and the above process is repeated to produce a further updated version of total electric field along S_1. This process is repeated until the mean square difference in the field quantities between each iteration reaches an acceptable level. The iteration procedure is found to converge quite rapidly (10 to 20 iterations), even for extremely approximate initial estimates of the total electric and magnetic fields. Furthermore, since the iterative procedure consists solely of vector inner products, the iterative solution process is directly applicable to high speed vector processes computer systems.

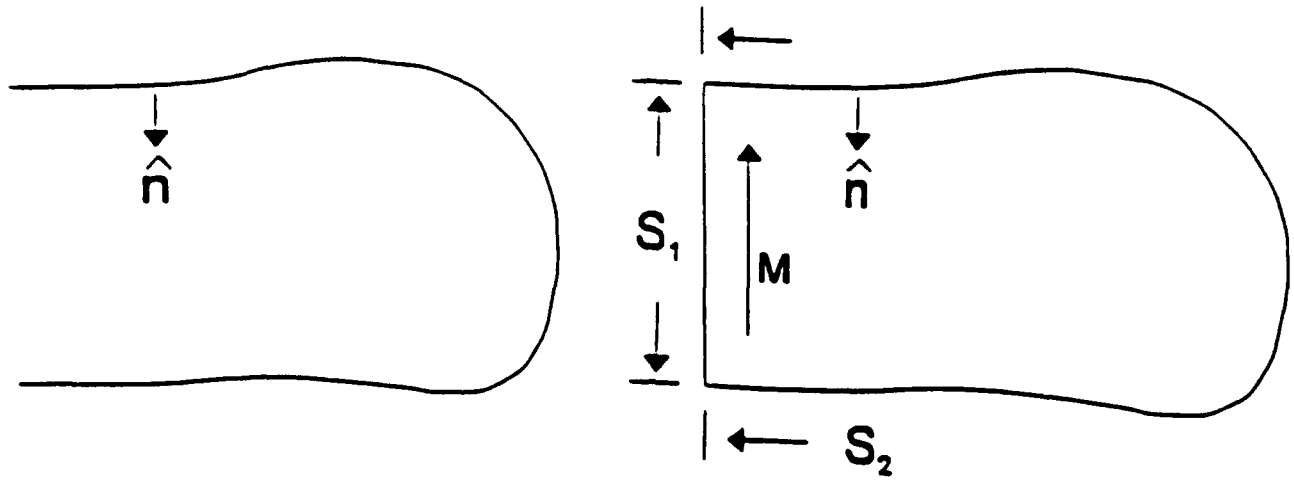

(a) Cavity Contour

(b) Internal Cavity Problem

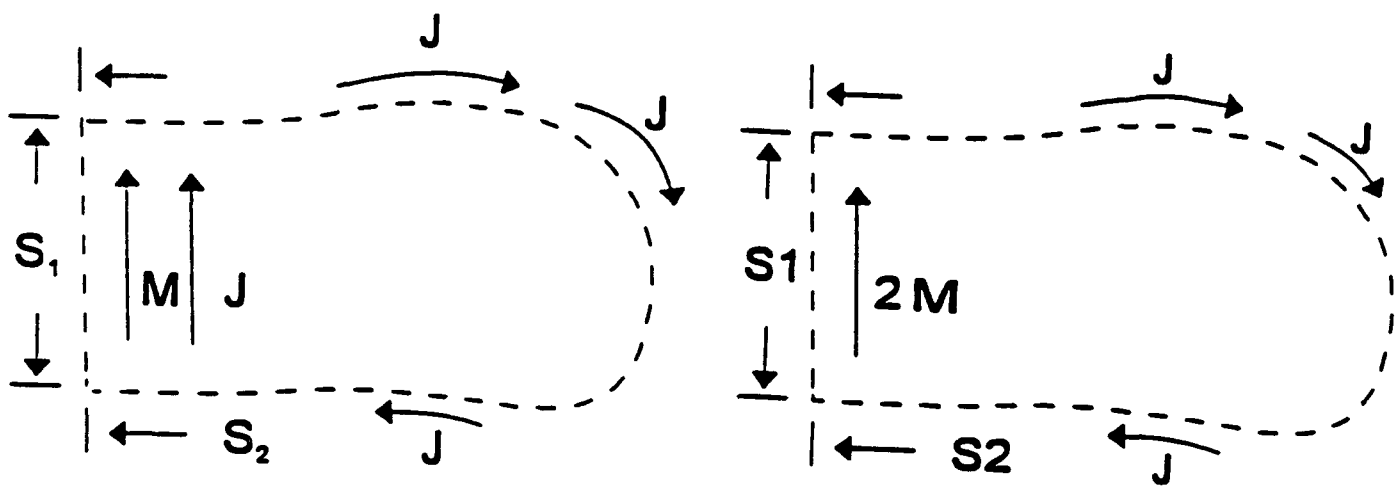

(c) Equivalent Current Model

(d) Image Theory Model

Figure 2 Cavity Models

4 Results

The iterative technique was used to calculate the scattered electric fields at the apertures of various rectangular cavities, and the aperture fields were integrated to produces RCS predictions for the cavities. These RCS predictions were compared with those produced by other techniques (see figures 3a-c). Since the external scattering from the cavities were not included in the iterative RCS predictions, the predictions obtained were expected to give good agreement in only those regions where the internal scattering problem is dominant. As can be seen from figures 3a-c, the RCS levels predicted by the iterative technique are in very good agreement with the RCS levels predicted by other methods in those regions where the internal scattering problem is dominant (approximately 0 to 30 degrees for the graphs presented). These regions being the main beams of the aperture's radiation pattern. The iterative RCS predictions for those regions outside the main beams of the aperture's radiation pattern tend to drop off quite rapidly which is a promising sign since for these regions the external scattering problem is expected to be dominant.

As a further check on the performance of the iterative code, a 2-dimensional TE Finite-Difference, Time-Domain (FDTD) code was developed to compute the total electric fields about the test cavities. Figure 4a shows the total electric fields about a 6λ by 6λ, 2-dimensional rectangular cavity. As can be seen from figure 4a all known wave propagation phenomena are present in the FDTD calculation including the diffracted waves from the edges of the cavity, the traveling waves along the sides of the cavity, and the modal propagation inside the cavity. Because of the completeness of the FDTD solution, the total electric fields calculated by the FDTD code were treated as the exact solution and used as a reference for comparison with the iterative code. Figure 4b shows a comparison between the aperture fields calculated by the FDTD code and the iterative code. Although the two curves are not identical, they both have the same behavior and their differences are attributed to the initial approximation that the electromagnetic coupling between the internal scattering and external scattering problem is negligible. Thus, based on the above results, it was concluded that the iterative technique does an effective job of accurately calculating the total electric fields at the aperture of the cavity. It also should be noted that the run time of the iterative code was approximately 120 times faster than the FDTD code.

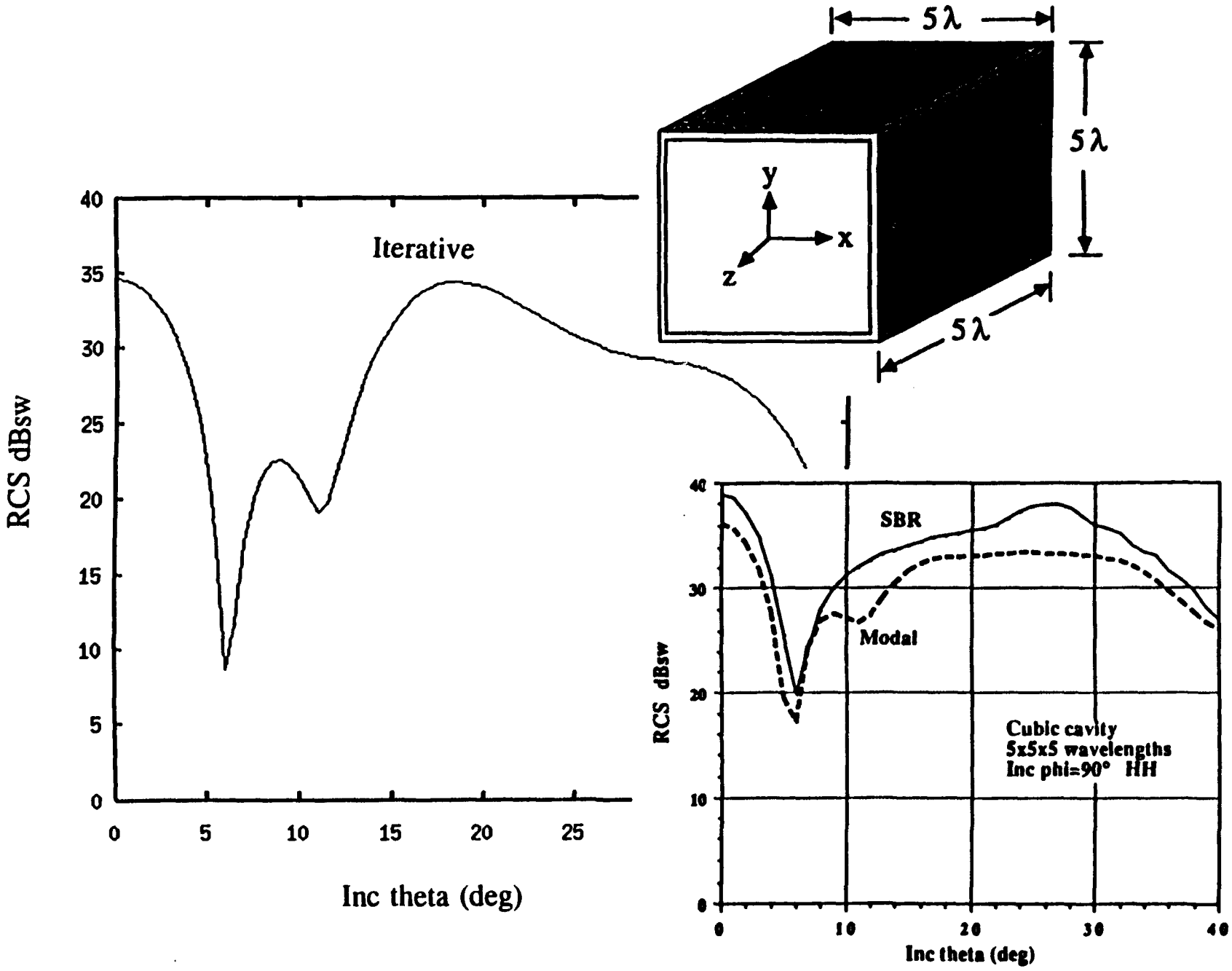
5λ
5λ
5λ
y
x
z
Iterative
RCS dBsw
Inc theta (deg)
0
5
10
15
20
25
30
35
40
SBR
Modal
Cubic cavity
5x5x5 wavelengths
Inc phi=90° HH
RCS dBsw
Inc theta (deg)

Figure 3a

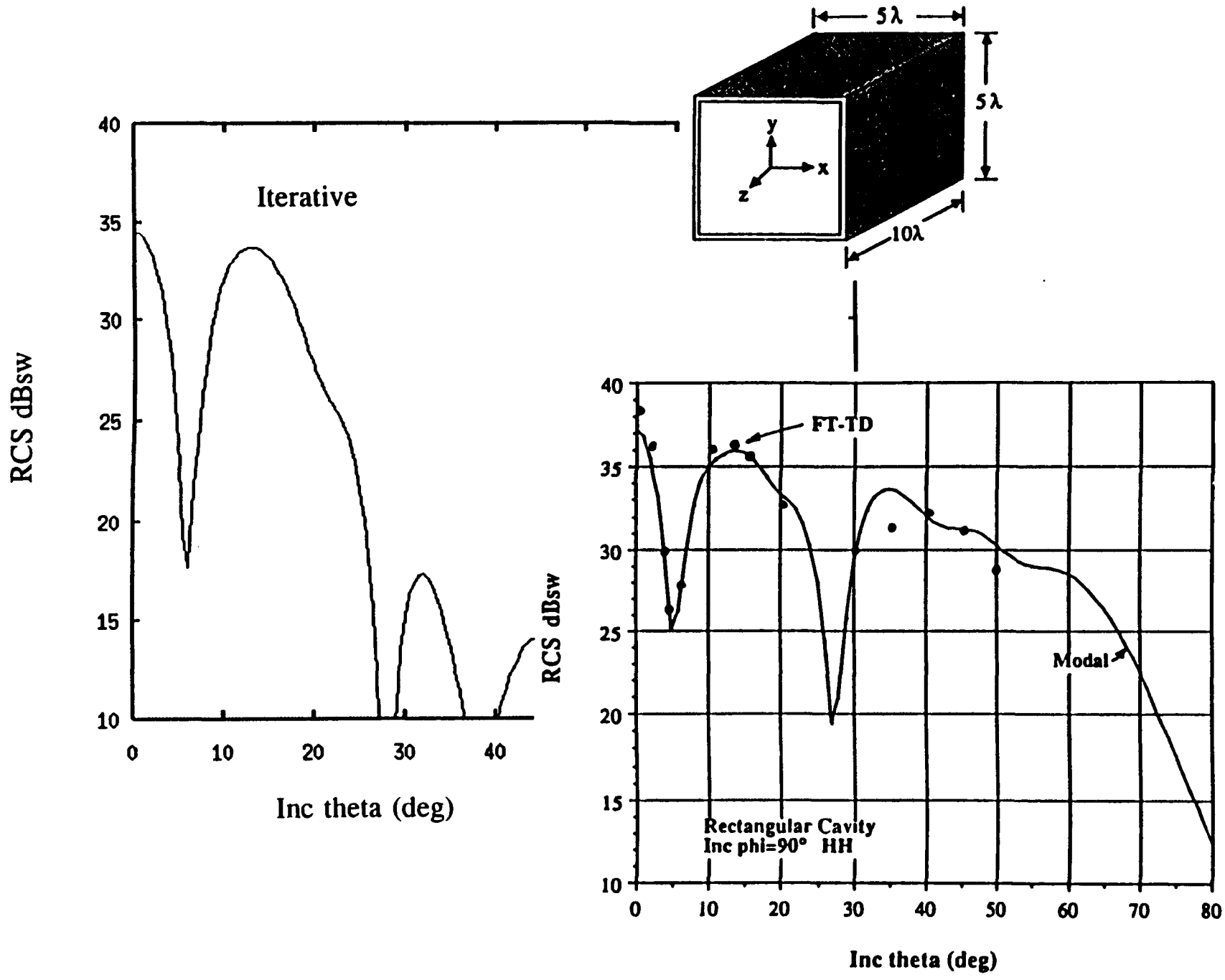
5λ
5λ
10λ
y
x
z
Iterative
RCS dBsw
Inc theta (deg)
FT-TD
Modal
Rectangular Cavity
Inc phi=90° HH
RCS dBsw
Inc theta (deg)

Figure 3b

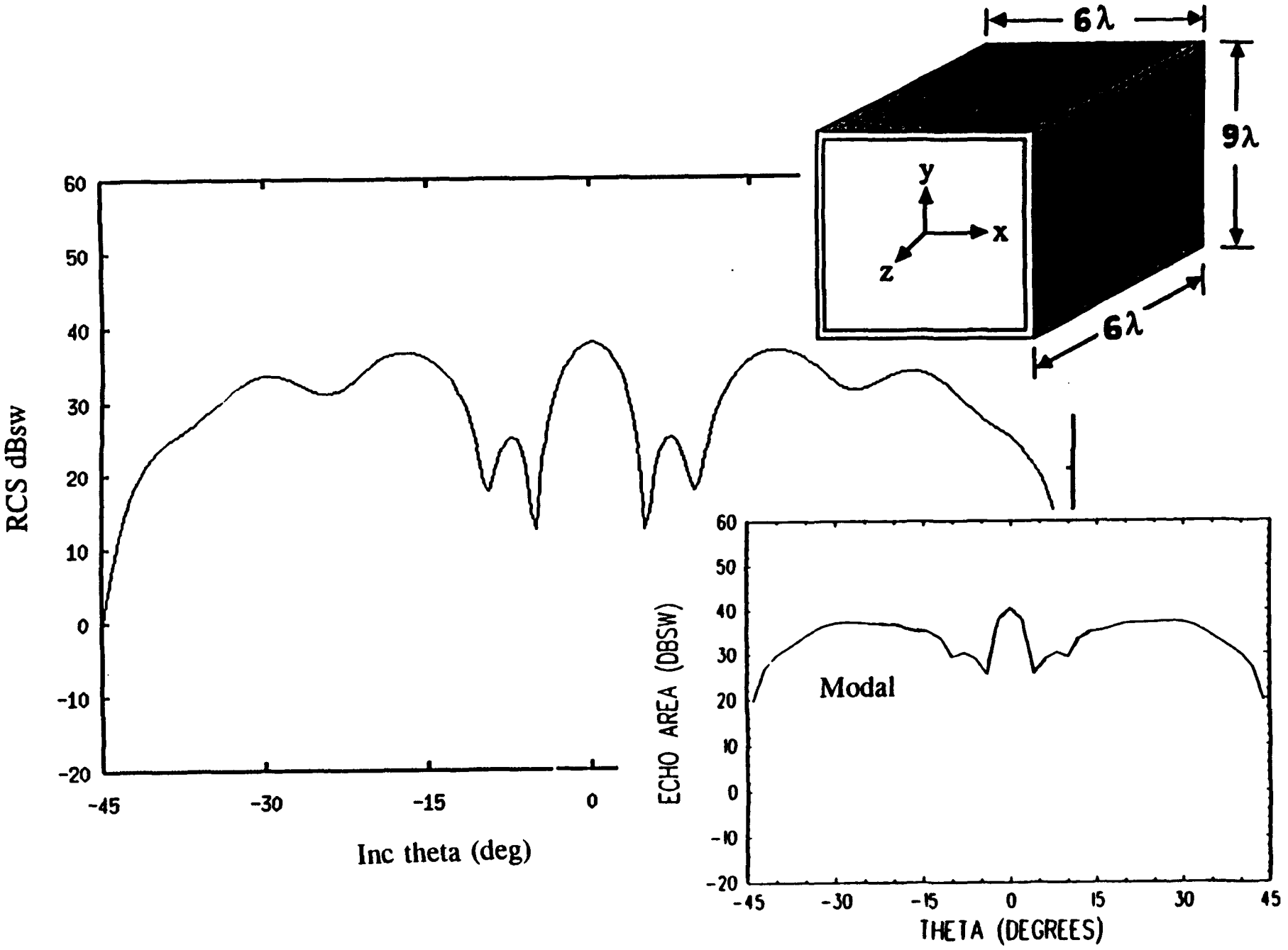
6λ
9λ
6λ
y
x
z
RCS dBsw
60
50
40
30
20
10
0
-10
-20
-45
-30
-15
0
Inc theta (deg)
ECHO AREA (DBSW)
Modal
60
50
40
30
20
10
0
-10
-20
-45
-30
-15
0
15
30
45
THETA (DEGREES)

Figure 3c

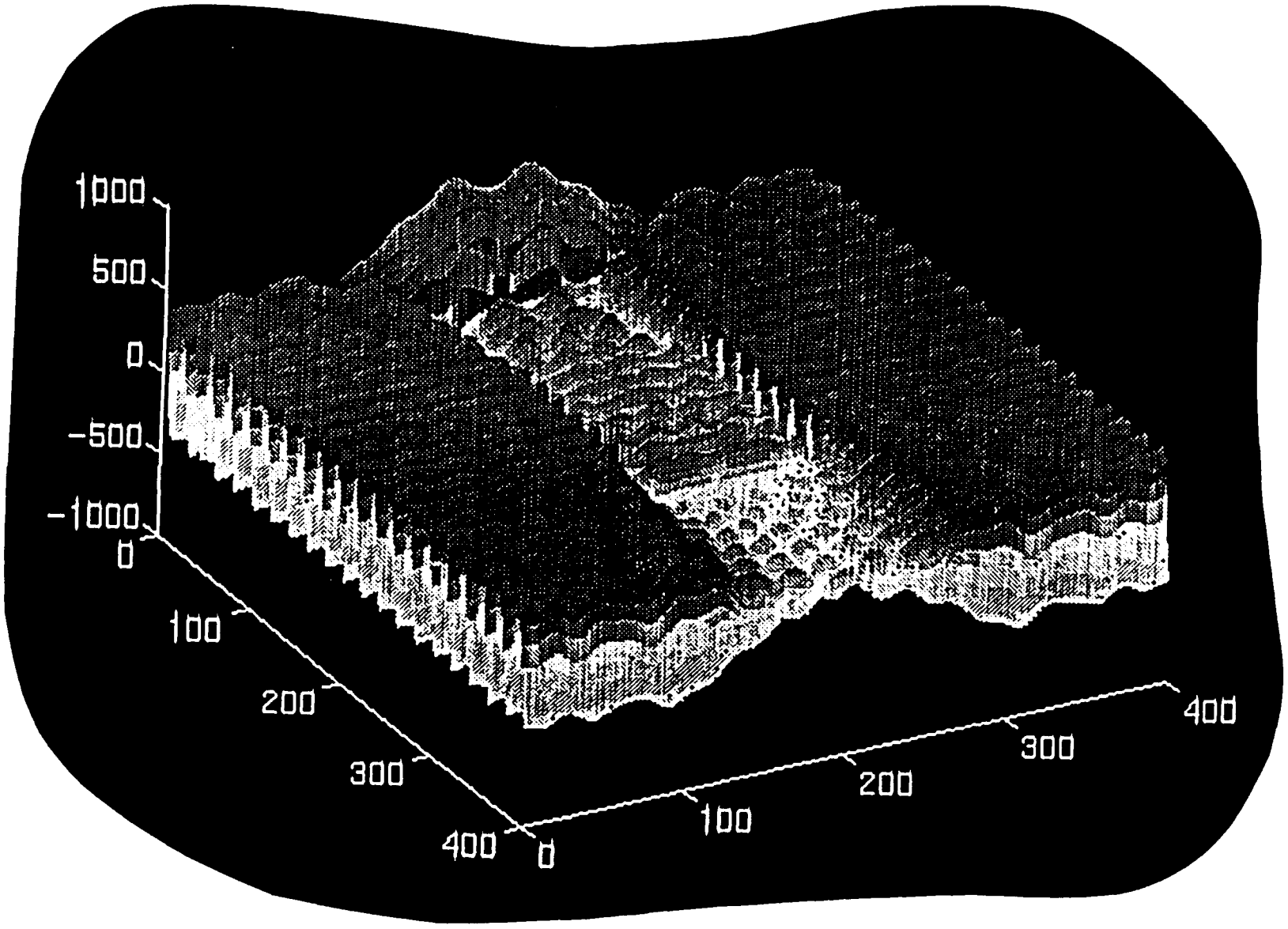

Figure 4a Total Field Surrounding a Cavity

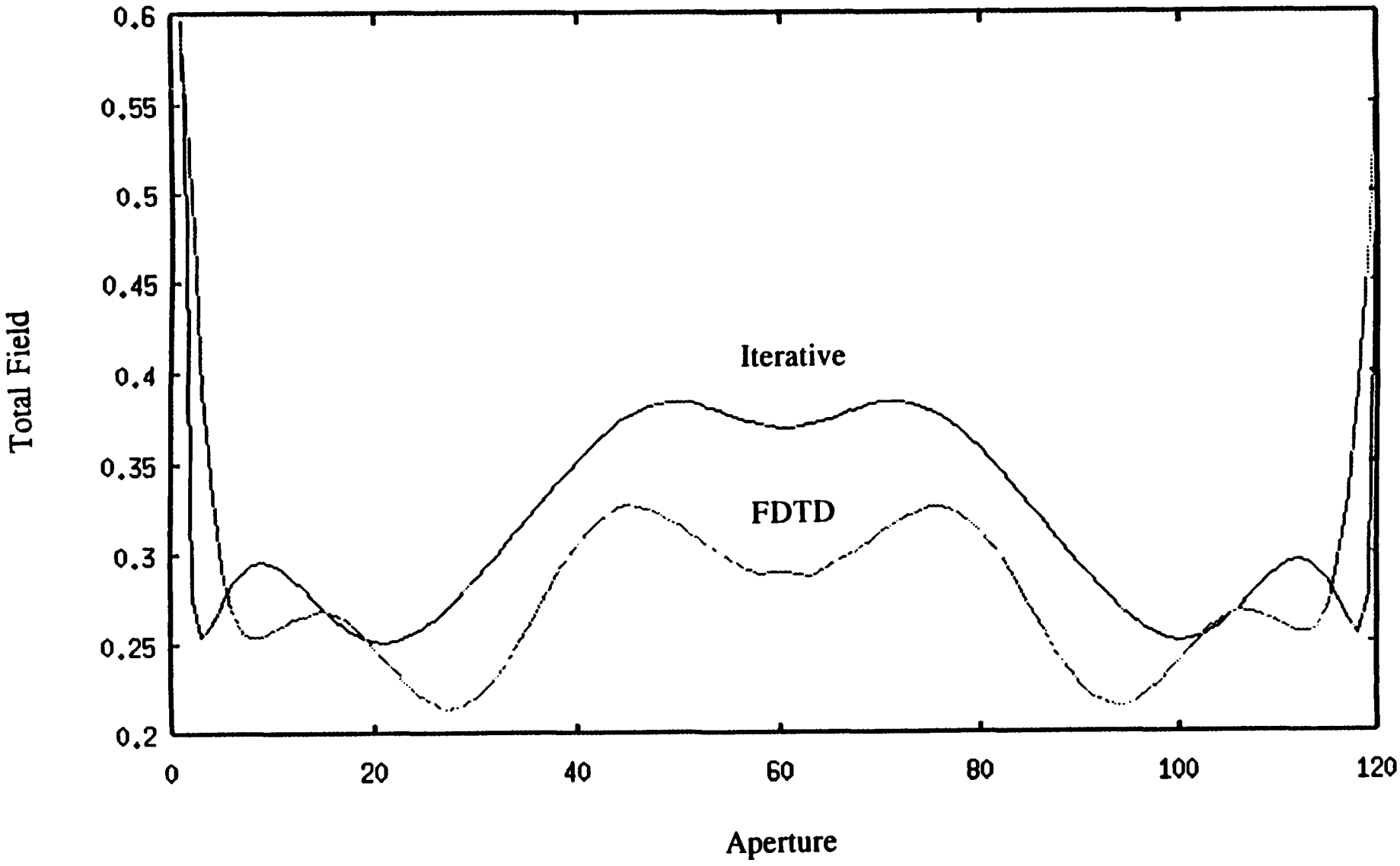

Figure 4b Comparison of Aperture Fields

5 Future Work

Based upon the accurate performance of the 2-dimensional iterative code, it is purposes to up-grade the current computer program to a complete, fully functional, 3-dimensional code. The process of up-grading the current code will consist of the following steps. First, both the discretized MFIE and EFIE need to be appropriately derived in 3-dimensions. Then, a computer code needs to be developed to apply the discretized equations to an ACAD inputed cavity geometry. Second, an appropriate data format needs to be developed to store the calculated field quantities along the surface of the cavity. This data format needs to be developed such that the data may be directly vector processed. Next, the new code needs to be thoroughly tested to insure all areas of the code are working correctly. The testing will be performed by the comparison of the computed aperture fields with those previously calculated by existing codes. Once the accuracy of the new code has been validated, the code will then be vectorized to obtain maximum efficiency. Standard Work-Station, vector processing, will be used to preform this part of the up-grade. Finally, an interface program will be written such that the new code can be directly interfaced with the current X-PATCH RCS prediction code.

References

[1] H. Ling, R. Chou, and S. W. Lee, "Shooting and Bouncing Rays: Calculating RCS of an Arbitrary Cavity," *IEEE Trans. on Antennas and Propagation*, Vol. AP-37, No. 2, pp. 194-205, Feb. 1989.

[2] R. J. Burkholder and P. H. Pathak, "High-Frequency Electromagnetic Scattering by Open-Ended Waveguide Cavities," *Radio Science*, Vol. 26, pp. 211-218, Jan.-Feb. 1991.

[3] H. Ling, "RCS of Waveguide Cavities: A Hybrid Boundary-Integral/Modal Approach," *IEEE Trans. on Antennas and Propagation*, Vol. AP-38, No. 9, pp. 1413-1419, Sept. 1990.

[4] T. J. Kim and G. A. Thiele, "A Hybrid Diffraction Technique - General Theory and Applications," *IEEE Trans. on Antennas and Propagation*, Vol. AP-30, Sept. 1982.

[5] Li Shi-zhi and G. A. Thiele, "A Hybrid Theory of Diffraction for the RCS Calculation of Ogive-Like Bodies," *Radio Science*, Vol. 19, Nov.-Dec. 1984.

[6] M. Kaye, P. K. Murthy, and G. A. Thiele, " An Iterative Method for Solving Scattering Problems," *IEEE Trans. on Antennas and Propagation*, Vol AP-33, Nov. 1985.

[7] P. K. Murthy, K. C. Hill and G. A. Thiele, "A Hybrid-Iterative Method for Scattering Problems," *IEEE Trans. on Antennas and Propagation*, Vol. AP-34, Oct. 1986.

[8] R. P. Penno, G. A. Thiele and P. K. Murthy, "Scattering from a perfectly Conducting Cube Using HIM," Special Issue of *IEEE Proceeding*, on Radar Cross-Section, Vol. 77,May 1989.

[9] N. Morita, N. Kumagai, and J. R. Mautz, Integral Equations Methods for Electromagnetic, Artech House Inc., Boston, 1991.

[10] R. F. Harrington, Time-Harmonic Electromagnetic Fields, McGraw-Hill Book Company, New York, 1961.

GENERAL - PURPOSE ELECTROMAGNETIC MODELING OF COPLANAR WAVEGUIDE STRUCTURES IN MICROWAVE AND MILLIMETER - WAVE PACKAGES

Todd W. Nuteson
Graduate Student Research Associate
Department of Electrical Engineering
Wright State University
Dayton, OH 45435

Final Report for:
AFOSR Summer Graduate Student Research Program
Wright Laboratory, WPAFB

Sponsored by:
Air Force Office of Scientific Research
Bolling A[illegible]e Base, Washington, D.C.

September 1993

GENERAL – PURPOSE ELECTROMAGNETIC MODELING OF COPLANAR WAVEGUIDE STRUCTURES IN MICROWAVE AND MILLIMETER – WAVE PACKAGES

Krishna Naishadham, Assistant Professor
Department of Electrical Engineering
Wright State University
Dayton, OH 45435

ABSTRACT

Coplanar transmission lines and coplanar waveguide (CPW) discontinuities have been analyzed by the finite–difference time–domain (FDTD) method. The FDTD computational mesh is truncated by imposing absorbing boundary conditions on the walls, thus simulating outgoing waves appropriate to an open structure. The residual reflection from these boundaries introduces significant error in the frequency-domain parameters derived by Fourier transformation of the time–domain voltages and currents calculated by FDTD at appropriate reference planes. In this research, we have developed a new computationally-efficient method called the geometry rearrangement technique (GRT) to cancel the dominant contribution to the residual reflection from absorbing boundaries. We have applied the GRT to compute the effective dielectric constant of coplanar lines as a function of frequency, and the computed results have been found to be in good agreement with published data, thus indicating the effectiveness of the GRT in canceling residual reflection from absorbing boundaries. We have developed a computer program to calculate the S–parameters of CPW discontinuities. As a test case, we have computed the S–parameters of a coplanar line with an air–bridge, and the results are in excellent agreement with measurements reported elsewhere. We are continuing to validate our program by investigation of other CPW discontinuities such as L–bend with air–bridges and/or dielectric overlay, open-circuited stub, etc. This research is applicable to efficient characterization of MMIC elements and discontinuities, and high–density microwave and millimeter–wave packages, which are currently being investigated in aerospace research. We conclude the report with a summary of potential aerospace–related problems which can be solved with the tools developed in this research.

GENERAL - PURPOSE ELECTROMAGNETIC MODELING OF COPLANAR WAVEGUIDE STRUCTURES IN MICROWAVE AND MILLIMETER - WAVE PACKAGES

Krishna Naishadham

I. INTRODUCTION

A wide variety of transmission lines, discontinuities and components are employed in both microwave and high–speed digital circuits to accomplish various design objectives. These structures employ microstrip, coplanar waveguide (CPW), coplanar slotline, or a similar environment to support signal propagation, and are not amenable to characterization over a wide range of frequency, geometrical and physical parameters by simple quasi-static methods [1]–[3] or canonical measurements [4]. Therefore, the general-purpose analysis of these transmission line structures tends to be difficult and computer–intensive. With the high density of integrated circuits available today in both high–speed digital circuits and microwave and millimeter–wave integrated circuits (MMICs), the electronic packaging that encompasses these circuits has become very sophisticated and must be accurately characterized for reliable circuit design. For example, multilayer packaging incorporates vias which connect signal lines from one layer to another, or air bridges and wire bonds to connect the chip to a circuit component. Because these discontinuities can introduce complicated frequency–dependent capacitive and inductive effects, radiate energy, and excite unwanted package modes in the circuits, reliable methods of analysis are needed to develop equivalent circuit models and general–purpose CAD tools for these discontinuities. This report summarizes our effort to develop such tools for the analysis of CPW transmission lines and discontinuities. The CPW configuration has received considerable atten–tion in the recent past because of several factors which include the ease of circuit interconnection, low radiation loss, and the promising flip-chip packaging technique [5], [6].

A few accurate methods have been applied to analyze coplanar waveguides and CPW discontinuities. Knorr and Kuchler [7] determined the dispersion characteristics and characteristic impedance of CPWs using the spectral–domain method of moments (MoM). Similar analysis by Hasnian et al. [8] yielded the dispersion characteristics of picosecond pulses in CPWs. A full–wave analysis of CPW and slotline using the finite difference time domain (FDTD) method has been performed by Liang et al. [9] to extend the dispersion characteristics into the terahertz regime. The analyses of CPW discontinuities, however, have been quite sparse in comparison with CPWs. Simons and Ponchak [10] presented for the first time equivalent circuit models derived from measured S–parameters for open circuit, series gap, symmetric step and right angle bend CPW discontinuities. Dib et al. [11] analyzed shielded CPW discontinuities with air bridges using the spectral domain moment method. The air bridge, however, was not considered as an integral part of the MoM computation in [11]. Rittweger et al. applied the FDTD method for a full three–dimensional analysis of a CPW band–reject filter with air bridges [12]. Omar and Chow [13] obtained the S–parameters of a CPW with air bridges using the moment method and a simplified representation of the Green's functions in terms of complex images.

In this report, we employ the FDTD method to analyze CPWs and CPW discontinuities. A novel technique based on transmission line analysis is used to cancel the spurious reflection from the far–end absorbing boundary used to terminate the FDTD computational mesh. The method is illustrated by application to CPW transmission lines with and without air bridges, and CPW right angle bends. The FDTD method is chosen over other techniques, such as the MoM, because (a) a single time–domain simulation provides characterization of the discontinuities from DC well into the sub–millimeter wave frequency regime, (b) it can be readily extended to analyze multilayered package structures, and complicated, yet realistic configurations such as a right angle bend compensated by a dielectric overlay in the inner slot [10], packages lined with walls made of absorbing material, etc. Unlike the moment method, the FDTD method does not involve cumbersome analytical preprocessing pertinent to the derivation of Green's functions, and the solution of a system of linear equations by the inversion of a large dense matrix.

II. FINITE DIFFERENCE TIME DOMAIN METHOD

In this section, we summarize the salient features of the FDTD method, adopting the notation in [14]. The propagation of the fields in the structure of interest is governed by the Maxwell's equations

$$\mu \frac{\partial \mathbf{H}}{\partial t} = -\nabla \times \mathbf{E} \tag{1}$$

$$\epsilon \frac{\partial \mathbf{E}}{\partial t} = -\nabla \times \mathbf{H} \tag{2}$$

The media are assumed to be isotropic, lossless and piecewise homogeneous. The problem is discretized over a finite three–dimensional computational volume consisting of rectangular cubes, known as Yee unit cells. The six field components in (1) and (2) are interleaved in space on the six faces of the unit cell [14, Fig. 1]. Such an arrangement automatically satisfies the continuity of the tangential field components. The spatial and time derivatives in Maxwell's equations are replaced by their central difference approximations defined over the surface of the unit cell, resulting in a set of nodal E–fields, and a corresponding orthogonal set of nodal H–fields. The reader is referred to [14, eqs. (3)–(8)] for the finite difference approximations of the nodal fields derived from (1) and (2). With this scheme, the H–field node is displaced in space from the E–field node by half space step, and is updated (in time) one–half time step ahead of the E–field. This half–step staggering of the fields in time and space allow for the solution of the difference equations by using an explicit, iterative, leap–frog scheme, whereby the field at a given position and time instant is updated in an explicit manner utilizing the nearest–neighbor fields. For modeling dielectric interfaces, the interface is assumed to pass through the center of a unit cell, and a dielectric constant equal to the average of those of the two adjacent media is enforced at the interface. Since the material constants can vary arbitrarily from cell to cell, the FDTD method can conveniently analyze structures filled with arbitrarily inhomogeneous media. Conducting surfaces are treated by setting the tangential electric field components to zero.

The computational domain must be truncated into a region which is of finite and manageable size.

This is accomplished by introducing fictitious boundaries, where the so–called absorbing boundary conditions (ABCs) [15], [16] are specified locally such that the reflection from these boundaries is minimal. Thus, these boundaries simulate the condition of outgoing waves appropriate to open–region problems. The use of ABCs makes it feasible to solve a wide variety of microwave circuit and packaging problems using the FDTD method. For the structures considered in this report, the pulses on the transmission lines will be assumed to be normally incident on the mesh walls (or absorbing boundaries), so that Mur's first–order ABC can be used. We implement this ABC in difference–form as

$$E_0^{n+1} = E_1^n + \frac{v\,\Delta t - \Delta\ell}{v\,\Delta t + \Delta\ell}\left[E_1^{n+1} - E_0^n\right] \tag{3}$$

where E_0 represents the tangential electric field component on the mesh wall, E_1 represents the same component one node inside of the mesh wall, v is the maximum velocity of light in the computational volume, the superscript n is the time index, $\Delta\ell$ and Δt are the spatial and time steps, respectively. For a stable solution, the maximum time step is restricted by

the Courant condition [14, eq. (9)]. The side walls should be chosen far enough from the circuit in consideration so that the fringing fields which propagate tangential to the walls have neglible amplitude on the walls. This is especially critical for CPWs, whose transverse fields are quite spread out in phase, and whose absorbing boundaries on the sides have a metal sheet sandwiched between media with different propagation velocities. In Sec. III, we will address a novel method, termed as the Geometry Rearrangement Technique (GRT), which we have developed to minimize influence of the reflection from absorbing boundaries.

The excitation pulse used in this research has been chosen to be Gaussian in shape since its Fourier transform is also Gaussian centered at zero frequency. This property makes it useful in the analysis of frequency–dependent characteristics of planar transmission lines and discontinuities. The parameters of the Gaussian pulse are chosen according to the criteria detailed in [17]. The frequency-dependent circuit parameters are computed as described in [14].

III. GEOMETRY REARRANGEMENT TECHNIQUE

The FDTD computational domain is artificially terminated by absorbing boundaries in order to make the problem size manageable. Since these boundaries are not completely transparent, the results obtained by the FDTD method are subject to error caused by the reflection from the boundaries. Although various methods such as superabsorption [16] have been proposed to minimize this reflection in the time domain, the error is still large in the frequency domain, since the Fourier transform is very sensitive to even relatively small error caused by imperfect boundaries. For example, when the FDTD method is used to calculate the effective dielectric constant of a microstrip transmission line with the first-order Mur boundary condition [15], we have found that the frequency–domain result shows periodic oscillation with a peak value around 10–20% of the result predicted by an empirical dispersion formula [18]. This large error is caused by imperfect absorbing boundaries. In this research, we have developed a new simple method called the geometry rearrangement technique which can minimize the reflection from the far–end absorbing boundary to a much smaller level than possible by using conventional ABCs. An attractive feature of the GRT is that an accurate numerical result can be obtained directly from the Fourier–transformed frequency–domain data. In this section, we will summarize the main feature of this method. The reader is referred to [18] for more details. The improvement of the computed FDTD results on CPWs, accomplished by using the GRT, is demonstrated in the next section. Although we describe the method below for calculating the effective dielectric constant, we have successfully applied GRT to compute accurately the S-parameters of planar circuit discontinuities [19].

The conventional method of calculating the effective dielectric constant with the FDTD method [17] is by Fourier transformation of the voltage (or the electric field) at two different points on the transmission line. With V_{p1} and V_{p2} denoting the transforms of voltages at the points P_1 and P_2 (see Fig. 1), we have

$$e^{-\gamma(\omega)\Delta\ell} = \frac{V_{p1}}{V_{p2}} \tag{4}$$

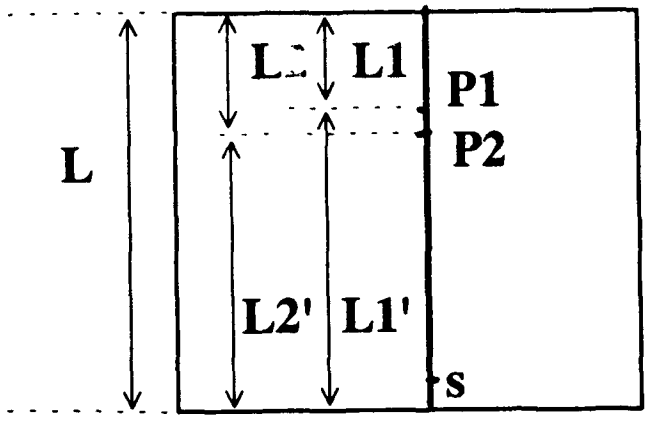

Fig. 1. Transmission line

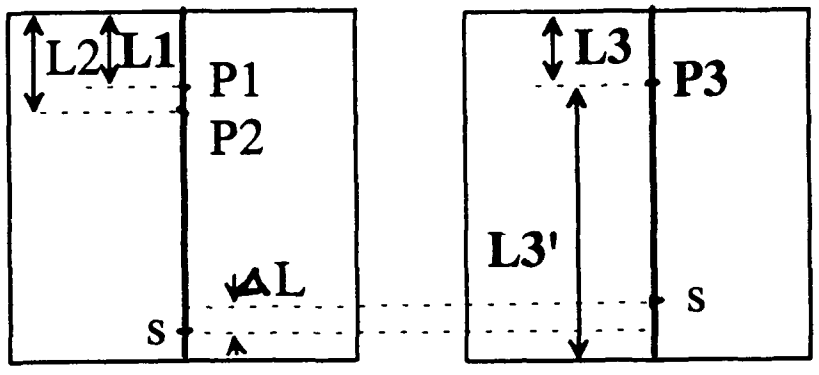

Fig. 2. Two identical transmission lines with source relocation in the second

where

$$\gamma(\omega) = \alpha(\omega) + j\beta(\omega) \tag{5}$$

$$\Delta\ell = \ell_2 - \ell_1 \tag{6a}$$

$$\beta(\omega) = \frac{1}{\Delta\ell} \operatorname{Ang}\left[\frac{V_{p1}}{V_{p2}}\right] \tag{6b}$$

The effective dielectric constant is given by

$$\epsilon_{reff}(\omega) = \frac{\beta^2(\omega)}{\omega^2 \epsilon_0 \mu_0} \tag{7}$$

where ω is the angular frequency and μ_0, ϵ_0 are the constitutive parameters of free space. We now examine how errors caused by reflection from the absorbing boundaries influence the computed dielectric constant. Let the reflection coefficient at the far-end boundary be Γ_f and that at the source-end boundary be Γ_s. Assume that the reflection caused by side, top and bottom walls is very small compared to that caused by the two end walls indicated above. The voltages V_{p1} and V_{p2} would then be the superposition of an incident wave and multiply reflected waves:

$$V_{p1} = V_{p1in}\left[1 + \Gamma_f e^{-2\gamma(\omega)\ell_1}\left[1 + \Gamma_s e^{-2\gamma(\omega)\ell_1'}\left[1 + \Gamma_f e^{-2\gamma(\omega)\ell_1}(1 + \ldots)\right]\right]\right] \tag{8}$$

$$V_{p2} = V_{p2in}\left[1 + \Gamma_f e^{-2\gamma(\omega)\ell_2}\left[1 + \Gamma_s e^{-2\gamma(\omega)\ell_2'}\left[1 + \Gamma_f e^{-2\gamma(\omega)\ell_2}(1 + \ldots)\right]\right]\right] \tag{9}$$

where V_{p1in}, V_{p2in} are incident voltages at points P_1, P_2. Eqs. (8) and (9) can be summed up in closed form:

$$V_{p1} = V_{p1in}\frac{1 + \Gamma_f e^{-2\gamma(\omega)\ell_1}}{1 - \Gamma_f\Gamma_s e^{-2\gamma(\omega)\ell}} \tag{10}$$

$$V_{p2} = V_{p2in}\frac{1 + \Gamma_f e^{-2\gamma(\omega)\ell_2}}{1 - \Gamma_f\Gamma_s e^{-2\gamma(\omega)\ell}} \tag{11}$$

where $\ell = \ell_1 + \ell_1' = \ell_2 + \ell_2'$. From (4), (10) and (11), we obtain:

$$e^{-\gamma(\omega)\Delta\ell} = \frac{V_{p1in}}{V_{p2in}} \frac{1 + \Gamma_f e^{-2\gamma(\omega)\ell_1}}{1 + \Gamma_f e^{-2\gamma(\omega)\ell_2}} \tag{12}$$

$\gamma(\omega)$ calculated from the above equation has an error caused by Γ_f The true value of $\gamma(\omega) \equiv \tilde{\gamma}(\omega)$ should be calculated from

$$e^{-\tilde{\gamma}(\omega)\Delta\ell} = \frac{V_{p1in}}{V_{p2in}} \tag{13}$$

for the transmission line without boundaries (without reflections).

2.1. *Source Relocation*

If $\ell_1 = \ell_2$ in eq. (12), eq. (12) would be the same as eq. (13), which means $\gamma(\omega) = \tilde{\gamma}(\omega)$. But this cannot be realized on the single transmission line, since the two points P_1 and P_2 coalesce into one and $\Delta\ell$ becomes zero. However, if two transmission lines with the same characteristics are used instead of one, as in Fig. 2, we can use voltage V_{p3} at point P_3 on the second transmission line to *simulate* the voltage V_{p2} at point P_2 on the first transmission line. This is accomplished by moving the *source* in the second line (identical tothat in the first line) by a distance $\Delta\ell$ closer to the far–end boundary, so that the distance between P_3 and the source location S_2 on the second line is the same as the distance between P_2 and the source location S_1 on the first line. Eq. (12) then becomes:

$$e^{-\gamma(\omega)\Delta\ell} = \frac{V_{p1in}\,[1 + \Gamma_f e^{-2\gamma(\omega)\ell_1}]}{V_{p3in}\,[1 + \Gamma_f e^{-2\gamma(\omega)\ell_3}]} = \frac{V_{p1in}}{V_{p3in}} \tag{14}$$

since $\ell_3 = \ell_1$ and $V_{p3} = V_{p2}$. Therefore, the result calculated from voltages at the two points P_1, P_3 on the two transmission lines with the source simply relocated in the second, is an accurate numerical result. It does not contain the error introduced by Γ_f or Γ_s. A similar result can be obtained by moving the far–end boundary in the second line $\Delta\ell$ closer to the source, keeping the source position unchanged [18]. The latter rearrangement, called *boundary relocation*, would be convenient in those instances when

the reflection from the side–walls is significantly affected by the source location, such as CPW with low dielectric constant substrates [9].

IV. TEST RESULTS AND DISCUSSION

We first present computed results for the effective dielectric constant and characteristic impedance of a coplanar transmission line and compare our results with [9] to validate the FDTD algorithm.

The parameters used in the comptuation are (see Fig. 3):

Dielectric constant of the substrate	$\epsilon_r = 13.0$
Width of the center strip	$W = 0.135$ mm
Slot width	$S = 0.065$ mm
Width of the lateral strips	$W_\ell = 1$ mm
Thickness of the substrate	$h = 0.5$ mm
Cell size	$\Delta x = \Delta y = \Delta z = 0.0135$ mm
Time step	$\Delta t = 0.0176$ ps
Number of cells	$Nx \times Ny \times Nz = 85 \times 120 \times 60$
Number of time steps	$N = 4096$

The same geometry (Fig. 3) has been analyzed by using FDTD in [9]. However, instead of using the time–consuming superabsorption boundary condition [9], we use the simple first–order Mur condition. We use the magnetic wall symmetry around the $x = 0$ plane to reduce size of the computational domain.

Unlike the microstrip transmission line, the electric field distribution in the CPW is loosely bound to the substrate over the slots. It is difficult to simulate accurate absorbing boundary conditions on the side, top and bottom walls. Although the field of the wave traveling longitudinally along the CPW is mainly concentrated in the slot, the fringing field spreads out laterally away from the slot [20], and does not decay to small values near the absorbing boundary walls on the sides. To better simulate the distribution of the field in the slot, the amplitude of the Gaussian pulse for the excitation field is chosen as [20]:

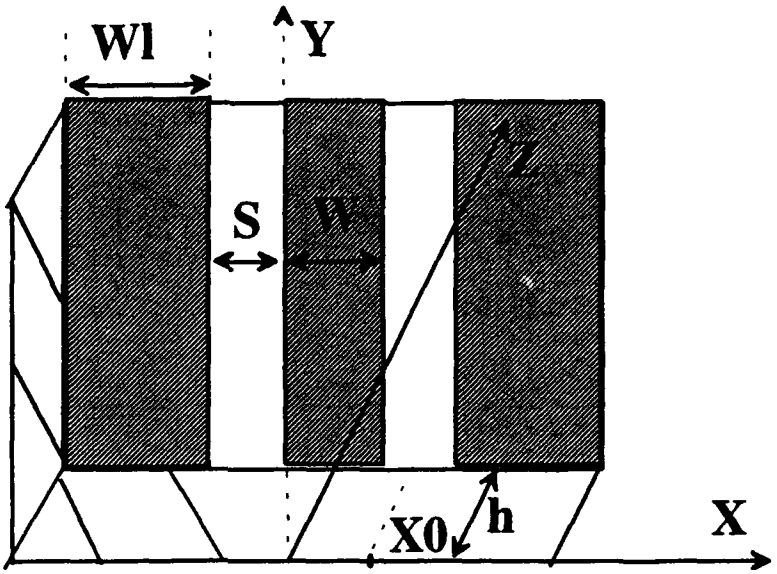

Fig. 3. Coplanar waveguide geometry

$$E_x = C\left[1-\left[\frac{2(x-x_0)}{S}\right]^2\right]^{-\frac{1}{2}}, \ |x-x_0| < \frac{S}{2} \tag{15}$$

at the air–dielectric interface, and as

$$E_x = C\left[1+\left[\frac{2(x-x_0)}{S}\right]^2\right]^{-\frac{1}{2}}, \ |x-x_0| < \frac{S}{2} \tag{16}$$

for a few cells above and below the air–dielectric interface over the excitation plane. In (15) and (16), C is an arbitrary constant and x_0 denotes the center of the slot (Fig. 3).

The numerical results for the CPW are shown in Figure 4. Four curves are shown — the conventional Fourier transform result, the GRT result, least squares fit to the GRT result, and an empirical result from [8]. It is observed that the maximum difference between the geometry rearrangement and the least squares results is less than 1.5 percent. The conventional Fourier transform result oscillates around the least squares or the geometry rearrangement result, but the difference between the conventional Fourier transform and the least squares is more than 12 percent. The least squares fit to the GRT result agrees reasonably well with the empirical formula. Therefore, considerable improvement in the accuracy of the effective dielectric constant can be obtained by using the geometry rearrangement technique with a simple absorbing boundary condition instead of the conventional FDTD implementation.

The characteristic impedance of the coplanar line depicted in Fig. 3 has been computed using FDTD, and is displayed in Fig. 5 as a function of frequency. Excellent agreement is observed between our result and that in [9, Fig. 6a].

Next, we consider a coplanar line with an air–bridge. The geometry is the same as that in Fig. 3, but an air–bridge with a height of 0.0135 mm, a width of 0.027 mm, and a length of 0.189 mm, has been positioned 0.729 mm from the $z = 0$ plane. The two S–parameters, S_{11} and S_{21}, where port 1 is located 0.594 mm from the $y = 0$ plane and port 2 is located 0.675 mm from the far–end wall, have been computed as described in [14], and compared with the measurements in [21]. The results, shown in Figs. 6 and 7, are in good agreement. No measured results are available beyond 30 GHz.

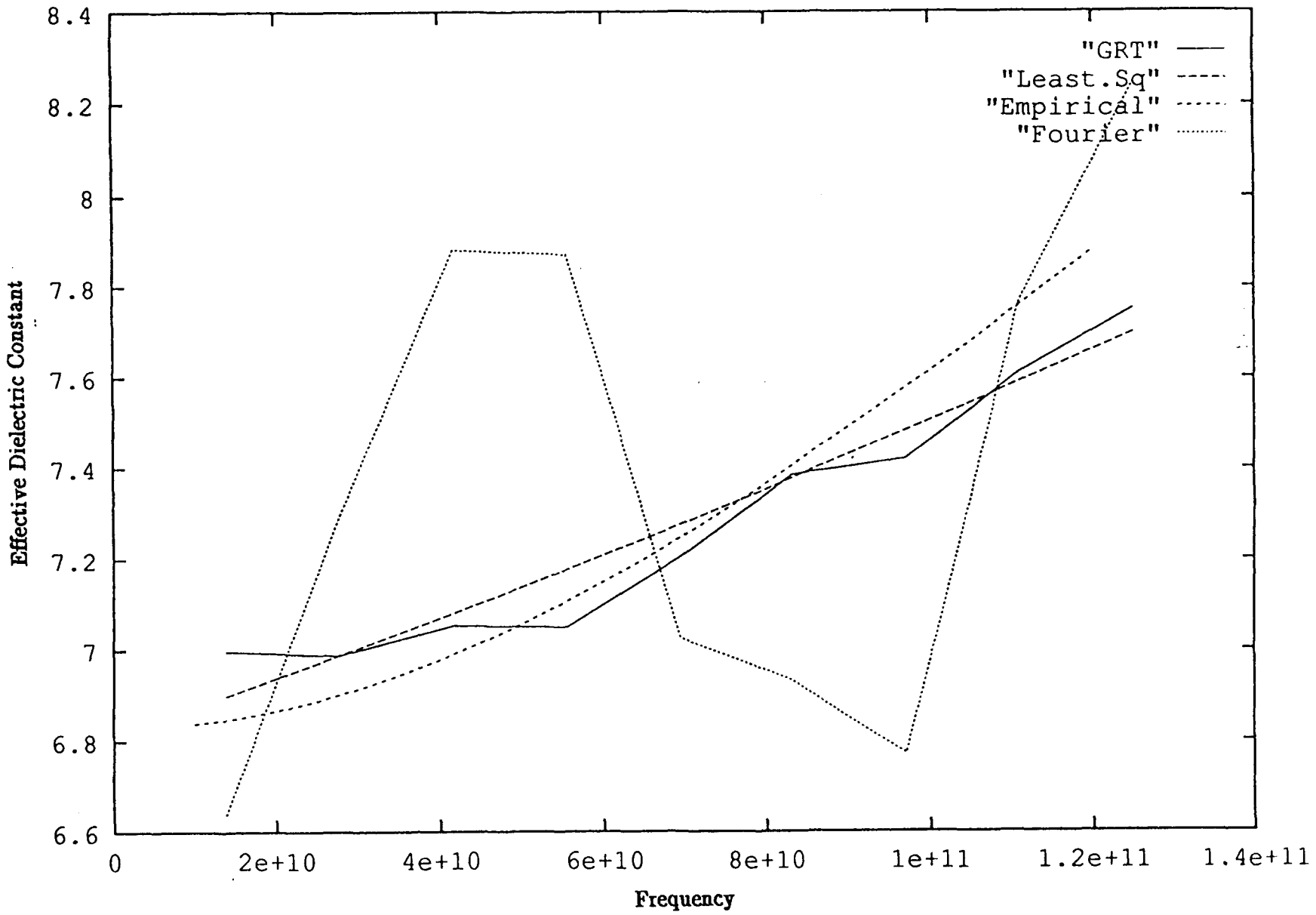

Fig. 4 Effective dielectric constant for the coplanar transmission line shown in Fig. 3.

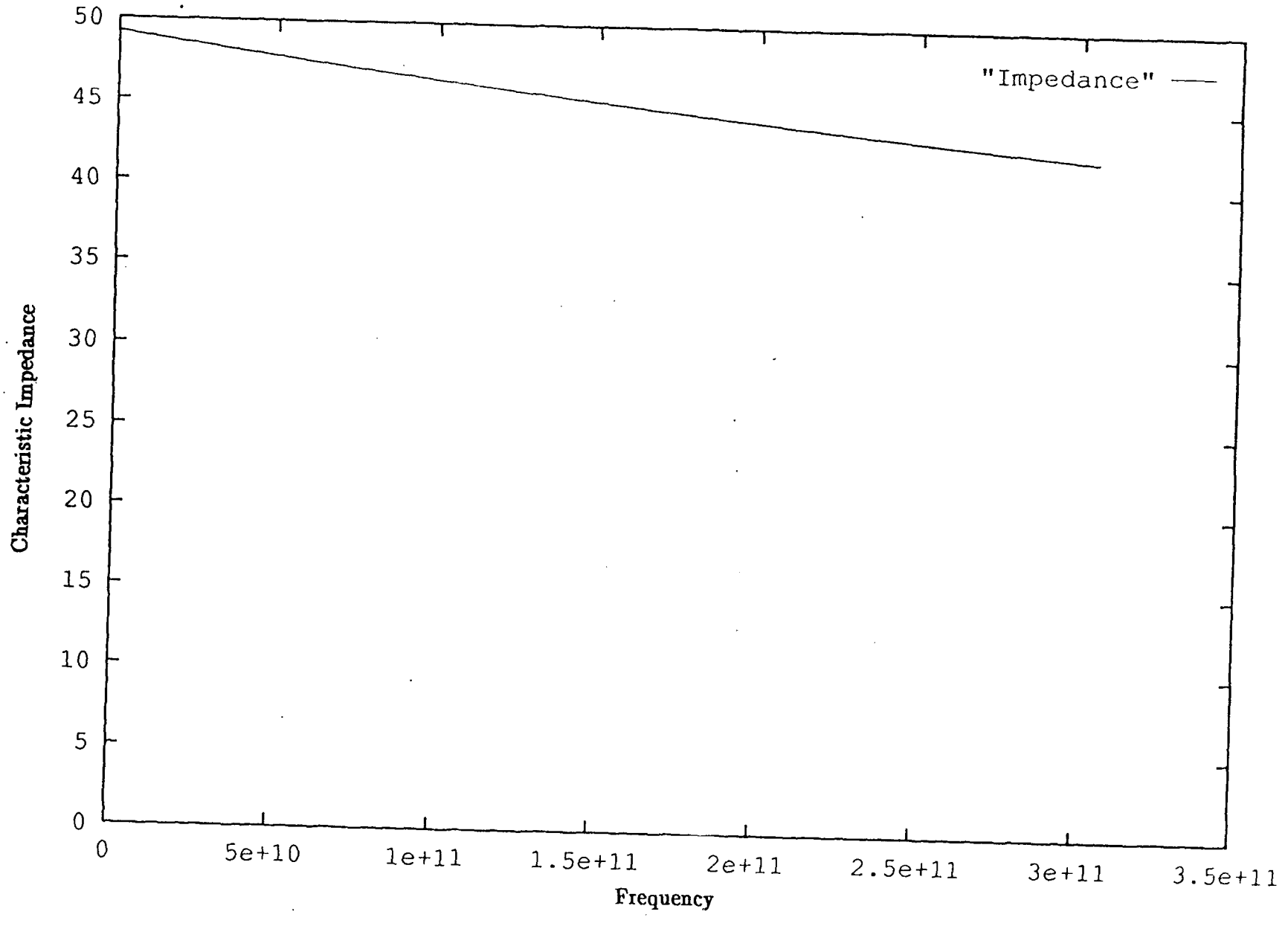

Fig. 5 Characteristic impedance of the coplanar transmission line shown in Fig. 3.

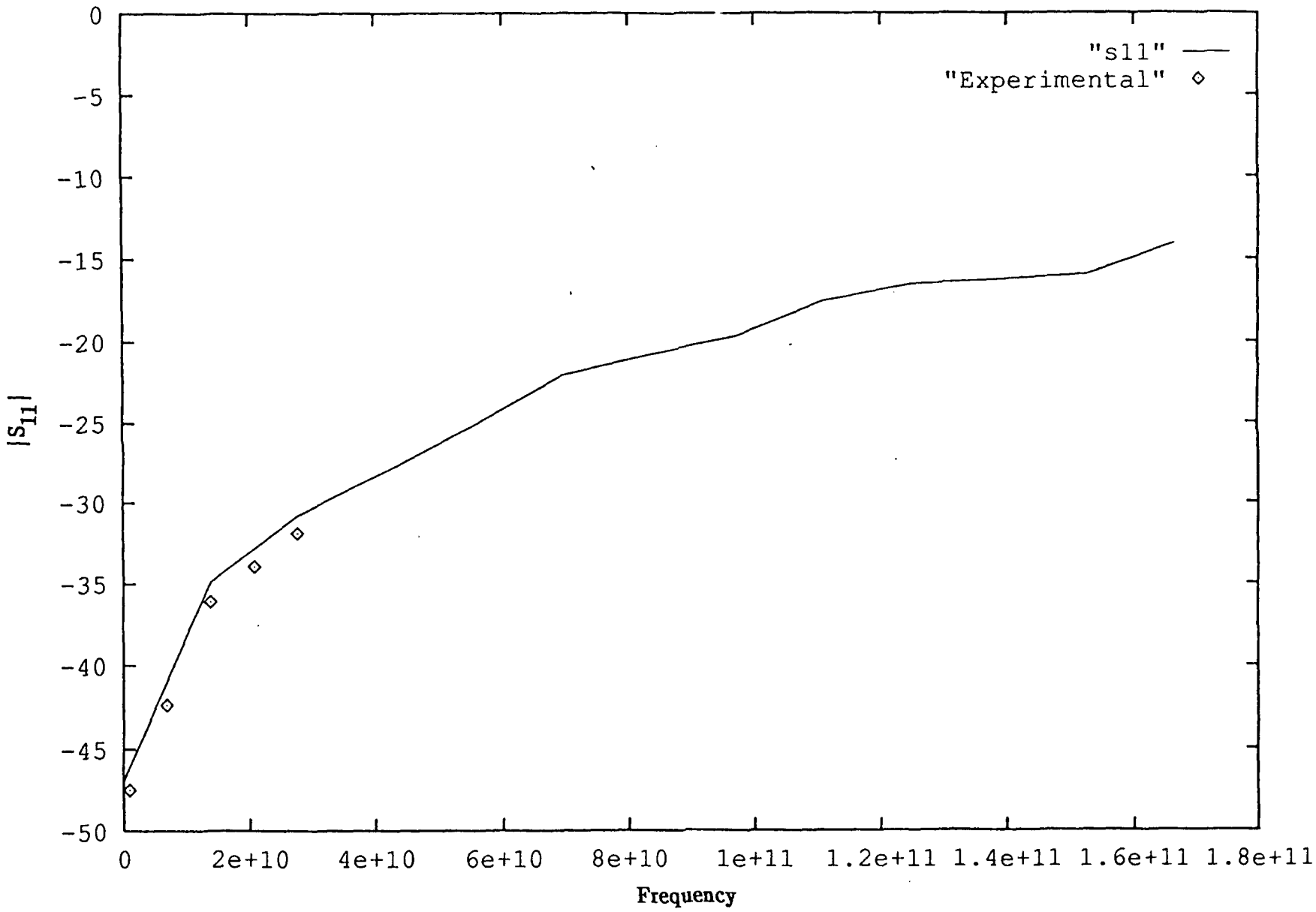

Fig. 6 $|S_{11}|$ **for the CPW in Fig. 3 with an air–bridge added.**

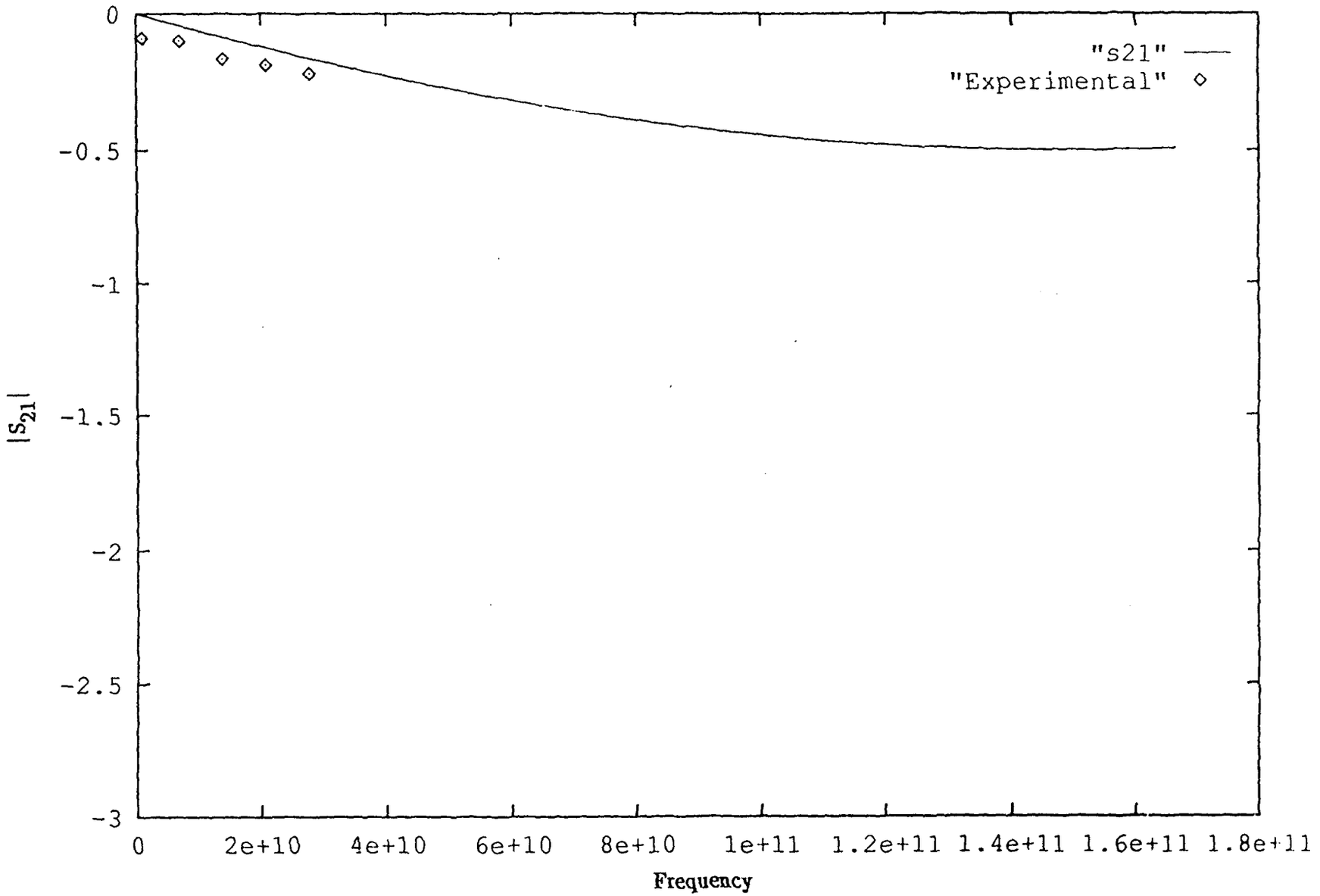

Fig. 7 $|S_{21}|$ for the CPW in Fig. 3 with an air–bridge added.

V. SUMMARY AND CONCLUSIONS

We have applied the finite–difference time–domain technique to analyze coplanar transmission lines and discontinuities. Unlike the microstrip geometry, the fields in CPW are spread out in space, and the absorbing boundaries used to terminate the computational mesh need special care. Although advanced boundary conditions such as superabsorption may be used, we have developed a simple method known as the geometry rearrangement technique for the FDTD analysis of planar transmission lines and discontinuities. We have determined the frequency–dependent effective dielectric constant of microstrip lines [18] and CPW, and computed results are found to be in good agreement with those obtained from empirical formulas and published literature. We are currently applying this method to compute the S–parameters of passive planar components in both microstrip and CPW configurations, and are examining how one may use th reflection coefficient estimated in the GRT to improve the FDTD result further. In comparison with advanced boundary conditions such as superabsorption, the GRT can save computer memory as well as computational time, and is considerably easier to implement on the computer. Also, the GRT *directly* minimizes the error introduced by Fourier transform operation without any need for curve–fitting. Our computed characteristic impedance for coplanar lines also agrees well with published data.

As a test case for CPW discontinuities, we have used our FDTD program to compute the S–parameters of a CPW with air–bridge. The computed results show excellent agreement with experimental data in [21]. We are currently applying the FDTD method to analyze other CPW structures such as bends and stubs in a multilayered structure with air–bridges and dielectric overlays on discontinuities.

VI. FUTURE WORK

The time span available on the AFOSR Summer Research Program is quite short for a comprehensive investigation. Given adequate resources, we wish to apply our FDTD algorithm to investigate the following problems relevant to MMICs, high–speed digital circuits, high–density microwave and millimeter–wave packaging:

a) study the influence of walls lined with surface–impedance, lossy or absorbing boundaries on the CPW characteristics and on coupling between discontinuities,

b) study the resonant behavior of packages lined with metallic walls and/or partitions — in particular the resonant coupling, Q–factors and losses,

c) extension of our algorithm to CPW discontinuities with inclined edges, such as mitered CPW bends,

d) develop and validate a design–base of equivalent circuits and S–parameters for CPW discontinuities in a general multilayered environment,

e) a thorough investigation of the loss mechanism in CPWs well into the terahertz regime.

REFERENCES

[1] C. Wei, R. F. Harrington, J. R. Mautz, and T. K. Sarkar, "Multiconductor transmission lines in multilayered dielectric media, "*IEEE Trans. Microwave Theory Tech.*, vol. MTT–32, no. 4, pp. 439–450, 1984.

[2] M. Kirschning, R. H. Jansen, and N. H. L. Koster, "Accurate model for open end effect of microstrip transmission lines," *Electron. Lett.*, vol. 17, pp. 123–125, 1981.

[3] P. Silvester and P. Benedek, "Microstrip discontinuity capacitance of right–angle bends, T–junctions, and crossings," *IEEE Trans. Microwave Theory Tech.*, vol. MTT–21, pp. 341–346, 1971.

[4] M. Caulton, J. J. Hughes, and H. Sobol, "Measurements on the properties of microstrip transmission lines for microwave integrated circuits," *RCA Review*, vol. 27, pp. 377–391, 1966.

[5] E. E. Davidson and G. A. Katopis, "Package electrical design," in *Microelectronics Packaging Handbook*, (R. R. Tummala and E. J. Rymaszewski, eds.), New York, NY: Van Nostrand Reinhold, ch. 3, pp. 111–165, 1989.

[6] Department of Defense (DoD) Advisory Group on Electron Devices (AGED) Special Technology Area Review (STAR) Report on *Microwave Packaging Technology*, February 1993.

[7] J. B. Knorr and K. Kuchler, "Analysis of coupled slots and coplanar strips on dielectric substrates," *IEEE Trans. Microwave Theory Tech.*, vol. MTT–23, no. 7, pp. 541–548, 1975.

[8] G. Hasnain, A. Dienes, and J. R. Whinnery, "Dispersion of picosecond pulses in coplanar transmission lines," *IEEE Trans. Microwave Theory Tech.*, vol. MTT–34, no. 6, pp. 738–741, 1986.

[9] G. Liang, Y. Liu, and K. K. Mei, "Full–wave analysis of coplanar waveguide and slotline using the time–domain finite–differenc method," *IEEE Trans. Microwave Theory Tech.*, vol. MTT–37, no. 12, pp. 1949–1957, 1989.

[10] R. N. Simons and G. E. Ponchak, "Modeling of some coplanar waveguide discontinuities," *IEEE Trans. Microwave Theory Tech.*, vol. MTT–36, no. 12, pp. 1796–1803, 1988.

[11] N. I. Dib, P. B. Katehi, and G. E. Ponchak, "Analysis of shielded CPW discontinuities with air bridges," in *Proc. IEEE Microwave Theory and Techniques mposium*, pp. 469–472, 1991.

[12] M. Rittweger, M. Abdo, and I. Wolff, "Full–wave analysis of coplanar discontinuities considering three–dimensional bond wires," in *Proc. IEEE Microwave Theory and Techniques Symposium*, pp. 465–468, 1991.

[13] A. A. Omar and Y. L. Chow, "A solution of coplanar waveguide with air–bridges using complex images," *IEEE Trans. Microwave Theory Tech.*, vol. 40, no. 11, pp. 2070–2077, 1992.

[14] D. M. Sheen, S. M. Ali, M. D. Abouzahra, and J. A. Kong, "Application of the three-dimensional finite–difference time–domain method to the analysis of planar microstrip circuits," *IEEE Trans. Microwave Theory Tech.*, vol. 38, no. 7, pp. 849–857, 1990.

[15] G. Mur, "Absorbing boundary conditions for the finite difference approximation of the time domain electromagnetic field equations," *IEEE Trans. Electromagn. Compat.*, vol. EMC–23, no. 4, pp. 377–382, 1981.

[16] K. K. Mei and J. Fang, "Superabsorption — A method to improve absorbing boundary conditions," *IEEE Trans. Antennas Propagat.*, vol. AP–40, no. 9, pp. 1001–1010, 1992.

[17] X. Zhang, J. Fang, and K. K. Mei, "Calculations of the dispersive characteristics of microstrips by the time–domain finite–difference method," *IEEE Trans. Microwave Theory Tech.*, vol. MTT–36, no. 2, pp. 263–267, 1988.

[18] X. P. Lin and K. Naishadham, "Geometry Rearrangement Technique — A new method for the FDTD analysis of dispersion in planar transmission lines," *IEEE Trans. Microwave Theory Tech.*, submitted.

[19] X. P. Lin and K. Naishadham, "Application of the geometry rearrangement technique to the computation of S–parameters of microstrip discontinuities by the FDTD method," in preparation.

[20] S. B. Cohn, "Slot–line field components," *IEEE Trans. Microwave Theory Tech.*, vol. MTT–20, no. 2, pp. 172–174, 1972.

[21] A. A. Omar, Y. L. Chow, L. Roy, and M. G. Stubbs, "Effects of air–bridges and mitering on coplanar waveguide 90° bends: theory and experiment," in *Proc. IEEE Microwave Theory and Techniques Symposium*, pp. 823–826, 1993.

Optical Properties of $Al_xGa_{1-x}As/Al_yGa_{1-y}As$ Quantum Wells Grown by Molecular Beam Epitaxy Using Desorption Mass Spectrometry for Composition Control.

Leon Radomsky

Graduate Research Assistant
Department of Chemical Engineering, Materials Science
and Mining Engineering

Columbia University
1137 S.W. Mudd
New York, NY 10027

Final Report for:
Graduate Student Research Program
Wright Laboratory
Dayton, OH 45433

Sponsored by:
Air Force Office of Scientific Research
Bolling Air Force Base, Washington, D.C.

August 1993

Optical Properties of $Al_xGa_{1-x}As/Al_yGa_{1-y}As$ Quantum Wells Grown by Molecular Beam Epitaxy Using Desorption Mass Spectrometry for Composition Control.

Leon Radomsky
Graduate Research Assistant
Department of Chemical Engineering, Materials Science and Mining Engineering
Columbia University

Abstract

We report the ability to produce high optical quality $Al_xGa_{1-x}As/Al_yGa_{1-y}As$ quantum well structures by molecular beam epitaxy (MBE) using the in-situ sensor technique of desorption mass spectrometry (DMS) for composition control. Growth takes place at elevated substrate temperatures for which the Ga incorporation efficiency is significantly below unity. Under constant incident Ga and Al fluxes, there is a one to one correspondence between composition and Ga desorption rate $F_d(Ga)$. Continuous composition control is achieved by controlling the measured value of $F_d(Ga)$ to that required to achieve the desired composition, via feedback of the desorption error signal to the arsenic source valve. A decrease in incident arsenic flux $F_i(As_2)$ causes an increase in $F_d(Ga)$. In order to examine the ability of DMS-control to provide rapid and controllable composition variations, two (2) nominally identical $Al_xGa_{1-x}As/Al_yGa_{1-y}As$ square quantum well structures were grown using: 1) conventional composition control, and 2) $F_i(As_2)$/DMS-control. The structures were characterized by low temperature photoluminescence (PL) and room temperature photoreflectance (PR) spectroscopy. Excitonic transitions were observed only in the quantum well of the DMS control structure.This structure had a high PL efficiency and a narrow line width.

Optical Properties of $Al_xGa_{1-x}As/Al_yGa_{1-y}As$ Quantum Wells Grown by Molecular Beam Epitaxy Using Desorption Mass Spectrometry for Composition Control.

Leon Radomsky

1. Introduction

The ability to produce III-V epitaxial heterostructures with improved optical properties via molecular beam epitaxy (MBE) is of great technological importance. Recently it was shown [1] that the implementation of the technique of desorption mass spectrometry (DMS) in a real-time feedback loop for continuous monitoring and control of layer composition during growth provided superior composition control to that of conventional MBE under conditions for which desorption is significant. Compositionally graded AlGaAs structures for which the composition varied smoothly were produced and characterized. No attempt was made to produce sharp heterointerfaces, although it was shown [2] that by incorporating the incident arsenic flux $F_i(As_2)$ into the DMS-control loop, rise and fall times of less than 1 second can be achieved. Additionally, nominally constant composition AlGaAs layers grown under DMS-control were found to have superior optical properties compared to AlGaAs grown by conventional MBE, which is consistent with previous studies [1] showing improvement of AlGaAs optical quality at high substrate temperatures T_s.

This study examines the ability of DMS-control to provide for the growth of high quality $Al_xGa_{1-x}As/Al_yGa_{1-y}As$ square quantum well structures. Growth takes place at elevated substrate temperatures for which the Ga incorporation efficiency is significantly below unity. Under constant incident Ga and Al fluxes, there is a one to one correspondence between composition and Ga desorption rate $F_d(Ga)$. Continuous composition control is achieved by making the

measured value of $F_d(Ga)$ conform to the value that is required to achieve the desired composition, via feedback of the desorption error signal to either the substrate temperature controller or to the arsenic source valve. A decrease in incident arsenic flux $F_i(As_2)$ causes an increase in $F_d(Ga)$. In order to examine the ability of DMS-control to provide rapid and controllable composition variations, two (2) nominally identical $Al_xGa_{1-x}As/Al_yGa_{1-y}As$ square quantum well structures were grown using: 1) conventional MBE composition control, and 2) $F_i(As_2)$/DMS-control. Also, another structure with different aluminum mole fraction in the well was grown using $F_i(As_2)$/DMS control to examine the effect of Al mole fraction on the optical properties of square quantum well heterostructures. The structures were characterized by low temperature photoluminescence (PL) and room temperature photoreflectance (PR) spectroscopy.

2. Experimental Procedure

A detailed description of the growth apparatus can be found elsewhere and is not repeated here [1]. We use a commercial solid source III-V MBE growth chamber, equipped with a differentially pumped, cooled, shuttered, high resolution quadrupole mass spectrometer (QMS). The QMS and its housing are attached to the source flange center port and are aligned via a series of baffles such that only the substrate is imaged by the QMS ionization region.

For DMS controlled growth the incident Ga and Al fluxes must be chosen to enable the desired composition modulation. Figure 1 shows the range of AlGaAs composition available, when $F_d(Ga)$ is varied, for differing incident Ga/Al flux ratios. The Ga incorporation efficiency α_{Ga} is the ratio of the Ga incorporation rate to the incident Ga flux $F_i(Ga)$ and is given by:

It is seen from Fig. 1 that 1) high incident Ga/Al flux ratios

$$\alpha_{Ga} = 1 - \frac{F_d(Ga)}{F_i(Ga)} \qquad (1)$$

provide for the largest composition modulation, 2) the sensitivity of composition to α_{Ga} is greatest at low α_{Ga} values, 3) low x-values require high Ga/Al flux ratios. Additionally, the ability to control $F_d(Ga)$ is finite for intermediate values of α_{Ga} but vanishes at α_{Ga} = 0 and 1. Considering these issues, in order to produce $Al_{.5}Ga_{.5}As/Al_{.15}Ga_{.85}As/Al_{.5}Ga_{.5}As$ quantum wells the incident Ga/Al flux ratio was chosen to be 10, which provides for compositions of x = .5 and .15 at values of α_{Ga} = .1 and .57 respectively. The magnitude of incident Ga and Al flux were chosen to provide for reasonable growth rates. We used $F_i(Ga)$ = 1.0 ML/s and $F_i(Al)$ = 0.1 ML/sec to give growth rates of 0.2 ML/s and 0.67 ML/s at x = 0.5 and 0.15, respectively.

The gallium desorption rate, $F_d(Ga)$, is continuously monitored by the QMS. This rate is compared to the desired $F_d(Ga)$, which can be calculated from the aluminum mole fraction, x:

$$x = \frac{F_i(Al)}{F_i(Al) + F_i(Ga) - F_d(Ga)} \qquad (2)$$

where the incident aluminum flux, $F_i(Al)$, and the incident gallium flux, $F_i(Ga)$, are determined from reflective high energy electron diffraction (RHEED) oscillations observed at low substrate temperature. The resulting error signal is then minimized by appropriately varying $F_i(As_2)$ with the use of a stepper-motorized, valved arsenic cracker, because from the law of mass action,

$$F_d(Ga) \propto [F_i(As_2)]^{-1/2} \qquad (3)$$

as previously verified for GaAs and AlGaAs growth [3].

$F_d(Ga)$ can also be controlled by varying the power to the substrate heater because $F_d(Ga)$ exhibits an Arrhenius-like behavior with substrate temperature, T_s [3]:

$$\frac{\Delta F_d(Ga)}{F_d(Ga)} = \frac{E_a}{kT_s}\frac{\Delta T_s}{T_s}$$

where E_a is the activation energy for Ga desorption and k is Boltzmann's constant. However, a T_s/DMS structure was not grown because it was shown [2] that such structures have slower rise times and a large amplitude of "ringing" associated with PID controllers. This is due to the slower response and higher sensitivity of $F_d(Ga)$ to changes in T_s than in $F_i(As_2)$. The slower response of $F_d(Ga)$ to T_s setpoint change is largely due to the large thermal mass of the Mo substrate holder. The higher sensitivity of $F_d(Ga)$ to T_s than to $F_i(As_2)$ can be seen from equations 2 and 3; in fact a 5-6 fold change in $F_i(As_2)$ gives rise to the same change in $F_d(Ga)$ as a T_s setpoint change of less than 4% [1].

A 20 nm $Al_{0.5}Ga_{0.5}As$, 10 nm $Al_{0.15}Ga_{0.85}As$, 20 nm $Al_{0.5}Ga_{0.5}As$ quantum well heterostructure was first grown on top of 500 nm of GaAs by $F_i(As_2)$/DMS control at 720 °C (A) and by conventional composition control at 620 °C (B). In order to compare their optical and structural properties, low temperature photoluminescence (PL) and room temperature photoreflectance (PR) measurements were then performed on the structures. Another heterostructure (C), identical to A, with the exception of Al=0.25 in the well, was grown to compare the effect of aluminum mole fraction on the optical properties of heterostructures.

The PL spectra were excited with a tunable dye laser using

Styryl 9 dye, which was pumped with an Ar^+ ion laser. The maximum pump power used was approximately 500 mW cm^{-2}. All measurements were made at 2K with the sample immersed in liquid He. The spectra were analyzed with a high resolution 4-m spectrometer equipped with an RCA C31034A photomultiplier tube for detection.

3. Results and discussion

The DMS-control structures, which were grown at higher T_s, are expected to have better optical properties than the conventional MBE structure, due to the increase in surface mobility of the adsorbed species at higher substrate temperatures.

Fig. 2 shows the gallium desorption signal versus time for sample A, and Fig. 3 shows the same for sample C. F_d(Ga) of the low T_s structure (B) is insignificant. There is a slight irregularity in Fig. 2, but the signal in Fig. 3 is nearly identical to the desired gallium desorption profile. Expansion of this data (Fig. 4), shows a rise time (between 10% and 90%) to be approximately 1 second, similar to that found in [2]. The fast response in DMS-controlled structures indicates that monolayer composition control is possible with this approach, since all growth rates were below 1 ML/s.

The low temperature photoluminescence (PL) spectra of the conventional control structure (B) is shown in Fig. 5. Shown are the bound exciton, free to bound and donor acceptor pair transitions from the GaAs buffer layer. The peak at 1.5091 eV, on the low energy side of the bound excitons has been identified as H-band A [4,5]. No peak attributed to excitonic transitions (bound and/or free) in the AlGaAs well was observed. The spectra for the DMS control structure (A) is shown in Fig. 6. Shown are the bound exciton, H-band A (1.5101 eV), free to bound and donor acceptor

pair transitions from the GaAs buffer layer. A peak attributed to excitonic transitions (bound and/or free) in the AlGaAs well is shown In Fig. 7 at 1.7476 eV, corresponding to x=0.15. This peak was 9.5 times greater than the bound exciton peaks in Fig. 6, and is therefore shown on a separate figure. The observed peak attributed to AlGaAs well excitonic transitions had a peak width (FWHM) of 10 meV. A peak attributed to excitonic transitions (bound and/or free) in the AlGaAs well of sample C is shown in Fig. 8 at 1.9594 eV, corresponding to x=0.29. This peak had width (FWHM) of 20 meV. Therefore, a smoother desorption profile does not necessarily guarantee a narrower peak due to excitonic transitions in the well.

The PR spectra of the conventional control sample B (Fig. 9) show the signature of GaAs near 1.43 eV and features at 1.772 eV and 2.7174 eV corresponding to aluminum mole fraction (x) values of 0.24 (well) and 0.52 (barrier), respectively. The aluminum mole fraction for the well of this sample is off by 0.09, and is actually closer to sample C then sample A. PR spectra of sample A (Fig. 10) leads to x values of 0.17 in the well and 0.5 in the barrier. In DMS control structures, well established incident Al and Ga fluxes of 0.1 and 1 ML/sec respectively are always used. These fluxes are well calibrated over time, and RHEED is used only to check the incident fluxes. However, in conventional MBE growth, different incident Al and GA fluxes are used in each structure, and RHEED is only source to establish the new incident fluxes. It comes as no surprise that DMS control structure has a more accurate composition profile than a conventional MBE structure.

In conclusion, we report the ability to grow high optical quality $Al_xGa_{1-x}As/Al_yGa_{1-y}As$ quantum well structures by molecular beam epitaxy (MBE) using the in-situ sensor technique of desorption mass spectrometry (DMS) for composition control. The $F_d(Ga)$ rise times of 1 sec. indicate that monolayer composition control is possible with this approach. From the PL spectra, it can be seen

that the optical properties of this structure were superior to the structure grown by conventional MBE.

Acknowledgements

The author is thankful to K.R. Evans and C.R. Jones for their invaluable guidance and support, without whom this report would not be possible, and to D.C. Reynolds, R.E. Sherriff, John Hoelscher, Cole Litton, and Gary McCoy for their technical assistance. Work was performed at Wright-Patterson Air Force Base.

References

[1] K.R. Evans, R. Kaspi, C.R. Jones, R.E. Sherriff, V.Jogai and D.C. Reynolds, J. Crystal Growth **127**, 523 (1993).

[2] K.R. Evans, R. Kaspi, W.T. Cooley, C.R. Jones and J.S. Solomon, Proc. MRS Spring 1993 Meeting.

[3] J.M. Van Hove and P.I. Cohen, Appl. Phys. Lett. **47**, 726 (1985).

[4] See for ex. Y.R. Yuan, M.A.A. Pudensi, G.A. Vawter and J.L. Merz, J.Appl. Phys. **58**, 397 (1985); I.V. Kukushkin, K.V. Klitzing and K. Ploog, Phys. Rev., **B45**, 8509, (1988)

[5] D.C. Reynolds, L. Radomsky, V.Jogai, D. Look, K.R. Evans, et.al., to be published. (This work was also part of my summer project, but is not included in this report)

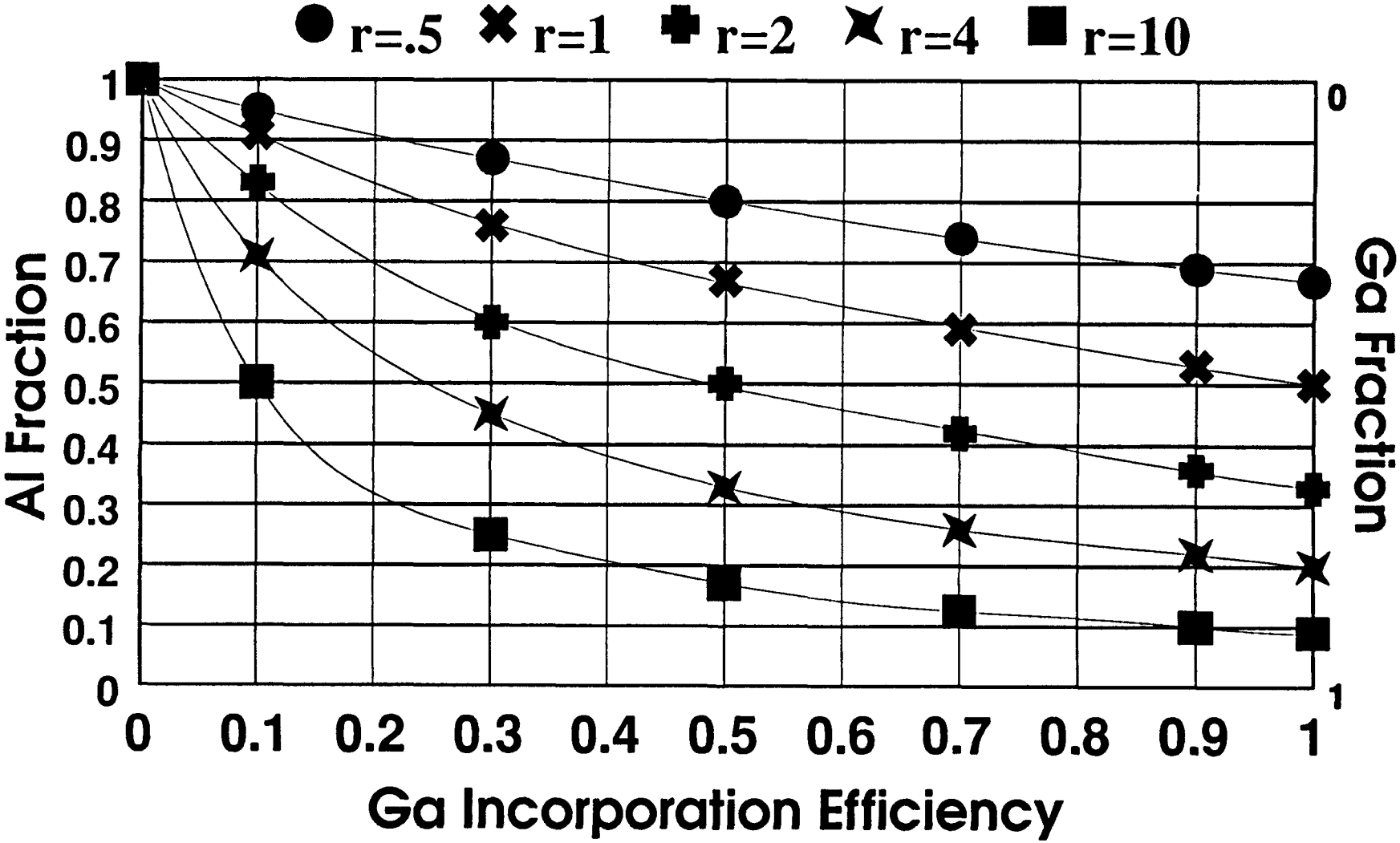
r=.5
r=1
r=2
r=4
r=10
Al Fraction
1
0.9
0.8
0.7
0.6
0.5
0.4
0.3
0.2
0.1
0
0
0.1
0.2
0.3
0.4
0.5
0.6
0.7
0.8
0.9
1
Ga Incorporation Efficiency
Ga Fraction
0
1

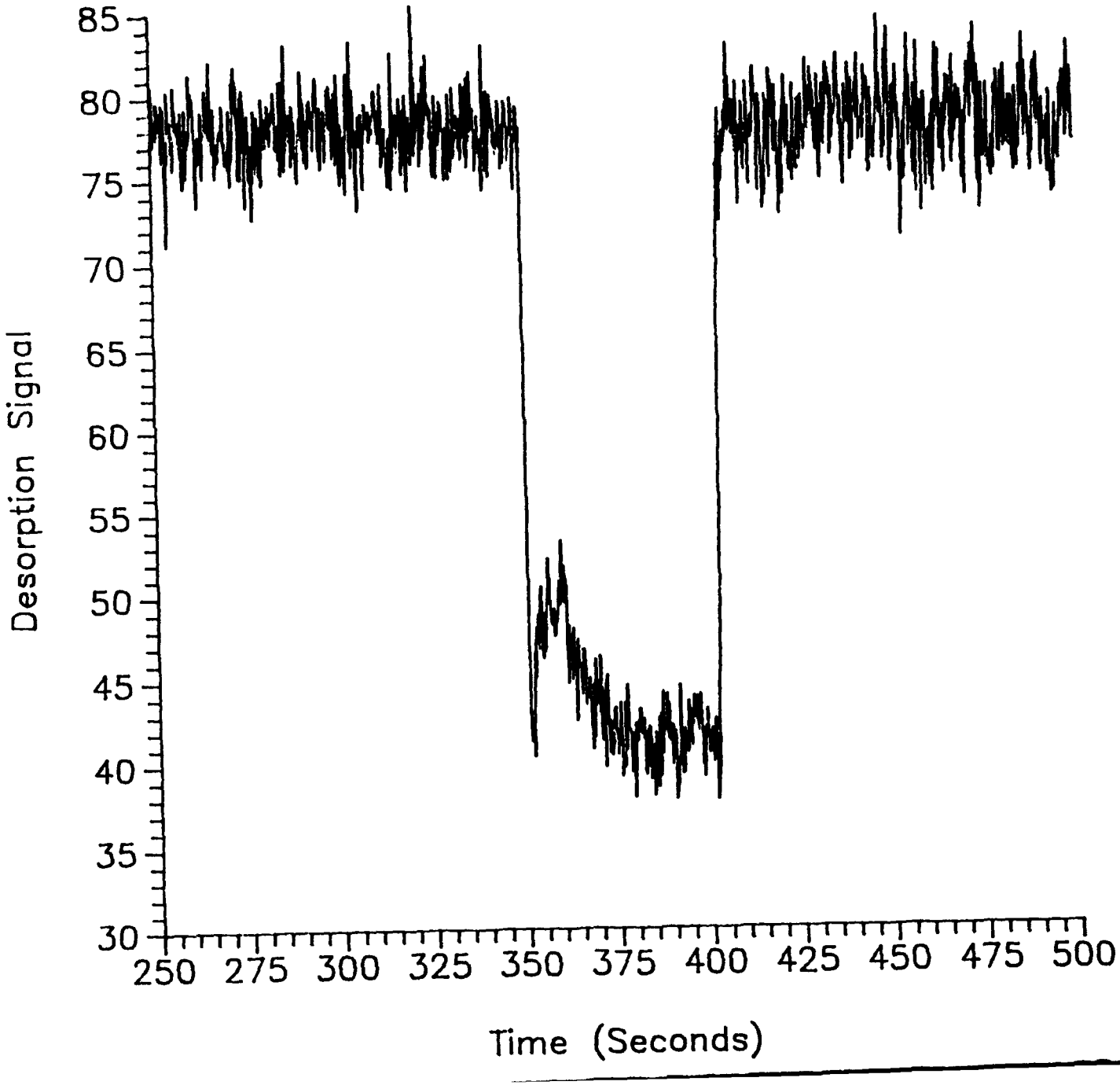
Desorption Signal
85
80
75
70
65
60
55
50
45
40
35
30
250
275
300
325
350
375
400
425
450
475
500
Time (Seconds)

FIGURE 3

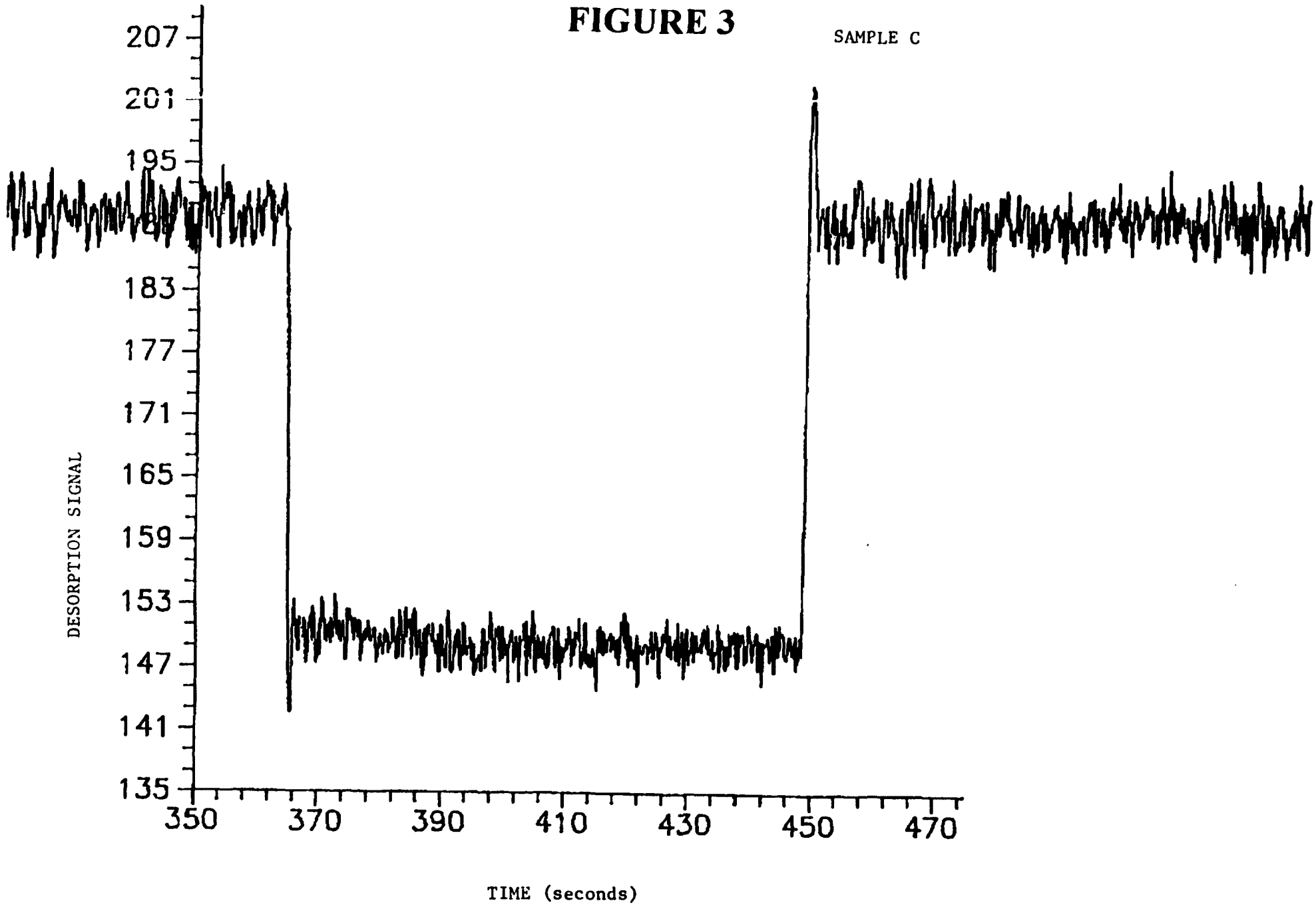
SAMPLE C
DESORPTION SIGNAL
207
201
195
183
177
171
165
159
153
147
141
135
350
370
390
410
430
450
470
TIME (seconds)

FIGURE 4

SAMPLE C

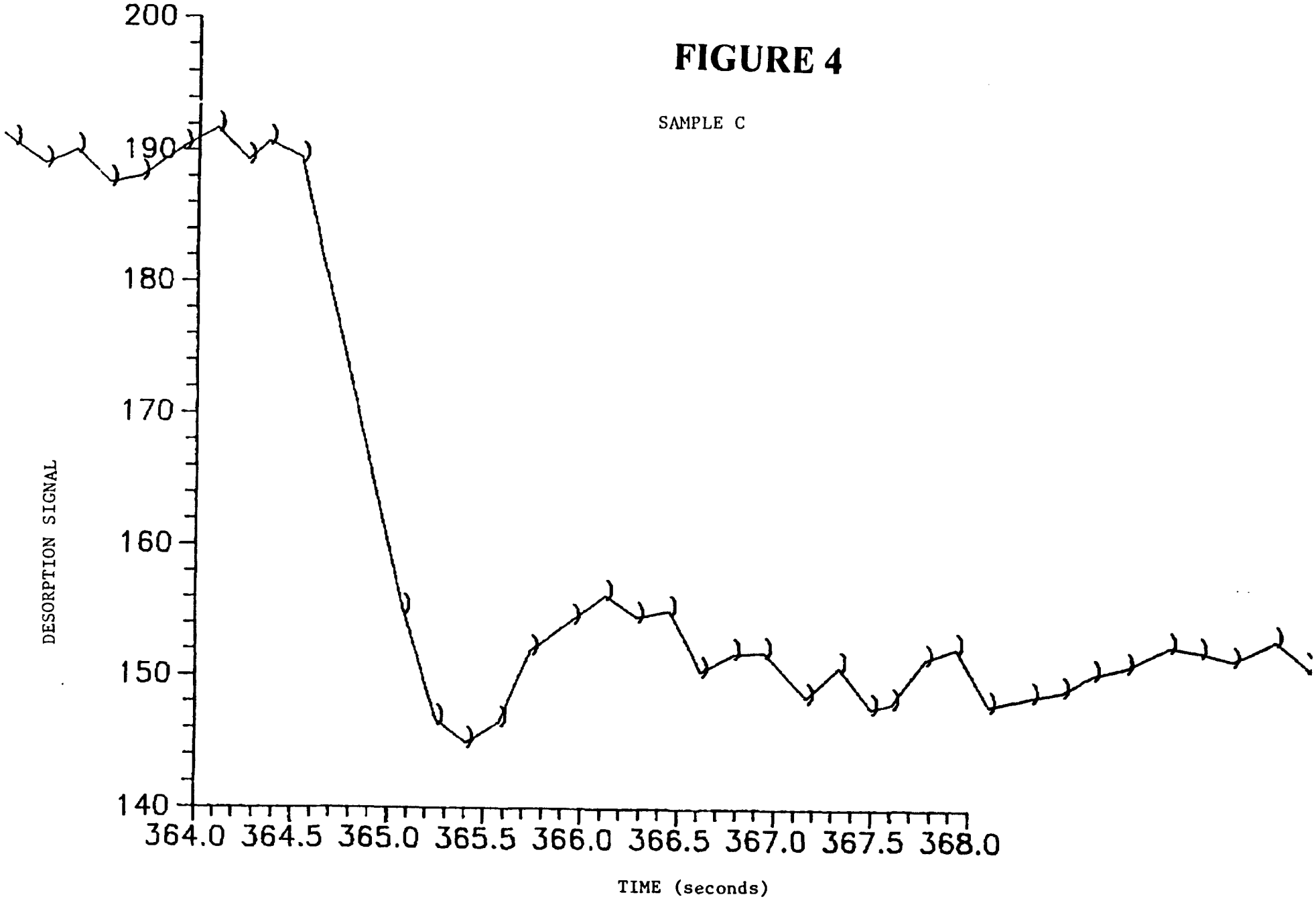

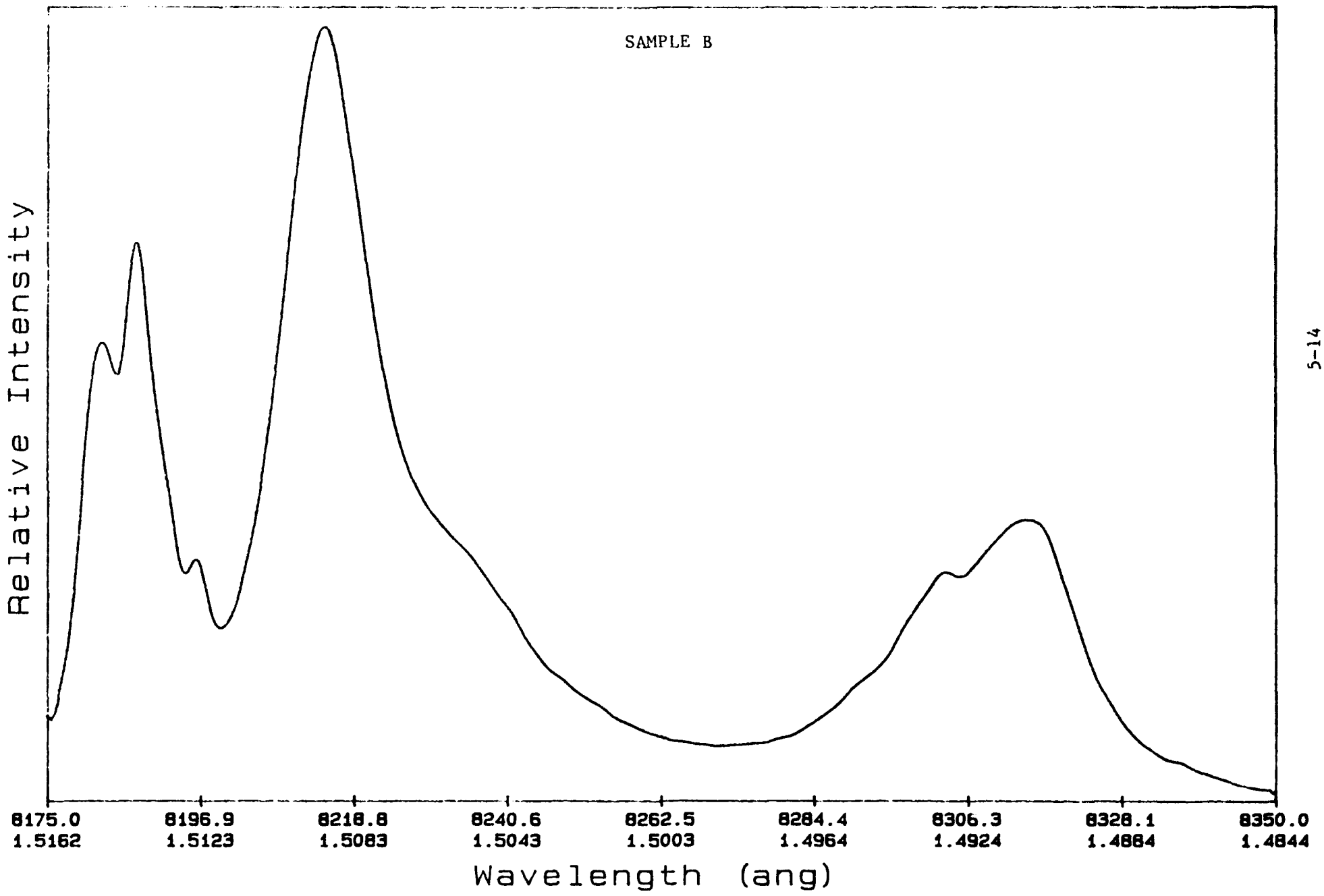
SAMPLE B
Relative Intensity
8175.0
1.5162
8196.9
1.5123
8218.8
1.5083
8240.6
1.5043
8262.5
1.5003
8284.4
1.4964
8306.3
1.4924
8328.1
1.4884
8350.0
1.4844
Wavelength (ang)

FIGURE 6

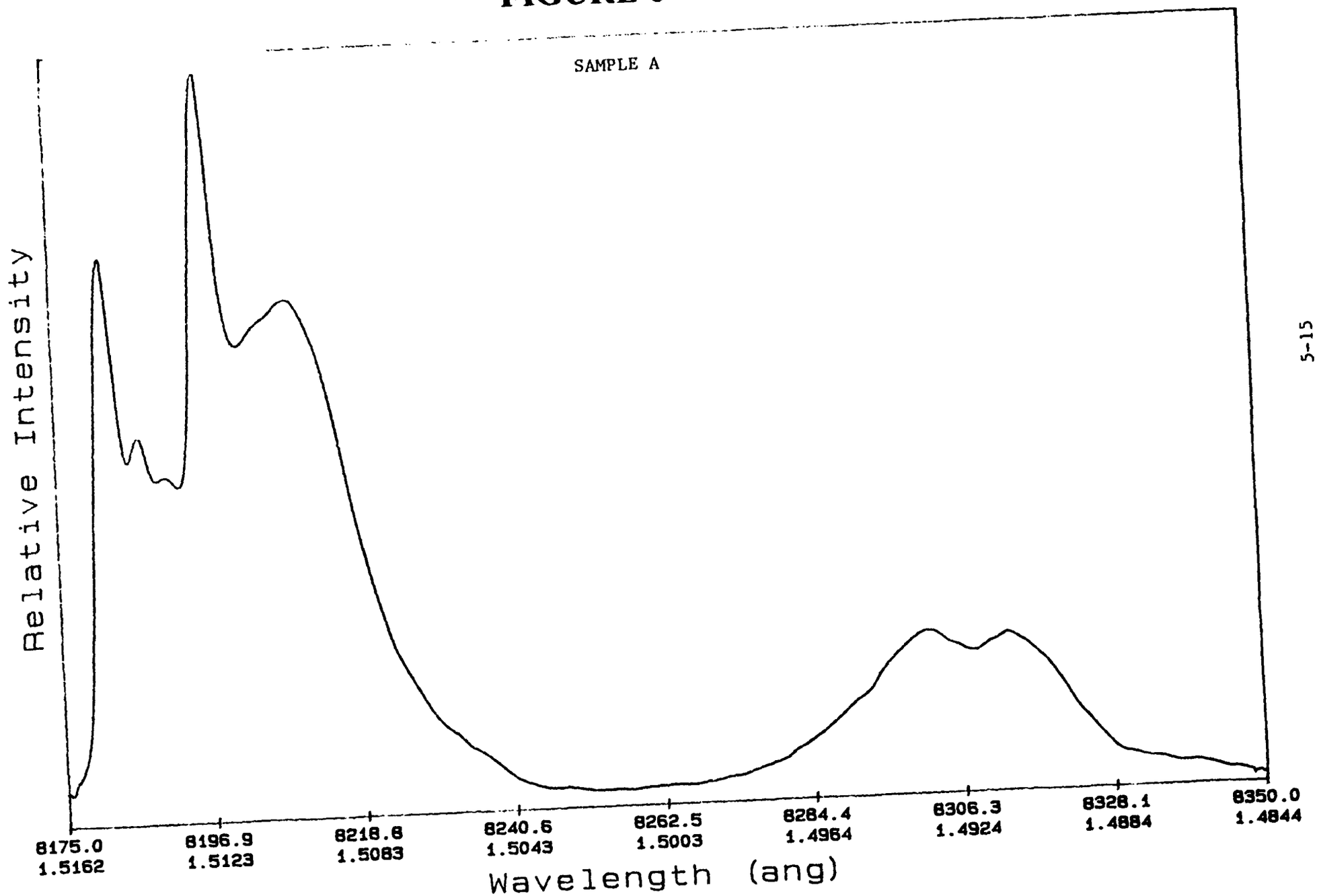
SAMPLE A
Relative Intensity
8175.0
1.5162
8196.9
1.5123
8218.8
1.5083
8240.6
1.5043
8262.5
1.5003
8284.4
1.4964
8306.3
1.4924
8328.1
1.4884
8350.0
1.4844
Wavelength (ang)

FIGURE 7

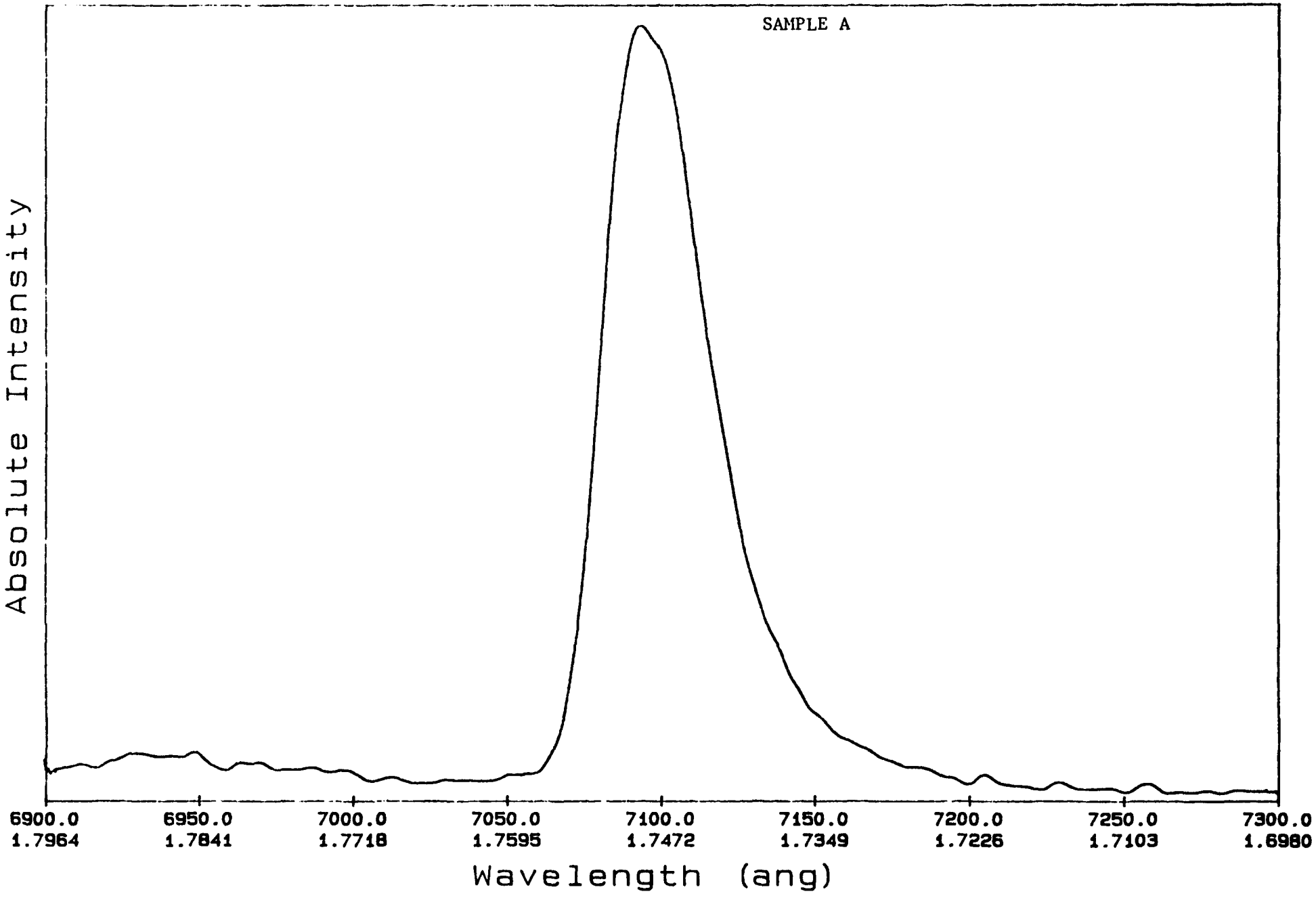
SAMPLE A
Absolute Intensity
6900.0
1.7964
6950.0
1.7841
7000.0
1.7718
7050.0
1.7595
7100.0
1.7472
7150.0
1.7349
7200.0
1.7226
7250.0
1.7103
7300.0
1.6980
Wavelength (ang)

FIGURE 8

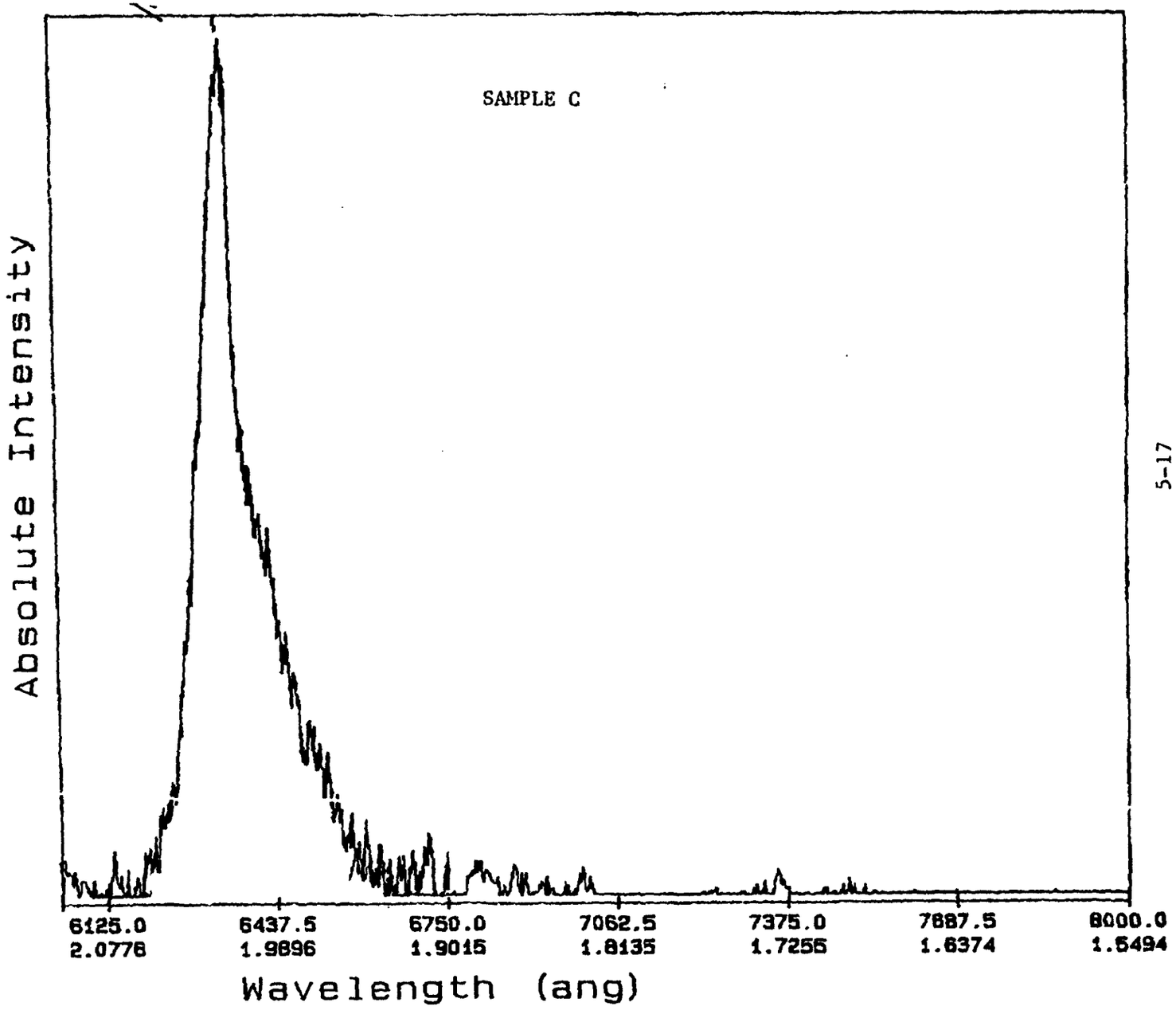
SAMPLE C
Absolute Intensity
6125.0
2.0776
6437.5
1.9896
6750.0
1.9015
7062.5
1.8135
7375.0
1.7255
7687.5
1.6374
8000.0
1.5494
Wavelength (ang)

FIGURE 9

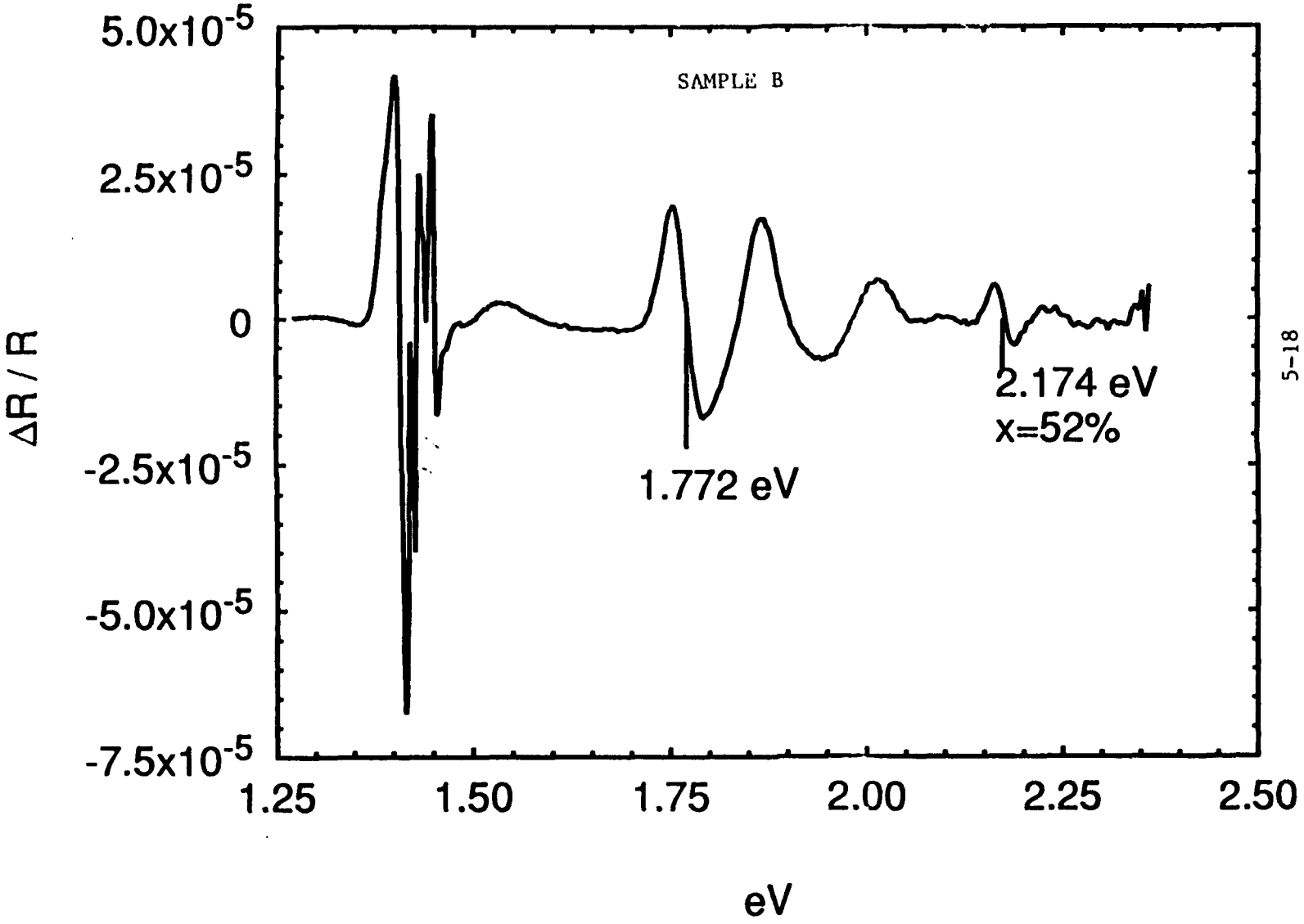
SAMPLE B
5.0x10-5
2.5x10-5
0
-2.5x10-5
-5.0x10-5
-7.5x10-5
ΔR / R
1.25
1.50
1.75
2.00
2.25
2.50
eV
1.772 eV
2.174 eV
x=52%

FIGURE 10

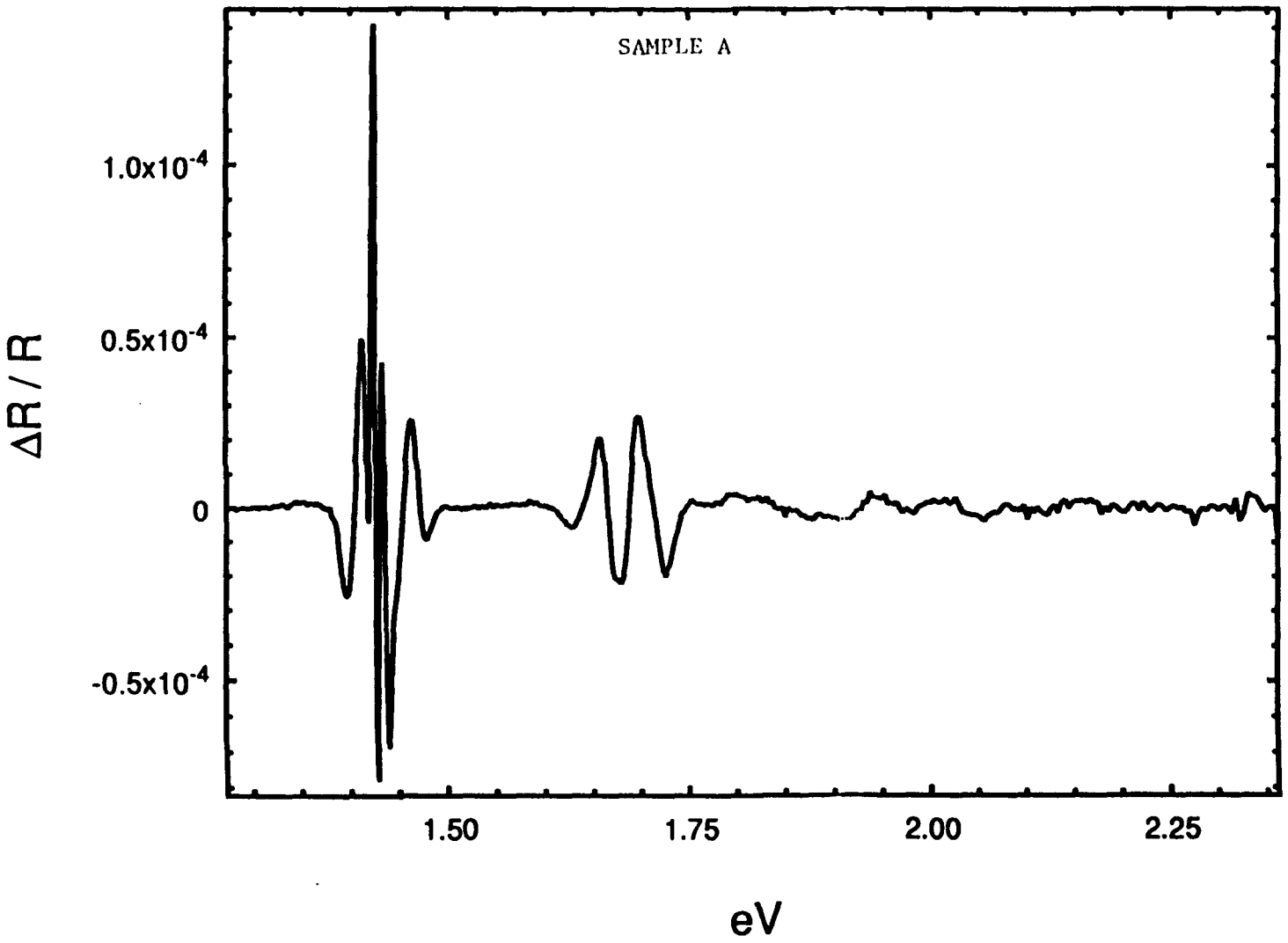

FEASIBILITY INVESTIGATION OF IN-HOUSE EDGE EMITTING SEMICONDUCTOR LASER FACET COATINGS

Vincent E. Stenger
Graduate Student
Department of Electrical Engineering
University of Cincinnati

The feasibility of reactive ion sputtering for deposition of high reflectivity dielectric stacks has been investigated. Two dielectric material systems were attempted; SiO_2/Si and Al_2O_3/Si. The specific laser material system was an InGaAs/GaAs/AlGaAs quantum well layer structure operating at about .92 um (Pseudomorphic InGaAs quantum well with GaAs optical guiding layers). During the course of the work, it was determined that cross contamination was occurring in the sputtering chamber between dielectric sputtering depositions and metal sputtering depositions performed for other projects. This contamination showed up in the form of absorbing dielectric layers and peeling metal layers. It was found that a moderate cleaning and pre-sputtering decontamination scheme was not sufficient to eliminate the contamination problems. An alternate reflector scheme utilizing a more basic Al/Si_3N_4 metal/insulator configuration (Si_3N_4 deposited by Chemical Vapor Deposition) was studied and fabrication was initiated. These coatings should theoretically yield reflectivities of up to 90% (vs. 35% for uncoated GaAs). Finally, MathCAD documents were developed to optimize multilayer designs, and to model ellipsometric measurements of the refractory coatings for extraction of optical constants and thicknesses.

INTRODUCTION

Although edge emitting lasers may often lase quite well without reflective end facet coatings, performance may be substantially enhanced by the addition of this relatively low cost step. In addition to passivation of facets (protection of surfaces from the elements during high temperature operation), high wavelength selectivity reflectance coatings offer lower threshold currents (scales linearly with reflectance of each facet) and higher mode locking thresholds. Mode locking threshold is the measure of the spectral purity of the optical output vs. power. Passivation of end facets is especially important for higher power operation, since there is usually significant facet absorption loss and catastrophic optical damage associated with uncoated facets. All this boils down to a faster, higher temperature, and more efficient laser. The purpose of this work was to determine if laser facet coatings could be performed with equipment currently available at the WL/ELRD WPAFB, Dayton, Ohio clean room facility.

METHODOLOGY

Figure 1 illustrates the addition of two common types of optical/passivation coatings suitable for laser end facets. In Fig 1a, the coating consists of a highly wavelength selective dielectric stack (DS) of alternating high-low index materials. The selectivity stems from the fact that the layers are all 1/4 design-wavelength optical thicknesses or .25 l/n). For no optical phase shifts at the interfaces (as in the case of non-absorbing dielectrics), and a top layer of high index, this structure will optically resonate at the design wavelength. This means the interface will be highly reflective to the design wavelength. On the other hand, removal of the top high index layer will tend to reduce this effect, tending toward a non-reflective coating. Conversely, if one were to flip the order of the high-low sequence, a highly anti-reflecting coating would be achieved (or use 1/2 l films for a destructive interference cavity).

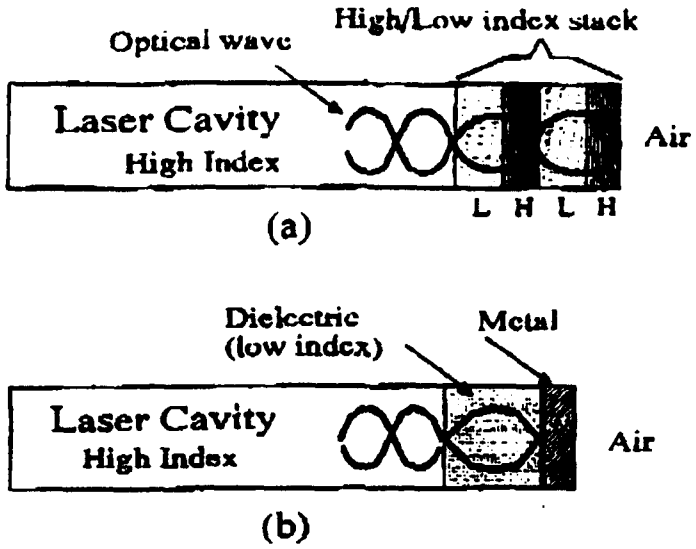

Fig 1 : Two types of semiconductor laser facet coatings
(a) Dielectric stack (DS), and (b) Insulator/metal (IM)

The big advantage of the DS scheme is in wavelength selectivity and flexibility of design. Sensitivity of the design to material refractory properties, thicknesses, and selective removal of high or low index layers offers a virtual continuum of reflectivity from 0 to near 1 (total reflection) around the operating wavelength. Reflectances approaching 1 (total reflection) are possible merely by the addition of more dielectric pair layers to the DS, or by using dielectric pairs of higher index differences. Figure 2 shows a typical sample plot of reflectance vs. DS layer structure[]. The reflectance as one deposits more layers is shown. These plots are typically derived empirically or by numerical analysis techniques.

< scan in the Al2O3/Si reflectance vs. depth plot >

Fig 2 : Reflectance plot for variation in the 1/4 wave dielectric stack structure

The IM design is simpler but also more constrained. The reflectance of the coating is determined to some extent by the thickness and composition of the insulator layer but chiefly by the type of metal used. There is very little wavelength selectivity since there is only one filtering layer (Si_3N_4 in this case). Furthermore, there is the danger that the metal layer may not survive the post-fabrication soldering/bonding process (especially if Gold or other delicate films were used). Finally, there is the issue that pinholing of the insulator layer would mean shorting out of the laser active region. On the plus side, the IM technique is inherently low cost, delivers repeatable reflectances up to .9 (typical for aluminum at about .85 um wavelength), and could be readily implemented with

the Si_3N_4 CVD and Al evaporator process available in-house. In addition, the Si_3N_4 CVD system has the added advantage that it is an almost isotropic deposition technique. That is, the vertical facet sidewalls are coated almost as well as the top surface of the sample. This means that no special fixturing of the laser "bar" samples would be necessary. This is in stark contrast to the DS design, which was to be implemented by the reactive ion sputtering technique.

Although DS structures have traditionally been deposited by e-beam evaporation[],[],[], there are others that have been successful at using reactive ion sputtering to deposit the dielectric materials [],[]. For this study, SiO_2 and Al_2O_3 test films were sputter deposited using in-house equipment. These test films served to determine the sputter process characteristics such as deposition rate and power for an optimum process, as well as film quality. Several DS structures were selected and implemented via sputtering, while IM structures were deposited by the alternate CVD/Evaporator process. Sputtering of dielectric coatings was performed on blank Silicon and GaAs substrates for a first phase characterization (thickness and n,k optical constants). In addition, two DS coatings (one 2-layer and one 4-layer) were deposited on blank Si and GaAs substrates to determine the multilayer characteristics of the sputtered DS coatings. Optical characteristics were determined by both single wavelength and spectroscopic ellipsometry. Design of all coatings was facilitated by the development of multilayer ellipsometry (variable polarization and incidence angle reflectance) calculation software (MathCAD). Calculation results for 70 degree incidence ellipsometry and normal incidence reflectance (using near zero degree ellipsometry equations) were compared to measured ellipsometry and spectroscopic normal reflectance measurements to confirm the spectroscopic optical characteristics of the individual films relative to the substrate , and of the multi-layers.

First phase design of the IM coatings was completed using the same software. Here, the GaAs was treated as the incident medium, the Si_3N_4 dielectric was the "top" film, while the highly absorbing/reflecting Aluminum film was treated as the "substrate". After a optimal nitride thickness was calculated, Si_3N_4/Al IM coatings of several Si_3N_4 thicknesses (around the calculated optimum) were deposited via plasma enhanced CVD (for Si_3N_4) and e-beam evaporation (for Al) on blank GaAs substrates. The GaAs substrates were subsequently thinned (by lapping) to enable backside GaAs/Coating reflectance spectroscopy measurements. A blank GaAs substrate was also thinned for comparative reflectance measurement purposes. The measurement would only be made over the GaAs transparent region ($l > 870$ nm). This would include the design wavelength of 920 nm.

EXPERIMENTAL

Dielectric Stack Sputterings

Sputterings were all performed in a Randex Model 2400-8J 8" sputtering system. Argon gas was used as the plasma gas source at plasma RF powers of 300 to 400 Watts typical. The target sources tested were Al_2O_3, Si, and SiO_2. Preparation of substrates included an Acetone-Methanol-Acetone-D.I. water degrease with a N_2 blow dry. Substrates were loaded onto the center of the sample stage, with a shadow mask resting or clamped on the surface. This mask served for step height measurements after deposition. The chamber was then sealed and pumped down to less than .1 mTorr. After the deposition pressure (20 mTorr typical) and Argon flow (57 ccm typical) was established, a 5 minute pre-sputter at 500 Watts was performed to clean the target. Manual tuning was performed to reduce reflected power to less than 5 Watts. The RF power was then reduced to the deposition power level, and the sample stage rotated to the deposition position for the given deposition time. At the end of the deposition, the RF power was cut, and the sample stage rotated back to the load/unload position. The chamber was then pumped back down to less than 10 mTorr to pump out residual gasses, then vented.

Step height measurements were performed on a DekTak mechanical stylus prober. Multiple incidence angle ellipsometer measurements were performed on a Gaertner auto-nulling ellipsometer connected to an IBM compatible computer and software. The Gaertner laser wavelength was a He-Ne line of 6328 Angstroms. The oxide film refractive index magnitude could be roughly determined from single film depositions on higher index substrates (Silicon), which enabled ellipsometry extraction of index magnitude and oxide thickness (these optically measured thicknesses were confirmed by the mechanical step height measurements). The single film Si depositions could not be as readily index characterized, however, since the expected index for the sputtered amorphous Si (n about = 3.8) was very close to the substrates (n = 3.7 for GaAs and n = 3.8 for Silicon substrates).

Since there were no readily available alternative substrates, the Si film index was to be verified through the ellipsometric analysis of multilayer depositions (Si on SiO_2 on Substrate, etc..). Table 1 lists all of the deposition settings and step height measurement results of sputtering runs performed in this work.

Table 1- Parameter settings and measurements of sputtering depositions in order of deposition

Sample ID	Target Material	Substrate	Sputter Power (W)	Sputter Time (min)	DekTak Step Ht (A)	Comments
GW6	Al_2O_3	Si	300	14	600-900	First Run; Poor Step
GW7	Al_2O_3	Si	300	20	1000-1200	Cleaved into two pieces
GW8	Al_2O_3	Si				Last Al_2O_3 Run
GW9	W	Si	300	10	1100-1200	10 min Pre-Sputter @ 500W 142 mW cm/ 4x less at anneal
GW10	SiO_2	Si	300	10	1,100	Deep purple color
GW11	SiO_2	Si	300	20	2000-3000	
GW12	W	Si	300	5' 15"	600-700	Co-deposit with R.Lee Sample same R as GW9/2x less at anneal
GW13	Si	Si	300	10	NA	Step mask slid off/cracked
GW14	Si	Si	300	15	300-400	ok
GW15	Si	Si	400	15' 30"	500	Dark Brown color
GW16	W	Si	300	5' 15"	450	Table low ; same R as GW9 2.5x less at anneal
GW??	W	Si	300	10	1,400	Table raised; thickness calib
GW19	Si	Si	400	15	600	Dot pattern; brownish color
GW20	SiO_2	Si	300	13' 20"		Arcing problem
GW21	Si	Si	400	15	600	Brownish purple/non-uniform
GW22	SiO_2	Si	300	13' 20"	1,400	
GW23	SiO_2 Si	Si	400 300	15 17	2100-2400 Overall	2-layer on Si $Si/SiO_2/Si$ Substrate
GW24	Si	GaAs	400	17	NA	Si on GaAs
GW25	SiO_2 Si SiO_2 Si	Si	300 400 300 400	17 15 17 15	NA	4-layer on GaAs Red pink to green color across wafer

Representatives of each medium (Si,SiO_2,Al_2O_3,GaAs substrate, Si Substrate) were measured by 70 degree incidence spectroscopic ellipsometry (SE). The ellipsometer used for this was a Rudolph S2000 system. The monochromater was set to sweep from 400 nm up to 850 nm (850 nm is the maximum wavelength for this system). It should be noted that in this work, the monochromator was located after the analyzer, hence light at all wavelengths from the source was incident on the sample. This can give rise to hysteresis through bleaching of

defects in the grown material. However, this did not seem to be a problem with the amorphous films of this work. SE results were input to the ellipsometry calculation program to verify the structure and performance of the multilayer coatings from 70 degree incidence single-wavelength ellipsometry (Gaertner). Y and D raw data was given by the system. The results of these measurements for the single film cases, as well as the expected (calculated) data, are given in Table 2. The "a-" prefix emphasizes that the films are amorphous (non-crystalline).

Table 2 Ellipsometry results of sputtered films (70° incidence angle)

Sample ID	Film	Assumed Thickness (A)	Calc #1 (from literature n.k)		Measured (Gaertner)		Calc #2 (from effective n.k)	
			Y(deg)	D(deg)	Y(deg)	D(deg)	Y(deg)	D(deg)
GW6	a-Al_2O_3	750	35	-110	10.82	153.9	12.4	-28.5
GW7	a-Al_2O_3	1,100	70	-140	11.99	152.6	13.7	-29
GW8*	a-Al_2O_3	1,100	70	-140	13.86	154.5	13.7	-29
GW10*	a-SiO_2	1,100	50	-100	49.7	87.23	38.2	-93.5
GW11	a-SiO_2	2,500	15	60	10.53	188.67	38.2	-93.8
GW22	a-SiO_2	1,400	80	50	69.83	105.91	38.2	-93.7
GW13	a-Si	300	14.2	-29	17.43	103.9	27.2	-87.5
GW14	a-Si	350	13.9	-32	22.57	89.29	28.5	-91
GW15*	a-Si	500	12.4	-35.5	31.81	72.48	31	-98
GW19	a-Si	600	11.6	-34	25.7	82.68	25.6	-100
GW20	a-Si	350	13.9	-32	78.08	120	28.5	-91
GW21	a-Si	600	11.6	-34	32.85	72.05	25.6	-100
GW24	a-Si	620	11.5	-33	36.7	67.63	31.5	-101
GW23 2-layer	Si SiO_2	600 1600	22.5	-58	30	270	33	-107
GW25 4-layer	Si SiO_2	600 1600	23	-64	23.6	84.4	32.5	-107
GW9	W	1,150	NC	NC	25.65	115.06	NC	NC
GW12	W	650	NC	NC	22.21	118.18	NC	NC
GW16	W	450	NC	NC	23.26	117.99	NC	NC
GW17	W	?	NC	NC	20.48	117.89	NC	NC
GW18	W	?	NC	NC	21.6	113.38	NC	NC

Note: NC = not computed

The first calculated values (Calc#1) were generated by the MathCAD ellipsometry program using $n(a\text{-}Al_2O_3) = 1.62$, $n(a\text{-}SiO_2) = 1.46$, $n(a\text{-}Si) = 3.8\text{-}.8j$, n of Si substrate = 3.8 - .17j, n of GaAs substrate = 3.7 - .65j Substrate data was measured directly, while the other values were gathered from literature. The second set of calculated values used effective indices measured from spectroscopic ellipsometry (see following) for the case of l = 632 nm. Measured effective indices will be seen to be especially valid at this wavelength due to the high absorption seen there (k > 1). (i.e. ellipsometry does not "see" the substrate effects at > 500 nm film thickness). Values used for Calc#2 were $n(a\text{-}Al_2O_3) = 3.8 - .8j$, $n(a\text{-}SiO_2) = .8 - 2.1j$, $n(a\text{-}Si) = 1 - 1.55j$. It is perhaps important to note that these calculated values apply especially to the particular samples measured spectroscopically (denoted by * in table), since there may be variations in the film characteristics from one sputtering run to the next. Note that the calculated D values are found to actually be "reference" angles for some of the cases (probably anomalies of the intrinsic "arg" function used). Using this observation, both of the Calc#2 values are seen to closely approach the measured values (especially Y). The Calc#1 values do not seem to even come close.

Representatives of the dielectric film materials used were measured spectroscopically on the Rudolph ellipsometer described earlier. The wavelength range was limited to 400 to 850 nm, so the design wavelength of 920 nm was not directly included. However, what the data did serve was to show that the films had an absorbing characteristic over a range of wavelengths near the design wavelength. This reinforced the metal-in-the-dielectric contamination theory. Fig 3 gives the calculated results of these measurements. It is important to note that the effective index should lie somewhere between the film index and the substrate index. Thus, if a k greater than the substrate is present, then this means that the film is very absorbing. The whole purpose for using dielectrics is that they are non-absorbing. Since the films are all seemingly absorbing, it is apparent that the films are not good dielectrics.

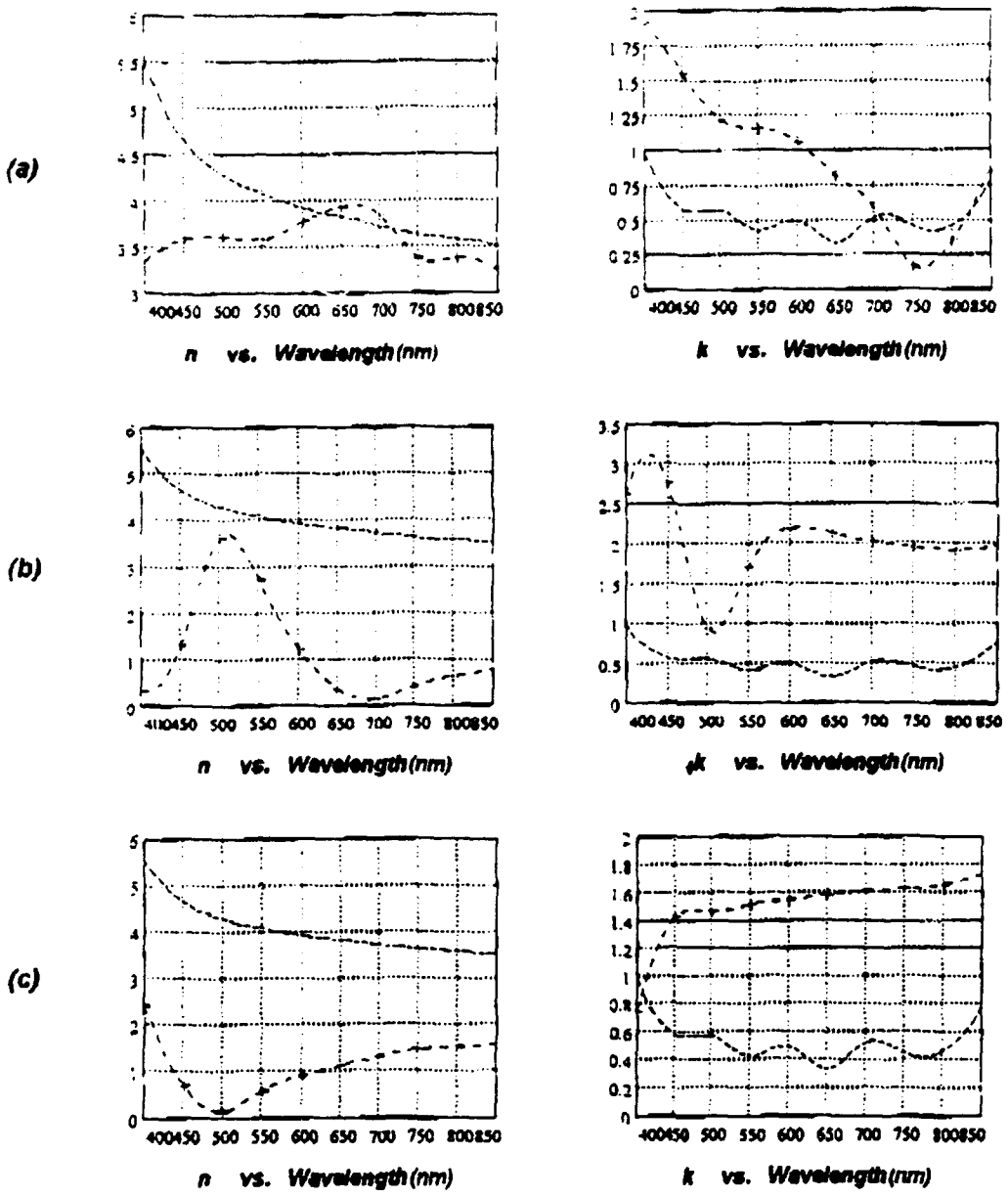

Fig 3 - Plots of effective n and k for the various dielectric film materials
(a) a-Al_2O_3 (GW8) (b) a-SiO_2 (GW10) (c) a-Si (GW15)
The dashed lines are the Silicon substrate values
Ellipsometry wavelength is 630 nm at 70° incidence

In addition to ellipsometry, the multilayer samples (GW23 and GW25) were measured by normal incidence reflectance spectroscopy. Normally incident "white" light (of known spectral characteristic) was directed normal to the sample, split, then angularly decomposed by a quartz prism onto a set of photodetectors. Results of calculated (expected) and measured spectroscopic normal reflectance for the two multi-layers are given in Fig 4. Two calculated plots are given. One assumes refractive indices taken from the literature. The other uses the effective indices measured on the Rudolph (Fig 3).

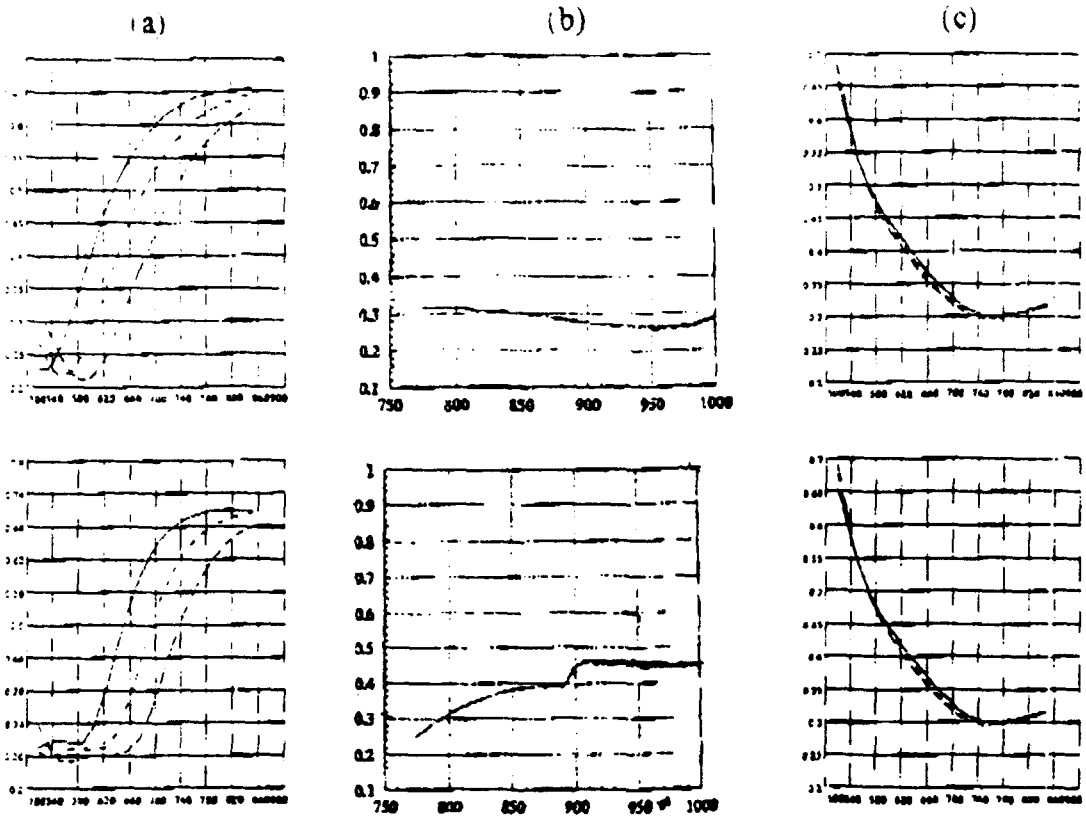

Fig 4 - Plots of calculated and measured reflectance for the two multilayer samples
(a) Calculated from literature n,k , (b) Measured ,
(c) Calculated using spectroscopic ellipsometer effective n,k measurements.
Top row is the 2-layer GW23, Bottom is 4-layer GW25
y axis is reflectance, x axis is wavelength (nm)

It is apparent from the plots that the multi-layers tended to be much closer to the absorbing layer calculation than to the plots calculated from reported film index values. That the measured 4-layer GW25 reflectance (lower middle) exhibits a characteristic substrate absorption kink at about 880 nm (GaAs band edge) indicates that the films for this sample are not quite as absorbing as some of the earlier runs measured spectroscopically on the ellipsometer. This could be due to the fact that more dielectrics were run (coating the chamber) right before, and during, this deposition.

CVD of Insulator / Metal Coatings

Design of IM coatings was performed using the same ellipsometry calculation software used for the DS work. Calculation of near-normal reflectance was performed using published n,k dispersion data for Aluminum (from Heavens), typical reported $n(Si_3N_4) = 2$, and the measured GaAs substrate n,k dispersion. Fig 5a shows the reflectance optimization plot around the design wavelength of 920 nm vs. nitride thickness. Fig 5b shows calculated reflectance over a range of wavelength for the optimum nitride thickness of about 1100 A. Calculated backside reflectance is for l = 920 nm for a transparent 3 mil GaAs substrate (used n(GaAs) = 3.56 at l = 920 nm, n(SiN) = 1.96, and n(Al) = 1.85 - 8j) .

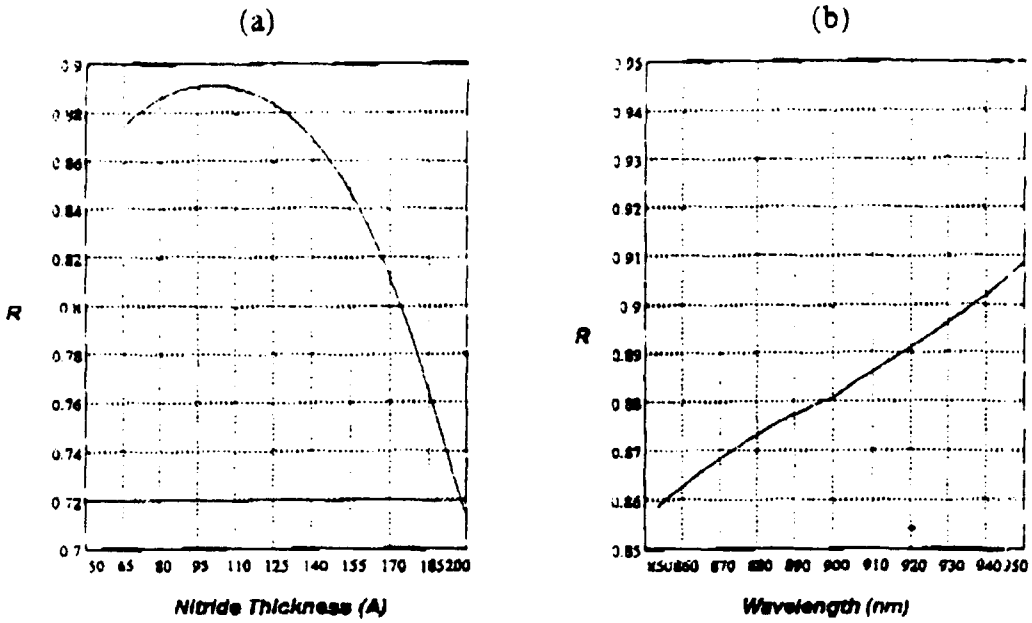

Fig 5 - Calculated reflectances for Incidence in GaAs
(a) vs. Nitride thickness at l = 920 nm, and
(b) vs. wavelength at optimum nitride thickness (about 1000 A)

Chemical vapor depositions of Si_3N_4 were performed using a Semi-Group CVD System 1000CC plasma enhanced CVD system. Ammonia, N_2, and dilute Silane were the gas sources. Growths were carried out at 350 °C, gas flows were set at Si_3H_4 = 16.8, N_2 = 25, and Ammonia = 10. RF power was fixed at 3.5 W and chamber pressure was set at 850.

After CVD of Si_3N_4 films, 750 to 1000 Angstroms of Aluminum was deposited by e-beam evaporation. Although reflectivity of Al saturates at about .9 at a thickness of about 300 Angstroms [] , a thicker layer was deposited to produce a hardier Al film, and to account for Al loss to oxidation. Initial reflectance measurements of the top Al film yielded Al reflectivities of about .8 from air ambient. That this was less than the reported .9 was attributed to oxidation of the aluminum surface (reflectance measurements were carried out days after the Al deposition). To facilitate GaAs back-side reflectivity measurements, the GaAs substrate side was thinned (manual lapping) to a thickness of about 3 mils. Reflectance measurements could then be taken from the substrate side relative to a blank 3 mil GaAs sample (lapped with the other samples). Table 3 tabulates the growth settings and measurements for the IM coating samples.

Table 3 Listing of growth settings and measurements for Si_3N_4 CVD samples

Sample ID	Growth Time (min)	Film Index @ 630 nm	Ellipsom Thickness (A)	Lapped Thickness (mil)	Comment/s
SING#1	?	1.92	1,100	3.2	Run around 7/13 93
SING#2	11.5	1.92	900	3.1	
SING#3	14.5	1.95	1,200	NA	Speckling (Hi-Vac problem)
SING#4	14.5	1.95	1,170	3	Re-run of SING#3
SING#5	11	1.92	895	2.9	
SING#6	15.5	1.97	1,260	3.3	
GaAs(B)	NA	NA	NA	3.4	Blank thinned GaAs

DISCUSSION OF RESULTS

DS Work

The multi-layers were found to possess an anti-reflecting character, in contrast to what was expected for a 1/4 wavelength air-high-low...high substrate index system that was deposited. Fig 4 showed reflectance plots for the various multilayer coatings. Despite calculated high reflectances for these multi-layers, the samples were found to possess nearly an antireflecting character.

The origin of the anti-reflecting characteristic of the coatings can be explained as the result of metal contamination generating additional absorption in the amorphous "dielectrics". During the course of this work, tungsten (W) metal sputterings were also performed to test for cross contamination of metal and dielectric films. It was discovered that a sandblasting of the removable sample holder, and extensive metal pre-sputter (before loading sample, with and without continuously rotating table) were not sufficient to prevent apparent dielectric contamination of metal depositions. The contamination was evident in the form of peeling tungsten layers after deposition of a Titanium sticking layer. This peeling could be the result of coherency stresses in the W film from contamination species (esp oxides). The actual contamination species has not yet been positively identified, though it has been noted that the peeling problem didn't start until dielectrics came into the picture. In addition, spectroscopic ellipsometry revealed that the "dielectric" films were actually highly absorbing over the wavelengths of interest (visible to near IR - see Fig 3). From this data, it was apparent that while the dielectric depositions were contaminating the metal films, the metal depositions were also contaminating the dielectric films (or the dielectric targets are not what they are labelled to be). This has been a classic "peanut butter and chocolate" mixing case. It is worth noting that the dielectrics were probably more readily contaminated by the metal, due to the easier re-sputtering of metal residues over dielectrics. (according to the sputtering system manufacturer, the difference may be a factor of almost 4 between Si and Au, but is about the same for Si and W).

After inserting measured effective refractive indices into the ellipsometry and reflectance calculations, it was found that the films were indeed highly absorbing, as evidenced by the close comparison of this calculation to the measured reflectances (see Fig 3b,c) and the ellipsometry data (Table 2).

After several dielectric sputterings and fruitless cleaning attempts, the entire rotating table and sample stage was sandblasted and dipped in a methanol solvent bath to eliminate virtually all previous sputtering residue from the chamber. "Virtually" means that there still existed a film along the extreme far walls of the chamber, where presumably no significant sputtering of residues would occur. This could be removed perhaps by a hand

power tool (drill with wire brush?). However, as of this writing, after extensive pre-sputtering coating of the chamber, the tungsten deposition problem has reportedly finally disappeared. It is worth noting that throughout this work, contact resistances of the tungsten films were not found to be a good indicator of "bad" metal films. Indeed, one W deposition which was performed right after several Si dielectric runs produced one of the best contact resistances to that date. Perhaps the refractive index information could be used here to measure contamination levels (see Table 2).

IM Coating Work

Since the sputtering of dielectrics was found to be incompatible with the metal sputterings, there is even more of a argument for the simpler IM coating technique. From the calculations, it evident that the IM coatings can increase the end facet reflectivities by up to 2 to 3 times from a bare GaAs facet (.35 typ for GaAs/Air). From Fig 5b, it was seen that the reflectivity should be fairly broad over wavelength. In terms of mode locking, this lack of wavelength selectivity should not pose a problem for the quantum well laser structures considered in this work. What now remains to be done is to actually test the samples already generated and verify the optimum nitride thickness, then try coating some actual lasers.

WHERE TO GO FROM HERE

As research funding becomes more and more scarce, it is becoming more important to consider the final goals of any project. Lately, it has been virtually a matter of Government decree that military research serve a dual military and commercial purpose. The use of fiber communications and electro-optic designs in avionics and detection is indisputable. That these technologies are used commercially, immediately in the form of long haul communications and video, is also obvious. It is also apparent that electro-optics and photonics will continue to play an ever strengthening role in military and commercial applications. To date, the research facilities at the avionics research facility at Wright Patterson AFB have been primarily concerned with the equally important "electro-" prefix of electro-optics. It will continue to be important to develop ultra-high speed electrical devices to exploit the enormous bandwidths of optical circuits, and for integration into faster computers. It is this author's opinion that the semiconductor laser project targeted by this work, although crucial for future avionics and fiber communications growth, will need more basic respect in the form of additional manpower and (fairly low cost) equipment if it is to realize it's full long term impact.

For this work, optical coatings could have enhanced device performance significantly at minimal cost in time and money (in-house work). Although the sputtering of dielectrics may have proven infeasible for this situation, one should not exclude some other possibilities. For instance, with additional gas sources, the same CVD system used to initiate IM coating work could be modified to grow Si/Si_3N_4 DS structures. A second possibility would be to commandeer an e-beam evaporator and assign it to optical coatings (noting that insulating films could also be used for electrical device applications). Finally, a dedicated sputtering system for dielectrics could also be implemented (depending on which is more readily available).

It is this author's sincere hope that the electro-optic activity at WPAFB (and the other military research establishments) will grow to a level which compliments the electrical device work already in place.

FINAL NOTE

As mentioned earlier, a MathCAD program was generated to perform ellipsometry and reflectance calculations. An example of this program is attached to the end of this report. Included in the program are index dispersion plots for the substrate and film materials investigated in this work. Ellipsometry equations used may be found in [] . The multilayer structure investigated in this particular case was the 2-layer GW23 sample with an ellipsometry incidence angle of 70 degrees. The first part of the program imports spectroscopic ellipsometry data

for calculation of material index dispersion data. This data is fed into the second part of the program, which calculates and plots the power reflectance, transmission, loss, and raw ellipsometry numbers (psi and delta) vs. wavelength and layer thicknesses, at the given incidence angle, for comparison to measured results. These comparisons may be found in the tables. This program may be readily applied to any multilayer system of materials. Given a rough initial design, the program may be used to optimize layer thicknesses for the desired reflectivity. The program may be used to model DS or IM coatings.

REFERENCES

TWO-DIMENSIONAL FINITE ELEMENT ANALYSIS OF LAMINATED COMPOSITE PLATES CONTAINING DISTRIBUTED PIEZOELECTRIC ACTUATORS AND SENSORS

Duane T. Detwiler
Graduate Research Associate
Department of Aeronautical and Astronautical Engineering

The Ohio State University
2036 Neil Ave Mall
Columbus, Ohio 43210-1276

Final Report for:
Summer Research Extension Program
Wright Laboratory

Sponsored by:
Air Force Office of Scientific Research
Bolling Air Force Base, Washington, D.C.

and

The Ohio State University

September 1993

Two-Dimensional Finite Element Analysis of Laminated Composite Plates Containing Distributed Piezoelectric Actuators and Sensors

Duane T. Detwiler
Graduate Research Associate
Department of Aeronautical and Astronautical Engineering
The Ohio State University

Abstract

A finite element formulation is developed to model the response of laminated composite plates containing distributed piezoceramic actuators and sensors. The equations of motion are derived using the variational principle with respect to the total structural and electrical potential energy. These equations of motion are converted to a two-dimensional finite element equation using a First Order Shear Deformation Laminated Plate Theory. The finite element equation is based on the QUAD4 isoparametric quadrilateral element which is currently used in such FEA codes as COSMIC/NASTRAN and ASTROS. This new piezoelectric finite element formulation will be incorporated into an FEA computer code and verified by comparison with published experimental results.

Two-Dimensional Finite Element Analysis of Laminated Composite Plates Containing Distributed Piezoelectric Actuators and Sensors

Duane T. Detwiler

Introduction

There has been a great deal of interest recently in the concept of active sensing and reactive "smart" structures by the research community. These smart structures contain a system of microsensors which monitor the internal strain of the structure caused by external vibrations, temperatures, or pressures. This information is input into control algorithms programmed into microprocessors which in turn activate a system of microactuators. These microactuators can change the shape of the structure and thereby the mass, stiffness, or energy-dissipation characteristics of the structure which effectively tailors the static or dynamic response of the structure. This type of smart system has applications in large space structures and satellites, aircraft and helicopter structures, automobiles, and automated manufacturing technology.[1-2]

The coupled mechanical and electrical properties of piezoelectric ceramics make them well suited for use as sensors and actuators in smart structures.[2-4] The direct and converse piezoelectric effects govern the interaction between the mechanical and electrical behavior of this type of material. The direct piezoelectric effect states that a strain applied to the material is converted to a charge. On the other hand the converse piezoelectric effect states that an electric potential applied to the material is converted to strain.

The high strength-to-weight ratio of fiber-reinforced laminated composite materials make them attractive for many aerospace applications. The use of these composites grows as advances in manufacturing technology progress. The construction of a laminated composite by stacking many thin layers together makes the integration of piezoceramic actuators and sensors possible. This integrated smart system would effectively increase the performance of the composite structure. There have been

several analytical analysis conducted to demonstrate the feasibility of this integrated concept for simple structures.[4-6]

The design and analysis of large complicated structures with integrated piezoelectric materials requires the development and implementation of finite element methods. Several of these finite element methods have been developed for laminated composite structures with integrated piezoelectric layers.[7-9] Most of these methods use solid three-dimensional hexahedron or brick elements. These elements display excessive shear stiffness as the element thickness decreases. This problem of shear locking was solved by adding three incompatible internal degrees of freedom to the element.[7-8] This makes the analysis of models using these elements complex and costly to solve. The use of two dimensional plate elements greatly reduces the problem size and the computation time.[10] The two-dimensional quadrilateral plate element developed by Hwang and Park is more efficient, but it is restricted to the modelling of collocated sensor and actuator pairs.[9]

The purpose of our research is to formulate a laminated composite plate with piezoelectrics as additional layers. This formulation, based on two-dimensional plate theory, is more realistic in the context of current applications. A three-dimensional model may be appealing in research but can be very cumbersome and expensive in modeling practical structures such as wings and control surfaces. This new piezoelectric plate element will be capable of modeling the static and dynamic response of laminated composite plates containing one or more piezoceramic activating or sensing layers subjected to mechanical and electrical loads. Each piezoelectric layer may be at an arbitrary distance from the mid-plane and may have a different voltage. (See figure 1.) The formulation of this new finite element will be verified by comparison with three-dimensional formulations and experimental results from literature.[11]

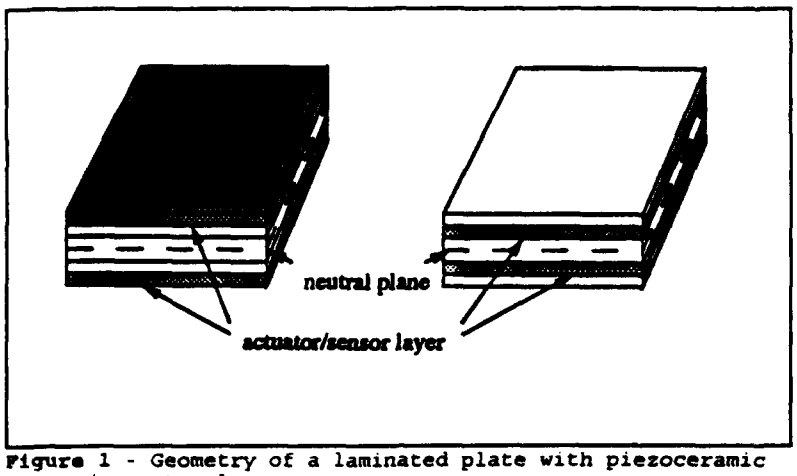

Figure 1 - Geometry of a laminated plate with piezoceramic sensor/actuator layers.

Derivation of Equations of Motion

The equations of motion for a material with coupled mechanical and electrical properties are based on the stress equations of motion

$$\sigma_{ij,i}+f_j=\rho\ddot{u}_j \tag{1}$$

and the charge equation of electrostatics

$$D_{i,i}=0 \tag{2}$$

where σ_{ij}, f_i, ρ, u_j, D_i are stresses, body forces, density, displacements, and electric flux density, respectively. These two equations can be combined by multiplying them by the appropriate quantities and integrating over the respective volumes

$$\int_V(\sigma_{ij,i}-\rho\ddot{u}_j)\,\delta u_j dV+\int_{Vp}D_{j,j}\delta\phi dVp=0 \tag{3}$$

where ϕ is the electric potential or voltage. The volume V represents the entire volume of the material while Vp is only the volume of the piezoelectric layers. The body forces are neglected in this equation.

The divergence theorem can be applied to equation (3) to rewrite it in a different form

$$\int_V \rho \ddot{u}_j \delta u_j dV + \int_V \sigma_{ij} \delta u_{j,i} dV + \int_{Vp} D_i \delta \phi_{,i} dV_p = \int_A n_i \sigma_{ij} \delta u_j dA + \int_{Ap} n_i D_i \delta \phi dAp \qquad (4)$$

This equation can be further rewritten by using the strain-displacement relationship

$$\epsilon_{ij} = \frac{1}{2}(u_{i,j} + u_{j,i}) \qquad (5)$$

and the electric field - electric potential relationship

$$E_i = -\phi_{,i} \qquad (6)$$

where ϵ_{ij} are the strains and E_i is the electric field strength vector. Substituting equations (5) and (6) into (4) produces

$$\int_V \rho \ddot{u}_i \delta u_i dV + \int_V \sigma_{ij} \delta \epsilon_{ij} dV - \int_{Vp} D_i \delta E_i dVp = \int_A T_i \delta u_i dA + \int_{Ap} Q \delta \phi dA \qquad (7)$$

were T_i are the tractions applied on the surface A and Q is the electrical charge applied on the surface of the piezoelectric A_p.

Finite Element Formulation

The finite element formulation is developed based on the QUAD4 plate element currently used in COSMIC/NASTRAN and ASTROS.[12] The QUAD4 is an isoparametric quadrilateral element which uses a bilinear variation of geometry and deformation within the element. The QUAD4 element has five degrees of freedom (dof) per node. Two additional dof per element are included to represent the electrical voltages of two different piezoelectric actuator/sensor layers. (See figure 2.)

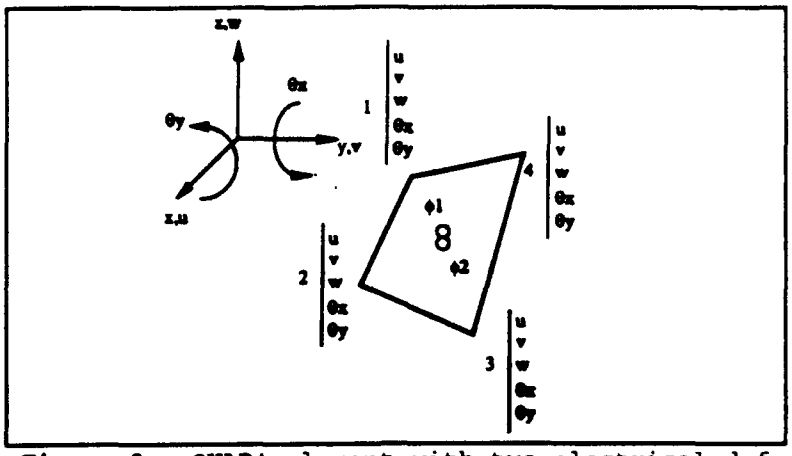

Figure 2 - QUAD4 element with two electrical dof

For every additional piezoelectric layer an additional voltage dof is needed per element. It is assumed that the strains vary linearly through the thickness. The QUAD4 element may be used to model the coupling of membrane and bending behaviors.

Displacement Functions

Two dimensional interpolation (shape) functions are used to define the geometry field at any point in the element cross-section. These shape functions relate the curvilinear coordinates in the nodal cartesian coordinate system to the element coordinate system. These shape functions and their derivatives are

$$N_i = \frac{1}{4}(1+\xi\xi_i)(1+\eta\eta_i) \tag{8}$$

$$\begin{aligned} \frac{\partial}{\partial}\frac{N_i}{\xi} &= \frac{1}{4}\xi_i(1+\eta\eta_i) \\ \frac{\partial}{\partial}\frac{N_i}{\eta} &= \frac{1}{4}\eta_i(1+\xi\xi_i) \end{aligned} \tag{9}$$

Shape functions can be used to express the element deformations in terms of nodal displacements

$$\{u(\xi,\eta)\}=\sum_{1}^{4} N_i(\xi,\eta)\{u\}_i \tag{10}$$

The electrical voltages are constant throughout the plane of the element

$$\phi_k(\xi,\eta)=\phi_k \tag{11}$$

Strain-Displacement Relationship

The strain-displacement relations for this element is based on the Mindlin first-order shear deformation plate theory[13] and equation (6).

$$\{\bar{e}\} = \begin{vmatrix} e_x^M \\ e_y^M \\ e_{xy}^M \\ e_x^B \\ e_y^B \\ e_{xy}^B \\ \gamma_{yz} \\ \gamma_{zx} \\ -E_{x_1} \\ -E_{y_1} \\ -E_{z_1} \\ -E_{x_2} \\ -E_{y_2} \\ -E_{z_2} \end{vmatrix} = \begin{vmatrix} \frac{\partial}{\partial x} & 0 & 0 & 0 & 0 & 0 & 0 \\ 0 & \frac{\partial}{\partial y} & 0 & 0 & 0 & 0 & 0 \\ \frac{\partial}{\partial y} & \frac{\partial}{\partial x} & 0 & 0 & 0 & 0 & 0 \\ 0 & 0 & 0 & z\frac{\partial}{\partial x} & 0 & 0 & 0 \\ 0 & 0 & 0 & 0 & z\frac{\partial}{\partial y} & 0 & 0 \\ 0 & 0 & 0 & z\frac{\partial}{\partial y} & z\frac{\partial}{\partial x} & 0 & 0 \\ 0 & 0 & \frac{\partial}{\partial y} & 0 & 1 & 0 & 0 \\ 0 & 0 & \frac{\partial}{\partial x} & 1 & 0 & 0 & 0 \\ 0 & 0 & 0 & 0 & 0 & \frac{\partial}{\partial x} & 0 \\ 0 & 0 & 0 & 0 & 0 & \frac{\partial}{\partial y} & 0 \\ 0 & 0 & 0 & 0 & 0 & \frac{\partial}{\partial z} & 0 \\ 0 & 0 & 0 & 0 & 0 & 0 & \frac{\partial}{\partial x} \\ 0 & 0 & 0 & 0 & 0 & 0 & \frac{\partial}{\partial y} \\ 0 & 0 & 0 & 0 & 0 & 0 & \frac{\partial}{\partial z} \end{vmatrix} \begin{vmatrix} u \\ v \\ w \\ \theta x \\ \theta y \\ \phi 1 \\ \phi 2 \end{vmatrix} \tag{12}$$

This relationship can be rewritten in the element coordinate system by substituting equation (9) into equation (12) and assuming the voltage potential is linear through the thickness of the piezoelectric layer and is grounded on one surface

$$\{\bar{\epsilon}\}=\sum_{i=1}^{4} [J]^{-1}[B]_i\{\bar{u}\}_i \tag{13}$$

where $[J]^{-1}$ is the inverse of the Jacobian Matrix

and

$$
[B]_i = \begin{vmatrix}
N_{i,1} & 0 & 0 & 0 & 0 & 0 & 0 \\
0 & N_{i,2} & 0 & 0 & 0 & 0 & 0 \\
N_{i,2} & N_{i,1} & 0 & 0 & 0 & 0 & 0 \\
0 & 0 & 0 & \zeta\frac{t}{2}N_{i,1} & 0 & 0 & 0 \\
0 & 0 & 0 & 0 & \zeta\frac{t}{2}N_{i,2} & 0 & 0 \\
0 & 0 & 0 & \zeta\frac{t}{2}N_{i,2} & \zeta\frac{t}{2}N_{i,1} & 0 & 0 \\
0 & 0 & N_{i,2} & 0 & N_i & 0 & 0 \\
0 & 0 & N_{i,1} & N_i & 0 & 0 & 0 \\
0 & 0 & 0 & 0 & 0 & 0 & 0 \\
0 & 0 & 0 & 0 & 0 & 0 & 0 \\
0 & 0 & 0 & 0 & 0 & \frac{1}{t1} & 0 \\
0 & 0 & 0 & 0 & 0 & 0 & 0 \\
0 & 0 & 0 & 0 & 0 & 0 & 0 \\
0 & 0 & 0 & 0 & 0 & 0 & \frac{1}{t2}
\end{vmatrix} \tag{14}
$$

where t1 and t2 are the respective thicknesses of the piezoelectric layers.

Stress-Strain Equations

The stress-strain equations are derived using the classical lamination theory which assumes:

(1) Each of the lamina is in a state of plane stress,

(2) All of the lamina are perfectly bonded,

(3) The bonds are infinitesimally thin and non-shear deformable.

This means the laminate behaves as a "single" layer with "special" properties. The stresses and strains are separated into membrane, bending, shear, and electrical components

$$\{\underline{\sigma}\} = [\underline{G}]\{\underline{\epsilon}\}$$

or

$$
\begin{vmatrix} \sigma_M \\ \sigma_B \\ \tau \\ D_1 \\ D_2 \end{vmatrix}
=
\begin{vmatrix}
[G_1] & [G_4] & 0 & [e_1]^1 & [e_1]^2 \\
[G_4] & [G_2] & 0 & [e_2]^1 & [e_2]^2 \\
0 & 0 & [G_3] & 0 & 0 \\
[e_1]^1 & [e_2]^1 & 0 & [\xi^s]^1 & 0 \\
[e_1]^2 & [e_2]^2 & 0 & 0 & [\xi^s]^2
\end{vmatrix}
\begin{vmatrix} \epsilon_M \\ \epsilon_B \\ \gamma \\ -E_1 \\ -E_2 \end{vmatrix} \tag{15}
$$

where the components for this "single" layer are assembled from the transformed plane stress constitutive relations of each lamina.

$$
\begin{aligned}
[G_{ij}]_1 &= \frac{1}{t}\sum_{k=1}^{N} [\bar{G}_{ij}]^k \ (z_k - z_{k-1}) \\
[G_{ij}]_2 &= \frac{1}{3I}\sum_{k=1}^{N} [\bar{G}_{ij}]^k \ (z_k^3 - z_{k-1}^3) \\
[G_{ij}]_4 &= \frac{1}{2t^2}\sum_{k=1}^{N} [\bar{G}_{ij}]^k \ (z_k^2 - z_{k-1}^2)
\end{aligned}
\tag{16}
$$

where $[G_{ij}]^k$ is the transformed moduli matrix for each lamina including the piezoelectric layers. z_k and z_{k-1} are the distances from the mid-plane of the laminate to the top and bottom of the kth lamina.

$$
\begin{aligned}
[e_{ij}]_1^p &= \frac{1}{t}[e_{ij}]^p (z_p - z_{p-1}) \\
[e_{ij}]_2^p &= \frac{1}{2t^2}[e_{ij}]^p (z_p^2 - z_{p-1}^2)
\end{aligned}
\tag{17}
$$

where $[e_{ij}]^p$ is the plane stress piezoelectric coefficient matrix for each piezoelectric layer p, and z_p and z_{p-1} are the distances from the mid-plane of the laminate to the top and bottom of the pth piezoelectric layer. The matrix $[\xi^s]^p$ is the permitivity at constant strain for the pth piezoelectric layer. These plane stress piezoelectric relations can be obtained from the three dimensional relations.[13]

$$
\begin{aligned}
[e] &= [d]\,[G] = \begin{vmatrix} 0 & 0 & e_{13} \\ 0 & 0 & e_{23} \\ 0 & 0 & 0 \end{vmatrix} \\
[\xi^s] &= -[\xi^\sigma] + [d]\,[G]\,[d]^T = \begin{vmatrix} \xi_{11}^s & 0 & 0 \\ 0 & \xi_{22}^s & 0 \\ 0 & 0 & \xi_{33}^s \end{vmatrix}
\end{aligned}
\tag{18}
$$

The transverse shear flexibility matrix $[G_3]$ is defined in terms of the transverse shear strain energy through the thickness. The transverse shear stiffness is numerically conditioned to enhance the accuracy of the element for a wide range of modeling practices.[12]

Finite Element Equation

The equilibrium equations (7) can now be written for each element in terms of the nodal displacements and the element voltages

$$[M]\{\ddot{u}\}+[\bar{K}]\{\bar{u}\}=\{\bar{F}\} \tag{19}$$

where [K] is the extended element stiffness matrix and [M] is the element mass matrix.[13] The stiffness matrix is integrated numerically by Gauss-quadrature integration method.[15]

$$[\bar{K}]=\sum\sum\sum [B]^T[\bar{G}]\,[B]\,W_\xi W_\eta W_\zeta \det[J] \tag{20}$$

where (ξ, η, ζ) are the Gaussian integration point coordinates and W_ξ, W_η, W_ζ are the associated weight factors.

Numerical Examples

The finite element formulation will be verified by modeling the experiment performed by Crawley and Lazarus and comparing the experimental results with finite element analysis.[11] This experiment was conducted using a cantilevered laminated composite plate with distributed G-1195 piezoelectric actuators and sensors bonded to the surfaces. (See figure 3.)

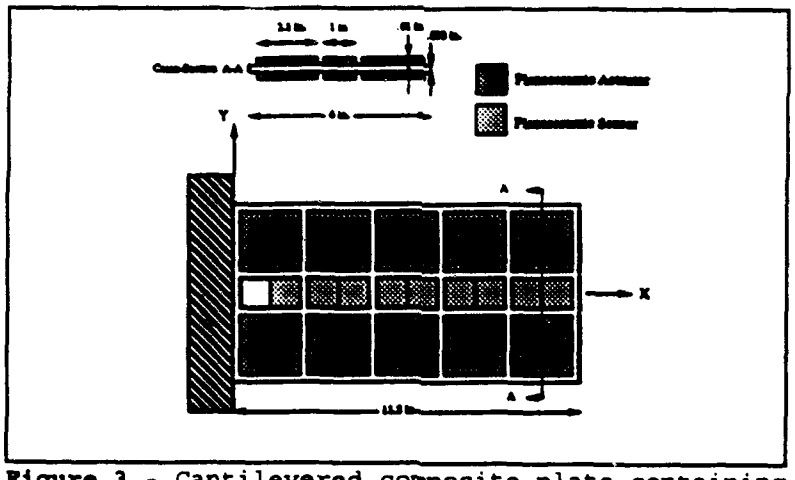

Figure 3 - Cantilevered composite plate containing distributed piezoelectric sensors and actuators

A constant voltage with an opposite sign was applied to the actuators on each side of the plate. The

deflections of the center line and both edges was obtained.

Further experiments will also be performed to verify the finite element analysis of the dynamic behavior of a plate with distributed piezoceramic actuators and sensors. Finally, several numerical examples will be shown to demonstrate the use of the computer code with control theory to control the shape and vibration of structures.

References

[1]Wada, B.K. "Adaptive Structures," *Proceedings of the AIAA/ASME/ASCE/ASC 30th SDM Conference*, AIAA, New York, pp 1-11.

[2]Gandhi, M.V. and Thompson, B.S., *Smart Materials andStructures*, Chapman & Hall, London, 1992.

[3]Tiersten, H.F., *Linear Piezoelectric Plate Vibrations*, Plenum Press, New York, 1969

[4]Crawley, E.F. and de Luis, J., "Use of Piezoelectric Actuators as Elements of Intelligent Structures," *AIAA Journal*, Vol.25, No.10, 1987 pp.1373-1385

[5]Wang, B.T., and Rogers, C.A., "Modeling of Finite-Length Spatially Distributed Induced Strain Actuators for Laminate Beams and Plates," *Journal of Int. Mat. Sys. and Struc.*,Vol.2,No.1,1991,pp38-58

[6]Lee, C.-K., O'Sullivan, T.C., and Chiang, W.-W., "Piezoelectric Strain Sensor and Actuator Design for Active Vibration Control, "*Proceedings of the AIAA/ASME/ASCE/AHS 32nd SDM Conf.*, AIAA, Washington, DC, 1991

[7]Tzou, H.S., *Piezoelectric Shells Distributed Sensing and Control of Continua*, KAP, Norwell, MA, 1993

[8]Ha, S.K., Keilers, C., and Chang, F.K., "Finite Element Analysis of Composite Structures Containing Distributed Piezoceramic Sensors and Actuators," *AIAA Journal*, Vol.30, No.3, 1992, pp.772-780

[9]Hwang, W.-S. and Park, H.C., "Finite Element Modeling of Piezoelectric Sensors and Actuators," *AIAA Journal*, Vol.31, No.5, 1993, pp.930-937

[10]Hughes, T.J.R., Taylor, R.L., and Kanoknukulchai, W., "A Simple and Efficient Finite Element for Plate Bending," *Int. J. Num. Meth. Engng.*, Vol.11, 1977, pp.1529-1543

[11]Crawley, E.F. and Lazarus, K.B., "Induced Strain Actuation of Isotropic and Anisotropic Plates, "*AIAA Journal*, Vol.29, No.6, 1991, pp.944-951

[12]Venkayya, V.B., Tischler, V.A., *QUAD4 Seminar*, WRDC-TR-89-3046, April, 1989

[13]Detwiler, D.T., "Finite Element Modeling of Laminated Composite Plates Containing Distributed Piezoelectric Actuators and Sensors Using the QUAD4 Isoparametric Quadrilateral Element.," M.S. Thesis, The Ohio State Univ., Columbus, OH, December, 1993

[14]Reddy, J.N., *Energy Variational Methods in Applied Mechanics*, John Wiley & Sons, Inc., 1984

[15]Bathe, K.-J., and Wilson, E.L., *Numerical Methods in Finite Element Analysis*, Prentice-Hall, Inc. 1976

FIRE SUPPRESSION TEST CELL (FSTC)
APPLICATIONS FOR HALON 1211 AND 1301 REPLACEMENT

Kevin R. Grosskopf, MSBC
Doctoral Candidate
College of Architecture

University of Florida
FAC 101
Gainesville, FL 32611-2032

Final Report for:
Graduate Student Research Program
Wright-Paterson Laboratory

Sponsored by:
Air Force Office of Scientific Research
Bolling Air Force Base, Washington, D.C.

and

University of Florida

July 1993

FIRE SUPPRESSION TEST CELL (FSTC)
APPLICATIONS FOR HALON 1211 AND 1301 REPLACEMENT

Kevin R. Grosskopf, MSBC
Doctoral Candidate
College of Architecture

Abstract

The Fire Suppression Test Cell (FSTC) is designed and fabricated for the purpose of testing fire suppression agents, techniques, and systems for implementation in Air Force facilities. The FSTC is being constructed under the supervision of the University of Florida (UF) under contract with the Applied Research Associates (ARA). This joint research initiative is producing a highly mobile "brilliant" structure maintaining the ability to analyze ozone depleting Halon 1211 and 1301 replacements using simulated delivery systems and extensive automation. This innovative project will rapidly assess potential Halon replacements, further reducing retrofit expenses to existing structures and ultimately revolutionizing fire detection and suppression technology.

The FSTC concept is anticipated to provide critical data on the complete spectrum of advanced streaming agents as cost effective, environmentally sensitive replacements for ozone depleting Halon 1211 and 1301. The FSTC will maintain the required long-term flexibility for analyzing future fire suppression techniques and clean air combustion technology.

FIRE SUPPRESSION TEST CELL (FSTC)
APPLICATIONS FOR HALON 1211 AND 1301 REPLACEMENT

Kevin R. Grosskopf, MSBC

Introduction

The Fire Suppression Test Cell (FSTC) is intended to evaluate agent performance while subjecting agents to a full range of fire events that are possible occurrences in Air Force facilities and installations. This design-build project involves the continued assessment of CFC and HCFC fire suppression replacement alternatives including CF_3I, HFC-23, perfluorobutane, HFC-227, EMAA, and cryogenic compounds for three-dimensional fire suppression using current fire suppression hardware.

The FSTC designed and fabricated under the supervision of the University of Florida will have two major areas, a test area of 500 ft^2 and a data collection and observation area of about 400 ft^2. The FSTC will be able to simulate a range of fire events that are possible occurrences in Air Force facilities, primarily CF_3Br installations. All necessary piping, controls, instrumentation, and data collection/analysis computers required to perform the testing will be included in this project. "Active" functions of the FSTC will involve fire suppression efficiency, toxicity, materials compatibility, and cost effectiveness. "Passive" functions (instrumentation) of the FSTC measure air flow and level, temperature, pressure, humidity, and other ambient characteristics that may influence test results.

Instrumentation is computer interfaced for rapid data acquisition. These sensor and data collection devices enable the FSTC to fully model and test fire suppressant performance under a variety of controlled and ambient conditions. All devices and instrumentation are provided adequate thermal and moisture protection for testing and wash-down activities. Adequate ventilation is also provided to minimize safety risks and to avoid damage as consequence of controlled test burns.

DEFINITION OF THE PROBLEM

The Air Force has utilized Halon 1211 and 1301 as standard streaming and total flood agents respectively for the past 20 years. The Montreal Protocol, the Clean Air Act of 1990, and DoD initiatives require the phase-out of these ozone depleting agents in both production and use as of 1 January 1994. As a consequence, all Air Force facilities recognized as "non-essential users" are required to implement new gaseous fire suppression agents as replacements for Halon. Laboratory and small-scale testing is currently being conducted to evaluate promising new agents. However, there exists no facility capable of conducting large-scale test burns under "real-time" conditions. Therefore, the FSTC must provide the life-cycle flexibility and endurance for evaluating several potential replacement alternatives.

METHODOLOGY

The method for determining the function and design of the FSTC structure must maintain both immediate and long-term applicability. Current design objectives involve simulated office spaces that are representative of Air Force facilities. Such "non-essential" structures using Halons are consequently targeted for replacement. Future FSTC objectives will include rapid detection and response systems, AFFF analysis, combustion spectronomy, and other potential programs requiring highly automated, controlled test facilities. Therefore, the FSTC must be designed to maintain the flexibility to expand and adapt to these emerging projects.

Instrumentation of the FSTC remains critical to the overall performance of the test cell. Instrumentation must consist of sensor devices, ambient controls, computer interfacing, and logic sequencing. This will allow all testing and data acquisition devices to operate at maximum efficiency. Similar to the structural core of the FSTC, the instrumentation must also maintain the flexibility to expand and adapt to changing instrumentation needs.

TEST CELL SPECIFICATIONS

Structural Requirements:

The pre-engineered structure is 30'-0" in width, 30'-0" in length, and approximately 12'-0" in height. The test area is 25'-0" x 20'-0" x 8'-0" in dimension consisting of 24"-30" sub-floor and 18"-24" ceiling spaces respectively. The test area is provided with finishes readily cleanable, weatherproof, and resistant to acidic corrosion. Partition walls separating observation and test areas are galvanized panels with urethane foam cores. Partition walls achieve a flame spread 30 or lower, smoke generation of less than 500, and a thermal conductivity factor (K) of less than 0.2 BTU per hour. Heat transfer (U) does not exceed 0.08 (R-13) for partition walls.[1]

The observation area is provided view ports into the testing area at sub-floor, floor, and ceiling locations. View port windows consist of 1'-0" x 2'-0" minimum dimension. Doors consist of 3'-8" x 7'-0" minimum clearance. All doors and view ports are capable of resisting 2-6 psi. All doors and view ports meet UL and NFPA fire standards for typical test facilities and are fully weatherproof. Flooring in the test area consists of raised grid panels and extend 24"-30" from the existing foundation. Access panels are 18" x 18" to 24" x 24" in dimension. Access panels maintain a water resistant integrity and a laminate finish. The floor within the observation area consists of conventionally metal framed 3/4" T & G OSB. Ceiling construction is standard 2'-0" x 4'-0" aluminum grid and inset acoustical panels. Acoustical panels are laminate finished fiber or epoxy finished MR gypsum.

An impermeable 80 mil. polyethylene liner is provided to contain potentially hazardous substrates during washdown processes. The liner is placed over the existing foundation and the 12" x 12" cast-in-place (CIP) curb. The CIP curb supports the load bearing walls and observation partitions of the FSTC. The CIP curb consists of a 12" x 12" grade beam of 2500 psi concrete reinforced with two #5 rebar fastened to #5 dowels grouted into the existing foundation 10'-0" o.c.. The 20'-0" x 25'-0" existing surface below the test area is grouted to achieve a 0.0625"/1'-0" slope to the collection pan above the polyethylene liner.

Mechanical Requirements:

The test cell is provided with a 2,000 cfm minimum exhaust system for ventilating the sub-floor, test area, and ceiling spaces. A 6'-0" x 6'-0" venting hood with flex-duct is provided for movement to various test locations within the 20'-0" x 25'-0" test area. The hood duct ventilation system is connected to the exhaust tower unit and vented to the exterior of the existing facility. The exhaust tower unit is capable of venting one or all three zones in addition to the venting hood simultaneously or individually. Static grilles are placed on the exterior test cell walls to allow ventilation from the sub-floor, test room, and ceiling zones. A piping system and control system is provided for injecting test fire suppressant agents. The suppression system consists of piping suspended from the structural ceiling below the finish (acoustical) ceiling. The piping consists of a main header and riser of 1.5" inert diameter and shall be capable of supplying reduced laterals and orifices to .5".

A sum pump for collecting sub-floor washdown is provided to transfer substrate wastewater from 50 a gallon equivalent collection pan to a 500 gallon above grade, mobile collection container outside of the existing. The test area is provided a .5" hose bibb for washdown purposes. A steel sink for non-potable purposes is located in the observation area. Separate HVAC systems and controls for the test cell and observation area is used. The test cell is further equipped with a 2.5 ton minimum unit supplying 2 room registers within the test area and a sub-floor plenum equipped with four finish floor grilles. The observation area is served by a 1.5 ton minimum unit. All duct work is galvanized and is adequately fire and corrosion resistant. All test area mechanical systems are separate of observation area mechanical systems. All test area mechanical systems are operable from a centralized point of control within the observation area.

Electrical Requirements:

Fire detectors, sensors, and other specialty instrumentation are located in all three zones. A warning light for test initiation is provided. The electrical supply consists of single phase service. The electrical service maintains a minimum 200 amp capacity with a power interrupt for test cell supply within the centralized control station in the observation area. The panel is located at the point of penetration into the hangar facility. A trip main is placed into a sub-panel within the observation and control area with positive cut-off to the test area. All supply electrical service and low voltage instrumentation wiring is placed in water-proof EMT conduit. All conduit for low voltage wiring is capped 6" below the finish access floor in the test area for instrumentation modifications. Lighting is provided to all three zones for test observation purposes. Lighting in the ceiling and sub-floor interstitial spaces consists of 60 watt incandescent lamps. Lighting in the observation and test areas consists of 24" x 48" troffer fixtures with four florescent lamps each. All test area electrical systems are separate of observation area mechanical systems. All test area electrical systems are operable from centralized control automation within the observation area.

INSTRUMENTATION SPECIFICATIONS

Thermocouple Probes and Assemblies:

Thermocouple probes are rigid on a self supportive stand and provided high temperature duplex ceramic insulated wire to the point of termination EMT junction. High temperature overbraided ceramic fiber insulated thermocouples are used in addition to rigid thermocouple probes for select applications requiring "flex" wire thermistors. Thermocouples and probes are tip sensitive with 0.3 second response and data acquisition time (1/8" probe dia. minimum). Thermocouples and probes are able to withstand temperatures exceeding 1700°F to 2100°F. Ceramic connectors are to withstand 1000°F. Thermocouples and wire consist of HT type "K" sheathed two-wire with grounded junctions. Duplex ceramic insulted teflon wire provides 30' lead from fire wall penetration of the observation area to the point of thermocouple connection within the test area. Four inch floor surface boxes (2) provide 4 - 1/8" x 20' thermocouple leads each.[2]

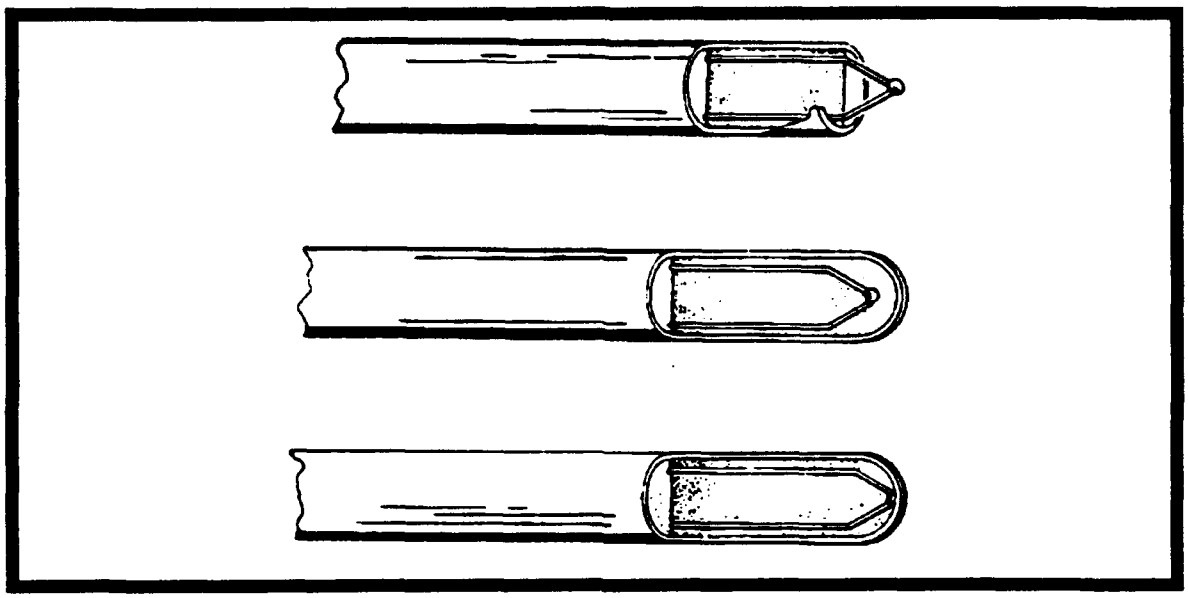

Figure 1 Thermocouple and probe junctions.

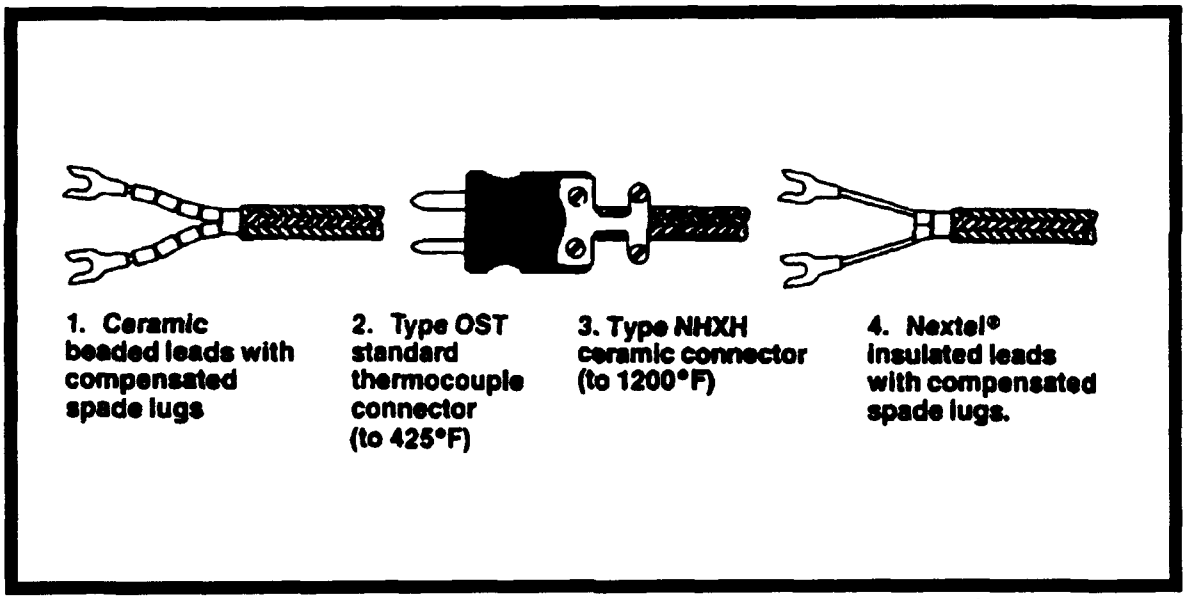

Figure 2 Thermocouple and insulated wire termination connections.

Flow and Level

Analog signature for O_2, CO, and CO_2 measurement is provided. Flowmeters for mass flow and level (low) must be able to withstand temperatures of 120°F. Flowmeters for vortex flow and level (high) must be able to withstand temperatures of 175°F. Pitotmeters may be used if flow and level measurement close to the burn subject the instrument to temperatures in excess of 175°F up to 800°F and pipe diameter is 2" minimum.[3]

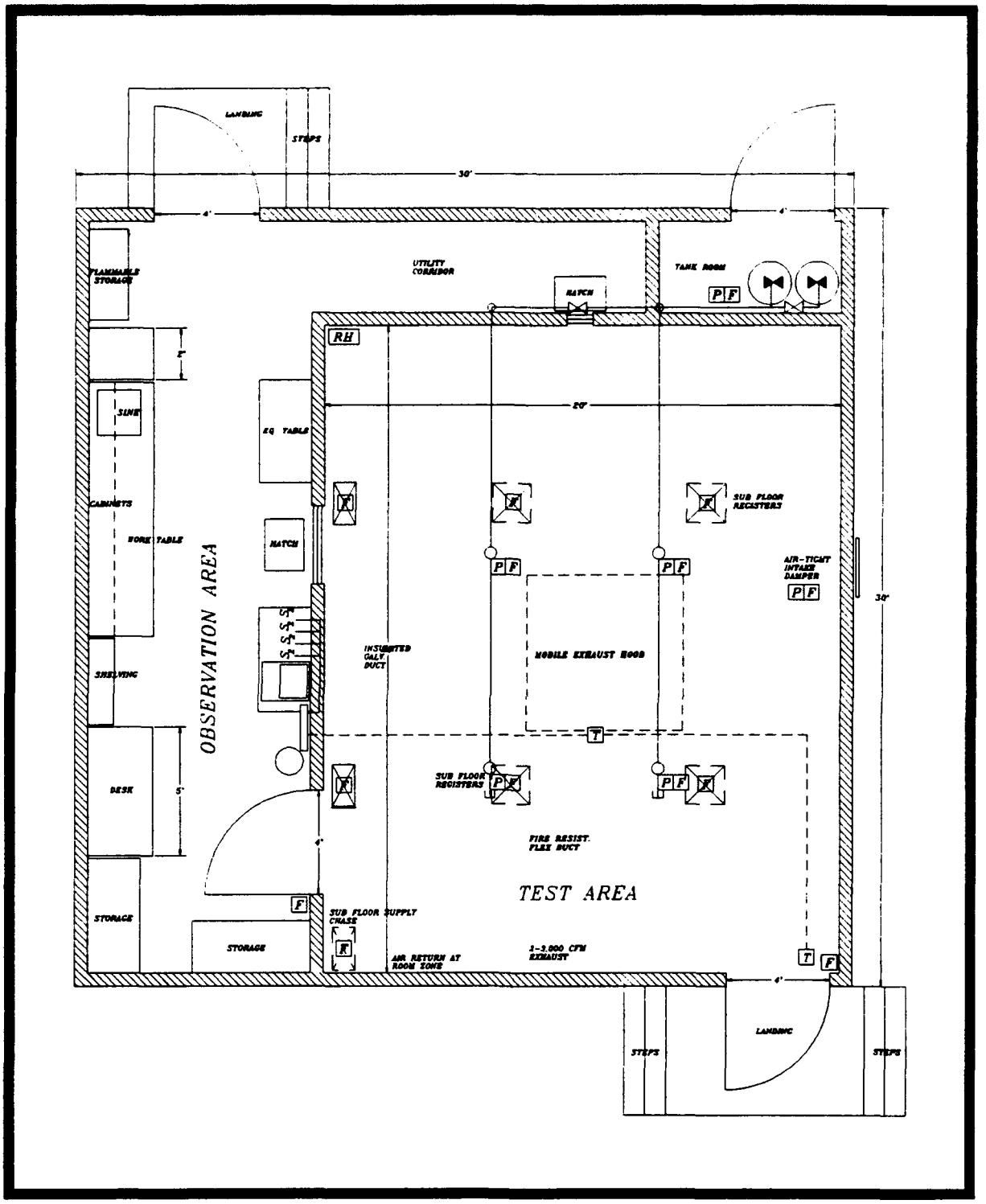

Figure 3 Test cell instrumentation and support equipment layout.

Pressure transducers

Typical ambient and test pressures developed within the test area are 0-6 psi (min/max). Developed pipe pressure, (frictional) loss, and reaction time is evaluated for suppressant under varying pressure. Pressure transducers are able to withstand temperatures to 185°F.[3]

Computer Interface and Data Acquisition

DOS 6.0 compatible software for simultaneous multiple data collection interfacing is provided. 3-dimensional graphic imagery for temperature measurement distribution at predetermined intervals can be provided throughout test sequencing. Spreadsheet data acquisition and interpolated graphing capability is provided within sensor relays. Interface boards operating at required A/D enables input (A/D) / output (D/A) at required voltage DC unless resistance is required to reduce voltage.

CONCLUSION

At the present time, the FSTC is currently under construction and no test or performance evaluations are currently available. The second phase of the project involving the FSTC instrumentation will initiate at the conclusion of FSTC construction. Temperature sensor devices will be placed intermittent intervals for accurate temperature measure prior to burn, ignition, and subsequent suppression. Probe sensor devices may be places in "tree" formation at vary probe lengths (subsequent distances from the fire) to acquire three-dimensional temperature distribution both horizontally and vertically. Flex thermocouples may be suspended or fastened to the FSTC or appropriate testing apparatus. Flex thermocouples may be immersed up to 12" in typical pan fire burns.

Flow and level will be monitored for active fire suppression agents (aerosols, CF_3I, CF_3Br) using 3/4" piping or greater. Flow and level may additionally be implemented for air flow through static grilles, HVAC registers, and returns to evaluate passive effects on fire behavior and suppression performance under a variety of air flow rates and patterns. Such systems will measure air velocity, ambient temperature, and static pressure. Vortex

shedding flowmeter systems are to be implemented to measure min/max flow and level for semi liquid/gaseous (aerosol), gaseous, and steam fire suppressant alternatives. Pressures developed in agent tanks (or other sources), piping, and orifices may be measured to assess fire suppressant performance under varying pressures. Pressures developed within the test areas as a result of suppression may be monitored. Effectiveness of passive pressure systems such as HVAC registers and returns, exhaust louvers, and static grilles may also be monitored.

Maximum and minimum values for temperature, flow, pressure, and R.H. must be obtained to practically and economically implement proper devices. Sensor devices capable of analyzing structural stress, strain, and torsion as a result of fire and fire suppression activities is also available. Finally, sensor device material selection must consider potential adverse effects of hydrocarbon, sulfuric, and halogen substrates on instrumentation as a result of exposure to fuels and suppressants targeted for FSTC use.

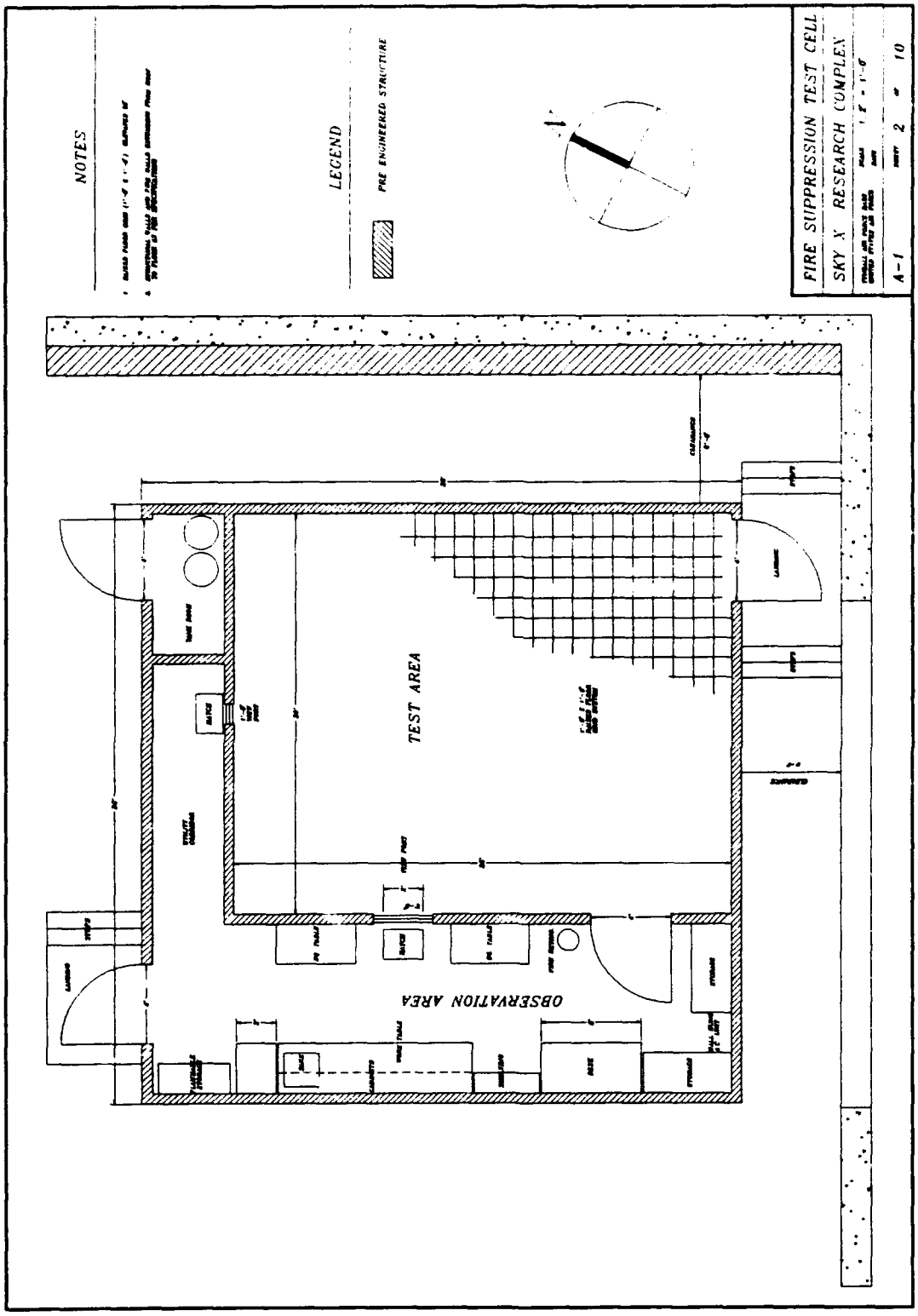

Figure 4 A-1: Fire Suppression Test Cell plan.

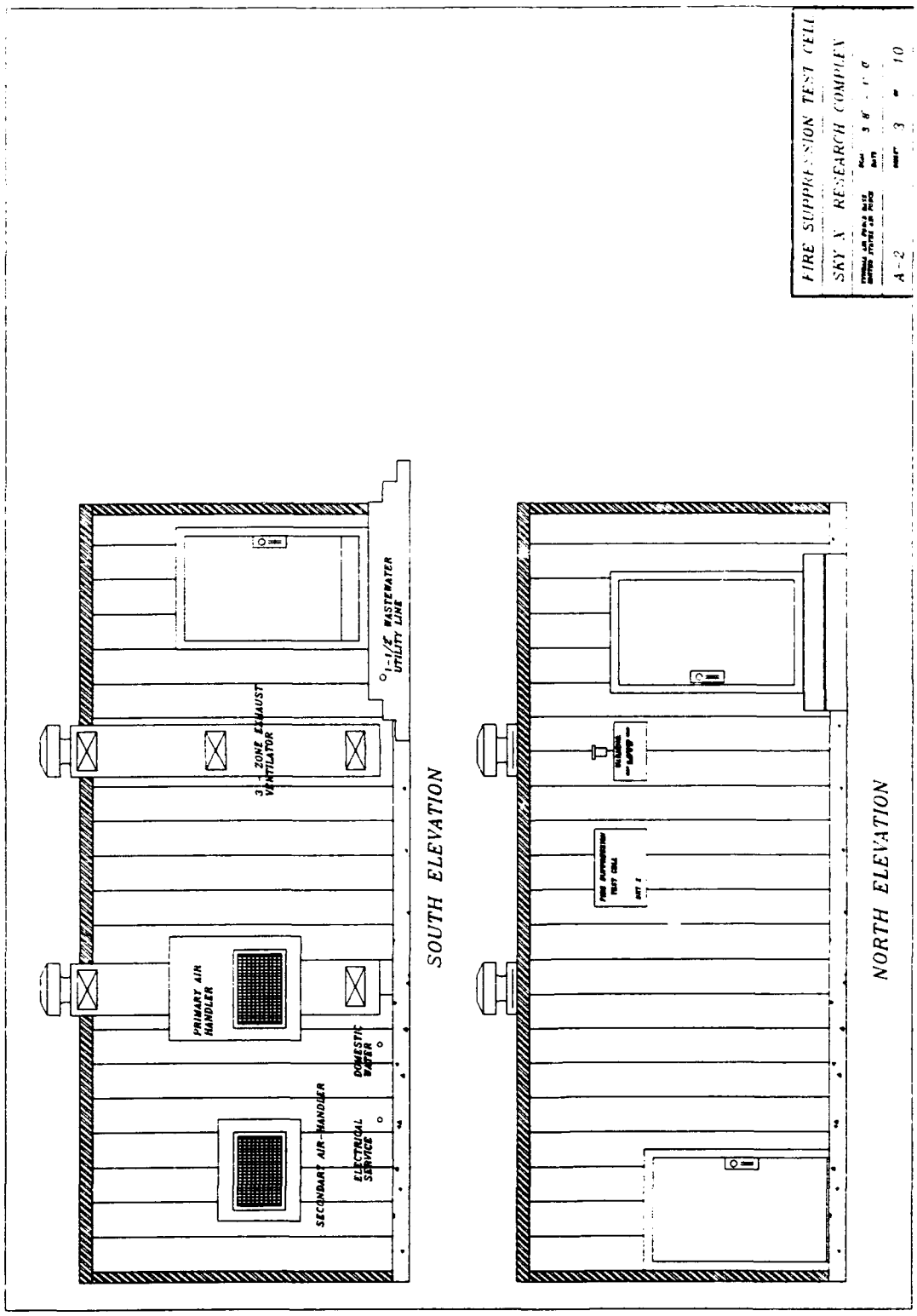

Figure 5 A-2: Architectural elevations.

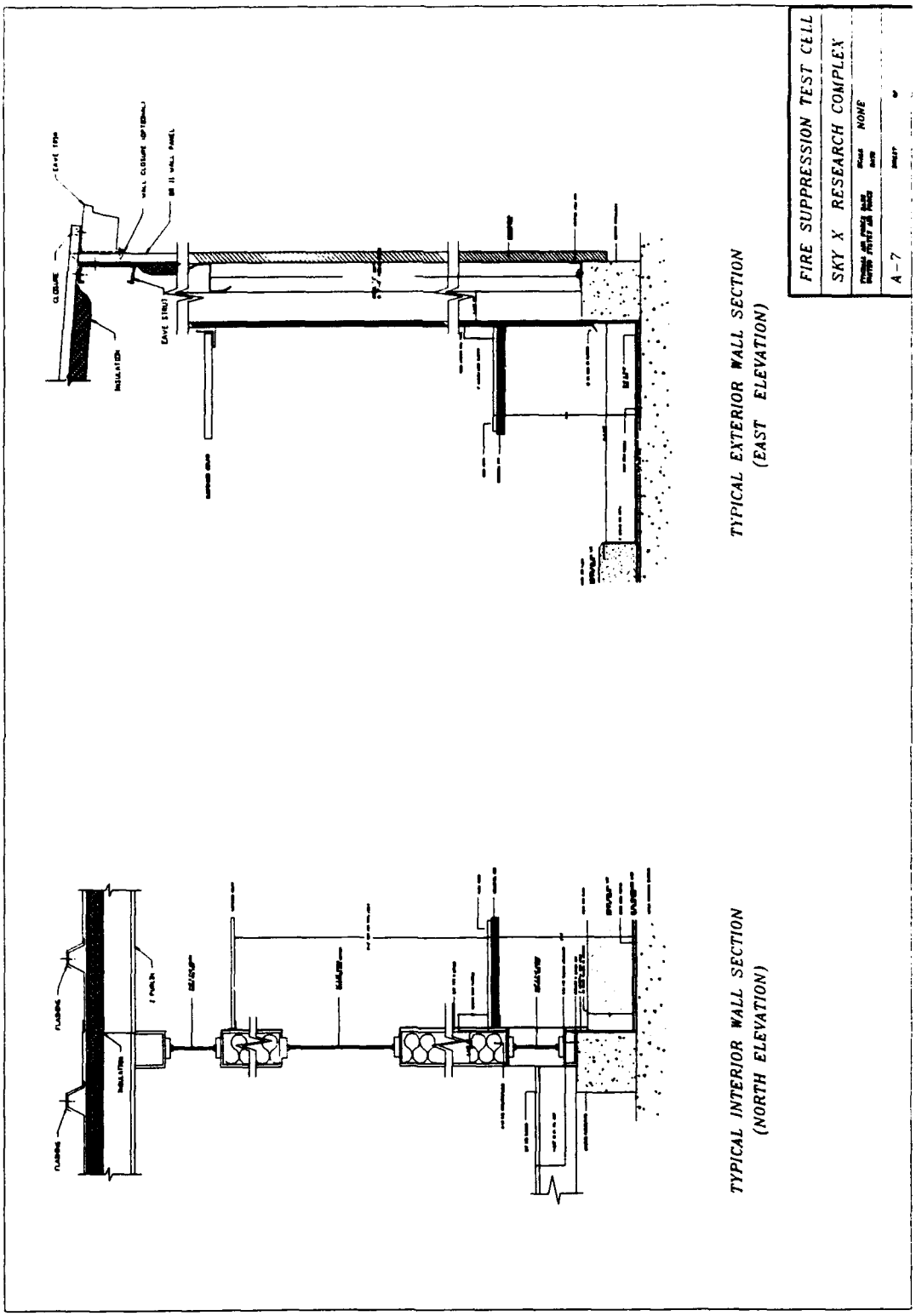

Figure 6 A-5: FSTC wall details and section plan.

REFERENCES

1. Comer, Don. Design Specifier's Manual. Kansas City, Butler Pre-Engineering Systems: 1993.

2. Omega Technology Company. The Temperature Handbook. Stamford, Omega: 1992.

3. Omega Technology Company. The Flow and Level Handbook. Stamford, Omega: 1992.

A Study of Delamination of Graphite - Epoxy Panels Due to Impact with 1/2" Diameter Steel Spheres

John T. Lair
Graduate Student
Department of Civil Engineering

University of New Orleans
Lake Front Campus
New Orleans, LA 70148

Final Report for:
Graduate Student Research Program
Wright Laboratory

Sponsored By:
Air Force Office of Scientific Research
Bolling Air Force Base, Washington D.C.

and

Wright Laboratory
WL/FIV
Wright-Patterson Air Force Base, Dayton OH

December 1993

A Study of Delamination of Graphite - Epoxy Panels Due to Impact with 1/2" Diameter Steel Spheres

John T. Lair
Graduate Student
Department of Civil Engineering

Abstract

Carbon graphite - epoxy composite panels that had been impacted with 1/2" steel spheres at velocities from 399 feet/sec to 5981 feet/sec were studied. After soaking the damaged region in a dye solution, the laminates were pyrolyzed and deplied to reveal the ply-by-ply area of delamination. Delamination and hole areas were quantified and are presented on a per-ply and velocity basis.

A Study of Delamination of Graphite - Epoxy Panels Due to Impact with 1/2" Diameter Steel Spheres

John T. Lair
Graduate Student
Department of Civil Engineering

Introduction

Carbon graphite fiber - epoxy composites are a structural material currently being used in aircraft and other applications. These composites consist of layers of carbon graphite held together by epoxy. The carbon graphite fibers are exceptionally strong and stiff resulting in a material that gives greater strength and stiffness per unit weight than steel or aluminum. The direction of the fibers in the composite may be varied from layer to layer to result in stiffness and strength directional properties best suited to the application at hand. Quasi-isotropic lay-ups are schemes to vary the fiber directions so that in the plane of the panel, the properti are approximately the same in all directions.

Problem discussion

Under impact conditions carbon graphite - epoxy composites do not react the same as metals. Where as metals fail by denting, petaling and shearing (each according to the projectile velocity) composites fail through delamination, tensile fiber failure, and eventually shear with increased velocities. Delamination is a separation of the layers of carbon graphite through loss of adhesion of the epoxy. Carbon

graphite - epoxy composites have been shown to delaminate upon being impacted by a projectile by several researchers such as Cantwell [1] and Hong and Lui [2]. Cantwell used a 6 mm (0.236 in), 1 gram (15.432 grain) projectile on ± 45 layup panels at velocities up to about 219 m/s (718 feet/sec). Hong and Lui used a cylindrical projectile 12.5 mm (0.492 in) dia. X 25 mm (0.984 in) long on various layups at velocities up to about 100 m/s (328 feet/sec). Both test series remained below the V_{50} for the subject material[1]. Impacts on aircraft are often expected to occur at higher velocities. Research performed in conjunction with this paper identifies damage distribution (through out the laminate) as a function of past V_{50} impact velocity. Identification and prediction of this complex damage state is of interest for repair and estimation of residual strength of damaged composite structures.

Methodology

The research describe in this paper was carried out on carbon graphite - epoxy panels $[(0/90/+45/-45)_4]_s$ of type AS4/3501-6 (carbon graphite type / epoxy type), provided by Wright Laboratory[2]. The manufacture of the panels was of

---

1 The V_{50} is the impact velocity at which a projectile will pass through a target 50 percent of the time. For the panels used in this experiment this impact velocity is about 375 ft/sec.

2 $[(0/90/+45/-45)_4]_s$ Represent the layup of the individual plies in the panel. The numbers represent the angle in degrees that the axis of the fibers lay along for each ply, the subscript 4 indicates that the

superior quality and resulted in clean data.

All laminates were penetrated by 1/2" diameter steel spheres. Spheres were chosen to eliminate the possibility of the projectile tumbling and impacting the target with an unpredictable presented impact area. Projectiles were propelled through the use of a light-gas gun for velocities below 2,200 feet/sec and through a 20 mm cannon for velocities above 2,200 feet/sec.

Projectile velocities were obtained redundantly by a series of light-screens, break-papers and inductance coils for the lower velocities, and by break-papers and inductance coils for the higher velocities. Multiple velocity measurement methods were used to verify velocity accuracy Light-screens were not employed at the higher velocities due to erratic functioning of the light-screens directly in front of the muzzle blast.

After being impacted, panels were pyrolized using a method developed by Freeman [3] and described by Harris [4]. A solution of ethyl alcohol containing 10 percent by weight of gold chloride was prepared for use as a dye agent. The bottom of the hole through the laminate was covered with a sheet of paraffin and the edges of the sheet sealed with hot paraffin. The gold chloride solution was then poured in and left to soak into the fractured region overnight. On the following day any

---

layup between the parentheses is repeated 4 times and the subscript S indicates the layup is symmetric about the centerline.

remaining solution was then poured out and the panel left to dry for one day. Panels were then pyrolyzed at 400 degrees Celsius for about 25 minutes, or until the plies started to separate. After the panels cooled, the edges of the outermost ply were reinforced with adhesive tape and an identifying label attached. The outer [illegible]ly was then removed with the assistance of a scalpel. The procedure of ply reinforcement, identification, and removal was then repeated for each remaining ply in the laminate. This procedure resulted in 31 plies (vs 32 in the laminate) because the centerline plies did not have a fiber angle mismatch and could therefore not be separated. In the following analysis, the center two plies have been assumed to act as one ply and no delamination is assumed between them.

The delamination area and hole area[3] associated with each ply was determined by image analysis. The image analysis system, supplied by Wright Laboratory, consisted of a 386SX computer with a True Vision "TARGA" image grabbing board a monochrome camera and "Java" image processing software (by Jandel). Several images of known size were first measured to ensure the accuracy of the system (estimated at about 0.0005 square inch for this application). Stained laminates were observed in a darkened room using two light sources whose direction was adjusted until the maximum amount of gold was

---

[3] Hole is here defined as the region where material was physically sheared (removed) from the lamina.

visible while avoiding glare on the ply surface. Computation of area was done automatically using the edge following capability of the "JAVA" software and the program's capability to set all pixels in the image below a chosen level to black. Results of the survey were then plotted using "SIGMA PLOT" (by Jandel).

Results

Total delamination and hole areas are plotted versus impact velocity in Figure 1. Delamination and hole data on a ply-by-ply basis are presented in Figures 2 through 11. It is noted again that the middle two plies are treated as one in these figures as they could not be separated due to a lack of fiber angle change between them.

Conclusions

It is apparent from Figure 1 that the hole size initially increases with impact velocity, stays constant for a range of impact velocities then slowly increases. What is less intuitive is that delamination area at first decreases (over velocities from V_{50} to about 2,500 feet/sec) then begins to increase after impact velocities in excess of 3,500 feet/sec are attained. Changes in delamination as a function of impact velocity are believed due to varying damage mechanisms. Czarnecki [5] has theorized that the initial decrease in delamination is due to the location where the projectile meets the reflected tensile stress wave. This theory is supported by the higher areas of

delamination on plies adjacent to the rear face (Figures 2 through 7). The increase in delamination and hole area at impact velocities higher than 3,500 feet/sec is not easily explained. It has been suggested by Mayer [6] that this increase is due to more energy being available at the higher impact velocities and that this increase could be explained by a percolation type theory.

Acknowledgements

I wish to thank Dr. A. Mayer and Mr. G. Czarnecki for their support and guidance in this research. I also wish to extend my gratitude to Wright Laboratories for their support.

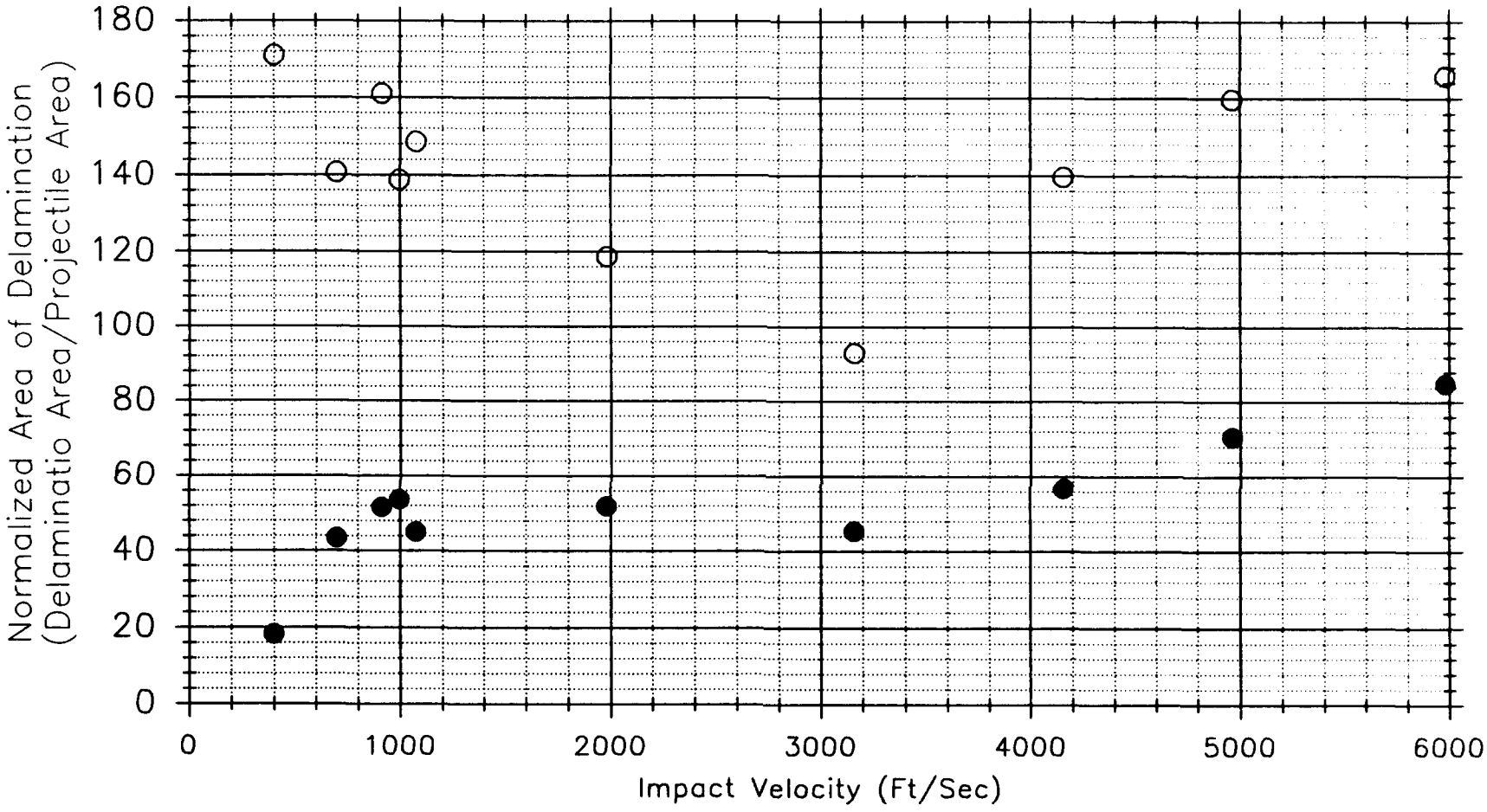

Figure 1
Hole and Delamination Area
Versus Impact Velocity, Deply Method

● Hole Area

○ Total Delamination Area

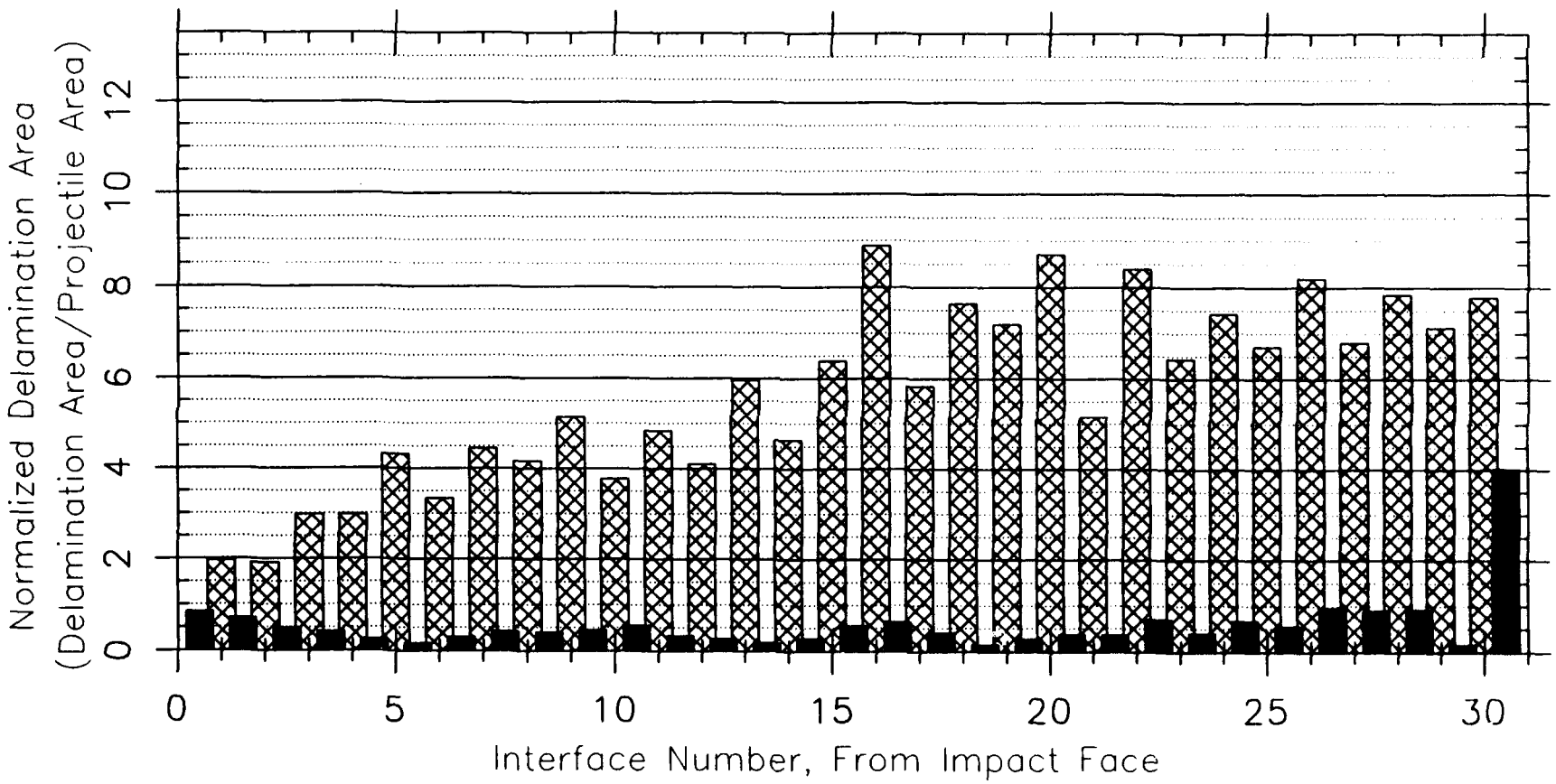

Figure 2

Delamination and Hole Area of Individual Plies

For Panel Impacted at 399 Ft/Sec

Delamination

Hole

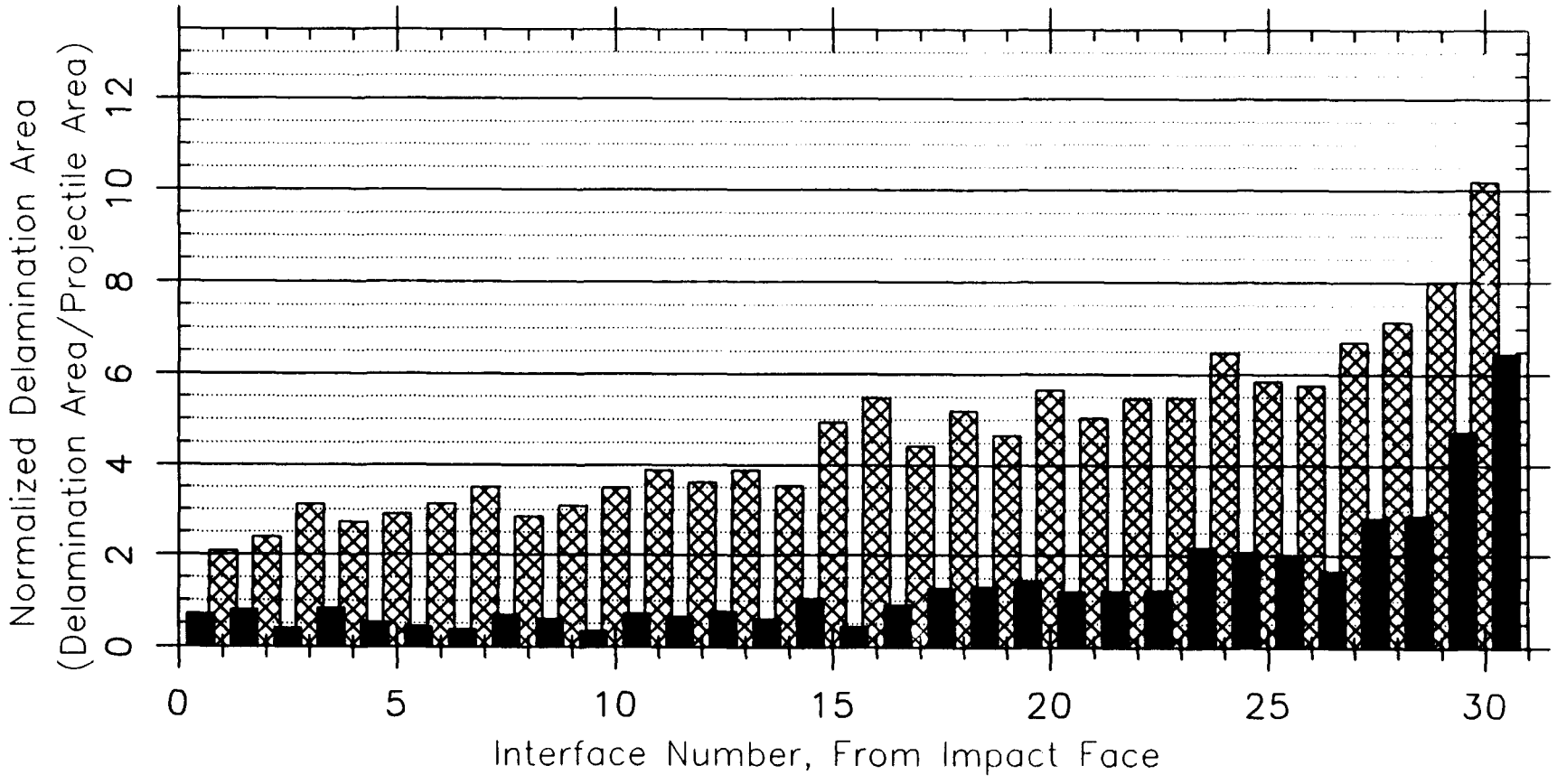

Figure 3

Delamination and Hole Area of Individual Plies

For Panel Impacted at 697 Ft/Sec

Delamination

Hole

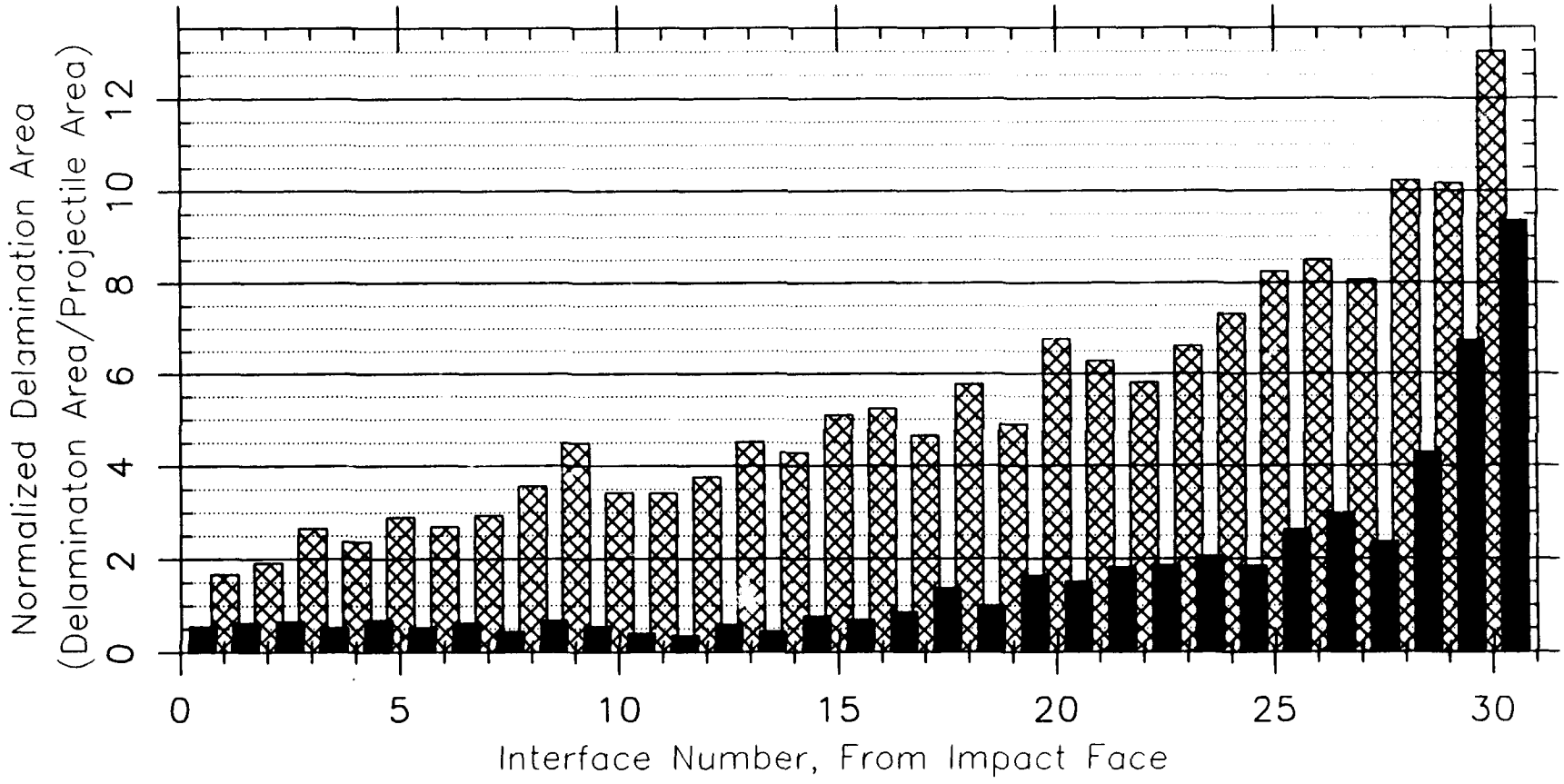

Figure 4

Delamination and Hole Area of Individual Plies

For Panel Impacted at 913 Ft/Sec

Delamination

Hole

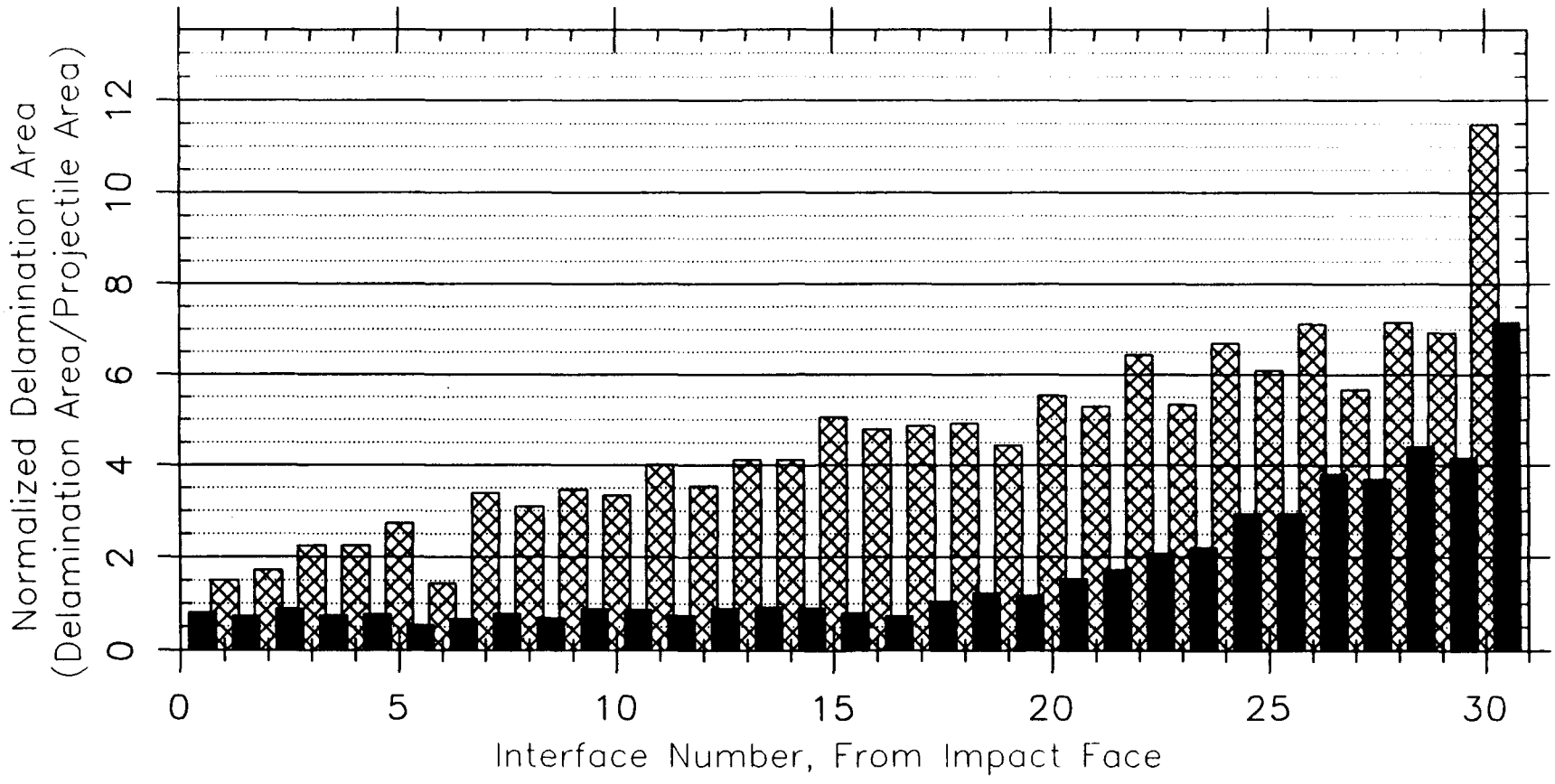

Figure 5

Delamination and Hole Area of Individual Plies

For Panel Impacted at 996 Ft/Sec

Delamination

Hole

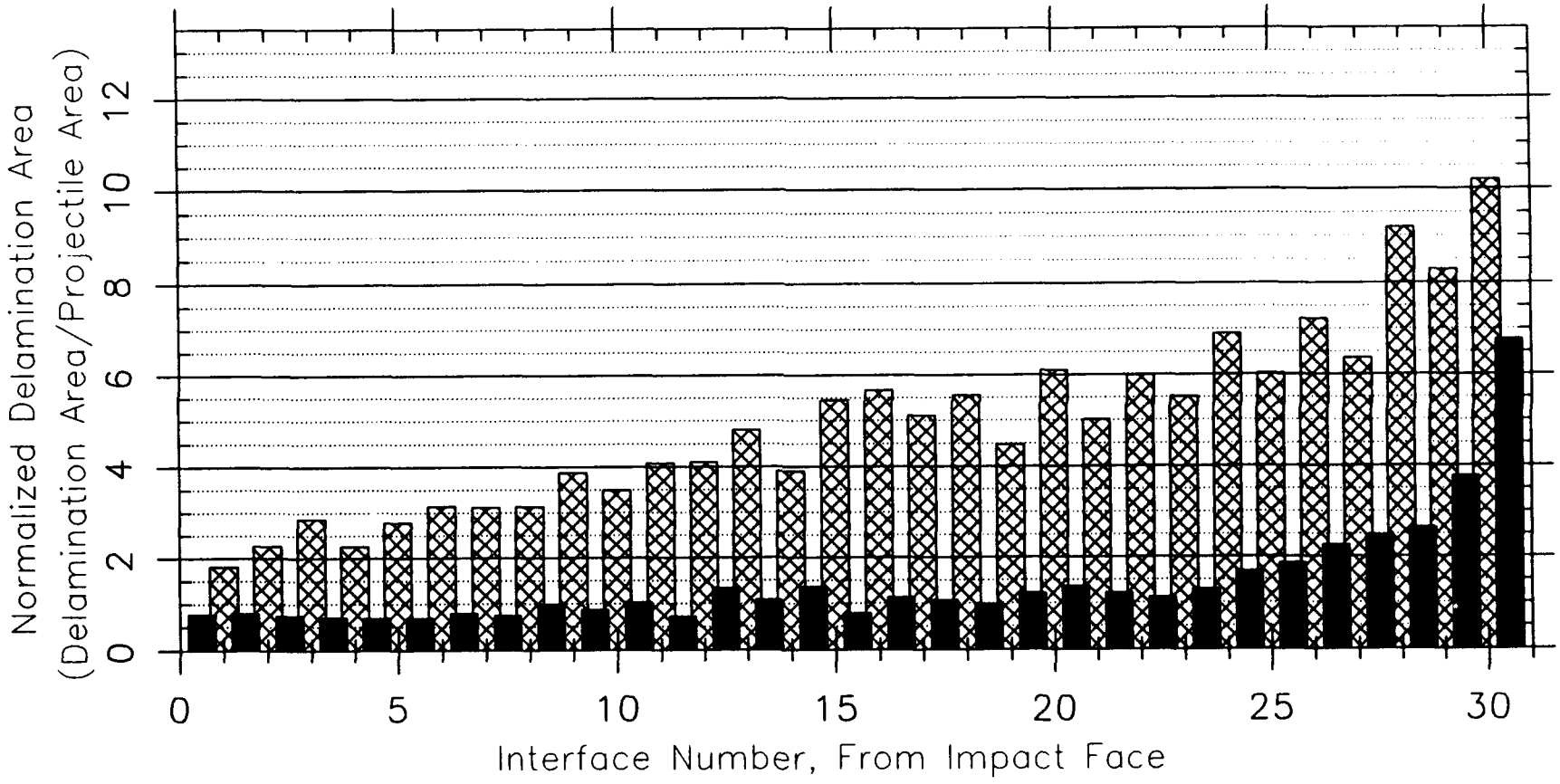

Figure 6

Delamination and Hole Area of Individual Plies

For Panel Impacted at 1074 Ft/Sec

Delamination

Hole

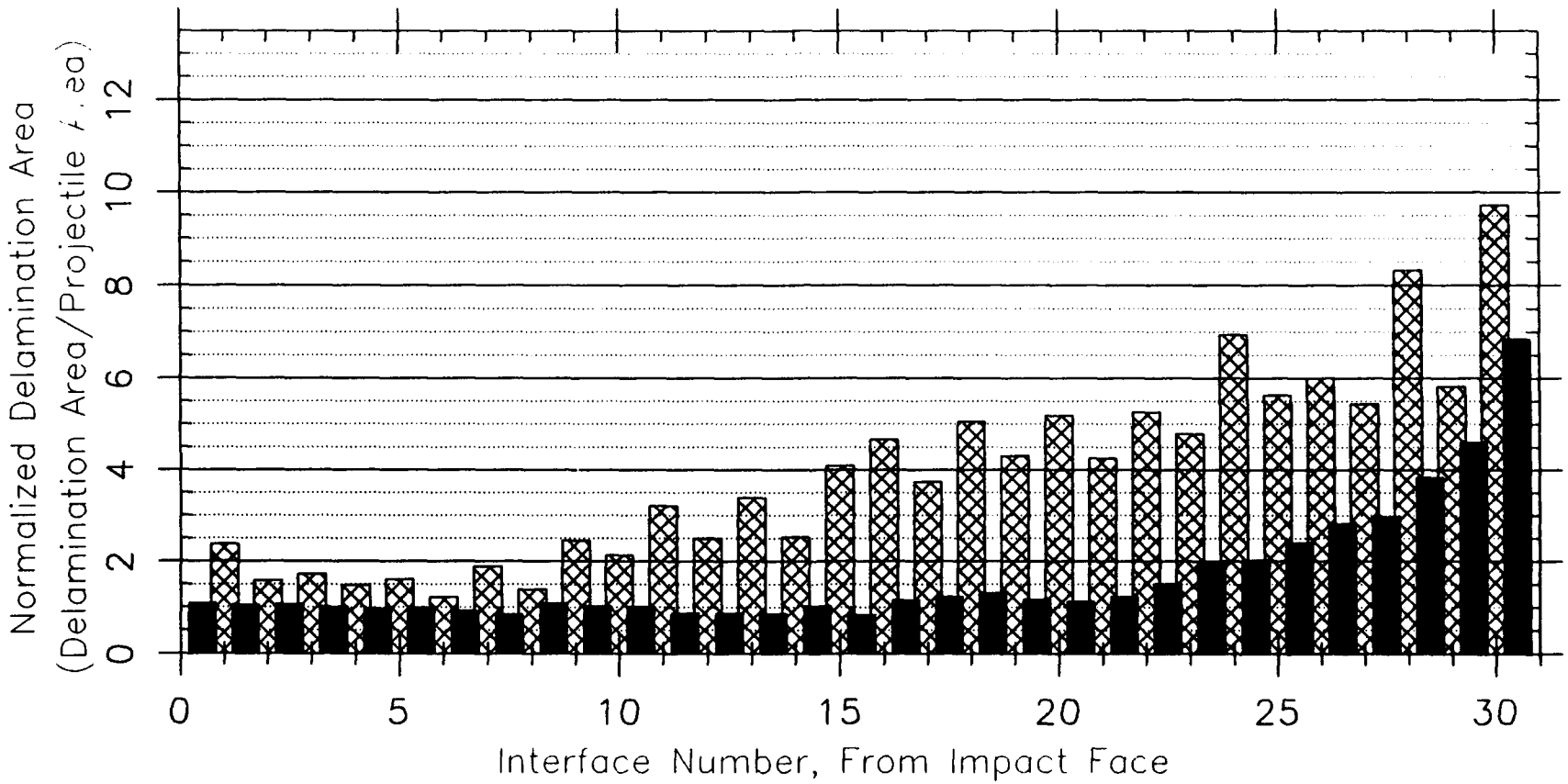

Figure 7

Delamination and Hole Area of Individual Plies

For Panel Impacted at 1982 Ft/Sec

Delamination

Hole

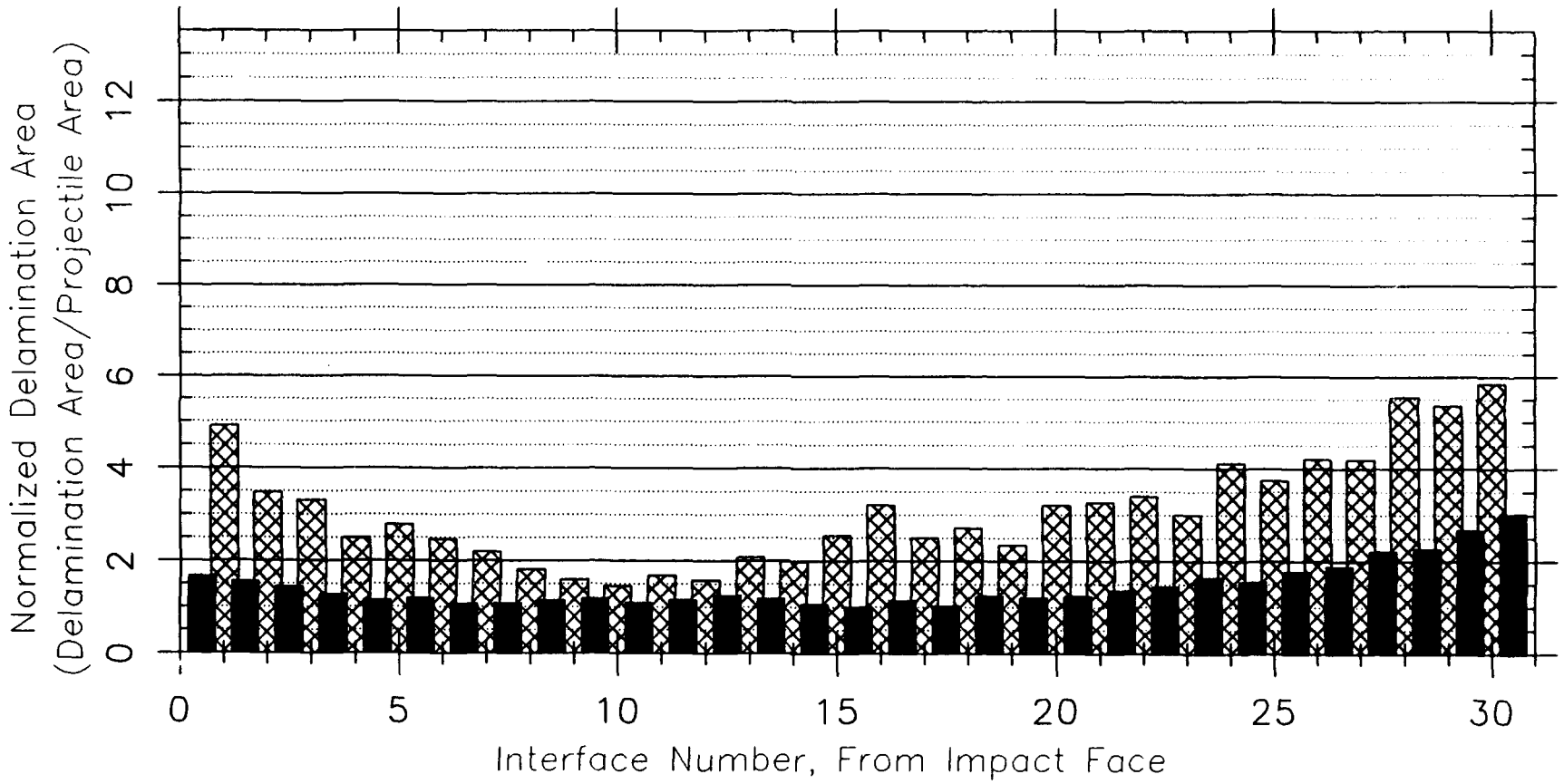

Figure 8

Delamination and Hole Area of Individual Plies

For Panel Impacted at 3157 Ft/Sec

Delamination

Hole

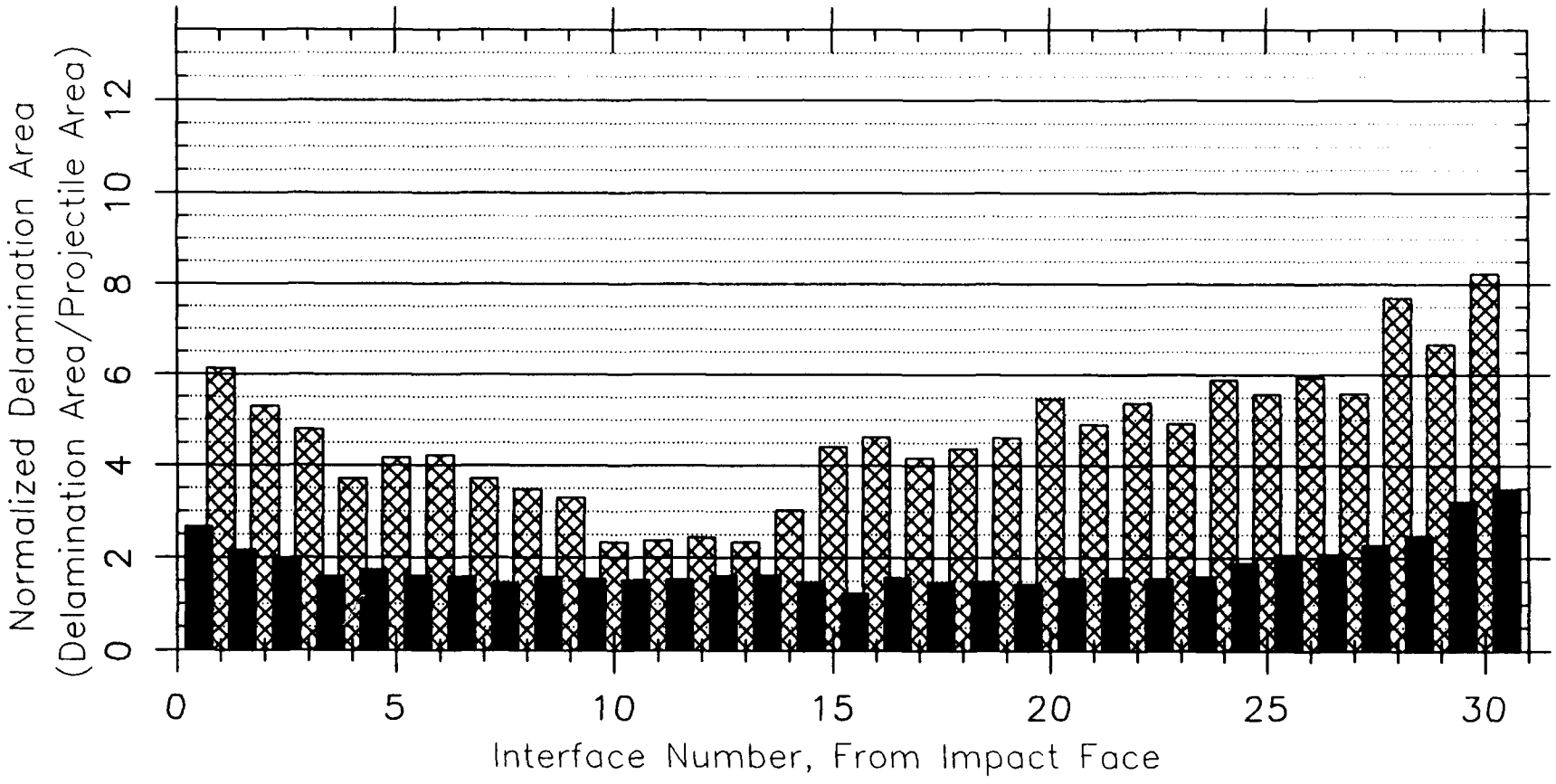

Figure 9

Delamination and Hole Area of Individual Plies

For Panel Impacted at 4157 Ft/Sec

Delamination

Hole

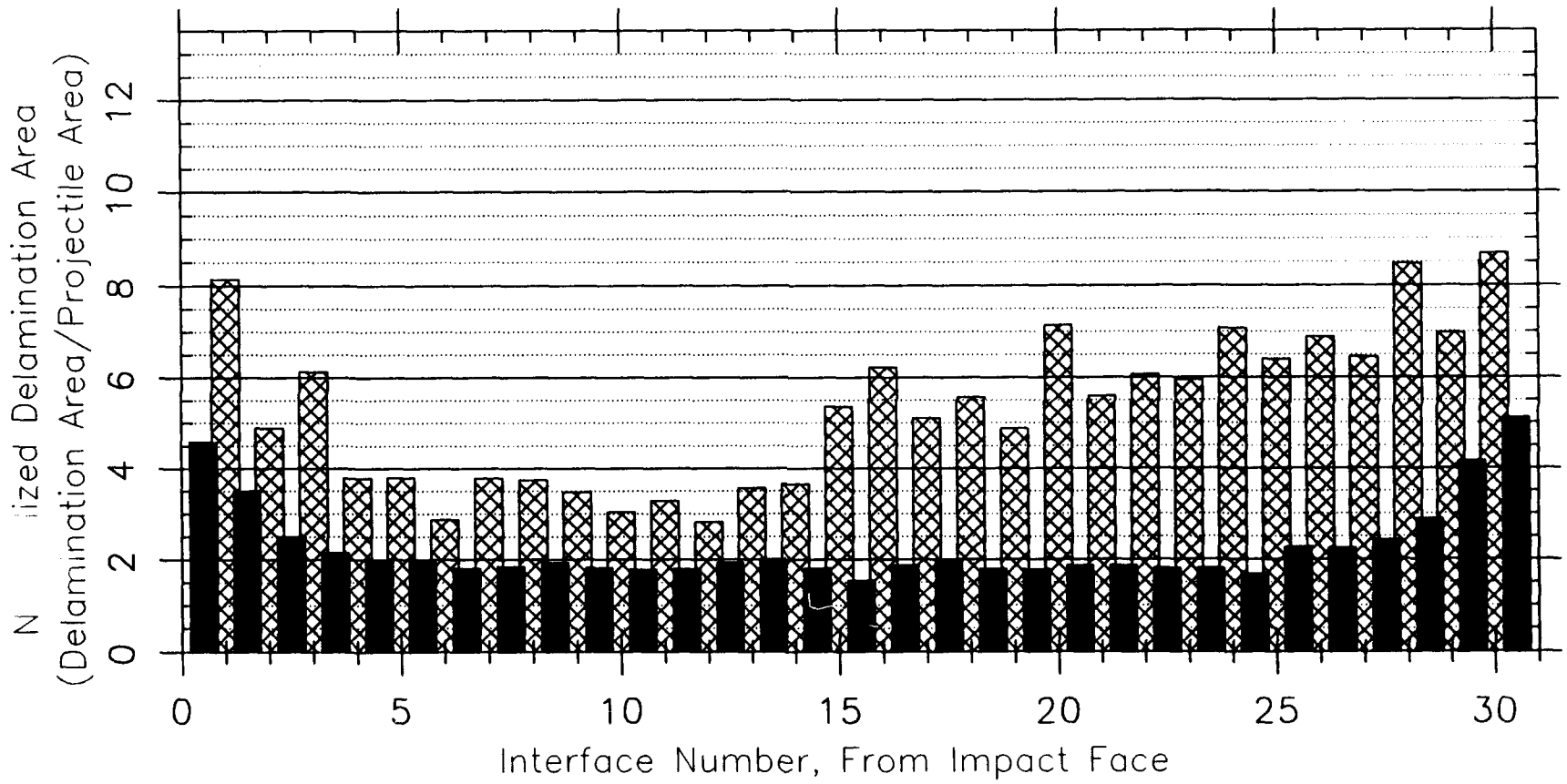

Figure 10

Delamination and Hole Area of Individual Plies

For Panel Impacted at 4963 Ft/Sec

Delamination

Hole

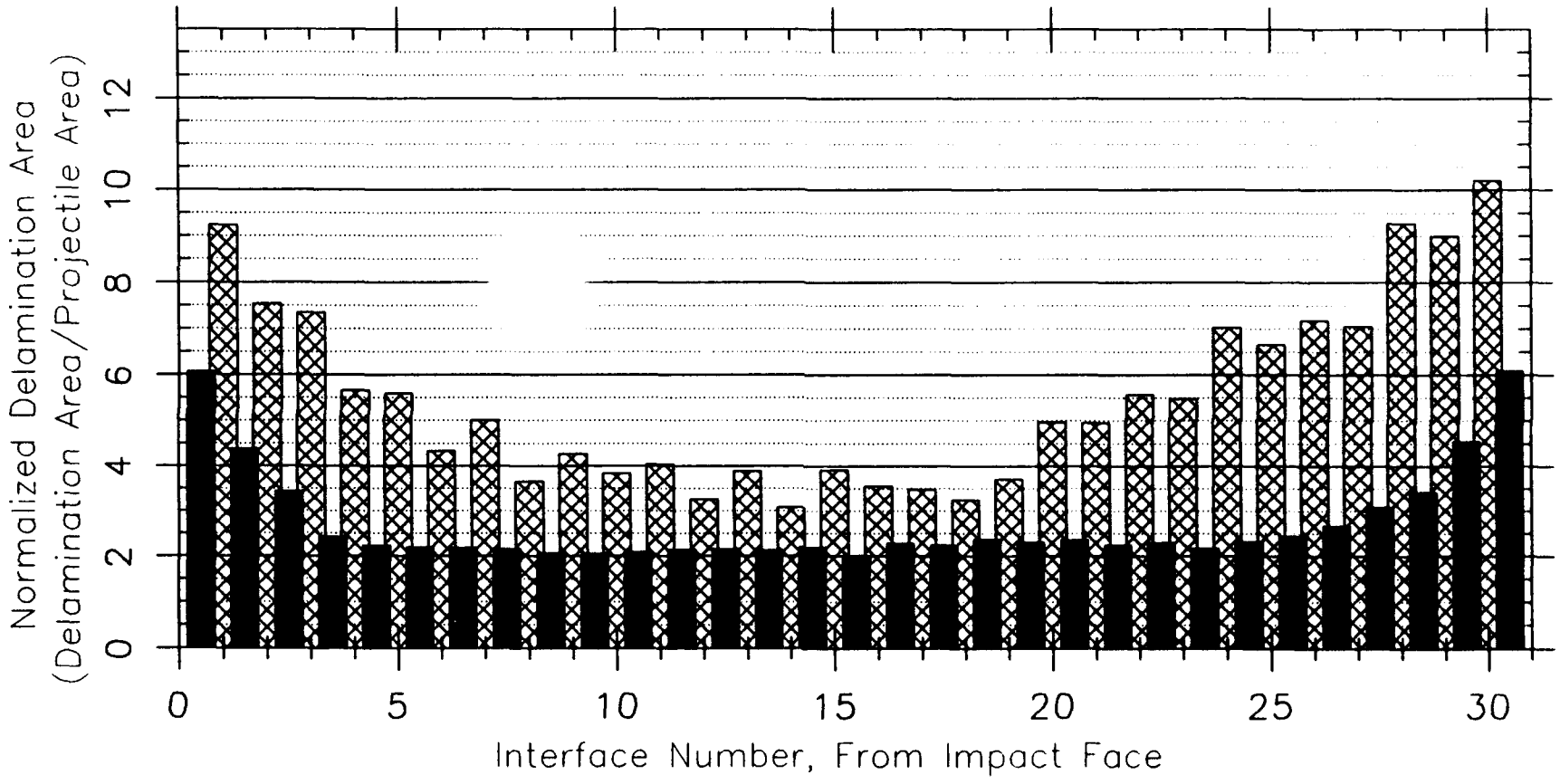

Figure 11

Delamination and Hole Area of Individual Plies

For Panel Impacted at 5981 Ft/Sec

Delamination

Hole

References

[1] Cantwell, W.J., "The Influence of Target Geometry on the High Velocity Impact Response of CFRP", Composite Structures, 1988, Volume 10, pages 247 - 265

[2] Hong, S. and Liu, D., "On the Relationship Between Impact Energy and Delamination Area", Experimental Mechanics, June 1989, pages 115 - 120

[3] Freeman, S.M., "Characterization of Lamina and Interlaminar Damage in Graphite-Epoxy Composites by the Deply Technique" Composite Materials: Testing and Design (Sixth Conf.), ASTM STP 787, ed. I.M. Daniel, ASTM, pages 50 - 62 (1982)

[4] Harris, C.E., "Damage Evaluation by Laminate Deply", Society of Experimental Mechanics , pages 147 - 149

[5] Czarnecki, G.J., "A Preliminary Investigation of Dual Mode Fracture Sustained by Graphite/Epoxy Laminates Impacted by High-Velocity Spherical Metallic Projectiles", Masters Thesis, University of Dayton, Dayton OH, April 1992

[6] Mayer, A., Personal correspondence between Mr. Lair and Dr. Mayer, June 1991 - Aug 1993

DELAMINATION DAMAGE AND ENERGY EXCHANGE FROM PENETRATING IMPACT OF SPIRAL STAIRCASE LAYUP COMPOSITE PLATES

MOHAMMED A. SAMAD

Graduate Student

Department of Mechanical Engineering

University of New Orleans

Lake front, New Orleans

Louisiana 70043.

Final Report for:

Graduate Student Research Program

Wright Laboratory

Sponsored by:

Air force Office of Scientific Research

Bolling Air Force Base, Washington, D.C.

August 1993

DELAMINATION DAMAGE AND ENERGY EXCHANGE FROM PENETRATING IMPACT OF SPIRAL STAIRCASE LAYUP COMPOSITE PLATES

MOHAMMED A. SAMAD
Graduate Student
Department of Mechanical Engineering
University of New Orleans

ABSTRACT

The change in delamination damage and energy exchange due to impact of composite plate (graphite/epoxy) was studied, using spiral staircase layup. The 4 different layups are

A) $[(0/90)_8]_s$, B) $[(0/+45/90/-45)_4]_s$,

C) $[(0/+22.5/+45/+67.5/90/-67.5/-45/-22.5)_2]_s$, and

D) $[(0/+11.25/+22.5/+33.75/+45/+56.25/+67.5/+78.75/90/-78.75/-67.5/-56.25/-45/-33.75/-22.5/-11.25)]_s$, impacted with a 1/2 inch steel sphere at a low and high velocities.

DELAMINATION DAMAGE AND ENERGY EXCHANGE FROM PENETRATING IMPACT OF SPIRAL STAIRCASE LAYUP COMPOSITE PLATES

Mohammed A. Samad

INTRODUCTION:

This research program was a continuation of work started last year 1992, summer, sponsored by Air Force office of Scientific research. The experimental work was done in Wright Laboratory, at WL/FIVS. The primary objective of this research is to continue the program stared last summer, the research was design to study experimentally the effect of mismatch angle between adjacent ply on delamination damage and energy exchange due to impact.

The composite plates (graphite epoxy) 5" X 5", 32 ply, were impacted with 1/2 inch steel sphere at a series of low and high velocities (velocity from 400 to 6000 ft/sec), using 4 different constant angle change layup to be A) $[(0/90)_8]_s$, B) $[(0/+45/90/-45)_4]_s$, C) $[(0/+22.5/+45/+67.5/90/-67.5/-45/-22.5)_2]_s$, and D) $[(0/+11.25/+22.5/+33.75/+45/+56.25/+67.5/+78.75/90/-78.75/-67.5/-56.25/-45/-33.75/-22.5/-11.25)]_s$. 16 panels of low velocity (velocity from 400 to 2000 ft/sec) were

deplied last year, 4 panels from each layup to determine exact delamination damage of each ply caused by impact, by using image analyzer. 20 more panels deplied of high velocity this summer (velocities are 2200 fps, 3000 fps, 4000 fps, 5000 fps, and 6000 fps), 5 panels from each layup.

METHODOLOGY:

After the panels were impacted at a known velocities, gold chloride is used to determine the delamination area. A number of procedure has to done to deply a panel. First of all a Wax wall is built over the hole of the plate to hold gold chloride. Gold chloride is poured in the panel for 2 days and soaked. After 2 days the panel is heated in furnace for approximately about half hour at 800 degrees. When the panel is heated at that temperature, gold chloride turned into gold and deposited on the delamination area of each ply. The panel is heated at high temperature to burn the matrix, it helps in deplying plies easily. A white paint line is drawn on each ply across the gold to measure delamination area under image analyzer.Image analyzer system consist of a camera, RBG color monitor, and a computer. Figure 1 shows the image analyzer. When a ply is placed under the camera, and an image of the ply is displayed on the monitor. By using JAVA software the area under the

white paint can be calculated. This procedure is repeated for 32 ply to calculate the total delamination damage for each panel. By same technic the hole area for each ply also calculated. Delaminaton damage of each ply and the hole area is plotted, the total delamination damage is correlated with initial velocity as shown in graphs.

To continue this research program, more than 140 panel of 4 different layup were impacted with 1/2 inch steel sphere at different velocities, with improved method for calculating initial velocity and residual velocity. To study the non penetrating damage below ballistic limit (V_{50}) many panels of different layup were impacted with 1/2 inch steel sphere at 200 fps and 300 fps.

FIGURE 1

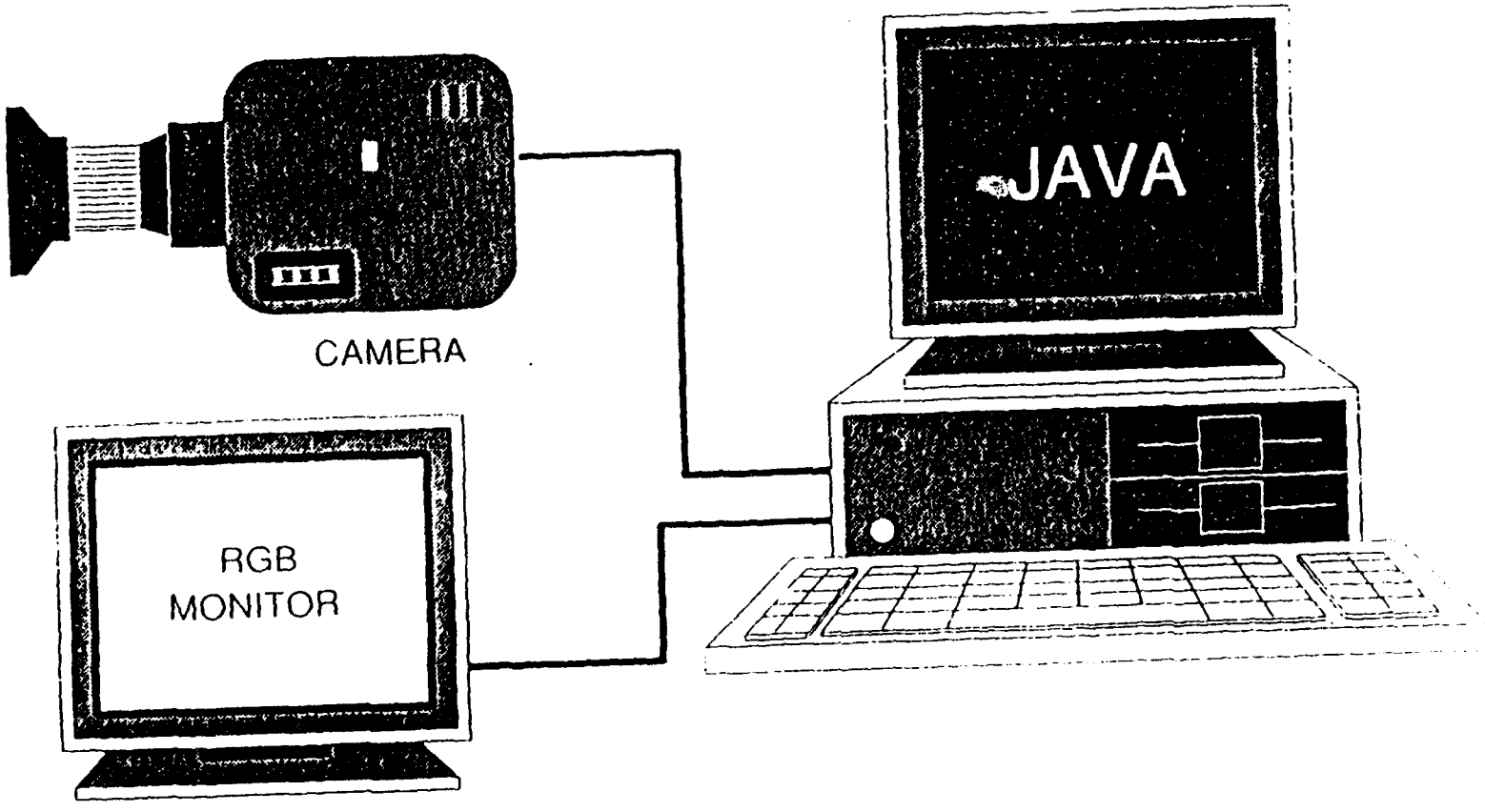

The Image Analysis System

PANEL LAYUP: 0/90

Panel	Intial Velocity	Delamination Area
1	397.00	31.715498
2	697.00	26.756778
3	1001.00	25.767780
4	1990.00	21.817380
5	2231.3	17.674760
6	3070.00	18.300870
7	4181.60	24.835160
8	4902.00	26.856870

Panel Layup: 0/45

Panel	Velocity	Delamination area
F.10.7	398	35.964815
F.9.2	696	28.513492
F.10.9	1091	26.804500
F.10.1	2008	19.449140
F.9.7	3148.9	23.226480
F.9.8	4050.0	24.822260
F.8.1	4933.0	32.792100
F.8.3	5937.2	36.359250

TABLE 1

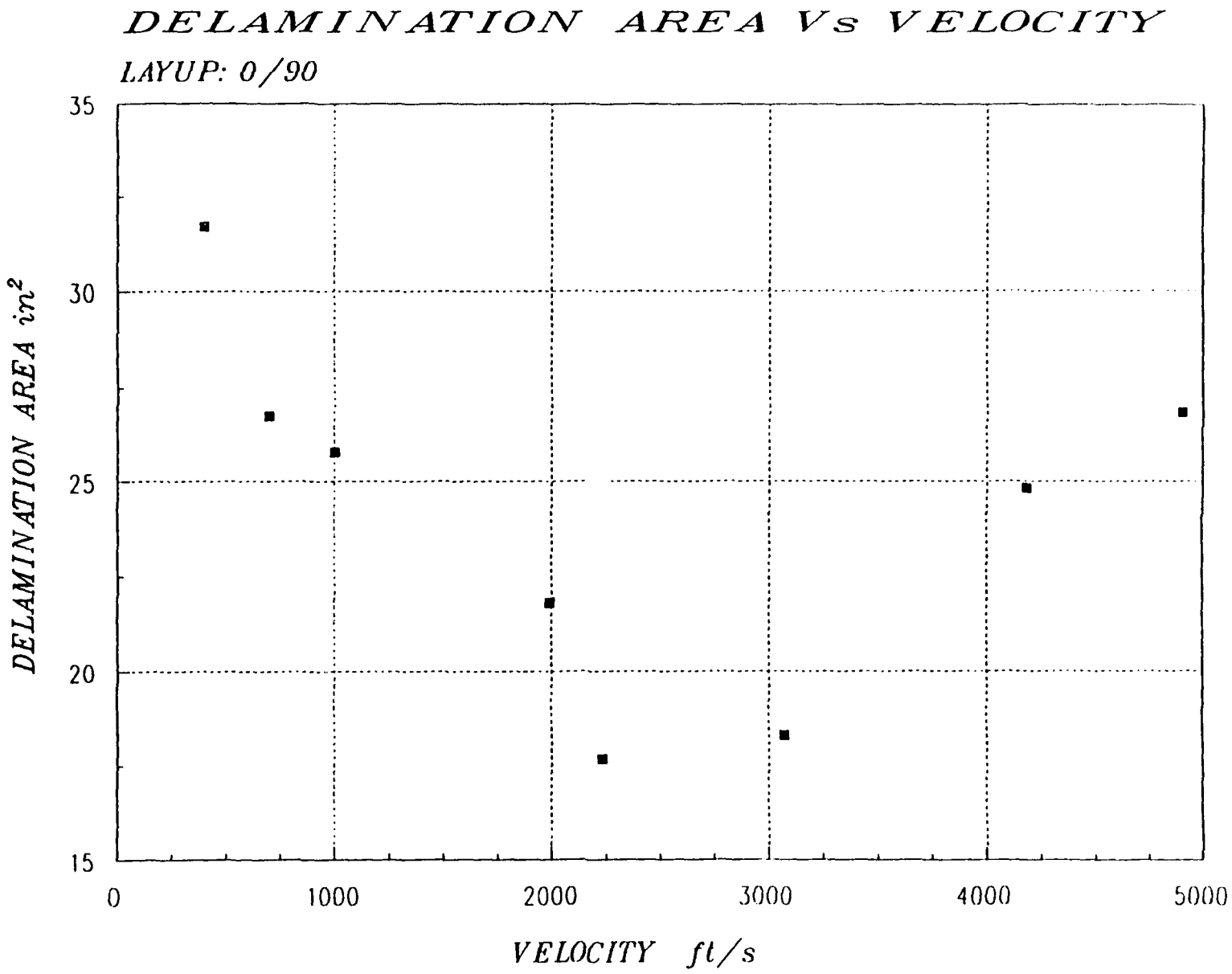
DELAMINATION AREA Vs VELOCITY
LAYUP: 0/90
DELAMINATION AREA in²
35
30
25
20
15
0
1000
2000
3000
4000
5000
VELOCITY ft/s

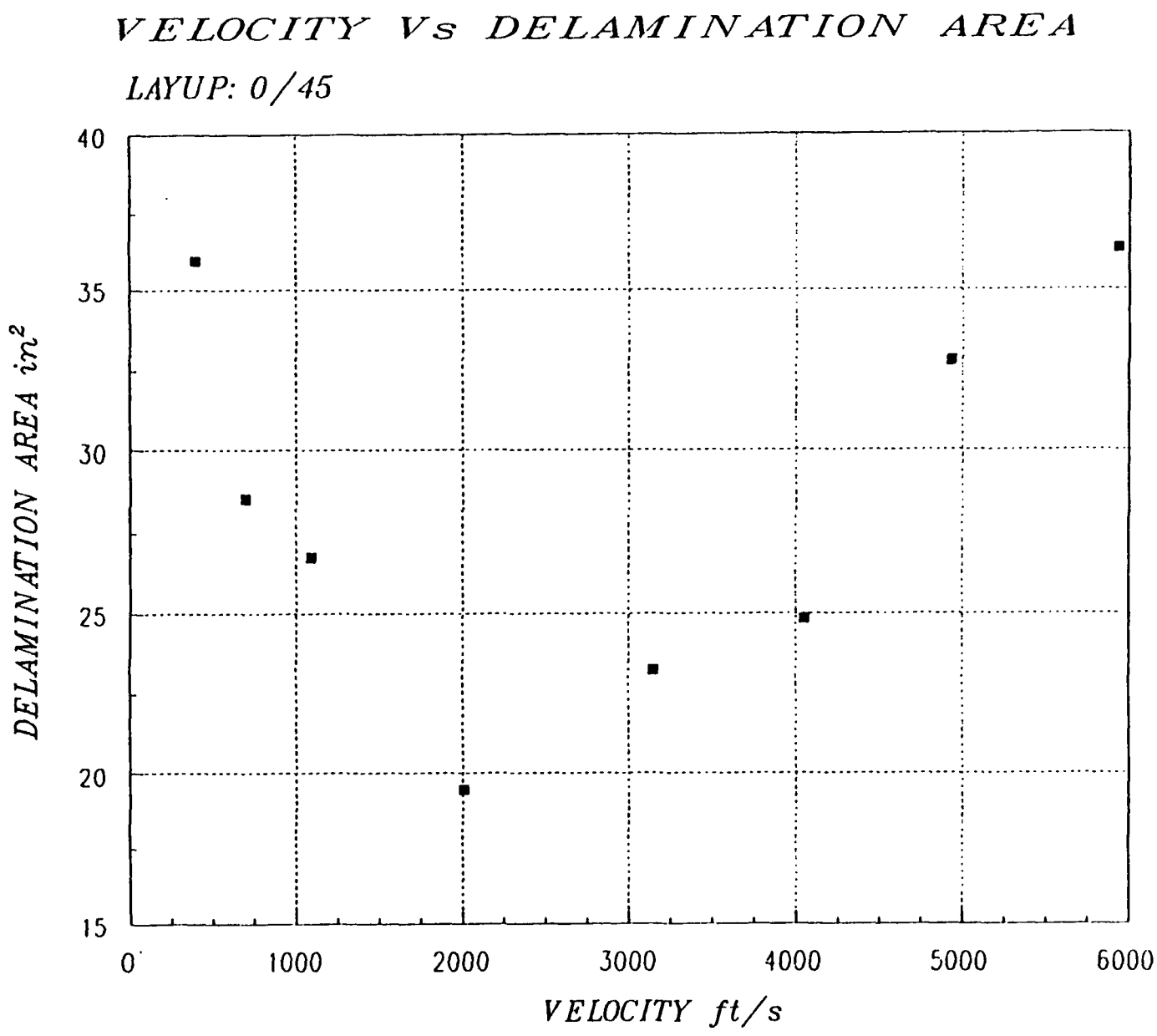
VELOCITY Vs DELAMINATION AREA
LAYUP: 0/45
DELAMINATION AREA in²
40
35
30
25
20
15
0
1000
2000
3000
4000
5000
6000
VELOCITY ft/s

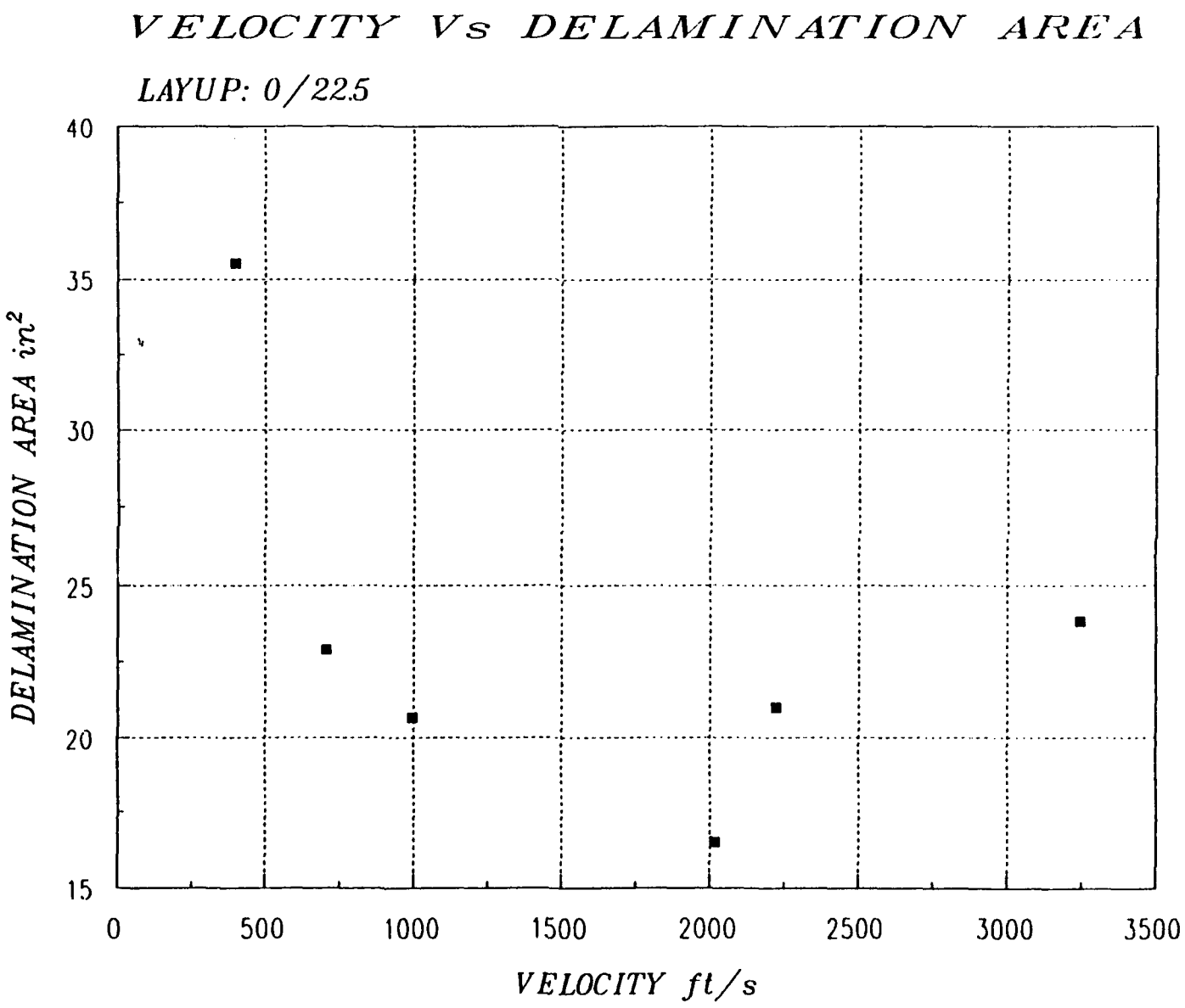
VELOCITY Vs DELAMINATION AREA
LAYUP: 0/22.5
DELAMINATION AREA in²
40
35
30
25
20
15
0
500
1000
1500
2000
2500
3000
3500
VELOCITY ft/s

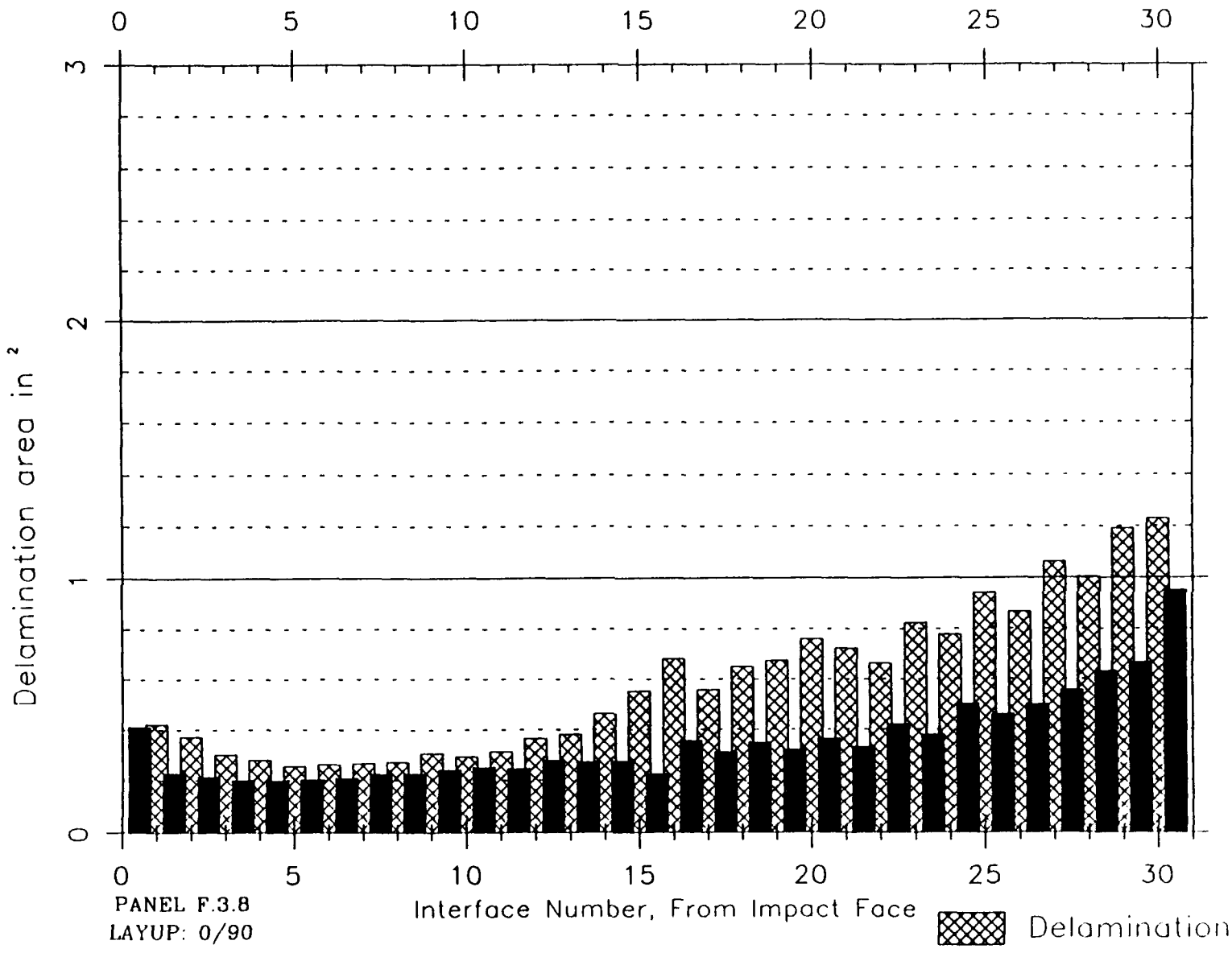

Delamination and Hole Area of Individual Plies
Panel Impacted at 2231.3 fps

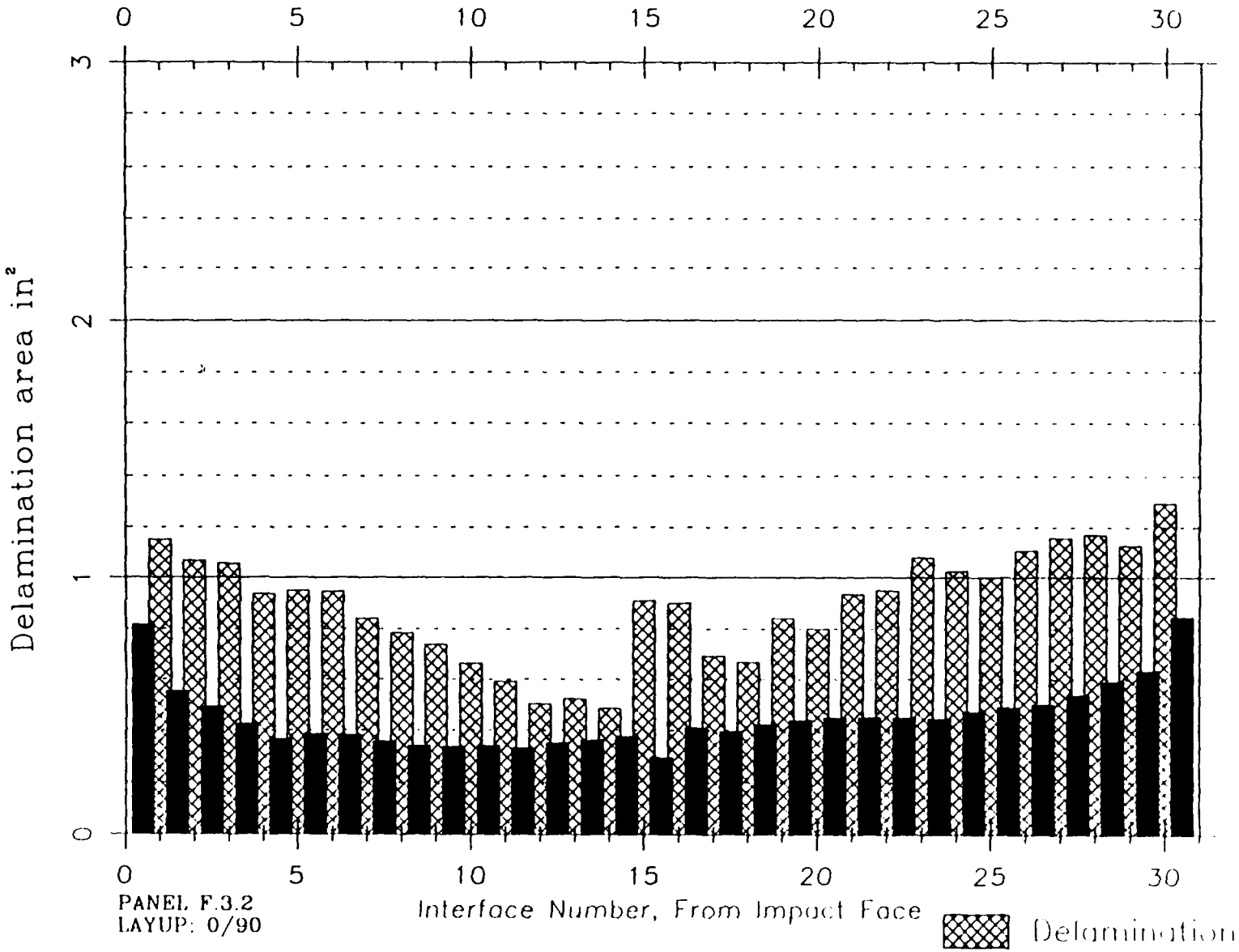

Delamination and Hole Area of Individual Plies
For panels impacted at 4902 fps

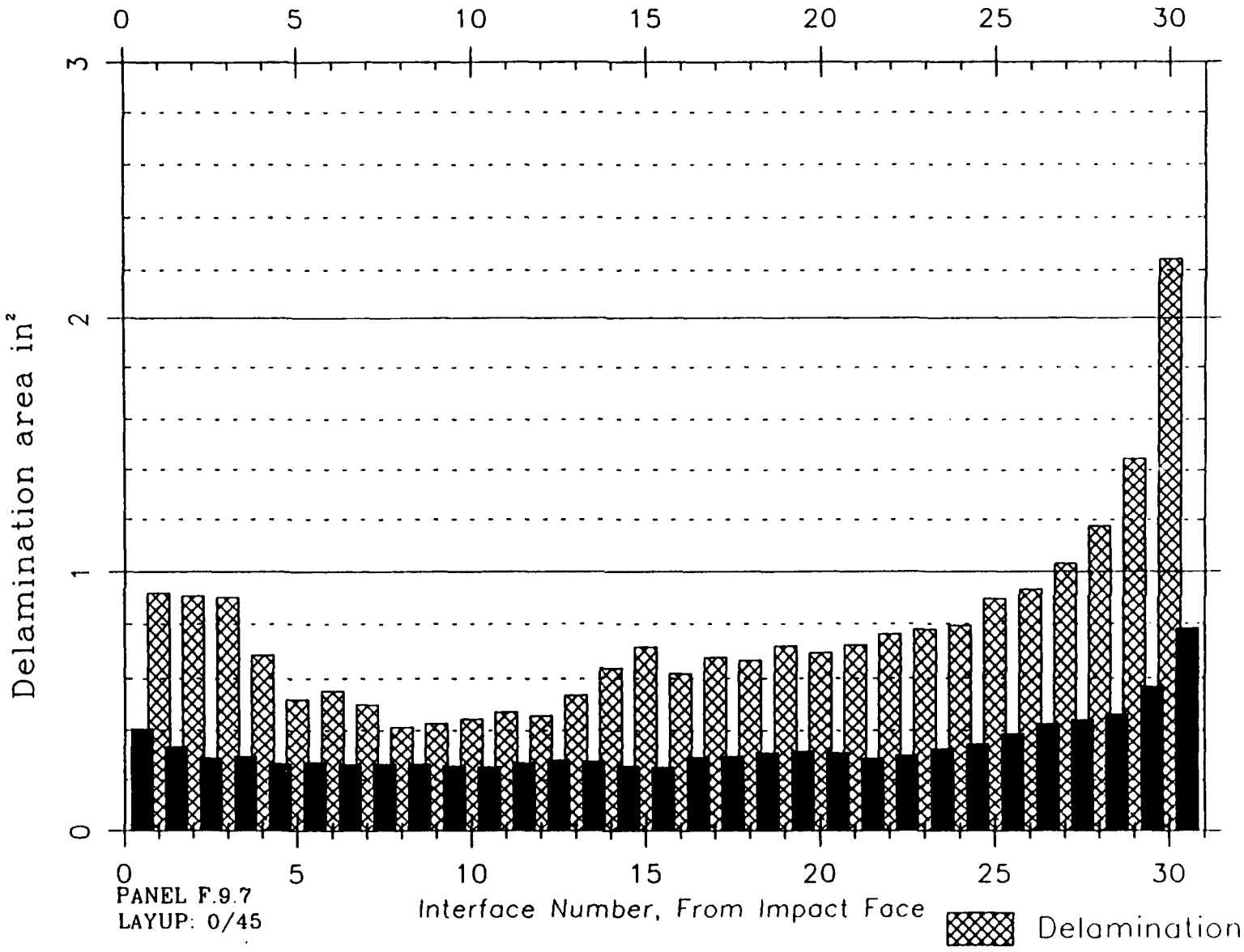

Delamination and Hole Area of Individual Plies
For panel impactked at 3184.9 fps

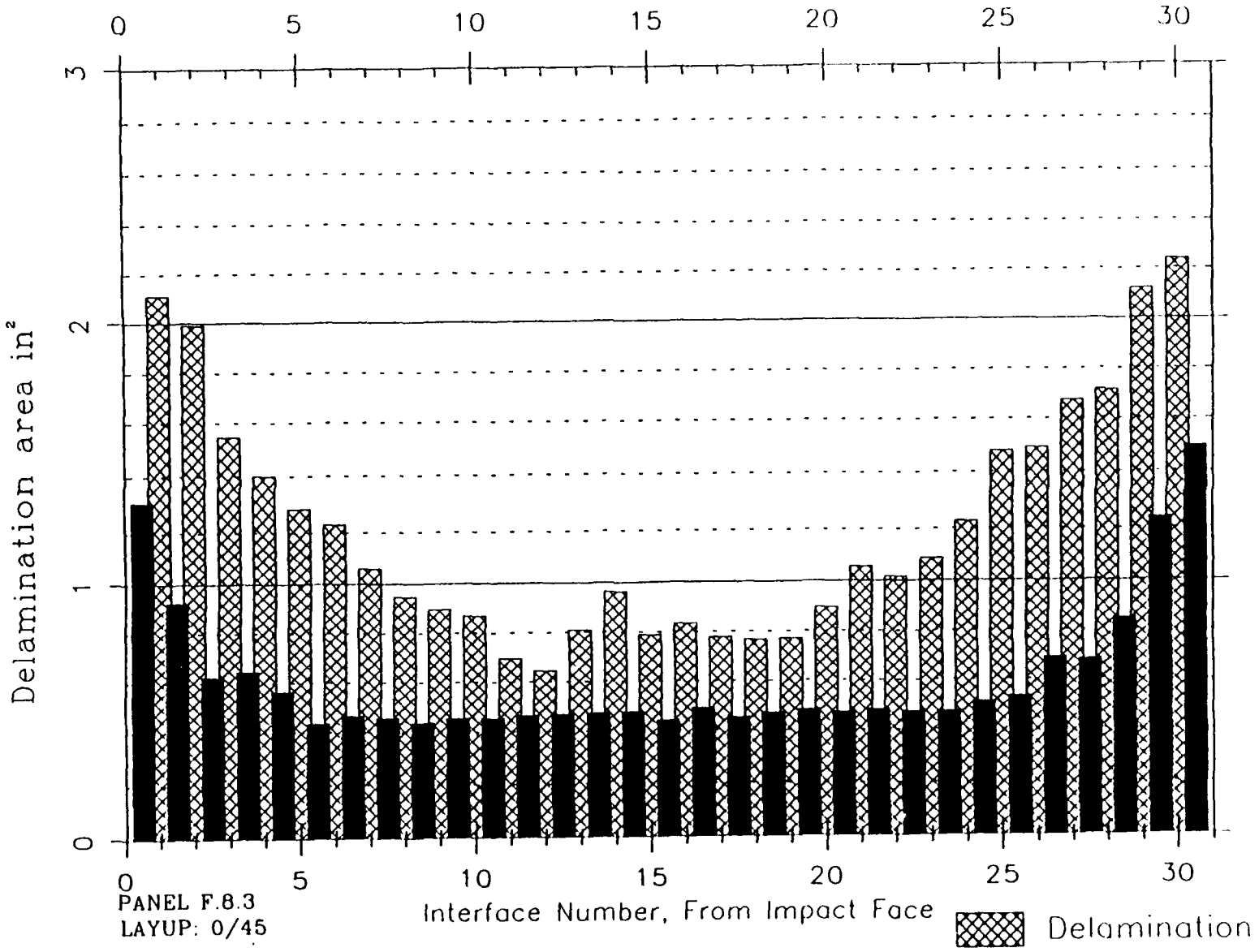

Delamination and Hole Area of Individual Plies
For panel impacted at 5937.2 fps

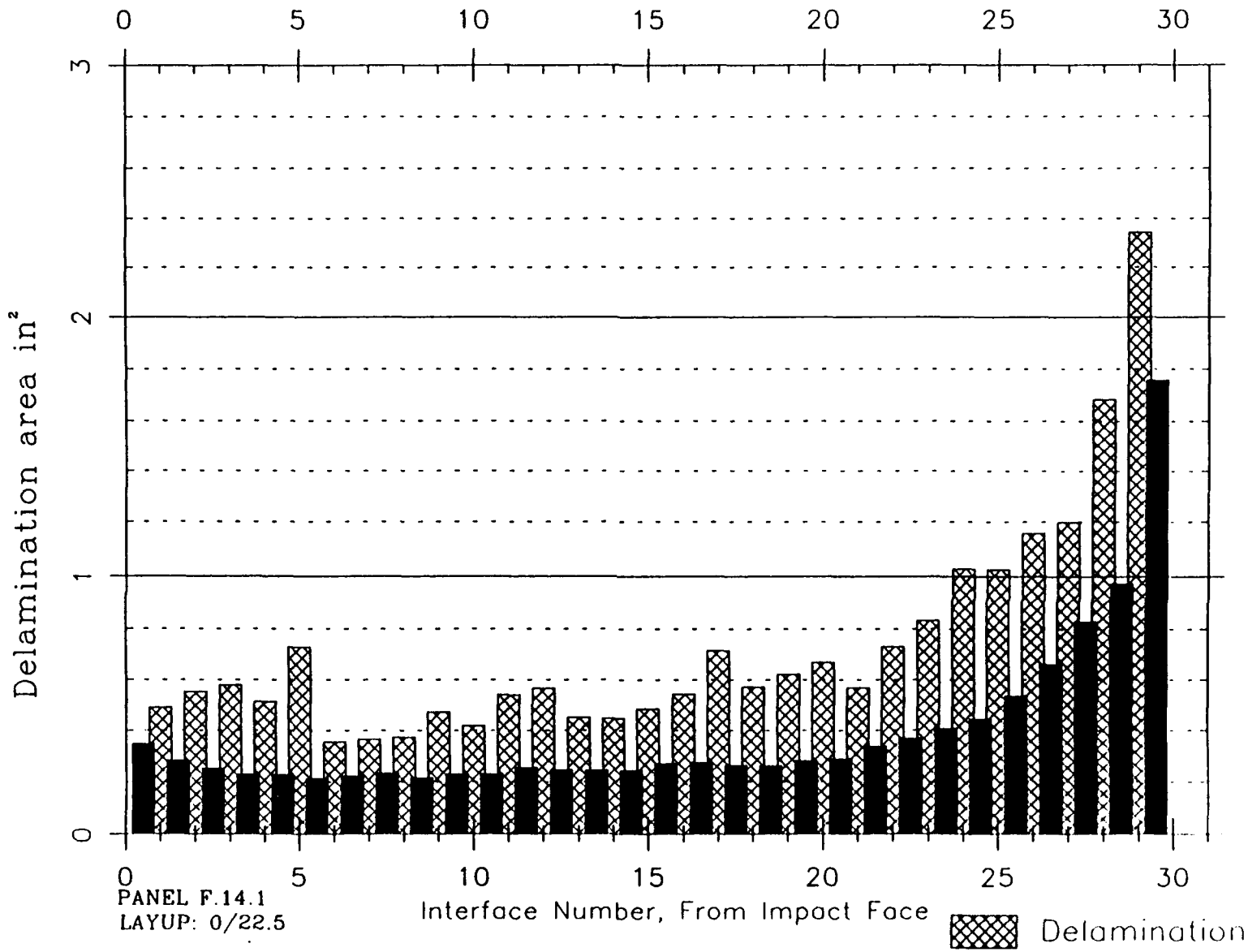

Delamination and Hole Area of Individual Plies
For panel impactked at 2220.0 fps

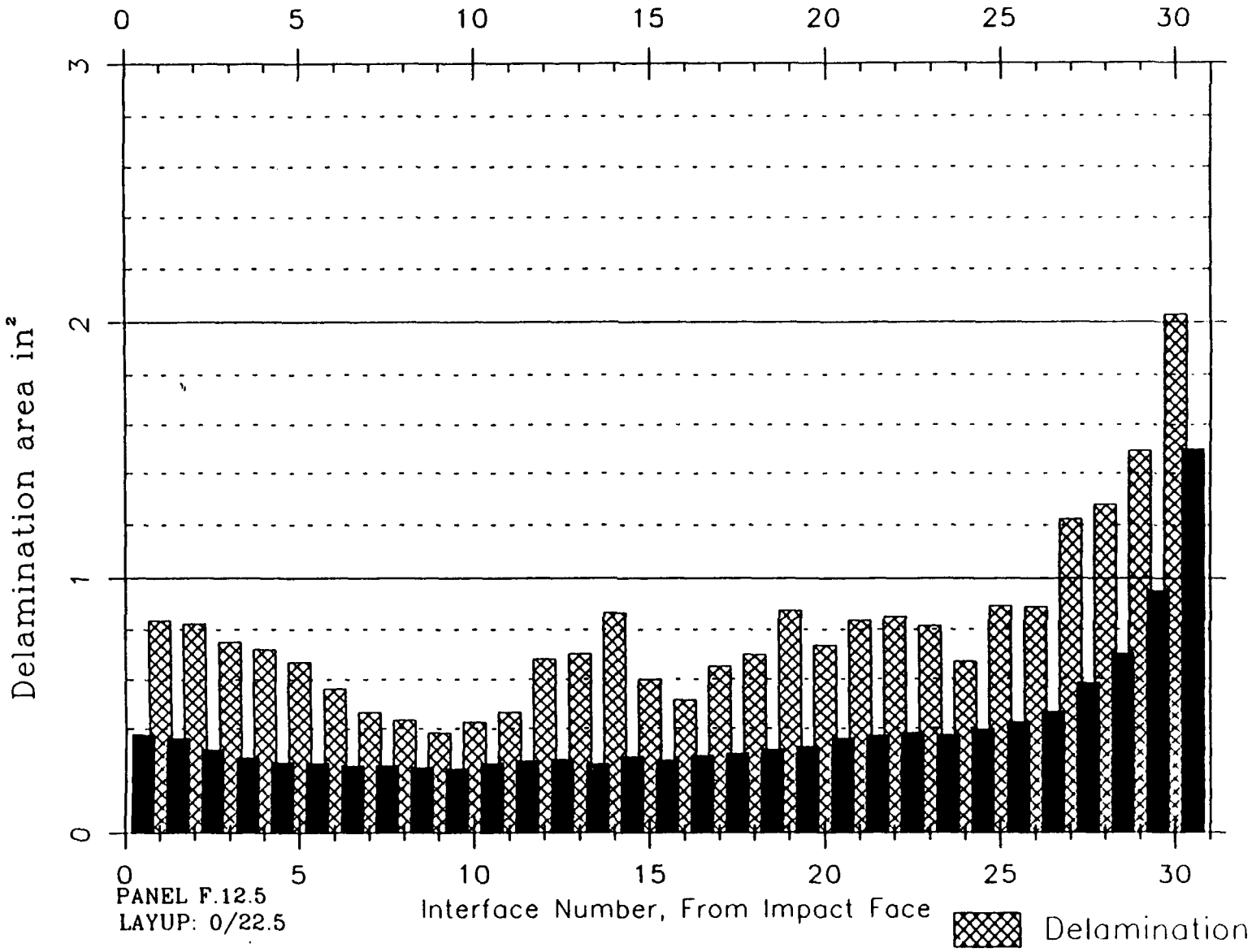

Delamination and Hole Area of Individual Plies
For panel impactked at 3245.0 fps

CONCLUSION:

The delamination damage for 4 different layup are calculated by deplying method. Total 9 panels were deplied for each layup. The delamination area is maximum at 400 fps for all layup, as the velocity increases, first of all delamination area decreases to a certain velocity and then increases with increase in velocity. In (0/90) layup delamination area is maximum at 400 ft/sec and decreases until the velocity is 2200 ft/sec, as the velocity increase above 2200 fps, the delamination increases as shown in the graph on page 8, also delamination damage for other layup as shown on page 9 and 10.

ACKNOWLEDGEMENT

The author wish to thank the Air Force office of Scientific Research for sponsorship of this research. Also I would like to thank to WL/FIVS group, at wright laboratory for allowing me to use their facility, specially to Greg Czarnecki for helping me throughout the summer and to Suresh B. Maryala, Graduate student of UNO for helping me.

I am particularly grateful to Dr. Arnold H. Mayer, who provide technical support from the beginning to make my research successful and to my Professor Dr. David Hui for his endless support.

A STUDY OF TIRE CARCASS FATIGUE FAILURE DUE TO PURE MECHANICAL DEGRADATION

Robert E. Seydel, III
Graduate Student
Department of Aerospace Engineering
University of Missouri - Rolla
Rolla, MO 65401

Final Report for:
Graduate Student Research Program
Landing Gear Systems Section
Flight Dynamics Directorate
Wright Laboratory
WPAFB, OH 45433

Sponsored by:
Air Force Office of Scientific Research
Bolling Air Force Base, Washington, D.C.

August 1993

A STUDY OF TIRE CARCASS FATIGUE FAILURE DUE TO PURE MECHANICAL DEGRADATION

Robert E. Seydel, III
Graduate Student
Department of Aerospace Engineering
University of Missouri - Rolla

Abstract

Isothermal fatigue studies were performed on tire carcass coupons. Results were compared to studies performed without temperature control for the determination of the relative contributions of mechanical and thermal fatigue. As expected, coupon lifetime without thermal effects was greater than with thermal effects. It was found that at low stress values material properties like tan δ were primarily dependent on temperature effects, while at higher stress values, these properties were more dependent on mechanical effects. This was due to lack of damage caused by mechanical fatigue at lower stresses, leading to longer lifetime and therefore more time for chemical changes.

A STUDY OF TIRE CARCASS FATIGUE FAILURE DUE TO PURE MECHANICAL DEGRADATION

Robert E. Seydel, III

I. Introduction

In previous studies of tire carcass fatigue, coupons cut from four-ply carcass material were subjected to cyclic tension-tension loading. These studies have shown that the coupons accumulate heat during loading. Therefore, thermal effects were probably a contributing factor (in addition to mechanical fatigue) to the degradation and eventual failure of the specimen besides mechanical fatigue. To quantify the thermal contribution, it was proposed to perform isothermal experiments so that degradation would be solely mechanical. With comparison to results under the same loading and frequency conditions where both mechanical and thermal degradation took place, this allowed for the determination of the relative contribution of each.

II. Objective

The objective of this study was to determine the effect of thermal degradation on a tire carcass coupon at various frequencies and loading conditions.

III. Experiments

The composite used was a symmetric, angle ply (+/- 38 degrees) laminate of rubber matrix reinforced with nylon fiber, four plies thick. Laminate panels, with approximate dimensions of 8" X 3" X .2", were supplied by the Goodyear Tire & Rubber Company. Coupons were cut from these panels to the dimensions of 4" by approximately .75" using a three axis waterjet cutting system. Coupons were placed in the grips so as to give a gage length of 2".

Specimens were tested to failure by sinusoidal, tensile loading. Frequencies tested were 10, 20 and 30 Hz. At each frequency maximum load was varied from 100 to 350 pounds in 50 pound increments, with minimum load kept constant at 36 pounds. Testing was performed using a Material Testing System (MTS) machine.

The MTS recorded load, displacement and temperature versus time at each data sampling. Load and displacement were read by actuators integral to the MTS machine, and average surface temperature of the specimen was read by an infrared sensor directed at the

center of the specimen. Based on an estimation of lifetime, sampling interval was varied so that at least 10 data samples would be taken for each test. At each sample, five cycles of data were recorded, and sampling rate was varied with frequency to record 20 points per cycle.

Several tests were run without cooling to complete the previous uncooled test matrix. This was required to allow for comparison with results from cooled testing.

For the remainder of the testing, coupons were cooled by blowing air across them. Air was directed upon the two sides of the coupon through holes in two copper tubes connected to a manifold. Rubber tubing connected the manifold to a compressed air source at a pressure of 400 psi. For the 10 Hz experiments, the velocity and cooling of the air created by expansion from the tubing were enough to cool the specimen. For 20 Hz, this set-up was modified by adding coiled copper tubing between the rubber tubing and the manifold, and submerging these coils in an ice bath. This set up was further modified for 30 Hz experiments by adding liquid nitrogen in a metal container within the ice bath to freeze the ice bath. For longer tests, nitrogen was periodically added to maintain the temperature of the ice.

IV. Results and Discussion

As the preset loadings were not actually reached for all tests, actual stresses were calculated from the data files; the largest errors in stress amplitude occurred at higher loadings at 30 Hz.

Attempts to maintain a constant temperature were most successful for lower loadings and frequencies, as shown in Table 1. For uncooled experiments temperatures exceeded 200° for every frequency, but for cooled experiments temperatures maintained depended on the frequency. At 10 Hz, operating temperatures were kept under 88°F (T_{amb}=80°) for all loads except 350 lb, where a temperature of 95° was recorded. At 20 Hz, temperatures were kept under 100° except at 300 lb, where temperatures reached 115°. Finally, at 30 Hz temperatures were usually kept under 120°, except for the first runs of the 200 lb and 300 lb cases, which were run while the liquid nitrogen system was still being developed.

Cycles to failure are also given in Table 1. The lifetimes for each loading condition appeared to correlate well for 200 lb and higher loads, but loads less than 200 lb gave quite

disparate results. There were apparent cases of coupon failure at or near the grips, including these cases, so it was decided to replace the toothed grips with knurled grips. Coarse knurled grips were the final selection, as medium knurling allowed coupon slippage. Data for the lower loads with the coarse knurled grips showed drastic improvement, while data for higher loads showed little change, so these values were used, and the old data was not considered.

To compare results at different frequencies, as well as to demonstrate the effects of cooling, durability, that is the true time to failure, was calculated, and results are listed in Table 2. Durability was calculated by dividing the lifetime (in cycles) by the frequency, giving it units of seconds. As shown in Figures 1 and 2, durability increased with decreasing frequency and decreasing load. Cooling increased durability, except at the highest load and frequency where it did not make any difference. The amount of increase in life increased with decreasing load and frequency, meaning that the importance of thermal effects increases under these conditions. This is because at smaller maximum stresses, a greater part is played by chemical processes (Bartenev and Zuyev, 212). Also visible in Figures 1 and 2 is that the curve fits are parallel on the log-log plots, meaning that these power curves have the same exponent. The equations for each curve fit are given on the graphs.

Also investigated was the variation of hysteresis area and tan δ with the degradation of the coupon; all calculated results can be found in Tables 4-9. From the displacement and loading data, the area of the hysteresis loop (H) was calculated, which is equivalent to the heat loss per volume per cycle. The variation of H with stress and frequency are shown in Figures 3 and 4; H increases with both increasing stress and frequency. Comparing Figures 3 and 4, H does not change with cooling, that is heat loss per cycle is the same. From this area, tan δ can be calculated from the formula (Clark, 28):

$$\tan\delta = \tan(\sin^{-1}(\frac{H}{\pi\sigma_0\varepsilon_0}))$$

where σ_0 and ε_0 are half of the stress and strain amplitude, respectively. As shown in Figure 5 and 6, higher frequencies gave higher tan δ's for the same temperature; comparing the plots higher loadings also gave higher tan δ's. For the cooled samples at lower loadings, for

example 150 lb as shown in Figure 5, tan δ remained nearly constant, while for the uncooled samples tan δ appeared to decrease with increasing temperature. However, at higher loadings, tan δ decreased almost as much for the cooled specimens as for the uncooled specimens. Therefore, it appears that for determination of tan δ, at lower loads thermal (or chemical) effects dominate, while at higher loads, mechanical effects dominate.

Recommendations

It was clearly demonstrated that cooling coupons increases fatigue lifetime. However, for many experiments temperature was not maintained so the exact variance of lifetime with particular temperatures could not be determined. Therefore it is recommended that future studies employ better isothermal temperature control, such as an environmental chamber.

Modification of the grips allowed for more consistent results for lower loadings. However, as these grips were not available for all tests it is recommended that the remainder of tests where coupons failed at the grips be repeated with the new grips.

For lower loads, tests ran for longer than one day, so it was required to stop tests and restart them the next day. As this allows for an unknown amount of recovery in the coupon, it is recommended that in the future a method be developed to run the tests continuously to allow better comparison with other tests.

Acknowledgements

The author wishes to express graditude to Paul Ulrich, Aivars Petersons and Dr. Arnold Mayer for his participation in the summer research program. Thanks are due to Martin Vogel of SRL for assistance in performing experiments, and Deborah Kennedy for past experimental results and suggestions. The author also thanks Dr. Mangal Chawla for direction in planning experiments, analyzing data and preparing this report.

References

G. M. Bartenev and Yu. S. Zuyev, Strength and Failure of Visco-Elastic Materials, Pergammon Press, New York, 1968.

Samuel K. Clark, editor, Mechanics of Pneumatic Tires, U.S. Department of Transportation.

Table 1: Cycles to Failure and Failure Temperature of Cooled Specimens

Load (lb)	Frequency					
	10 Hz		20 Hz		30 Hz	
	N_f	T_f(°F)	N_f	T_f(°F)	N_f	T_f(°F)
350	529	91	511	99	458	117
350	424	92	610	98	535	90
300	2602	85	1450	111	1296	144
300	1580	87	1134	115	780	95
250	9880	82	6056	95	3060	119
250	6055	83	6997	92	3377	90
200	17494	87	24226	90	19060	106
200	21707	84	19550	87	13458	131
150	21013*	83	617735	105	170570	124
150	760900	83	1019911	85	427775	87
100	54949*	87	47056*	82		
100	27567*	84	not run		not run	

* Grip failure, not plotted

Table 2: Cycles to Failure and Failure Temperature of Uncooled Specimens

Load (lb)	Frequency					
	10 Hz		20 Hz		30 Hz	
	N_f	T_f(°F)	N_f	T_f(°F)	N_f	T_f(°F)
350	359	161	412	168	503	142
350	271	152	494	155	395	157
300	626	178	964	177	643	168
300	788	176	774	162	717	185
250	1331	209	1970	171	1316	214
250	1370	192	1506	171	1803	238
200	4942	214	5662	252	2881	231
200	5582	208	4574	259	4819	272
150	13988	144	28314	227	19061	269
150	9121	171	15942	241	14649	269
100	20911	106	46906	162	157575	185
100	not run		18161	144	16142	193

Table 3: Durability for various loads and frequencies, demonstrating the effect of cooling

	10 Hz		20 Hz		30 Hz	
Load (lb)	with cooling	no cooling	with cooling	no cooling	with cooling	no cooling
350	48	32	28	23	15	15
300	173	71	65	41	25	23
250	797	135	326	87	102	52
200	1960	526	1094	226	542	128
150	76090	1155	30887	920	9973	562

Table 4: Mechanical properties at various stages of life
10 Hz, no cooling

Load (lb)	Property	Percentage of Fatigue Life				
		0	25	50	75	90
200	H	.13017	.12325	.11817	.1215	.13856
	E"	5.9699	3.8178	3.0612	2.8393	2.5607
	tan δ	.13545	.10571	.092262	.089505	.08942
	E'	44.074	36.118	33.179	31.722	28.637
	E*	44.476	36.319	33.320	31.849	28.751
	T (°F)	103	153	184	197	207
250	H	.21235	.22462	.21174	.20985	.21925
	E"	7.5875	5.8229	4.1022	3.5761	3.0742
	tan δ	.15348	.13300	.10858	.10154	.098056
	E'	49.436	43.780	37.779	35.221	31.352
	E*	50.015	44.166	38.001	35.402	31.502
	T (°F)	85	109	139	159	176
300	H	.28151	.28522	.28583	.28683	.2855
	E"	8.9859	7.4059	5.2759	4.6363	3.9174
	tan δ	.16425	.14610	.12184	.11531	.10686
	E'	54.708	50.690	43.303	40.207	36.661
	E*	55.441	51.228	43.624	40.473	36.870
	T (°F)	86	98	129	148	164
350	H	.39486	.42976	.44389	.43851	.45455
	E"	9.2678	8.0166	6.9553	5.4922	4.9268
	tan δ	.16202	.15043	.14119	.12614	.12047
	E'	57.201	53.290	49.262	43.542	40.898
	E*	57.947	53.890	49.750	43.887	41.193
	T (°F)	90	99	109	127	137

Table 5: Mechanical properties at various stages of life
20 Hz, no cooling

Load (lb)	Property	Percentage of Fatigue Life				
		0	25	50	75	90
200	H	.14652	.1576	.16201	.1695	.18912
	E"	5.2060	4.4371	2.8759	2.5468	2.1187
	tan δ	.14355	.13492	.11199	.10565	.10196
	E'	36.265	32.887	25.681	24.106	20.780
	E*	36.637	33.185	25.841	24.240	20.888
	T (°F)	109	138	212	242	253
250	H			.24479		
	E"			3.8383		
	tan δ			.12227		
	E'			31.391		
	E*			31.625		
	T (°F)			170		
300	H		.28175	.28779	.30607	.31373
	E"		7.5016	6.0285	5.1673	4.2616
	tan δ		.15356	.13695	.12776	.12111
	E'		48.853	44.019	40.447	35.186
	E*		49.426	44.430	40.775	35.444
	T (°F)		95	125	153	177
350	H	.32215	.39099	.43493	.48271	.51740
	E"	10.518	8.2263	6.4242	5.1595	4.2827
	tan δ	.17815	.16654	.15087	.13962	.13658
	E'	59.040	49.395	42.581	36.954	31.357
	E*	59.970	50.076	43.063	37.312	31.648
	T (°F)	83	90	107	136	154

Table 6: Mechanical properties at various stages of life
30 Hz, no cooling

Load (lb)	Property	Percentage of Fatigue Life				
		0	25	50	75	90
200	H	.14852	.18928	.19318	.19683	.19877
	E"	6.6659	4.5700	3.3211	2.9717	2.4734
	tan δ	.15883	.13883	.12308	.11514	.11194
	E'	41.970	32.919	26.984	25.810	22.095
	E*	42.496	33.235	27.187	25.980	22.233
	T (°F)	82	139	193	225	247
250	H	.21458	.27749	.28938	.32793	.31786
	E"	8.2355	6.0170	4.4397	3.8267	3.3026
	tan δ	.17440	.16245	.14147	.13159	.12974
	E'	47.221	37.039	31.383	29.080	25.456
	E*	47.933	37.525	31.695	29.330	25.669
	T (°F)	82	108	149	185	208
300	H	.34883	.43518	.47105	.52277	.51177
	E"	9.4129	7.3236	6.2880	5.1519	4.5672
	tan δ	.17958	.16629	.15775	.14075	.13618
	E'	52.417	44.042	39.860	36.604	33.538
	E*	53.256	44.646	40.353	36.965	33.847
	T (°F)	87	100	117	151	168
350	H	.25657	.41112	.47315	.51759	.62500
	E"	13.406	9.0575	6.1602	5.3309	5.8743
	tan δ	.19670	.18508	.15924	.15076	.15000
	E'	68.153	48.938	38.686	35.360	39.1631
	E*	69.459	49.769	39.174	35.759	39.601
	T (°F)	81	88	107	121	137

Table 7: Mechanical properties at various stages of life
10 Hz, with cooling

Load (lb)	Property	Percentage of Fatigue Life				
		0	25	50	75	90
200	H	.11759	.11941	.11984	.12645	.12687
	E"	5.3701	5.3712	5.2542	5.4006	5.2917
	tan δ	.13950	.13955	.13824	.14078	.13752
	E'	38.495	38.489	38.008	38.362	38.478
	E*	38.867	38.862	38.369	38.740	38.884
	T (°F)	81	83	84	83	83
250	H	.21018	.21199	.21886	.23941	.24498
	E"	5.2347	4.8066	4.7292	4.3195	4.1590
	tan δ	.14421	.14084	.13811	.13993	.13700
	E'	36.300	34.128	34.243	30.869	30.357
	E*	36.676	34.465	34.568	31.170	30.641
	T (°F)	80	81	80	81	82
300	H	.28421	.29658	.29659	.30850	.32472
	E"	5.8804	5.3396	5.0673	4.7050	4.4838
	tan δ	.14761	.14428	.13945	.13768	.13684
	E'	39.838	37.009	36.338	34.173	32.767
	E*	40.269	37.392	36.689	34.496	33.072
	T (°F)	80	82	84	84	85
350	H	.36472	.38935	.39746	.41898	.46722
	E"	7.5994	6.4632	5.7321	4.8212	4.6489
	tan δ	.16487	.15565	.14826	.13933	.13737
	E'	46.093	41.524	38.661	34.602	33.842
	E*	46.715	45.024	39.084	34.937	34.160
	T (°F)	82	84	87	90	91

Table 8: Mechanical properties at various stages of life
20 Hz, with cooling

Load (lb)	Property	Percentage of Fatigue Life				
		0	25	50	75	90
200	H	.14622	.15711	.16047	.16199	.17652
	E"	4.5337	4.3913	4.2623	4.1092	4.2978
	tan δ	.13950	.14112	.13973	.13903	.14062
	E'	32.499	31.116	30.503	29.556	30.563
	E*	32.814	31.425	30.799	29.840	30.864
	T (°F)	78	82	85	86	86
250	H	.24111	.24958	.25144	.25102	.28640
	E"	5.7565	4.7902	4.2934	3.9024	3.8377
	tan δ	.15723	.14743	.13875	.13239	.12490
	E'	36.613	32.492	30.942	29.476	30.726
	E*	37.063	32.843	31.239	29.733	30.965
	T (°F)	78	86	87	89	91
300	H		.36705	.39282	.40523	.42644
	E"		6.2555	5.1800	4.5748	4.1463
	tan δ		.16155	.14766	.14080	.13934
	E'		38.723	35.081	32.492	29.757
	E*		39.225	35.461	32.813	30.044
	T (°F)		90	100	106	111
350	H	.35719	.42221	.42864	.45821	.47167
	E"	7.3944	6.9778	5.1328	4.7400	3.9164
	tan δ	.17681	.16926	.14883	.14327	.13521
	E'	41.820	41.225	34.488	33.086	28.965
	E*	42.469	41.811	34.868	33.424	29.229
	T (°F)	70	74	83	90	95

Table 9: Mechanical properties at various stages of life
30 Hz, with cooling

Load (lb)	Property	Percentage of Fatigue Life				
		0	25	50	75	90
200	H	.16389	.17385	.17741	.17993	.18778
	E"	6.1728	5.1422	5.1190	4.8864	4.7165
	tan δ	.16919	.15596	.15419	.15285	.15325
	E'	36.484	32.972	33.198	31.968	30.777
	E*	37.003	33.370	33.590	32.339	31.136
	T (°F)	82	95	94	96	97
250	H	.26074	.28158	.30648	.30128	.29019
	E"	6.3964	5.0049	4.0637	3.6161	3.2461
	tan δ	.15723	.14743	.13875	.13239	.12490
	E'	38.337	33.264	29.323	27.527	25.474
	E*	38.867	33.639	29.603	27.763	25.680
	T (°F)	72	86	105	117	119
300	H	.20676	.38440	.38679	.37742	.38595
	E"	12.629	6.1080	4.3178	3.6387	3.2459
	tan δ	.19081	.15443	.12965	.11959	.11789
	E'	66.186	39.552	33.303	30.426	27.533
	E*	67.380	40.021	33.582	30.643	27.723
	T (°F)	76	97	122	135	144
350	H	.19992	.37959	.47061	.52994	.54749
	E"	17.038	10.424	7.1221	5.3578	5.0694
	tan δ	.20169	.18449	.16493	.14536	.14638
	E'	84.477	56.503	43.276	36.856	34.631
	E*	86.178	57.457	43.858	37.243	35.000
	T (°F)	74	81	92	114	117

Fig 1: Durability vs Stress with Cooling

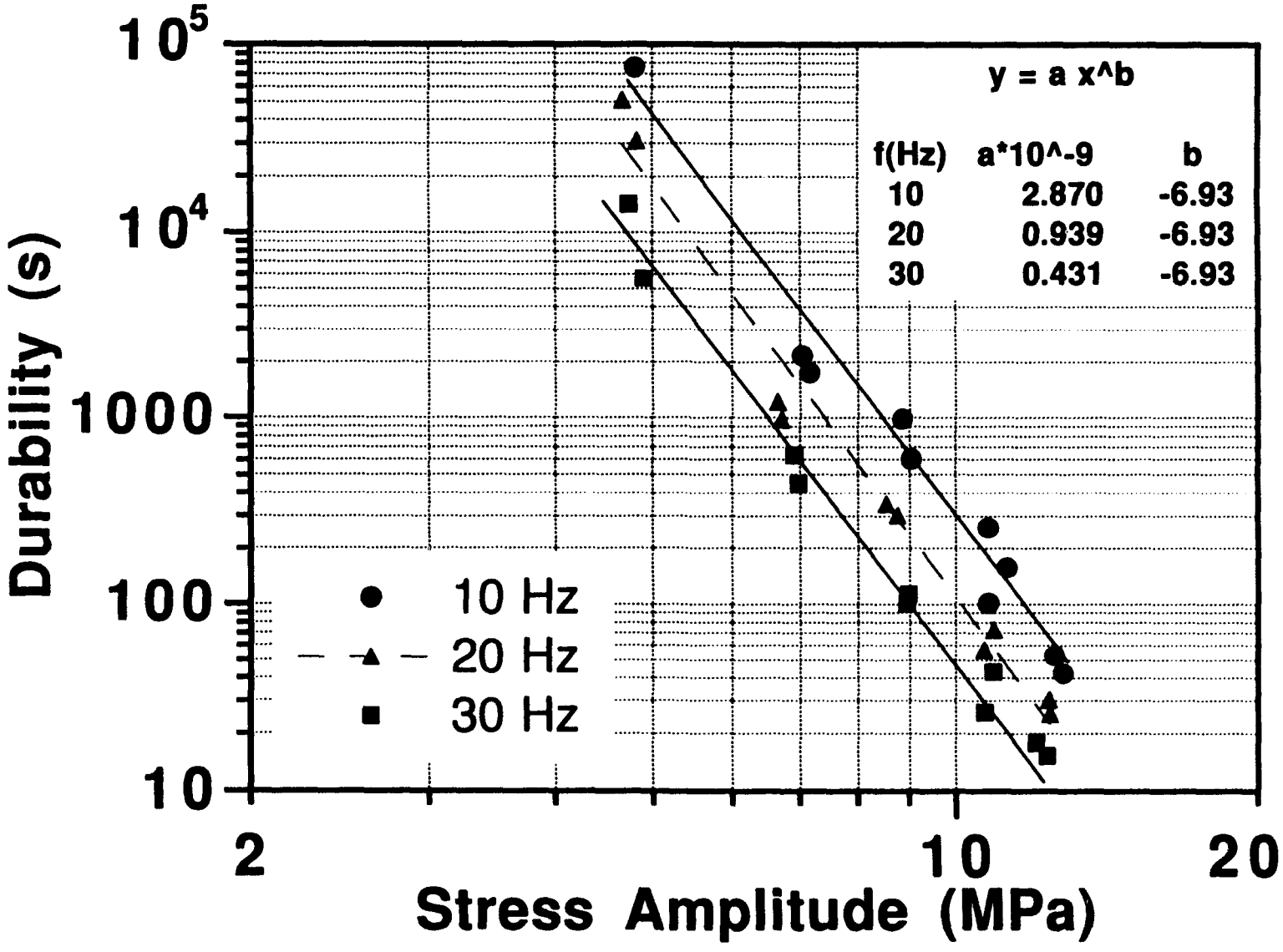

Fig 2: Durability vs Stress no cooling

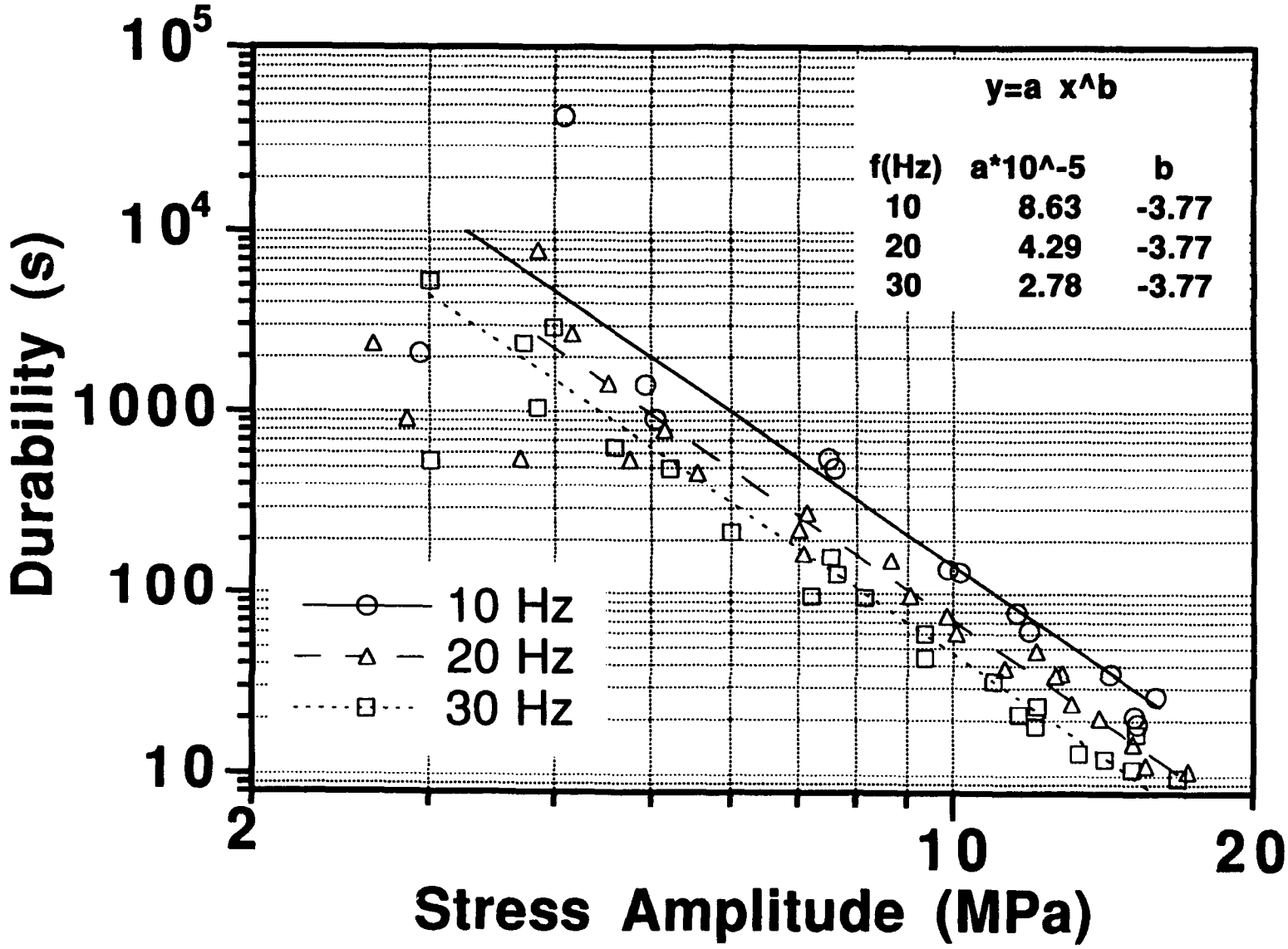

Fig 3: Hysteresis Areas vs Stress with cooling, 10 & 30 Hz

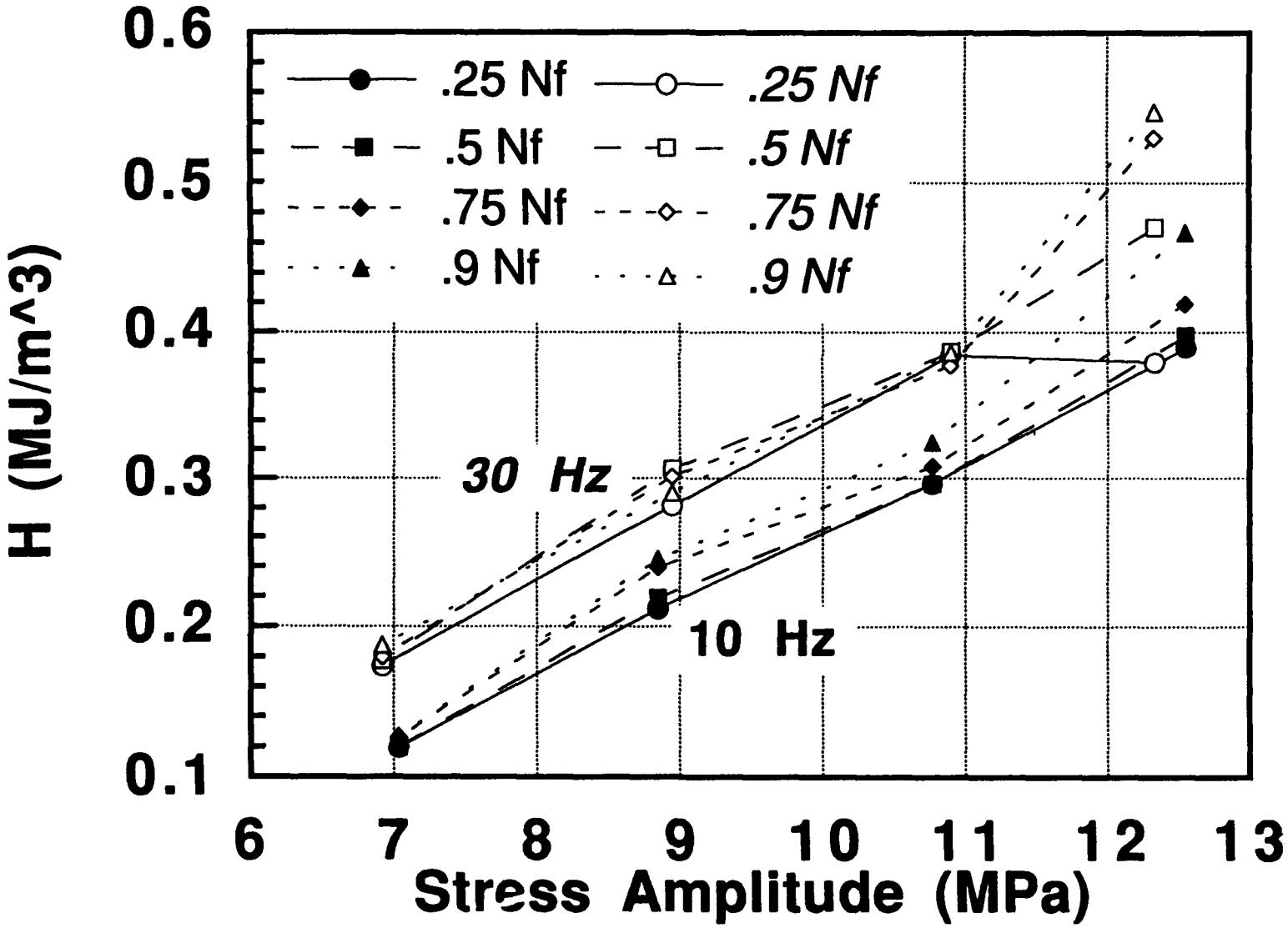

Fig 4: Hysteresis Area vs Stress no cooling, 10 & 30 Hz

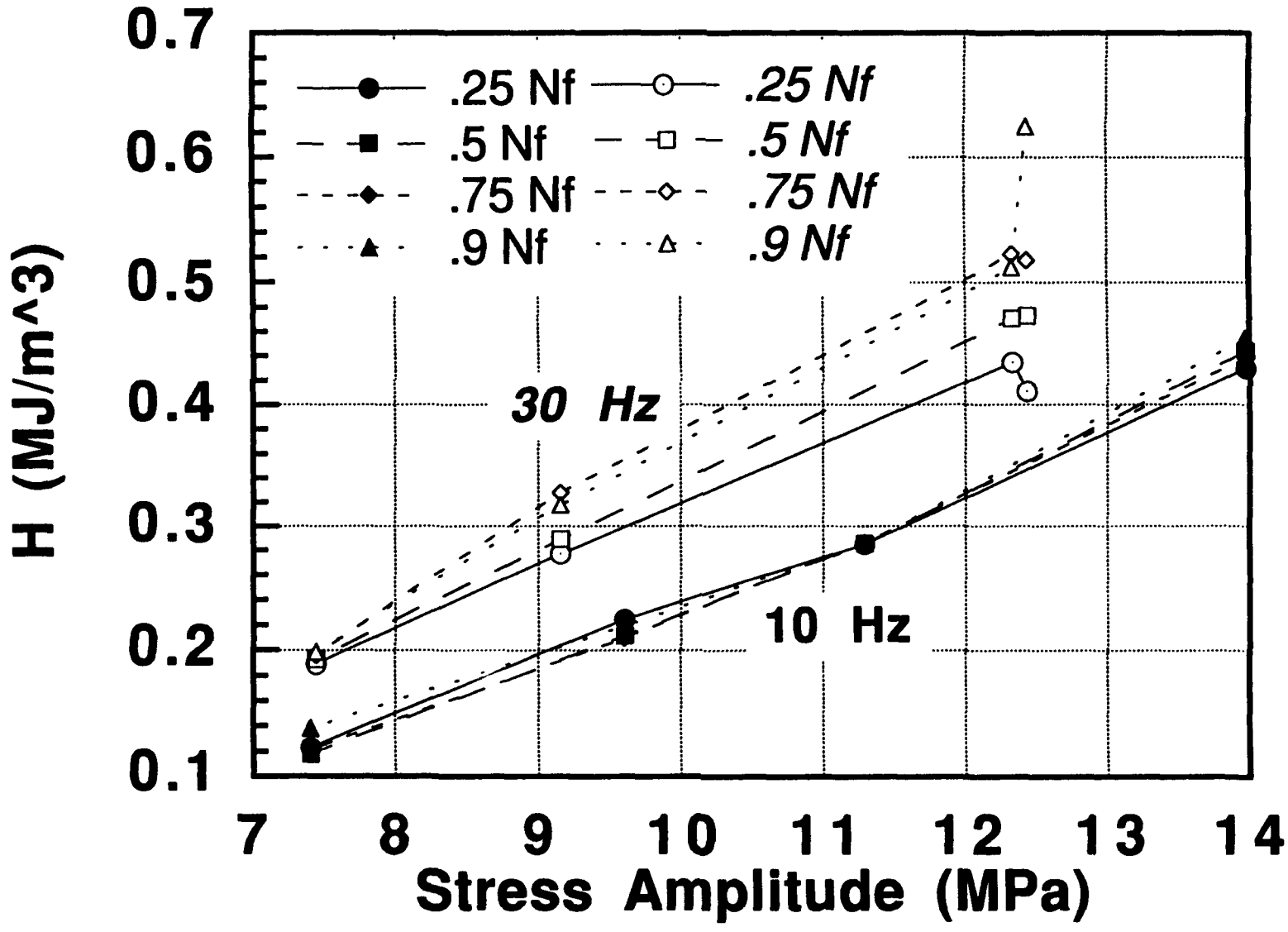

Fig 5: Tan Delta vs Temperature 150-36 Pounds

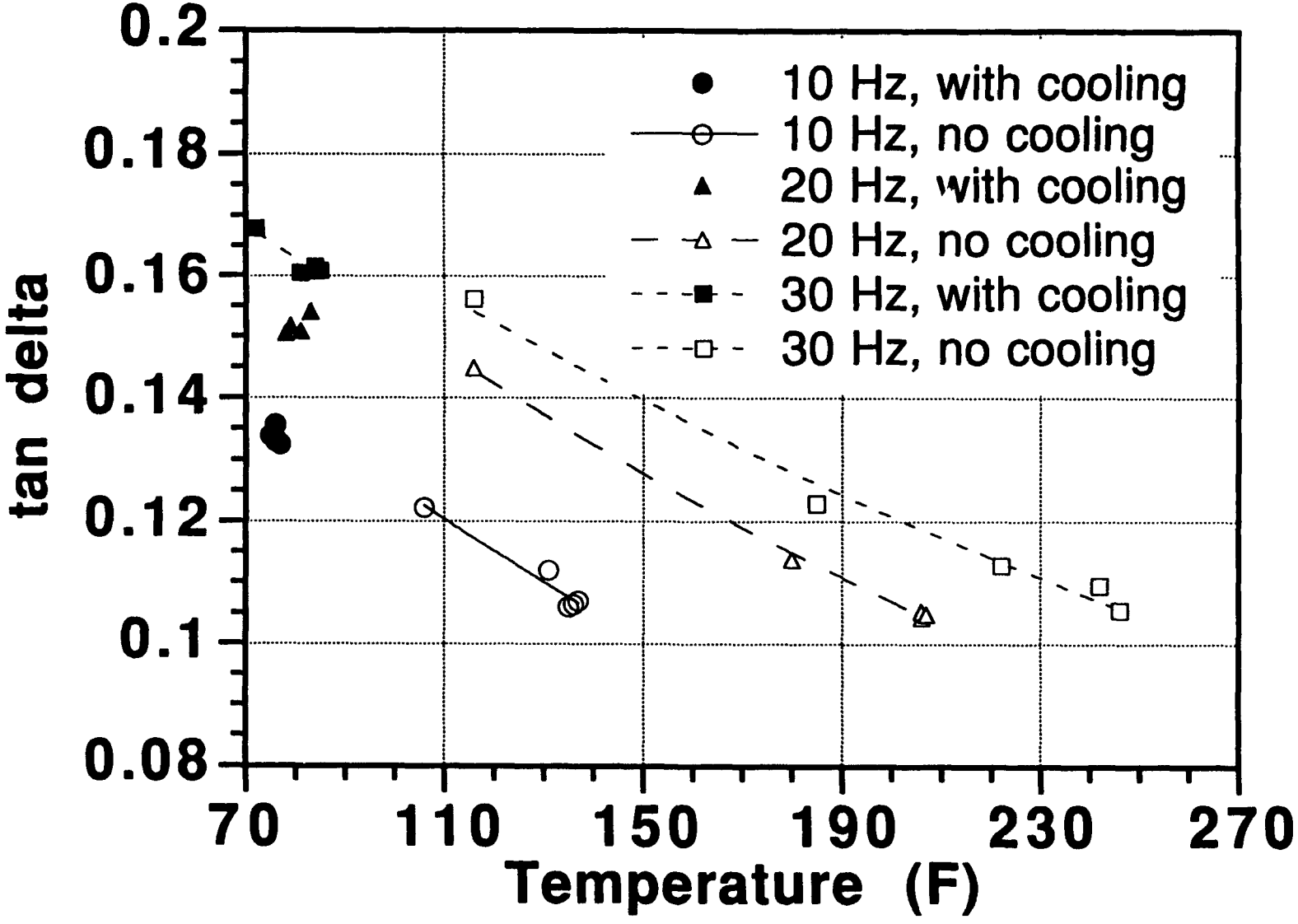

Fig 6: Tan Delta vs Temperature 350-36 Pounds

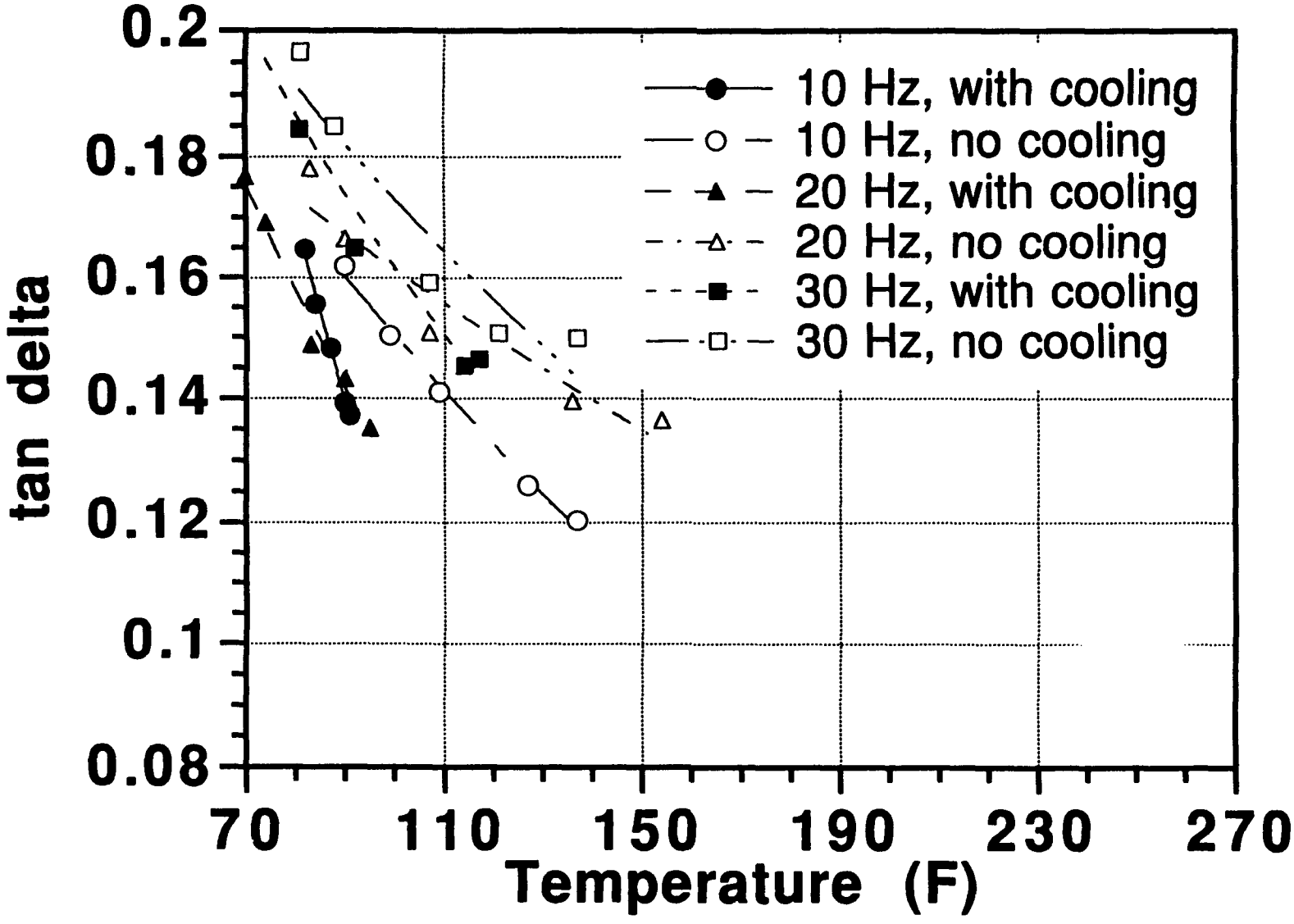

CONTACT LAW FOR LOW-VELOCITY IMPACT OF COMPOSITE MATERIALS

Rob Slater
Graduate Research Assistant
Department of Mechanical, Industrial, and Nuclear Engineering

University of Cincinnati
Cincinnati, OH 45221-0072

Final Report for:
Graduate Student Research Program
Wright Laboratory

Sponsored by:
Air Force Office Of Scientific Research
Bolling Air Force Base, Washington, D.C.

September 1993

CONTACT LAW FOR LOW-VELOCITY IMPACT OF COMPOSITE MATERIALS

Rob Slater
Department of Mechanical, Industrial, and Nuclear Engineering
University of Cincinnati

ABSTRACT

Low-velocity impact damage is a critical consideration in the design of composite laminates for aircraft structures. Composite materials offer high stiffness and strength at a significant weight savings over metals. Low-velocity impact damage is a particularly insidious problem because it is difficult to detect by visual inspection. These impacts occur during the course of normal flight and maintenance operations and often leave only a small, shallow dent on the impact surface. But there may be significant interior and backface damage to the laminate. In order to design composite materials for impact tolerance, it is necessary to develop methods to model composite structures and simulate the loads. A contact law describes the relationship between the indentation of an impacting object into the target and the transmitted force. A modified Hertzian theory is commonly used. This model requires experimental data and only predicts the total force as a function of indentation. For more accurate determination of the stresses which cause impact damage, a contact law which predicts the distribution of force in the contact area is necessary.

INTRODUCTION

Composite materials are frequently considered in the design of aircraft structures. They offer high stiffness and strength at a significant weight savings over metals. There are distinct differences in the design criteria for metal and composite structures. Fracture and fatigue are the key concerns in the service life of metal structures. Design of composites is driven by concerns such as delaminations at the discontinuities, voids, wrinkles, and low-velocity impact by foreign objects. Laminated composites are particularly susceptible to low-velocity impact damage. These impacts occur during normal operations due to hail or stones blown around a runway by jet engines or during maintenance operations due to tool drop of footsteps. The damage mechanisms associated with low-velocity impacts include matrix cracking, ply delamination, and fiber breakage. Delamination is particularly troublesome because serious internal and back-face damage may be present even though the damage on the impact face appears to be quite minor. It is often not detected during routine visual inspection because the visible damage is slight. Significant reductions in strength and stiffness may result. The design criteria for composites generally require tolerance of a certain level of impact, defined either as an impact energy or a maximum surface indentation, which must be tolerated without significant degradation of service life. The simplest measure of impact is the kinetic energy of the impactor; i.e. an object of known mass

impacting at a known velocity. Establishing rational design criteria for low-velocity impacts is the subject of numerous investigations. Characterization of initial damage and its propensity to propagate under service loading are important considerations in the development of the design criteria. In addition, impact may occur at any point of a structure, so a panel must be designed to resist impact at any location. There are numerous local stress raisers in actual aircraft panels such as cutouts, ply drops, and stiffeners which must be considered in designing for impact damage tolerance. It is prohibitively expensive to perform laboratory tests on every composite panel configuration in an aircraft and difficult to correlate results from coupon tests to built-up structures. A more prudent course is to develop analytical criteria and validate them with experiments.

In order to design for impact tolerance, it is necessary to develop methods to model composite structures and simulate the loads. Numerous researchers have attempted to determine a methodology for predicting damage in a composite laminate subject to impact [1-5]. There are a number of variables which must be considered in the analysis of such events. Sensitivity to changes in materials, stacking sequence and panel thickness are significant. Boundary conditions in numerical models and experimental setups are difficult to match except by trial and error. Various failure theories have been offered to predict the size, shape, and location of damage for a given state of stress, but there is little consensus about what mechanisms are at work. In

short, no general method exists to predict in an arbitrary composite laminate due to an arbitrary impact.

Finite element methods have frequently been used to evaluate the stress field in an impacted laminate and correlate levels of stress components to experimentally observed damage [6-8]. The stress gradients are very high in the region where the impactor strikes the target and the immediate vicinity, so in order to find the stresses accurately, a refined element mesh is required. The contact force should be distributed over the numerous nodes of this region. As with all analyses involving contact, problems arise in predicting the size of the contact area because it varies non-linearly with transmitted force. Knowledge of the relationship between the indentation of the impacting body in the target and the magnitude and distribution of the contact force is essential for accurate modeling and determination of the stresses which cause damage. A contact law which predicts total force without the details of its distribution may be sufficient to model the gross deformations of the target under impact loading, but will not allow a model to be as accurate in predicting the stresses which cause the matrix cracking and delaminations representative of low-velocity impact. The objective of the summer's research was to develop a simple analytical method for determining the relationship between distribution of contact pressure and indentation of a transversely isotropic plate being acted on by a rigid spherical impactor with a known force. By a series of analyses using varying contact forces, a contact law may be devised.

SUMMARY OF SUMMER RESEARCH

The research conducted this summer was under the supervision of Dr. Greg Schoeppner, WL/FIBC. Dr. V.B. Venkayya, WL/FIBR, was also a major contributor of technical advice and direction. The majority of the work was in developing a new contact law for use in analyzing low-velocity impact of composite materials. An abstract for a paper to be presented was submitted for the upcoming AIAA Structures, Structural Dynamics, and Materials Conference on this topic. The remaining time was spent on other technical interests such as aeroelasticity and smart structures.

There has been an interest in the area of low-velocity impact of composites dating back approximately twenty years, and a great deal of material on this topic has been published in scientific journals. Many researchers have attempted to develop a comprehensive theory to explain the response of composite laminates to impact, estimate the post-impact damage, and predict the residual strength of the damaged structure. This has proved to be quite a difficult task. The procedure for completely analyzing an impact event can be broken down into four phases:

1. Loads Definition

The forces transmitted to the composite structure by the impacting body must be determined. The loading is frequently expressed as a function of the impacting body's indentation into the target. The distribution of the contact force on the surface of

the target is difficult to calculate. It is theoretically infinite for the initial point impact, but then spreads out over a growing finite area. Strain rate effects and plastic behavior of both the impactor and the target materials are important, as there have been instances observed in which multiple contacts occur during a single impact event [7]. The force-indentation relationship changes during unloading and reloading.

2. Laminate Response

A suitable model for the laminate must be determined. The complexity of this model depends strongly on the type of information desired. If the gross response of the panel is all that is required, a smeared plate theory may be sufficient. But if damage is to be predicted, a discrete laminate theory is necessary to evaluate the stresses layer-by-layer through the thickness. The commonly used first-order shear deformation plate theories lead to discontinuities in the stresses at the interfaces, so a more computationally intense formulation is required.

3. Damage Criteria

For a given state of stress in a laminate, this model must be capable of predicting the onset and propagation of damage. Properties of the laminate will change as damage occurs, so the model must be continually updated as the analysis proceeds. Knowledge of the material's behavior beyond the elastic range and its fracture characteristics are needed. The damage modeling must

deal with failed material (cracked matrix and broken fibers) by either removing it or treating it with revised properties.

4. Residual Strength Calculation

For a panel with known interior damage, a theory must be developed to predict the residual strength and stiffness. Strength in compression is often significantly reduced. Laminate symmetry is destroyed, introducing bending-stretching coupling effects which may not be accounted for in the design. Local buckling of delaminated areas at interfaces near the surface may occur. It is even possible to see local buckling under tensile loading due to Poisson's effect and the marked difference in stiffness of a single ply in the fiber and transverse directions. Global buckling can occur at reduced loads.

Of these four aspects, the second and fourth seem to be the furthest developed. Plate theory was a topic of great interest even before the development of composites. The extension of research on these materials has paralleled their increasing use in engineered structures. Residual strength models have not received the same volume of attention, but researchers have been able to demonstrate the capability to predict post-impact characteristics for composite laminates with known, although admittedly simplistic, damage states. The third consideration in the analysis of impact, damage prediction, has recently been the focus of several researchers. Unfortunately the state of the art is not as advanced as for the

first two topics. Several different theories have been proposed to predict the onset of damage at a specified level of stress in a laminate.

The analysis of contact between two bodies dates back to the work of Hertz in the late 19th century [10]. Today many of these same solutions form the basis of contact laws for composites. The basic form of the results are:

$$F=ka^n$$

F = contact force

k = contact stiffness

a = indentation

n = constant

Unfortunately, composite materials have characteristics which often invalidate the assumptions necessary to solve the equations analytically. A composite laminae is highly orthotropic, and exhibits strain-rate-dependent effects. For most impacts the stresses will be large enough to cause the material to fail locally so plastic behavior must be included in the model. Friction between the impactor and target on the surface adds tangential forces.

For these reasons experimental force-indentation data do not agree well with the classic Hertzian law. Researchers have thus turned to experimentally determined contact laws for purposes of modeling. A relationship developed by Tan and Sun [10] has become widely accepted as accurate and is frequently cited in publications

by other authors. It is assumed that during the initial loading of an undamaged laminate force versus indentation obeys the Hertzian relationship with a nonlinear (3/2) power. The stiffness of the laminate is unique to each material and stacking sequence and is determined by fitting a curve to experimental data. Upon unloading, the relationship is different. The force is a function of the maximum force during the loading phase, indentation depth and the critical indentation. Critical indentation defines the depth at which permanent deformation begins and must be determined by experiment for each material and stacking sequence.

For certain ratios of impactor mass/velocity and target stiffness, multiple contacts occur. The impactor transfers the majority of its momentum to the laminate, which then breaks contact with the now relatively slow-moving impactor. As the target rebounds from its maximum displacement (it essentially vibrates freely), it re-contacts the impactor before the impactor bounces clear of the target. The contact law has yet a third relationship for this reloading phase. It was found that the 3/2 power relationship no longer holds. Again the exponent must be found experimentally, and often 2 or 5/2 fits the data better. Results from tests such as these are frequently used by other investigators as the contact law of choice in their models. The obvious disadvantage of this method is that the tests require expensive equipment, expertise, and large amounts of time to perform. For every combination of impactor and target material (including stacking sequence) and geometry, a separate test is required.

Investigators who do not have the facilities available to perform their own tests are limited to scarce published data.

The contact law under development is based upon the theory of elasticity. For cases involving torsionless axisymmetry, solutions can be found for a host of loading and boundary conditions [11]. By a series of derivations the problem of a constant distributed load over a finite radius acting on an isotropic half space can be solved. This pressure-displacement relationship is the basis for the contact law. The solutions show that stresses diminish rapidly at distances a few contact radii from the original contact point, so the assumption of a semi-infinite target to represent a plate will give more accurate results for thicker laminates. Axisymmetry is utilized to reduce the problem from that of three dimensions to two. Thus, the contact surface can be modeled as a single radial line. Since the surface ply of a composite laminate is orthotropic, modifications must be made to account for the assumption of isotropy. The equations upon which the analysis is based follow:

$$\delta = \frac{4(1-\nu^2)P\rho}{\pi E}\int_0^{\pi/2}\sqrt{1-\left(\frac{r}{\rho}\right)^2\sin^2\Phi}\,d\Phi \quad , \text{for } r \le \rho$$

$$\delta = \frac{4(1-\nu^2)Pr}{\pi E}\left[\int_0^{\pi/2}\sqrt{1-\left(\frac{\rho}{r}\right)^2\sin^2\Phi}\,d\Phi - \left\{1-\left(\frac{\rho}{r}\right)^2\right\}\int_0^{\pi/2}\frac{d\Theta}{\sqrt{1-\left(\frac{\rho}{r}\right)^2\sin^2\Theta}}\right] \quad , \text{for } r > \rho$$

δ = transverse deflection

r = radial coordinate

P = constant pressure

ρ = radius of area over which pressure acts

E,ν = material properties of half-space

The contact area is represented by N overlapping constant pressure elements extending radially from the axis of symmetry. There is one node common to all elements at the center of the area. The second node of each element discretizes the contact area into regularly spaced sub-radii. Each node has a single translational degree of freedom in the transverse direction. A representation of the model appears in the figure below. Influence coefficients relating the elemental pressures to the nodal displacements are derived from the elasticity equations. A set of initial displacements is determined based on the user-specified parameters of the problem.

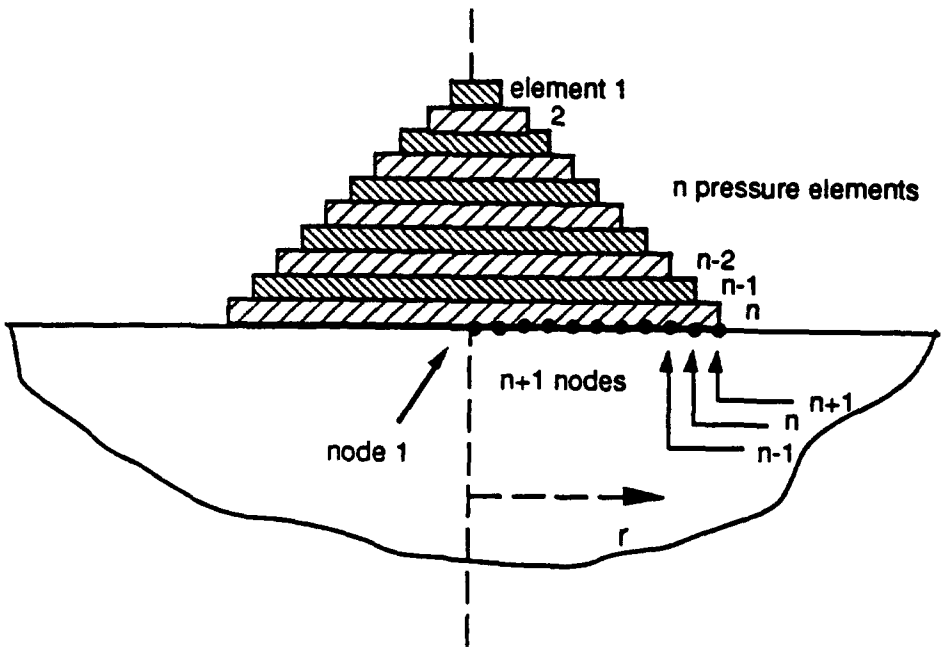

At the end of each iteration, the validity of the solution is checked based on three criteria:

1) Equilibrium

   The sum of the elemental pressures multiplied by their corresponding areas must equal the applied force.

2) Edge Pressure

   The pressure in the outermost element must approach zero at the edge of the contact zone. Since the contact area is divided into discrete areas, the pressure in this element cannot equal zero, or else there would be no contact.

3) Contact/Separation

   There must be continuous contact between the target and impactor in the assumed contact region and separation outside the contact region. For the geometry chosen, a spherical impactor on a flat target, contact cannot be broken at a given radius and re-established at a greater radius.

When these three conditions are satisfied a solution has been found and iteration stops. It was found that satisfying all three conditions simultaneously is difficult due to the non-linearity of the problem. Specifically, the size of the contact area varies rapidly with changing load.

The original solution method relied on a heuristic approach to solving the equations. But the rate of convergence depended very

strongly on the initial estimate of the displacements. In an effort to find more accurate solutions, optimization methods were investigated.

Optimization refers to any of a number of algorithms which seek to minimize a mathematical function, called the objective function. In addition, extra requirements to be satisfied, known as constraints, may be placed on the solution. The parameters from which the objective function and constraints are constructed are the design variables. Although mathematical in theory, optimization techniques have been of great interest to engineers as a means of solving difficult systems of non-linear equations which frequently arise, or for finding the "best" solution to a problem of many variables which has no exact solution. If the important physical phenomena in an engineering system can be accurately described by an objective function and constraints, a numerical method can often be found which will provide satisfactory solutions when analytical methods do not.

For the contact problem, several equations have been derived relating surface pressure and displacement. It is desirable to use these equations as the basis for the objective function and constraints, since they are known to govern the physical system. For a similar contact problem, optimization techniques were applied to the Rayleigh-Ritz method [12]. Rayleigh-Ritz is an energy method which requires a mathematical function to describe the internal strain energy of the elastic body. It was noted that it is difficult to find a function which satisfies the kinematic boundary

conditions for a contact problem and gives reasonable solution accuracy.

The first approach is to make the objective function by rearranging the equilibrium equation. The optimization routine would seek to minimize the absolute value of the difference between the sum of the pressures multiplied by their respective areas and the applied force. The conditions of the edge pressure approaching zero and the contact/separation condition would be imposed as constraints. A second approach would be to use the edge pressure criterion as an objective function, and the other two as constraints.

RESULTS OF SUMMER RESEARCH

During the Summer Graduate Student Research Program a technique for determining the contact force-indentation relationship for low-velocity impact of composite materials has been under development. This contact law is critical for modeling of impact events. Present methods require experimental results to determine several parameters. Different combinations of impactor and target materials require separate tests. Due to the non-linearity of the contact phenomenon, it is very difficult to extrapolate results or predict behavior when no experimental results are available.

The new method also gives information about the distribution of the contact pressure underneath the impactor. This is particularly useful for performing finite element analyses where the contact forces must be applied at several discrete points. The stress gradients are extremely high in the contact zone, so in order to accurately model impact and be able to track the stresses which initiate damage, this type of precision is necessary. The contact laws which are currently used do not provide such information.

CONCLUSIONS

A new method for analytically determining the force-indentation relationship for impact on laminated composites was investigated. A program is under development which seeks to reduce the amount of experimental data necessary for modeling of impact events. The method is based upon equations derived from the theory of elasticity. An experimental plan for validating the theoretical aspects of this method will be proposed.

Additionally, other numerical methods will be investigated to study contact problems. These include modeling for commercially available codes such as ANSYS, which solves transient dynamics problems with a conventional implicit solution scheme, and DYTRAN, which uses an implicit scheme to solve the system of equations. The explicit solution method is advantageous for problems involving high-velocities and/or large deformation. For a low-velocity impact problem, it is not clear which method will have the advantage in computation cost.

REFERENCES

1. Finn, S.R. and Springer, G.S., Delaminations in composite plates under transverse static loads - A model. Composite Structures, 23 (1993) 177-190

2. Finn, S.R. and Springer, G.S., Delaminations in composite plates under transverse static loads - Experimental results. Composite Structures, 23 (1993) 191-204

3. Choi, H.Y. and Chang, F.K., A Model for Predicting Damage in Graphite/Epoxy Laminated Composites Resulting from Low-Velocity Point Impact. Journal of Composite Materials, 26 (1992) 2134-2169

4. Liu, D., Impact-Induced Delamination - A View of Bending Stiffness Mismatching. Journal of Composite Materials, 22 (1988) 674-692

5. Robinson, P. and Davies, G.A.O., Impactor Mass and Specimen Geometry Effects In Low-Velocity Impact of Laminated Composites. International Journal of Impact Engineering, 12 (1992) 189-207

6. Lee, J.D., Du, S., and Liebowitz, H., Three-Dimensional Finite Element and Dynamic Analysis of Composite Laminate Subjected to Impact. Computers and Structures, 19 (1984) 807-813

7. Sun, C.T. and Chen, J.K., On the Impact of Initially Stressed Composite Laminates. Journal of Composite Materials, 22 (1988) 490-504

8. Wu, H.T. and Springer, G.S., Impact Induced Stresses, Strains, and Delaminations in Composite Plates. Journal of Composite Materials, 22 (1988) 533-560

9. Hertz, H., Uber die Beruhrung fester Elastischer Korper. Journal Reine Angle Math, 92 (1881) 155

10. Tan, T.M. and Sun, C.T., Use of Statical Indentation Laws in the Impact Analysis of Laminated Composite Plates. Journal of Applied Mechanics, 52 (1985) 6-12

11. Timoshenko, S.P. and Goodier, J.N., Theory of Elasticity, 3rd Edition, McGraw-Hill, 1970

12. McDonald, E.S., Optimization Techniques For Contact Stress Analysis, M.S. Thesis, Naval Postgraduate School, Monterey, California, 1992

A SELF-TUNING PIEZOELECTRIC VIBRATION ABSORBER

Thomas F. Starchville Jr.
Graduate Student
Department of Aerospace Engineering

The Pennsylvania State University
233 Hammond Building
University Park, PA 16802-1401

Final Report for:
Graduate Student Research Program
Wright Laboratory

Sponsored by:
Air Force Office of Scientific Research
Bolling Air Force Base, Washington, D.C.

August 1993

A SELF-TUNING PIEZOELECTRIC VIBRATION ABSORBER

Thomas F. Starchville Jr.
Graduate Student
Department of Aerospace Engineering
The Pennsylvania State University

Abstract

A self-tuning piezoelectric vibration absorber is presented. This device, similar to a mechanical vibration absorber, has to be tuned to a particular structural vibration mode in order to be effective. The absorber presented here will tune itself to a particular mode and track that mode if it varies in frequency. A set of experiments were designed and conducted to demonstrate the self-tuning absorber. A cantilevered beam was used as the base structure with its second mode as the target frequency for the absorber. Design of the absorber consisted of a pair of lead zirconate titanate (PZT) tiles on the structure shunted by an inductor-resistor circuit. This produced an electrical resonance that could be tuned to the desired structural mode. The performance criterion for the absorber was determined from a ratio of the RMS response of the absorber to the RMS response of the structure. A simple control system was designed using only the change in slope of the RMS ratio as criteria to increase or decrease the electrical resonance of the shunt. Experiments using coarse, fine, and a combination of frequency step-sizes are presented. Finally, the response of the absorber to an abrupt change in system parameters is also examined.

A SELF-TUNING PIEZOELECTRIC VIBRATION ABSORBER

Thomas F. Starchville Jr.

INTRODUCTION

In the past several years, researchers have begun using piezoelectric devices for structural vibration suppression. These devices transform electrical energy to mechanical energy and vice versa. Vibration absorbers using piezoelectric devices have been presented by Hagood and von Flotow [1], Hagood and Crawley [2], Edberg et. al. [3], and Hollkamp [4]. A single-mode absorber is created by connecting a simple inductor-resistor network across a piezoelectric actuator. The inductance combined with the inherent capacitance of the piezoelectric produces an electrical resonance which when properly tuned to a vibration mode will absorb energy from the structure.

Also recently, Smith et. al. [5] have demonstrated an adaptive absorber using a viscoelastic material (VEM) as the spring for a single-degree-of-freedom mechanical absorber. The stiffness of the VEM can be varied with temperature, thereby varying the tuning of the absorber. A controller tunes the absorber to suppress a vibration mode and keeps the absorber tuned to that mode even if its frequency shifts.

A self-tuning adaptive piezoelectric absorber is presented in this report. The theory behind the device will be discussed and analytical simulations provided. Finally, the absorber will be demonstrated experimentally on a cantilevered beam with attached lead zirconate titanate (PZT) tiles.

THEORY

The design of the mechanical vibration absorber is straightforward if the frequency of a vibration mode is known [6,7]. However, if the frequency is unknown or varying, an adaptive scheme must be used. The ratio of RMS response of the absorber to the RMS response of the structure is used as the absorber's

performance criterion by Reference [5]. A natural choice for the performance criterion would have been the RMS response of the structure, but this choice is good only if the magnitude of the disturbance is consistent. The RMS ratio performance criterion eliminates the need for a consistent disturbance, and as shown in Figure 1, the RMS ratio is a maximum (δ = 1.043) near the .imum RMS structural response (δ = 1.025). (Note that δ is the tuning ratio, which is the absorber frequency divided by the structures' natural frequency.)

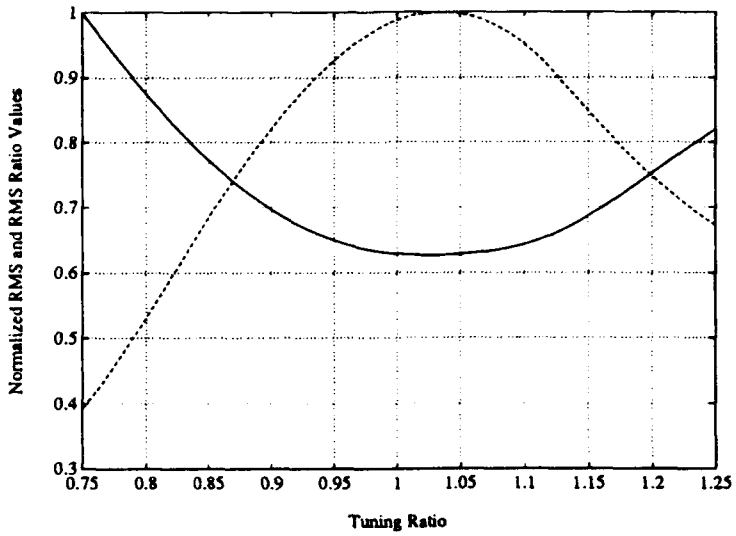

Figure 1. The mechanical vibration absorber (ζ = 5%, mass ratio of 0.1) is applied to an undamped system. Shown is the RMS response of the system (solid) and the ratio of the absorber RMS response to the system RMS response (dashed) as the tuning ratio (δ) varies.

A piezoelectric damping device can be created by applying an electrical shunt across a piezoelectric actuator that is attached to a structure. When the shunt consists of an inductor and resistor in series, the inductor together with the inherent capacitance of the piezoelectric creates an electrical resonance. This resonance can be tuned so that it coincides with a structural resonance, creating a device similar to the mechanical absorber. Reference [1] gives a detailed analytical derivation of a piezoelectric absorber applied to an undamped mechanical structure. The derivation specifies the inductance and resistance to achieve optimal vibration suppression.

A self-tuning piezoelectric absorber can be made by adaptively tuning the electrical resonance. This can be done by adjusting the shunt inductance and resistance. As with the mechanical absorber, a performance criterion must be used to control the tuning. Again, the ratio of the absorber RMS to the system RMS response will be used. Figure 2 shows the performance of a piezoelectric absorber as the shunt is tuned, the RMS ratio is a maximum ($\delta = 0.9975$) near the minimum RMS structural response ($\delta = 1.025$).

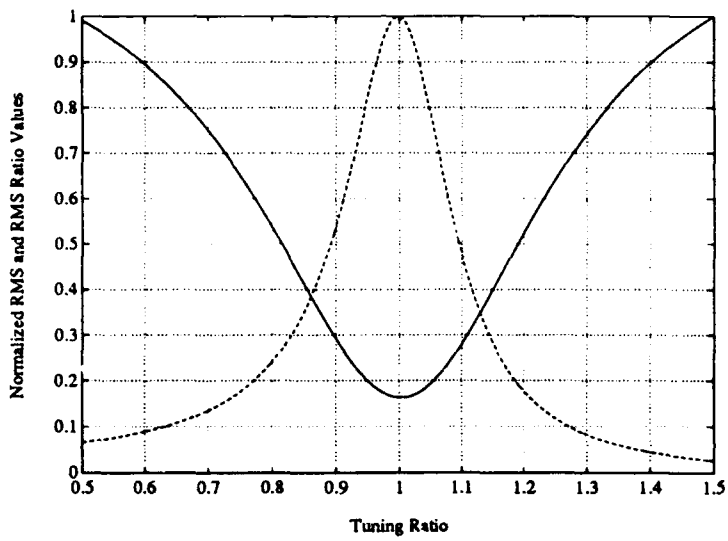

Figure 2. The piezoelectric vibration absorber performance as the tuning ratio varies. Shown is the RMS response of the system (solid) and the ratio of the absorber RMS response to the system RMS response (dashed).

The control based on the RMS ratio can be stated as: if the estimation of the slope of the RMS ratio is positive, increase the electrical frequency, otherwise decrease it by a set amount. A simulation of this control law is shown in Figure 3. In the simulation, the disturbance was a gaussian random variable whose variance in each iteration was modulated by a uniform random number (each iteration represents 5000 data points.) This represented a non-consistent excitation. As shown in the figure, the control keeps the piezoelectric absorber tuned to resonance.

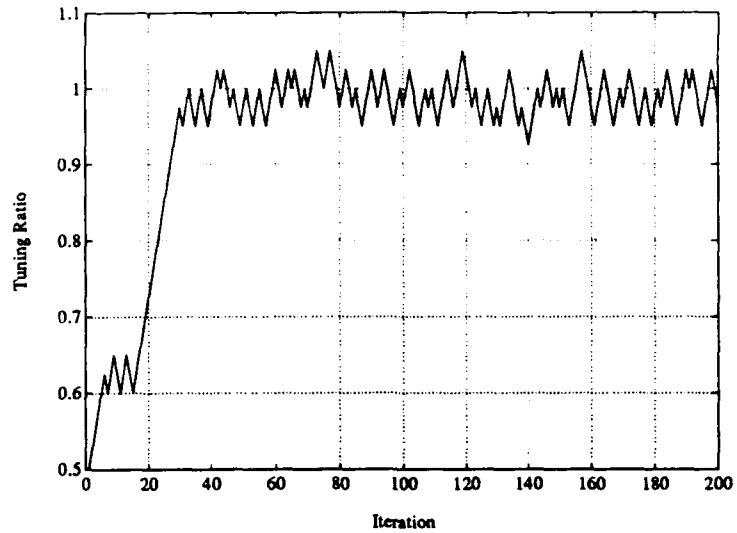

Figure 3. The piezoelectric vibration absorber; the inductance and resistance of the shunt is adjusted based on the RMS ratio estimated from simulated response of the system and the absorber.

EXPERIMENT

A set of experiments were conducted to verify the control theory. A cantilevered aluminum beam shown in Figures 4 and 5 was constructed for this purpose. Six pairs of PZT tiles (a tile on each side of the beam) are attached at the locations shown in Figure 4. One side of each tile is grounded to the beam and the other side is connected in parallel to the other tile in each pair. Synthetic inductors [8], schematic in Figure 6, are used in the shunt; these were chosen for ease of use. The effective inductance is linearly proportional to the value of an adjustable resistor which in this study was a motorized potentiometer. A PZT tile (one side of pair #5) was used as a disturbance; the input to the tile was a band limited (0-100 Hz) gaussian random signal.

An absorber was created using the PZT tiles at location 1. The second bending mode (41.87 Hz, 0.36% damping) was chosen as the mode to suppress. The synthetic inductor provided both the inductance and resistance of the shunt. Ideally, the synthetic inductor can create high inductance values without an associated resistance. Practically, there is an effective resistance.

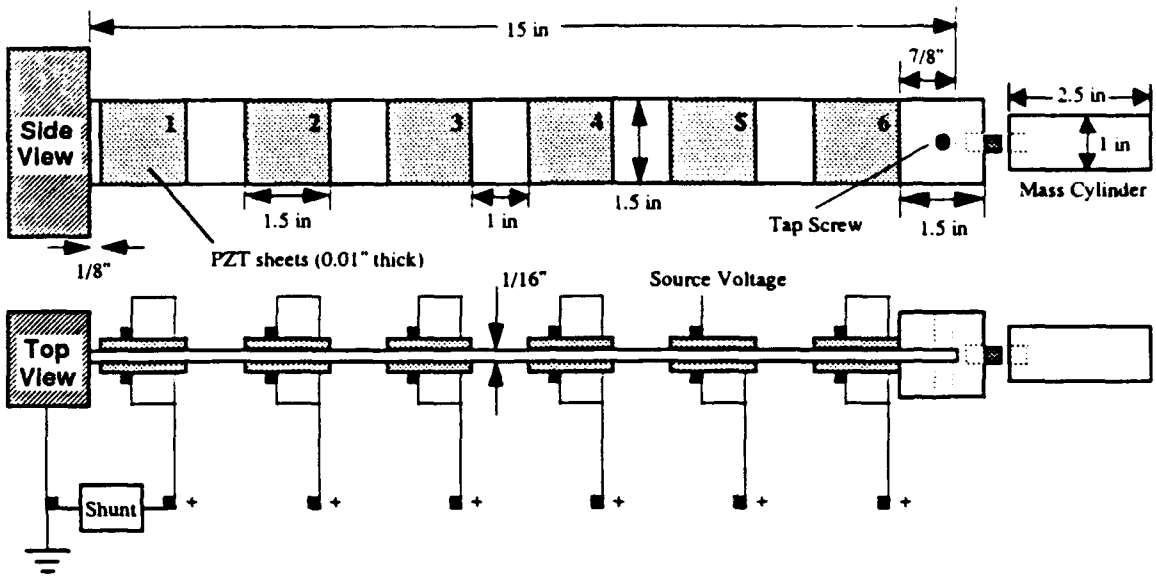

Figure 4. A schematic of the experimental cantilevered beam. Six pairs of PZT tiles are bonded to the structure. The absorber or shunt response is measured from PZT pair #1 and the system response is measured from PZT pair #4. One PZT sheet of pair #5 is used for excitation while the other side senses the excitation input to the structure.

(a)

(b)

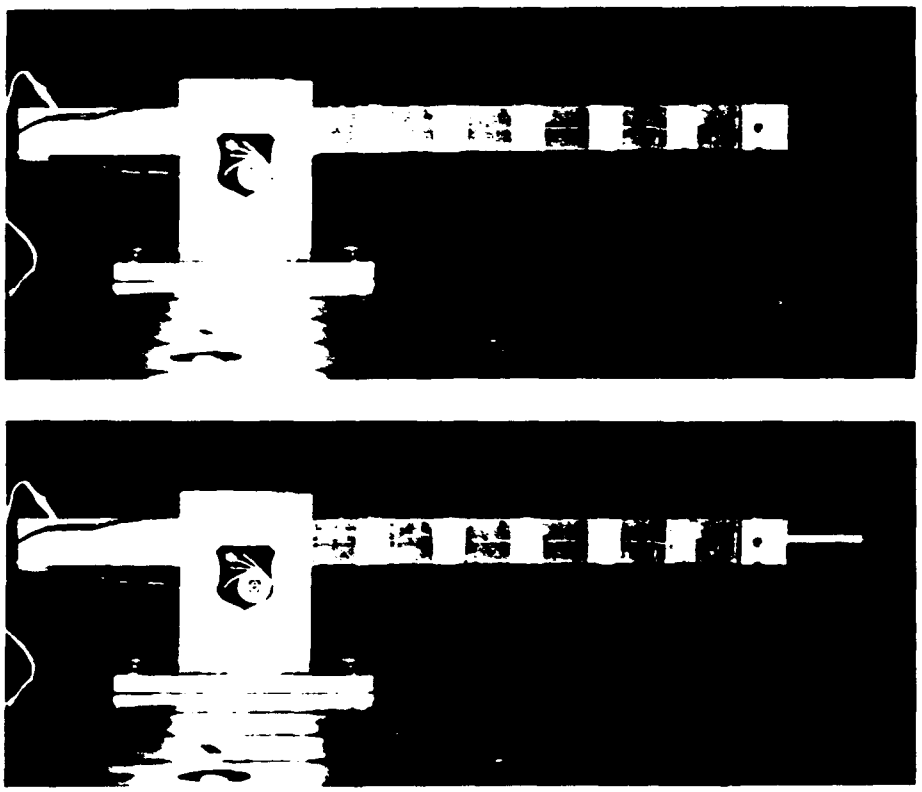

Figure 5. Photograph of the experimental beam (a) in base configuration and (b) with an added mass cylinder to abruptly change the parameters of the system.

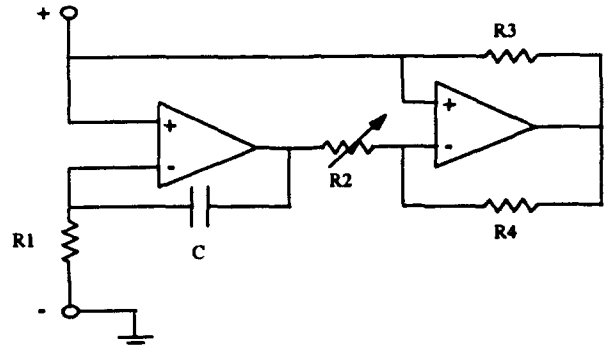

Figure 6. A synthetic inductor design using two operational amplifiers. For the experiments the inductance is controlled by selecting R2.

A personal computer with an analog-to-digital card was used to measure the voltage across the synthetic inductor (absorber response) and the voltage across the PZT tiles at location 4 (system response). The signals from each of the two PZT pairs were sent through a bank of filters to allow only the second mode to be measured. Two filters were necessary to "window" the desired frequency range: a high-pass butterworth filter was set for a cutoff frequency of 10 Hz and a low-pass elliptical filter was set for a cutoff frequency of 70 Hz. Software (see Appendix) was used to acquire the data, estimate the RMS response, and command the motorized potentiometer to change according to the control law. A Hewlett Packard Paragon system served as the source driver to produce the random input and measure the frequency response functions during the experiments. Figure 7 illustrates a schematic of the experimental setup.

A preliminary experiment was conducted to validate the performance criteria. Figure 8 shows the results of this preliminary experiment. Here, the tuning of the absorber was manually varied and RMS ratio estimated by the software. Since there was a large amount of uncertainty in the estimation of the RMS ratio, a polynomial fit to the data around the peak was used to more accurately predict the "optimal" tuning ratio. The RMS ratio is a maximum when the tuning ratio is very near unity ($\delta = 0.9678$, in this case). Although this value should be as close to unity as possible, it will be shown that performance of the absorber is not significantly diminished.

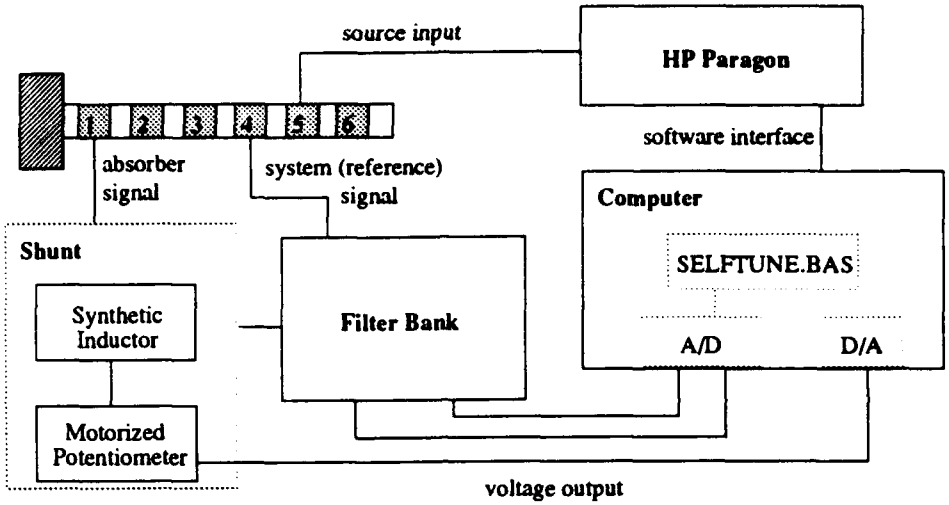

Figure 7. Schematic of the experimental setup. Signals from the absorber PZTs (pair #1) and system PZTs (pair #4) are passed through a filter bank with a frequency window of 10-70 Hz. Software on the computer estimates the signal RMS and determines a voltage to send to the motorized potentiometer.

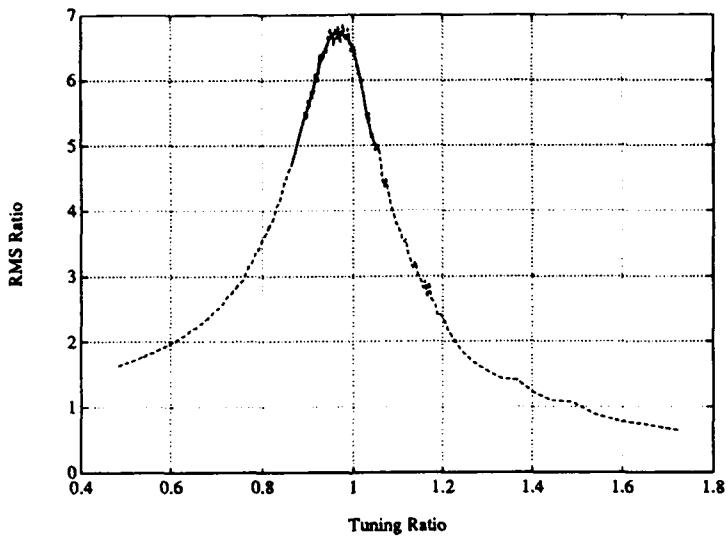

Figure 8. The experimentally determined RMS response ratio as a function of the piezoelectric absorber tuning. Each point uses 5 seconds of data sampled at 1000 Hz. Since there was uncertainty in estimating the RMS response, a fit was performed to better distinguish the peak ($\delta = 0.9678$).

After the preliminary experiments confirmed that the choice of the performance criterion was acceptable, experiments were conducted to allow the absorber to self-tune. The change in voltage to the motorized potentiometer resulted in a shift in the electrical resonance of the shunt; however, a linear change in

voltage did not correspond to a linear change in frequency. To achieve a constant change in the frequency domain, the following equation was used to determine the change in voltage:

$$\Delta Voltage = C(4095 - V_{command})^{3/2};\ 0 \le V_{command} \le 4095$$

where C is a constant to change the resolution of the step-size. Two values for C were used for the experiments: C=0.005 (coarse frequency change - 4 Hz) and C=0.001 (fine frequency change - 0.8 Hz).

A series of fine and coarse frequency change tests were conducted to determine the ability of the absorber to self-tune. The response for each case is shown in Figure 9; the potentiometer was given an initial command voltage of 1000. Note in the figure that the rise time of the absorber for the coarse tuning is fast (approximately 30 sec) due to the larger step-size in frequency. The response afterwards, however, dithers around the "optimal" tuning ratio (δ = 0.9678) by what would seem a significant amount. The rise time for the fine tuning case is very slow, but the oscillation about the "optimal" tuning is small.

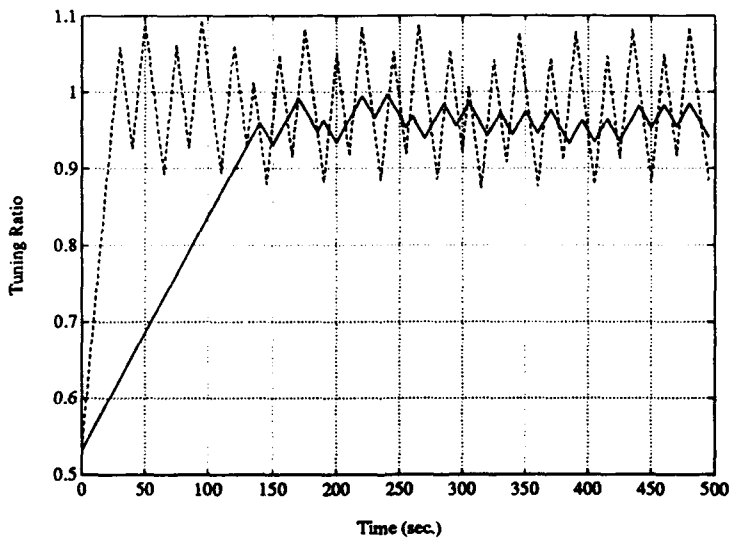

Figure 9. Experimental results for the piezoelectric vibration absorber when a coarse frequency adjustment of 4 Hz (dashed) and a fine frequency adjustment of 0.8 Hz (solid) are used.

To better understand the implications of the dithering around the "optimal" tuning ratio in Figure 9, Figures 10 and 11 should be considered. Five different frequency response functions (FRFs) are presented to

illustrate the addition of the electrical resonance when the absorber is: 1) optimally tuned (δ = 1.0), 2) tuned to the minimum of the dithering, 3) tuned to the maximum of the dithering, 4) tuned to the maximum RMS ratio (δ = 0.9678), and 5) turned off. Each of the four cases involving the absorber result in a decrease of the resonant peak. A comparison of the power from these FRFs normalized to the baseline (no shunt) is shown in Table 1. The power was calculated by the following equation:

$$Power = \int_{2\pi(10\,\mathrm{Hz})}^{2\pi(70\,\mathrm{Hz})} \left|H(j\omega)\right|^2 d\omega$$

Notice in Table 1 for the coarse and fine frequency changes, the highest reduction in power (85%) occurs when the absorber is optimally tuned; this was expected. Comparing this value to the cases when the absorber was allowed to self-tune using a coarse change, the range of power reduction is between 64% and 83%. This shows that even though the absorber is not able to stay exactly tuned throughout the experiment (due to RMS estimation uncertainty), it still significantly reduces the vibration energy.

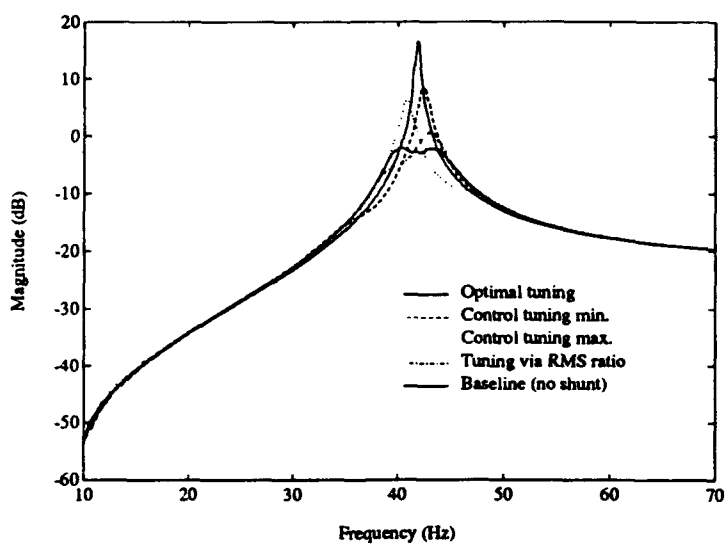

Figure 10. The experimentally measured frequency response functions for five conditions during a coarse frequency change self-tuning test.

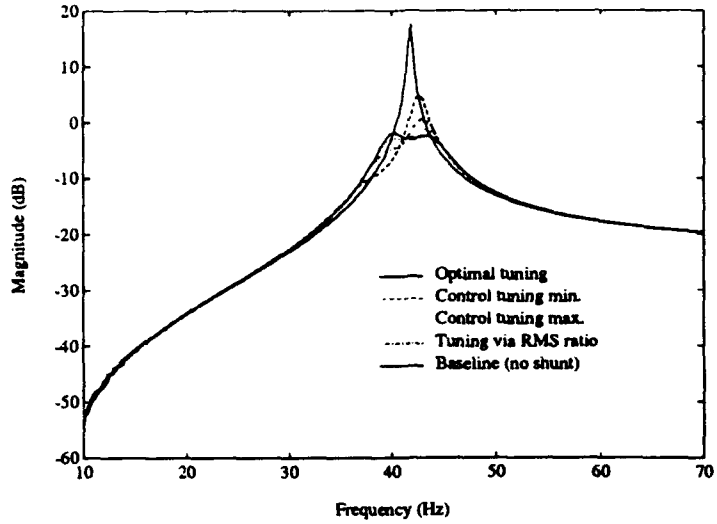

Figure 11. The experimentally measured frequency response functions for five conditions during a fine frequency change self-tuning test.

Table 1. Comparison of normalized power for five tuning conditions for a coarse frequency change (4 Hz) and a fine frequency change (0.8 Hz).

Tuning Condition	Coarse Frequency Change (4 Hz)		Fine Frequency Change (0.8 Hz)	
	Command Voltage	Normalized Power (%)	Command Voltage	Normalized Power (%)
Optimally tuned	3220	15.51	3220	15.10
Minimum of dithering	2948	35.85	3085	22.03
Maximum of dithering	3365	26.26	3214	15.13
Maximum RMS ratio	3162	16.99	3162	16.55
No shunt	----	100.00	----	100.00

The range of power reduction for the fine frequency change is noticeably smaller (78% - 85%). This shows that even though the rise time for this case is long, the overall performance of the absorber as it begins to tune is very good compared to a coarse frequency change. Ideally, one would want a compromise between the two cases. At the start of an experiment, a fast rise time is desirable (coarse frequency change) while after the

absorber begins to tune a small amount of variation around the "optimal" tuning ratio (fine frequency change) is desired.

The self-tuning response for a combination of the two frequency step-sizes is shown in Figure 12. Here, the constant, C, was initially set for a coarse change then halved after every ten iterations. Notice the fast rise time characteristic of the coarse step-size, but the amount of oscillation about the "optimal" tuning ratio is greatly reduced and even begins to settle after 250 seconds. This shows that the absorber remained tuned even with the uncertainty in estimating the RMS responses.

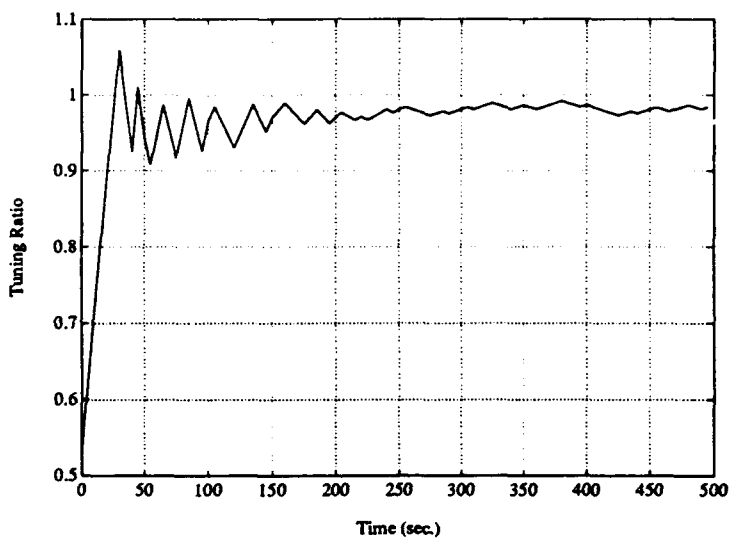

Figure 12. A self-tuning test using a combination of coarse and fine frequency step-sizes to achieve the best response possible. Initially, the constant, C, was set at 0.005 (coarse) and then halved every ten iterations (50 seconds).

Now that it has been demonstrated that the piezoelectric vibration absorber can self-tune to a particular structural mode, the system was subjected to an abrupt change to cause the frequency to shift. Causing an abrupt change in system parameters at a point during the experiment was accomplished by attaching a mass cylinder to the end of the beam as shown in Figures 4 and 5. The cylinder was made of aluminum, weighed 114.75 g, and reduced the frequency of the second mode from 41.87 Hz, 0.36% damping to 31.55 Hz, 0.35% damping. It was decided that this was a large enough change in frequency to test the self-

tuning of the absorber. The responses for coarse and fine frequency adjustments are presented in Figure 13. At the start of the self-tuning test, the motorized potentiometer was given a voltage command of 1000. The mass cylinder was added to the structure at 500 seconds into the experiment. Notice that the response for the first portion of the test is similar to that in Figure 9, the absorber does a better job self-tuning with the smaller frequency step-size. When the mass is applied and the frequency shifts, the absorber, in both cases, tracks the shift with excellent results.

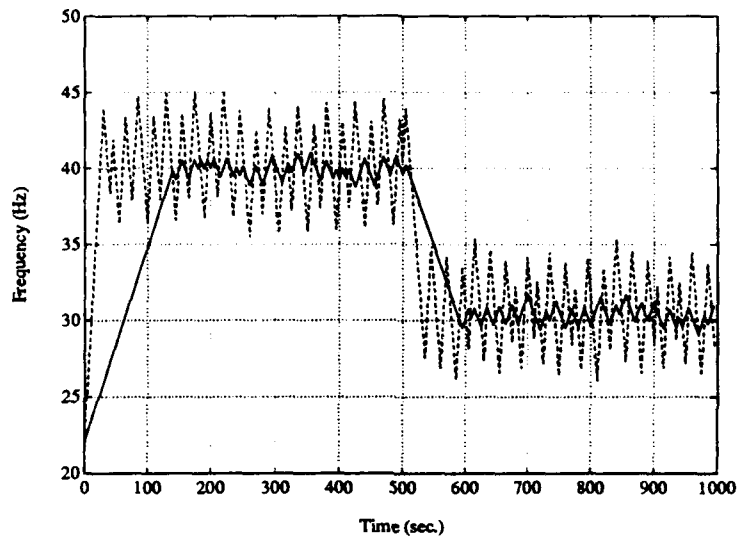

Figure 13. Self-tuning of the vibration absorber with an abrupt change in system properties during the experiment for a coarse (dashed) and fine (solid) frequency change. A mass cylinder was added to the end of the structure to reduce the second mode frequency from 41.87 Hz to 31.55 Hz.

CONCLUSIONS AND RECOMMENDATIONS

The design of a self-tuning piezoelectric vibration absorber has been presented. It was demonstrated that the absorber could tune itself to the second structural mode using both a coarse (4 Hz) and a fine (0.8 Hz) frequency step-size in the control law. The control law itself was designed for simplicity using the change in the RMS ratio slope to increase or decrease the electrical resonance of the shunt. Although there was some variation in the absorber around the "optimal" tuning ratio, this could be attributed to a fair amount of

uncertainty in estimating the RMS of the absorber and system. One way to improve this measure could be to use a longer data stream when performing the RMS calculation. This, however, would greatly increase the amount of time for the absorber to properly tune and as seen in the FRF power comparisons, the resulting reduction in vibration energy was still very favorable. The robustness or "tunability" of the absorber was examined by abruptly changing the system parameters to determine if once tuned and a change occurred, could it retune to the new frequency? A mass cylinder was added to the structure to reduce the second mode frequency and the absorber demonstrated that it could retune itself after this abrupt change.

A natural extension of this work would be the application of the self-tuning vibration absorber to two-dimensional structures such as vibrating plates. The theoretical analysis would be similar, however, a study into the placement of the absorber for best performance would need to be completed.

REFERENCES

[1] Hagood, N.W. and A. von Flotow, "Damping of Structural Vibrations with Piezoelectric Materials and Passive Electrical Networks," *Journal of Sound and Vibration*, Vol. 146, No. 2, 1991, pp. 243-268.

[2] Hagood, N.W. and E.F. Crawley, "Experimental Investigation into Passive Damping Enhancement for Space Structures," *Proceedings of the 30th AIAA/ASME/ASC/AHS Structures, Structural Dynamics and Materials Conference*, Mobile, AL, AIAA Paper 89-3439, pp. 97-109.

[3] Edberg, D.L., A.S. Bicos and J.S. Fechter, "On Piezoelectric Energy Conversion for Electronic Passive Damping Enhancement," *Proceedings of Damping '91*, Feb. 1991, San Diego, CA, Paper GBA-1.

[4] Hollkamp, J.J., "Multimodal Passive Vibration Suppression with Piezoelectrics," *Proceedings of the 34th AIAA/ASME/ASC/AHS Structures, Structural Dynamics and Materials Conference*, La Jolla, CA, AIAA Paper 93-1683, pp. 3227-3237.

[5] Smith, K.E., J.R. Maly and C.D. Johnson, "Smart Tuned-Mass Dampers," *Proceedings of the ADPA/AIAA/ASME/SPIE Conference on Active Materials and Adaptive Structures*, Nov. 1991, Alexandria, VA, pp. 19-22.

[6] Den Hartog, J.P., Mechanical Vibrations, McGraw-Hill Book Co., New York, 1956.

[7] Timoshenko, S., D.H. Young and W. Weaver, Vibration Problems in Engineering, John Wiley, New York, 1974.

[8] Chen W.-K., Passive and Active Filters, John Wiley, New York, 1986.

APPENDIX

```
'*************************************************************************
'*                                                                       *
'*                  A SELF-TUNING PIEZOELECTRIC DAMPER                   *
'*                                                                       *
'*                       Last Modified 29-Jul-1993                       *
'*                 Thomas F. Starchville Jr., PENN STATE                 *
'*                                                                       *
'*   The following Quick-BASIC program is designed to actively tune a    *
'*   a vibration damper. Data from two PZT pairs is read via an A/D and  *
'*   an RMS ratio value is found. A simple control law determines        *
'*   whether the inductance of the damper should be increased or de-     *
'*   creased. A D/A card sends a voltage out to a motorized potent-      *
'*   iometer. Three different functions may be performed with this       *
'*   program: 1) calibration of the damper system, 2) self-tuning of     *
'*   the damper, 3) user-defined output from the D/A.                    *
'*                                                                       *
'*************************************************************************

'**  Define arrays and subroutines  ****************************************
DIM D%(8), DAT%(10000), CHAN%(10000), SUM(2)
COMMON SHARED D%(), CHAN%(), DAT%()
DECLARE SUB CIO16 (MD%, BYVAL DUMMY%, F%)
'**  Define the data acquisition session parameters  **********************
   NPTS% = 500          'Number of samples to be taken from each channel
   NCHAN% = 2           'Number of channels to be scanned
   NMAX% = 10000        'Total number of samples to be taken
   DSETS% = 10          'Number of data sets for the RMS calculation
   LOOPS% = 10          'Number of loops before program checks with user
   VENTRYS% = 221       'Number of entries in the voltage calibration file
   DIRECT% = 1          'Initial slope direction for control law
   AMPL5 = 1            'Amplification of absorber signal
   AMPL6 = 2            'Amplification of system signal
   C = .005             'Step-size resolution constant
'**  Perform desired program function  *************************************
   GOSUB FUNCT
'**  Loop for the RMS calculation  *****************************************
   COUNTER% = 1
   RATIO.OLD = 0
10 GOSUB RMSSUM
'**  Prompt user to continue control algorithm or quit  ******************
   GOSUB DONE
'**  End program  ******************************************************
   CLOSE #1
   END
'**  Program Subroutines  **************************************************
FUNCT:
110   CLS
      LOCATE 3, 5: PRINT "Enter the function you wish to perform:"
      LOCATE 5, 10: PRINT "(1)  System Calibration"
      LOCATE 6, 10: PRINT "(2)  Self-Tuning Experiment"
```

```
      LOCATE 7, 10: PRINT "(3)  User-Defined Command Output"
      LOCATE 8, 10: PRINT "(4)  Quit Program"
      LOCATE 10, 5: INPUT "Choice ? ", CHOICE%
      IF CHOICE% = 1 THEN GOSUB CALIBRTE
      IF CHOICE% = 2 THEN GOSUB TUNING
      IF CHOICE% = 3 THEN GOSUB USER
      IF CHOICE% = 4 THEN END
      RETURN
CALIBRTE:
      CLS
      LOCATE 3, 5: PRINT "**  Calibration of System  **"
      LOCATE 6, 5: INPUT "Enter a data OUTPUT file name (w/ ext):  ", FILE$
      OPEN FILE$ FOR OUTPUT AS #1
      LOCATE 7, 5: INPUT "Enter a cmd INPUT file name (w/ ext):  ", VIN$
      OPEN VIN$ FOR INPUT AS #2
      WRITE #1, "Iteration,RMS A,RMS B,RMS Ratio,Pot Setting"
      '**  Place the potentiometer at an initial position  ****************
      INPUT #2, VOLT%
      GOSUB START
      RETURN
TUNING:
      CLS
      LOCATE 3, 5: PRINT "**  Self-Tuning Experimental Run  **"
      LOCATE 6, 5: INPUT "Enter a data OUTPUT file name (w/ ext):  ", FILE$
      OPEN FILE$ FOR OUTPUT AS #1
      WRITE #1, "Iteration,RMS A,RMS B,RMS Ratio,Pot Setting"
      '**  Place the potentiometer at an initial position  ****************
      LOCATE 8, 5
      INPUT "Enter a starting voltage command (0-4095):  ", VOLT%
      GOSUB START
      RETURN
USER:
100   CLS
      LOCATE 3, 5: PRINT "**  User-Defined Single Command Output  **"
      LOCATE 6, 10: INPUT "Enter a command to output (0-4095):  ", VOLT%
      GOSUB DA
      LOCATE 10, 5: PRINT "Enter (1) to do again or (2) go to main menu"
      LOCATE 13, 10: INPUT "Choice ?  ", CHOICE2%
      IF CHOICE2% = 1 THEN GOTO 100
      IF CHOICE2% = 2 THEN GOTO 110
      RETURN
START:
      LOCATE 10, 5: PRINT "Please wait, allowing the system to stabilize."
      '**  Send the voltage to the potentiometer  **************************
      GOSUB DA
      SLEEP 10
      RETURN
RMSSUM:
      CLS
      IF CHOICE% = 1 THEN NUMBER% = VENTRYS%
      IF CHOICE% = 2 THEN NUMBER% = LOOPS%
      FOR ITER% = 1 TO NUMBER%
```

```
      GOSUB PRTHEAD
      SUM(1) = 0: SUM(2) = 0            'Initialize the data sums
      PASS% = 1
      FOR I = 1 TO DSETS%
         IF CHOICE% = 1 THEN
            LOCATE 12, 20: PRINT "Volt Command = "; VOLT%
         END IF
         IF CHOICE% = 2 THEN
            LOCATE 11 + ITER%, 5: PRINT ITER%
            VOUT = 1.220421E-03 * VOLT% - 3.192633E-04
            LOCATE 11 + ITER%, 54: PRINT VOLT%
            LOCATE 11 + ITER%, 64: PRINT VOUT
         END IF
         '**  Perform the data acquisition  ****************************
50       GOSUB INITA
         GOSUB AD
         LOCATE 6, 15
         PRINT "          Pass"; PASS%; "completed."
         '**  Calculate the sum of the data squared for the current  ***
         '**  pass and check for clipping (out of range data)        ***
         FOR K = 0 TO NCHAN% - 1
            TEMPSUM(K + 1) = 0
         NEXT K
         FOR J = 0 TO NPTS% - 1
            FOR K = 0 TO NCHAN% - 1
               TEMPDATA% = DAT%(J * NCHAN% + K)
               IF TEMPDATA% < -2040 OR TEMPDATA% > 2040 THEN
                  LOCATE 6, 15
                  PRINT "          Redoing Pass"; PASS%; "     "
                  GOTO 50
               ELSE
                  TEMPSUM(K + 1) = TEMPSUM(K + 1) + TEMPDATA% ^ 2
               END IF
            NEXT K
         NEXT J
         FOR K = 0 TO NCHAN% - 1
            SUM(K + 1) = SUM(K + 1) + TEMPSUM(K + 1)
         NEXT K
         '**  End RMS summation loop  ***********************************
         PASS% = PASS% + 1
      NEXT I
   '**  Calculate RMS values and RMS ratio  ****************************
   GOSUB RMS
   '**  Implement control law (CHOICE%=2 only)  ************************
   IF CHOICE% = 2 THEN
      GOSUB CONTROL
      GOSUB PRTOUT
   END IF
   '**  Get next voltage value from file (CHOICE%=1 only)  *************
   IF CHOICE% = 1 AND ITER% < VENTRYS% THEN
      INPUT #2, VOLT%
      LOCATE 6, 15: PRINT "                                    "
```

```
      END IF
      WRITE #1, ITER%, RMSA, RMSB, RATIO.NEW, OLDVOLT%
      '**  Send voltage change to potentiometer ***************************
      GOSUB DA
      NEXT ITER%
      RETURN
PRTHEAD:
        IF CHOICE% = 1 THEN
           LOCATE 3, 5
           PRINT "Entry"; ITER%; "data acquisition in progress..."
           END IF
        IF CHOICE% = 2 THEN
           LOCATE 3, 5
           PRINT "Loop"; COUNTER%; "data acquisition in progress ..."
           LOCATE 10, 5: PRINT "Iter"
           LOCATE 10, 12: PRINT "Absorber": LOCATE 11, 14: PRINT "RMS"
           LOCATE 10, 26: PRINT "System": LOCATE 11, 27: PRINT "RMS"
           LOCATE 10, 39: PRINT "RMS Ratio"
           LOCATE 10, 54: PRINT "Command": LOCATE 11, 55: PRINT "Volts"
           LOCATE 10, 65: PRINT "Estimated": LOCATE 11, 66: PRINT "Voltage"
        END IF
        RETURN
DA:
      BA% = 864                          'CIODDA-06 Base I/O Address
      CH% = 0                            'D/A Channel Output
      LOADR% = BA% + CH% * 2             'Construct low address of DAC
      HIADR% = BA% + CH% * 2 + 1         'Construct high address of DAC
      LOBYTE% = VOLT% AND 255                'Construct low byte of data
      HIBYTE% = (VOLT% - LOBYTE%) / 256      'Construct high byte of data
      OUT LOADR%, LOBYTE%                    'Output low byte through D/A
      OUT HIADR%, HIBYTE%                    'Output high byte through D/A
      SLEEP 2        'Pause to allow potentiometer to move into position
      RETURN
INITA:
      F% = 0                    'Error flag
      MD% = 0                   'Mode of operation (initialize A/D)
      D%(0) = &H300             'CIO-16ADJR-AT Base I/O Address
      D%(1) = 2                 'Interrupt level
      D%(2) = 1                 'DMA level
      CALL CIO16(MD%, VARPTR(D%(0)), F%)
      IF F% <> 0 THEN PRINT "A/D MODE"; MD%; "ERROR # "; F%: END
      RETURN
AD:
      MD% = 50                              'Mode of operation (take data)
      F% = 0                                'Error flag
      D%(0) = 0                             'Channel no. of lower scan limit
      D%(1) = D%(0) + NCHAN% - 1            'Channel no. of upper scan limit
      D%(2) = 1                             'Sampling frequency (KHz)
      D%(3) = 0                             'Sampling frequency (hundreds Hz)
      D%(4) = NCHAN% * NPTS%                'Total no. of samples to be taken
      IF D%(4) > NMAX% THEN
         PRINT "Increase DATA & CHAN array sizes to: "; D%(4): END
```

```
      END IF
      D%(5) = VARPTR(DAT%(0))          'Array pointer for DATA
      D%(6) = VARPTR(CHAN%(0))         'Array pointer for CHAN
      D%(7) = 1                        'External Trigger - 0=On,1=Off
      D%(8) = 0                        'Voltage range +/- 5 volts
      CALL CIO16(MD%, VARPTR(D%(0)), F%)
      IF F% <> 0 THEN PRINT "A/D MODE"; MD%; "ERROR # "; F%: END
      RETURN
RMS:
      RMSA = (SQR(SUM(1) / (DSETS% * NPTS%)) * 5) / (AMPL5 * 2048!)
      RMSB = (SQR(SUM(2) / (DSETS% * NPTS%)) * 5) / (AMPL6 * 2048!)
      IF RMSB = 0 THEN
         RATIO.NEW = 1
      ELSE
         RATIO.NEW = RMSA / RMSB
      END IF
      RETURN
CONTROL:
      DIRECT% = DIRECT% * SGN(RATIO.NEW - RATIO.OLD)
      DELTA% = ((4095 - VOLT%) ^ 1.5) * C
      IF DELTA% < 5 THEN DELTA% = 5
      OLDVOLT% = VOLT%
      IF DIRECT% = -1 THEN
         VOLT% = VOLT% - DELTA%
      ELSE
         VOLT% = VOLT% + DELTA%
      END IF
      IF VOLT% < 0 THEN VOLT% = 0
      IF VOLT% > 4090 THEN VOLT% = 4090
      RATIO.OLD = RATIO.NEW
      RETURN
PRTOUT:
      LOCATE 11 + ITER%, 11: PRINT RMSA
      LOCATE 11 + ITER%, 24: PRINT RMSB
      LOCATE 11 + ITER%, 38: PRINT RATIO.NEW
      LOCATE 6, 15: PRINT "                                        "
      RETURN
DONE:
      LOCATE 3, 5: PRINT "                                          "
      LOCATE 6, 15: PRINT "Data acquisition completed !!"
      SOUND 1000, 3
      LOCATE 23, 3
      INPUT "Press <c> to continue or <q> to quit ...  ", KEY$
      IF KEY$ = "c" OR KEY$ = "C" THEN
         CLS
         COUNTER% = COUNTER% + 1
         'C = C / 2!
         GOTO 10
      END IF
      IF KEY$ = "q" OR KEY$ = "Q" THEN RETURN
```

Rapid Design Systems Features Development

Barry Caslin
Graduate Student
Department of Computer Science

Wright State University
Dayton, Ohio 45435

Final Report for:
Graduate Student Research
Materials Directorate/ Wright Laboratory

Sponsored by:
Air Force Office of Scientific Research
Wright-Patterson AFB, OH

and

Wright State University

Rapid Design Systems Features Development

Barry Caslin

Abstract

This paper describes the Feature-Based Design Environment of the Rapid Design System. As well as desired and realized updated under development.

The Rapid Design System

The Rapid Design System (RDS) is a project of the Materials Directorate, a unit of the Air Force's Wright Laboratory. The goal of the project is to reduce design and production time and improve quality, particularly for small lot size jobs. The technical approach is to couple feature-based design with a memory that can retrieve past designs based on similarities to the current design, providing a "corporate history" function that enables the designer to profit from the experience of the past.

There are four major "environments" within the RDS. They are:

- The Feature-Based Design Environment (FBDE) is used to create a specification of the part's geometry. This is done by adding, modifying, or deleting features from the part model. The features handled by the FBDE are form features, which give the nominal geometry of the part, and Geometric Dimensioning and Tolerancing (GD&T) features, which specify the allowable deviation of a manufactured part from the ideal shape given by the form features. The FBDE has the ability to do some constraint checking and constraint satisfaction. See Figure 1 for a list of currently supported features.
- The Fabrication Planning Module takes the part specification (the collection of form and GD&T features), and produces a process plan for machining. The process plan includes tool selections, operation sequencing, tool paths, and feeds and speeds.
- The Inspection Planning and Evaluation Module (IPEM) takes the part specification and produces a process plan for inspection. Currently, only inspection by a 3-axis coordinate measurement machine is supported.
- The Episodal Associative Memory provides for retrieval of past designs based on similarities with a given design. Search is based on geometric similarity; however, other types of search (e.g., based on functional similarity) will be supported in the future.

The Rapid Design System (RDS) is a high-level design system that incorporates expert knowledge about producibility and inspectibility. A feature-based approach is used to

describe part geometry, manufacturing information and inspection information. In traditional CAD systems, design information is represented in terms of geometric and topological primitives (points, lines, surfaces, vertices, edges, faces, etc.) and text. Feature-based design is an attempt to establish a higher level of representation, i.e., primitives (features) which have meaning and are interpretable by both the design system and the designer. It is also the intent of the designers of the RDS system to make this feature based system very intuitive and simple for the designer to use, which today means using a Graphical User Interface (GUI). It was my task to update and modify the tool set available so it would meet the needs of the designers and future consumers.

Feature Attributes

The shape of an individual feature can be controlled using attributes of the feature. For features whose basic geometries are simple shapes such as rectangular block or cylinder, a small set of attributes can completely specify the shape.

Evaluating the Part Model

In order to determine the shape of the part, the part model must be *evaluated.* This is done within the solid model using boolean operations. Starting with the starting feature, adding the material of the positive features, and removing the material of the negative features. The algorithm is as follows:

```
algorithm evaluate(part_model)
result ← transformed_geometry(starting_feature of part_model);
remaining_features ← sequence{{all features of part_model except
  the starting_feature});
for each feature F in remaining_features do
    if F is a positive feature then
        result ← result ∪ transformed_geometry(F);
    elseif F is a negative feature then
        result ← result - transformed_geometry(F);
    elseif F is a modifier feature then
        result ← result modified by F;
    endif;
endfor;
return result;
end evaluate;
```

In the above algorithm, transformed_geometry(F) represents the basic geometry of F, transformed to the world coordinate system. "∪" represents the set union operation, and "–" represents the set difference operation.

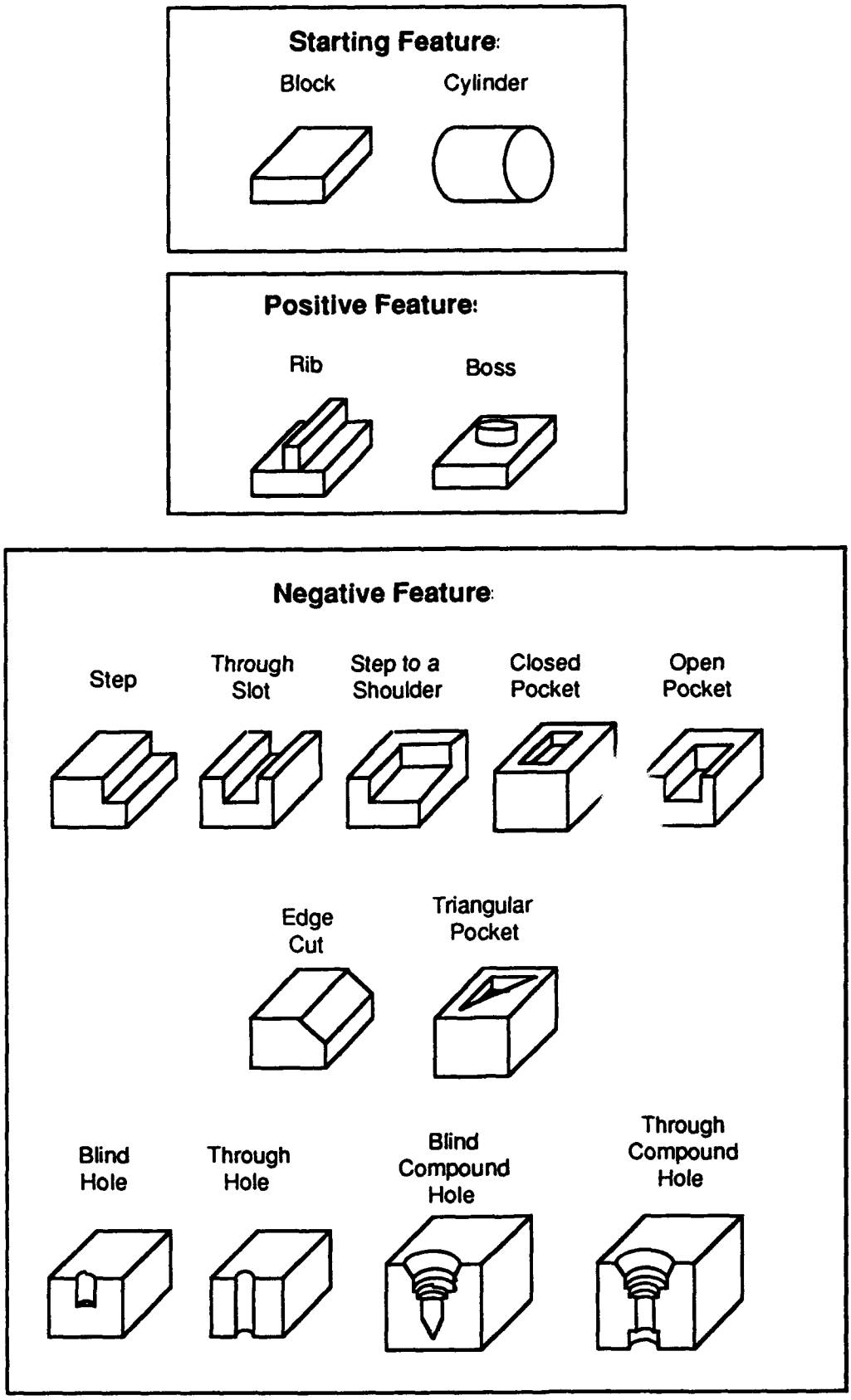

Figure 1: Features currently supported by the FBDE

Positioning of Features

As mentioned earlier, most features have a basic geometry consisting of either a rectangular block or a cylinder. It might seem that there is no need to have more than one feature with any given basic geometry. To see why this is not the case, consider the case of a pocket and a step to shoulder, which both have a block as their basic geometry. The difference is that the pocket normally has four walls, while the step to shoulder has two walls, and thus can be thought of as modifying a *corner* of the geometry. Referring to Figure 2, we can give the location of the pocket by specifying surface A, and distances d_1 and d_2. On the other hand, we can the position of the step to shoulder by specifying surfaces B, C and D. This leads to the notion of "attachments."

A feature F is said to be *attached* to a surface S if one of the surfaces of the (basic geometry of) F is constrained to lie on S. In the case of negative features such as holes, pockets, and slots, S represents the surface of the material into which the feature is cut. In the case of positive features such as ribs and bosses, it represents the surface to which the feature is "glued." Note that this cutting or gluing operation is a logical operation which helps to conceptualize the shape of the part; there is not requirement that the part actually be manufactured this way.

A surface to which a feature is attached is called an "attachment surface." Each positive or negative feature has at least one attachment surface. Some features have more than one attachment surface: a through hole has two (the top and bottom), and as we have already seen, a step to shoulder has three.

In the present implementation, an attachment surface is assumed to be a face of another feature instance. Therefore, to select the attachment surface, we can select an "attachment

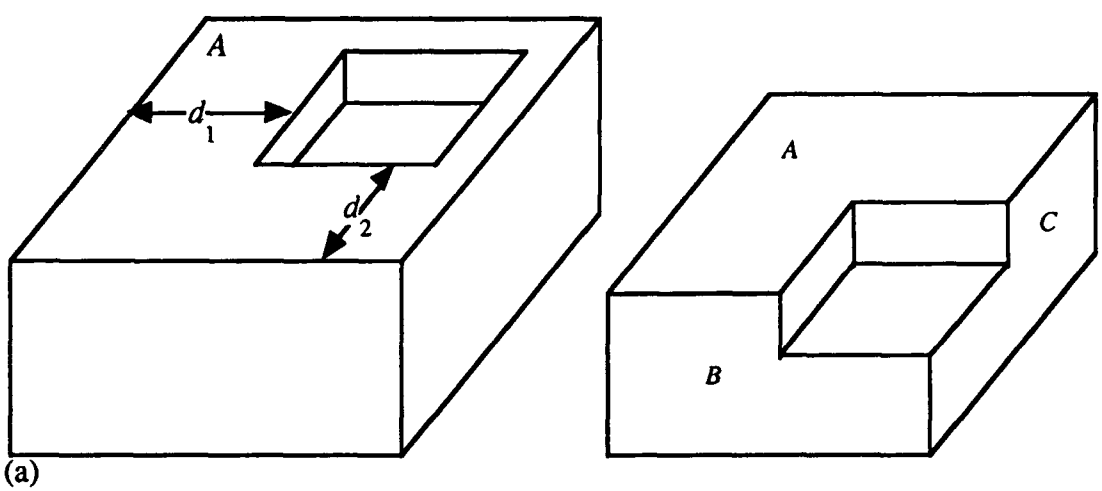

Figure 2: Positioning of (a) a slot (b) a step to shoulder

object" (a feature instance) and a face of (the geometry of) that object, called the "attachment face."

Depending on the feature, there will be 0, 1 or 2 translational degrees of freedom after the attachment surfaces have been specified. This translation will be on the attachment surface. Figure 2 illustrates cases with 0 and 2 degrees of freedom. The translation amounts are called *offsets*. Offsets may be specified with respect to any edge which lies on the attachment face.

The use of attachment and offset faces is illustrated in Figure 3.

Generic (non-prismatic) feature description

The generic (non-prismatic) feature can be an extrusion of an arbitrary two-dimensional profile, although in principle any three-dimensional solid could be used. The designer designs by adding and deleting features, and by modifying the attributes of already existing features. Feature can be categorized into three based on how they modify the geometry. *Positive features* , represent an addition of material; *negative features* , represent the removal of material, and *modifier features* , modify existing geometry, and can either cause addition or removal of material. Each feature has a number of *attributes* which must be given values in order fully specify the feature. Attributes are used to specify the internal dimensions of a feature, the relationship of a feature to other features, and other miscellaneous items. Each positive or negative feature has a *basic geometry*. For example, the basic geometry of a rectangular pocket is a block; the basic geometry of a hole is a cylinder. The basic geometry of a part is specified in a local coordinate system, and is generally centered around the origin. The attributes of the feature which are used to specify its relation to other features can then be used to determine the position of the feature's geometry in the world coordinate system.

Description of Research

The RDS was a system which runs on a Sun work station and runs under UNIX. The RDS exists within a Emacs environment and is coded in Common LISP under a package called Wisdom which has many features which allows the programmer to interact with the part geometry, as well as allowing the user to manipulate the GUI in a fairly efficient manner. Also at times it was necessary to program in C.

Figure 3: Starting block with a through slot attached to it, then a blind hole attached to the through slot.

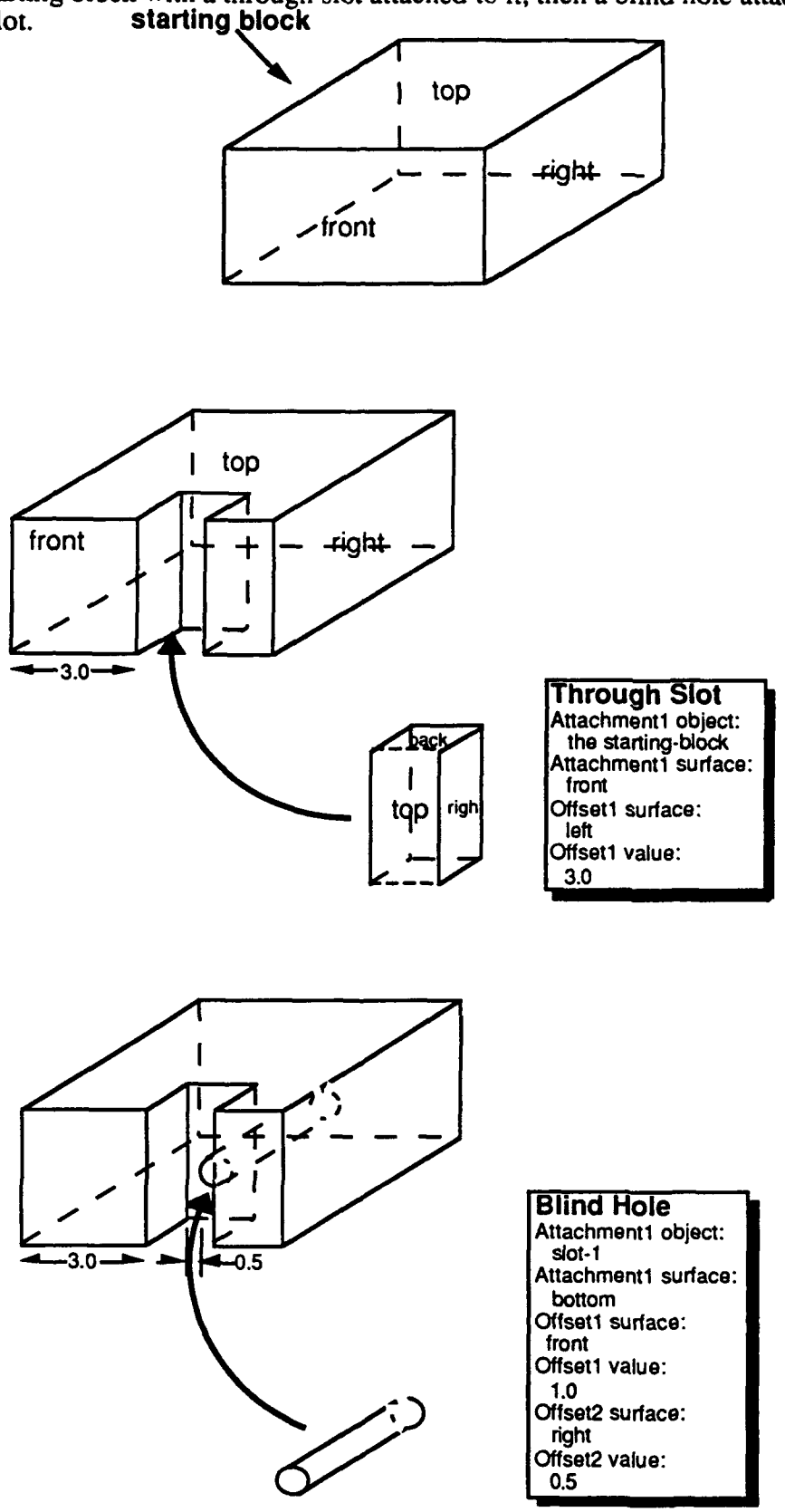

In completing this project I had to learn Emacs, Wisdom, Common LISP, UNIX system support and some X-windows programming. To accomplish the intended goals of this project the rules for a generic feature where laid down and further developed and a generic starting block was added to the partmodel.

MECHANISMS OF OHMIC CONTACT FORMATION IN Al-Ge-Ni/n-GaAs CONTACTS

Verlyn Fischer
Graduate Student
Department of Materials Science and Engineering

University of Florida
258 Rhines Hall
Gainesville, FL 32601

Final Report for:
Graduate Student Reasearch Program
Wright Laboratory

Sponsored by:
Air Force Office of Scientific Research
Bolling Air Force Base, Washington, D.C.

September 1993

MECHANISMS OF OHMIC CONTACT FORMATION IN Al-Ge-Ni/n-GaAs CONTACTS

Verlyn Fischer
Graduate Student

Abstract

Gallium arsenide regrowth has been shown to occur in Ni-Ge/n-GaAs contacts by thin film X-ray diffraction measurements before and after heat treatments at 500C. Specific contact resistance, as determined by the transmission line method, was related to the extent of GaAs regrowth. A fully regrown layer produced the smallest ohmic contact resistance and occured when the Ni:Ge ratio was 1:1.

MECHANISMS OF OHMIC CONTACT FORMATION IN Al-Ge-Ni/n-GaAs CONTACTS

Verlyn Fischer

Introduction

Gallium arsenide (GaAs) is a semiconductor whose unique properties make it an indispensable material. Since it has a direct band gap it can be used in making solid state diodes and lasers which find uses in medicine, industry, and military areas. Electro-optical computer systems have been built in which calculation is handled entirely by light beams. The data transition back and forth from light to electricity is managed using GaAs. Fiber optic communication systems utilize GaAs technology and allow calls to be transfered optically which is far quicker than standard electrical technology. A direct band gap semiconductor makes electrical transitions quicker than an indirect band gap semiconductor, such as silicon, so quicker devices can be manufactered. Transistors and amplifiers can now opertate in the gigahertz range using GaAs technology and are used in phase array radar systems, signal processors, space based electronic detection systems, tracking devices and digital transmitter-receivers (Sclater, 1988). Gallium arsenide devices are more radiation hard than silicon since the Fermi level is pinned at the crystal surface. As a result, devices constructed with GaAs are able to operate adequately in radioactive enviornments such as X-ray instrumentation, nuclear power plant facilities, and outer space.

Ohmic contacts are metal-semiconductor junctions which allow electricity to flow from the metal to the semiconductor with very little power loss and very little heating in the contact. This is

important since the properties of semiconductors are drastically altered by sever temperature. For instance, gallium arsenide laser efficiency degrades with increasing temperature. In addition, ohmic contacts exhibit linear current-voltage behavior. Ohmic contact formation and optimization is an increasingly important subject of study since every semiconducting device has at least one ohmic contact. Although many useful devices have been constructed with GaAs using present ohmic contact technology there is room for improvement which is driven by the need for quicker, more efficient semiconductor devices. There are many characteristics which describe an ohmic contact; they include specific resistivity, corrosion resistance, lateral diffusion, interface homogenaeity, and reliabilty. To date, the Au-Ge-Ni alloyed system is the commercially favored ohmic contact. As technological demands increase, Au-Ge-Ni contacts will not be able to fit the parameter space required and other contact systems will become increasingly important. One such system, the Al-Ge-Ni contact, has been recently developed and studied. Substituting Al for Au in the commercially conventional contact system, Au-Ge-Ni, provides larger thermal conductivity, greater edge definition, and better interface morphology.

Developing better ohmic contacts requires knowledge about the mechanisms that produce ohmic contacts. A simple "Edisonial" approach will prove impractical due to the large number of variables involved. But determining what mechanisms are responsible for GaAs ohmic contact formation will allow contact systems to be custom designed. To date there are numerous competing theories about the mechanisms of conduction and many results which conflict with these theories in the literature. More likely than not, conduction in GaAs ohmic contacts is a combination of related mechanisms. Thorough systematic studies will eventually unravel the mystery. In this work, the affect of Ge during ohmic contact formation in the Al-Ge-Ni/n-GaAs contact system will be studied. In the following section a thumbnail sketch of the theories of ohmic contact formtion will be presented and problems with the theories be discussed.

Ohmic Contact Formation Mechanisms

Electrical conduction between metals and semiconductors is impeded by a potential energy barrier at the metal-semiconductor interface. In ohmic contacts charge carriers pass by the potential energy barrier either by going over it or by tunneling through it. A potential energy diagram of the metal-semiconductor interface is shown in figure 1. For most semiconductor-metal junctions the height of the potential energy barrier, Φ_{Bn}, is a function of the electron affinity of the semiconductor, X, and the metal's work function, Φ_m, given by the following equality,

$$\Phi_{Bn} = \Phi_m - X$$

It would seem that creating a highly conductive contact would simply involve using a low work function metal since this would create a small potential energy barrier. However, Fermi energy level pinning takes place which serves to lock the Fermi energy level at midband gap at the semiconductor surface regardless of doping type and fixes the barrier height at greater than 0.8eV regardless of the metal used which is too large to conduct adequately. It has been generally accepted that the GaAs surface is pinned under most circumstances although there is some controversy about whether metal-GaAs reactions can unpin the Fermi energy level and form low work function alloys (Woodall, 1981).

Since pinning eliminates conduction over the barrier, conduction though the barrier by quantum mechanical tunneling must be taking place. The tunneling probabilty is dependant on the potential energy barrier height and width. A smaller and thinner barrier will increase the tunneling probability. Through quantum mechanical calculations it has been shown that increasing the doping concentration in the semiconductor narrows the barrier width and increases the tunnelling probability. Again it seems easy enough to produce an ohmic contact: just use highly doped semiconductors. However, device requirements sometimes forbid the use of highly doped semiconductor substrates. Fortunately there are a number of available avenues. Epitaxial growth

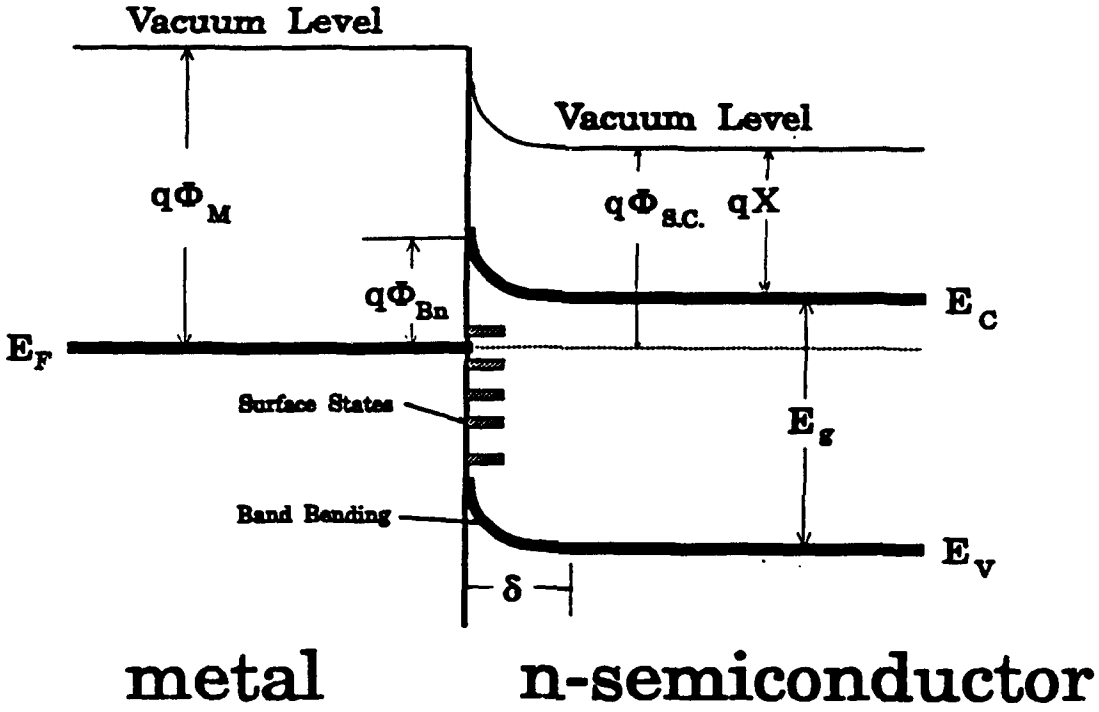

δ = depletion depth
Φ_M = metal work function
Φ_{Bn} = barrier height
E_F = Fermi energy level
E_g = band-gap energy
E_C = conduction band minimum energy
E_V = valance band maximum energy
X = semiconductor electron affinity
$\Phi_{s.c.}$ = semiconductor work function
q = carrier charge

Figure 1. Energy level diagram of a metal-semiconductor junction illustrating the potential energy barrier at the interface.

of a highly doped surface region to which an ohmic contact could be created is possible but very impractical since epitaxial growth of semiconductors is a slow, time consuming process. It is also possible to deposit metals on the semiconductor which, when heated, will react with the semiconductor to either produce a highly doped surface region or a defect structure which will increase tunnelling. The latter is the most typically used technique used today to form ohmic contacts to GaAs.

A metal-semiconductor reaction which produces a highly doped interface region can be imagined to occur in one of three ways. Although each method has been supported in the literature there are inconsistencies with each explanation. The first method involves the diffusion of dopant, deposited with the metals, from the metal into the GaAs surface region. Since Ge is an n- and p-type dopant, it makes intuitive sence that its diffusion from the Au-Ge-Ni metallization to the GaAs surface would produce a highly doped surface region. However, the diffusivity of Ge in GaAs at contact treatment temperatures (500C) is too low to allow sufficient diffusion to reduce the potential energy barrier width. Also, it has not been entirely explained how the Ge chooses its lattice site in GaAs although it has been speculated that the As concentration at the interface and the surface Fermi energy level may play a considerable role. If Ge sits on a Ga site it acts as a donor and if it sits on an As site it acts as an acceptor. In conflict with the proposed theory of dopant diffusion from the metal to the semiconductor is the study by Roedel *et al* (1993). It was shown that Al-Sn-Ni metallizations produced ohmic contacts to n- and p-type GaAs even though Sn is not an acceptor in GaAs and should not produce a heavily doped p-region.

The second method involves the decomposition of GaAs during metal-semiconductor heat treatment, the regrowth of GaAs, and incorporation of the dopant from the metal solution into the GaAs lattice. Once again, this explanation doesn't explain the behavior of Al-Sn-Ni contacts. In a Raman scattering study on Au-Ge ohmic contacts by Kirillov and Chung, it was shown that Ge wasn't responsible for forming a heavily doped region (Kirillov, 1987). Although it has been shown that regrowth of GaAs occurs during heat treatment (Sands, 1988), (Li, 1991), (Holloway,

1991), it has also been shown that ohmic contacts form even when there is no dopant present in the metallization such as Au and Ag contacts to n-GaAs (Fischer, 1993). These observations led to the third method of forming a heavily doped region.

Segregation of dopant from the GaAs during GaAs decomposition is the third means by which a heavily doped region could form. It is possible that during the decomposition of GaAs in the presence of a reactive metal, such as Ni, Pd, Au, and Ag, the dopant in the GaAs remains at the interface. This may occur due to the low solubility of the dopant in the newly forming ternary or higher order metallization. In any case, it has been shown that Si did accumulate in the surface region of decomposed n-GaAs (Holloway, 1991). The formation of the heavily doped region could either occur due to diffusion of the dopant back into the GaAs (uphill diffusion) or regrowth of the GaAs and incorporation of the dopant which is in excess at the interface. Diffusion is unlikely because dopant (Si and Zn) diffusivities in GaAs are very small (Lide, 1990). In addition to diffusion, regrowth after segregation may occur but evidence indicates that it doesn't produce a heavily doped region (Kirillov, 1987). For instance, Holloway showed that Si wasn't in higher concentrations at regrown areas of Au/n-GaAs contacts

Although it has been shown that highly doped surface regions will indeed decrease the barrier width and increase the tunnelling probability, it is unclear whether the formation of a heavily doped surface region takes places during metal-semiconductor reactions. Instead there may be another mechanism which increases the tunnelling probability. Defects, such as vacancies, antisites, and dislocations, are sources of carrier traps and interface states. It is conceivable that these traps and states may be in the potential barrier region allowing the charge carrier to hop its way across the barrier. This is supported in the literature. For instance Ni/n-GaAs contacts are typically rectifying even after heat treatment but become ohmic with ion bombardment (Sebestyn, 1982). Furthermore, it is common practice to sand blast Si and Ge surfaces prior to metal deposition which creats a near amourphous layer full of detects to get ohmic contacts. Tunnel diodes were shown to develope "excess" current which was related to defects (Parker,

1969),(Chynowfth, 1960),(Kirillov, 1987) and Mossbauer spectroscopy has been used to identify a defect complex, $Te_{As}V_{Ga}^{-}$, which increases conduction in Au/Te/n-GaAs contacts.

Knowing which mechnism is responsible for the conduction of charge in GaAs ohmic contacts will eventually allow better ohmic contacts be manufactured increasing device performance and reliability. Since there is extensive conflict regarding how various contact systems react with GaAs to produce a highly doped region for conduction by tunnelling, a correlation between the semiconductor surface defect density, the phases present in the metallization, and the specific contact resistance will attempt to be found in order to offer an explanation for the formation of ohmic contacts to GaAs after metal-semiconductor reaction.

Experiment

Samples were produced using As-capped 1μm thick MBE grown GaAs (100) doped with Si to 3.2×10^{17} cm^{-3} which was grown on semi-insulating GaAs. Wafers were placed into an adsorbtion roughed, ion pumped ultra-high vacuum electron beam evaporation system and pumped down to 2×10^{-8} Torr. The system was then baked to achieve pressures less than 6×10^{-10} Torr. Samples were heated *in situ* to a temperature of 530C in order to remove the As cap. A pressure burst indicated that the As had indeed been flashed. After the samples cooled to below 50C, a shadow mask was moved into place in order to form transmission line contact strips but only masked 1/4 of the sample. An eight layer contact structure starting with Ni and alternating between Ni and Ge, was deposited on two samples while only Ni was deposited on one. Before a layer was deposited on the wafer the source material was heated, while the wafer was facing away from the source, until 100A of material had been evaporated to ensure that the source material was clean before deposition took place. Evaporation rates were between 1 and 2A/s as measured by an Inficon quartz crystal ocsillator. Three samples were produced each having a total contact thickness of 1000A. The contact layer thicknesses for each of the three samples is listed in table 1.

Table 1. Metallization layer thicknesses for eight layer contact structure.

Sample	Stoichiometry	Ni Layer Thickness (A)	Ge Layer Thickness (A)
A	Ni	1000*	
B	NiGe	80	170
C	$Ni_{12}Ge_{19}$	110	140

* Sample A has only one layer.

As-deposited samples were then transfered to a Rigaku Geigerflex X-ray Thin Film Diffractometer (TFXRD) operating with an incident angle of 4 degrees. Measurements were taken from 25 to 110 degrees. After TFXRD measurements were taken, current-voltage (I-V) measurements were taken on a Keithly 196 Voltmeter and 228 Power Supply and specific contact resistance was calculated by the transmission line method (Williams, 1984). The samples were then heated for 30s intervals in forming gas (3.94%H_2, 96.06%N_2) until I-V measurements indicated that the contact resistance had just passed a minimum. Only two heat treatments (one minute total) were neccessary for the contact structures containing Ge while the Ni/GaAs contact resistance didn't change after several 30s heat treatments and one 15min heat treatment After heat treatment, TFXRD data were recorded.

Results

Current-voltage data was used to calculate the effective barrier height (Sze, 1981) on rectifying contacts while the specific contact resistance was calculated for ohmic contacts (Williams, 1984). The Ni/GaAs contact (sample A) remained rectifying with little change in the effective barrier height. The NiGe/GaAs contact (sample B) was ohmic as deposited and a decrease in specific contact resistance was measured after heat treatment. The $Ni_{12}Ge_{19}$/GaAs contact (sample C) was rectifying as deposited but turned ohmic with heat treatment. See table 2 for the effective barrier heights, F_B, and specific contact resistances, R_c, of the rectifying and ohmic contacts respectively.

Table 2. Current-Voltage Results Before and After Heat Treatment

Sample	Stoichiometry	I-V Characteristic Before Heat Treatment	I-V Characteristic After Heat Treatment
A	Ni	F_B=0.356eV	F_B = 0.367eV
B	NiGe	$R_c = 5.5x10^{-5}$ Wcm^2	R_c= $2.4x10^{-6}$ Wcm^2
C	$Ni_{12}Ge_{19}$	F_B= 0.353eV	R_c= $1.6x10^{-5}$ Wcm^2

Specific contact resistivity is an important ohmic contact parameter which is often minimized as much as possible. For this reason it is important to point out a noticable trend. Sample A, which is entirely Ni, remained rectifying while both the Ni-Ge samples (B and C) turned ohmic and sample C (with a Ni:Ge ratio equal to 1:1) had the lowest contact resistance. The mechanism responsible and its importance will be discussed shortly.

X-ray diffraction data before and after heat treatment for samples A, B, and C indicated which phases were initially present and what product phases developed. Spectra for the Ni/n-GaAs, NiGe/n-GaAs, and $Ge_{12}Ni_{19}$/n-GaAs contacts are presented in figures 2, 3, and 4 respectively. Phases were identified using powder diffraction files as compiled by the International Centre for Diffraction Data. Peaks associated with given phases are labeled as such. These spectra will not contain all the peaks associated with a given phase as listed in powder diffraction files since the samples are not in powder form but instead are thin films. In thin films, crystals assume preferred orientations which causes some peaks to be diminished while other are absent. When the phases present before and after heat treatment for each of the samples is tabulated (as in table 3) it becomes clear that there are even subtle differences between closely related samples such as the NiGe/n-GaAs and $Ge_{12}Ni_{19}$/n-GaAs.

Figure 2. XRD spectra of Ni/n-GaAs system before and after heat treatment at 500C for 18min. Heat treatment produces Ni_2GaAs and NiAs product phases.

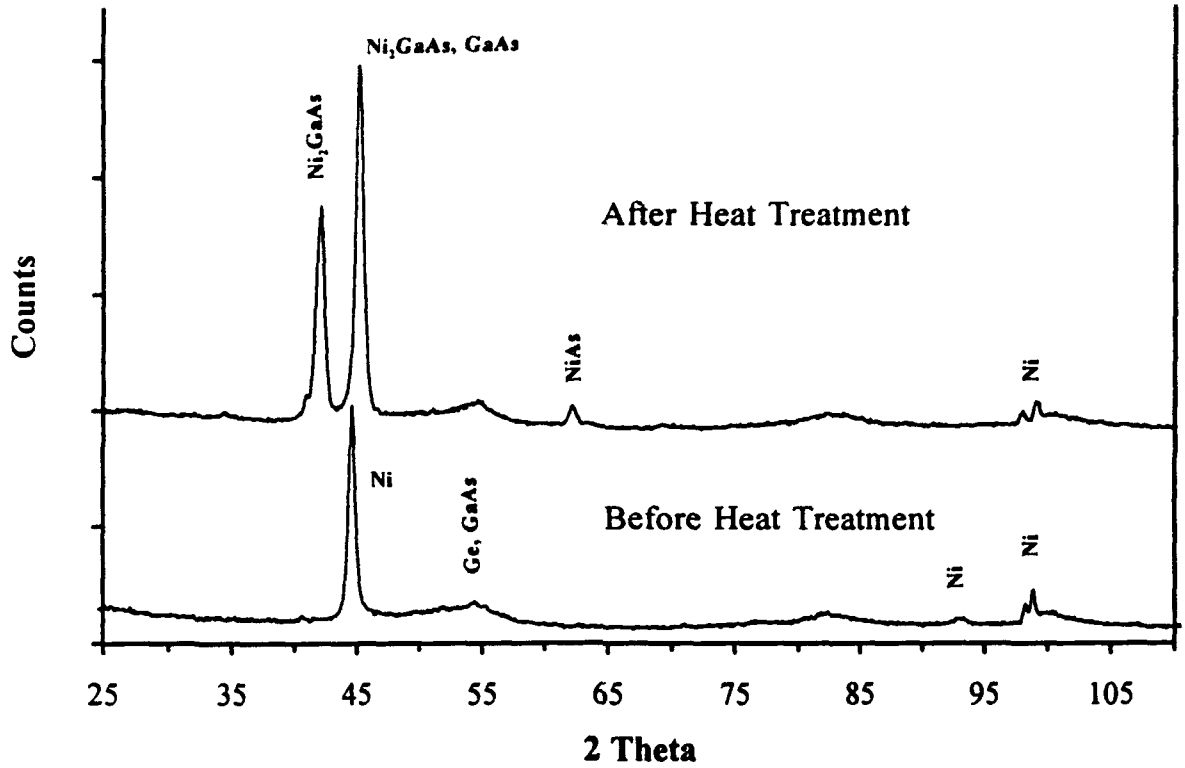

Figure 3. XRD spectra of NiGe/n-GaAs system before and after heat treatment at 500C for 1 min. Heat treatment produces the NiGe product phase.

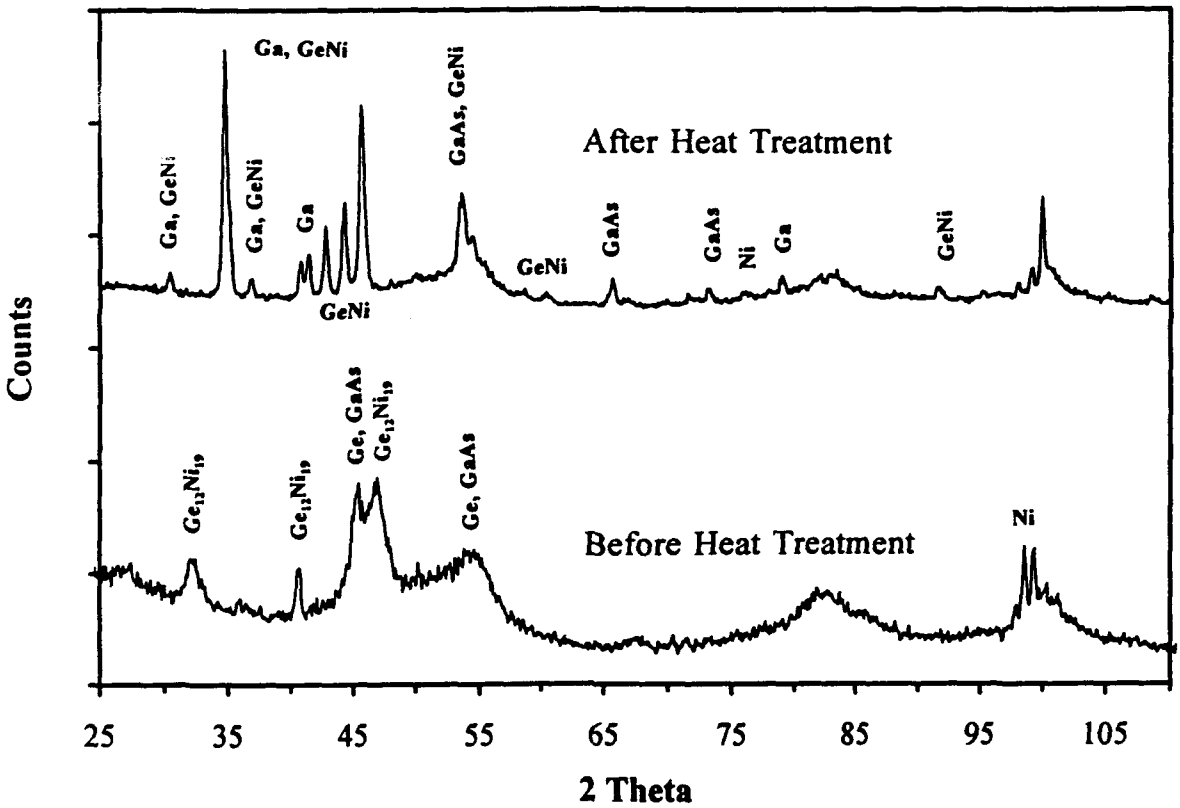

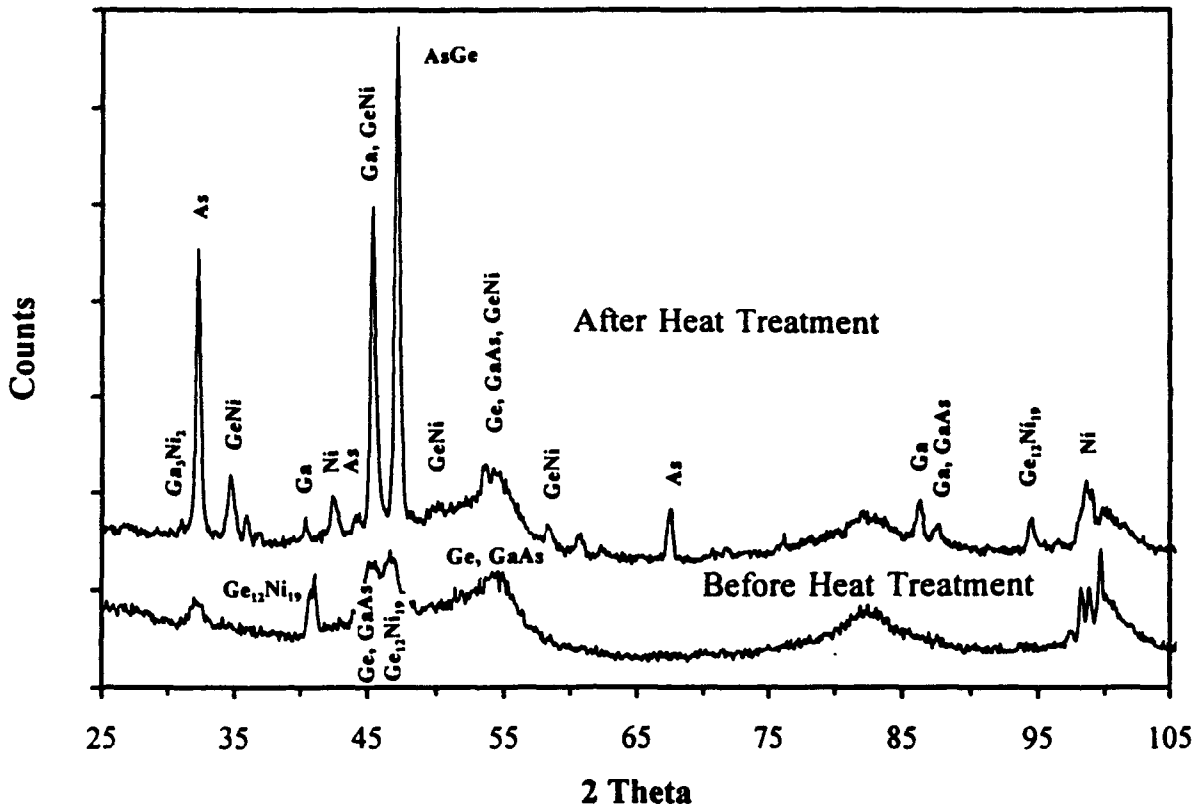

Figure 4. XRD spectra of $Ni_{19}Ge_{12}$/n-GaAs system before and after heat treatment at 500C for 1 min. Heat treatment produces NiGe, AsGe, Ga_3Ni_2, and elemental As and Ga phases.

Table 3. Phases Present Before and After Heat Treatment at 500C.

Sample	Composition	Phases Present Before Heat Treatment	Phases Present After Heat Treatment
A	Ni	Ni GaAs	Ni Ga NiAs Ni_2GaAs GaAs
B	NiGe	Ni Ge $Ge_{12}Ni_{19}$ GaAs	Ni Ge Ga GeNi GaAs
C	$Ge_{12}Ni_{19}$	Ni Ge GaAs $Ge_{12}Ni_{19}$	Ni Ge Ga As GeNi AsGe beta-Ga_3Ni_2 GaAs

Discussion

From the TFXRD data it is possible to develop a reaction path model for Ni-Ge/n-GaAs contacts during heat treatment and provide reasons for the apparently different I-V behavior of the three samples studied. It has been shown that Ni reacts with GaAs to form a binary compound, NiAs, and a ternary compound, Ni_2GaAs. The formation of these compounds do not aid in producing an ohmic contact. In the Ni-Ge/n-GaAs systems a Ni layer is in immediate contact with the GaAs surface and it can be assumed that the same phases form initially as did in the Ni/n-GaAs system. However, since there are no indications that these phases are present in the Ni-Ge/n-GaAs samples after heat treatment then it stands to reason that these phases decomposed to form more energetically favorable phases such as the NiGe phase. Some of the excess Ga and As left over after Ni_2GaAs and NiAs decomposes combines to form regrown GaAs. This has already been shown to occur in a number of metal/GaAs systems as mentioned earlier. The reaction path model

is illustrated in figure 5. When Ni is in immediate contact with GaAs and is heat treated it reacts with the GaAs to form two compounds and some excess Ga. This has been observed in sample A. By combining this model with the XRD data for the NiGe/n-GaAs system, a reaction path is proposed in which the NiAs and Ni_2GaAs compounds form initially and decompose in the presence of Ge to form NiGe and regrow the decomposed GaAs. As shown in the figure, even at room temperature, reactions between the Ni and Ge are taking place to form $Ni_{12}Ge_{19}$. Sample C, which has a Ni:Ge ratio of 19:12, has a slightly more complicated reaction path due to the excess Ni. Like sample B, the Ni and Ge reacted at room temperature to form the $Ni_{19}Ge_{12}$ compound. Early in the reaction Ni reacts with the GaAs to form NiAs and Ni_2GaAs and these compounds decompose in the presence of Ge to form the stable compound NiGe. The excess Ni which has no Ge with which to form NiGe reacts with the Ga instead to form Ga_3Ni_2 and the As which now has no Ga to react with to form regrown GaAs, reacts with the small amounts of free Ge to form AsGe. The important difference between the two Ni-Ge/GaAs systems is the extent to which the GaAs regrew. When the Ni:Ge ratio is 1:1 then the Ni is fully removed to allow complete regrowth to occur while an excess of Ni produces an incomplete regrowth of GaAs.

Unique to this study is the dependence of the specific contact resistivity on contact stoichiometry. The lower resistivity in the NiGe/n-GaAs contact is attributed to the fact that there are sufficient amounts of Ge to completely react with the Ni in order to fully decompose the Ni_2GaAs and NiAs compounds. This is not true in the $Ge_{12}Ni_{19}$/n-GaAs system where there is an excess of Ni and compounds such as AsGe and β-Ga_3Ni_2 phases exist after heat treatment. From these observations, the mechanism responsible for the formation of an ohmic contact is related to the regrowth of GaAs. Incomplete regrowth produces ohmic contacts while complete regrowth produces better ohmic contacts.

At present one can only speculate as to why a fully regrown GaAs layer produces a lower resistivity ohmic contact. A number of theories have been presented earlier. For example the regrown layer could incorporate Ge or Si, freed after GaAs decomposed, which would act as a

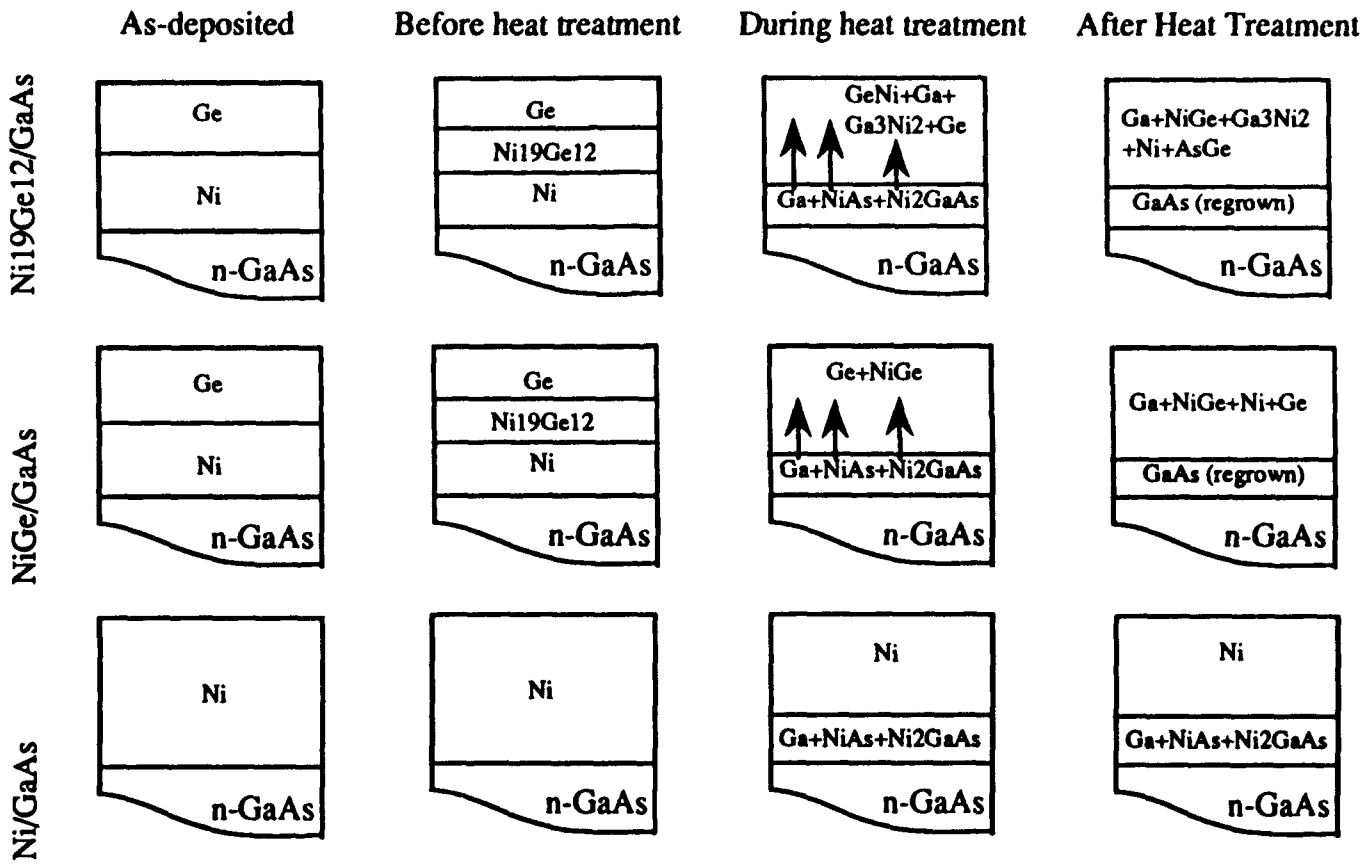

Figure 5. Model of reaction paths taken during 500C heat treatment describing the formation of regrown GaAs.

donor an a Ga site and produce a highly doped region at the metal-semiconductor interface. As mentioned earlier this would permit tunneling which would lead to an ohmic contact. It is also possible that regrown GaAs is sufficiently defected to allow tunneling to occur by defect assisted tunneling mechanisms. In either case the larger the depth of the regrown region the better the tunneling properties. For instance, the depletion depth of highly doped GaAs (10^{19} cm^{-3}) is 60A. A regrown layer with the appropriate thickness which is suffeciently doped will have better transposrt properties than a thin equally well doped layer. A graded Ge-GaAs bandgap is not a possible explanation since the electron affinity of Ge is nearly equal to GaAs and the presence of Ge-GaAs phases were not detected.

Conclusions

Gallium arsenide regrowth occurs in Ni-Ge/n-GaAs ohmic contacts as shown by X-ray diffraction data. It has been shown that the extent of regrowth influences the specific contact resistivity and a 1:1 ratio of Ni:Ge produces lower specific resistivity contacts than a 19:12 ratio. The mechanisms responsible for forming an ohmic contact resulting from GaAs regrowth have been discussed and further study is necessary to determine exactly what mechanism is responsible. Further studies will include secondary ion mass spectroscopy (SIMS) depth profiling which will investigate the doping concentrations in the regrown GaAs region and tunneling electron microscopy (TEM) which will determine the defect density in the newly regrown GaAs layer. Once the mechanism is found for ohmic contact formation then future studies will probably center around finding ways to utilize this mechanism to its maximum benefit.

Another study which will supplement this one is an XRD measurement on an Al-Ge-Ni/n-GaAs contact after heat treatment which will indicate the affect Al has on the contact reaction path. It is speculated that Al is a quick diffusion path for Ge so in effect it acts as a sink for Ge and produces a Ni:Ge ratio greater than 1:1 which degrades contact performance. Based on this

speculation it may prove beneficial to use a two step heat treatment, one after Ni and Ge deposition to regrow the GaAs layer and another after Al deposition in order to bond the Al to the NiGe layer, which will produce low resistivity ohmic contacts with out sacrificing the practical benefits of using Al.

Acknowledgments

This work was able to progress in a timely manner with the help of Michael Capano, Richard Bach, and Jim Hierholzer and they are highly appreciated. The use of current-voltage and heat treatment equipment was instrumental in this work and I would like to thank William Thomas, Steve Smith, and Dave Tomich for their help. Molecular beam epitaxially grown n-GaAs was fashioned by Kurt Eyink and that and his tutorial on the technique is highly appreciated as was Neil McDevitt's help with other analytical techniques.

I would like to extend special thanks to Steve Fenstermaker for having an open ear and for his diligent work during sample preparation and analysis. To Bill Lampert, I am especially grateful. His guidance during this project and his continued support and interest has not only made this very rewarding but also exceptionally fun.

Works Cited

Chynowfth, A.G., Feldmann, W.L., Logan, R.A., Excess Tunnel Current in Silicon Esaki Junctions, *Physical Review*, **121**:684, 1960.

Fischer, V.M., *Ohmic Contact Formation to GaAs and AlGaAs via Sulfur Passivation and Dopant Segregation*, Masters Thesis, University of Florida, 1993.

Holloway, P.H., Yeh, L.L., Powell, D.H., Brown, A., Mechanism of Forming Ohmic Contacts to GaAs, *Appl. Phys. Lett.*, **59**:947, 1991.

Li, B., Holloway, P.H., Regrowth of a GaAs Layer for n-GaAs Ohmic Contacts, *J. Appl. Phys.*, **71**:4385, 1992.

Lide, D.R., *CRC Handbook of Chemistry and Physics*, CRC Press, Boston, 1990.

Parker, G.H., Mead, C.A., Tunneling in CdTe Schottky Barriers, *Physical Review*, **184**:780, 1969

Roedel, R.J., Davito, D., West, W., Adams, R., Ohmic Contacts to p- and n-type GaAs made with Al-Sn-Ni, *J. Electrochem. Soc.*, **40**: 1450, 1993.

Sands, T., Marshall, E.D., Wang, L.C., Solid-phase regrowth of compound semiconductor by reaction-driven decomposition of intermediate phases, *J. Mater. Res.*, **3**:914, 1988.

Sclater, N., *Gallium Arsenide IC Technology*, TAB Books, Inc., Blue Ridge Summit, PA 1988.

Sebestyen, T., Models for Ohmic contacts on graded crystalline or amorphous heterojuctions, *Solid State Electronics*, 25:543, 1982.

Sze, S.M., *Physics of Semiconductor Devices*, 2nd. ed., John Wiley & Sons, New York, 1981.

Williams, R.E., *Gallium Arsenide Processing Techniques*, Artech House Inc., Dedham, MA, 1984.

Woodall, J.M., Freeouf, J.L., GaAs metallization: some problems and trends, *J. Vac. Sci. Technol.*, **19**:794, 1981.

Single Crystal 6H Silicon Carbide studied using

Temperature Dependent Hall and Optical Absorption

by

Jason Jenny
Department of Materials Science and Engineering
Carnegie-Mellon University
Pittsburgh, PA 15213

Final Report for:
Graduate Student Research Program
Wright Laboratory
Wright-Patterson AFB

Sponsored by:
Air Force Office of Scientific Research
Bolling Air Force Base, Washington, D.C.

September 1993

Abstract

The refinement of Silicon Carbide as a semiconductor will allow for the development of high-power, high-temperature solid state devices. Along this vein, the properties of single crystal 6H SiC grown by several companies were evaluated using temperature dependent Hall effect and optical absorption. The optical absorption experiments yielded information related to the bound excitons in SiC, Vanadium inter band absorption, and another unknown element absorption. On the basis of the slope of the temperature dependent Hall data, the activation energies of the impurities could be discerned, which led to the chemical identification of Nitrogen, Boron, Aluminum, and potentially another unknown element as common impurities in this set of samples.

Table of Contents

	Page
Introduction	16-4
Data with Discussion	16-4
N Doped n-type	16-4
XX Doped n-type	16-5
Undoped p-type	16-6
Al Doped p-type	16-6
Results	16-7
References	16-7

Table of Figures

Figure 1-Log Concentration vs 1/T of N doped SiC	16-8
Figure 2-Absoprtion of N bound excitons	16-9
Figure 3-Broad absorption spectrum of N doped samples	16-10
Figure 4-Log Concentration vs. 1/T of XX doped SiC	16-11
Figure 5-Log Concentration vs. 1/T of undoped p-type samples	16-12
Figure 6-Broad absorption spectrum of undoped p-type samples	16-13
Figure 7-Absorption of B bound excitons	16-14
Figure 8-Log Concentration vs. 1/T of Al doped sample	16-15
Figure 9-Broad absorption spectrum of Al doped samples	16-16

Introduction

The utilization of silicon carbide as an electronic material could open many doors in terms of solid state design and device fabrication. This summer project was focused in the analysis of single crystal 6H-silicon carbide. The crystals fabricated by sources 1, 2, and 3 were done so by a physical vapor transport mechanism. The crystals from source 4 were grown using the Lely growth technique. The two analysis tools that were used were optical absorption from 2100nm to 400nm using a Cary spectrometer run at 10K. The other tool was a computer-controlled, high-impedance, temperature dependent Hall probe which scanned temperature from 20K to 350K in fields of up to 10T. This paper will be used to report the data collected as well as discussion of important results. It is grouped by distinguishing the important sample types which were studied over the summer.

Data with Discussion

The classification of the data as mentioned before will be of a grouping nature. For each group of sample types, a corresponding log concentration versus inverse temperature plot will be shown for the hall effect, and an intensity versus wavelength plot for the absorption experiments. The groups of sample types are as follows: N doped n-type, XX[1] doped n-type, undoped p-type, and Al doped p-type.

N doped n-type

These crystals were manufactured by source 1 and the levels of doping were of moderately high levels as is shown in figure 1 of the appendices. From the slope of the line in figure

[1] XX refers to an unknown element, but found in large concentrations

1, the activation energy of the nitrogen donor in SiC is shown to be 85 meV which corresponds to the value noted in the literature.[1]

The absorption spectra for this type of sample evinced the characteristic[2] bound exciton peaks at 410nm and 413nm (figure 2), which further confirmed the presence of nitrogen in the samples. In the wider spectrum (figure 3), the presence of Vanadium[3] is noted at 1309, 1311, 1348, 1352, and 1388nm. Additionally, an unknown peak also is in evidence in the wide spectrum (figure 3). Currently, we are in the process of characterizing this peak, but as of yet nothing is known about this set of peaks, save an excerpt in a German student's thesis which makes a cursory note of its presence[4].

XX doped n-type

Samples which fell into this group were provided by source 4. A fitting routine extracted energy levels of 60 and 100meV from the concentration plot in figure 4. While the samples were n-type, nitrogen which is the most common impurity in SiC was virtually ruled out as the main donor source in these samples. This observation has mild support in the literature as reference[5] has been made to an unknown impurity in 3C SiC whose energy was closer to the conduction band than nitrogen (as is the case here). The impurity noted in that work could very well be the same impurity noticed in these samples.

Due to a time constraint, the optical characteristics of these samples were not measured. This omission is not critical, because nobody has noted the presence of other bound excitons other than that of boron and nitrogen, therefore the chemical identity could not be determined via optical means. These samples require a chemical analysis like SIMS to determine the nature of this unknown donor.

Undoped p-type

This class of samples has proven to be the most interesting, because the typical impurity in SiC is nitrogen, which makes the sample n-type. In these samples provided by source 2, there seems to be a p-type dopant which seems to overshadow the nitrogen. The growers have found a way to remove excess nitrogen, but in the process have revealed a new common impurity.

A computer fit of the concentration curve of figure 5 reveals an excitation energy of 330meV, which corresponds to that of boron. A potential explanation is that boron contaminated the graphite which was used as a furnace element during the crystal growth.

Optical absorption of these samples reveals a photo-ionization band which extends to about 1200nm, as evidenced in figure 6. Additionally, the samples absorbed light of wavelengths 429, 433, 437nm, which may be the energies of excitons bound to the major impurity (see figure 7).

Al-doped p-type

These samples were provided by source 3, and are commercially grown crystals. The Hall effect yielded an excitation energy of 210meV, which corresponds to that of aluminum acceptors[7], but these crystals were purchased as Al doped wafers, so this energy was expected.

The optical experiments which were conducted showed that these were virtually free of defects which can be seen in the wavelength range from 400 to 2100nm (from figure 9).

The only noticeable feature in these samples was the free carrier tail from 600nm to the edge of the spectral range.

Results

The purpose of this research was to analyze the common impurities of SiC which exist in the samples which were examined. The results of this study show while the purposefully doped samples seemed to follow the standard observed trends, the undoped samples tended to have significant quantities of dopants. The significant result of this survey is that further purification of samples is required for the proper device isolation required for the operation of solid state devices.

References

1. The Ionization Energy of Nitrogen Donors in 6H and 15R SiC by S.H. Hagen and C.J. Kapteyns, Philips Res. Repts., vol. 25, pp 1-7, 1970

2. I.S. Gorban' and A.P. Krokhmal', Sov. Phys.-Sol. St., vol. 12, no. 13, pp. 699-700, Sept 1970

3. J. Schneider, H.D. Muller, K. Maier, W. Wilkening, F. Fuchs, A. Dornen, S. Leibenzeder, and R. Stein, Appl. Phys. Lets., vol. 56, pp. 1184, 1990

4. Hong Zhang, PhD. thesis, (Friedrich-Alexander-Universitat Erlangen-Nurnberg, 1990)

5. B. Segall, S.A. Alterovitz, H.J. Haughland, and L.G. Matus, Appl. Phys. Lets., vol. 49, pp. 584, 1986

6. H. J. van DAAL, PhD. thesis, (University of Amsterdam, 1964)

7. Ibid

Fig 1

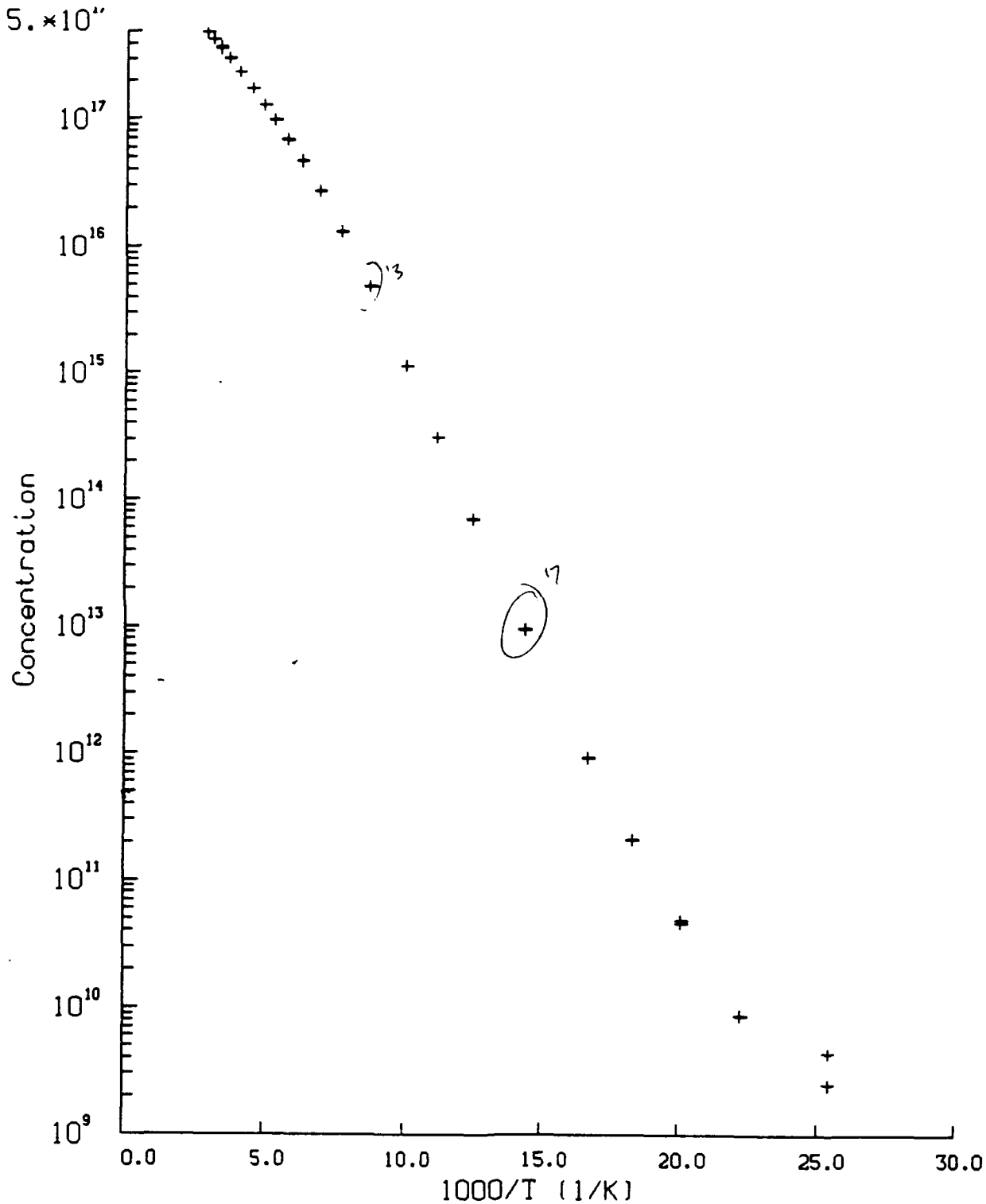
5.×10¹⁸
10¹⁷
10¹⁶
10¹⁵
10¹⁴
10¹³
10¹²
10¹¹
10¹⁰
10⁹
Concentration
0.0
5.0
10.0
15.0
20.0
25.0
30.0
1000/T (1/K)
13
17

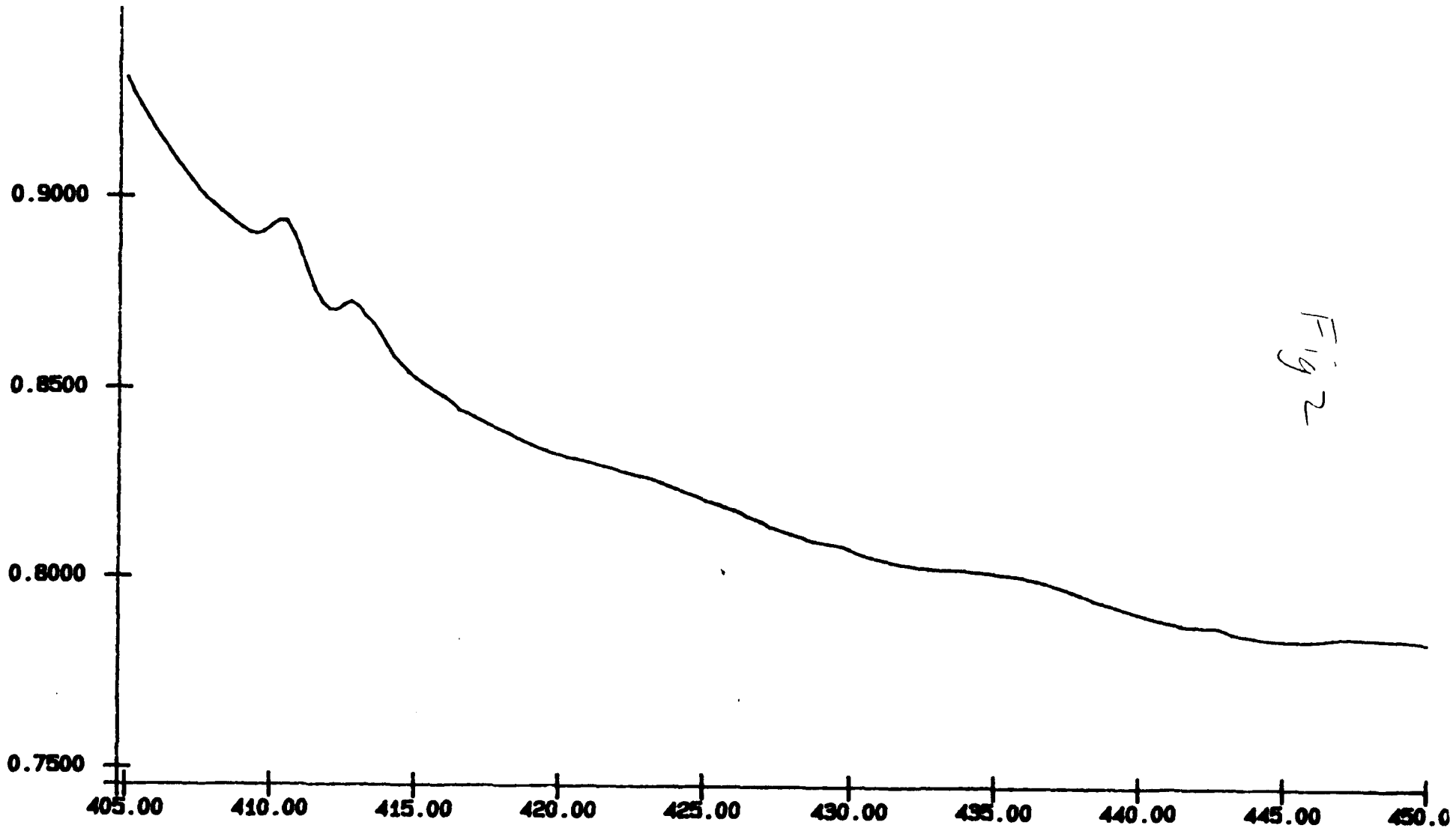
0.9000
0.8500
0.8000
0.7500
405.00
410.00
415.00
420.00
425.00
430.00
435.00
440.00
445.00
450.0

Fig 2

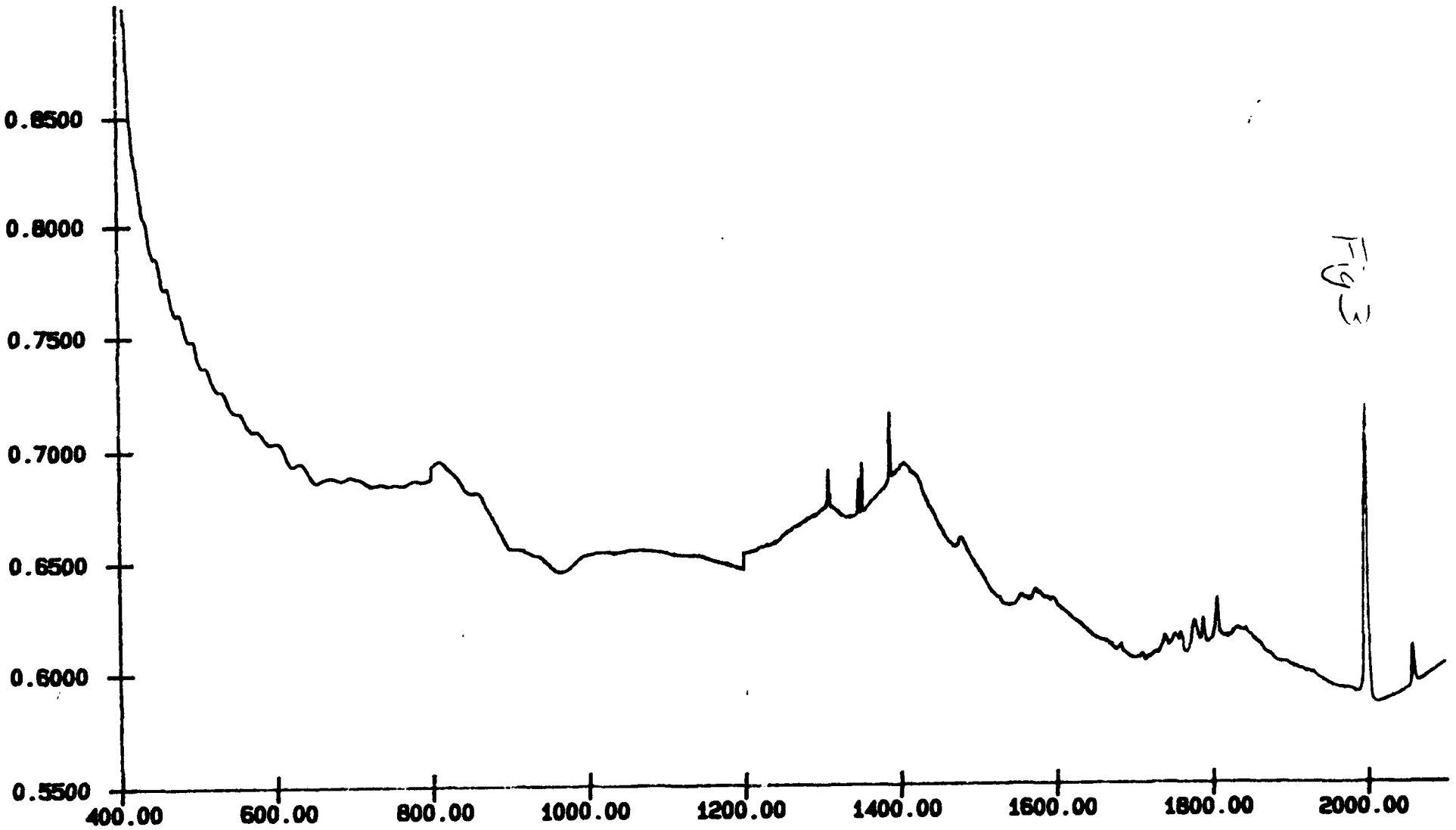
0.8500
0.8000
0.7500
0.7000
0.6500
0.6000
0.5500
400.00
600.00
800.00
1000.00
1200.00
1400.00
1600.00
1800.00
2000.00

Fig 3

Fig 4

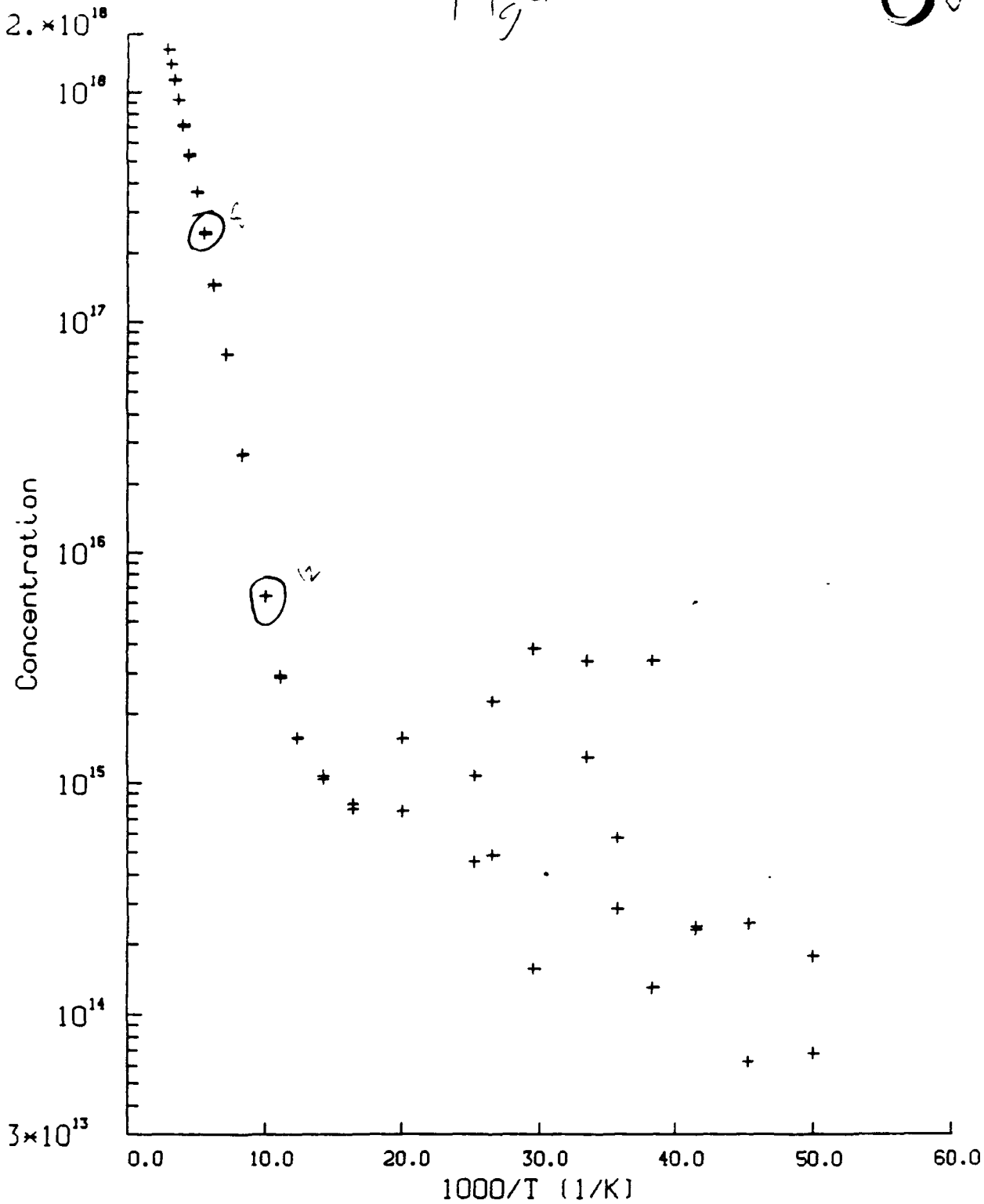
2.×10^18
10^18
10^17
10^16
10^15
10^14
3×10^13
Concentration
0.0
10.0
20.0
30.0
40.0
50.0
60.0
1000/T (1/K)

Fig 5

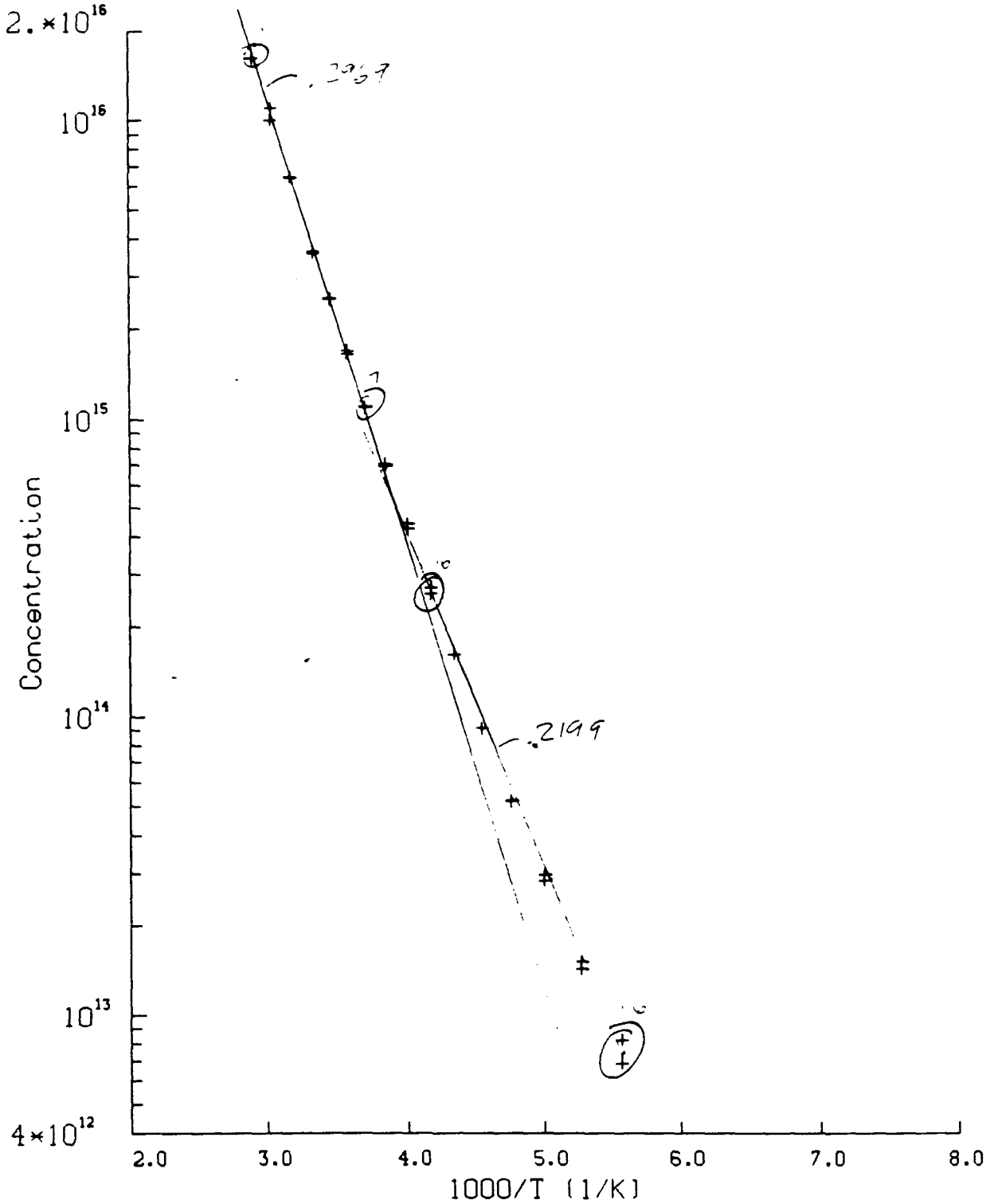
2.*10^16
10^16
10^15
10^14
10^13
4*10^12
Concentration
2.0
3.0
4.0
5.0
6.0
7.0
8.0
1000/T (1/K)
.2199

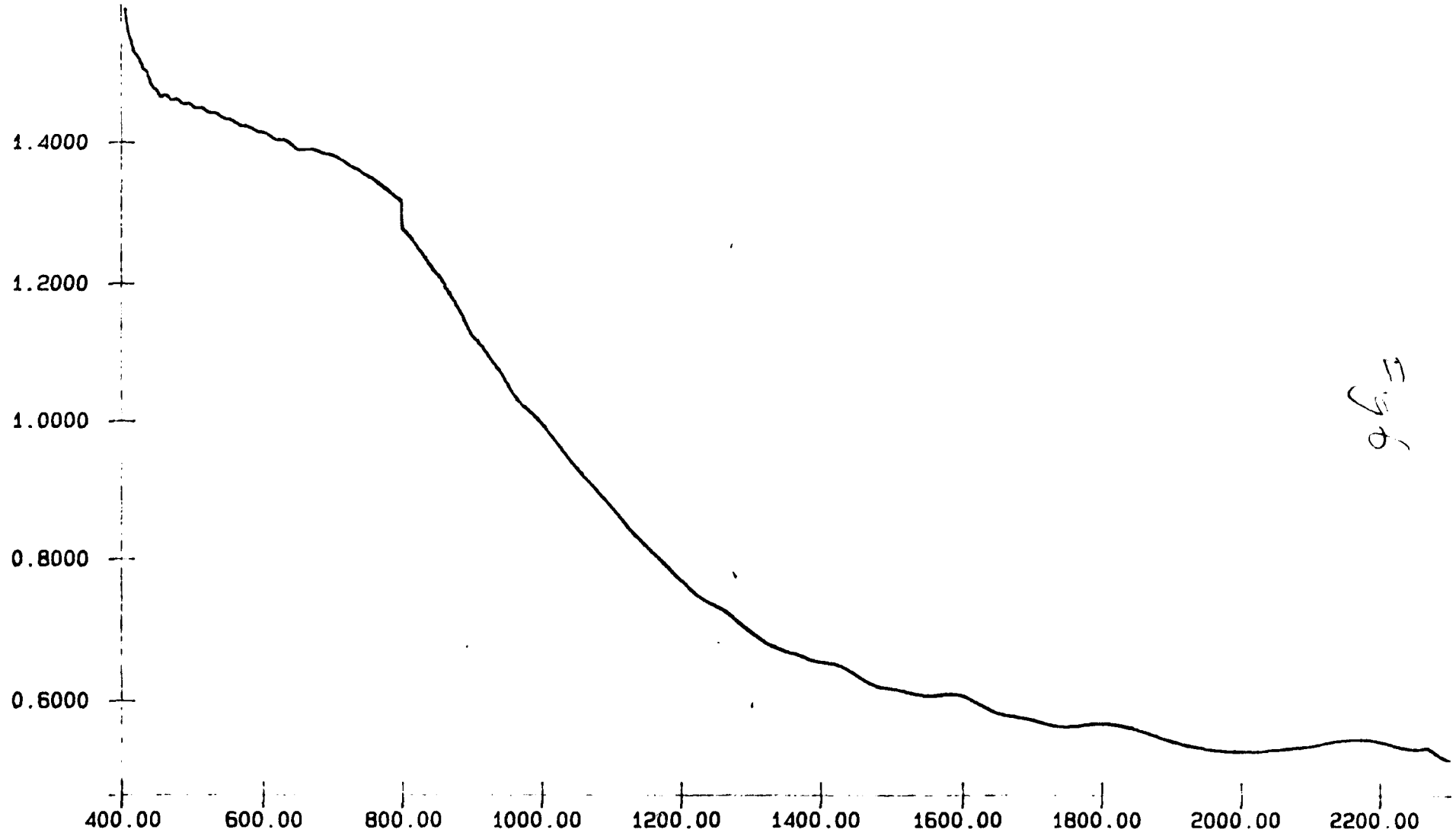
1.4000
1.2000
1.0000
0.8000
0.6000
400.00
600.00
800.00
1000.00
1200.00
1400.00
1600.00
1800.00
2000.00
2200.00

Fig 6

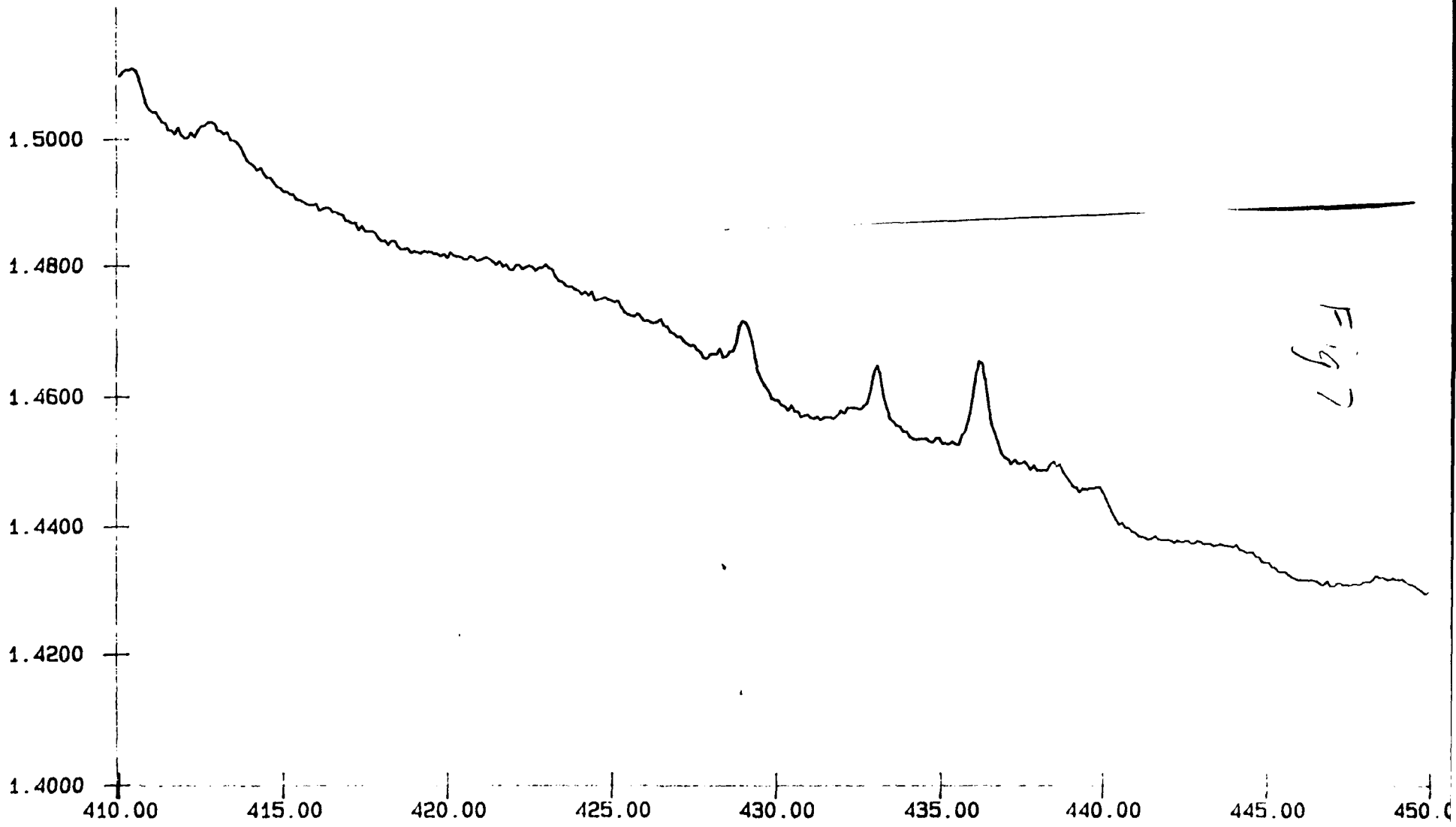
1.5000
1.4800
1.4600
1.4400
1.4200
1.4000
410.00
415.00
420.00
425.00
430.00
435.00
440.00
445.00

Fig 7

Fig 5

fit got .213

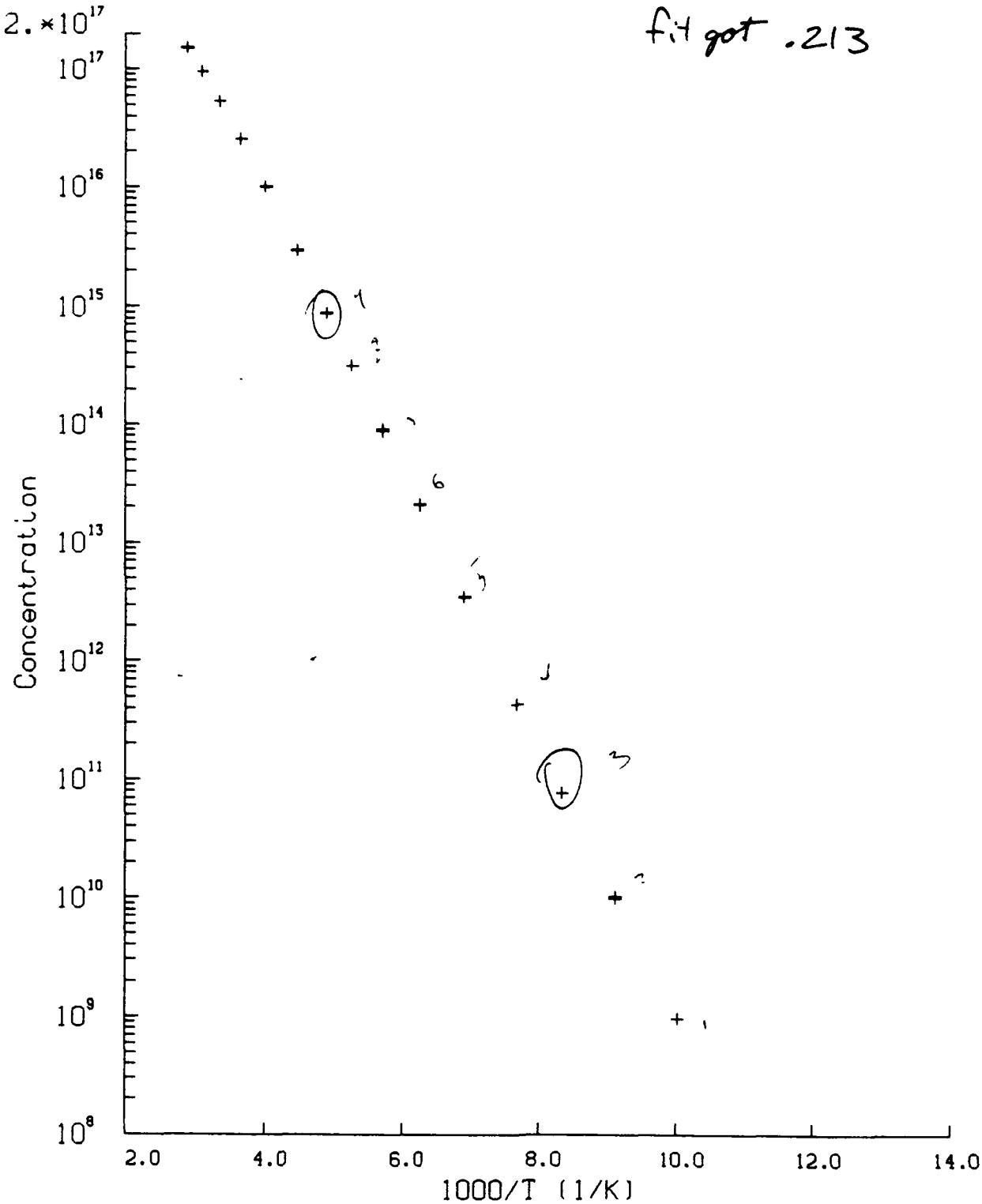

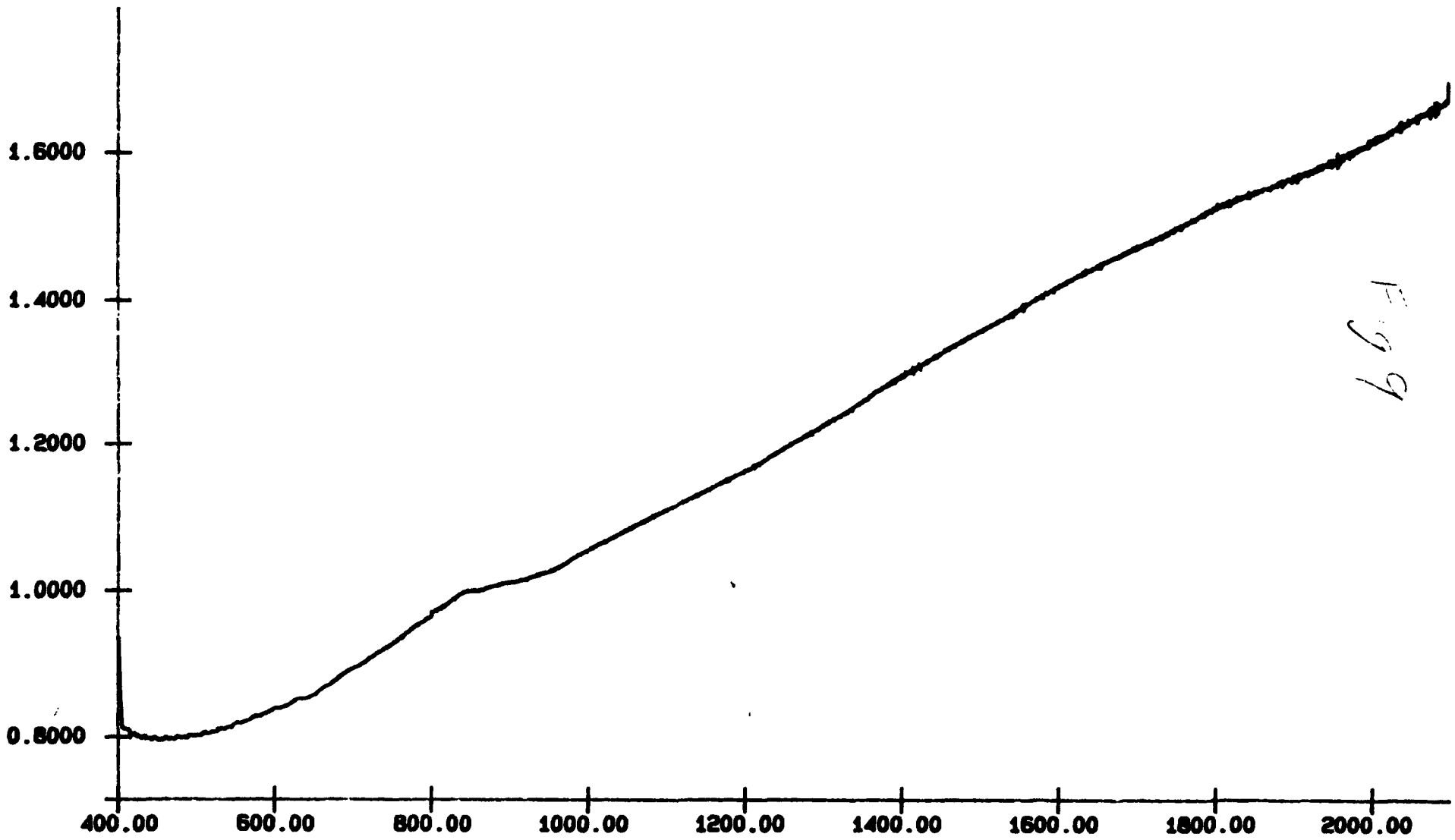
1.6000
1.4000
1.2000
1.0000
0.8000
400.00
600.00
800.00
1000.00
1200.00
1400.00
1600.00
1800.00
2000.00

Fig 9

DESIGN OF AN INTEGRATED WAVEGUIDE OPTICAL PARAMETRIC OSCILLATOR

David H. Naghski

Graduate Research Assistant

Department of Electrical and Computer Engineering

University of Cincinnati

Mail Location 30

Cincinnati, OH 45221-0030

Final Report for:

Graduate Student Research Program

Wright Laboratory Materials Lab, WL/MLPJ

Wright-Patterson Air Force Base

Sponsored by:

Air Force Office of Scientific Research

Bolling Air Force Base, Washington, D.C.

September 1993

DESIGN OF AN INTEGRATED WAVEGUIDE OPTICAL PARAMETRIC OSCILLATOR

David H. Naghski
Graduate Research Assistant
Department of Electrical and Computer Engineering
University of Cincinnati

Abstract

The theoretical design of an integrated waveguide Optical Parametric Oscillator has been performed. The device will be made of Aluminum Gallium Arsenide which allows the widespread growth and processing knowledge of this material to be utilized. The results of a number of computer simulations are presented and it is shown that it should be possible to build such a device without extreme material growth or processing requirements. The effective index approximation is used for planar and channel waveguide analysis and a brief outline of the requirements for parametric oscillation is given. The outline of a photolithographic mask for device processing is presented.

DESIGN OF AN INTEGRATED WAVEGUIDE OPTICAL PARAMETRIC OSCILLATOR

David H. Naghski

Introduction

The concept of an Optical Parametric Oscillator (OPO) is nearly as old as the laser itself. Work began in the early 60's and the first tunable OPO was constructed by Giordmaine and Miller in 1965[1]. Since that time, work has involved broadening the wavelength coverage, increasing the conversion efficiency, and to improving the linewidth characteristics.

There have been a number of tunable coherent sources developed over the years such as dye lasers and more recently the Ti:Sapphire laser. However, the wavelengths of these sources are restricted to the visible and near infra-red (NIR) and the tuning range is relatively narrow. On the other hand OPO's offer the potential of continuously tunable coherent radiation from the ultra-violet (UV) to the far infra-red.

Optical parametric oscillation is a well known nonlinear process and the theory has been described extensively in the literature[2]. We will confine the present discussion to a few of the concepts which drive our theoretical design considerations. In the parametric oscillation process a "pump" wave of frequency ω_p impinges on a nonlinear material and the interaction produces two other frequencies ω_s (the "signal") and ω_i (the "idler"). Conservation of energy requires that $\omega_p = \omega_s + \omega_i$. Conservation of momentum constrains the possible values of ω. This constraint operates on the wavevectors and requires that $k_p = k_s + k_i$. In fact some phase mismatch is allowed, that is

$\Delta k = k_p - k_s - k_i$. However for large values of Δk the conversion efficiency is too low for the oscillation threshold to be exceeded.

Many devices use a birefringent nonlinear crystal as the oscillator material. The birefringence allows exact phase matching between the pump, signal, and idler frequencies. Tuning can be achieved by several techniques. The crystal temperature must be closely controlled due to the temperature dependence of the crystal refractive indices. Therefore, tuning will result from changes of the crystal temperature. Alternatively, rotation of the crystal changes the orientation of the ordinary and extraordinary axes relative to the pump polarization and results in wavelength tuning.

Recently there has been much interest in making OPO's using nonlinear materials in a thin film waveguide configuration. There are a number of reasons that make this configuration desirable. It is possible to achieve optical parametric oscillation in non-birefringent materials through the use of "quasi"-phase matching. Thus the door is opened to the use of many more materials and the wavelength range of OPO's can be extended. Some materials that have been considered are many of the common ternary and quaternary materials that have become popular in the semiconductor laser industry. In fact, a theoretical study of this type of oscillator using AlGaAs was made in 1970. Material processing limitations, present at that time, prevented the realization of such a device. Theoretically the threshold power necessary for oscillation should be drastically reduced by the increased confinement provided by channel optical waveguides. Use of channel waveguide technology allows for the possibility of integration of pump source and oscillator sections of the final device. Furthermore, integration with other electro-optic functional blocks can be envisaged. Finally smaller quantities of high

quality crystalline material are needed when the thin film configuration is used. This can be advantageous when trying to observe oscillation attributes of new materials when large crystals of high quality cannot yet be grown.

These are the basic reasons motivating the building of a thin film OPO. $Al_{1-x}Ga_xAs$ will be used because, as a semiconductor, its processing has become relatively advanced (second only to silicon). It also has been widely used in efforts to achieve optoelectronic integrated circuits. The waveguide material is optically transparent from approximately 900 nm (depending on x, the concentration of aluminum) to over 18 μm. It has a relatively large nonlinear coefficient which means lower oscillation thresholds. Additionally it has been found that the nonlinearity can be enhanced when the material is grown as a superlattice.

In the following section the channel waveguide design will be presented. Next the requirements for quasi-phase matching in a channel waveguide will be developed. Another section will describe the requirements of a photolithographic mask necessary for fabricating the OPO. Finally the evaluation procedures will be outlined.

Channel Waveguide Analysis

Again we will not deal with the theoretical details of optical waveguide analysis as this is covered extensively elsewhere[3]. The commonly used effective index analysis was employed for our calculations. Several FORTRAN programs were developed to perform effective index analyses on a slab guide structure consisting of up to a total of nine slab and/or superlattice layers.

Properties for a slab waveguide were computed first and used to direct the design for a channel guide. Figure 1 shows a schematic of the chosen waveguide structure. The material is grown by MOCVD (Metal Organic Chemical

Vapor Deposition) on a GaAs substrate. First, a buffer layer is grown which acts to allow better crystal orientation to take place. Then the guide structure is grown which consists of upper and lower cladding layers composed of $Al_{.3}Ga_{.}As$ surrounding the guide region. A thin cap layer is grown on the top to prevent ox dation of the high aluminum concentration upper layer.

Figure 2 shows the mode indices as a function of the superlattice region thickness for three wavelengths. The superlattice layer thickness was fixed at 50 Å, while the number of layers was varied to change the layer thickness. The desired guide thickness should be convenient for optical coupling. The guide thickness must also support at least one mode at the longest wavelength of interest. However, this upper wavelength must be chosen with discretion because as it gets longer more modes will be supported at the pump wavelength. This allows multimode coupling of pump power and therefore decreased power available for parametric conversion.

The chosen guide region thickness of 1.250 μm is indicated by the arrow in Fig. 2. All following discussion will apply to a guide of this thickness. It is seen that two modes are supported at the pump wavelength of 0.9 μm. Figure 3 shows the mode structure for this guide as a function of wavelength. For parametric conversion from the TM pump mode (shorter wavelength) to the TE signal mode (longer wavelength), the cutoff wavelength is approximately 3.4 μm. Figure 4 shows the amplitude profile for several modes supported by this guide structure. The figure depicts a TE polarized pump field at 0.9 μm and a TM polarized degenerate signal field at 1.8 μm.

Figure 5 shows the single mode cutoff channel width as a function of etch depth for this guide thickness and several different wavelengths. Figure 5a shows the values for TE modes while Fig. 5b shows the results for TM modes.

The guide is single mode for parameters below a given wavelength curve. That is, in Fig. 4a a 3 μm wide guide, etched to a depth of 2000Å will be single mode at a wavelength of 1.8 μm but multimode at 0.9 μm. It is desired to keep the guide single mode at the 1.8 μm wavelength. The figure indicates that for channel widths in the 2 to 5 μm range, the etch depths should be approximately 5000Å. For deeper etch depths, the curves end where the effective index approximation reaches modal cutoff.

Conditions for Quasi-Phase Matching

Parametric conversion occurs between TE modes of the pump wavelength and TM modes of the signal and idler wavelengths, or vice versa. A wider conversion bandwidth is possible by choosing the TM(pump) to TE(signal/idler) conversion because longer wavelength TE modes are supported.

Direct phase matching requires that the effective index of each mode involved in the parametric process be equal. Figure 2 shows that no crossing (that is, equality) of the modes at different wavelengths occurs. The amount of difference in the indices is proportional to the momentum mismatch, Δk. This mismatch can be overcome by perturbation of the guide indices. We have chosen the method of etching a grating into the upper surface of the guide. This shallow grating periodically perturbs the guide thickness and thereby the refractive index.

The grating period is found by working with the two conservation equations given earlier,

$$\omega_p = \omega_s + \omega_i \qquad (1) \qquad \text{and} \qquad k_p = k_s + k_i + \Delta k \qquad (2)$$

We can rewrite $\omega = \frac{kc}{n} = \frac{2\pi}{\lambda}\frac{c}{n}$ where c is the speed of light. Substituting into (1) and (2) and rearranging yields

$$\lambda_s = \frac{\lambda_i - \lambda_p}{\lambda_i \lambda_p} \quad (3) \qquad \Lambda = \left(\frac{n_p}{\lambda_p} - \frac{n_i}{\lambda_i} - \frac{n_s}{\lambda_s}\right)^{-1} \quad (4)$$

where $\Lambda = \frac{2\pi}{\Delta k}$ is the grating period. At this point we consider the case of degenerate parametric oscillation, that is $\lambda_i = \lambda_s = 2\lambda_p$. Then $n_i = n_s$ and (4) can be rewritten

$$\Lambda = \left(\frac{n_p}{\lambda_p} - \frac{n_s}{2\lambda_p} - \frac{n_s}{2\lambda_p}\right)^{-1} \quad (5)$$

Simplifying (5) yields the grating period for degenerate oscillation: $\Lambda_d = \frac{\lambda_p}{\Delta n}$ where $\Delta n = n_p - n_s$ is the difference in the effective indices of the pump and degenerate signal wavelengths.

Figure 6 shows the grating period required for quasi-phase matching as a function of signal wavelengths for several pump wavelengths. It is seen that the minimum value of Λ occurs for degenerate oscillation. Also note that the value of Λ is on the order of several microns. The fabrication of gratings with this period is well within the capabilities of common photolithographic processing.

At this point we make note that the computations made to this point have only considered the slab waveguide geometry. Computations were made to try and account for the actual channel waveguide geometry of the oscillator. In the context of the effective index approximation these computations are not

always accurate, particularly as the guide approaches modal cutoff. However, the qualitative aspects are maintained.

Figure 7 shows the grating period necessary for degenerate oscillation as a function of pump wavelength for two channel widths and a variety of channel etch depths. The figure shows that the effects of considering the channel waveguide geometry are minimal as the grating period is in the same range as indicated in Fig. 6. The breakdown of the effective index approximation is clearly indicated by the discontinuities in the TE to TM coupling curves. These discontinuities occur when the approximation reaches a cutoff mode and the predicted values are considered inaccurate.

Photolithographic Mask Design

Because it is anticipated that the final devices will not operate exactly as predicted (due to obvious approximations in the analysis and material unknowns) it was decided to design a mask that provided a variation of device characteristics, thus increasing the probability that at least one device would be successful.

From the computer analyses it was decided that channel widths of 2, 3, and 4 μm would be useful for experimental evaluation. These are wide enough to be fabricated without special care and yet maintain the desired modal characteristics. The chosen material composition will present low optical loss for a pump wavelength between 0.85 and 1.00 μm. From Fig. 7 the grating period should be between 5 and 6 μm for TM to TE conversion. It was decided to use four different periods, 5.0, 5.5, 6.0, and 6.5 μm.

The first mask level is a benchmark etch. This was included in the design to provide alignment for the guide and grating levels in case the etch on the waveguide level (Level 2) is not deep enough to be visible.

Figure 8 shows the schematic appearance of the second and third mask levels which define the channel guides and the gratings respectively. The guides on Level 2 are arranged in sets of three of each width. The guide length is 25 mm. The first guide is masked from the grating etch by the third level and thus acts as a control guide allowing evaluation of guide quality. The second and third guides of each set receive grating etches of 8 and 11 mm interaction lengths respectively. This will allow evaluation of conversion efficiency. The grating etch is 10 μm wide. This assures that the index perturbation effected by the grating will be uniform over the effective guide width even if some misalignment is present between the two levels. Four of the grating levels will be made, one for each grating period. Thus a finished sample will contain a number of channels with a single grating period.

Oscillator Experimental Evaluation

It is planned to use a Ti:Sapphire laser for the evaluation of the finished samples. This laser is tunable with useful output in the 0.85 to 1.00 μm range. It is reasoned that as the pump wavelength is scanned, degenerate conversion will occur at some wavelength. Whether or not this conversion results in oscillation or only fluorescence will depend upon the conversion efficiency, coupling efficiency, quality of the guides, and available pump power

Conclusion

We have presented a thorough theoretical design for an Aluminum Gallium Arsenide thin film integrated Optical Parametric Oscillator. In depth computer analysis has been performed leading to a reasonable experimental design. The design includes a great deal of flexibility that allows a reasonable expectation of experimental success.

Bibliography

[1] J. A. Giordmaine and R. C. Miller, "Tunable coherent parametric oscillation in $LiNbO_3$ at optical frequencies," Physical Review, vol. 14, pp. 973, 1965.

[2] R. L. Byer, "Parametric Oscillators and Nonlinear Materials," in Nonlinear Optics, ed. P G Harper, and B S Wherrett. (London: Academic Press, 1977) pp. 47-160.

[3] A. W. Snyder and J. D. Love, Optical Waveguide Theory, (London: Chapman and Hall, Ltd, 1983)

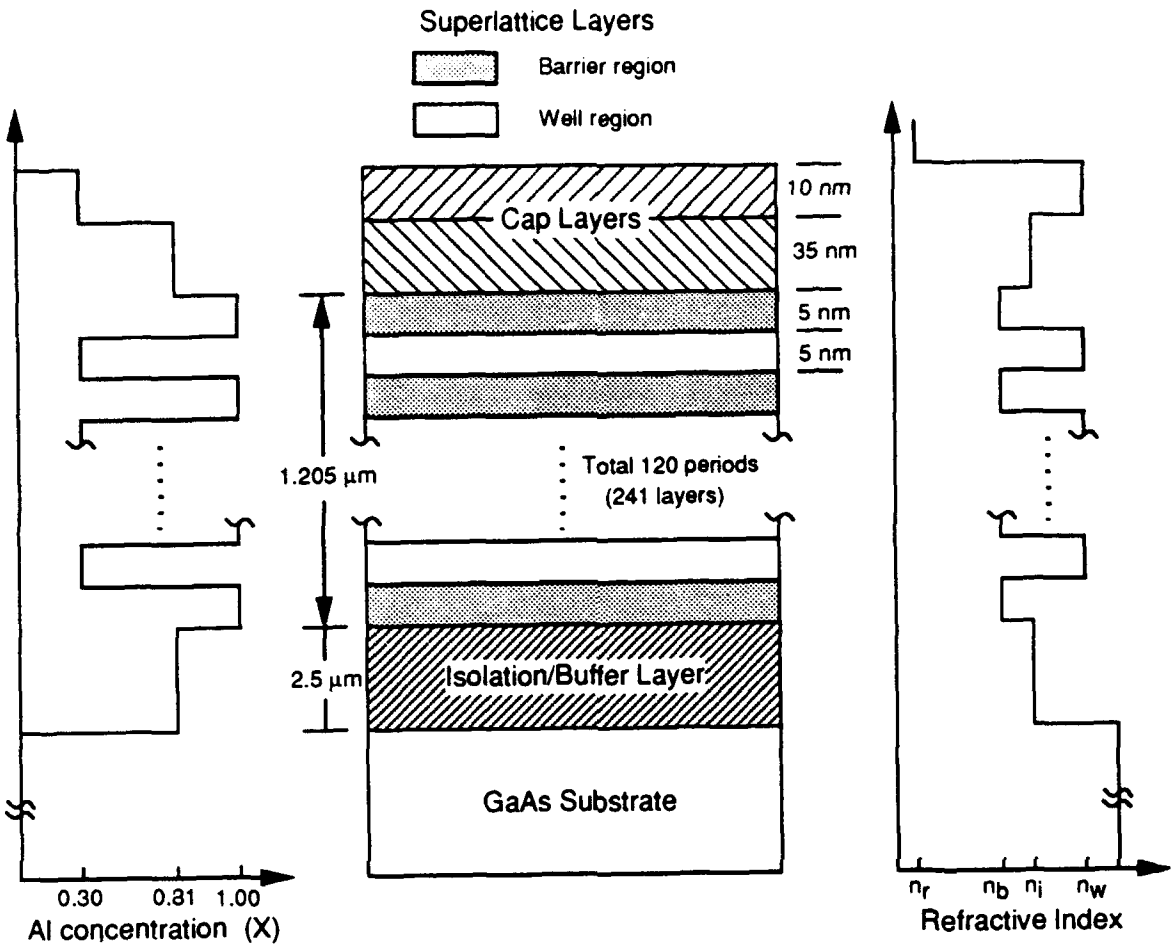

Layer	Thickness	Aluminum Conc. (x) in the AlGaAs Layers
Top Layer 1	10 nm	30 %
Top Layer 2	35 nm	81 %
MQW Structure		
Barrier	5 nm	100 %
Well	5 nm	30 %
Barrier	5 nm	100 %
|	|	|
Well	5 nm	30 %
Barrier	5 nm	100 %
Isolation Layer	2.5 µm	81 %
Substrate		0 %

Fig. 1. Schematic description of the waveguide material structure.

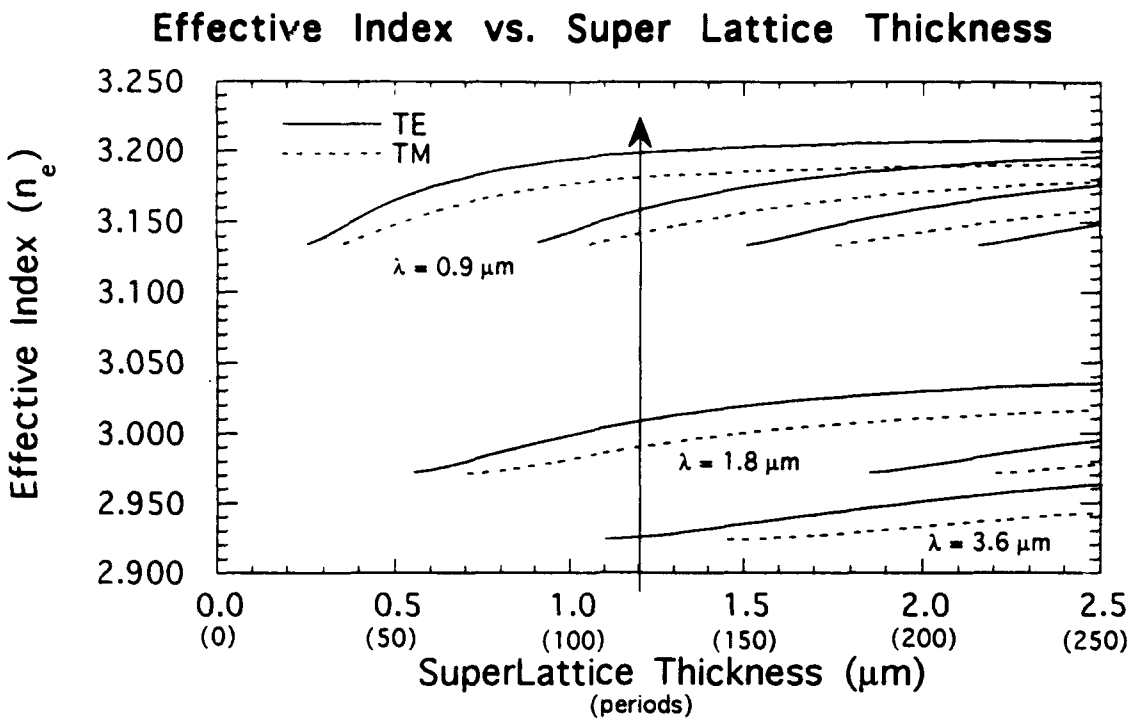

Fig. 2. Mode effective index as a function of the thickness of the superlattice region in a planar guide. The arrow indicates the thickness chosen for the oscillator, which consists of 120 superlattice periods. (Total guide thickness is 1.250 μm)

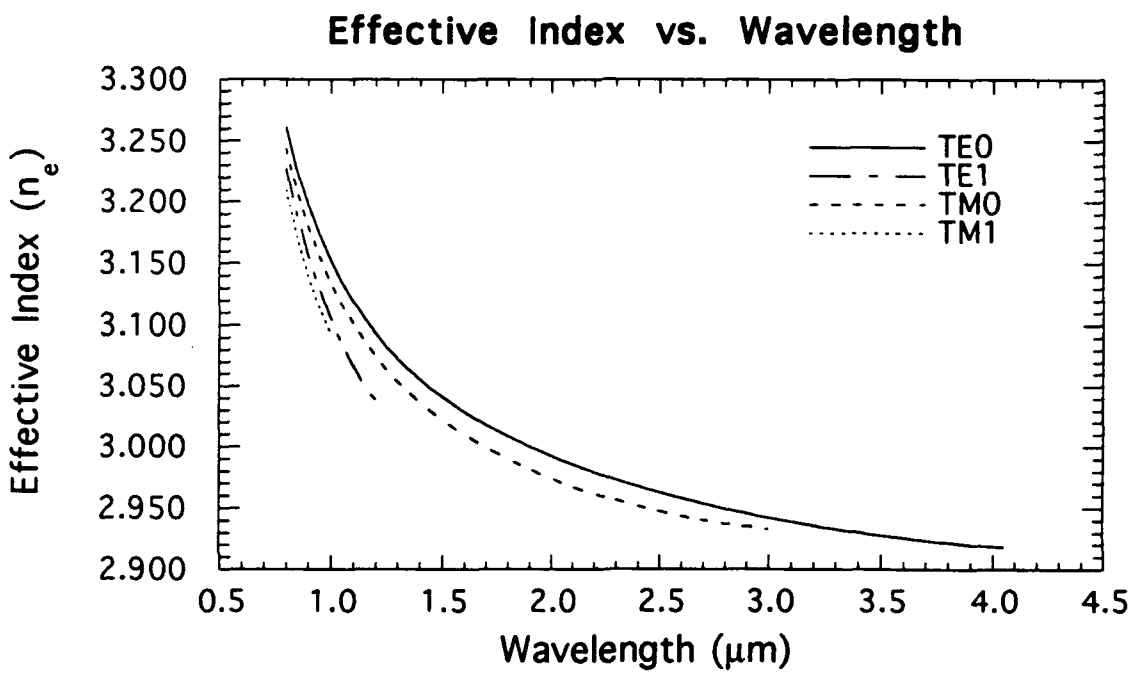

Fig. 3. Mode effective index as a function of wavelength for the 1.25 μm thick planar guide.

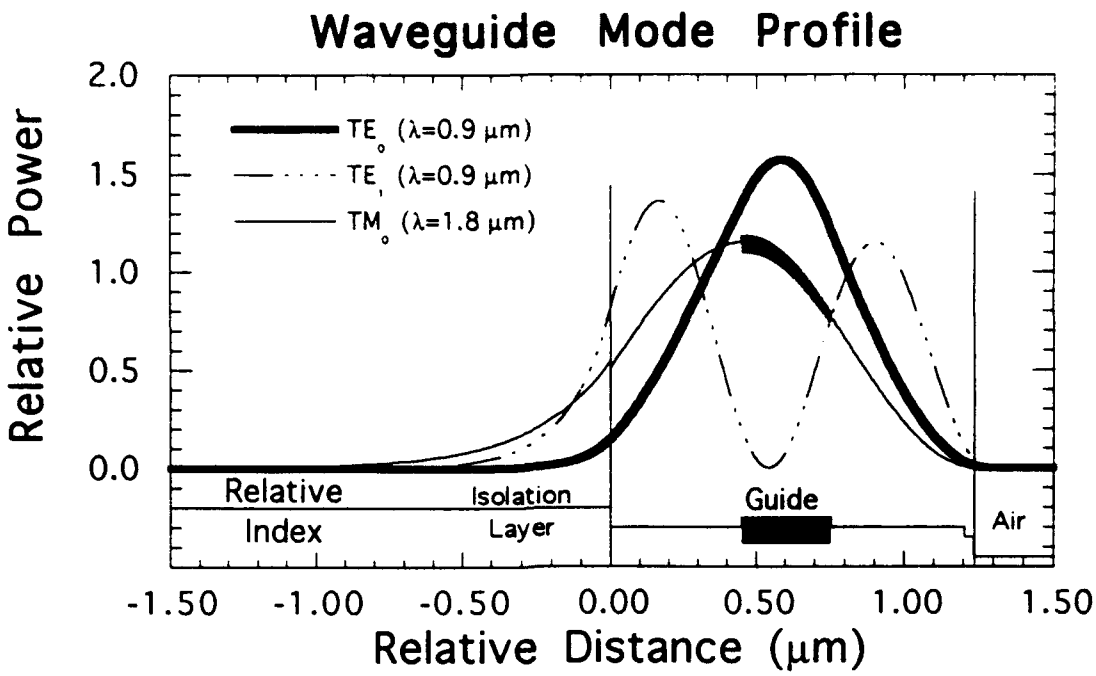

Fig. 4. Amplitude profiles for several modes supported by the 1.25 μm thick planar guide at the degenerate oscillation wavelength.

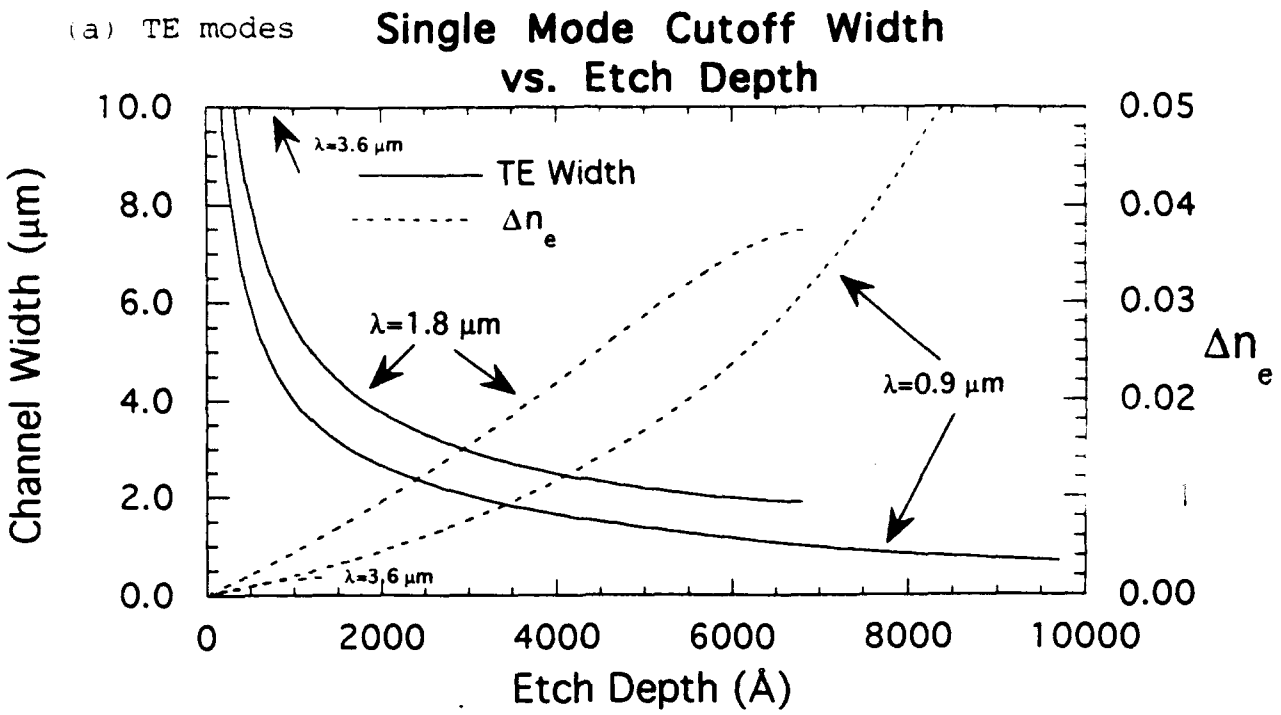

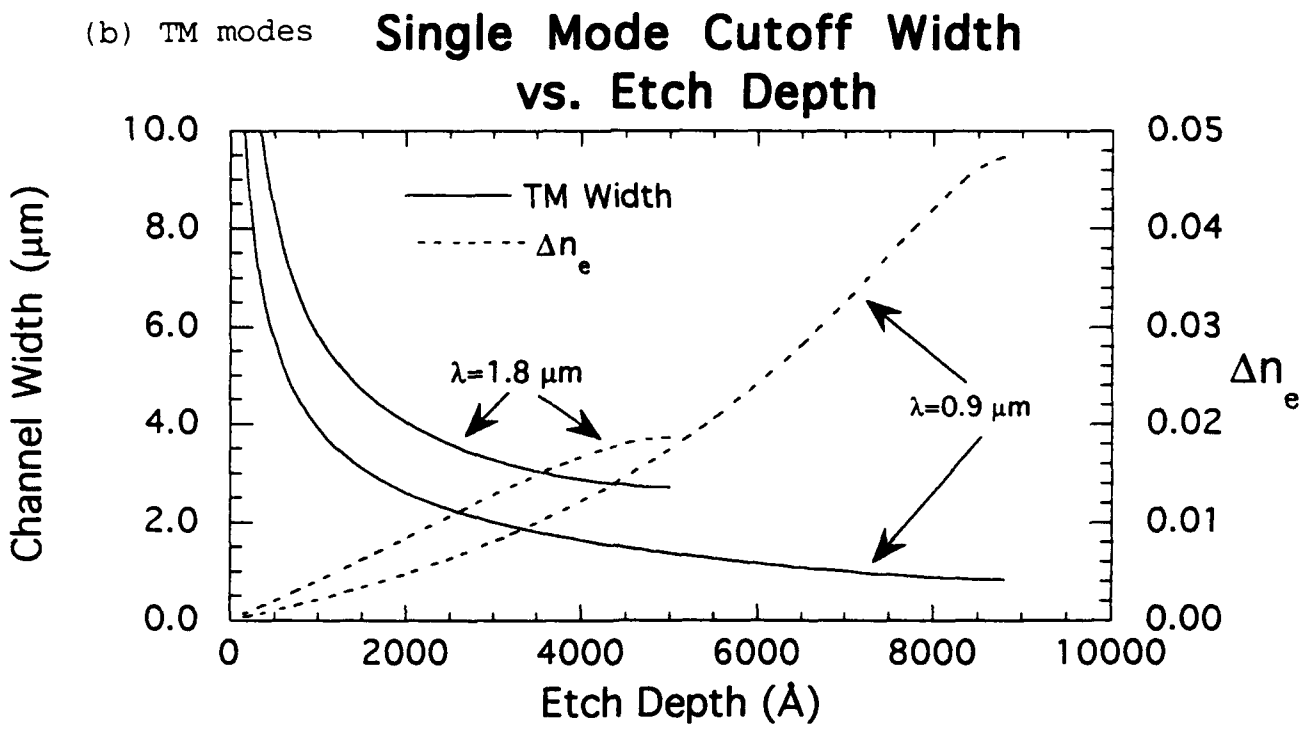

Fig. 5. Channel guide width for single mode cutoff as a function of etch depth for the 1.25 μm thick planar structure at various wavelengths. The guides support only a single mode for width and etch depth values below the given wavelength curve. The curves discontinue at planar cutoff.

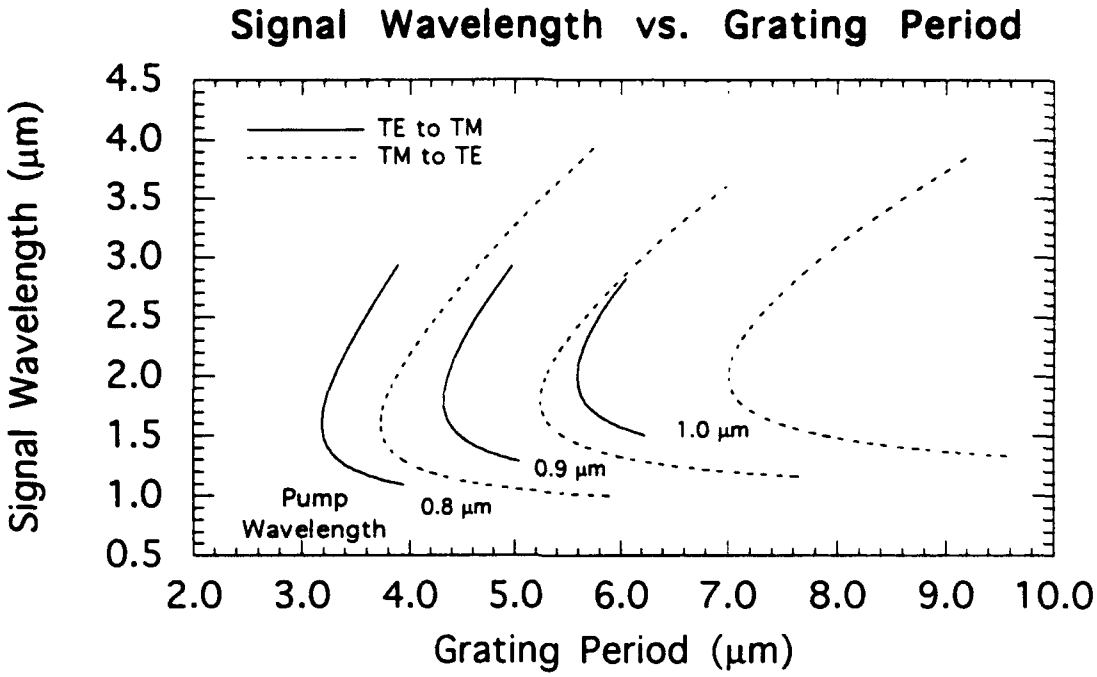

Fig. 6. Signal wavelength as a function of the grating period for three pump wavelengths.

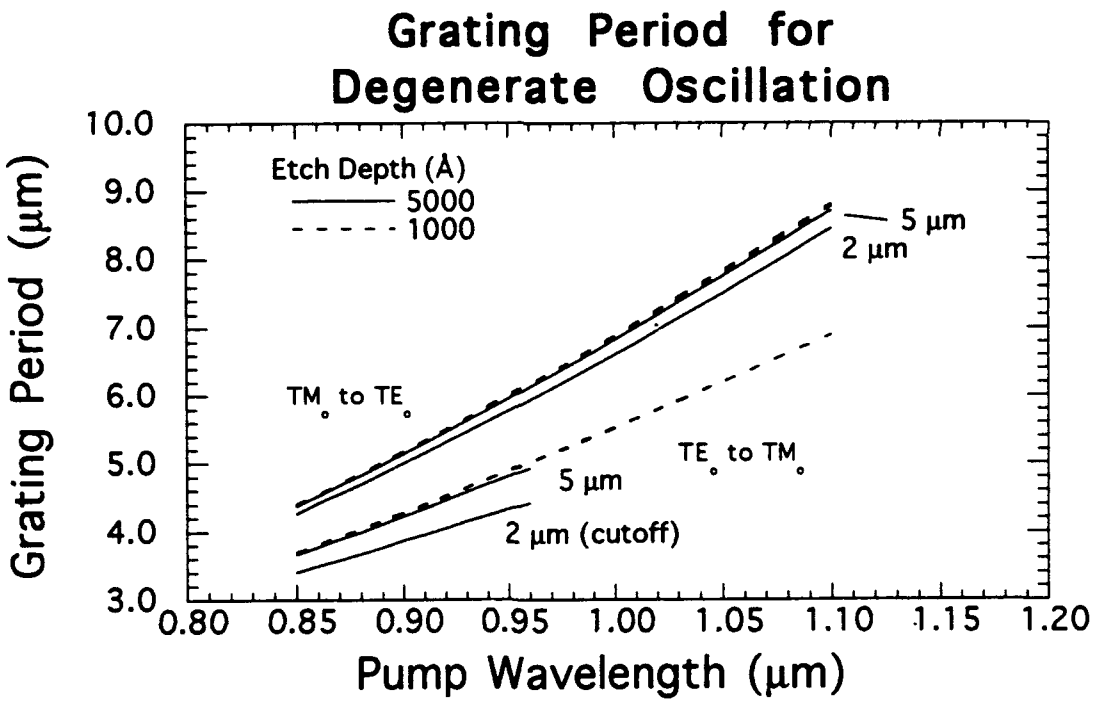

Fig. 7. Grating period as a function of pump wavelength for degenerate oscillation. Computations are for 2 µm and 5 µm channel waveguides at etch depths of 1000 and 5000 Å (the 2 µm values are lower for each data set). Note that the TMo mode at the degenerate wavelength is completely cutoff in the planar guide etched to 5000Å. The values for the 2 µm guide in the TEo to TMo conversion are affected by this much more than the values for the 5 µm guide.

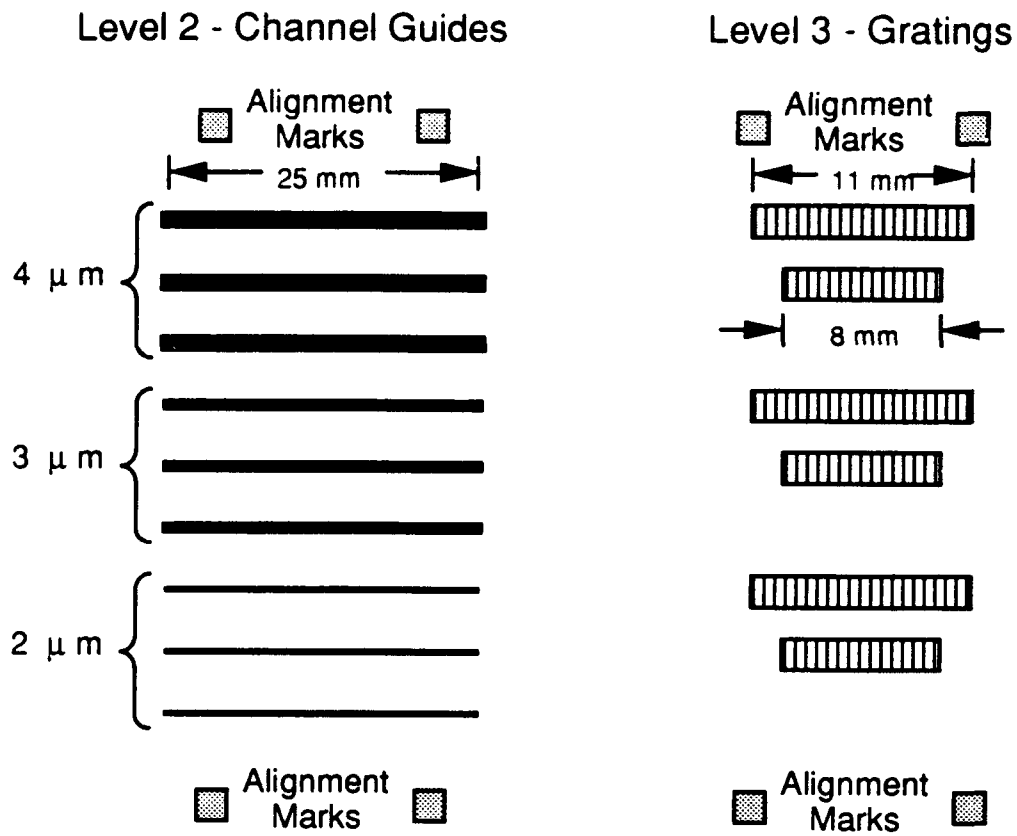

Fig. 8. Schematic diagram of the photolithographic mask layout. The distance between the guides is 100 μm, and the distance between alignment marks is 1100 μm. The pattern between alignment marks was repeated seven times. The grating sections are 10 μm wide. There are four different Level 3 patterns, one each for the 5.0, 5.5, 6.0, and 6.5 μm grating periods.

Ronald Neaffer's report not available at time of publication.

CRYSTAL STRUCTURE OF CHOLESTERYL-4-VINYLBENZOATE

Edward Peter Socci

Graduate Student

Department of Materials Science & Engineering

University of Virginia

Thornton Hall

Charlottesville, VA 22903-2442

Final Report for:

Graduate Student Research Program

Wright Laboratory

Sponsored by:

Air Force Office of Scientific Research

Bolling Air Force Base, Washington, D.C.

September 1993

CRYSTAL STRUCTURE OF CHOLESTERYL-4-VINYLBENZOATE

Edward Peter Socci
Graduate Student
Department of Materials Science & Engineering
University of Virginia

Abstract

The structure of cholesteryl-4-vinylbenzoate was determined by X-ray diffraction. The molecule is elongated, with the benzoate group oriented out of the plane of the tetracyclic core. Molecules pack anti-parallel, with overlap between either aliphatic tails or tetracyclic cores. These two types of interactions (overlap) are similar to the two packing modes that co-exist in the liquid crystalline phase.

CRYSTAL STRUCTURE OF CHOLESTERYL-4-VINYLBENZOATE

Edward Peter Socci

Introduction

The Laser Hardened Materials Branch of the Materials Laboratory, Wright Laboratory is interested in organic materials with highly ordered molecular structure for nonlinear optical purposes. One class of materials under investigation are thermotropic liquid crystalline compounds, especially those based upon cyclic siloxane backbones.

The first compound exhibiting liquid crystallinity was an ester of cholesterol discovered by Reinitzer in 1888 (Reinitzer, 1888). Since then the liquid crystalline properties of a number of steroidal-based esters (Shibaev & Freidzon, 1989) have been examined. The crystal structures of cholesterol-based materials, most notably those with pendant n-alkanoate ester groups, have also been studied in an attempt to obtain information relating the conformation and packing in the crystalline state to packing in the liquid crystalline phase.

Craven and co-workers (Craven & Guerina, 1979; Guerina & Craven, 1979; Pattabhi & Craven, 1979; Sawzik & Craven, 1979; Sawzik & Craven, 1980a; Sawzik & Craven, 1980b) have observed three distinct packing modes which are dependent upon the length of the pendant n-alkanoate spacer group. Compounds with short spacer lengths (6-8 carbons) exhibit a monolayer structure in which the molecules pack antiparallel. The methyl side groups pendant on the tetracyclic core interlock, leading to efficient packing. Structures of compounds with medium length spacers (9-12 carbons) are comprised of two non-symmetry related molecules in the unit cell that differ mainly in the conformations of the n-alkanoate groups. The tetracyclic cores in these anti-

parallel molecules are approximately orthogonal. Compounds with longer spacer groups (13-18 carbons) pack in a bilayer structure in which the molecules are oriented antiparallel. The tetracyclic cores between adjacent molecules do not overlap. Differences in these three packing types have been compared with the variations in packing behavior observed in the liquid crystalline phases (Sawzik & Craven, 1979). Others (Sato & Yano, 1987) have correlated conformations in the crystalline state with the ability of a compound to exhibit liquid crystallinity.

As part of our program aimed toward the development of ordered, optically clear thin films a series of cholesteryl-4-alkenebenzoate materials was synthesized (Bunning, 1992; Gresham, McHugh, Bunning, Klei, Samulski, & Crane, 1993). These compounds were attached to cyclic siloxane backbones . X-ray diffraction measurements of the liquid crystalline phase of these macromolecules indicate the co-existence of two molecular packing schemes (Bunning, Klei, Samulski, Crane, & Linville, 1991; Bunning, Klei, Samulski, Adams, & Crane, 1993) Type I packing consists of nearly fully interdigitated cholesteryl molecules packed antiparallel with a molecular repeat distance (as measured from X-ray diffraction) corresponding to the calculated length of an extended conformation of the molecule. Type II packing consists of antiparallel mesogens packed with overlap only among the aliphatic tails. The relative amounts of type I and II packing can be controlled by altering several variables including the terminal spacer length. This paper examines the structure of vinylbenzoate substituted cholesterol compounds. Materials with other alkene benzoate spacers are also being studied. Trends in the crystalline packing as a function of alkene-benzoate spacer length may offer insight into the packing behavior in the liquid crystalline phase.

Experimental Methods

The title compound ($C_{36}H_{52}O_2$, F.W.=516.78) was synthesized using a mild esterification reaction of vinylbenzoic acid and cholesterol. Experimental details are available elsewhere (Bunning, 1992). Colorless parallelepiped crystals were obtained by recrystallization from ethyl acetate. A crystal of approximate dimensions 0.37 by 0.30 by 0.27 mm was mounted on a glass fiber with its long axis approximately parallel to the φ axis of the goniometer. Preliminary examinations of the crystal and subsequent data collection were performed on an Enraf-Nonius CAD-4 diffractometer equipped with graphite monochromated Mo Kα radiation (λ=0.71073 Å). A rotation (about φ) Polaroid was taken and indicated the crystal was of diffraction quality.

Unit cell dimensions were obtained from a least square fit of 25 reflections with $18.02° \leq 2\theta \leq 23.48°$. The orthorhombic cell parameters and calculated volume are: a=13.755(2) Å, b=24.817(3)Å, c=9.101(2)Å, and V=3101.6 $Å^3$. There are four molecules per unit cell (Z=4).

Intensities were measured at 294 K in a $\omega/2\theta$ scan mode. A total of 5035 reflections in the range of $2° \leq 2\theta \leq 60°$ and $0 \leq h \leq 19$, $0 \leq k \leq 34$, $0 \leq l \leq 12$ were measured. Three intensity monitoring reflections (measured every 120 reflections) showed a decay of 1.79% over approximately 72 hours of data collection. Absorption and decay corrections were applied (μ=0.061). Examination of reflections for systematic absences led to the choice of space group $P2_12_12_1$ (#19).

The phase problem was successfully solved using the direct method program SIR88 (Spagna, R & Viterbo, D., 1989). Structure factors were calculated with scattering factors from the International Tables of X-ray Crystallography (International Tables for Crystallography, 1974). Full matrix

least-squares refinement where the minimized function was $\Sigma w(|Fo| - |Fc|)$ was performed. Non-hydrogen atoms were first refined isotropically and then anisotropically. The 1470 reflections with $F>2\sigma(F)$ were used in the refinement. Hydrogen atoms were added at calculated positions to the structure model and set as fixed riding atoms. The final cycle of refinement included 243 variable parameters. The final R factor was 0.071 and the weighted R factor was 0.064. The largest shift/error for a parameter was equal to 0.02. All calculations were performed on a Micro-VAX II computer using Enraf-Nonius' MolEN software. The SYBYL computer modeling program (Tripos Associates, 1991) was used to visualize the molecular packing. A summary of experimental details is given in Table 1. The fractional coordinates and isotropic equivalent temperature factors of the non-hydrogen atoms are listed in in Table 2 of the appendix.

Table 1. Experimental Details

Formula	$C_{36}H_{52}O_2$
Formula Weight	516.78
F(000)	1136
Crystal Dimensions	0.37 x 0.30 x 0.27 mm
Radiation	Mo Kα
Temperature	294 K
Crystal Form	Orthorhombic
Space Group	$P2_12_12_1$
Cell Constants	a=13.755(2) Å
	b=24.817(3) Å
	c=9.101(2) Å
Volume	3101.6 $Å^3$
Z	4
Density (calc.)	1.10 g/cm^3
Absorption Coeff.	0.061
Scan type	$\omega/2\theta$
Max 2Q	59.94°
Reflections Measured	5066 total
	5035 unique
Corrections	Lorentz-polarization
	Numerical absorption (0.9768-0.9906)
Observations	1470 with $F>2\sigma(F)$
Parameters	243
R	0.071
wR	0.064
Goodness of fit	1.912
Max shift/error	0.02

Discussion

Bond lengths bond angles and torsion angles are compiled in Tables 4, 5 and 6, respectively. A thermal-ellipsoid plot of the molecule (without hydrogen atoms) along with the numbering scheme employed is shown in Figure 1. Bond lengths and angles in the phenyl ring of the benzoate ester compare well with conventional aromatic bond lengths and angles. The benzoate moiety lies out of the plane of the tetracyclic core (illustrated in Figure 2) as indicated by the C2 C3 O3 C28 torsion angle of 152.2(6)°. The C35-C36 bond length (1.30(1)Å) is consistent with accepted values for carbon-carbon double bonds, indicating that dimerization did not occur during X-ray exposure. The C28-O28 (1.199(8)Å) carbonyl and C28-O3 (1.352(8)Å) ester bonds are in agreement with accepted values. Boat and chair conformations (illustrated in Figure 2) are both present in the tetracycles consistent with results from the n-alkanoate cholesterol series. Large thermal vibrations are observed in the two terminal methyl groups of the aliphatic tail (C26 and C27). In general, the molecule adopts an extended conformation along the b axis.

The anti-parallel molecules pack pairwise in the unit cell as shown in Figure 3. There is a staggered repeat along the a axis of molecules packed with either overlapping aliphatic tails or overlapping tetracyclic cores (Figure 4). The overlapping cores are tilted with respect to each other. The phenyl ring of the benzoate group lies approximately parallel to the tetracyclic core of the neighboring molecule. The methyl groups of adjacent molecules do not interlock.

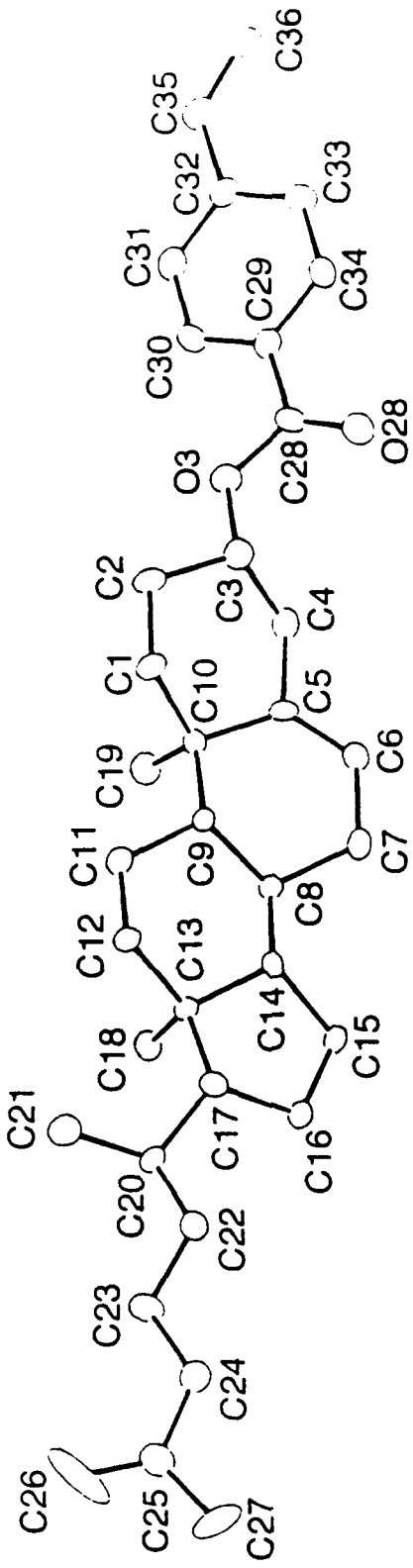

Figure 1: Molecular structure of the title compound along with the atom numbering scheme. H atoms are omitted. Thermal ellipsoids (ORTEPII; Johnson, 1976) are drawn at the 50% probability level.

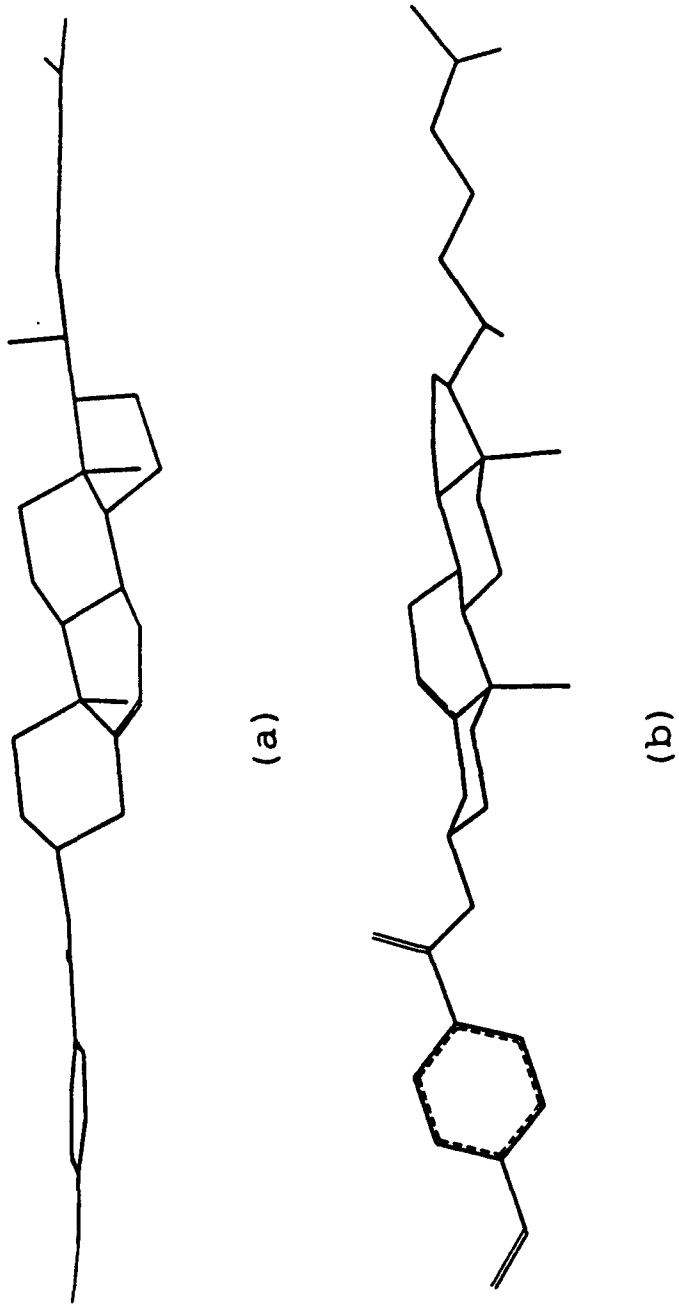

Figure 2: Illustrations showing the benzoate moiety out-of-plane with the tetracyclic core (a) and boat-chair ring conformations of the tetracyclic core (b).

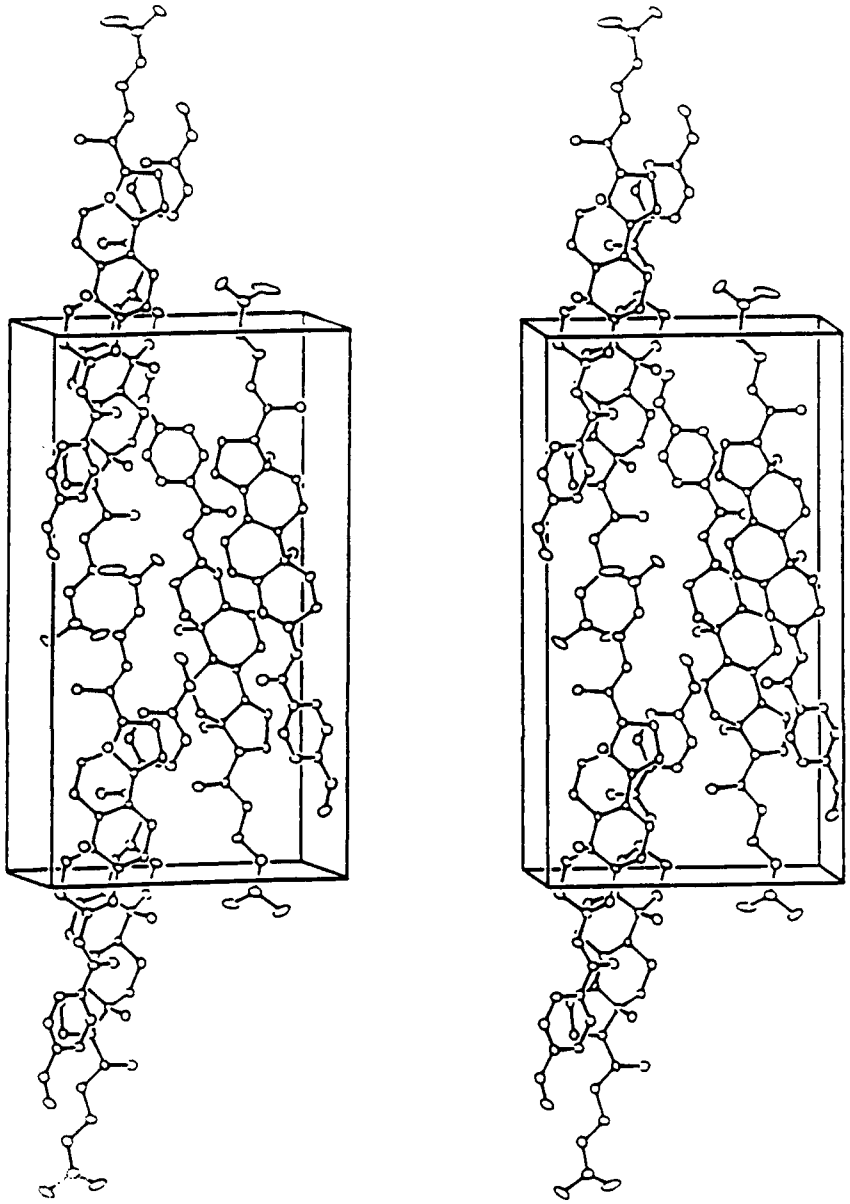

Figure 3: An ORTEPII plot of the unit cell. The c axis is perpendicular to the plane of the paper; the a and b axes are horizontal and vertical, respectively.

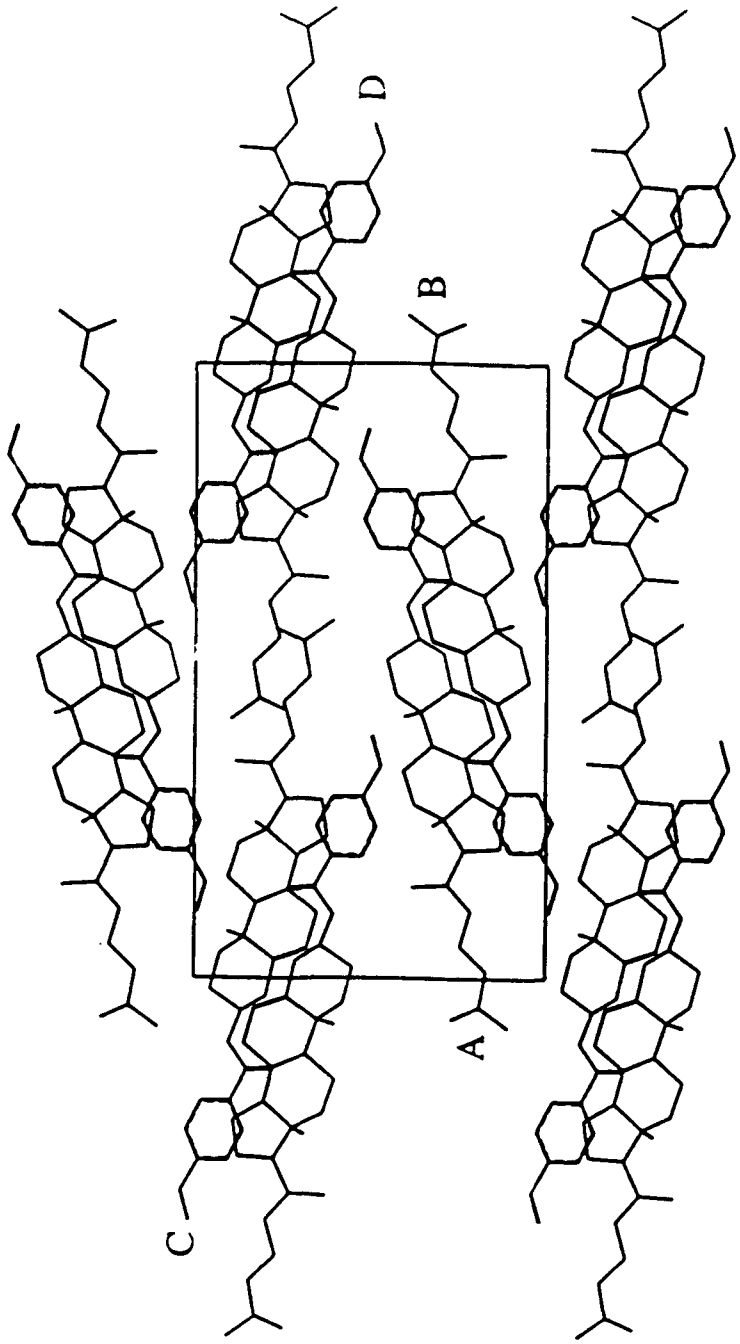

Figure 4: Projection of the cholesteryl-4-vinylbenzoate crystal structure down the c axis. Molecular interaction types are staggered along the a axis. A-B and C-D separation distances are given in the text.

The types of interactions exhibited in the solid state have features reminiscent of those observed in the liquid crystalline state (described in the introduction) of cholesteryl-4-vinylbenzoate substituted siloxanes. Type I liquid crystalline packing approximates that of antiparallel molecules in the solid state where tetracyclic cores overlap. An end-to-end spacing (along the b-axis) between atoms A and B (shown in Figure 4) of 27.5 Å qualitatively agrees with a 26 Å d-spacing observed for type I packing in the liquid crystalline state. An end-to-end spacing (along the b-axis) between atoms C and D shown in Figure 4 of 45.1 Å qualitatively agrees with an observed (in the liquid crystalline state) type II d-spacing of 47 Å. In the liquid crystalline phase, the amount of type II packing is presumably dictated by steric interactions among aliphatic tails of neighboring molecules. As conditions increase the mobility of the cholesterol molecules (e.g. modification of spacer group length), the amount of type II packing decreases relative to type I packing. We are currently studying the progression of these two packing modes in the crystal structures of cholesterol molecules substituted with longer spacer groups.

References

BUNNING, T.J., KLEI, H.E., SAMULSKI, E.T., CRANE, R.L., and LINVILLE, R.J. (1991). *Liq. Cryst.*, **10(4)**, 445-456.

BUNNING, T.J. (1992). Ph.D. Dissertation, University of Connecticut.

BUNNING, T.J., KLEI, H.E., SAMULSKI, E.T., ADAMS, W.W., & CRANE, R.L. (1993). *Mol. Cryst. Liq. Cryst.*, **231**, 163-174.

BURLA, M.C., CAMALLI, M., CASCARANO, G.,GIACOVAZZO, C., POLIDORI, G.,SPAGNA, R. &VITERBO, D. (1989). ***SIR***. J. Appl. Cryst. **22**, 389-393.

CRAVEN, B.M. & GUERINA, N.G. (1979). *Chem. Phys. Lipids*, **24**, 157-166.

FAIR, C.K. (1990). ***MolEN***, An Interactive Intelligent System for Crystal Structure Analysis, User Manual, Enraf - Nonius, Delft, The Netherlands.

GRESHAM, K.D., MCHUGH, C.M., BUNNING, T.J., KLEI, H.E., SAMULSKI, E.T., & CRANE, R.L. (1993). *Am. Chem. Soc., Polym. Prep.*, **34(1)**, 594-595.

GUERINA, N.G. & CRAVEN, B.M. (1979). *J. Chem. Soc. Perkin Trans. II.*, 1414-1419.

International Tables for X-Ray Crystallography, **Vol. IV**, The Kynoch Press, Birmingham, England, 1974

JOHNSON, C. K. (1976). ***ORTEPII***. Report ORNL-5138. Oak Ridge National Laboratory, Tennessee, USA.

PATTABHI, V. & CRAVEN, B.M. (1979). *J. Lipid Res.*, **20**, 753-759.

REINITZER, F. (1888). *Monatsh. Chem.*, **9**, 421-441.

SATO, T. & YANO, S. (1987). *Mol. Cryst. Liq. Cryst.*, **144**, 179-184.

SAWZIK, P. & CRAVEN, B.M. (1979) in Liquid Crystals, S. CHANDRASEKHAR, Ed., Bangalore, India. 171-178.

SAWZIK, P. & CRAVEN, B. M. (1979). *Acta. Cryst.*, **B35**, 895-901.

SAWZIK, P. & CRAVEN, B. M. (1980). *Acta. Cryst.*, **B36**, 3027-3033.

SAWZIK, P. & CRAVEN, B. M. (1980). *Acta. Cryst.*, **B36**, 215-218.

SHIBAEV, V.P. & FREIDZON, YA. S. (1989) in Side Chain Liquid Crystal Polymers, C. B. MCARDLE, Ed., Blackie; Glasgow, pp 260-286.

SYBYL program and manual, release 5.4, Tripos Associates, 1991.

Appendix

Table 2. Fractional Coordinates and Equivalent Anisotropic Thermal Parameter for Cholesteryl-4-vinylbenzoate

Atom	x	y	z	U_{eq}
O3	0.3961(3)	0.1037(2)	0.4407(5)	5.5(1)
O28	0.2672(3)	0.1459(2)	0.3399(6)	6.4(1)
C1	0.4243(5)	-0.0405(3)	0.3309(9)	5.8(2)
C2	0.4511(5)	0.0178(3)	0.371(1)	6.0(2)
C3	0.3609(5)	0.0523(3)	0.3872(9)	5.0(2)
C4	0.2907(5)	0.0285(3)	0.4934(8)	5.2(2)
C5	0.2676(5)	-0.0305(2)	0.4595(7)	4.0(2)
C6	0.1774(5)	-0.0480(3)	0.4510(8)	4.9(2)
C7	0.1485(4)	-0.1050(3)	0.4282(9)	5.1(2)
C8	0.2313(4)	-0.1445(2)	0.4498(7)	3.6(2)
C9	0.3219(4)	-0.1225(2)	0.3722(8)	3.5(2)
C10	0.3552(4)	-0.0671(2)	0.4400(8)	3.7(2)
C11	0.4032(5)	-0.1639(2)	0.3628(8)	5.0(2)
C12	0.3712(5)	-0.2187(2)	0.3078(8)	4.4(2)
C13	0.2875(4)	-0.2415(2)	0.3994(6)	3.3(1)
C14	0.2055(4)	-0.1997(2)	0.3912(7)	3.7(1)
C15	0.1180(4)	-0.2288(2)	0.4561(8)	4.7(2)
C16	0.1332(4)	-0.2879(3)	0.4098(9)	4.9(2)
C17	0.2346(4)	-0.2917(3)	0.3381(8)	4.3(2)
C18	0.3208(5)	-0.2527(3)	0.5578(7)	5.2(2)
C19	0.4039(5)	-0.0752(3)	0.5871(8)	5.9(2)
C20	0.2809(4)	-0.3478(3)	0.3536(9)	4.7(2)
C21	0.3822(5)	-0.3514(3)	0.290(1)	8.3(3)
C22	0.2148(5)	-0.3906(3)	0.2860(8)	5.5(2)
C23	0.2436(5)	-0.4481(3)	0.3086(9)	6.7(2)
C24	0.1694(5)	-0.4888(3)	0.259(1)	6.6(2)
C25	0.1874(6)	-0.5461(3)	0.275(1)	9.9(3)
C26	0.2671(8)	-0.5670(4)	0.294(2)	27.4(6)
C27	0.1041(7)	-0.5805(3)	0.227(1)	13.1(4)
C28	0.3425(5)	0.1475(3)	0.4059(8)	4.6(2)
C29	0.3908(5)	0.1981(3)	0.4526(7)	4.3(2)
C30	0.4756(5)	0.1980(3)	0.5340(8)	5.2(2)
C31	0.5192(5)	0.2457(3)	0.5715(8)	5.7(2)
C32	0.4818(5)	0.2945(3)	0.5275(8)	4.8(2)
C33	0.3966(5)	0.2944(3)	0.4489(8)	5.4(2)
C34	0.3513(5)	0.2469(3)	0.4125(8)	5.1(2)

Appendix (con't)

Table 2 (con't)

Atom	x	y	z	U_{eq}
C35	0.5325(6)	0.3444(3)	0.5643(9)	6.5(2)
C36	0.5071(6)	0.3936(3)	0.534(1)	7.6(2)
H1A	0.3927	-0.0392	0.2380	7.3*
H1B	0.4813	-0.0618	0.3236	7.3*
H2A	0.4824	0.0168	0.4644	7.9*
H2B	0.4933	0.0336	0.3010	7.9*
H3	0.3273	0.0523	0.2959	6.6*
H4A	0.2324	0.0490	0.4931	6.6*
H4B	0.3202	0.0305	0.5875	6.6*
H6	0.1280	-0.0218	0.4655	6.5*
H7B	0.0978	-0.1132	0.4955	6.5*
H7A	0.1247	-0.1082	0.3305	6.5*
H8	0.2448	-0.1492	0.5513	4.5*
H9	0.3040	-0.1142	0.2738	4.2*
H11A	0.4253	-0.1688	0.4608	6.5*
H11B	0.4551	-0.1512	0.3035	6.5*
H12B	0.3467	-0.2137	0.2110	5.8*
H12A	0.4241	-0.2432	0.3054	5.8*
H14	0.1907	-0.1911	0.2919	4.6*
H15A	0.0592	-0.2144	0.4179	6.3*
H15B	0.1183	-0.2251	0.5600	6.3*
H16B	0.1320	-0.3108	0.4933	6.9*
H16A	0.0835	-0.2984	0.3432	6.9*
H17	0.2345	-0.2882	0.2341	5.3*
H18A	0.3654	-0.2818	0.5622	5.9*
H18B	0.2650	-0.2609	0.6150	5.9*
H18C	0.3507	-0.2210	0.5951	5.9*
H19C	0.4275	-0.0414	0.6208	7.1*
H19B	0.3567	-0.0885	0.6541	7.1*
H19A	0.4562	-0.1000	0.5803	7.1*
H20	0.2868	-0.3532	0.4565	6.9*
H21A	0.3780	-0.3570	0.1873	9.5*
H21B	0.4164	-0.3805	0.3341	9.5*
H21C	0.4158	-0.3187	0.3093	9.5*
H22A	0.2094	-0.3827	0.1841	7.1*
H22B	0.1527	-0.3870	0.3310	7.1*
H23A	0.2597	-0.4547	0.4083	9.3*

Appendix (con't)

Table 2 (con't)

Atom	x	y	z	U_{eq}
H23B	0.2993	-0.4534	0.2488	9.3*
H24B	0.1116	-0.4801	0.3109	9.7*
H24A	0.1590	-0.4839	0.1566	9.7*
H25	0.1862	-0.5489	0.3788	12.4*
H26A	0.3012	-0.5498	0.2165	18.8*
H26B	0.2675	-0.6048	0.2794	18.8*
H26C	0.2913	-0.5630	0.3914	18.8*
H27A	0.1046	-0.6149	0.2722	13.7*
H27B	0.1085	-0.5847	0.1230	13.7*
H27C	0.0454	-0.5623	0.2504	13.7*
H30	0.5025	0.1646	0.5650	6.8*
H31	0.5778	0.2445	0.6267	6.6*
H33	0.3698	0.3277	0.4170	7.4*
H34	0.2911	0.2489	0.3576	7.9*
H35	0.5911	0.3410	0.6188	8.5*
H36A	0.545	0.423	0.559	9.9*
H36B	0.448	0.399	0.477	9.9*

Starred atoms were refined isotropically. Anisotropically refined atoms are given in the form of the isotropic equivalent displacement parameter defined as: $(4/3) * [a^2*B(1,1) + b^2*B(2,2) + c^2*B(3,3) + ab(\cos\gamma)*B(1,2) + ac(\cos\beta)*B(1,3) + bc(\cos\alpha)*B(2,3)]$

GAS CHROMATOGRAPHY ANALYSIS OF PHENOLIC-CARBON COMPOSITE PYROLYSIS

Kimberly A. Trick
Graduate Research Assistant
Department of Chemical and Materials Engineering

University of Dayton
300 College Park
Dayton, OH 45469

Final Report for:
Graduate Student Research Program
Wright Patterson AFB, OH

Sponsored by:
Air Force Offfice of Scientific Research
Bolling Air Force Base, Washington, D.C.

September 1993

GAS CHROMATOGRAPHY ANALYSIS OF PHENOLIC-CARBON COMPOSITE PYROLYSIS

Kimberly A. Trick
Graduate Research Assistant
Department of Chemical and Materials Engineering
University of Dayton

Abstract

A fundamental step in the processing of carbon-carbon materials is the pyrolysis of cured phenolic-carbon composites. This reaction, which converts the phenolic matrix to one of amorphous carbon, is not well characterized. An understanding of the reaction kinetics could lead to improved processing of carbon-carbon materials. Analysis of the pyrolysis using thermogravimetric analysis and infrared spectroscopy techniques have identified four reaction stages. An investigation of the benefit of using gas chromatography to analyze the gas products of phenolic/carbon composite pyrolysis to further increase the understanding of the reaction kinetics has been made.

GAS CHROMATOGRAPHY ANALYSIS OF PHENOLIC-CARBON COMPOSITE PYROLYSIS

Kimberly A. Trick

1. INTRODUCTION

Carbon-Carbon, a composite material consisting of a carbon fiber in an amorphous carbon matrix, is a low density material which retains excellent mechanical properties to temperatures above 3000°F. [1] While initial research and development of carbon-carbon was pursued to meet the light-weight thermal protection requirements of the space shuttle, it has now found a number of other uses. [1-3] It is used for ablative heat protection in rocket nozzles, as a heat sink and structural friction material in aircraft brakes and race car clutches, in structural components of turbine engines to reduce weight and increase efficiency, and as a biocompatible material.

However, the processing of carbon-carbon is expensive. Long cycle times are required and development of processing cycles is accomplished largely by trial and error. The most common method of manufacturing carbon-carbon is to impregnate a carbon fiber preform with an organic precursor such as phenolic resin. The preform is then pyrolyzed to transform the matrix into amorphous carbon. A cycle of reimpregnation followed by pyrolysis is repeated until the desired part density is achieved.

The first carbonization step, involving pyrolysis of cured phenolic, is considered the longest most critical step in the manufacturing process. To avoid part damage and scrap, first carbonization is performed at very slow rates. The pyrolysis of phenolic resin matrix results in the production of gaseous by-products. The diffusion of these gases through the developing porous matrix is limited. Trapped gases result in stresses within the composite and can cause part defects such as delaminations. Slow heating rates are used to limit gas production and thus keep stresses below a critical value. Because the pyrolysis reaction

is not well understood, a large factor of safety must be used when developing processing cycles. This leads to very long cycle times. Also, the limited understanding of the reaction kinetics requires that process cycles be developed largely by trial and error.

To advance the state of carbon-carbon processing, it is essential that the reaction kinetics of the pyrolysis of the phenolic matrix be understood. Thermogravimetric analysis and infrared spectroscopy techniques have been used to study the weight loss during pyrolysis and the chemical state present at various stages of pyrolysis.[4] These methods have identified four stages of the pyrolysis reaction. It is proposed that gas chromatography analysis of the pyrolysis gas products will provide additional information concerning the reaction kinetics. An experimental set-up and procedure is presented.

2. DISCUSSION OF PROBLEM

Thermogravimetric analysis of Fiberite SC1008 phenolic/carbon prepreg with Amoco heat-treated T300 carbon fibers in an eight-harness satin weave has been reported.[4] Specimens were taken from an eight-ply, warp-aligned composite panel cured to 340°F in an autoclave. The samples, 2.5 cm square, 0.25 cm thick and weighing approximately 2.3 gm, were pyrolyzed in a nitrogen atmosphere. Three constant linear heating rates, 0.5^{o} C/min, 1.0^{o} C/min and 10.0^{o} C/min, were investigated. Thermogravimetric weight loss data was obtained during pyrolysis.

Weight loss curves obtained from thermogravimetric analysis (TGA) are shown in Figure 1. The weight loss curves are seen to shift to higher temperatures with increased heating rate. This is an indication that the controlling reaction mechanism is temperature dependent. The TGA data has been used to estimate the apparent kinetic parameters of the pyrolysis reaction using the Friedman derivative [5] and the Flynn and Dickens isoconversional diagnostic plot [6] methods of kinetic analysis of TGA data. The calculated apparent activation energy is plotted versus fiber-free percent weight remaining in Figure 2. The plot has four regions defined in terms of percent weight remaining. In the first region, from the start of pyrolysis to approximately 90% resin remaining, the overall activation energy is constant at 14 kcal/mol. The

processing temperature ranges from 27°C to 300°C in this first region. In the second region, from 90% to 80% resin remaining, the activation energy increases from 14 kcal/mol to 80 kcal/mol. The third region of the activation energy as a function of percent weight remaining curve extends from 80% to 50% resin weight remaining. The activation energy is constant at 80 kcal/mol. In this region the processing temperature increases from 403°C to 600°C. The higher activation energy during this time of the reaction, when the temperature is higher, would be expected as stronger bonds are likely to be breaking. In the fourth region, below 50% resin weight remaining, the activation energy decreases.

At each of the three heating rates investigated, 0.5° C/min, 1.0° C/min and 10.0° C/min, individual samples were pyrolyzed to 300°C, 400°C, 600°C and 800°C for infrared spectroscopy evaluation.[4] The resulting spectra were analyzed at specific wavenumbers 1320 cm^{-1}, 1256 cm^{-1}, and 1200 cm^{-1} relating to the benzene ring, and 3015 cm^{-1}, 2960 cm^{-1}, 2925 cm^{-1}, and 2853 cm^{-1} associated with aromatic and aliphatic carbon-hydrogen stretches. The progression of the matrix material from phenolic to amorphous carbon was identified in the progressive flattening of the spectra. No rate dependent difference was reported in spectra of samples pyrolyzed at different rates to the same temperature. Evidence of the existence of an intermediate structure, possibly diphenyl-ether, was reported.

This previous work suggests that the pyrolysis reaction can be modeled as a number of steps, each with constant overall apparent kinetics. The analysis of gas products using gas chromatography could help to further define these stages. A description of the application of gas chromatography to the analysis of gaseous by-products of phenolic-carbon pyrolysis, including an experimental set-up and procedure, has been developed.

3. METHODOLOGY

3.1 Gas Chromatography

Gas chromatography is a well understood, widely used analysis technique. [7-11] Chromatographic separation involves the partitioning of a sample between two phases: stationary and mobile. The proportions in which a component distributes itself between the two phases differs for each component of a compound. This difference in mobility results in the different sample components separating into discrete bands. In the case of gas chromatography the sample is vaporized onto the head of a chromatographic column, mixes with an inert carrier gas flow and partitions between this gaseous mobile phase and a stationary liquid phase immobilized on the surface of an inert solid.

The distribution of a component between the mobile and stationary phases can be described by a partition ratio or coefficient, K, which is essentially an equilibrium constant for the transfer of a component between the mobile and stationary phases.

$$K = \frac{C_s}{C_m} \qquad 1$$

where C_S and C_m are the molar concentrations of the component in the stationary and mobile phases respectively. This partition ratio is a function of the sample component, the liquid phase and the column temperature.

The time it takes, after a sample is injected, for a component band to exit the chromatograph is termed the retention time, t_r. The total retention time consists of two parts.

$$t_r = t_m + t_s \qquad 2$$

The first term, t_m, is the dead time and is the time it takes a component which never enters the stationary phase to exit the column. Thus it is the time each component is present in the mobile phase. The

second term, t_s, is the net retention time and is the difference between the total retention time, t_r, and the dead time, t_m. The net retention time of a component is a function of the component's partition ratio. Sample components with high vapor pressure above the stationary phase and weak intermolecular interactions with the stationary phase have a lower partition ratio and leave the column earlier.

The output of a chromatographic process is a time versus response chart which is generated by some type of detector capable of detecting the amount of eluting substance at a given time. Standards must be used to identify the eluting components. Due to axial diffusion of components in the mobile phase and the fact that mass transfer between the mobile and stationary phases is slow relative to the convective mass transfer from carrier gas flow, individual components do not form sharp peaks but rather form bands with gaussian distributions. The efficiency of a chromatographic column is expressed as a relationship between the length of time the solute spends in the column and the amount of band broadening which takes place. Efficiency is characterized by the theoretical plate number, N. The theoretical plate number is calculated from the retention time and peak width as measured on the time axis of the chromatogram.

$$N=5.54(t_r/b_{0.5})^2 \text{ or}$$

$$N=16(t_r/b_B)^2 \qquad 3$$

where t_r is the total retention time, $b_{0.5}$ is the peak width at half height, and b_B is the width at the peak base. Another related term used to describe column efficiency is plate height, H.

$$H=L/N \qquad 4$$

where L is the length of the column. The efficiency of a column increases as the number of plates increases and the plate height decreases. Very high efficiency columns can obtain plate numbers as high at 1,000,000 and plate heights less than 0.1 mm. It is important to note that for the characteristic

plate height and number of plates to be meaningfully used to compare two columns, the same compound must be used in their determination.

The resolution of a chromatogram is a description of the separation of adjacent peaks. The resolution of two peaks is large if the peak widths are small compared to the difference in their retention times. With a low efficiency column it is possible that the widths of adjacent peaks could be so broad they overlap each other. The resolution of a low efficiency column can be increased by adjusting factors which alter the retention times of the components, factors such as the column temperature profile. Thus high resolution is achieved either by high efficiency narrow peaks or large retention time differences. Essentially the degree of resolution and the time necessary for a separation is a function of six parameters. Three parameters, column length, column internal diameter, and film thickness are a function of the column and must be specified when selecting a column. The remaining three parameters, carrier gas, carrier gas velocity, and column temperature are easily changed operational parameters.

In order to use the separation technique of gas chromatography for quantitative and qualitative analysis of samples a detector must be used which generates an electrical signal proportional to the composition of the gas eluting from the column. Either measurement of a physical property of the carrier gas or the sample component alone can be made. Two of the most common detectors are the flame ionization detector (FID) and the thermal conductivity detector (TCD). The FID mixes the effluent from the column with hydrogen and air. The mixture is then ignited electrically and the organic compounds present produce ions and electrons create a current which is recorded. The FID is mass-sensitive, responding to the number of carbon atoms entering the detector per unit time. The TCD is based upon changes in the thermal conductivity of the gas stream brought about by the presence of analyte molecules. The detector consists of two elements, sensing and reference. Pure carrier gas flows over the reference element and effluent gas flows over the sensing element. The difference in thermal conductivity between the carrier gas and effluent gas determines the detector's response. The TCD is concentration-sensitive, responding to the concentration of a component in the carrier gas.

Gas chromatographs are also coupled with mass spectrometers which serve not only to detect the appearance of analytes but also provide information about their identity. The gas chromatograph/mass spectrometer is the combination of two analytical investigative instruments. Basically, the gas chromatograph is used to separate a mixture so that each component is individually introduced into the mass spectrometer for analysis. The mass spectrometer is useful for identification and determination of the structure of a compound. It provides information on the sample molecular weight and the pieces that constitute the sample molecules. A molecule is passed through an electron beam where is becomes ionized and/or breaks into fragment ions. Once the ions are formed they are detected and analyzed by various methods. Such methods include: time-of-flight which measures the time it takes for ions to travel a given distance, magnetic sector which determines the magnetic force needed to bend the ion path, and quadrupole methods which use oscillating fields to control ion path. In all methods the ion mass is detected.

3.2 Application of GC to Phenolic Pyrolysis

Gas chromatography coupled with a mass spectrometer has been used to investigate the reaction kinetics of phenolic pyrolysis. [12-15]. Ouchi and Honda [15] worked with neat phenolic resin and reported species evolved as a function of temperature range as listed in Table 1.

Seibold [14] used this data as well at TGA data reported by Ouchi and Honda to estimate the volume of individual gases produced during phenolic pyrolysis. Seibold's findings are listed in Table 2.

4. EXPERIMENTAL PROCEDURE

To further investigate the pyrolysis of phenolic/carbon composite material, an experimental set-up and procedure using gas chromatography to analyze gas products is proposed. It is known that both fixed gases, such as carbon dioxide, carbon monoxide and hydrogen, and higher molecular weight substances, such as phenol and cresol, are products of the pyrolysis process. The

Table 1 Gases Evolved from Phenolic Pyrolysis as a Function of Temperature[15]	
Temperature Increment ^{o}C	Species Evolved
100 - 200	H_2O
200 - 300	LMS *
300 - 400	H_2O, LMS *, CO_2
400 - 500	H_2O, LMS *, CO_2, C_2H_6, H_2, CO, CH
500 - 600	H_2O, CO_2, C_2H_6, H_2, CO, CH_4
600 - 700	H_2O, CO_2, C_2H_6, H_2, CO, CH_4
700 - 800	H_2O, H_2, CO

* LMS = lower molecular substances.

Table 2
Volume of Gases Evolved by Pyrolysis of Phenolic Resin [14]

TEMPERATURE INCREMENT*		VOLUME OF GASES EVOLVED (ML/G)**								CUMULATIVE
°C	°F	H_2O	LMS	CO_2	C_2H_6	H_2	CO	CH_4	TOTAL	TOTAL (ML/G)***
100-125	212-257	7.56							7.56	7.56
125-150	257-302	11.25							11.25	18.81
150-175	302-347	15.95							15.95	34.76
175-200	347-392	7.00	27.01						34.01	68.77
200-225	392-437	1.89	5.96						7.85	76.62
225-250	437-482		6.13						6.13	82.75
250-275	482-527		6.32						6.32	89.07
275-300	527-572		8.14						8.14	97.21
300-325	572-617	2.29	10.15	0.02					12.46	109.67
325-350	617-662	7.17	13.90	0.03					21.10	130.77
350-375	662-707	13.03	15.77	0.04					28.84	159.61
375-400	707-752	21.70	20.25	0.04	0.01				42.00	201.61
400-425	752-797	25.40	20.79	0.04	0.01	0.44			46.68	248.29
425-450	797-842	23.90	17.95	0.05	0.02	1.85	0.64	0.82	46.23	293.52
450-475	842-887	18.80	9.17	0.07	0.02	3.87	1.54	1.67	34.94	328.07
475-500	887-932	14.95	2.01	0.08	0.04	12.60	3.90	4.37	38.03	366.40
500-525	932-977	11.20		0.09	0.08	20.00	9.23	6.43	47.03	413.52
525-550	977-1022	10.50		0.10	0.09	29.00	9.32	10.15	59.16	472.68
550-575	1022-1067	9.80		0.15	0.13	38.20	8.32	12.50	70.10	542.78
575-600	1067-1112	8.30		0.16	0.15	43.80	11.70	13.70	78.01	620.79
600-625	1112-1157	7.87		0.12	0.13	51.30	8.33	9.30	76.25	697.04
625-650	1157-1202	6.86		0.11	0.11	51.50	6.46	8.20	74.52	771.56
650-675	1202-1247	7.35		0.12	0.10	52.20	6.84	4.28	70.89	842.45
675-700	1247-1292	7.54		0.11	0.07	48.60	6.83	3.30	66.65	909.10
700-725	1291-1337	4.85		0.06	0.03	40.50	5.13	1.14	60.70	969.80
725-750	1337-1382	4.25		0.03	0.01	46.00	4.17	0.50	57.04	1026.84
750-775	1382-1427	3.24		0.02		43.60	2.17		49.03	1075.87
775-800	1427-1472	2.92		0.01		31.10	1.92		35.95	1111.82
800-825	1472-1517	2.47				25.10	1.14		28.71	1140.53
825-850	1517-1562	2.19				19.56	0.56		22.32	1162.85
850-875	1562-1607	2.30				17.80			20.19	1183.04
875-900	1607-1652	2.19				15.84			18.03	1201.07

* PYROLYSIS RATE = 2°C/MINUTE
** THE VOLUMES SHOWN ARE THE VOLUME OF GASES EVOLVED AT THE GIVEN 25°C TEMPERATURE INCREMENT
*** THE CUMULATIVE TOTAL VOLUME IS THE SUM OF THE VOLUME OF GASES EVOLVED AT THE GIVEN 25°C TEMPERATURE INCREMENT PLUS THE VOLUMES EVOLVED AT THE PREVIOUS INCREMENTS

developed procedure consists of two separate set-ups, one for the analysis of the fixed gases and one for analysis of the higher molecular weight substances. The fixed gases are analyzed using a gas chromatogram equipped with a TCD detector. During pyrolysis of the composite in a Cahn thermobalance, grab samples are taken from the vent line of the balance and directly injected into the gas chromatograph. Standards are used to identify the gas products and perform qualitative analysis The higher molecular weight products are analyzed using gas chromatography coupled with mass spectrometry. During pyrolysis of the composite in a tube furnace, effluent gas samples are condensed in a cold trap. The condensed material is then dissolved in an appropriate solvent such as normal hexane and subsequently analyzed using a gas chromatogram coupled to a mass spectrometer for qualitative and quantitative analysis.

The same sampling matrix is used for analysis of fixed gases and higher molecular weight products. Effluent gas samples are obtained and analyzed at 25° increments in the temperature range of 300°C to 800°C. Additional samples are obtained at isothermal holds of 400°C, 525°C, 600°C and 800°C. The entire sampling matrix is repeated at three linear heating rates, 0.5°C/min, 1.0°C/min, and 10.0°C/min.

5. CONCLUSION

Investigation of the literature and analysis of earlier experimental work has led to the development of a procedure to use gas chromatography to further analyze the reaction kinetics of phenolic-carbon pyrolysis. The procedure is designed to further define the four stages of reaction identified by previous investigation using thermogravimetric analysis and Fourier transform infrared spectroscopy.

6. REFERENCES

1. Brahney, "Carbon-Carbon Heat Means Strength," ***Aeorspace Engineering***, June 1987.

2. Buckely, J.D., "Carbon-Carbon, an Overview," ***Ceramic Bulletin***, Vol. 67, No. 2, 1988.

3. Reed, I., "A True Case of Black Magic," ***Autoweek***, Aug. 10, 1987, pp 38-39.

4. Trick, K.A. and T.E. Saliba, "Pyrolysis Reaction Kinetics: A Critical Knowledge For Intelligent Processing Of Carbon-Carbon" ASC 8th Technical Conference, Oct. 19-21 1993, Cleveland OH.

5. Friedman, H.L.,"Kinetics of Thermal Degradation of Char-Forming Plastics from Thermogravimetry. Application to a Phenolic Resin.," ***Journal of Polymer Science:Part C***, No. 6, 1964, pp 183-195.

6. Dickens, B. and J.H. Flynn, "Thermogravimetry Applied to Polymer Degradation Kinetics," ACS Advances in Chemistry Series Vol. 20B, C.D. Craver, Ed., ACS, Washington, D.C., 1983, pp 209-232.

7. Skoog D.A. and J.J. Leary, ***Principles of Instrumental Analysis 4th ed.***, Saunders College Publishing, New York, 1992,.pp 579-627.

8. Schomburg G., ***Gas Chromatography: A Practical Course***, VCH Publishers Inc., New York, 1990.

9. Cowper, C.J. and A. J. DeRose, ***The Analysis of Gases by Chromatography***, Pergamon Press, New York,1983.

10. Freeman, R.R., ***High Resolution Gas Chromatography Second ed.***, Hewlett-Packard Co., 1981.

11. Jennings, W., ***Gas Chromatography with Glass Capillary Columns Second ed.***, Academic Press, New York,1980.

12. Sullivan, E., "Thermal Degradation of Epoxy Novolac-Phenol Formaldehyde Novolac Resin Systems", ***Journal of Applied Polymer Science***, Vol 42, 1991, pp 185-1827.

13. Pardee, W. J., M. R. Mitchell and A. Gupta, "Effect of Carbonization Kinetics on In-Process Mechanical Properties," in ***Intelligent Processing of Materials, ed.*** Wadley and Eckhart, The Minerals, Metals & Materials Society, Warrendale, PA, 1990, 195-205.

14.Seibold, R. W., "Carbonization of Phenolic Resin", MDAC Paper WD 2426, McDonnell Douglas Astronautics Company -West,January 1975.

15. Ouchi, K. and H. Honda, "Pyrolysis of Coal I-Thermal Cracking of Phenolformaldehyde Resins Taken As Coal Models", ***Fuel***, Vol. 38, 1959, pp 429-443.

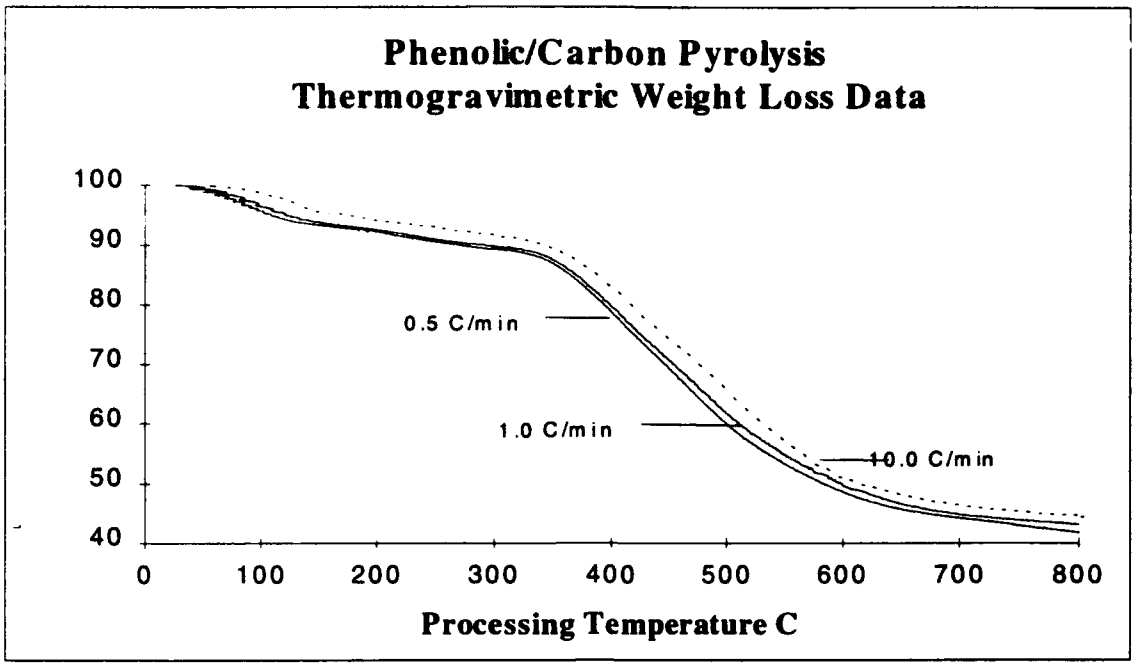

Figure 1 - Phenolic/carbon composite thermogravimetric analysis. Percent resin remaining as a function of process temperature when heated at constant linear heating rates of 0.5°C/min, 1.0°C/min, and 10.0°C/min. [4]

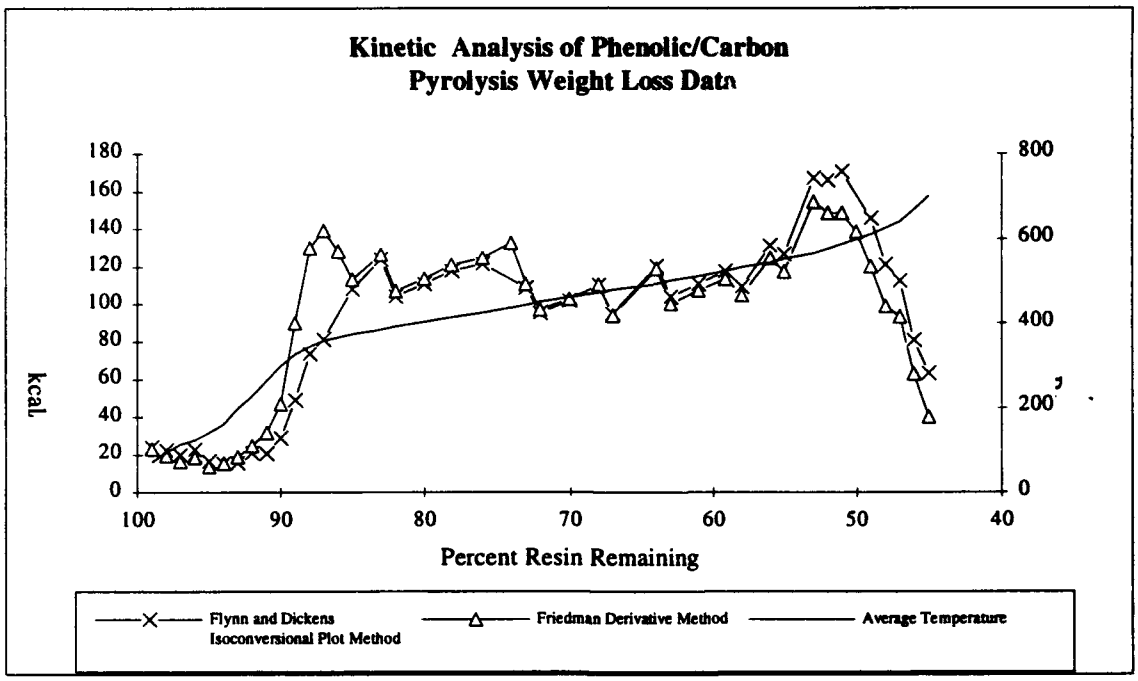

Figure 2 - Kinetic analysis of phenolic/carbon composite thermogravimetric data. Apparent activation energy as a function of percent resin remaining.[4]

SUPERRESOLUTION OF PASSIVE MILLIMETER WAVE IMAGES

Paul Burns
Graduate Student
Department of Electrical Engineering

Auburn University
Auburn, AL 36849

Final Report for:
Summer Graduate Student Research Program
Wright Laboratory/MNGS
Eglin Air Force Base, FL 32542-5434

Sponsored by:
Air Force Office of Scientific Research
Bolling Air Force Base, Washington D. C.

August 1993

Superresolution of Passive Millimeter-Wave Images

Paul D. Burns
Graduate Student
Department of Electrical Engineering
Auburn University

Abstract

Techniques for the reconstruction of millimeter-wave images were investigated. Computer simulations were run for constrained iterative deconvolution (CID) and fast constrained iterative deconvolution (FCID). A new approach to FCID is described. The results of each of these simulations are presented and their effectiveness is evaluated.

Superresolution of Passive Millimeter-Wave Images

Paul D. Burns

Introduction

Passive millimeter-wave imaging has shown promise to be an effective imaging sensor under atmospheric conditions that would seriously impede the performance of infrared sensing devices. Fog, rain, smoke, and dust are all examples of conditions which hamper the performance of infrared sensors. They do not, however, seriously attenuate millimeter-wave frequencies. The trouble with millimeter-wave (MMW) images is their low cross range resolution. This low resolution severely limits its usefulness. However, the resolution may be increased by digital signal processing techniques. This paper explains the superresolution algorithms I explored with the purpose of remedying this inherent problem of millimeter-wave imaging. It then describes the outcome of the simulations I wrote testing each approach.

Background

The problem of image reconstruction arises in the case of passive millimeter-wave imaging with the blurring effect of the antenna and noise corruption from sensors. It turns out that the antenna blurring can be modeled as a convolution operation between an uncorrupted image and the antenna's point spread function [1]. Hence, this problem can be classified as a deconvolution problem. That is, since the antenna acts essentially as a linear system, one can undo its effects on an image by some sort of inverse filtering.

Since the antenna pattern is assumed to be known, the direct approach would be to pass the blurred image through a system which is the actual inverse of the point spread function. However, antenna patterns are generally low pass, so inverting them will result in extreme overamplification of high frequency noise (where the fourier transform of the point spread

function is zero.) Perhaps the best approach to this is to come up with an iterative scheme which attacks the problem indirectly and whose progress can be monitored.

Another important point is that the reconstruction cannot be done by a linear system. This is because part of the image's spectrum is cut off by the low-pass filtering of the antenna. Therefore, in order for a reconstructive approach to be effective, it must be able to restore lost frequencies. This cannot be done with a linear system, so a nonlinear approach is needed. Here, the iterative approach is useful again in that it can be nonlinearized by using nonlinear constraints. In fact, this is just what is done in constrained iterative deconvolution (CID).

Simple iterative deconvolution is just inverse filtering, iteratively. To illustrate how it is done, let the fourier transform of the antenna pattern be $H(\omega)$. Next define $T(\omega)=1-\lambda H(\omega)$. Notice that

$$\lambda/(1-T(\omega)) = \lambda/[1-(1-\lambda H(\omega)) = 1/H(\omega),$$

and that

$$\lambda/(1-T(\omega)) = \lambda\sum^{\infty}_{n=0} T^{n}(\omega)\,. \qquad (1)$$

Hence the antenna's inverse can be obtained by iteratively adding terms to the geometric sum in (1). Convergence of the sum is garanteed if $|T(\omega)|=|1-\lambda H(\omega)|<1$, for all ω. Hence, λ must be chosen to ensure that the sum converges. Without constraints, however, computing this sum will just give the inverse system - which is undesireable.

In CID, nonlinear constraints are applied to the sum iteratively. In this case, we used a nonnegativity constraint, which clips all negative portions of the iterative output to zero. This constraint is based on the knowledge that the noncoherent received signal should be nonnegative. The following is the CID update equation.

$$x_{k+1}(n) = C[\lambda y(n)+t(n)*x_k(n)]$$

$x_k(n)$ is the kth estimate of the high resolution image and $y(n)$ is the blurred image. C represents

the nonlinear constraint operator and * represents the linear convolution operator. The constraint, C, allows the blurred image to increase its high frequency content - effectively increasing its resolution.

The problem with CID is the large number of computations required to reasonably restore the image. This makes it expensive to implement in real time. To improve its efficiency, Richards et al [1] developed the fast constrained iterative convolution (FCID) algorithm. FCID works by changing the way the geometric sum for $H^{-1}(\omega)$ is constructed. Instead of just adding one term to the sum each iteration, one rewrites the sum as

$$(1+T(\omega))(1+T^2(\omega))(1+T^4(\omega)) \ldots = \prod_{m=0}^{\infty}(1+T^b(\omega)), \text{ where } b=2^m.$$

As this product is expanded, one can see that each product term adds the equivalent of 2^m terms to the geometric series in equation (1). This greatly increases the rate at which the sum is computed, but the number of times the nonlinear constraint is applied is decreased in direct proportion. This causes problems with performance which will be outlined below. The update equations used for FCID are

$$x_{k+1}(n)=C[x_k(n)+t_k(n)*x_k(n)] \quad \text{and}$$

$$t_{k+1}(n)=t(n)*t(n)$$

where * indicates convolution and C represents the nonlinear constraint. It is assumed that $x_0(n)=\lambda y(n)$, where y(n) is the received image. A problem with FCID is its instability. The algorithm often converges for a few iterations, but it will diverge suddenly. The progress of the algorithm can be monitred, however, but only at the cost of complicating things and slowing convergence. Another problem is that it has bad asymptotic properties. That is, if left alone, FCID won't converge to a single solution. In fact, it will continue to spread the image's spectrum into high frequencies indefinitely. A side effect of this tendency is to force everything in the image to be point targets. Ad hoc solutions to these two shortcomings of FCID were presented in [1], but they do not overcome the problems well enough to make FCID a feasable algorithm

when dealing with extended targets.

One way was found which improves the performance of the FCID algorithm. If the assumption is made that target features are strictly dictated by edges in an image, then those features will appear as spikes in the derivative image. Since FCID tends to enhance spikes, it is natural to think that FCID would restore the derivative image better than the original. One potential problem is the noise amplification properties of differentiation. This could be largely overcome with a low-pass filter before FCID is applied, however. Because of the nonnegativity constraint that was used, FCID cannot restore the derivative image directly (while the original image is strictly nonnegative, its derivative has no such restriction). One must split the derivative into its positive and negative halves and perform the FCID algorithm separately on each.

Our own version of the FCID takes advantage of its high frequency enhancing properties. We differentiated the image, divided it into its positive and negative parts, applied FCID to each half, and recombined and integrated the final result to obtain the resolution enhanced image. This is called the differentiate, integrate, and deconvolve (DID) method. Figure 1 illustrates this process in a block diagram. DID can also be implemented using the original CID algorithm, or any image reconstructing algorithm for that matter. In fact, using CID in the DID guideline significantly improves the quality of image reconstruction over the original CID. The computational requirements, however, are greater than that of CID alone.

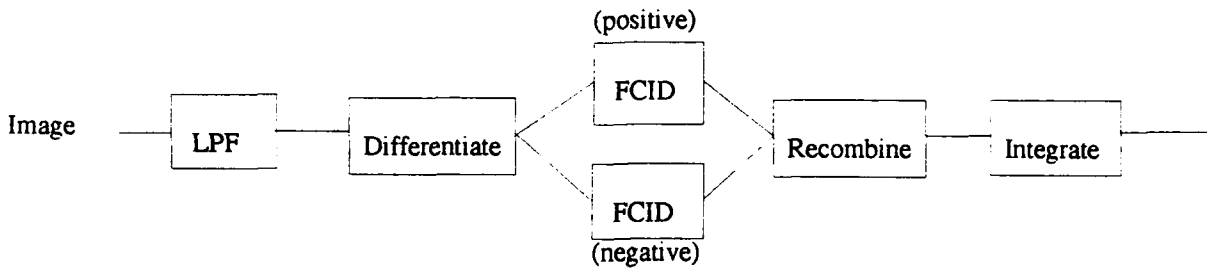

Figure 1: Block diagram of DID scheme

Simulation Results

All of the following simulations were written in the C programming language by the author. The computing was performed on a Sun workstation. The simulations were intended to illustrate the performance of CID, FCID, and the new DID (in conjunction with FCID) and to evaluate the latter under the influence of various antenna widths and SNR's. The simulations are first presented for the noise-free case to illustrate the performance of stand-alone CID and FCID. Next, a more extensive study of DID incorporating FCID is presented.

The artificial one-dimensional image that is used for all of the performance simulations here is shown in Figure 2. Since no previous results were available on the performance of FCID on extended targets, we constructed an image with a target having a wide span. This image was convolved with the antenna pattern, which was a sinc^2 pulse, to obtain the blurred image. This noiseless blurred signal (see Figure 3) was deblurred by the CID algorithm. Many of the features that were lost in the blurred signal were restored after implementing the algorithm. The restored image is shown in Figure 4. The problem is that it takes many iterations in order for CID to reasonably restore an image. The image shown resulted after 50 iterations.

The fast CID algorithm takes much fewer iterations to get to the same point in the geometric series as the slow algorithm. However, as you can see in Figure 5, the restored image looks nothing like the original (after 25 iterations). The reason is because of the algorithm's tendency to overemphasize high frequencies. This tendency is, in turn, a result of the algorithm's bad asymptotic properties. The corrective approach (taking the derivative and separating the positive and negative parts) resulted in better restoration. However, an exhaustive test was performed to more thoroughly evaluate the new approach to the FCID. Figures 6-11 illustrate the results using this method for the extended target. The deblurred images show the steps quite a bit better than the blurred images. The quality of the deblurred images depends on the width of the

main lobe of the antenna's point spread function and the severity of the noise.

There are three parameters that I varied to test the performance of DID: the value of lambda, the SNR caused by sensors and various electronic equipment, and the width of the antenna's main lobe. The value of lambda that was chosen is 0.03. It was found that a larger value would cause the algorithm to be unstable, but decreasing its size tended to dull the effectiveness of the restoration. The relative power of the noise didn't become a significant factor until the SNR dipped below 30 dB or so. At 20 dB, the noise is severe enough to be felt through the differentiation process. Therefore, with more severe noise, the spikier the image is at the input to FCID. One would expect, then, that the output of the FCID's will be garbled with spikes resulting from the noise. This distortion is minimized, however, by the integration. The steps that appear at the output of the algorithm are caused by the spikiness of the FCID output. When this is integrated, it appears as a series of small steps. As the noise gets stronger, the steps grow larger.

The width of the antenna's point spread function limits the algorithm in its ability to restore features of a target. For larger beamwidths, the algorithm has an increasingly difficult time restoring the image. In the simulations, the one-dimensional images were composed of 256 points. In the original unblurred image, the steps have a width of 50 points. When the ant beamwidth is 35 or less, the DID can give reasonable results (see Figure 6.) However, whe .e width approaches or exceedes 50 (the width of the steps in the example image), then the amount of restoration decreases rapidly (Figures 10-11.) Even for the wider beamwidths, however, the output of the algorithm uncovers some crude features that aren't present before it is applied.

One unfortunate side effect of using FCID to implement DID is caused by FCID's insensitivity to relative amplitudes. The algorithm is good at detecting edges, but doesn't necessarily preserve their relative sizes. Therefore, when the output of the FCID's are recombined and integrated, the rough features are present, but, as can be seen in Figures 6-11,

there is some error where the image doesn't return to zero. The severity of this distortion is mainly dependent on the antenna beamwidth.

Conclusions

The FCID algorithm was indeed faster than the slow CID, but its convergence properties are undesireable and it fares poorly when one is interested in deconvolving extended targets from the antenna pattern. I have tried to improve the latter deficiency of FCID using the DID scheme outlined above. While the scheme does indeed improve FCID's response to extended targets, it doesn't give a startling improvement in resolution compared to the slow CID. For the computational cost, however, the method is a good improvement. DID works better when coupled with the slower CID algorithm [3], but the computational cost is greater.

Bibliography

[1] M. Richards and C. Barnes, "Super Resolution in Low Signal-to-Clutter Ratios for Millimeter Wave Seekers," AFATL-TR-90-62, Air Force Armament Laboratory, Eglin AFB, September 1990.

[2] Z. Ding, "Resolution Enhancement of Passive Millimeter Wave Imaging," AFATL technical document, Air Force Armament Laboratory, Eglin AFB, August 1993.

Figure 2: Original Image

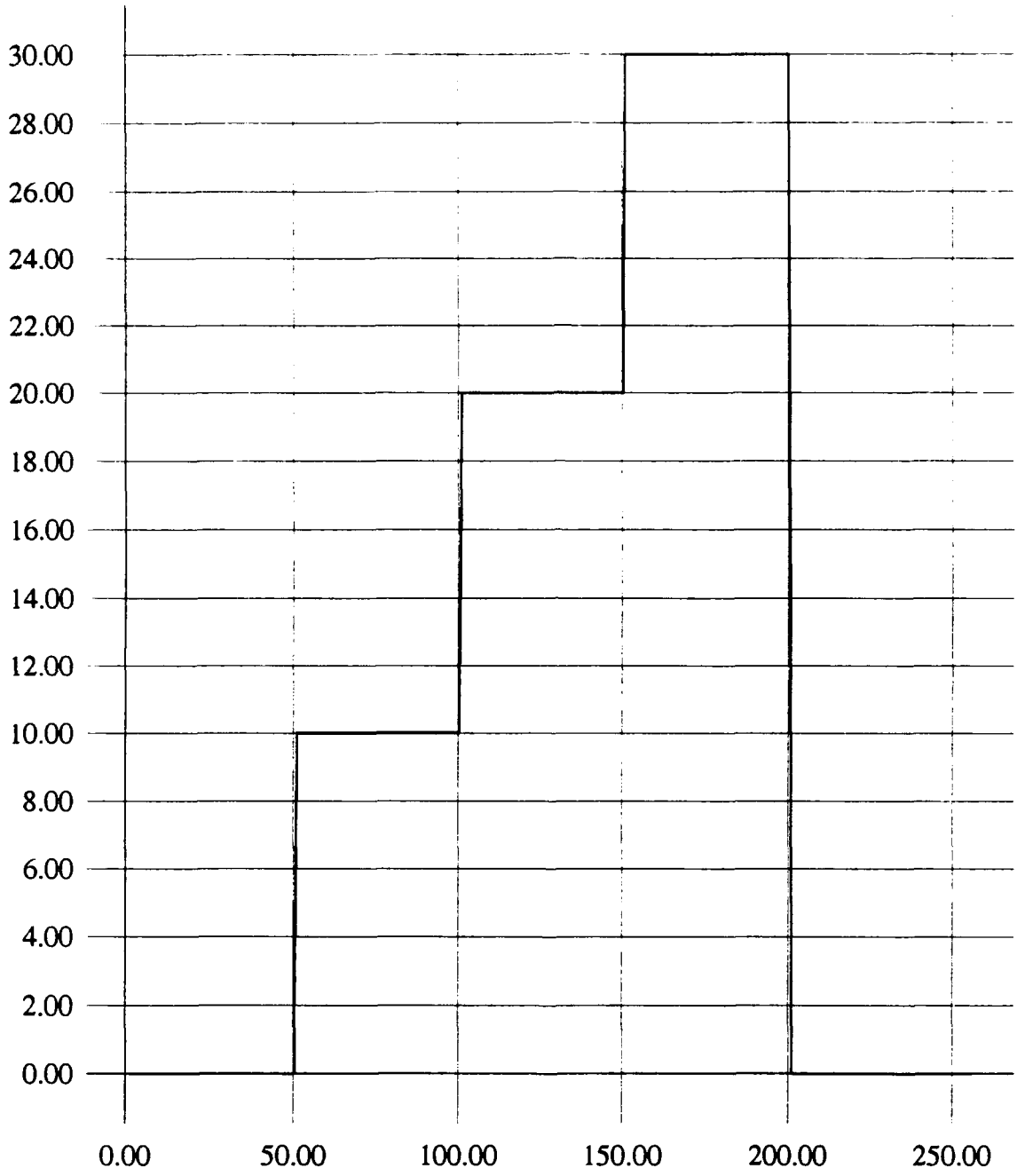

Figure 3: Noiseless blurred image

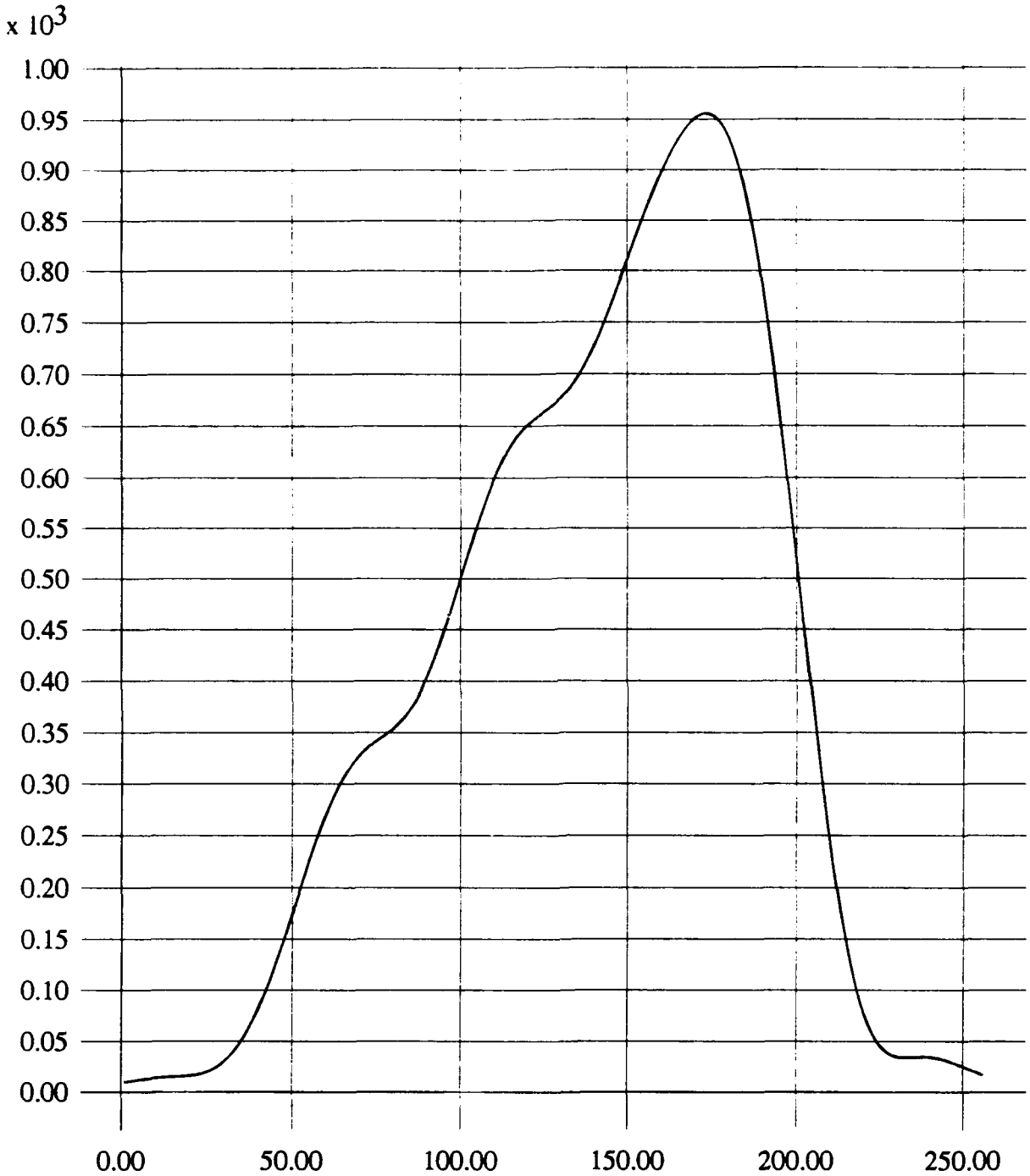

Figure 4: Noiseless reconstruction by CID after 50 iterations

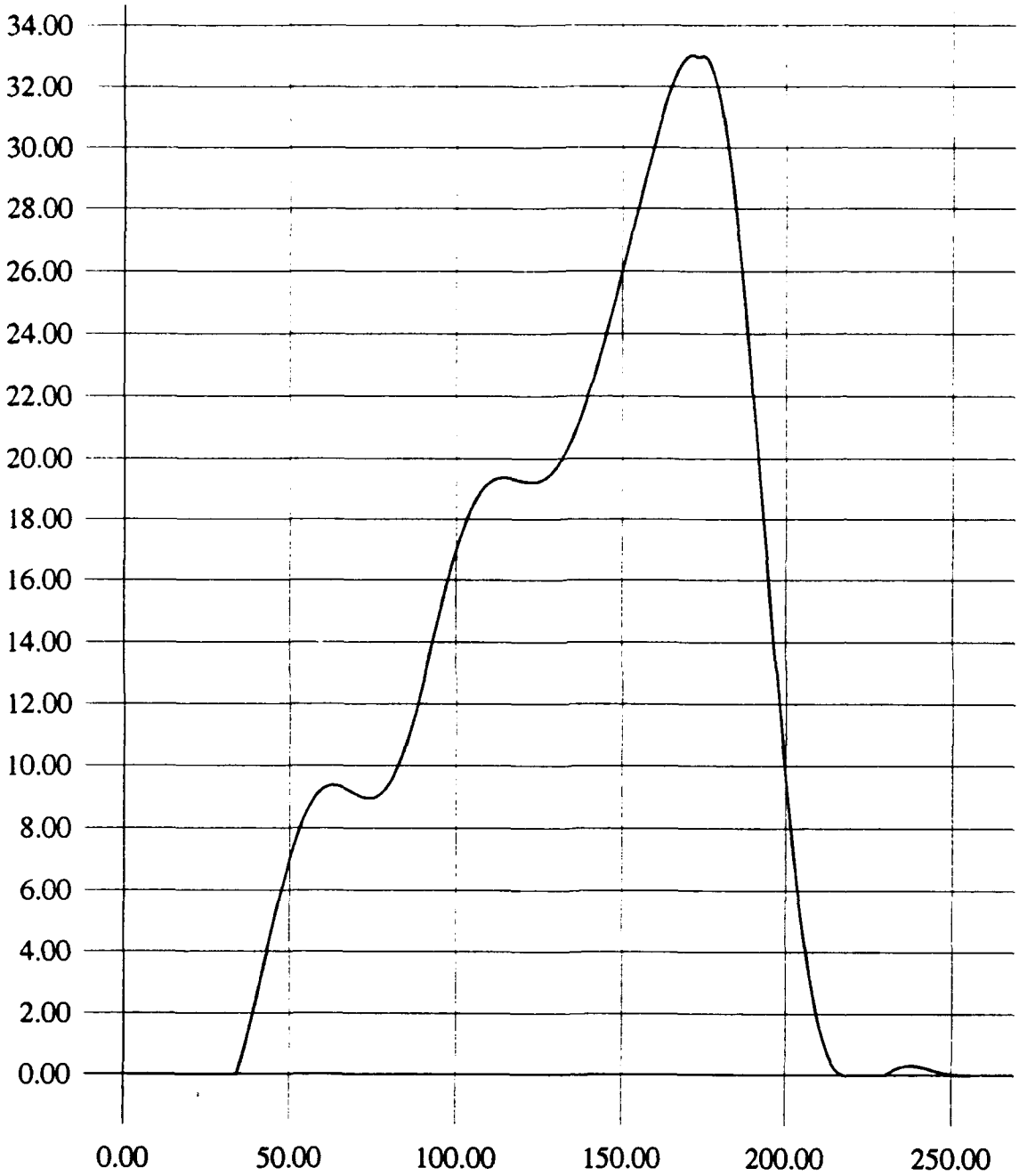

Figure 5: Noiseless reconstruction using FCID after 25 iterations

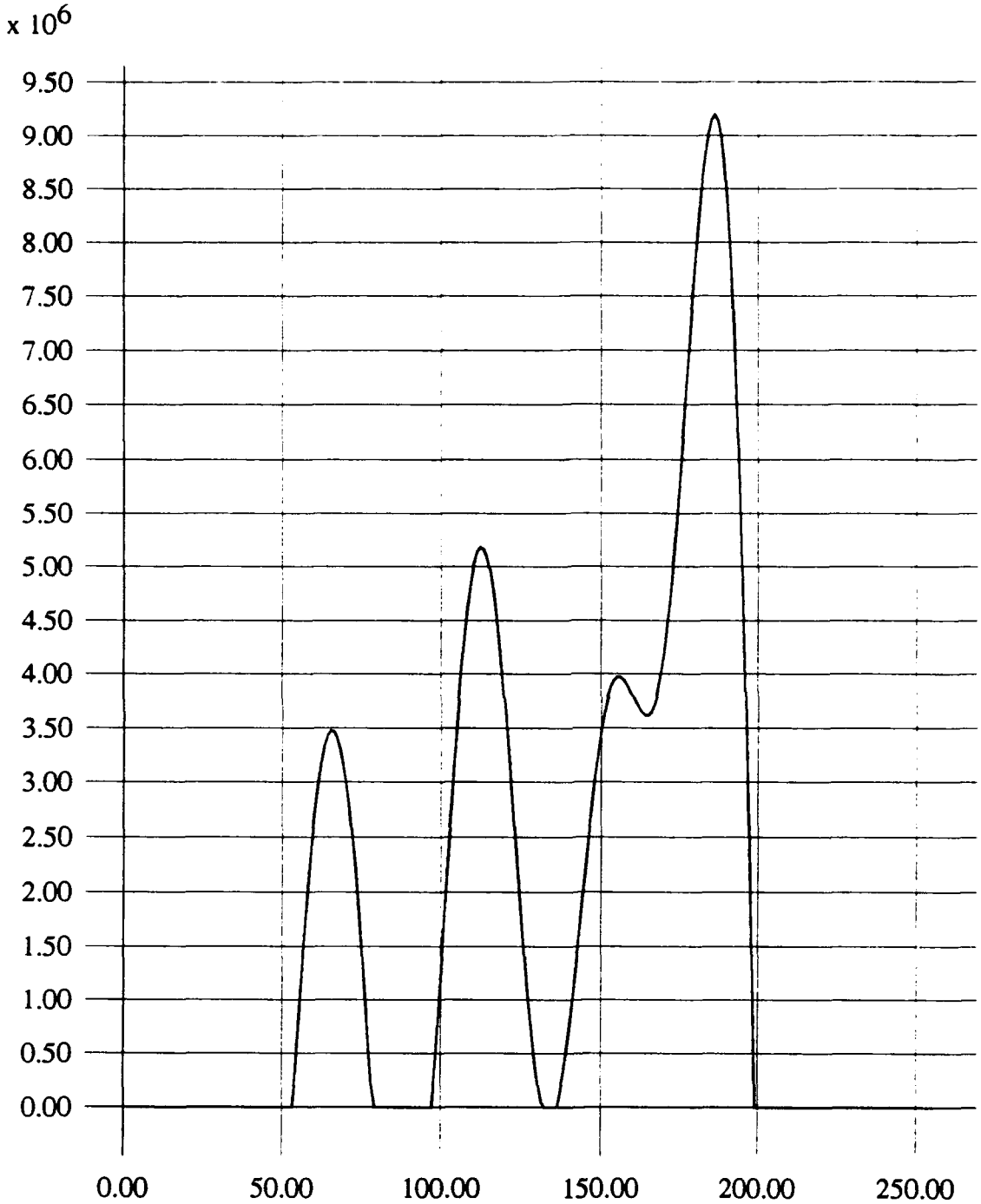

Figure 6: DID noiseless reconstruction with a beamwidth of 35

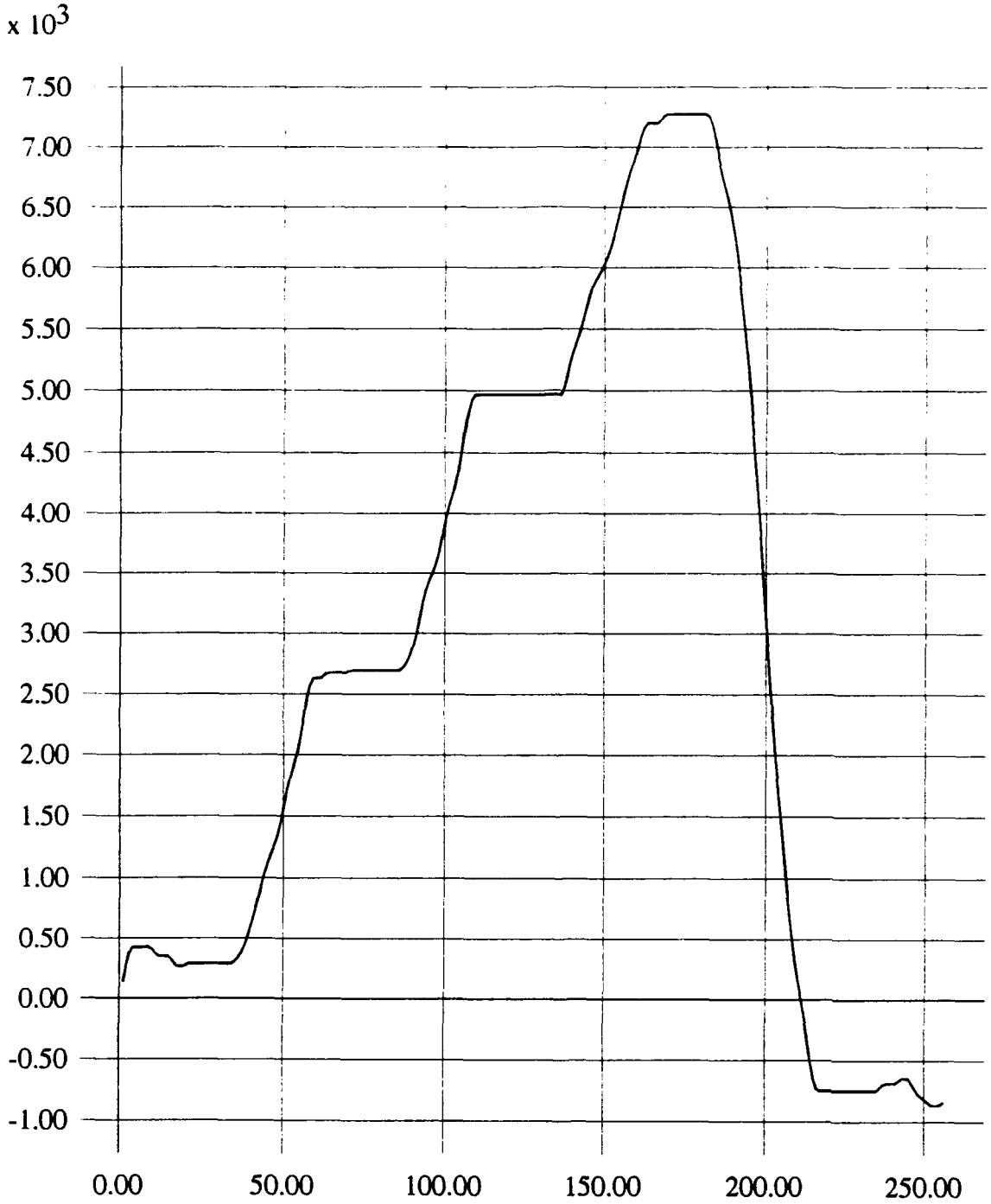

Figure 7: DID with antenna beamwidth 35 and SNR 30 dB

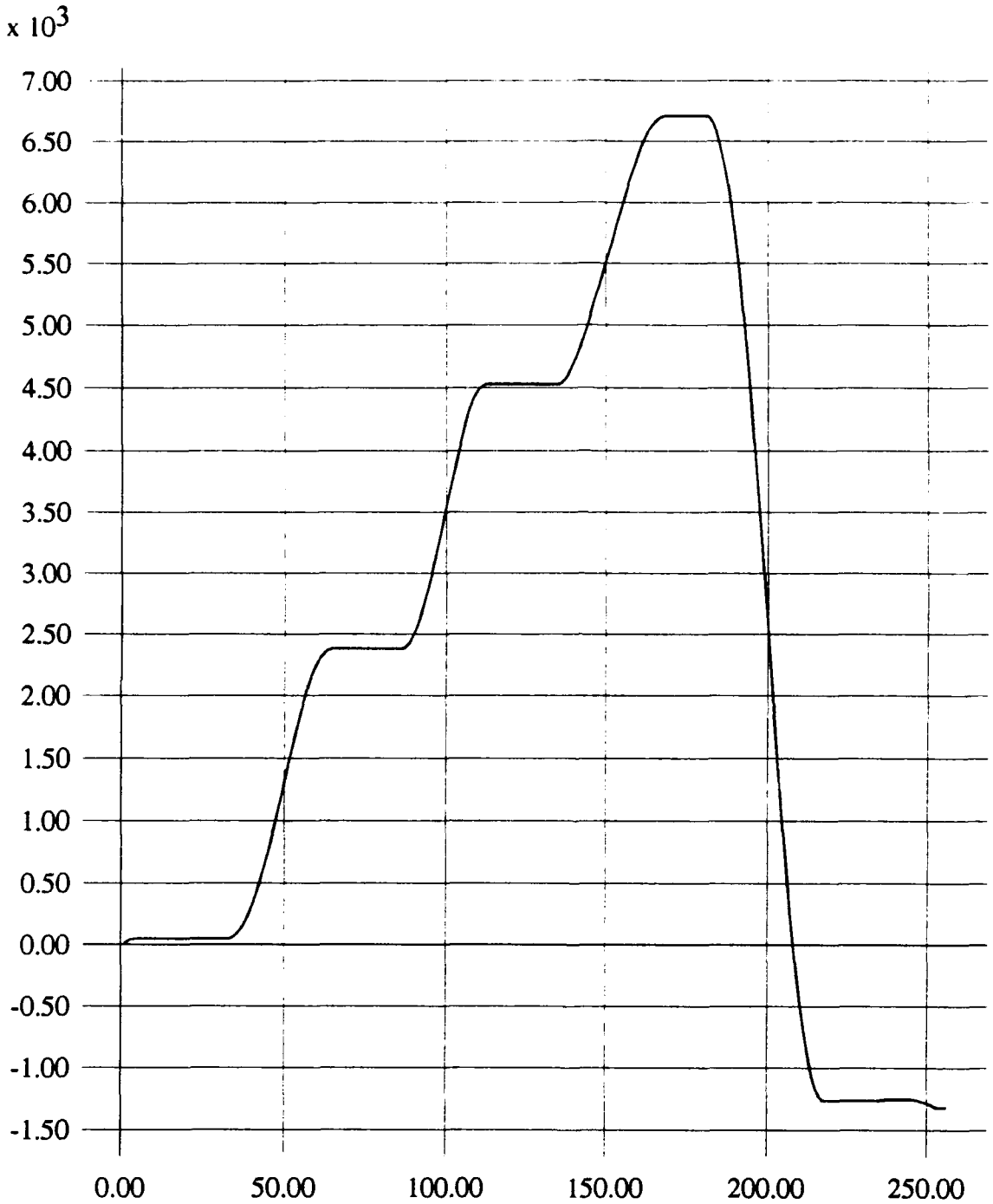

Figure 8: DID with antenna beamwidth 35 and SNR 20 dB

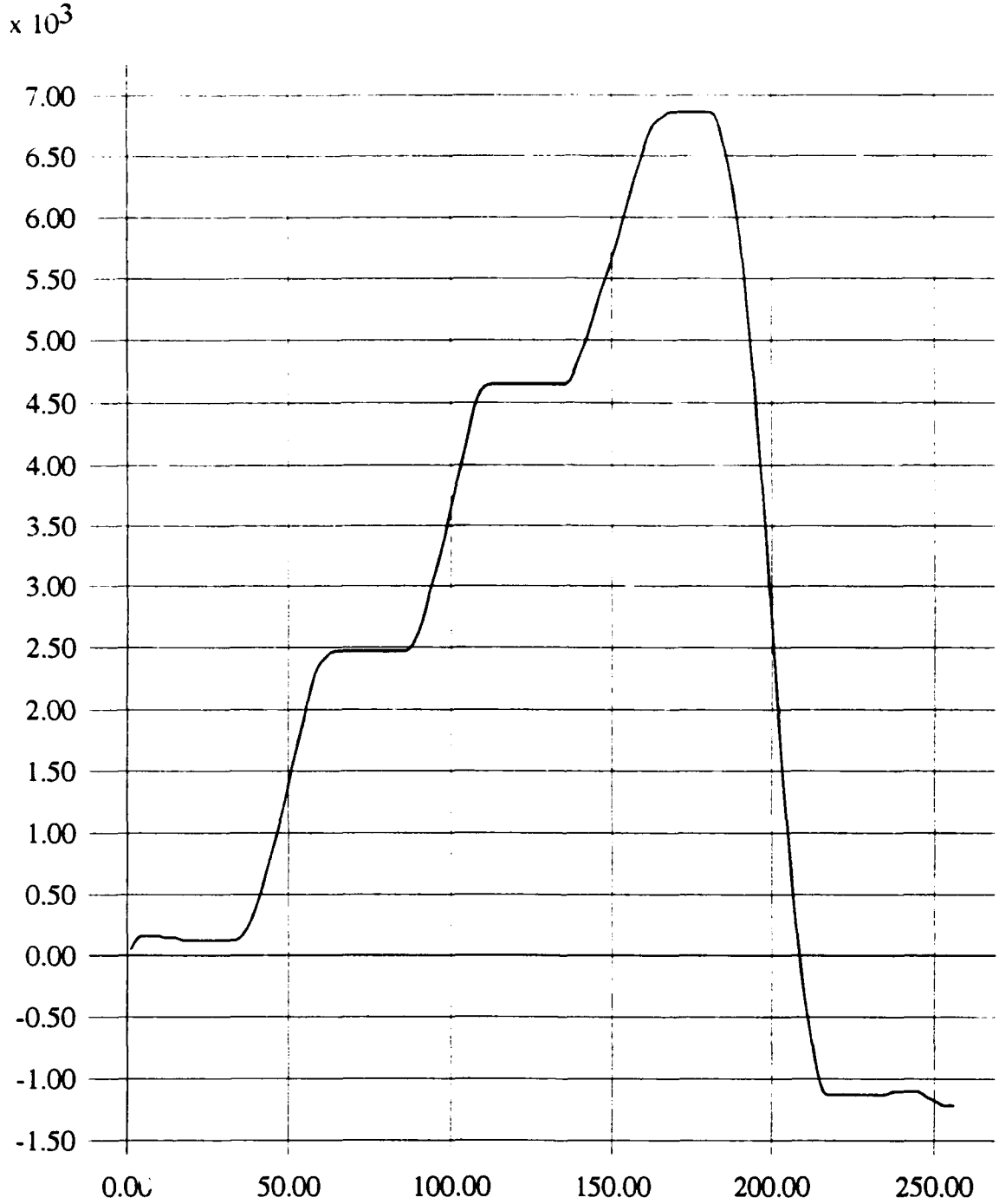

Figure 9: DID with antenna beamwidth 35 and SNR 15 dB

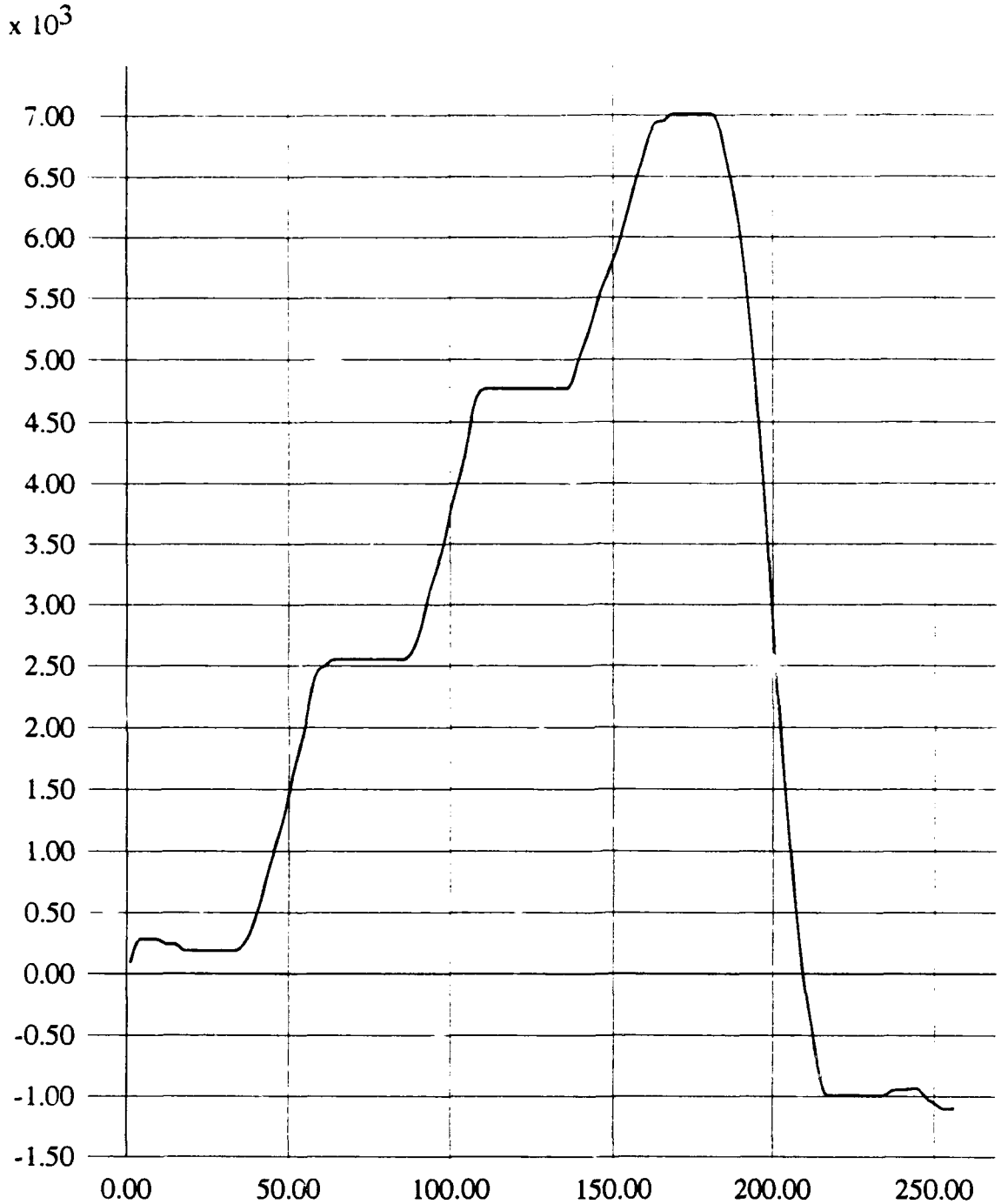

Figure 10: DID with antenna beamwidth 45 and SNR 30 dB

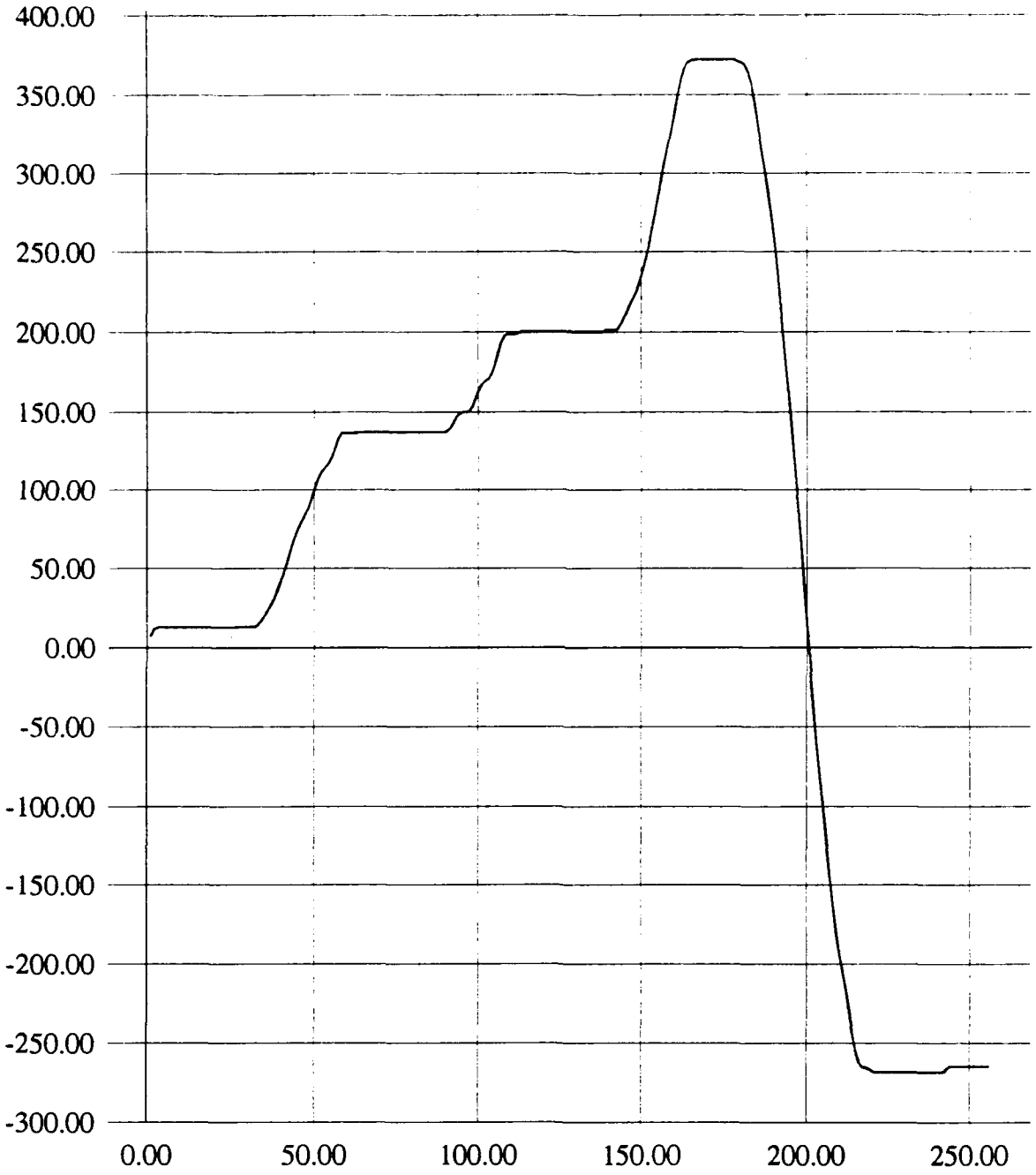

Figure 11: DID with antenna beamwidth 55 and SNR 30 dB

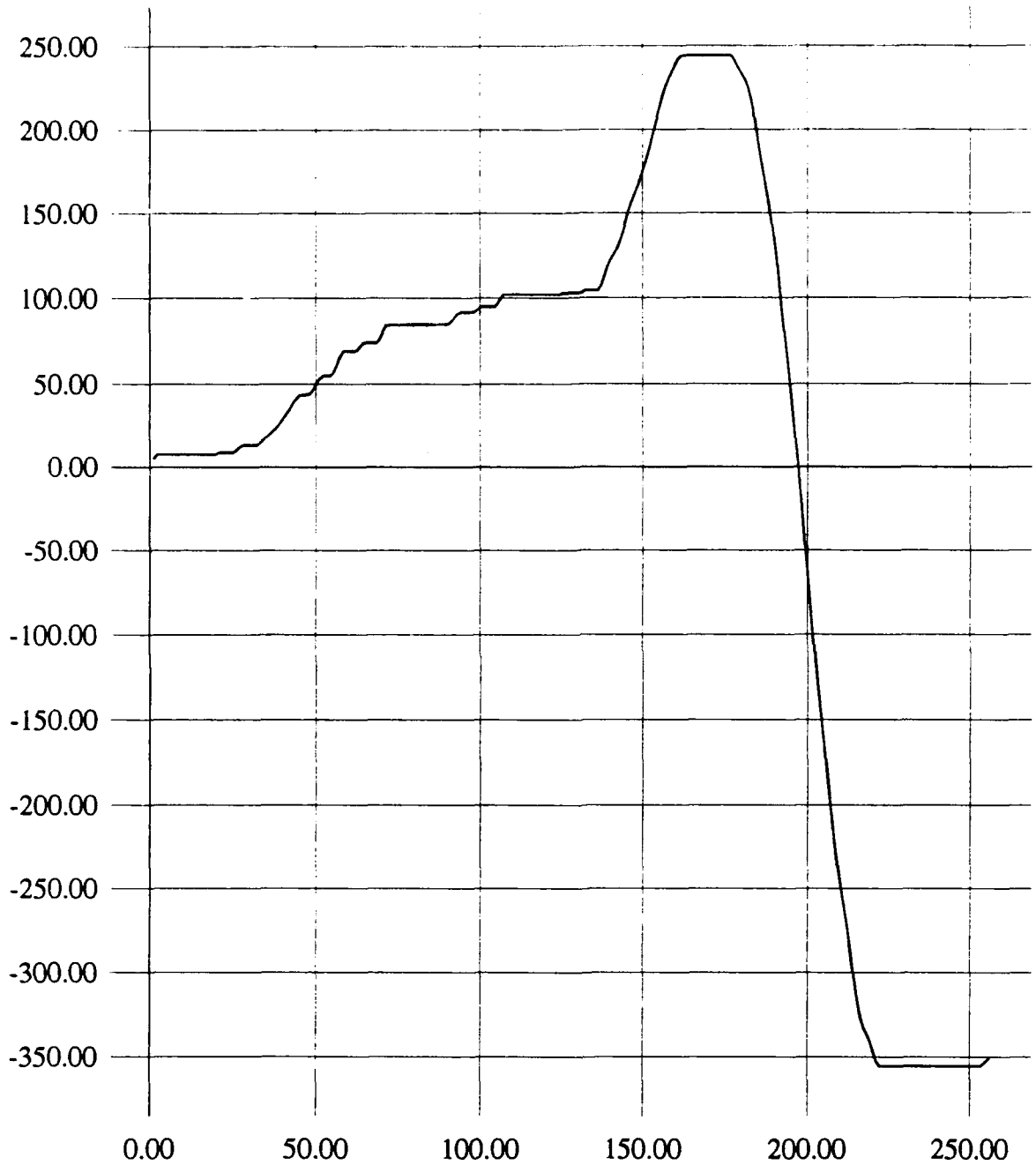

INFLUENCE OF PENETRATOR AND TARGET PROPERTIES ON PENETRATION MECHANICS

E. Eugene Callens, Jr.
Associate Professor
J. Scott McMurtry
Graduate Student
Department of Mechanical and
Industrial Engineering

Louisiana Tech University
Ruston, LA 71272

Final Report for:
Summer Research Program
Wright Laboratory

Sponsored by:
Air Force Office of Scientific Research
Bolling Air Force Base, Washington, D.C.

September 1993

INFLUENCE OF PENETRATOR AND TARGET PROPERTIES ON PENETRATION MECHANICS

E. Eugene Callens, Jr.
Associate Professor
J. Scott McMurtry
Graduate Student
Department of Mechanical and
Industrial Engineering
Louisiana Tech University

Abstract

A previously developed quasi-steady wave mechanics model for penetration of structural targets is modified to include an improved model for the initial and terminal transients. The improved model is then utilized in the parametric study of the influence of penetrator and target properties on penetration depth. The wave mechanics model not only predicts the trends in penetration with variation in these properties, but it also delineates the kinematic mechanisms that are responsible for these trends. It is shown that the combination of high penetrator strength and low target strength produces a local maximum in the plot of penetration depth versus impact velocity. The wave mechanics model shows that the observed decrease in penetration depth with increasing impact velocity is due to flow initiation in the high strength penetrator. For high strength targets, the strength of the penetrator is shown to have little influence on penetration depth. However, for low strength targets, increased penetration results from increased penetrator strength. The effect of penetrator L/D on the ratio of penetration depth to original penetrator length is shown to be very pronounced for L/D's less than 6 but diminishing to near insignificance for L/D's greater than 12. The wave mechanics model shows that the L/D effect is due entirely to the initial and terminal transients. The effects of target strength, penetrator strength, and penetrator density on penetration depth into concrete targets is also presented.

INFLUENCE OF PENETRATOR AND TARGET PROPERTIES ON PENETRATION MECHANICS

E. Eugene Callens, Jr.
J. Scott McMurtry

INTRODUCTION

The work reported in Ref. 1 indicates that excellent agreement with experimental data is obtained for a properly formulated one-dimensional quasi-steady wave mechanics model of the penetration processes for blunt, cylindrical penetrators. The necessity of employing a wave mechanics model is rooted in the observation that the total time for the penetration process exclusive of the terminal transient is usually less than 200 microseconds. The corresponding deceleration levels are typically more than one million times greater than the standard value of gravitational acceleration. Thus, the classical differential equations for rigid body mechanics cannot adequately describe the time resolved response of either the penetrator or target material.

A major advantage of a realistic model of the governing physical mechanisms over a straight forward correlation of experimental data is that the physically based model can delineate the processes that cause the observed and predicted data trends. For example, the interaction between the hydrodynamic flow stress and the structural stresses in the penetrator and target dictate at what penetrator velocities flow is initiated in the penetrator and/or target. The initiation of flow, in turn, has a dramatic effect on the penetrator and target response as is illustrated in the parametric studies reported below.

The current work employs a wave mechanics model to conduct a parametric study of the effects of target and penetrator compressive strength and density as well as the penetrator length to diameter ratio on penetration depth. The study covers the entire velocity range from those values where penetration is initiated and material strength effects are dominant to the hypervelocity values where material strength effects are insignificant and the penetration process is hydrodynamic in nature. The range of material densities and strengths includes all engineering materials, and the penetrator length to diameter ratios range from 1 to 50.

QUASI-STEADY WAVE MECHANICS MODEL

The quasi-steady wave mechanics model used in this study is presented in Ref. 1 and summarized below. The governing equations are the conservation of momentum, the conservation of mass, and a velocity component kinematic relationship.

The penetrator/target interface momentum equation is

$$S'_P + \rho'_P U^2{}_{PF} = \rho'_T U^2{}_{TF} + S'_T \qquad (1)$$

where

S'_P = Stress in compressed penetrator
S'_T = Stress in compressed target
ρ'_P = Density of compressed penetrator
ρ'_T = Density of compressed target
U_{PF} = Penetrator flow velocity
U_{TF} = Target flow velocity

The one-dimensional wave continuity equation in the penetrator is

$$\rho'_P = \rho_P \left(\frac{V_{WP}}{V_{WP} - U_{PP}} \right) \qquad (2)$$

and for the target

$$\rho'_T = \rho_T \left(\frac{\overline{V}_{WT}}{\overline{V}_{WT} - \overline{U}_{PT}} \right) \qquad (3)$$

where

ρ_P = Penetrator initial density
ρ_T = Target initial density
V_{WP} = Penetrator wave velocity
$\overline{V}_{WT}$ = Mean target wave velocity in the bow region
U_{PP} = Penetrator particle velocity
$\overline{U}_{PT}$ = Mean target particle velocity

The particle velocity is the change in velocity associated with the passage of the disturbance wave. The kinematic relationship between the various velocity components is given by

$$V_P = U_{PF} + U_{PP} + U_{TF} + \overline{U}_{PT} \qquad (4)$$

where V_P = Velocity of the free end of the penetrator.

The velocities in the penetrator and target before and after the disturbance waves are shown schematically in Fig. 1 relative to the interface.

The wave velocities are given by

$$\overline{V}_{WT} = C_{WP} + S_{IT}\,\overline{U}_{PT} \tag{5}$$

$$V_{WP} = C_{WP} + S_{IP}\,U_{PP} \tag{6}$$

where

C_{WP} = Zero pressure wave velocity in the penetrator
C_{WT} = Zero pressure wave velocity in the target
S_{IP} = Hugoniot constant for the penetrator material
S_{IT} = Hugoniot constant for the target material

The stress in the compressed penetrator is given by

$$S_P' = \rho_P\,U_{PP}\,V_{WP} \quad for \quad U_{PF} = 0 \tag{7}$$

$$S_P' = \rho_P\,U_{PPM}\,V_{WP} \quad for \quad U_{PF} > 0 \tag{8}$$

$$U_{PPM} = \frac{C_{SP}\,\sigma_{SP}}{\rho_P\,V_{WP}} \tag{9}$$

$$C_{SP} = \nu_P^{-1} \tag{10}$$

where

U_{PPM} = Maximum penetrator particle velocity
C_{SP} = Penetrator free surface maximum stress constant
ν_P = Poisson's ratio for the penetrator material
σ_{SP} = Penetrator compressive stress

From these relationship[illegible]s observed that either the penetrator particle velocity or flow velo[illegible] is known for any condition. If the interface pressure is below the maximum allowable penetrator stress, the flow velocity is zero, and the particle velocity is the variable. If the interface pressure is above the maximum penetrator stress, the particle velocity is at its known maximum value and the flow velocity is the variable.

The stress in the compressed target is given by

$$S_T' = \rho_T\,\overline{U}_{PT}\,\overline{V}_{WT} \quad for \quad U_{TF} = 0 \tag{11}$$

$$S_T' = \rho_T\,\overline{U}_{PTM}\,\overline{V}_{WT} \quad for \quad U_{TF} > 0 \tag{12}$$

$$\overline{U}_{PTM} = \frac{C'_{ST}\,\sigma_{ST}}{\rho_T\,\overline{V}_{WT}} \tag{13}$$

$$C'_{ST} = C^2{}_{ST} = \nu^{-2}{}_T \tag{14}$$

where

U_{PTM} = Maximum mean target particle velocity
C'_{ST} = Target confined surface maximum stress constant
C_{ST} = Target free surface maximum stress constant
ν_T = Poisson's ratio for the target material
σ_{ST} = Target compressive stress

As in the case of the penetrator, either the target particle velocity or flow velocity is known for any condition. The penetrator deceleration is determined by the wave mechanics. In this model the compression wave that originates at the penetrator/target interface upon impact is tracked in the penetrator as it travels back and forth between the interface and the free end. The compression wave reflects from the free end as an expansion wave and the penetrator free-end velocity decreases by twice the particle velocity with each reflection.

When the expansion wave reflects from the interface, the sum of the penetrator and target variable velocities decrease by twice the particle velocity. The new values of these velocities are determined from the interface momentum equation and the velocity component kinematic relationship. Again, the particle velocity changes sign with each wave reflection.

The penetrator traveling wave is tracked until the penetrator velocity falls below the target flow initiation velocity. When this occurs the developed penetration phase is complete and the remainder of the penetration process is a terminal transient cylindrical expansion of the target stress and a spherical expansion of the penetrator flow stress as presented below. The change in penetrator length due to the developed penetration phase is

$$\Delta L_{PD} = -\int (\, U_{PP} \pm U_{PP}\,)\; dt \tag{15}$$

The change is crater depth due to the developed penetration phase is

$$\Delta L_{CD} = \int (\, U_{TP} + \overline{U}_{PT}\,)\; dt \tag{16}$$

The final crater diameter at each penetration location is given by

$$\frac{D_C}{D_P} = \sqrt{\frac{\rho_P' \overline{U}^2{}_{PF} + C_{ST}\sigma_{ST}}{C_{ST}\sigma_{ST}}} \qquad (17)$$

where D_P = penetrator initial diameter.

INITIAL AND TERMINAL TRANSIENT MODELS

The initial and transient models have been modified from those presented in Ref. 1. The time for the initial transient is taken to be the time for the passage of the lateral release wave in the penetrator

$$\Delta t_{IT} = \frac{R_P}{V_{WPTS}} \qquad (18)$$

where

V_{WPTS} = Penetrator transverse impact shock velocity.

The crater length due to the initial transient is given by

$$L_{CI} = (U_{PTS} - \overline{U}_{PTM}) \Delta t_{IT} \qquad (19)$$

where

U_{PTS} = Target shock particle velocity

The length of penetrator loss during the initial transient expansion is obtained from a form of the velocity kinematic relationship

$$\Delta L_{PI} = -(V_{PI} \Delta t_{IT} - L_{CI}) \qquad (20)$$

The terminal transient model is a combination of a spherical penetrator flow stress expansion and a cylindrical target particle momentum expansion. The crater length due to the spherical expansion of the penetrator flow stress is

$$L_{CTPF} = \sqrt{\frac{\rho_P' U^2{}_{PF}}{C_{ST}\sigma_{ST}}} - 1 \qquad (21)$$

The crater length due to the cylindrical expansion of the target particle momentum is

$$L_{CTPM} = R_{PR} \left(\frac{\overline{U}_{PTFI}}{U_{PTFS}} - 1 \right) \tag{22}$$

where

U_{PTFI} = Mean target particle velocity when the penetrator velocity equals the target flow initiation velocity

U_{PTFS} = Free surface target particle velocity

Also the reference radius for the cylindrical expansion is

$$R_{PR} = \frac{V_{WTL}}{V_{WTT}} R_P \tag{23}$$

where

V_{WTL} = Target longitudinal wave velocity

V_{WTT} = Target transverse wave velocity

R_P = Penetrator radius

The total crater length due to the terminal transient is

$$L_{CT} = L_{CTPF} + L_{CTPM} \tag{24}$$

The time for the penetrator flow stress expansion is

$$t_{TTPF} = \frac{R_P}{2\, U_{PF}} \left(\frac{L_{CTPF}}{R_P} \right)^2 \tag{25}$$

and the time for the target particle expansion is

$$t_{TTPM} = \frac{R_{PR}}{\overline{U}_{PTFI}} \left[.5 \left(\frac{L_{CTPM}}{R_{PR}} \right)^2 + \left(\frac{L_{CTPM}}{R_{PR}} \right) \right] \tag{26}$$

The total time for the terminal transient expansion is

$$t_{TT} = t_{TTPF} + t_{TTPM} \tag{27}$$

COMPUTATIONAL RESULTS

The above equations constitute a comprehensive model for the complete terminal ballistics process including the initial transient, the developed penetration regime, and the final transient. The model predicts crater depth, penetrator velocity, and penetrator length as a function of time as well as the final crater diameter as a function of crater depth.

The equations have been programmed using the True BASIC language and the program is readily solved on a personal computer. Typical run times are 15 seconds on a 25-MHz 386 PC with a math coprocessor.

Fig. 2 presents data in terms of the ratio of penetration depth to original penetrator length (P/L) for tungsten alloy penetrators into rolled homogeneous armor (RHA) targets. The calculated P/L results are compared with data from Ref. 2 for length to diameter ratios (L/D) of 3, 6, and 12 and penetrator impact velocities (VPI) from 600 to 1600 m/s. The predictions show the experimentally observed L/D effects. Both the experiment and calculations show a change in slope at an impact velocity of approximately 800 m/s. This corresponds to the velocity at which the RHA target reaches the maximum confined surface stress and begins to flow.

Fig. 3 shows the same agreement within the experimental uncertainty for a mild steel penetrator into an aluminum target for L/D = 3. The experimental data from Ref. 3 extend from an impact velocity of approximately 900 m/s where target and penetrator strength effects are very significant to 5000 m/s where the penetration process is approximately hydrodynamic.

Figs. 4 and 5 compare the calculated results with experimental data from Ref. 4 for tungsten into ST52 steel and a penetrator L/D of 10.4. Two calculated curves are presented which correspond to the range of compressive strength quoted for ST52 steel. Fig. 4 presents the comparisons for crater depth, and Fig. 5 presents the comparisons for crater diameter. The agreement is seen to be excellent over the entire velocity range from 600 to 3600 m/s.

The effect of target strength on penetration depth for high and low strength penetrators is shown in Figs. 6 and 7, respectively. Both plots show increasing penetration with decreasing target strength as expected. However, for the combination of high penetrator strength and sufficiently low target strength, Fig. 6 shows a local maximum in penetration depth occurring at moderate impact velocities. The wave mechanics code clearly indicates that this decrease in penetration depth with increasing velocity is due to flow initiation in the high strength penetrator.

This phenomenon is further investigated in Figs. 8 and 9 where the effect of penetrator strength on penetration depth is presented for high and low strength targets, respectively. For high strength targets, the strength of the penetrator has little influence on penetration depth (Fig. 8).

However, for low strength targets, there is significantly more penetration associated with increasing penetrator strength at moderate to high impact velocities (Fig. 9). The local maxima are present for all but the two lowest strength penetrators. At impact velocities above 3,000 m/s, the curves are seen to coalesce due to the fact that even the highest strength penetrators are flowing under the influence of the high interface pressure. The penetration depth continues to increase with increasing velocity above 3,000 m/s due to terminal transient effects.

The effect of target density on penetration depth is presented in Figs. 10 and 11 for high and low strength targets, respectively. At high velocities, the penetration depth increases as target density decreases as expected. However, the curves cross at low velocities indicating that there is a regime where low density, high strength targets are more resistant to penetration than high density, high strength targets (Fig. 10). The wave mechanics model shows that this is due to the higher target flow initiation velocities associated with the lower target densities. This also suggests that the superior penetration resistance of ceramics over metals at low to moderate velocities may be due in part to the lower densities of the ceramics in addition to the obvious advantage of higher compressive strengths. Fig. 11 also shows that the penetration local maximum phenomenon is very pronounced for very low density targets.

Figs. 12 and 13 show the effect of penetrator density on penetration depth for high and low strength targets, respectively. The anticipated characteristic of increasing penetration with increasing density is observed in both figures. Fig. 13 shows that the local maxima occur for low strength targets if the penetrator density is sufficiently large.

Fig. 14 presents the effect of L/D on penetration depth for L/D of 1, 3, 6, 12, 20, and 50. The penetrator and target material properties are typical of a tungsten alloy penetrator into RHA. Low values of L/D are observed to have substantially high relative penetration compared to the higher L/D's. However, as L/D increases the difference diminishes and becomes nearly insignificant for L/D above 12. The wave mechanics model shows that the L/D effect is due entirely to the initial and terminal transients. There is no difference in the relative penetration of different L/D penetrators in the developed penetration regime.

The effect of target strength, penetrator strength, and penetrator density on penetration depth into concrete is shown in Figs. 15, 16, and 17, respectively, for a penetrator L/D of 12. Fig. 15 illustrates that the penetration depth has a local maximum for concrete strengths below 20,000 psi for a tungsten alloy penetrator. For normal structural strength concrete between 3,000 and 5,000 psi, the effect is quite pronounced. The consequence

of this phenomenon is that there is a limit on the impact velocity to achieve maximum penetration in concrete. The same effect is observed in Figs. 16 and 17 for all but the two lowest penetrator strengths and densities.

It is concluded that the wave mechanics model is very effective in the delineation of the effects of penetrator and target characteristics on penetration mechanics. Not only are the trends in penetration depth apparent but, more importantly, the physical mechanisms that drive these trends are exposed. The mechanisms are dynamic in nature and produce results that may not be anticipated from consideration of static material properties.

REFERENCES

1. Callens, E. Eugene, Jr. and J. Scott McMurtry, "One-Dimensional Wave Mechanics Model for Terminal Ballistics," Final Report for AFOSR Summer Research Program, Aug. 1992.
2. Tate, A., K. E. B. Green, P. G. Chamberlain, and R. G. Baker, "Model Scale Experiments of Long Rod Penetration," Proc. Fourth Int. Symp. Ballistics, Oct. 1978.
3. Christman, D. R., A. B. Wenzel, and J. V. Gehring, "Penetration Mechanisms of High-Velocity Rods," Proc. of the Seventh Hypervelocity Impact Symp., Tampa, FL, Vol. V and VI, Experiments, Nov. 17-19, 1964.
4. Hohler, V., and A. J. Stilp, Penetration of Steel and High Density Rods in Semi-infinite Steel Targets," Int. Symp. on Ballistics, 1977.

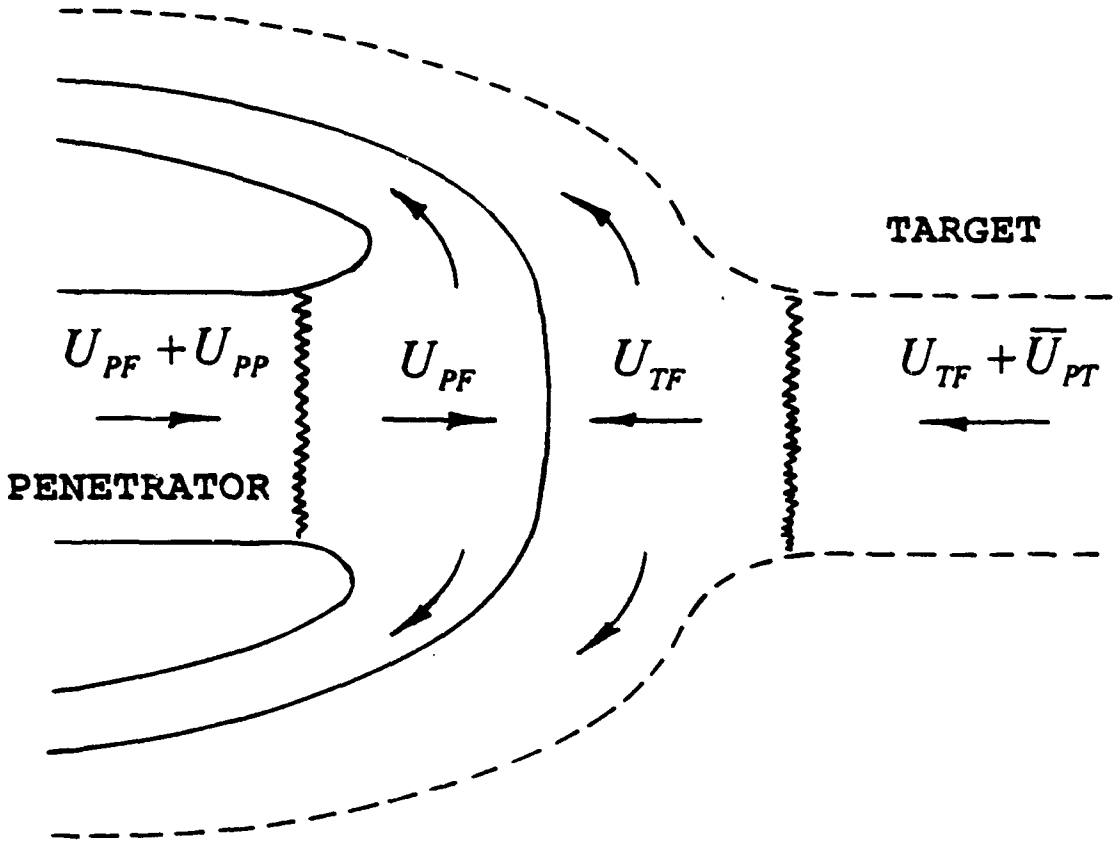

FIG. 1. FLOW AND PARTICLE VELOCITIES RELATIVE TO THE INTERFACE

FIG. 2. TUNGSTEN INTO RHA, L/D = 3, 6, 12

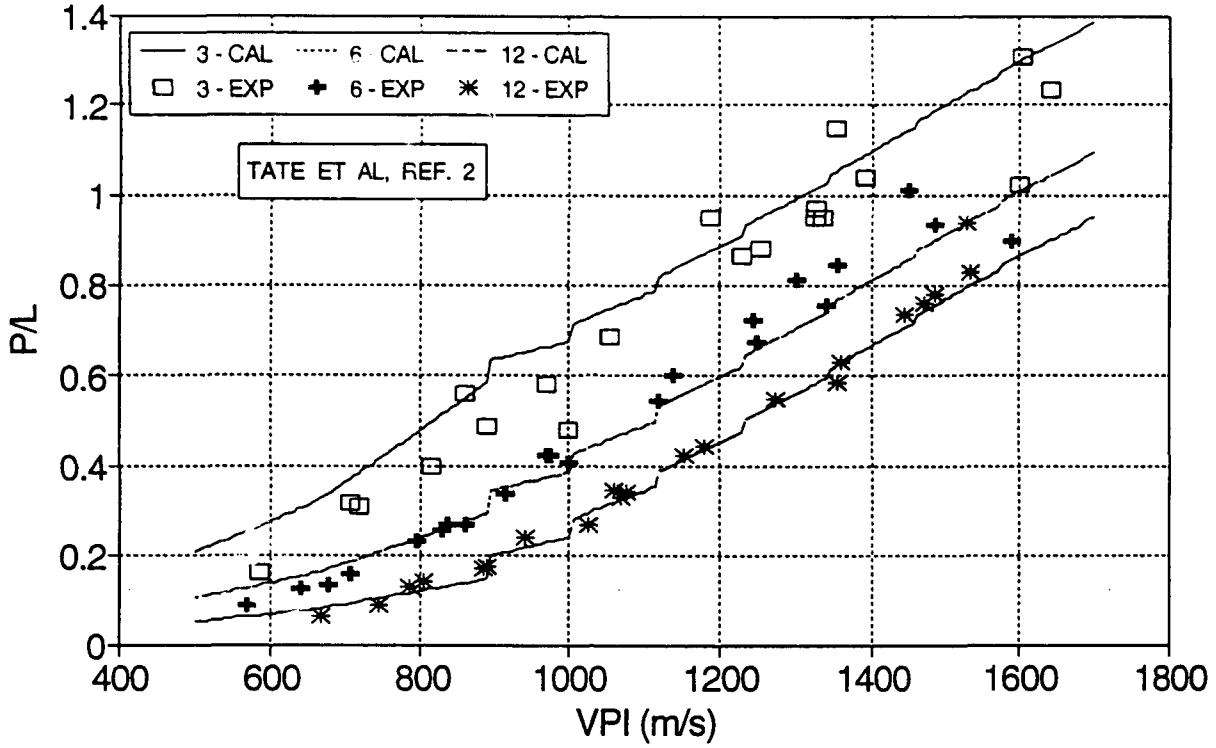

FIG. 3. MILD STEEL INTO AL, L/D = 3

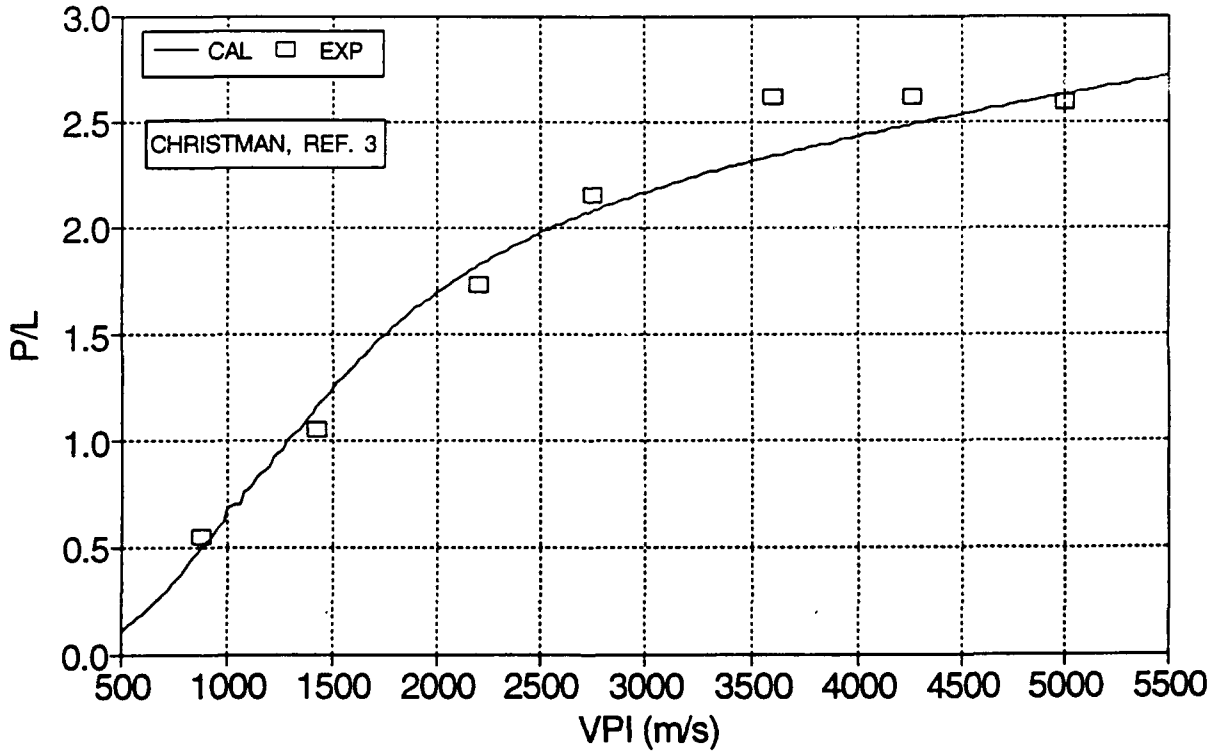

FIG. 4. TUNGSTEN INTO ST52 STEEL, L/D = 10.4, CRATER DEPTH

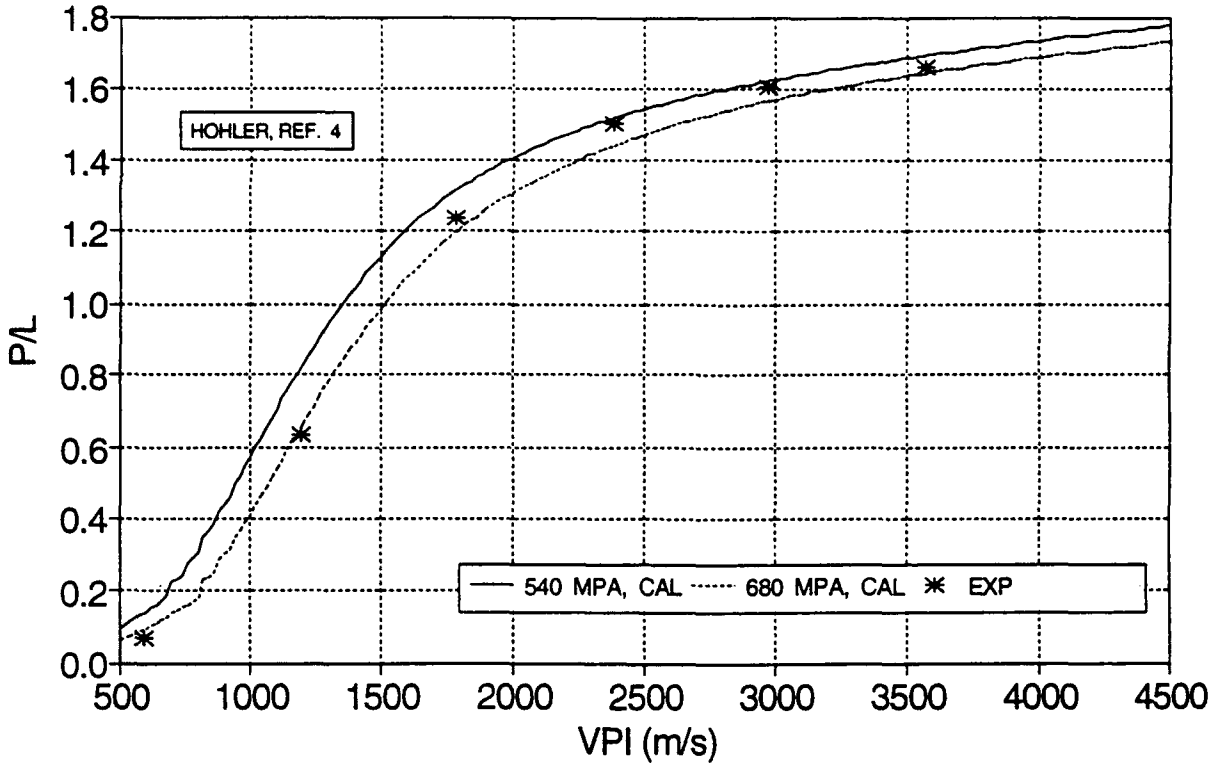

FIG. 5. TUNGSTEN INTO ST52 STEEL, L/D = 10.4, CRATER DIAMETER

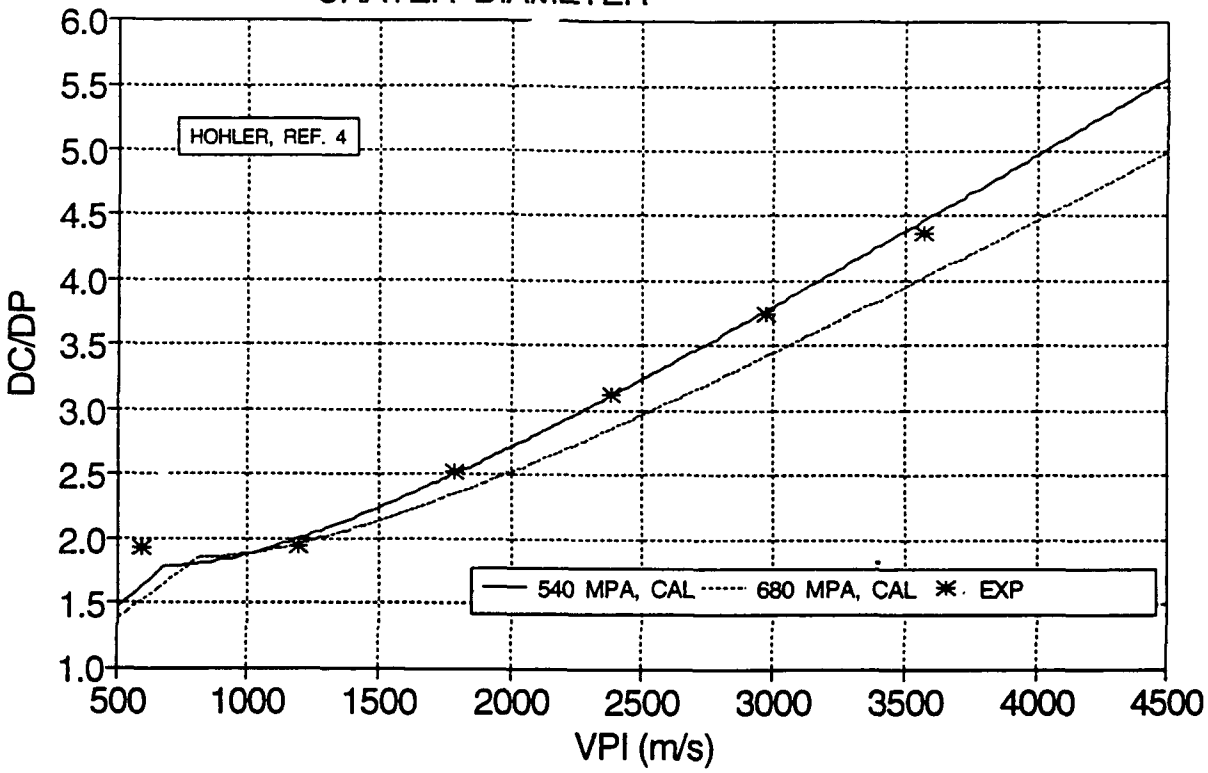

FIG. 6. EFFECT OF TARGET STRENGTH ON PENETRATION DEPTH, HIGH STRENGTH PENETRATOR

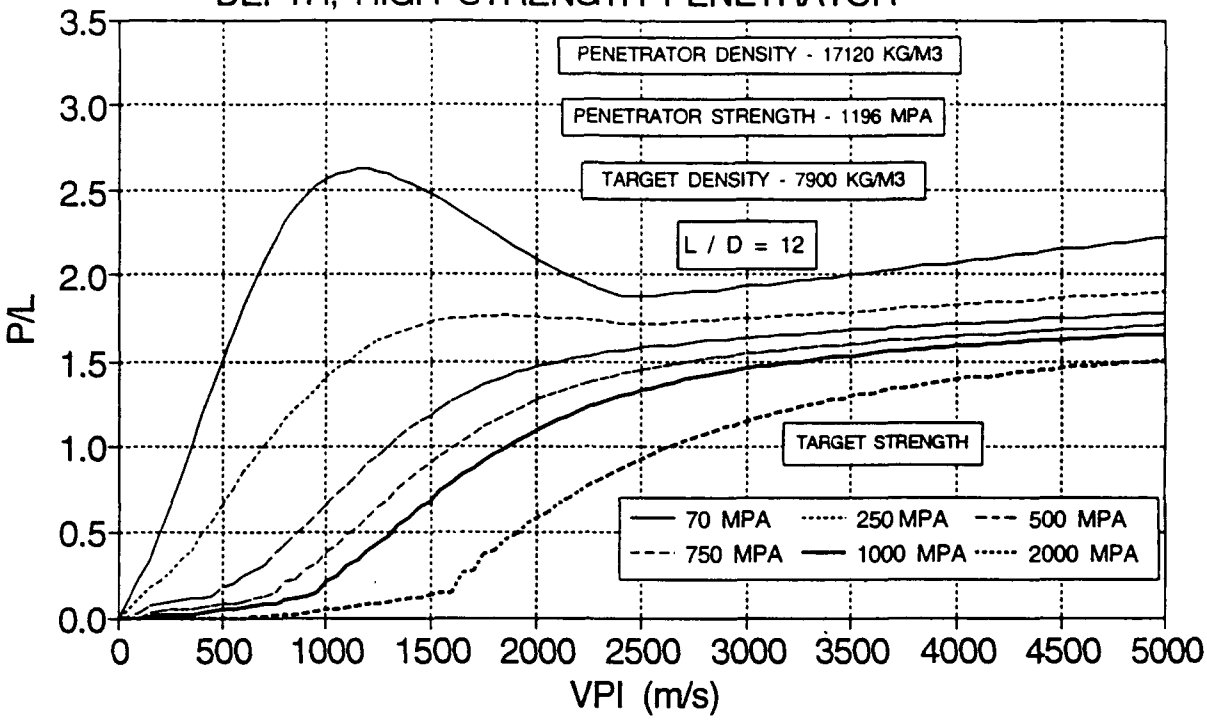

FIG. 7. EFFECT OF TARGET STRENGTH ON PENETRATION DEPTH, LOW STRENGTH PENETRATOR

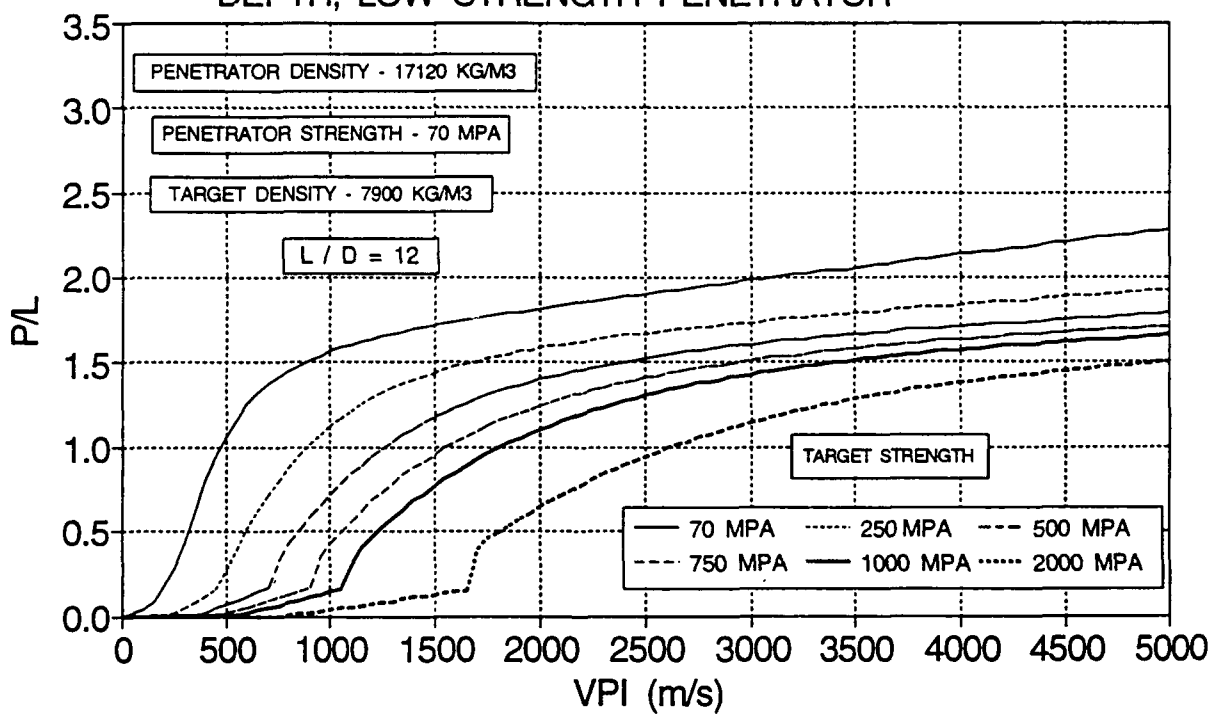

FIG. 8. EFFECT OF PENETRATOR STRENGTH ON PENETRATION DEPTH, HIGH STRENGTH TARGET

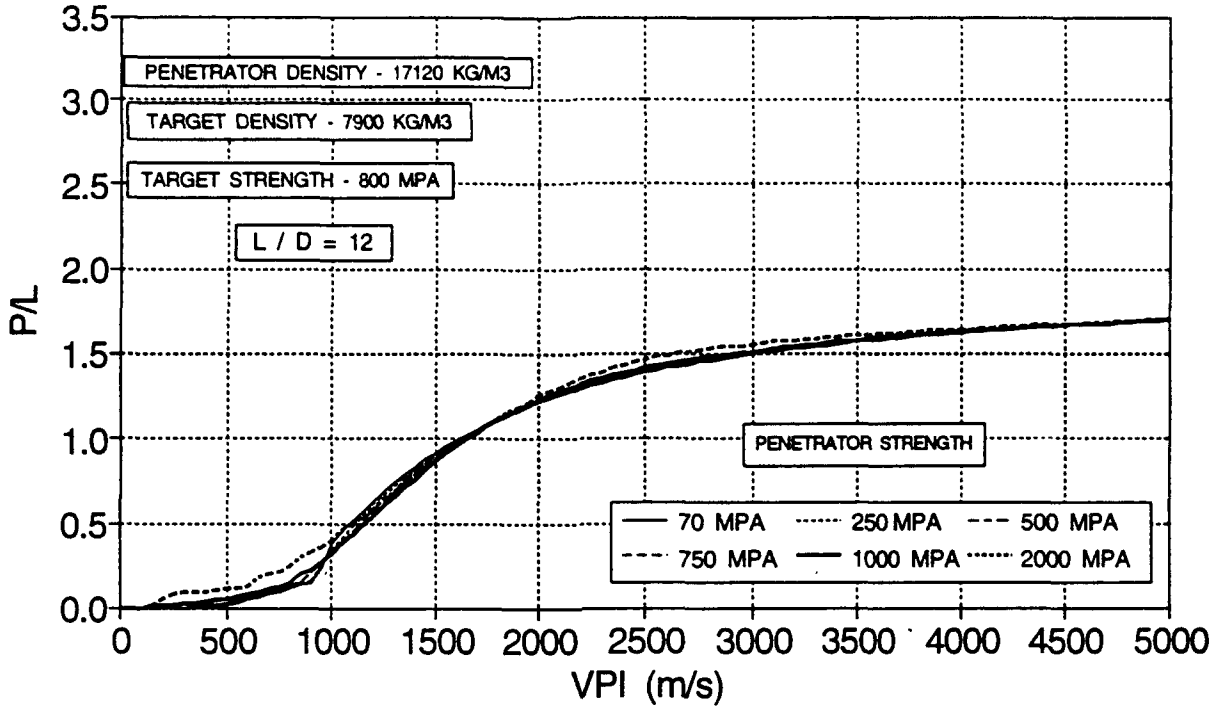

FIG. 9. EFFECT OF PENETRATOR STRENGTH ON PENETRATION DEPTH, LOW STRENGTH TARGET

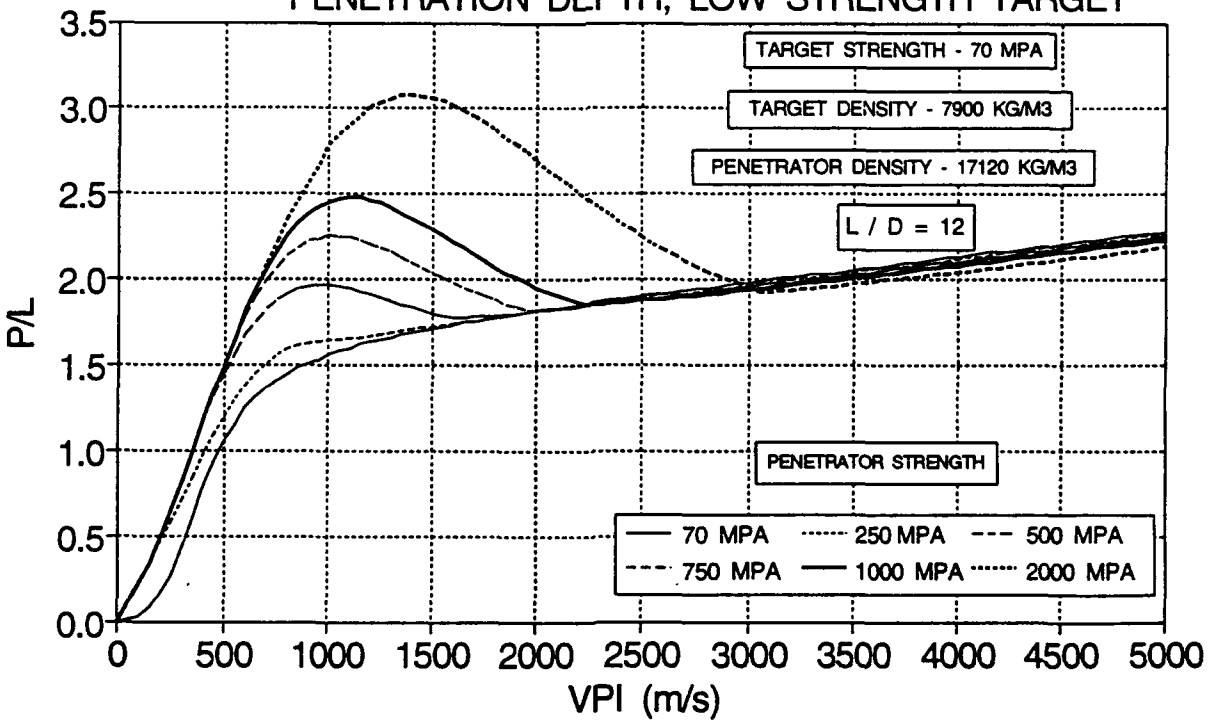

FIG. 10. EFFECT OF TARGET DENSITY ON PENETRATION DEPTH, HIGH STRENGTH TARGET

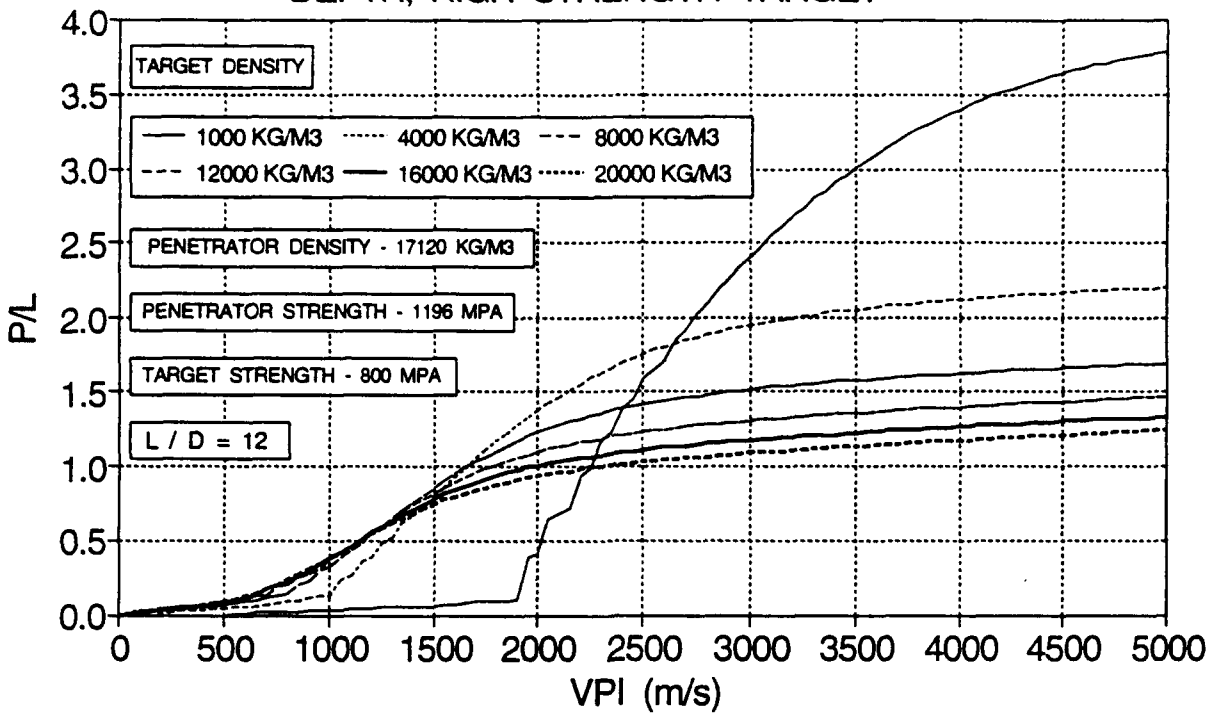

FIG. 11. EFFECT OF TARGET DENSITY ON PENETRATION DEPTH, LOW STRENGTH TARGET

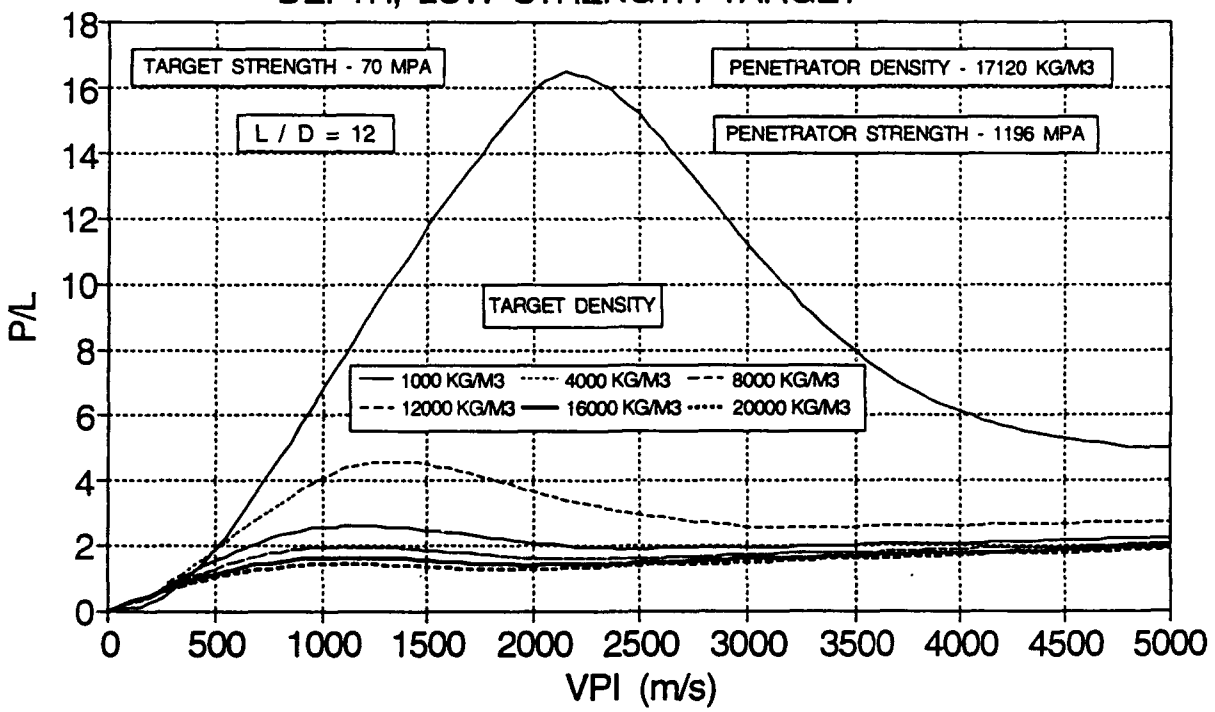

FIG. 12. EFFECT OF PENETRATOR DENSITY ON PENETRATION DEPTH, HIGH STRENGTH TARGET

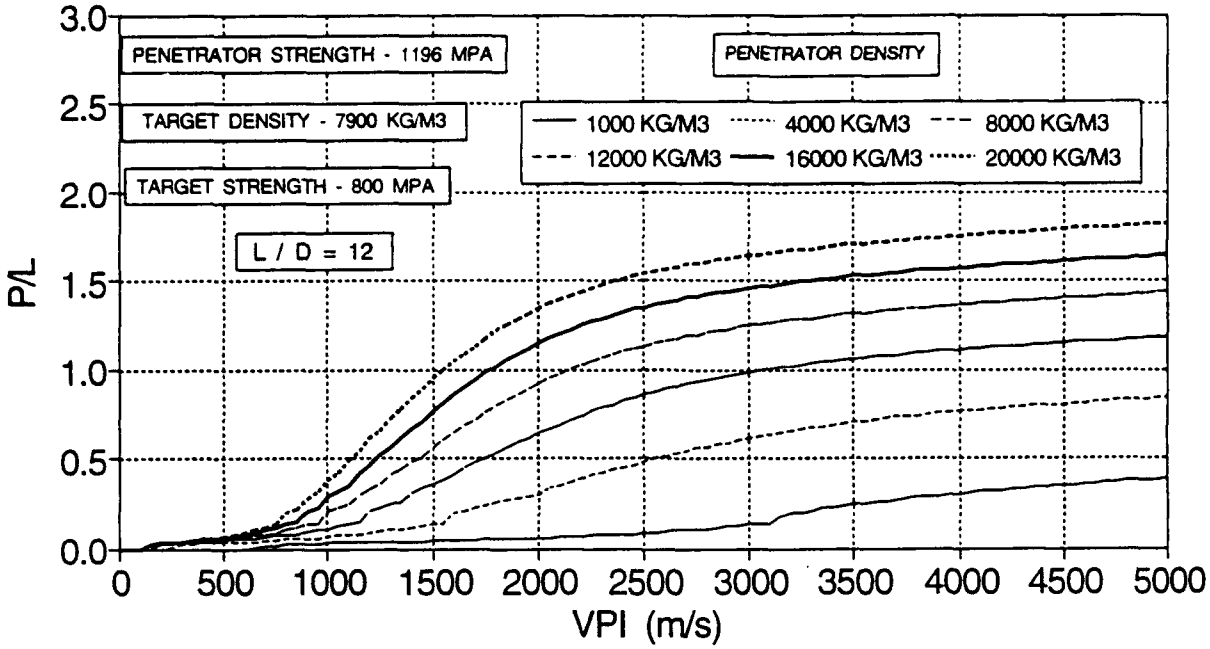

FIG. 13. EFFECT OF PENETRATOR DENSITY ON PENETRATION DEPTH, LOW STRENGTH TARGET

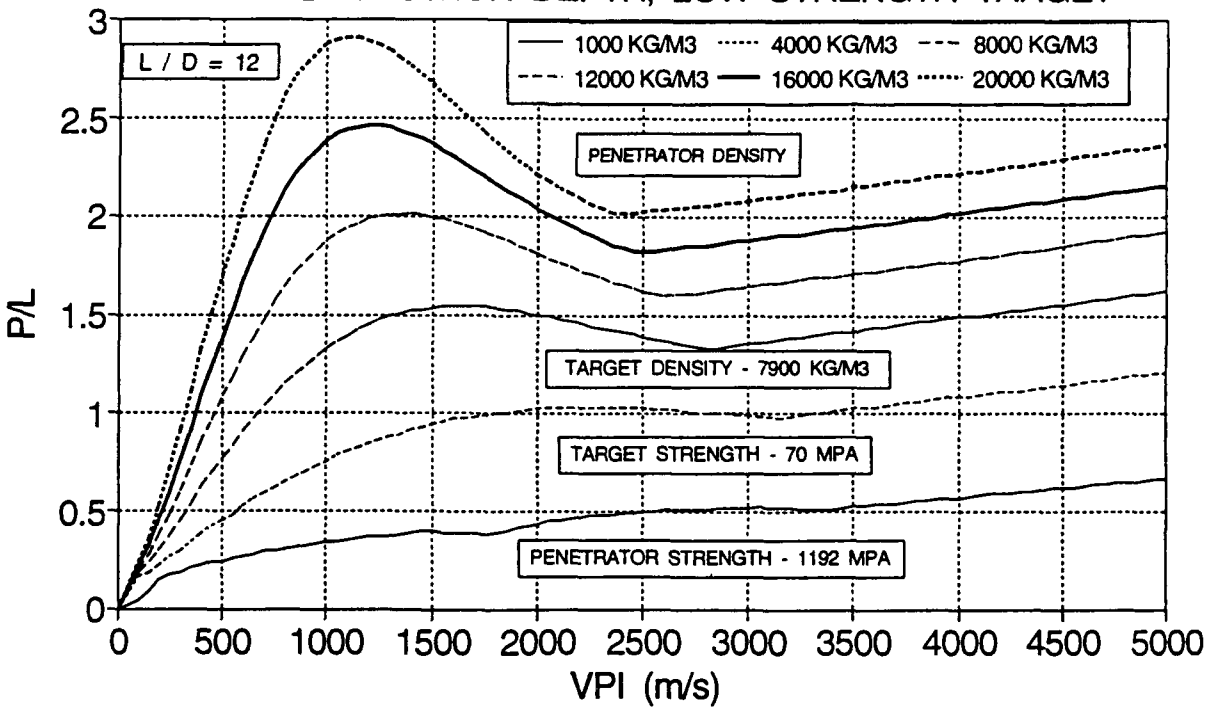

FIG. 14. EFFECT OF L/D ON PENETRATION DEPTH

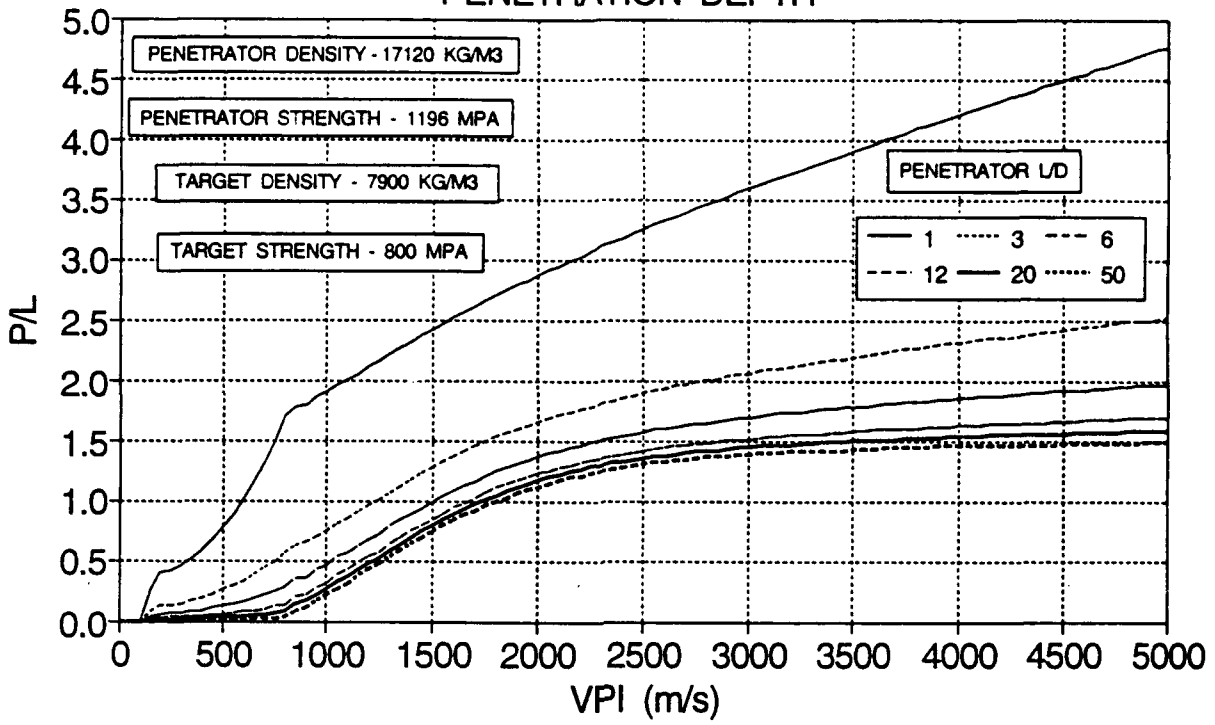

FIG. 15. EFFECT OF TARGET STRENGTH ON PENETRATION DEPTH FOR CONCRETE

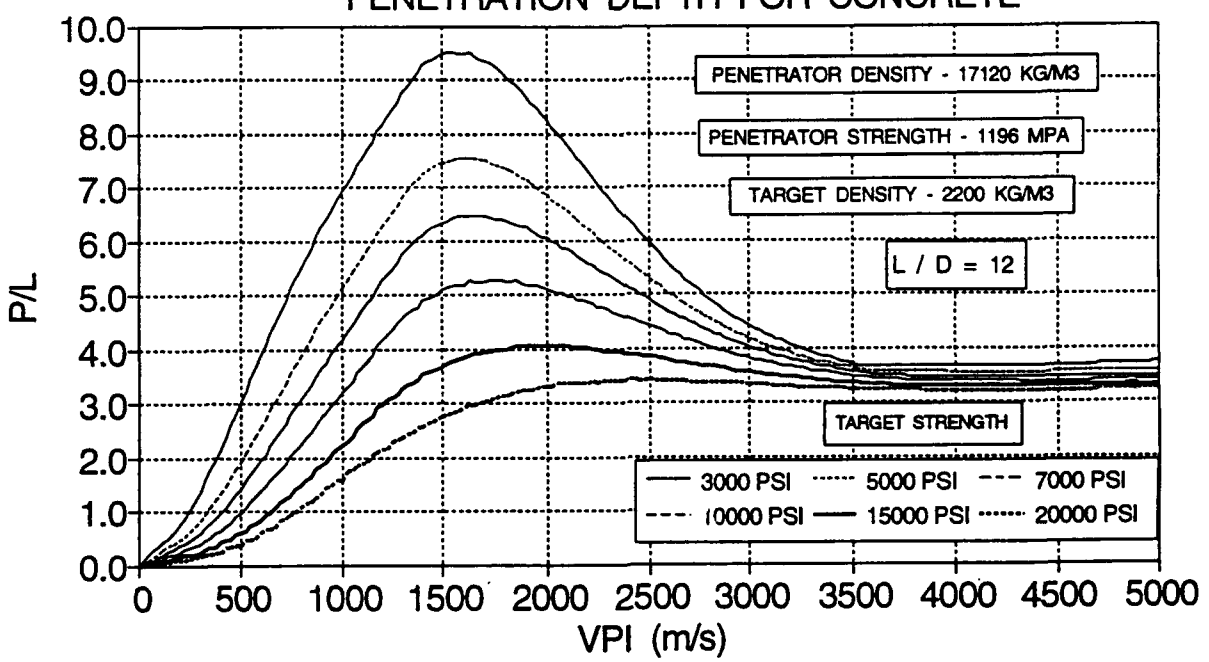

FIG. 16. EFFECT OF PENETRATOR STRENGTH ON PENETRATION DEPTH FOR CONCRETE

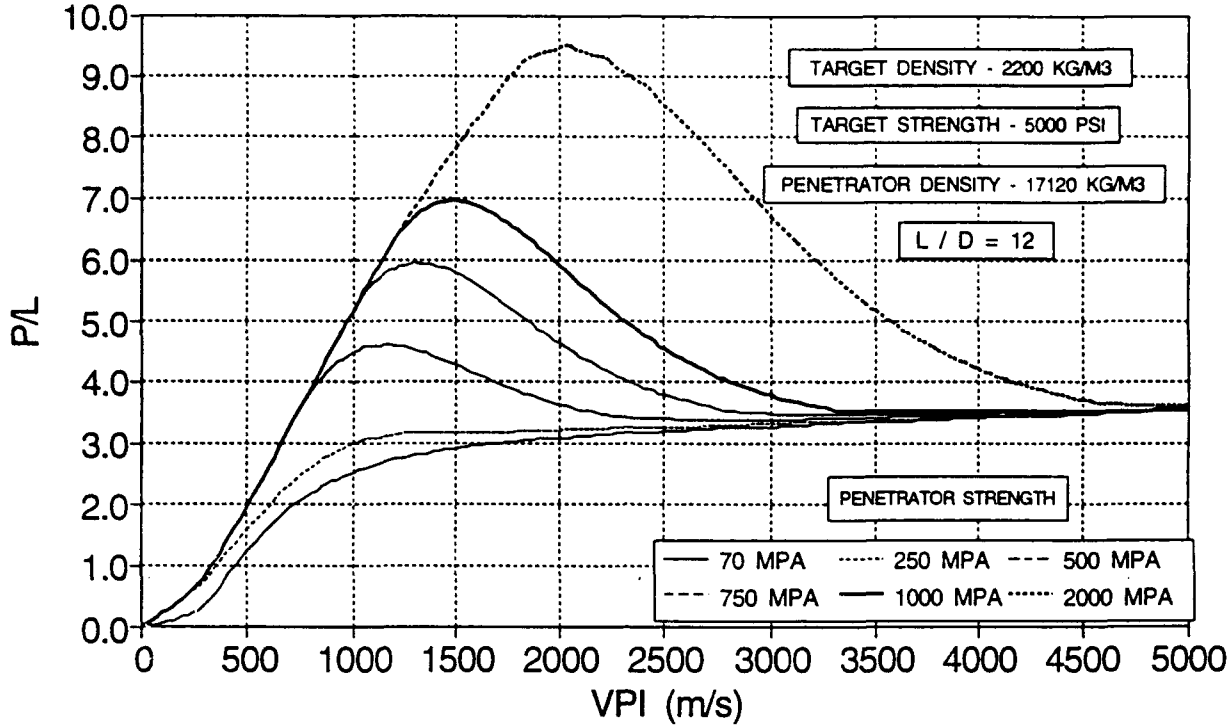

FIG. 17. EFFECT OF PENETRATOR DENSITY ON PENETRATION DEPTH FOR CONCRETE

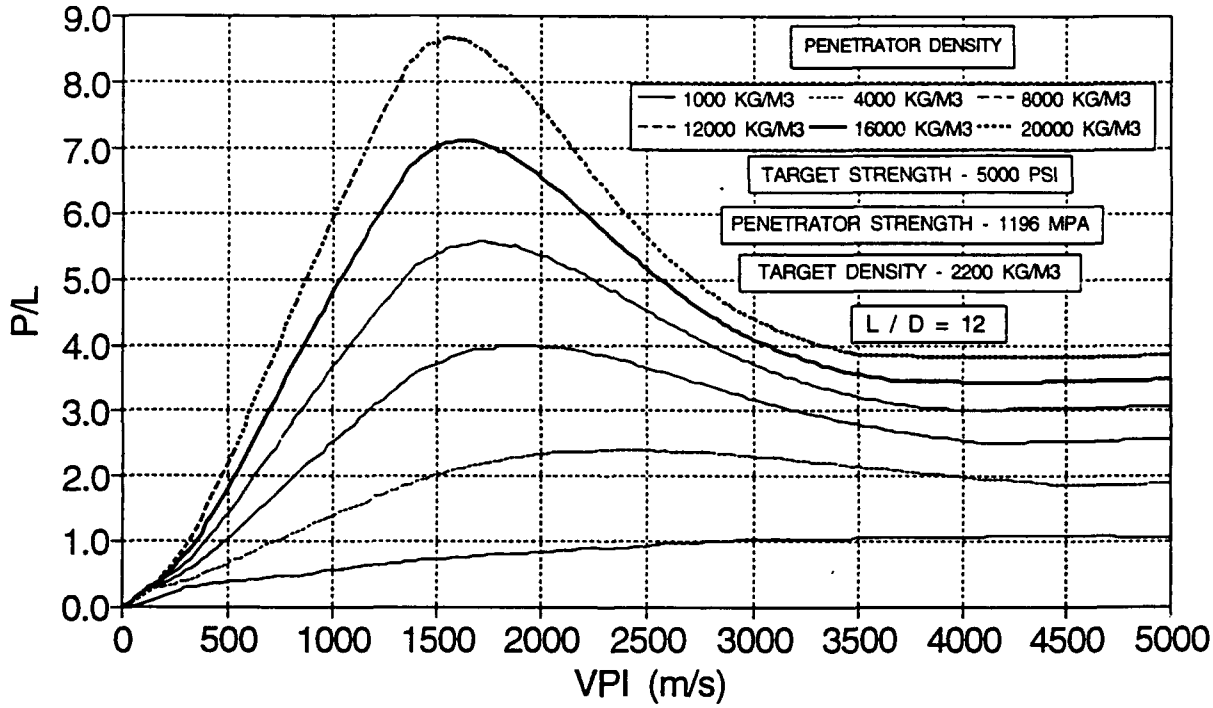

ANALOG SIGNAL CHARACTERIZATION CIRCUIT

Michael Olson
Electrical Engineering Graduate Student

Florida State University
College of Electrical Engineering
2525 Pottsdamer Road
Tallahassee, FL 32310

Final Report for:
Graduate Student Research Program
Wright Laboratory Armament Directorate

Sponsered by:
Air Force Office of Scientific Research
Bolling Air Force Base, Washington D.C.

August 1993

ANALOG SIGNAL CHARACTERIZATION CIRCUIT

Michael G. Olson
Electrical Engineering Graduate Student
College of Electrical Engineering
Florida State University

Abstract

An analog signal characterizer is one that will take is an analog signal and characterize it apart from other signals. The circuit consists of three main modules, each giving a different characteristic of the signal. Three modules were used instead of just one, to better characterize the signal. The analog approach, as opposed to the digital was taken in this case, because the timing of the analog circuit was much faster than the digital. The circuitry used in creating an analog signal characterizer was designed, tested and debugged until a working circuit was obtained.

ANALOG SIGNAL CHARACTERIZATION CIRCUIT

Michael G. Olson

Introduction

Signal characterization is of necessity in many electrical engineering applications today. The proposed design for the analog signal characterizer consists of three modules. Three modules are used here to get a better understanding of the signal, and thus, better characterization is obtained. Each takes the same input wave, and analyzes it in a different way. The first module takes the absolute value of the signal, and then integrates the signal over a set time period in order to obtain a final voltage stored on the integrators capacitor. The second module takes the same signal and first differentiates it before taking the absolute value and integrating it. The third module takes the second derivative of the signal before taking the absolute value and integrating it. Each of these modules will run in parallel with each other, and a series of vectors will be output for each time interval, so one can classify the wave at specific time intervals.

Methodology

The design of the analog signal characterizer consists of three main modules. Each of these main modules consists of separate stages. These stages when cascaded correctly will form the modules. Some of the individual stages are the differentiator, absolute value circuit, integrator (with clear), differential to single-ended converter, and a sample and hold circuit. Each of these will now be discussed.

The differentiator is a circuit that will accept any signal at its input, and deliver the derivative of the signal at its output. The derivative of an analog signal will be obtained through the use of discrete circuitry. The circuit shown in figure 1 will be the one used. In order to fully understand this circuit, the characteristic equations of the

circuit will be derived. The current across the capacitor, i_1, is as follows: $i_1 = C\frac{dv_{in}}{dt}$. By knowing that the voltage between input terminals is equivalent to zero, the output voltage can be obtained by the use of Kirchhoff's voltage law. Thus, the output voltage is, $v_{out} = -i_2 R$. In an operational amplifier, the input currents are both equivalent to zero. Applying Kirchhoff's current law yields $i_1 = i_2$. This information can then be applied to obtain a final expression for the output voltage, $v_{out} = -RC\frac{dv_{in}}{dt}$.

The absolute value circuit is a device that will output the absolute value of an input signal, i.e., $v_{out} = |v_{in}|$. This circuit is sometimes called a full wave rectifier circuit. The problem here is that most full wave rectifiers incorporate diodes in such a manor that the rectified portion of the signal has a voltage loss equal to the diodes voltage drop. In this design a circuit is needed that will not give us any voltage loss. In other words, a precision full wave rectifier, or a true absolute value circuit is needed.

The absolute value circuit used will be the one shown in figure 2. The top half of the circuit shows an op-amp in the follower configuration, with a diode in its negative feedback path. If the input voltage into this half of the circuit is positive, then the voltage of the op-amp's output will also be positive. This means that the diode will conduct and the positive voltage at the input of this half of the circuit will be "mirrored" at the output. If the voltage of this half of the circuit is negative, then the voltage at the output of the op-amp will also be negative. This means that the diode will be thrown into its reverse-bias state, and no current will flow through it. Thus we have a precision half wave rectifier with transfer curve like the following:

The bottom half of the circuit shows an op-amp in the inverting mode with a diode in its negative feedback path. If the two resistors are matched, the gain of the inverting amplifier is, g=-1. If the input voltage into the bottom half of the circuit is negative, then the voltage at the output of the op-amp will go negative. Thus, throwing the diode into

its reverse-bias state. If the input voltage is negative, then the voltage at the output of the op-amp is negative, and the diode will conduct. This means that the circuit has the following transfer curve:

Since the two circuits, the top and the bottom, work in parallel, the two transfer curves may be added directly to obtain the final output transfer curve, which is:

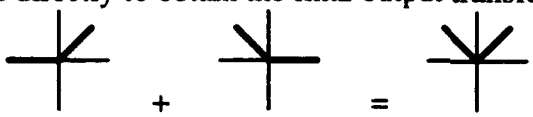

The integrator is a device that will accept any signal as input, and deliver an integrated version of the signal to the output. The circuitry used to do the integration is the shown in figure 3. If the capacitor is initially uncharged, and v_{in} is made positive at time t=0, then the current through R_1 is, $i_1 = \frac{v_{in} - v_-}{R_1} \equiv \frac{v_{in}}{R_1}$. Since $v_+ \equiv v_-$, the voltage at v_{out} *must change at the same rate as* v_c. With this knowledge and the use of the capacitors v-i relationship, the following expression is obtained: $\frac{dv_{out}}{dt} = \frac{-i_1}{C} = \frac{-v_{in}}{R_1 C}$. Integrating this equation, the following expression for the final output voltage is obtained:

$$V_{out}(t) = \frac{-1}{R_1 C}\int_0^t v_{in}dt.$$

The design calls for slight modifications to be made to the integrator stage. A clear enable is needed. The integrator will be used to store charges, and then be discharged so it may store another charge. This is done by adding switches as shown in figure 4. During the integrating time, the switches are set as to allow the capacitor to charge. And during the discharge time, the switches are set to separate the capacitor from the rest of the circuit and allow the capacitor to discharge through resistors.

The value of the capacitor must be read at continuos time intervals. Therefore, a second branch of each module is needed that will integrate the signal as the other branch is discharging the capacitor from the previous charge. This second branch will include all

the integrator and all stages after the integrator stage. A block diagram of the three modules are given in figure 5.

An integrator stores charge differentially across a capacitor, but in order to send this voltage into another stage, a voltage in reference to ground is needed. To do this, the circuit in figure 6 is examined. This circuit takes the voltages at each end of the capacitor in the integrator and subtracts them to get a voltage in reference to ground. As long as the operational amplifier stays in its linear region, superposition may be used to define the circuit. First v_1 is grounded, and the circuit becomes a simple inverting amplifier with a gain of $v_{out} = \frac{-R_2}{R_1} v_2$. If v_2 is grounded next, the circuit is equivalent to a non-inverting amplifier with a gain of, $v_{out} = \frac{R_2 + R_1}{R_1} v_1$. Thus, the transfer function of the entire circuit is $V_{out} = \frac{R_2 + R_1}{R_1} v_1 - \frac{R_2}{R_1} v_2$. The circuit would be much easier to work with if the amplification factors of both v_1 and v_2 were the same. Therefore, a voltage divider with a gain of $m = \frac{R_2}{R_1 + R_2}$ is added to the v_+ terminal to attenuate v_1. The output equation of the circuit is now, $v_{out} = \frac{R_2}{R_1}(v_1 - v_2)$.

In order to get the final output values into a vector form, a sample and hold and switching circuitry is needed. The sample and hold will keep the voltage of the capacitor in the integrator constant, so it may be read into a vector. Next switches will be used so that the only signal at the output of the circuit will be the final voltage stored on the integrators capacitor at the end of the specified time period.

Results

The properties of the different stages were each tested individually, before they were cascaded together. This was done by passing wave forms through the circuit and

analyzing the results. After each stage passed the tests and was working correctly, they were then cascaded together one stage at a time to make sure they were still functioning correctly. Once all stages were cascaded together, each main module was tested.

When a differentiator differentiates a signal that has a very large slope, or essentially a discontinuity with infinite slope, it forms a spike. The algorithms used by the simulation programs, Pspice, and Analog Work Bench, had trouble dealing with the discontinuities of the signal. The simulation programs try to "track" this output signal, but after a spike occurs the simulation program has trouble finding the signal again to track. If there is a low error tolerance, then the program may not find the signal again, and hence give an error. If the error tolerance is increased, then the signal will "flutter" after the spike until the program is able to catch the signal again and track it. The computer cannot manipulate a differential equation in the same way that a person can by hand. This is because of the assumptions that people make as they work a differential equation. The computer does the best it can do by using mathematical equations to represent the differential equation. Even though the output signal of a differentiator may flutter a little bit, this is only because of the computer not being able to represent a true differential equation and it is not an error. The output of the differentiator that was used is shown in figure 8. The input signal was the one shown in figure 7.

The absolute value circuit's output is shown in figure 9. As can be seen the circuit returns the true absolute value signal of the input wave shown in figure 7. The integrator was tested after is was cascaded with the absolute value circuit. The output of this circuit is shown in figure 10. The sample and hold circuits output is shown in figure 11.

The output vector for the module 1 (no differentiation) with the non-ideal input wave shown in figure 12, is shown in figure 7. As seen, the value out of the integrator at the end of 50 μs, is held for 50 μs. The second branch of the module then takes over and the value of the integrator at the end of the next 50 μs is then held for another 50 μs.

The signal is then feed back and forth between the two branches of the module in order to hold the values of the integrator at the end of each 50 μs.

Conclusion

The circuit was tested extensively, and worked as proposed. This design process was the first stage in completely designing this circuit. The next step would be to transfer this design all onto one substrate, while still keeping the overall properties of the circuit. Also, this step did not take into account stress analysis, packaging, etc. This step was just to see if the design was feasible. This design was found to work properly, and will be designed further, in order to obtain a final product.

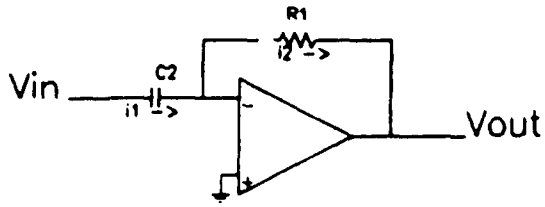

Figure 1

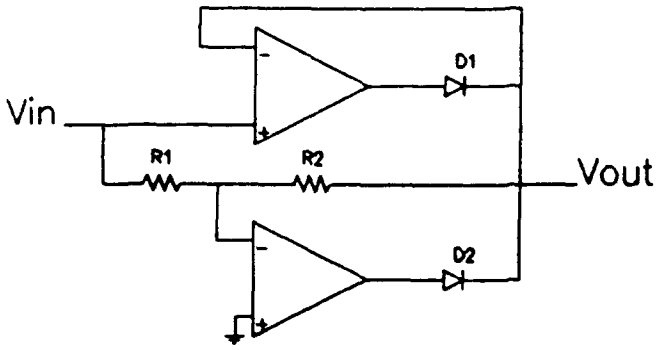

Figure 2

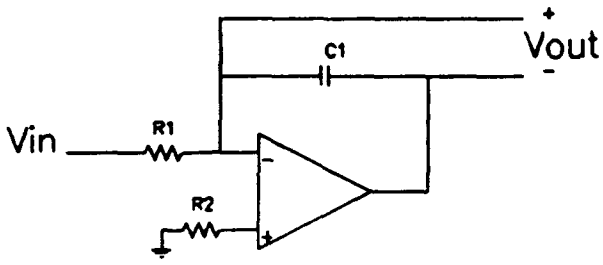

Figure 3

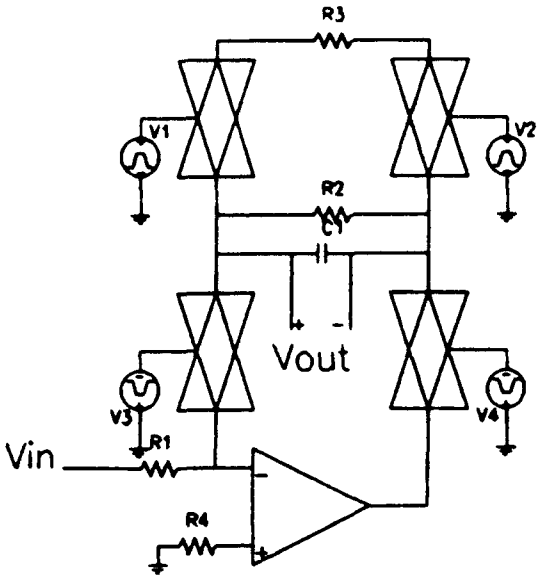

Figure 4

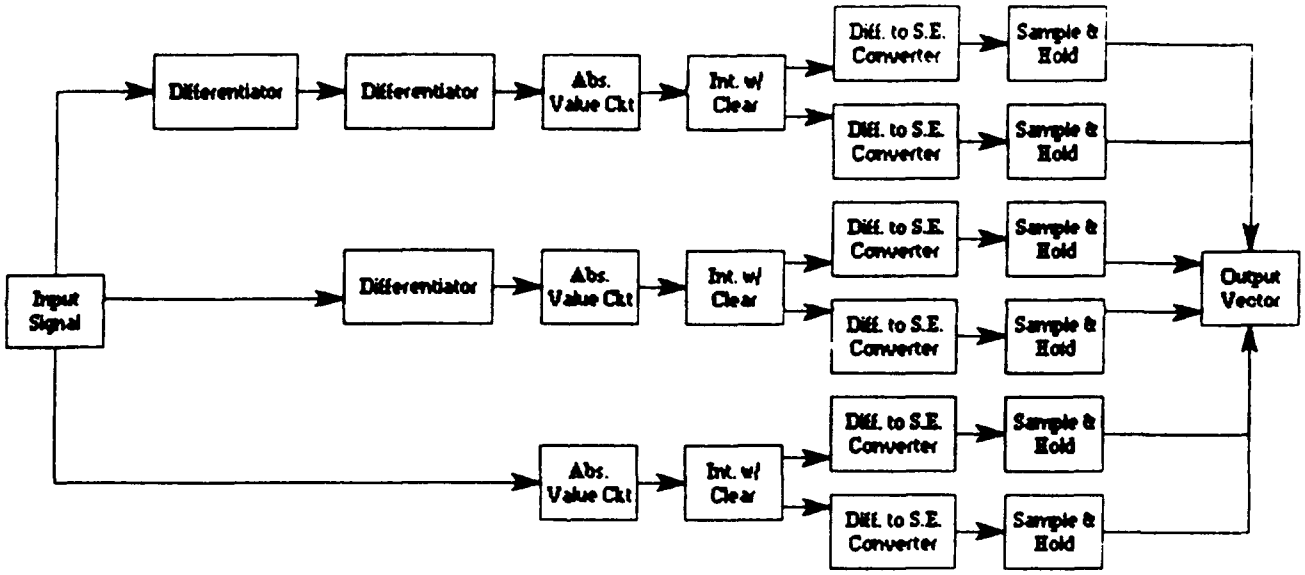

Figure 5

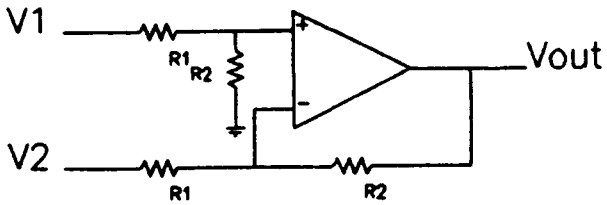

Figure 6

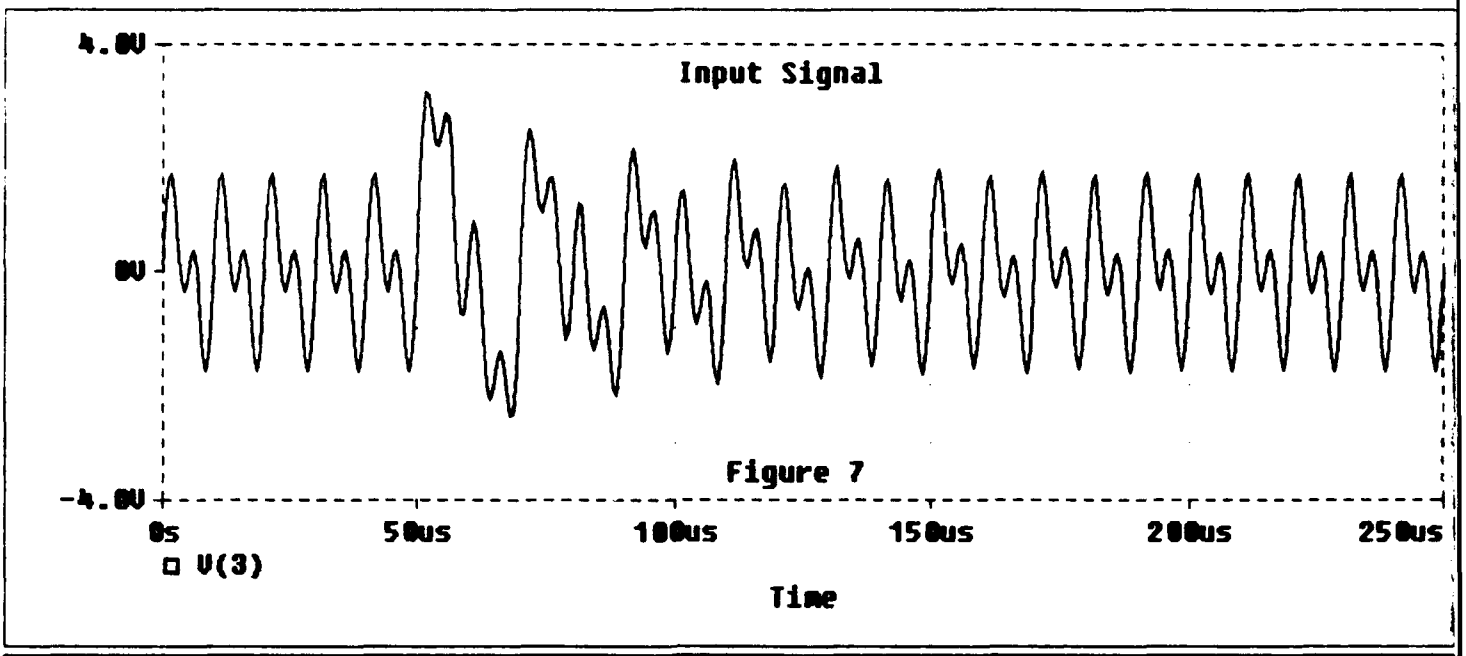

Figure 7

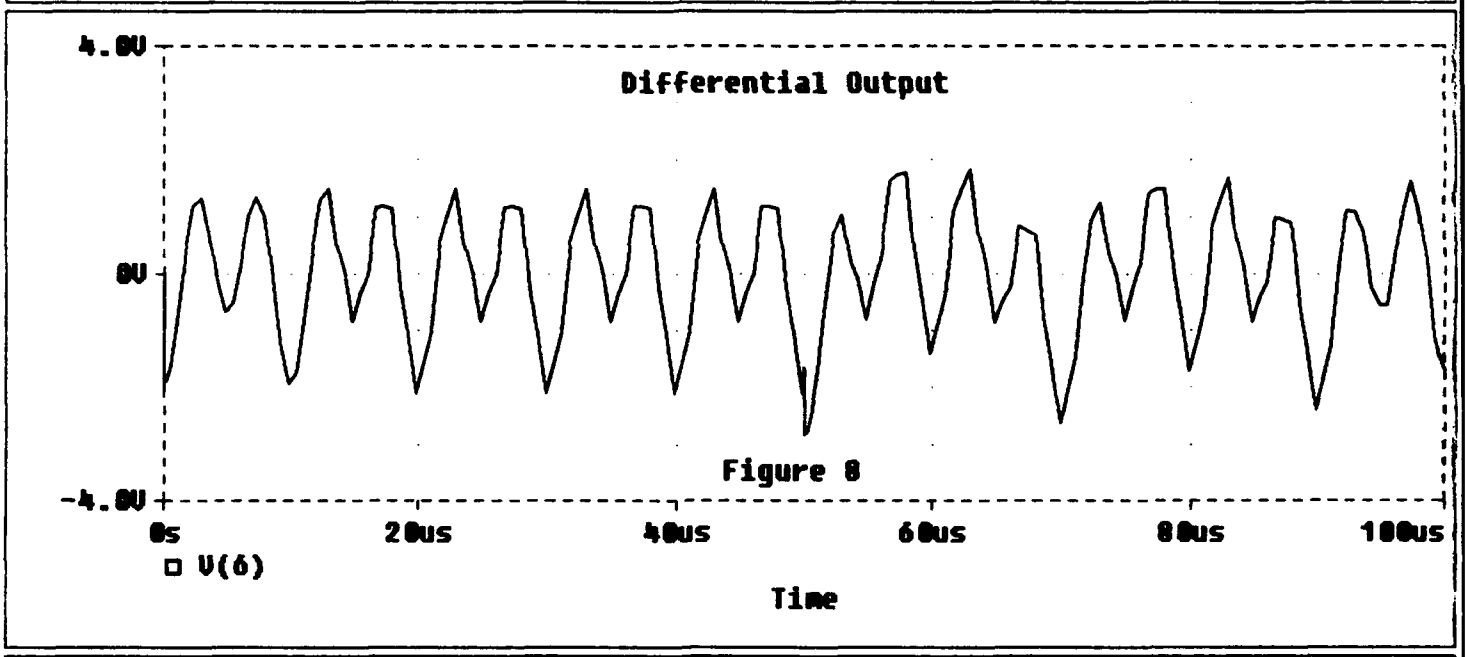

Figure 8

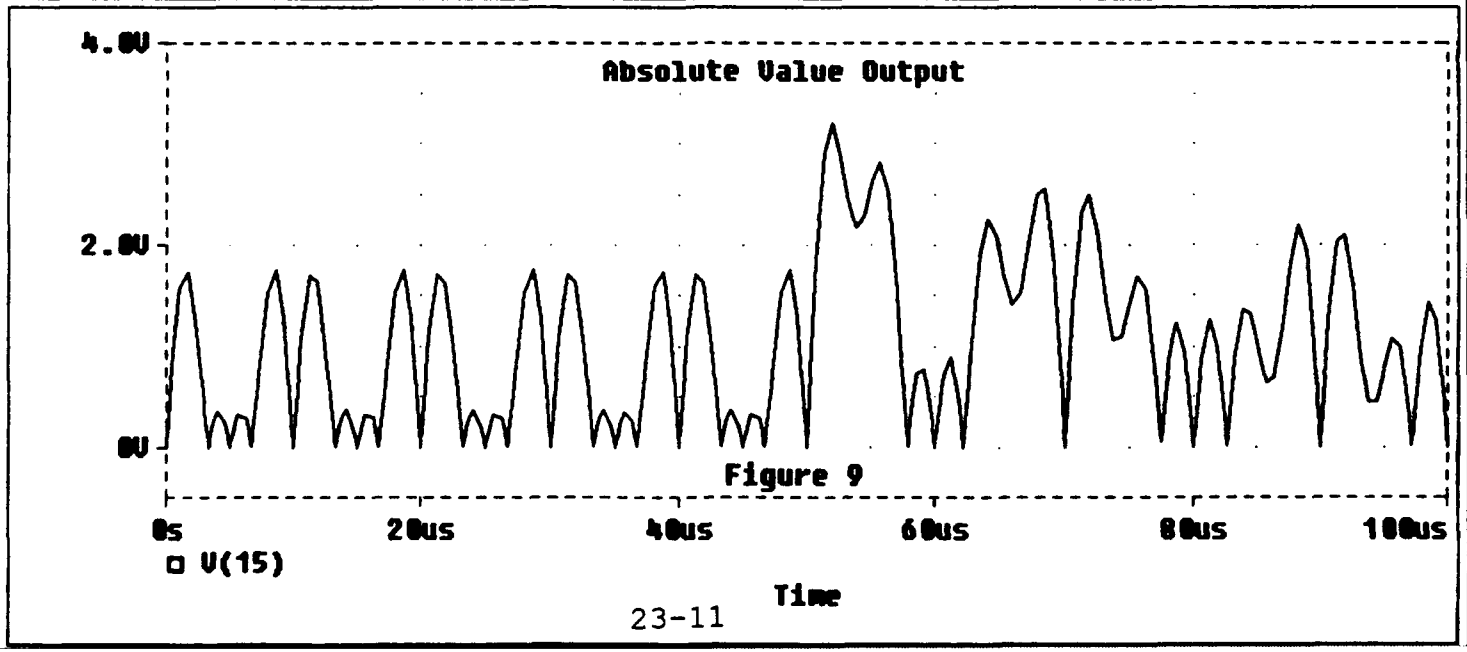

Figure 9

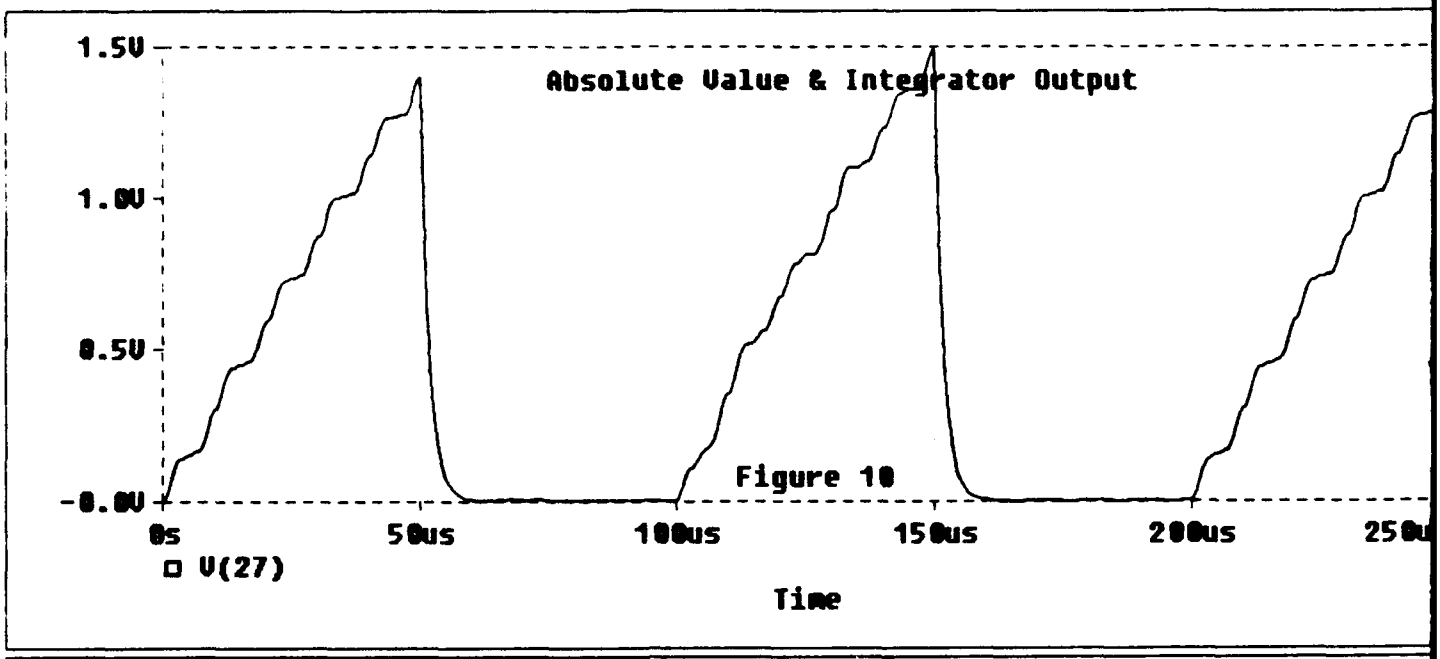

Figure 10

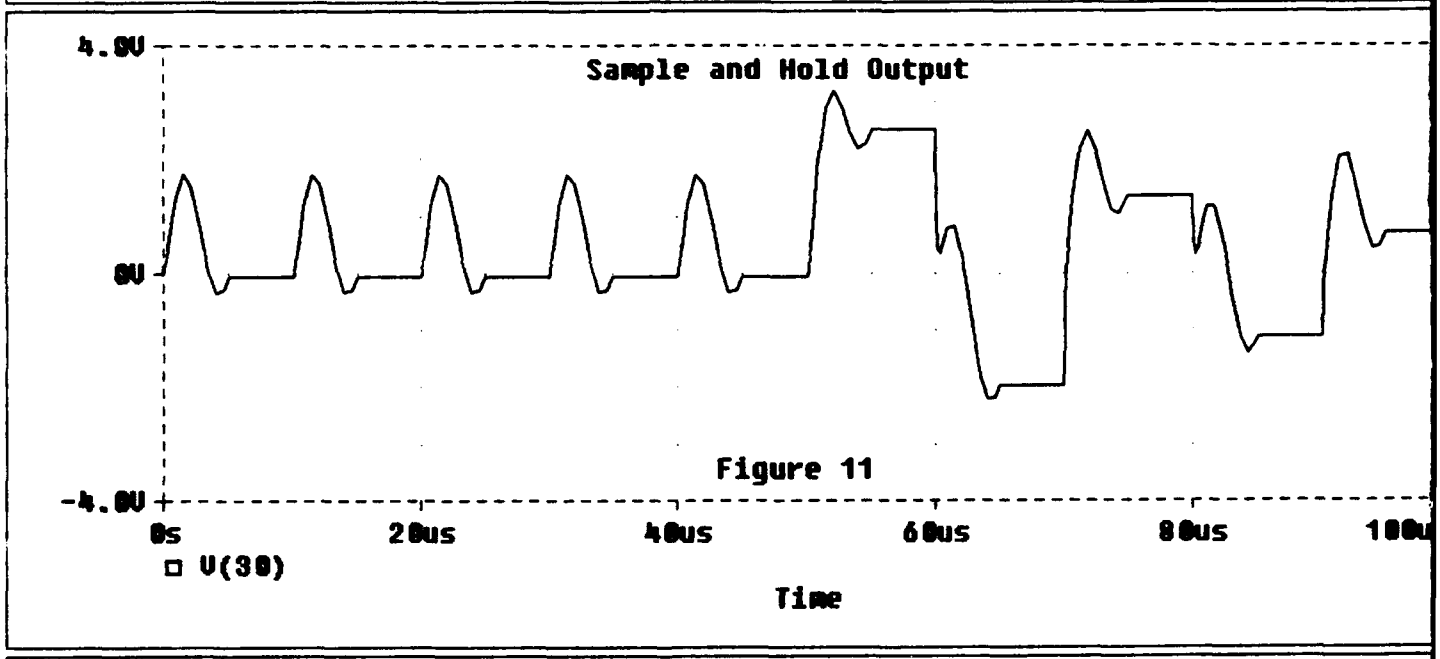

Figure 11

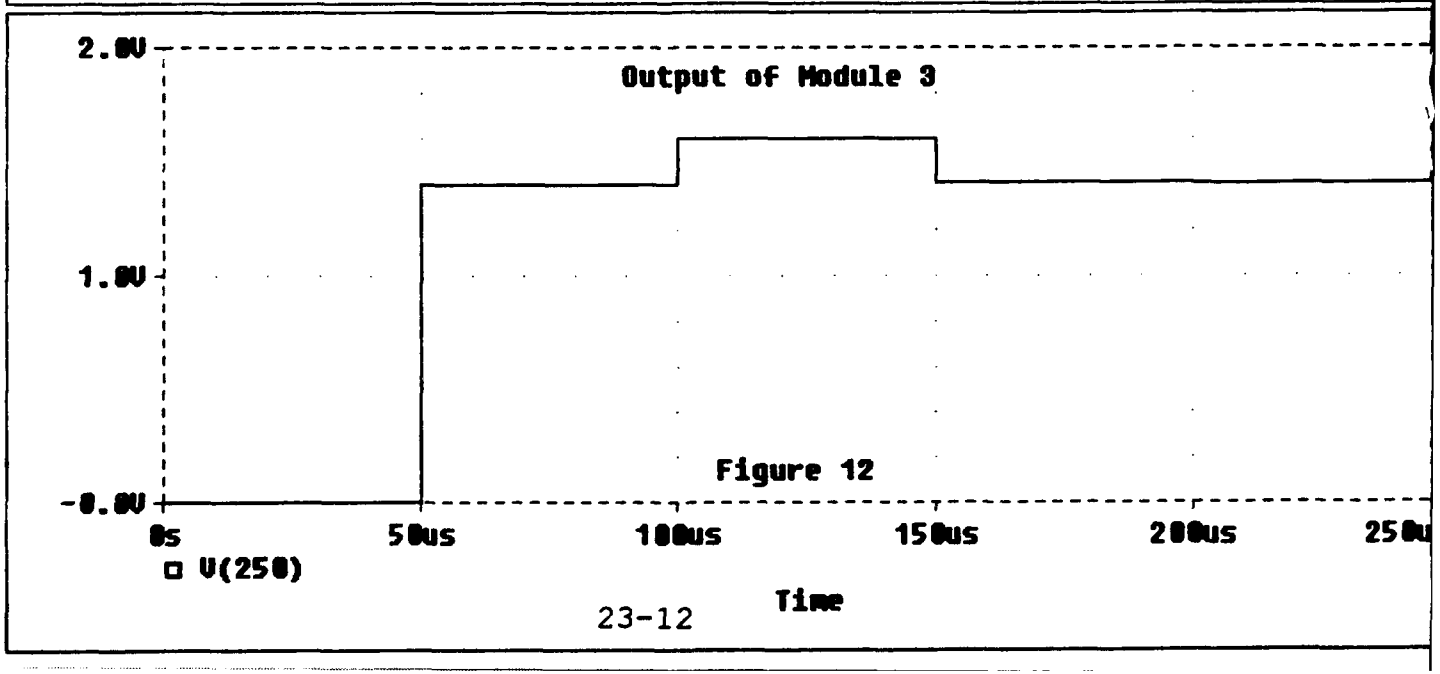

Figure 12

Polarization Considerations for Optical Correlators

Daniel J. Reiley
Physics Department
University of Alabama in Huntsville
Huntsville, AL 35899
(205)895-6417x318

Final Report for:
Graduate Student Research Program

Sponsored by:
Air Force Office of Scientific Research,
Bolling AFB, Washington, DC
at
Wright Laboratory, Eglin AFB, FL

September, 1993

Polarization Considerations for Optical Correlators

Daniel J. Reiley
Physics Department
University of Alabama in Huntsville
Huntsville, AL 35899
(205)895-6417x318

Abstract

The effect on polarization errors on the performance of optical correlators is examined. These errors are examined in the example of a matched-filter correlator with spatial light modulators which are nominally amplitude-only modulators. The modulators consist of a retarder oriented at 45° with spatially varying magnitude followed by a polarizer at either 0° or 90°. Three errors are considered - 1) misorientation of the input polarization state, misorientation of the polarizer, and nonlinear eigenpolarizations for the retarder. The first error is shown to reduce the height of the correlation peak. The second error is shown to reduce the height of the correlation peak and increase the background noise. The Third error has no effect. Following the discussion of polarization errors in optical correlators is a broad discussion of polarization analysis of optical systems. This discussion presents the underlying theory of the preceding section.

I. Polarization Considerations for Optical Correlators

Optical correlators can be sensitive to instrumental polarization. This sensitivity is due to the fact that many optical correlators use spatial light modulators which are actually polarization modulators. A twisted nematic modulator, for example, operates by inducing a spatially varying polarization pattern. A polarizer can be placed after the modulator to produce either phase modulation or amplitude modulation. Even modulators such as dichromated gelatin holograms can be polarization-sensitive. Due to the inherent anisotropy of these types devices, they tend to have some diattenuation.

This report presents a polarization analysis for a very particular type of correlator. A method is presented which calculates the effects of imperfect modulators on the quality of the correlation.

Nominal arrangement

The modulator analyzed in this report is a nominally amplitude-only modulator. The modulator consists of a linear retarder followed by a linear polarizer. The fast axis of the retarder is chosen to be at 0°, and the pass axis of the polarizer is chosen to be at 45° to the fast axis of the retarder. The input state is chosen to be at 90° to the polarizer. This scheme is shown in Figure 1.

$\vec{E}_{in}$ is the input polarization state, which is uniform over the object plane. $\vec{E}_{obj}$ Is the polarization state immediately after the input modulator; this polarization state will be modulated across the object plane. $\vec{E}_{fil-}$ Is the polarization state immediately before the filter plane modulator; this polarization state will be modulated across the filter plane. $\vec{E}_{fil+}$ Is the polarization state immediately after the filter plane modulator; this polarization state will be modulated across the filter plane. $\vec{E}_{img}$ Is the polarization state in the image plane; the variation of this polarization state will include the correlation peak.

In scalar diffraction theory, the derivation for the diffraction peak would go something like this: The field amplitude in the input plane is the transmission of the input filter times the (uniform) input field

$$E_{obj} = \tau_{obj} E_{in}, \qquad 1$$

where τ_{obj} is the transmission of the input filter. The field amplitude immediately before the filter is proportional to the Fourier transform of the field in the object plane,

$$E_{fil-} \propto \mathcal{F}\{E_{obj}\} \qquad 2$$

$$\mathcal{F}\{\tau_{obj} E_{in}\}$$

Since the input field is uniform, we can take the Fourier transform on the filter transmission instead of the input field,

$$E_{filt-} \propto \mathcal{F}\{\tau_{obj} E_{in}\}$$
$$= \mathcal{F}\{\tau_{obj}\} E_{in} \qquad 3$$

The field immediately beyond the filter is the field in front of the filter time the transmission function of the filter, τ_{filt},

$$E_{filt+} = \tau_{filt} E_{filt-}$$
$$\propto \tau_{filt} \mathcal{F}\{\tau_{obj}\} E_{in} \qquad 4$$

The field in the image plane is proportional to the Fourier transform of the field immediately after the filter,

$$E_{obj} \propto \mathcal{F}\{E_{filt+}\}$$
$$= \mathcal{F}\{\tau_{filt} \mathcal{F}\{\tau_{obj}\}\} E_{in} \qquad 5$$

We will consider simple matched filters of the form

$$\tau_{filt} = \mathcal{F}\{\tau_{tar}\} \cos k x_0 \qquad 6$$

where τ_{tar} is the pattern of the target. For this situation, the field in the image plane is a delta function whose height is proportional to the convolution between the object and the target,

$$E_{img} \propto \mathcal{F}\{\mathcal{F}\{\tau_{tar}\} \cos k x_0 \mathcal{F}\{\tau_{obj}\}\} E_{in}$$
$$= (\tau_{tar} \otimes \tau_{obj}) E_{in} \delta(x - x_0) \qquad 7$$

where $\delta(x)$ is a delta function centered at x and $\otimes$ represents a convolution operation.

In vector diffraction theory, we replace the scalar field amplitudes with Jones vectors, and we replace the scalar transmission functions with Jones matrices. The Jones vectors will describe the change in field amplitude across a beam, as well as the change in phase and polarization state. The Jones matrices will describe the change in amplitude, phase, and polarization state at each interface in the system. Since many spatial light modulators are really polarization modulators, working with the Jones calculus has the advantage that it can accurately describe what is physically happening to the light at each interface.

In vector diffraction theory, the derivation for the diffraction peak would go something like this: The field in the input plane is the transmission of the input filter times the (uniform) input field

$$\vec{E}_{obj} = \mathbf{J}_{obj} \vec{E}_{in}, \qquad 8$$

where $\mathbf{J}_{obj}$ is the Jones matrix of the input filter. The field immediately before the filter is proportional to the Fourier transform of the field in the object plane,

$$\vec{E}_{filt-} \propto \mathcal{F}\{\vec{E}_{obj}\}$$
$$= \mathcal{F}\{\mathbf{J}_{obj} \vec{E}_{in}\} \qquad 9$$

ince the input field is uniform, we can take the Fourier transform on the filter's Jones matrix istead of the input field,

$$\vec{E}_{filt-} \propto \mathcal{F}\{\mathbf{J}_{obj}\vec{E}_{in}\}$$
$$= \mathcal{F}\{\mathbf{J}_{obj}\}\vec{E}_{in}$$

he field immediately beyond the filter is the field in front of the filter times the Jones matrix of the lter, $\mathbf{J}_{filt}$,

$$\vec{E}_{filt-} = \mathbf{J}_{filt}E_{filt-}$$
$$\propto \mathbf{J}_{filt}\mathcal{F}\{\mathbf{J}_{obj}\}E_{in} \qquad 10$$

he field in the image plane is proportional to the Fourier transform of the field immediately after ie filter,

$$\vec{E}_{obj} \propto \mathcal{F}\{\vec{E}_{filt-}\}$$
$$= \mathcal{F}\{\mathbf{J}_{filt}\mathcal{F}\{\mathbf{J}_{obj}\}\}\vec{E}_{in} \qquad 11$$

his paper considers the proper forms for the filter's Jones matrix such that the height of the orrelation peak represents the correlation between the object and the target.

$$\vec{E}_{peak} \propto (\tau_{tar} \otimes \tau_{obj}) \qquad 12$$

The Jones matrix for our nominal modulator, shown in Figure 1, is

$$\mathbf{J} = \mathbf{J}_{polarizer}\mathbf{J}_{retarder} = \frac{1}{2}\begin{bmatrix} 1 & 1 \\ 1 & 1 \end{bmatrix}\begin{bmatrix} e^{i\delta} & 0 \\ 0 & e^{-i\delta} \end{bmatrix} \qquad 13$$

here δ is the retardance. For small amounts of retardance, this Jones matrix is

$$\mathbf{J} \cong \frac{1}{2}\begin{bmatrix} 1 & 1 \\ 1 & 1 \end{bmatrix}\begin{bmatrix} 1+i\delta & 0 \\ 0 & 1-i\delta \end{bmatrix} \qquad 14$$

he Jones vector for the nominal input state is

$$\vec{E} = \frac{1}{\sqrt{2}}\begin{bmatrix} 1 \\ -1 \end{bmatrix} \qquad 15$$

herefore, the transmission of the modulator is proportional to the retardance of the retarder,

$$\vec{E}_{mod} = \mathbf{J}_{polarizer}\mathbf{J}_{retarder}\vec{E}_{in}$$
$$\cong \frac{1}{2}\begin{bmatrix} 1 & 1 \\ 1 & 1 \end{bmatrix}\begin{bmatrix} 1+i\delta & 0 \\ 0 & 1-i\delta \end{bmatrix}\frac{1}{\sqrt{2}}\begin{bmatrix} 1 \\ -1 \end{bmatrix} = i\delta\frac{1}{\sqrt{2}}\begin{bmatrix} 1 \\ 1 \end{bmatrix} \qquad 16$$

o obtain an amplitude transmission proportional to the object, it is possible to write a retardance attern on the modulator such that

$$\delta(x,y) = \tau(x,y) \qquad 17$$

We consider a correlator like the one shown in Figure 2. The input beam is uniformly polarized at 45°. The input modulator is a spatially varying retarder at 0° followed by a uniform polarizer at -45°. The fourier plane modulator is a spatially varying retarder at 0° followed by a uniform polarizer at +45°. For this arrangement, the electric field immediately after the filter is

$$\begin{aligned}\vec{E}_{filter} &\propto \mathbf{J}_{filter}\mathcal{F}\{\mathbf{J}_{obj}\}E_{in} \\ &= \mathbf{J}_{polarizer-}\mathbf{J}_{retarder2}\mathcal{F}\{\mathbf{J}_{polarizer-}\mathbf{J}_{retarder2}\}\frac{1}{\sqrt{2}}\begin{bmatrix}1\\1\end{bmatrix}\end{aligned} \tag{18}$$

Since the polarizer is uniform, we can multiply its Jones matrix out of the Fourier transform,

$$\begin{aligned}\vec{E}_{filter} &\propto \mathbf{J}_{polarizer-}\mathbf{J}_{retarder2}\mathbf{J}_{polarizer-}\mathcal{F}\{\mathbf{J}_{retarder1}\}\frac{1}{\sqrt{2}}\begin{bmatrix}1\\1\end{bmatrix} \\ &= \frac{1}{2}\begin{bmatrix}1 & 1\\1 & 1\end{bmatrix}\begin{bmatrix}1+i\delta_2 & 0\\0 & 1-i\delta_2\end{bmatrix}\frac{1}{2}\begin{bmatrix}1 & -1\\-1 & 1\end{bmatrix}\mathcal{F}\left\{\begin{bmatrix}1+i\delta_2 & 0\\0 & 1-i\delta_2\end{bmatrix}\right\}\frac{1}{\sqrt{2}}\begin{bmatrix}1\\1\end{bmatrix}\end{aligned} \tag{19}$$

We then distribute the Fourier transform through the retarder matrix

$$\vec{E}_{filter} \propto \frac{1}{2}\begin{bmatrix}1 & 1\\1 & 1\end{bmatrix}\begin{bmatrix}1+i\delta_2 & 0\\0 & 1-i\delta_2\end{bmatrix}\frac{1}{2}\begin{bmatrix}1 & -1\\-1 & 1\end{bmatrix}\begin{bmatrix}1+i\mathcal{F}\{\delta_2\} & 0\\0 & 1-i\mathcal{F}\{\delta_2\}\end{bmatrix}\frac{1}{\sqrt{2}}\begin{bmatrix}1\\1\end{bmatrix} \tag{20}$$

By setting the retardance of the first retarder equal to the object function ($\delta_1 = \tau_{object}$) and the retardance of the filter retarder proportional to the target function ($\delta_2 = \tau_{tar}\cos kx_0$), we find the electric field immediately after the filter to be

$$\begin{aligned}\vec{E}_{filter} &\propto \frac{1}{2}\begin{bmatrix}1 & 1\\1 & 1\end{bmatrix}\begin{bmatrix}1+i\mathcal{F}\{\tau_{tar}\}\cos kx_0 & 0\\0 & 1-i\mathcal{F}\{\tau_{tar}\}\cos kx_0\end{bmatrix}\frac{1}{2}\begin{bmatrix}1 & -1\\-1 & 1\end{bmatrix}\begin{bmatrix}1+i\mathcal{F}\{\tau_{obj}\} & 0\\0 & 1-i\mathcal{F}\{\tau_{obj}\}\end{bmatrix}\frac{1}{\sqrt{2}}\begin{bmatrix}1\\1\end{bmatrix} \\ &= \frac{1}{\sqrt{2}}\begin{bmatrix}1\\1\end{bmatrix}\mathcal{F}\{\tau_{tar}\}\mathcal{F}\{\tau_{obj}\}\cos kx_0\end{aligned} \tag{21}$$

The electric field in the image plane is then proportional to the convolution of the object with the target,

$$\begin{aligned}\vec{E}_{img} &\propto \mathcal{F}\{\vec{E}_{filter}\} \\ &= \frac{1}{\sqrt{2}}\begin{bmatrix}1\\1\end{bmatrix}\tau_{tar}\otimes\tau_{obj}\delta(x-x_0)\end{aligned} \tag{22}$$

So, for the ideal polarizers and ideal retarders in this system, the electric field in the image is the same as for the result from scalar diffraction theory.

We now consider the effects on the previous analysis for several small error in polarization of the input beam, polarizers, and retarders,

Polarization error #1: Improperly polarized input beam

The Jones vector for a slightly elliptical input polarization state is

$$\vec{E}_{in} = \frac{1}{\sqrt{2}}\begin{bmatrix} 1 \\ 1 \end{bmatrix} + i\frac{a}{\sqrt{2}}\begin{bmatrix} 1 \\ -1 \end{bmatrix}, \qquad 23$$

where a is the ratio of the major axis of the polarization ellipse to the minor axis of the polarization ellipse. Since we already have the polarization aberration function for the nominal system, we can readily find the electric field immediately following the filter,

$$\vec{E}_{out} \propto \frac{1}{2}\begin{bmatrix} 1 & 1 \\ 1 & 1 \end{bmatrix}\begin{bmatrix} 1 + i\mathcal{F}(\tau_{tar})\cos kx_0 & 0 \\ 0 & 1 - i\mathcal{F}(\tau_{tar})\cos kx_0 \end{bmatrix}\frac{1}{2}\begin{bmatrix} 1 & -1 \\ -1 & 1 \end{bmatrix}\begin{bmatrix} 1 + i\mathcal{F}(\tau_{obj}) & 0 \\ 0 & 1 - i\mathcal{F}(\tau_{obj}) \end{bmatrix}\left(\frac{1}{\sqrt{2}}\begin{bmatrix} 1 \\ 1 \end{bmatrix} + i\frac{a}{\sqrt{2}}\begin{bmatrix} 1 \\ -1 \end{bmatrix}\right)$$

$$= \frac{1}{\sqrt{2}}\begin{bmatrix} 1 \\ 1 \end{bmatrix}\left(-a\cos kx_0 + i\mathcal{F}(\tau_{tar})\cos kx_0)\mathcal{F}(\tau_{obj})\right) \qquad 24$$

For this situation, the height of the correlation peak is reduced to

$$\vec{E}_{peak} \propto \frac{1}{\sqrt{2}}\begin{bmatrix} 1 \\ 1 \end{bmatrix}(i\tau_{tar} \otimes \tau_{obj} - a\tau_{tar}) \qquad 25$$

Since a can be real or imaginary, this result is applicable for both a misoriented linear input polarization state and a slightly elliptical input polarization state.

Polarization error #2 - misoriented polarizer in the input plane

The Jones matrix for a slightly misoriented polarizer in the input plane is

$$J_{polarizer} = R(-a)\frac{1}{2}\begin{bmatrix} 1 & -1 \\ -1 & 1 \end{bmatrix}R(a) \cong \frac{1}{2}\begin{bmatrix} 1-2a & -1 \\ -1 & 1+2a \end{bmatrix}, \qquad 26$$

where we have dropped terms of order a^2 and higher. We can readily substitute the new Jones matrix for the polarizer into equation __ to find the electric field immediately following the filter.

$$\vec{E}_{out} \propto \frac{1}{2}\begin{bmatrix} 1 & 1 \\ 1 & 1 \end{bmatrix}\begin{bmatrix} 1 - i\mathcal{F}(\tau_{tar})\cos kx_0 & 0 \\ 0 & 1 - i\mathcal{F}(\tau_{tar})\cos kx_0 \end{bmatrix}\frac{1}{2}\begin{bmatrix} 1-2a & -1 \\ -1 & 1+2a \end{bmatrix}\begin{bmatrix} 1 + i\mathcal{F}(\tau_{obj}) & 0 \\ 0 & 1 - i\mathcal{F}(\tau_{obj}) \end{bmatrix}\frac{1}{\sqrt{2}}\begin{bmatrix} 1 \\ 1 \end{bmatrix}$$

$$= \frac{1}{\sqrt{2}}\begin{bmatrix} 1 \\ 1 \end{bmatrix}\left(a - a\cos kx_0 + i\mathcal{F}(\tau_{tar})\cos kx_0)\mathcal{F}(\tau_{obj})\right) \qquad 27$$

For this situation, the height of the correlation peak is reduced to

$$\vec{E}_{peak} \propto \frac{1}{\sqrt{2}}\begin{bmatrix} 1 \\ 1 \end{bmatrix}(i\tau_{tar} \otimes \tau_{obj} - a\tau_{tar}) \qquad 28$$

Furthermore, the error in the input polarization state adds a background field in the image plane. This electric field reduces the contrast between the correlation peak and the noise. The amplitude of this background is,

$$\vec{E}_{background} \propto \frac{1}{\sqrt{2}}\begin{bmatrix} 1 \\ 1 \end{bmatrix}a\tau_{obj} \qquad 29$$

Polarization error #3 - elliptical eigenstates for the retarder

An elliptical retarder has a Jones matrix,

$$J_{ell\ ret} = \begin{bmatrix} 1 + i\tau & 2a\tau \\ 2a\tau & 1 - i\tau \end{bmatrix} \qquad 30$$

Its eigenvalues differ in phase,

$$\xi_s = 1 + i\tau \tag{31}$$

$$\xi_p = 1 - i\tau \tag{32}$$

so it is a weak retarder. Its eigenvectors are elliptical

$$\vec{E}_s = \begin{bmatrix} 1 \\ -ia \end{bmatrix}, \tag{33}$$

$$\vec{E}_q = \begin{bmatrix} ia \\ 1 \end{bmatrix}, \tag{34}$$

so it is an elliptical retarder. Replacing the Jones matrices in Equation __ with this type of retarder gives an electric field in immediately after the filter of

$$\vec{E}_{pu} \propto \frac{1}{2}\begin{bmatrix} 1 & 1 \\ 1 & 1 \end{bmatrix}\begin{bmatrix} 1 + i\mathcal{F}\{\tau_{tar}\}\cos k x_0 & 2a\mathcal{F}\{\tau_{tar}\}\cos k x_0 \\ 2a\mathcal{F}\{\tau_{tar}\}\cos k x_0 & 1 - i\mathcal{F}\{\tau_{tar}\}\cos k x_0 \end{bmatrix}\frac{1}{2}\begin{bmatrix} 1 & -1 \\ -1 & 1 \end{bmatrix}\begin{bmatrix} 1 + i\mathcal{F}\{\tau_{obj}\} & 2a\mathcal{F}\{\tau_{obj}\} \\ 2a\mathcal{F}\{\tau_{obj}\} & 1 - i\mathcal{F}\{\tau_{obj}\} \end{bmatrix}\frac{1}{\sqrt{2}}\begin{bmatrix} 1 \\ 1 \end{bmatrix}$$

$$- \frac{1}{\sqrt{2}}\begin{bmatrix} 1 \\ 1 \end{bmatrix}\mathcal{F}\{\tau_{tar}\}\cos k x_0 \mathcal{F}\{\tau_{obj}\}) \tag{35}$$

To this order, the height of the correlation peak is not affected by nonlinear eigenstates in the retarder,

$$\vec{E}_{peak} \propto \frac{1}{\sqrt{2}}\begin{vmatrix} 1 \\ 1 \end{vmatrix}\tau_{tar} \otimes \tau_{obj} \tag{36}$$

II. Introduction

A fundamental principle governing polarization in optical design is the existence a function J_{sys} which describes the effect of optical systems on the propagation of polarized light. This function, called the polarization aberration function, calculates the phase, amplitude, and polarization state in the exit pupil for any ray with any polarization state in the entrance pupil. The polarization aberration function is an extension of the wavefront aberration function, which only calculates the phase accumulation along a ray path due to geometrical optical path length. The following sections describes the following topics in general terms:

* defining J_{sys}
* calculating J_{sys}
* interpreting J_{sys}
* controlling J_{sys}

Section III describes how to define J_{sys}. Two methods of defining the polarization aberration function are described: a three-dimensional calculus which is well-suited for calculating the polarization aberration function, and an extension of the Jones calculus which is well-suited for interpreting the polarization aberration function.

Section IV describes a technique to calculate J_{sys}. This technique, called "polarization raytracing," is an extension of the well-established field of geometrical raytracing. This section describes how to calculate the polarization aberration function for a ray path by multiplying a cascade of two types of matrices: a matrix for propagation between surfaces, and a matrix for reflection or refraction at surfaces.

Section V outlines two methods of interpreting J_{sys}: approximation methods and graphical methods. First, the section presents a Taylor series approximation which is suitable for interpreting the polarization aberration functions of radially symmetric systems. Then, three graphical methods for interpreting the polarization aberration function are presented.

Section VI briefly discusses methods of controlling J_{sys}. Two classes of techniques are described: minimizing the polarization effects of each surface and balancing polarization effects among surfaces.

III. Defining J_{sys}

This section defines the polarization aberration function. First, light's electric field is related to its polarization state. Next, two methods for defining the light's polarization state and systems' polarization are presented. Finally, the relationship between the polarization aberration function and the wavefront aberration function is discussed.

A ray's polarization state is defined using a polarization vector. The polarization vector is related to the electric field of a monochromatic electromagnetic plane wave by

$$\vec{E}(\vec{r},t) = Re\{\vec{E}e^{i(\omega t-\vec{k}\cdot\vec{r})}\}. \qquad 37$$

$\vec{E}$ is the ray's polarization vector and defines the ray's amplitude, phase, and polarization state. $\vec{E}(\vec{r},t)$ is the time-varying electric field, $\vec{k}$ is the ray propagation vector, $\vec{r}$ is position, t is time, ω is the angular frequency of the field, and $Re\{\}$ indicates the real part. The polarization aberration function is usually defined as a matrix which maps a rays' polarization vector in the entrance pupil to its polarization vector in the exit pupil.

$$\vec{E}_{ex\ pupil}(\vec{\rho},\vec{h}) = J_{sys}(\vec{\rho},\vec{h})\vec{E}_{ent.\ pupil}, \qquad 38$$

where $\vec{\rho}$ represents pupil coordinates and $\vec{h}$ represents object coordinates. The polarization aberration function is a function of ray coordinates because diattenuation, retardance, transmittance, and optical path length are different for each ray path through the system. This section describes two standard representations for the polarization vector: the polarization raytracing vector and the Jones vector. This section also describes two associated representations for the polarization aberration function: the polarization raytracing matrix and the Jones matrix.

The first representation of the polarization vector is called a "polarization raytracing vector." A polarization raytracing vector is a three-element, complex valued column vector,

$$\vec{E}_P = \begin{bmatrix} E_x \\ E_y \\ E_z \end{bmatrix}. \qquad 39$$

E_x, E_y, and E_z are the projections of the electric field along the $\hat{x}$, $\hat{y}$, and $\hat{z}$ axes. When the light's polarization state is defined as a polarization raytracing vector, the polarization aberration function is defined as a complex-valued, 9-element, square matrix,

$$\mathbf{J}_{sys} = \mathbf{P} = \begin{bmatrix} p_{xx} & p_{xy} & p_{xz} \\ p_{yx} & p_{yy} & p_{yz} \\ p_{zx} & p_{zy} & p_{zz} \end{bmatrix}. \qquad 40$$

This form of the polarization aberration function is called the "polarization raytracing matrix." Since the polarization raytracing matrix uses the global basis vectors, it is a particularly useful form of the polarization aberration function to use for calculating $\mathbf{J}_{sys}$.

A second representation of the polarization vector is a Jones vector. A Jones vector is a two-element, complex valued column vector,

$$\vec{E}_J = \begin{bmatrix} E_i \\ E_j \end{bmatrix}. \qquad 41$$

E_i and E_j are the projections of the electric field along the $\hat{i}$ and $\hat{j}$ axes. The $\hat{i}$ and $\hat{j}$ axes are chosen so that they form an orthonormal basis set with the ray vector, $\hat{k}$. When the light's polarization state is defined as a Jones vector, the polarization aberration function is defined as a Jones matrix,

$$\mathbf{J}_{sys} = \mathbf{J}_J = \begin{bmatrix} J_{11} & J_{12} \\ J_{21} & J_{22} \end{bmatrix}. \qquad 42$$

The Jones matrix is commonly-used, well-understood form for analyzing and understanding polarization properties, so it is a particularly useful form of the polarization aberration function for interpreting $\mathbf{J}_{sys}$

The Jones calculus is related to the polarization raytracing calculus by an orthogonal change in basis states. The Jones vector is related to the polarization raytracing vector by multiplication of an orthogonal matrix O,

$$\vec{E}'_P = \mathbf{O}\vec{E}_P = \mathbf{O}\begin{bmatrix} E_x \\ E_y \\ E_z \end{bmatrix} = \begin{bmatrix} E_x \\ E_y \\ 0 \end{bmatrix} = \begin{bmatrix} \vec{E}_J \\ 0 \end{bmatrix}, \qquad 43$$

where $\vec{E}_J$ is a Jones vector and $\vec{E}'_P$ is called an "extended Jones vector." The Jones matrix can be calculated from the polarization raytracing matrix by multiplication of two orthogonal matrices $\mathbf{O}_0$, and $\mathbf{O}_Q$,

$$\mathbf{J}_{sys}' = \mathbf{O}_Q^{-1}\mathbf{P}\mathbf{O}_0 = \mathbf{O}_Q^{-1}\begin{bmatrix} p_{xx} & p_{xy} & p_{xz} \\ p_{yx} & p_{yy} & p_{yz} \\ p_{zx} & p_{zy} & p_{zz} \end{bmatrix}\mathbf{O}_0$$

$$= \begin{vmatrix} J_{11} & J_{12} & 0 \\ J_{21} & J_{22} & 0 \\ 0 & 0 & 0 \end{vmatrix} = \begin{vmatrix} & \mathbf{J}_J & & 0 \\ & & & 0 \\ 0 & 0 & 0 & 0 \end{vmatrix}.$$

where the submatrix $\mathbf{J}_J$ is a four-element Jones matrix and $\mathbf{J}_{sys}'$ is called an "extended Jones matrix." $\mathbf{O}_Q$ and $\mathbf{O}_0$ account for the change in ray direction from surface 0 to surface Q. The choice of an orthogonal transformation is not unique; equations __ and __ represent necessary conditions, not sufficient conditions, for the choice of O. The choice of these orthogonal transformation involves many other considerations which are beyond the scope of this report.

Finally, we discuss the relationship between the polarization aberration function and the wavefront aberration function, $W(\vec{\rho},\vec{h})$. In the Jones calculus, the wavefront in the exit pupil can be separated into orthogonal polarization states,

$$\begin{aligned} \vec{E}_{J,\text{ex.pupil}}(\vec{\rho},\vec{h}) &= \mathbf{J}_{sys}(\vec{\rho},\vec{h})\vec{E}_{J,\text{ent. pupil}} \\ &= a_1(\vec{\rho},\vec{h})e^{i\delta_1(\vec{\rho},\vec{h})}\vec{E}_{J,\text{ent. pupil}} + a_2(\vec{\rho},\vec{h})e^{i\delta_2(\vec{\rho},\vec{h})}\vec{E}_{J,\text{orth.}}, \end{aligned} \qquad 45$$

where $\vec{E}_{J,\text{orth.}}$ is the polarization state which is orthogonal to the polarization state in the entrance pupil, $\vec{\rho}$ is the exit pupil coordinate, and $\vec{h}$ is the object coordinate $a_1(\vec{\rho},\vec{h})$ And $a_1(\vec{\rho},\vec{h})$ are the amplitudes in the exit pupil of $\vec{E}_{J,\text{ex.pupil}}$ and $\vec{E}_{J,\text{orth.}}$. $\delta_1(\vec{\rho},\vec{h})$ and $\delta_2(\vec{\rho},\vec{h})$ are the phases in the exit pupil of $\vec{E}_{J,\text{ex pupil}}$ and $\vec{E}_{J,\text{orth.}}$, measured with respect to a reference sphere. The wavefront aberration function can be defined as the phase in the exit pupil of the portion of the wavefront which is not coupled into the orthogonal polarization state,

$$\delta_1(\vec{\rho},\vec{h}) = 2\pi W(\vec{\rho},\vec{h}), \qquad 46$$

where the wavefront aberration function is defined in waves. This definition of the wavefront aberration function reduces to the definition from geometrical optics when no light is coupled into the orthogonal polarization state, $a_2(\vec{\rho}, \vec{h}) = 0$, and when there is no apodization, $a_1(\vec{\rho}, \vec{h}) = 1$. Under these conditions, equation __ reduces to

$$\vec{E}_{J,\text{ex.pupil}} = \mathbf{J}_{sys}\vec{E}_{J,\text{ent. pupil}} = e^{i2\pi W(\vec{\rho},\vec{h})}\vec{E}_{J,\text{ent. pupil}}, \qquad 47$$

which is the definition of the wavefront aberration function in geometrical optics.

IV. Calculating $\mathbf{J}_{sys}$

Calculating the polarization aberration function usually requires a polarization raytracing program. A polarization raytracing program can sample $\mathbf{J}_{sys}$ by calculating a polarization raytracing matrix for a grid of ray paths. This section describes how polarization raytracing programs can calculate the polarization raytracing matrix for a single ray path.

Polarization raytracing programs can calculate the polarization aberration function by calculating two types of matrices: propagation matrices and refraction matrices. The polarization raytracing matrix for a ray path is the matrix product of these constituent matrices,

$$\mathbf{P}_{sys} = \mathbf{P}_{Q-1,Q}\mathbf{P}_{Q-1}\mathbf{P}_{Q-2,Q-1}\cdots\mathbf{P}_{1,2}\mathbf{P}_{1}\mathbf{P}_{0,1}, \qquad 48$$

where $\mathbf{P}_{q-1,q}$ is the polarization raytracing matrix for propagation from surface $q-1$ to surface q, $\mathbf{P}_q$ is the polarization raytracing matrix for refraction at surface q, and Q is the total number of surfaces in the system. Propagation matrices are calculated by a straightforward extension of geometrical raytracing. Refraction matrices are calculated by combining geometrical optics with thin-film calculations.

Calculating the propagation matrix, $P_{q-1,q}$, requires a simple extension of geometrical raytracing. First, OPD_{q-1}, the optical path difference along the ray path between surface $q-1$ and surface q, is calculated using geometrical raytracing. Then, the polarization raytracing program constructs $P_{q-1,q}$, the propagation matrix. In isotropic media, the polarization state doesn't change between surfaces, so $P_{q-1,q}$ is the identity matrix times a phase factor proportional to OPD_{q-1},

$$\mathbf{P}_{q-1,q} = \begin{bmatrix} 1 & 0 & 0 \\ 0 & 1 & 0 \\ 0 & 0 & 1 \end{bmatrix} e^{iOPD_{q-1}2\pi/\lambda}, \qquad 49$$

where λ is wavelength. In non-isotropic media, light's polarization state can change on propagation, so the propagation matrix for these media is not proportional to the identity matrix.

To calculate $\mathbf{P}_q$, the refraction matrix, the polarization raytracing program combines geometrical raytracing and coating calculations. The refraction matrix is a product of several other matrices:

$$P_q = O_{\vec{r}_q \to \vec{r}_q} J'_q O_{\vec{r}_{q-1} \to \vec{r}'_{q-1}}$$

$$= O_{\vec{r}_q \to \vec{r}'_q} O_{sp'_q \to \vec{r}'_q} C_{sp_q \to sp'_q} O_{\vec{r}'_{q-1} \to sp_q} O_{\vec{r}_{q-1} \to \vec{r}'_{q-1}} \qquad 50$$

This matrix multiplication first uses $O_{\vec{r}_{q-1} \to \vec{r}'_{q-1}}$ to change from the global basis states into the local, $\{\hat{i}, \hat{j}, \hat{k}\}$, basis states. Next, J'_q, the extended Jones vector for the interface, accounts for the change in the light's polarization state. The extended Jones matrix for the interface is made up of three constituent matrices, $O_{\vec{r}'_{q-1} \to sp_q}$, $C_{sp_q \to sp'_q}$, and $O_{sp'_q \to \vec{r}'_q}$. $O_{\vec{r}'_{q-1} \to sp_q}$ changes the basis states from the local $\{\hat{i}, \hat{j}, \hat{k}\}$ basis into the $\{\hat{s}, \hat{p}, \hat{k}\}$ basis; $C_{sp_q \to sp'_q}$, a diagonal matrix, accounts for the change in phase and amplitude of the s- and p- polarization states; $O_{sp'_q \to \vec{r}'_q}$ changes from the s-p basis vectors into the local, ray-based basis vectors. Finally, $O_{\vec{r}'_q \to \vec{r}_q}$ changes from the local, ray-based basis vectors into the global basis vectors.

To calculate $O_{\vec{r}_{q-1} \to \vec{r}'_{q-1}}$, the matrix which changes from the global $\{\hat{x}, \hat{y}, \hat{z}\}$ basis states into the local $\{\hat{i}_{q-1}, \hat{j}_{q-1}, \hat{k}_{q-1}\}$ basis states, the polarization raytracing program must choose the local basis states. These basis states are set by convention and must form an orthonormal basis set with the ray vector, $\hat{i} \cdot \hat{j} = \hat{k} \cdot \hat{j} = \hat{k} \cdot \hat{i} = 0$. $O_{\vec{r}_{q-1} \to \vec{r}'_{q-1}}$ is

$$O_{\vec{r}_{q-1} \to \vec{r}'_{q-1}} = \begin{bmatrix} \hat{x} \cdot \hat{i}_{q-1} & \hat{y} \cdot \hat{i}_{q-1} & \hat{z} \cdot \hat{i}_{q-1} \\ \hat{x} \cdot \hat{j}_{q-1} & \hat{y} \cdot \hat{j}_{q-1} & \hat{z} \cdot \hat{j}_{q-1} \\ \hat{x} \cdot \hat{k}_{q-1} & \hat{y} \cdot \hat{k}_{q-1} & \hat{z} \cdot \hat{k}_{q-1} \end{bmatrix}. \qquad 51$$

$O_{\vec{r}'_{q-1} \to sp_q}$ is a rotation about the ray vector $\hat{k}_q$. To calculate $O_{\vec{r}'_{q-1} \to sp_q}$, the polarization raytracing routine must first calculate $\hat{s}_q$ and $\hat{p}_q$, the unit vectors parallel to the s- and p-polarization states. Since the s-polarization state is perpendicular to both the incident ray and the surface normal, $\hat{s}_q$ can be calculated using the cross product of the ray vector and the surface normal, $\hat{\eta}_q$,

$$\hat{s}_q = \hat{\eta}_q \times \hat{k}_{q-1} / |\hat{\eta}_q \times \hat{k}_{q-1}|. \qquad 52$$

Since the p- polarization state is perpendicular to both the s- polarization state and the incident ray, $\hat{p}_q$ can be calculated using the cross product of the ray vector and $\hat{s}_q$:

$$\hat{p}_q = \hat{k}_{q-1} \times \hat{s}_q. \qquad 53$$

$O_{\vec{r}'_{q-1} \to sp_q}$ is constructed from the unit vectors $\hat{s}_q$, $\hat{p}_q$, $\hat{i}_{q-1}$, and $\hat{j}_{q-1}$,

$$\mathbf{O}_{\vec{r}_{q-1}\to sp_q} = \begin{bmatrix} \hat{\imath}_{q-1}\cdot\hat{s}_q & \hat{\jmath}_{q-1}\cdot\hat{s}_q & \hat{k}_{q-1}\cdot\hat{s}_q \\ \hat{\imath}_{q-1}\cdot\hat{p}_q & \hat{\jmath}_{q-1}\cdot\hat{p}_q & \hat{k}_{q-1}\cdot\hat{p}_q \\ \hat{\imath}_{q-1}\cdot\hat{k}_{q-1} & \hat{\jmath}_{q-1}\cdot\hat{k}_{q-1} & \hat{k}_{q-1}\cdot\hat{k}_{q-1} \end{bmatrix} = \begin{bmatrix} \hat{\imath}_{q-1}\cdot\hat{s}_q & \hat{\jmath}_{q-1}\cdot\hat{s}_q & 0 \\ \hat{\imath}_{q-1}\cdot\hat{p}_q & \hat{\jmath}_{q-1}\cdot\hat{p}_q & 0 \\ 0 & 0 & 1 \end{bmatrix}. \qquad 54$$

To calculate $\mathbf{C}_{sp_q\to sp'_q}$, the polarization raytracing routine must calculate $\xi_{s,q}$ and $\xi_{p,q}$, the complex s- and p- eigenvalues for the interface. These calculations follow well-established algorithms from thin-film coating design. $\mathbf{C}_{sp_q\to sp'_q}$ Is a diagonal matrix with the s- and p-eigenvalues along the diagonal.

$$\mathbf{C}_{sp_q\to sp'_q} = \begin{bmatrix} \xi_{s,q} & 0 & 0 \\ 0 & \xi_{p,q} & 0 \\ 0 & 0 & 0 \end{bmatrix}. \qquad 55$$

To calculate $\mathbf{O}_{sp'_q\to\vec{r}'_q}$, the polarization raytracing routine must first calculate $\vec{k}_q$, the direction cosines after surface q. $\vec{k}_q$ is readily calculated using well-established methods from geometrical raytracing. The polarization raytracing routine then finds $\hat{p}'_q$, the unit vector parallel to the p-polarization state after reflection. Since the $\hat{s}_q$ vector doesn't change at the interface, $\hat{p}'_q$ can be calculated using the cross product of the new ray vector with $\hat{s}$,

$$\hat{p}'_q = \hat{k}'_q \times \hat{s}_q. \qquad 56$$

$\mathbf{O}_{sp'_q\to\vec{r}'_q}$ is calculated from the $\hat{s}$, $\hat{p}'_q$, $\vec{k}_q$, $\hat{\imath}_q$ and $\hat{\jmath}_q$ unit vectors,

$$\mathbf{O}_{sp'_q\to\vec{r}'_q} = \begin{vmatrix} \hat{s}_q\cdot\hat{\imath}_q & \hat{p}'_q\cdot\hat{\imath}_q & \hat{k}'_q\cdot\hat{\imath}_q \\ \hat{s}_q\cdot\hat{\jmath}_q & \hat{p}'_q\cdot\hat{\jmath}_q & \hat{k}'_q\cdot\hat{\jmath}_q \\ \hat{s}_q\cdot\hat{k}'_q & \hat{p}'_q\cdot\hat{k}'_q & \hat{k}'_q\cdot\hat{k}'_q \end{vmatrix} = \begin{bmatrix} \hat{s}_q\cdot\hat{\imath}_q & \hat{p}'_q\cdot\hat{\imath}_q & 0 \\ \hat{s}_q\cdot\hat{\jmath}_q & \hat{p}'_q\cdot\hat{\jmath}_q & 0 \\ 0 & 0 & 1 \end{bmatrix} \qquad 57$$

To calculate $\mathbf{O}_{\vec{r}'_q\to\vec{r}'_q}$, the polarization raytracing program needs only the local, ray-based basis vectors

$$\mathbf{O}_{\vec{r}'_q\to\vec{r}'_q} = \begin{vmatrix} \hat{\imath}_q\cdot\hat{x} & \hat{\jmath}_q\cdot\hat{x} & \hat{k}_q\cdot\hat{x} \\ \hat{\imath}_q\cdot\hat{y} & \hat{\jmath}_q\cdot\hat{y} & \hat{k}_q\cdot\hat{y} \\ \hat{\imath}_q\cdot\hat{z} & \hat{\jmath}_q\cdot\hat{z} & \hat{k}_q\cdot\hat{z} \end{vmatrix} \qquad 58$$

$\mathbf{P}_q$, the polarization raytracing matrix for a surface can be calculated by combining the constituent matrices as shown in equation __. $\mathbf{P}$, the polarization raytracing matrix for a ray path, can be calculated by multiplying the propagation matrices and refraction matrices as shown in equation __. $\mathbf{J}_{sys}$, the polarization aberration function, can be sampled by calculating the polarization raytracing matrix for grids of ray paths.

V. Interpreting J_{sys}

After a polarization raytracing program samples the polarization aberration function, the optical designer often must interpret the results to decide if the system's performance is acceptable. This section describes two types of methods for interpreting J_{sys}: approximation methods and graphical methods.

The first method for interpreting the polarization aberration function is to make approximations. A particularly useful approximation, called the "polarization aberration expansion," is a Taylor series expansion in pupil and object coordinates. The polarization aberration expansion for radially symmetric systems is

$$
\begin{aligned}
J_{sys} \cong\ & P_{0000}\begin{vmatrix} 1 & 0 \\ 0 & 1 \end{vmatrix} + P_{1200}h^2\begin{bmatrix} 1 & 0 \\ 0 & -1 \end{bmatrix} \\
& + P_{1111}h\rho\left(\cos\phi\begin{vmatrix} 1 & 0 \\ 0 & -1 \end{vmatrix} - \sin\phi\begin{bmatrix} 1 & 0 \\ 0 & -1 \end{bmatrix}\right) \\
& + P_{1022}\rho^2\left(\cos 2\phi\begin{vmatrix} 1 & 0 \\ 0 & -1 \end{vmatrix} - \sin 2\phi\begin{bmatrix} 1 & 0 \\ 0 & -1 \end{bmatrix}\right),
\end{aligned}
\tag{59}
$$

where ρ is the radial pupil coordinate, ϕ is the angular pupil coordinate, h is the object coordinate, and P_{0000}, P_{1200}, P_{1111}, and P_{1022} are called the "polarization aberration coefficients." The polarization aberration expansion systematizes the analysis of the polarization aberration function in two ways. First, the overall image quality can be understood by examining each of the terms in the series because each term has an identifiable effect on image quality. Second, unacceptably large terms can be systematically reduced because each term can be calculated on a surface-by-surface basis.

The second method for interpreting the polarization aberration function is to use graphical methods. In these methods, the relevant parameters are plotted as a function of exit pupil coordinate. These plots include exit pupil phase maps, exit pupil polarization maps, diattenuation pupil maps.

One graphical method for interpreting the polarization aberration function is an exit pupil phase map, shown in Figure 3. An exit pupil phase map plots the phase of a particular polarization state as a function of exit pupil coordinate. Figure3 is a plot of the phase of the horizontally polarized component of the light in the exit pupil when horizontally polarized light is incident. In the Jones calculus, this wavefront is described by

$$\vec{E}_{J\ \text{ex pupil}} = \begin{bmatrix} a_{11}e^{i\delta_{11}} \\ a_{21}e^{i\delta_{21}} \end{bmatrix} = \mathbf{J}(\vec{\rho},\vec{h})\begin{bmatrix} 1 \\ 0 \end{bmatrix}$$

$$= \begin{bmatrix} a_{11}e^{i\delta_{11}} & a_{12}e^{i\delta_{12}} \\ a_{21}e^{i\delta_{21}} & a_{22}e^{i\delta_{22}} \end{bmatrix}\begin{bmatrix} 1 \\ 0 \end{bmatrix}. \qquad 60$$

Figure 3 is a plot of δ_{11}, the phase of the first element in the Jones matrix. The exit pupil phase map is an incomplete description of an optical system's imaging properties because it gives no information about the wave's amplitude or polarization state or about the system's effect on the orthogonal polarization state. Nevertheless, the exit pupil phase map is sometimes a sufficient characterization of an optical system's performance, especially in systems which are not polarization-critical. In these systems, the phase of the first element in the Jones matrix is proportional to the wavefront aberration function, $\delta_{11} = W(\vec{\rho},\vec{h})2\pi/\lambda$; and the exit pupil phase map is a good indication of the sharpness of an image.

A second, more complete, graphical method for interpreting the polarization aberration function is an exit pupil polarization map, shown in Figure 4. A grid of rays with a uniform polarization state in the entrance pupil is traced through the optical system, and the polarization state is plotted in the exit pupil. For example, Figure 4 shows the wavefront in the exit pupil when vertically polarized light is incident. This wavefront can be represented in the Jones calculus by

$$\vec{E}_{J\ \text{ex pupil}} = \begin{bmatrix} a_{12}e^{i\delta_{12}} \\ a_{22}e^{i\delta_{22}} \end{bmatrix} = \mathbf{J}(\vec{\rho},\vec{h})\begin{bmatrix} 0 \\ 1 \end{bmatrix}$$

$$= \begin{bmatrix} a_{11}e^{i\delta_{11}} & a_{12}e^{i\delta_{12}} \\ a_{21}e^{i\delta_{21}} & a_{22}e^{i\delta_{22}} \end{bmatrix}\begin{bmatrix} 0 \\ 1 \end{bmatrix}. \qquad 61$$

The lines and ellipses on the plot describe the polarization ellipse of the transmitted light. The position of the arrow on each ellipse denotes phase, and the direction of the arrow distinguishes between left and right circularly polarized components. Figure 4 gives information about the amplitude and phase of two elements of the polarization aberration function, J_{12} and J_{22}.

VI. Controlling $\mathbf{J}_{sys}$

Once the polarization aberration function is calculated and interpreted, it often must be controlled so that the optical system will perform properly. This section describes two design methods to control the polarization aberration function: reducing the polarization aberrations of each surface and balancing polarization aberrations among surfaces.

The first design method to control the polarization aberration function is to reduce the polarization aberration coefficients for each surface in the system. One way to reduce a surface's polarization aberration coefficient is to choose the proper type of surface. For example, choosing a prism instead of a diffraction grating can greatly decrease the diattenuation and retardance of a ray path. A second way to reduce a surface's polarization aberration coefficient is to place a low-polarization coating on the interface. Low polarization coatings are optimized to have s- and p-eigenvalues which are nearly equal, $\xi_{s,q} \cong \xi_{p,q}$. When this condition is met, the surface's polarization aberration coefficient is nearly zero, and the polarization raytracing matrix for the surface is nearly proportional to the identity matrix,

$$C_{sp_q \to sp_q} \cong \xi_{s,q} \begin{vmatrix} 1 & 0 & 0 \\ 0 & 1 & 0 \\ 0 & 0 & 0 \end{vmatrix} \cong \xi_{p,q} \begin{bmatrix} 1 & 0 & 0 \\ 0 & 1 & 0 \\ 0 & 0 & 0 \end{bmatrix}. \qquad 62$$

A second way to control the polarization aberration function is to balance the polarization aberrations among surfaces. Figure 5 illustrates an example of balancing the polarization aberration coefficients for two fold mirrors with identical coatings. For the arrangement shown in figure 5a, the polarization aberrations of the two fold mirrors are not balanced because the s- and p- eigenpolarizations of each surface are aligned. The Jones matrix for the axial ray for this arrangement is

$$J_{sys} = \begin{vmatrix} \xi_p & 0 \\ 0 & \xi_s \end{vmatrix} \begin{vmatrix} \xi_p & 0 \\ 0 & \xi_s \end{vmatrix} = \begin{bmatrix} \xi_p^2 & 0 \\ 0 & \xi_s^2 \end{bmatrix}. \qquad 63$$

For the arrangement shown in Figure 5b, the polarization aberration of the two fold mirrors are balanced because the s- and p- eigenstates for the surface are crossed. The Jones matrix for the axial ray for this arrangement would be,

$$J_{sys} = \begin{vmatrix} \xi_p & 0 \\ 0 & \xi_s \end{vmatrix} \begin{bmatrix} \xi_s & 0 \\ 0 & \xi_p \end{bmatrix} = \xi_s \xi_p \begin{bmatrix} 1 & 0 \\ 0 & 1 \end{bmatrix}. \qquad 64$$

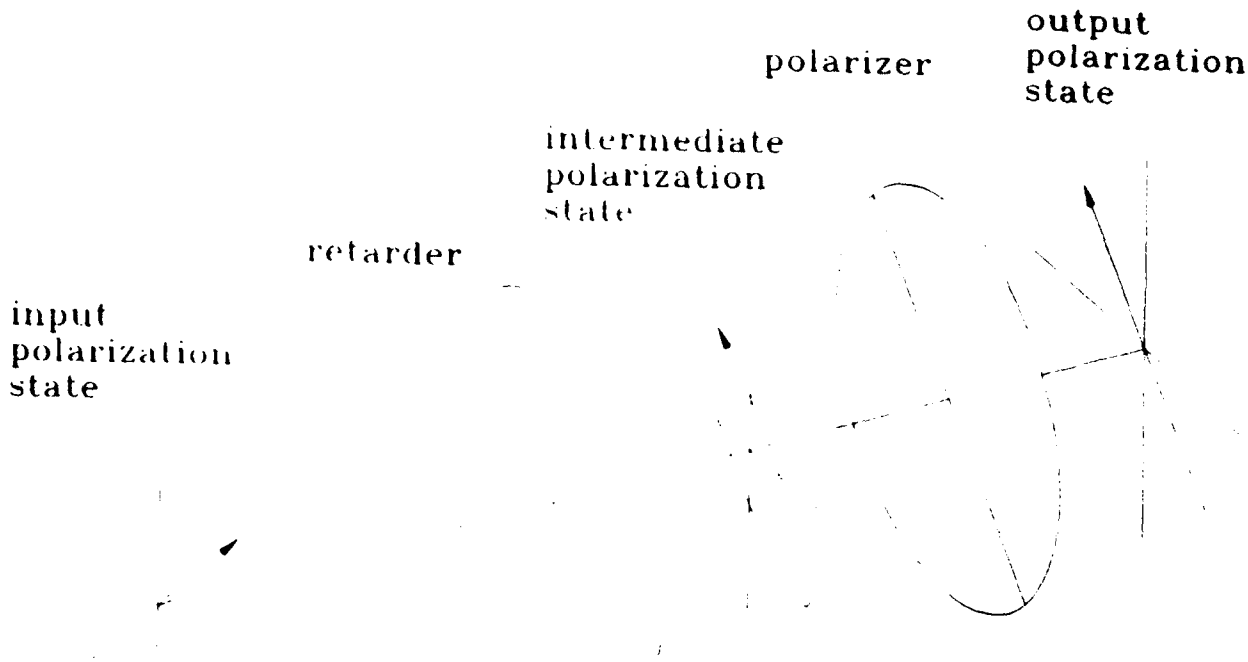

Figure 1: Modulator arrangement. This arrangement is commonly used in optical correlators for nominally amplitude-only modulation. This paper describes the effects of imperfections in the polarization elements on the correlation.

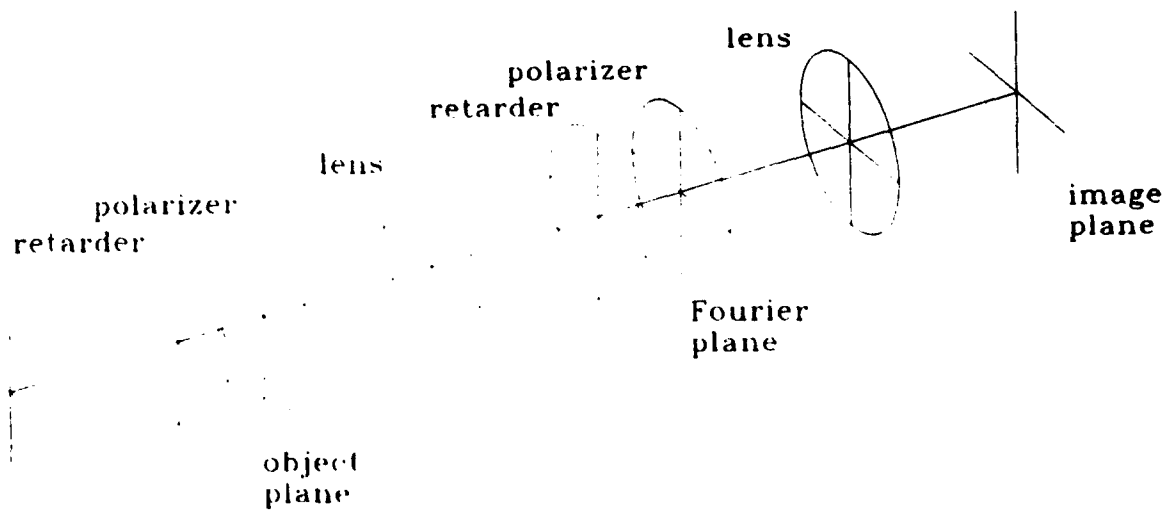

Figure 2: Correlator arrangement. This paper assumes a simple matched filter in the Fourier plane, and a typical 4f optical layout.

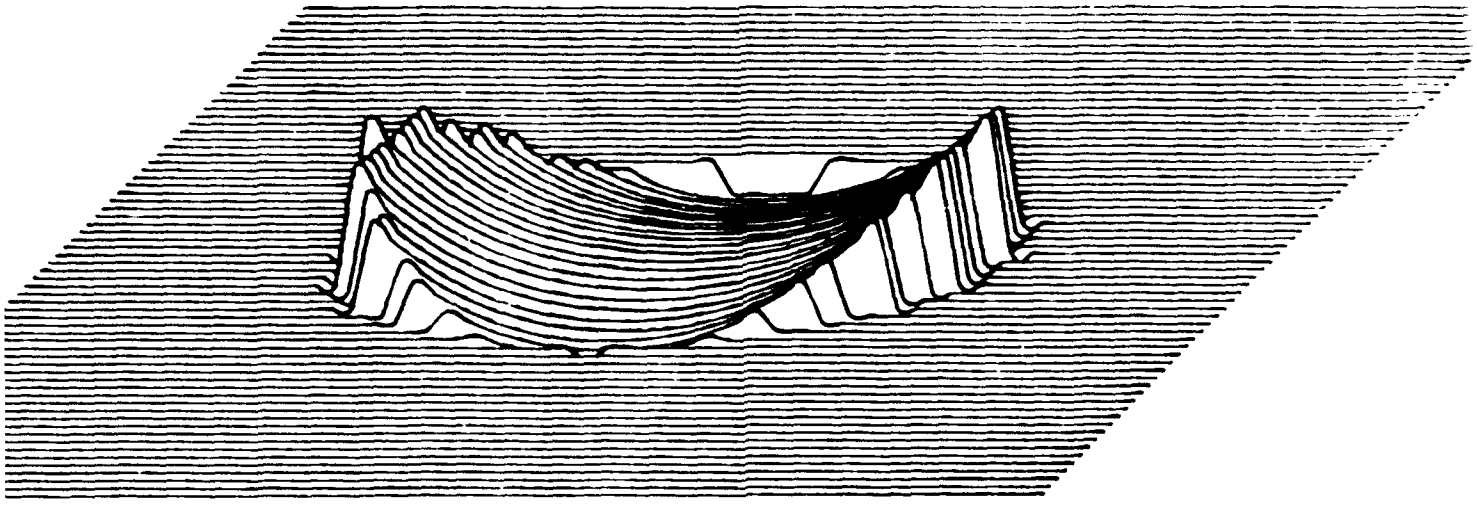

Figure 3: Exit pupil phase map.

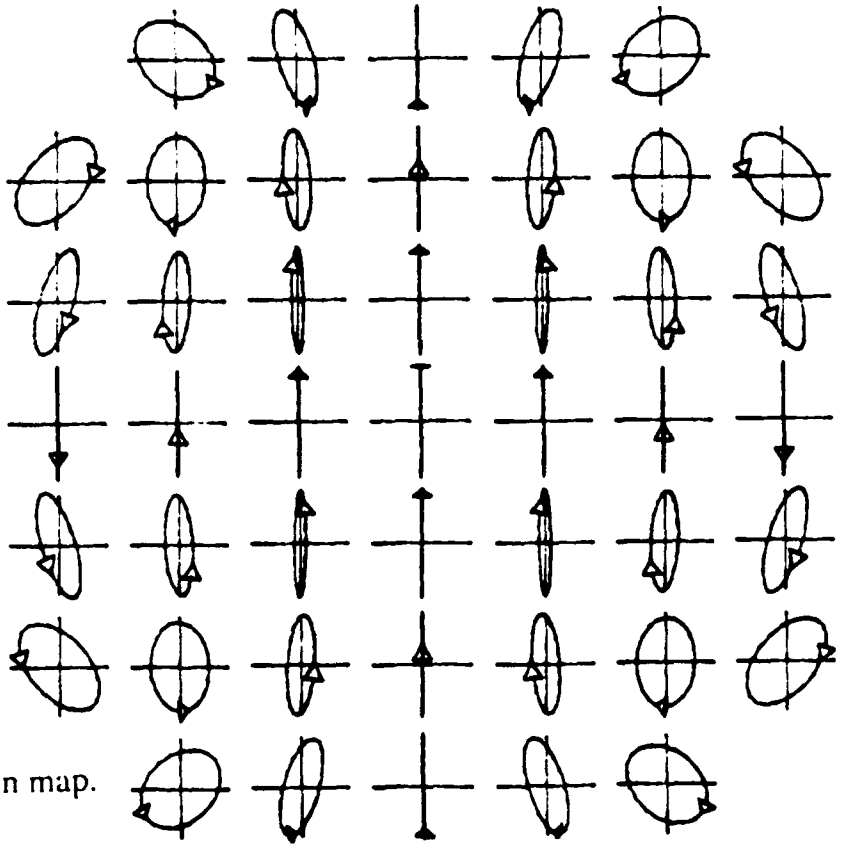

Figure 4: Exit pupil polarization map.

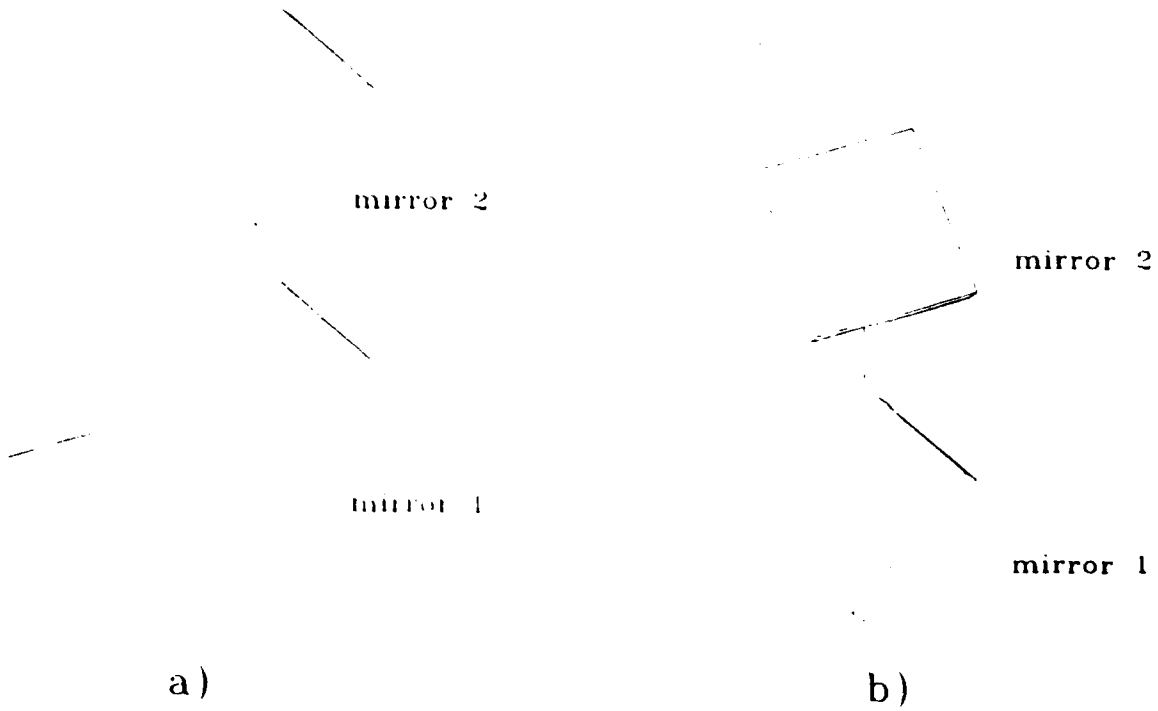

Figure 5: Two fold mirror arrangements. In figure 5a, the polarization aberrations add. In figure 5b, the polarization aberrations nearly cancel.

ANALYTICAL GUIDANCE LAWS FOR HOMING MISSILES

Donald T. Stansbery
Graduate Student
Faculty Advisor: S. N. Balakrishnan
Department of Mechanical and Aerospace Engineering
and Engineering Mechanics

University of Missouri-Rolla
Rolla, MO 65401

Final Report for:
Graduate Student Research Program
Wright Laboratory / Armament Directorate
Eglin Air Force Base, FL 32542

Sponsored by:
Air Force Office of Scientific Research
Bolling Air Force Base, Washington, D.C.

August 1993

ANALYTICAL GUIDANCE LAWS FOR HOMING MISSILES

Donald T. Stansbery
Graduate Student
Faculty Advisor: S. N. Balakrishnan
Department of Mechanical and Aerospace Engineering
and Engineering Mechanics
University of Missouri-Rolla

ABSTRACT

In this study polar coordinates are used to obtain an analytical guidance law for homing missiles. The closed form solution for the guidance law is developed using modern control techniques. To develop this control scheme, the dynamic equations of the target-intercept problem are decoupled. The decoupling of the radial and transverse coordinates is accomplished by introducing a pseudo-control in the radial direction. The commanded acceleration in the radial direction is determined through the use of pseudo-control and the commanded acceleration in the transverse direction is determined from the solution to a two-point boundary value problem. The two-point boundary value problem is solved through the use of the state transition matrix of the intercept dynamics. The optimal guidance law is also used to compare the solutions for other guidance laws such as True Proportional Navigation (TPN) and Ideal Proportional Navigation (IPN).

ANALYTICAL GUIDANCE LAWS FOR HOMING MISSILES

Donald T. Stansbery

I. INTRODUCTION

Most air-to-air missiles use some form of a control law called proportional navigation. The idea behind proportional navigation is to apply the missile commanded acceleration in a direction which will annul the line-of-sight rate so the missile will be on a collision course with its target. Various forms of proportional navigation exist, depending on the direction in which the missile commanded acceleration is applied. Two forms of proportional navigation which have closed form solutions are Ideal Proportional Navigation (IPN) and True Proportional Navigation (TPN). In IPN, the missile commanded acceleration is applied normal to the relative velocity. A closed form solution for IPN, for a maneuvering and non-maneuvering target, was developed by Yuan and Chern [5]. In TPN, the missile commanded acceleration is applied normal to the line-of-sight. A closed form solution for TPN, for a maneuvering and non-maneuvering target, was also developed by Yuan and Chern [6]. Other closed form solutions for TPN [8,9] have been developed but are complicated and difficult for comparison with other solutions. There is increased interest in using modern control techniques to develop optimal guidance laws which perform better than existing proportional navigation guidance laws [4, 7].

In this study polar coordinates are used to obtain a closed form solution for an optimal guidance law for a target-intercept problem [3]. The reason for formulating this problem in polar coordinates is that polar coordinates are the natural reference system to solve the target-intercept problem. In order to obtain a closed form solution for the commanded accelerations in the radial and transverse directions, the equations of the intercept dynamics must be decoupled. To decouple the dynamic equations a pseudo-control is introduced in the radial direction, which produces an optimal control problem in each direction. The closed form solution in the radial direction is found through the use of the pseudo-control and the closed form solution in the transverse direction is found by using the state transition matrix of the intercept dynamics. The closed form solution for the optimal guidance law for the target-intercept problem can then be compared with two forms of proportional navigation; IPN [5] and TPN [6].

The remainder of this paper is organized as follows: the optimal guidance law in polar coordinates is developed in Section II. This section also shows that the optimal guidance law results in two decoupled optimal control problems. In Section III, the state transition matrix for the intercept dynamics is used to produce a closed form solution for the missile transverse commanded acceleration with a maneuvering and non-maneuvering target. Section IV describes the approximations that can be made in the state transition matrix (STM) solution and compares the STM solution for the two-point boundary value problem with an iterative (ITR) method for solving the same problem. In Section V, the optimal guidance law for a maneuvering and non-maneuvering target is compared with two other guidance laws; IPN and TPN. The conclusions are summarized in Section VI.

II. OPTIMAL GUIDANCE LAW IN DECOUPLED POLAR COORDINATES [1, 2]

The dynamics of a two dimensional target-intercept problem as shown in Figure 1,

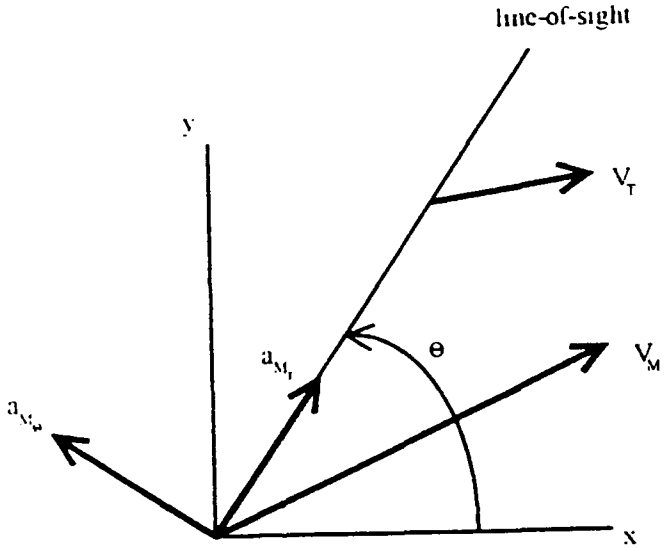

Figure 1

can be described in inertial polar coordinates by two coupled nonlinear differential equations.

$$\ddot{r} - r\dot{\theta}^2 = a_{T_r} - a_{M_r} \tag{1}$$

$$r\ddot{\theta} + 2\dot{r}\dot{\theta} = a_{T_\theta} - a_{M_\theta} \tag{2}$$

In these equations r is the relative range between the target and the missile, θ is the bearing angle, a_{T_r} and a_{T_θ} are the target accelerations in the radial and transverse directions respectively, and a_{M_r} and a_{M_θ} are the missile commanded accelerations in the radial and transverse directions respectively. Dots denote differentiation with respect to time. The target-intercept problem can be expanded into three dimensions by adding the dynamics in the elevation direction.

In order to decouple the dynamics in the radial and transverse directions a pseudo-control is defined in the radial direction as

$$a_{M_{r1}} = a_{M_r} - r\dot{\theta}^2 \tag{3}$$

By introducing the pseudo-control the dynamics in the radial and transverse directions are decoupled. This allows the commanded acceleration in each direction to be developed independent of the other.

Radial Commanded Acceleration

The equation of motion in the radial (line-of-sight) direction can be put into a state space form as

$$y = [r \;\; \dot{r}]^T$$

where

$$\dot{y}_1 = y_2 \tag{4}$$

$$\dot{y}_2 = a_{T_r} - a_{M_{r,l}} \tag{5}$$

In Eq. (5), a_{T_r} is the time varying model of the radial target acceleration which can be specified.

The optimal guidance law in the radial direction is obtained as a solution to minimizing the performance index, J_r , where

$$J_r = \frac{1}{2} S_{f_r} y_{1_f}^2 + \frac{1}{2} \int_0^{t_f} \gamma \, a_{M_{r,l}}^2 dt \tag{6}$$

where S_{f_r} is the weight on the terminal miss distance, y_{1_f} , and γ is the weight on the pseudo-control effort. The time-to-go, t_f , is approximated as $\frac{r}{|\dot{r}|}$, assuming that the relative velocity along the line-of-sight is maintained at a constant. The pseudo-control which minimizes the performance index in Eq. (6) is found to be

$$a_{M_{r,l}}(t) = \frac{t_f}{\gamma} \lambda_1(t) \tag{7}$$

where

$$\lambda_1(t) = \frac{S_{f_r}[y_1(t) + t_f y_2(t) + q_1(t)]}{1 + \frac{S_{f_r} t_f^3}{3\gamma}} \tag{8}$$

and

$$q_1(t) = \int_0^t \left(\int_0^t a_{T_r}(t) dt \right) dt \tag{9}$$

λ_1 is the Lagrangian multiplier which adjoins the differential constraint in Eq. (5) to the performance index in Eq. (6). The actual missile commanded acceleration in the radial direction can be obtained from Eq. (3) as

$$a_{M_r}(t) = a_{M_{r1}}(t) + r(t)\dot{\theta}^2(t) \tag{10}$$

The instantaneous values of the relative range, $r(t)$, and relative range rate, $\dot{r}(t)$, can be obtained through the integration of Eqs. (4) and (5).

Transverse Commanded Acceleration

The equation of motion in the transverse direction given by Eq. (2) can be rewritten as

$$\ddot{\theta} = -\frac{2\dot{r}\dot{\theta}}{r} + \frac{1}{r}a_{T_\theta} - \frac{1}{r}a_{M_\theta} \tag{11}$$

Since r and $\dot{r}$ are known from Eq. (4) and (5) they can be treated as functions of time only. This allows Eq. (11) to be expressed as a time-varying linear differential equation.

$$\ddot{\theta} = f(t)\dot{\theta} + g(t)a_{T_\theta} - g(t)a_{M_\theta} \tag{12}$$

where $f(t) = -\frac{2\dot{r}}{r}$ and $g(t) = \frac{1}{r}$.

The equation of motion in Eq. (12) can be put into a state space form as

$$z = [\theta \;\; \dot{\theta}]^T$$

where

$$\dot{z}_1 = z_2 \tag{13}$$

$$\dot{z}_2 = f(t)z_2 + g(t)a_{T_\theta} - g(t)a_{M_\theta} \tag{14}$$

In Eq. (14), a_{T_θ} is the time varying model of the transverse target acceleration which can be specified.

The optimal guidance law in the transverse direction is obtained as a solution to minimizing the performance index, J_θ, where

$$J_\theta = \frac{1}{2}S_{f_\theta}z_2^2 + \frac{1}{2}\int_0^{t_f}(\gamma_1 z_2^2 + \gamma_2 a_{M_\theta}^2)dt \tag{15}$$

where S_{f_0} is the weight on the final line-of-sight rate and γ_1 and γ_2 are the weights on the line-of-sight rate and the transverse commanded acceleration respectively.

The optimization of Eq. (15), which produces the minimizing control, results in a two-point boundary value problem:

$$\begin{bmatrix} \dot{z}_2 \\ \dot{\lambda}_2 \end{bmatrix} = \begin{bmatrix} f(t) & -\dfrac{g^2(t)}{\gamma_2} \\ -\gamma_1 & -f(t) \end{bmatrix} \begin{bmatrix} z_2 \\ \lambda_2 \end{bmatrix} + \begin{bmatrix} g(t) \\ 0 \end{bmatrix} a_{T_0}(t) \tag{16}$$

λ_2 is the Lagrangian multiplier which adjoins the state in Eq. (14) with the performance index in Eq. (15). The two-point boundary value problem can be solved numerically, by using the shooting method, or analytically if functional forms of $f(t)$ and $g(t)$ are known. The minimizing control in the transverse direction is given by

$$a_{M_0}(t) = \frac{\lambda_2(t)g(t)}{\gamma_2} \tag{17}$$

III. AN OPTIMAL GUIDANCE LAW SOLUTION USING STATE TRANSITION MATRIX

In this section, a solution to the two-point boundary value problem in Eq. (16) will be accomplished by using the state transition matrix of the intercept dynamics. This will produce a closed form solution for the minimizing control in the transverse direction. The solution to the two-point boundary value problem will first be found for a non-maneuvering target [2] and then the solution for a maneuvering target will be added.

Non-Maneuvering Target

Without target acceleration Eq. (16) can be written as

$$\dot{x}(t) = A(t)x(t) \tag{18}$$

where $x(t) = [z_2(t) \;\; \lambda_2(t)]^T$ and $A(t)$ is

$$A(t) = \begin{bmatrix} f(t) & -\dfrac{g^2(t)}{\gamma_2} \\ -\gamma_1 & -f(t) \end{bmatrix} \tag{19}$$

The solution to the homogeneous differential equation in Eq. (18) is

$$x(t) = \phi(t,\tau)x(\tau) \tag{20}$$

where $\phi(t,\tau)$ is the state transition matrix, which can be written in matrix form as

$$\phi(t,\tau) = \begin{bmatrix} \phi_{11}(t,\tau) & \phi_{12}(t,\tau) \\ \phi_{21}(t,\tau) & \phi_{22}(t,\tau) \end{bmatrix} \tag{21}$$

The state transition matrix can be found by solving the following equation:

$$\dot{\phi}(t,\tau) = A(t)\phi(t,\tau) \ , \quad \textit{with} \quad \phi(\tau,\tau) = I \tag{22}$$

where $A(t)$ comes from Eq. (19), $\phi(\tau,\tau)$ are the boundary conditions and I is the identity matrix. The time, τ, can be selected based on when the states, $x(\tau)$, are known(usually the states can be found at time, $\tau = 0$).

The earlier assumption that the closing velocity is constant, can be translated to

$$r(t) = -\dot{r}(t)(t_f - t) \tag{23}$$

Using this assumption, $f(t)$ and $g(t)$ can be written as explicit functions of time as

$$f(t) = \frac{2}{(t_f - t)} \tag{24a}$$

$$g(t) = \frac{t_f}{r_0(t_f - t)} \tag{24b}$$

By substituting Eqs. (24a) and (24b) into Eq. (19), $A(t)$ becomes

$$A(t) = \begin{bmatrix} \dfrac{2}{(t_f - t)} & -\dfrac{F}{(t_f - t)^2} \\ -\gamma_1 & -\dfrac{2}{(t_f - t)} \end{bmatrix} \tag{25}$$

where $F = \dfrac{t_f^2}{r_0^2 \gamma_2}$ or $F = \dfrac{1}{\dot{r}_0^2 \gamma_2}$.

Using Eq. (25) in Eq. (22) produces four scalar homogeneous differential equations.

$$\dot{\phi}_{11}(t,\tau) = \frac{2}{(t_f - t)}\phi_{11}(t,\tau) - \frac{F}{(t_f - t)^2}\phi_{21}(t,\tau) \tag{26}$$

$$\dot{\phi}_{12}(t,\tau) = \frac{2}{(t_f - t)}\phi_{12}(t,\tau) - \frac{F}{(t_f - t)^2}\phi_{22}(t,\tau) \tag{27}$$

$$\dot{\phi}_{21}(t,\tau) = -\gamma_1\phi_{11}(t,\tau) - \frac{2}{(t_f - t)}\phi_{21}(t,\tau) \tag{28}$$

$$\dot{\phi}_{22}(t,\tau) = -\gamma_1\phi_{12}(t,\tau) - \frac{2}{(t_f - t)}\phi_{22}(t,\tau) \tag{29}$$

Eq. (26) can be differentiated with respect to time, and Eq. (26) and (28) can be used to manipulated the result so that the differential equation is a function of $\phi_{11}(t,\tau)$ only. This produces the following equation

$$\ddot{\phi}_{11}(t,\tau) = \frac{2}{(t_f - t)}\dot{\phi}_{11}(t,\tau) + \frac{(F\gamma_1 + 2)}{(t_f - t)^2}\phi_{11}(t,\tau) \tag{30}$$

Similarly for $\ddot{\phi}_{12}(t,\tau)$, $\ddot{\phi}_{21}(t,\tau)$, $\ddot{\phi}_{22}(t,\tau)$ we get

$$\ddot{\phi}_{12}(t,\tau) = \frac{2}{(t_f - t)}\dot{\phi}_{12}(t,\tau) + \frac{(F\gamma_1 + 2)}{(t_f - t)^2}\phi_{12}(t,\tau) \tag{31}$$

$$\ddot{\phi}_{21}(t,\tau) = \frac{(F\gamma_1 + 2)}{(t_f - t)^2}\phi_{21}(t,\tau) \tag{32}$$

$$\ddot{\phi}_{22}(t,\tau) = \frac{(F\gamma_1 + 2)}{(t_f - t)^2}\phi_{22}(t,\tau) \tag{33}$$

If we assume a solution for $\phi_{21}(t,\tau)$ of the form

$$\phi_{21}(t,\tau) = K(t_f - t)^b \tag{34}$$

$$\dot{\phi}_{21}(t,\tau) = -Kb(t_f - t)^{b-1} \tag{35}$$

$$\ddot{\phi}_{21}(t,\tau) = Kb(b-1)(t_f - t)^{b-2} \tag{36}$$

Eqs. (34)-(36) can be put into Eq. (32), which produces a quadratic equation that is a function of b.

$$b^2 - b - (F\gamma_1 + 2) = 0 \tag{37}$$

The resulting solution for b is

$$b = \frac{1}{2} \pm \frac{1}{2}D \tag{38}$$

where

$$D = \sqrt{9 + 4F\gamma_1} \tag{39}$$

The solution for $\phi_{21}(t,\tau)$ can now be written as

$$\phi_{21}(t,\tau) = A_1(t_f - t)^{\frac{1}{2}(1-D)} + A_2(t_f - t)^{\frac{1}{2}(1+D)} \tag{40}$$

where A_1 and A_2 are constants to be determined from the boundary conditions in Eq. (22). Knowing the boundary condition for ϕ_{21}, at $t = \tau$, we can solve Eq. (40) for A_1 in terms of A_2.

$$A_1 = -A_2(t_f - \tau)^D \tag{41}$$

We will now use Eq. (28) to obtain $\phi_{11}(t,\tau)$ as a function of $\phi_{21}(t,\tau)$ and $\dot{\phi}_{21}(t,\tau)$.

$$\phi_{11}(t,\tau) = -\frac{1}{\gamma_1}[\frac{2}{(t_f - t)}\phi_{21}(t,\tau) + \dot{\phi}_{21}(t,\tau)] \tag{42}$$

$\dot{\phi}_{21}(t,\tau)$ in Eq. (42) can be found by differentiating Eq. (40) with respect to time. Substituting for $\phi_{21}(t,\tau)$ and $\dot{\phi}_{21}(t,\tau)$ in Eq. (42) produces a solution for $\phi_{11}(t,\tau)$ as a function of A_1 and A_2.

$$\phi_{11}(t,\tau) = -\frac{1}{2\gamma_1}[A_1(3 + D)(t_f - t)^{-\frac{1}{2}(1+D)} + A_2(3 - D)(t_f - t))^{-\frac{1}{2}(1-D)}] \tag{43}$$

Knowing the boundary condition for ϕ_{11}, at $t = \tau$, and A_1 as a function of A_2 from Eq. (41), we can solve for A_2.

$$A_2 = \frac{\gamma_1(t_f - \tau)^{\frac{1}{2}(1-D)}}{D} \tag{44}$$

Substituting Eq. (44) into Eq. (41) gives the solution for A_1 as

$$A_1 = -\frac{\gamma_1 (t_f - \tau)^{\frac{1}{2}(1+D)}}{D} \tag{45}$$

Since A_1 and A_2 are known, ϕ_{11} and ϕ_{21} can be found at any time t, provided that time τ is known.

If we assume the same type of solution for ϕ_{22},

$$\phi_{22}(t,\tau) = A_3 (t_f - t)^{\frac{1}{2}(1-D)} + A_4 (t_f - t)^{\frac{1}{2}(1+D)} \tag{46}$$

A_3 and A_4 can be determined in the same manner as A_1 and A_2. The resulting solutions for A_3 and A_4 are

$$A_3 = \frac{(D - 3)}{2D(t_f - \tau)^{\frac{1}{2}(1-D)}} \tag{47}$$

$$A_4 = \frac{(D + 3)}{2D(t_f - \tau)^{\frac{1}{2}(1+D)}} \tag{48}$$

Since A_3 and A_4 are known, ϕ_{12} and ϕ_{22} can be found at any time t provided that time τ is known. The solution for $\phi(t,\tau)$ is now complete.

In order to solve Eq. (20) for the states at time t, we must be able to determine the states at time τ. The states at time τ can be found by evaluating the states at the final time, t_f. From Eq. (20) the final states are

$$\lambda_2(t_f) = \phi_{21}(t_f,\tau) z_2(\tau) + \phi_{22}(t_f,\tau) \lambda_2(\tau) \tag{49}$$

$$z_2(t_f) = \phi_{11}(t_f,\tau) z_2(\tau) + \phi_{12}(t_f,\tau) \lambda_2(\tau) \tag{50}$$

From the terminal term of the performance index, $\lambda_2(t_f)$ is known to be

$$\lambda_2(t_f) = S_{f_0} z_2(t_f) \tag{51}$$

By substituting Eq. (50) into Eq. (51), $\lambda_2(t_f)$ can be found as a function of $\lambda_2(\tau)$ and $z_2(\tau)$.

$$\lambda_2(t_f) = S_{f_0} [\phi_{11}(t_f,\tau) z_2(\tau) + \phi_{12}(t_f,\tau) \lambda_2(\tau)] \tag{52}$$

By setting Eq. (52) equal to Eq. (49), $\lambda_2(\tau)$ can be found as a function of $z_2(\tau)$.

$$\lambda_2(\tau) = \frac{[S_{f_0}\phi_{11}(t_f,\tau) - \phi_{21}(t_f,\tau)]}{[\phi_{22}(t_f,\tau) - S_{f_0}\phi_{12}(t_f,\tau)]} z_2(\tau) \tag{53}$$

If the terminal term of the performance index is left out, $z_2(t_f)$ is zero and Eq. (50) can be used to solve for $\lambda_2(\tau)$.

$$\lambda_2(\tau) = -\frac{\phi_{11}(t_f,\tau)}{\phi_{12}(t_f,\tau)} z_2(\tau) \tag{54}$$

In the target-intercept problem the line-of-sight rate, z_2, is known at the initial time, $\tau = 0$ and $\phi(t_f,\tau)$ can be determined at $\tau = 0$, so λ_2 can be found at the initial time. The resulting solution to the homogeneous differential equation in Eq. (20) is

$$z_2(t) = (1 - \frac{t}{t_f})^{\frac{1}{2}(D-1)} z_2(0) \tag{55}$$

$$\lambda_2(t) = \frac{(D+3)}{2}\gamma_2 t_f \dot{r}_0^2 (1 - \frac{t}{t_f})^{\frac{1}{2}(D+1)} z_2(0) \tag{56}$$

By substituting Eq. (56) into Eq. (17), the minimizing control in the transverse direction can be expressed as

$$a_{M_\theta}(t) = -\frac{(D+3)}{2}\dot{r}_0\dot{\theta}_0(1 - \frac{t}{t_f})^{\frac{1}{2}(D-1)} \tag{57}$$

where the notation for $z_2(0)$, the line-of-sight rate, has been changed to $\dot{\theta}_0$ (the typical notation). If $t = 0$ is assumed to be the current time, the minimizing control in the transverse direction with a non-maneuvering target becomes

$$a_{M_\theta} = -\frac{(D+3)}{2}\dot{r}_0\dot{\theta}_0 \tag{58}$$

Maneuvering Target

The solution to the two-point boundary value problem for a maneuvering target can be obtained by adding the target acceleration to Eq. (18).

$$\dot{x}(t) = A(t)x(t) + B(t)u(t) \tag{59}$$

where $u(t) = [a_{T_e}]$ and $B(t) = [g(t) \;\; 0]^T$ from Eq. (16). To solve the two-point boundary value problem, the following equation must be used

$$x(t) = \phi(t,0)x(0) + \int_0^t \phi(t,\tau)B(\tau)u(\tau)d\tau \tag{60}$$

In Eq. (60), $\phi(t,\tau)$ and $\phi(t,0)$ are known from the solution to the two-point boundary value problem for a non-maneuvering target. Eq. (60) produces two scalar equations.

$$z_2(t) = \phi_{11}(t,0)z_2(0) + \phi_{12}(t,0)\lambda_2(0) + p_1(t) \tag{61a}$$

$$\lambda_2(t) = \phi_{21}(t,0)z_2(0) + \phi_{22}(t,0)\lambda_2(0) + p_2(t) \tag{61b}$$

where

$$p_1(t) = \int_0^t \phi_{11}(t,\tau)g(\tau)a_{T_e}(\tau)d\tau \tag{62a}$$

$$p_2(t) = \int_0^t \phi_{21}(t,\tau)g(\tau)a_{T_e}(\tau)d\tau \tag{62b}$$

In order to solve Eqs. (61a) and (61b) for the states at time t, we must be able to determine the states at the initial time. The states at the initial time can be found by evaluating the states at the final time, as was done for the non-maneuvering case. From Eqs. (61a) and (61b) the final states are

$$z_2(t_f) = \phi_{11}(t_f,0)z_2(0) + \phi_{12}(t_f,0)\lambda_2(0) + p_1(t_f) \tag{63}$$

$$\lambda_2(t_f) = \phi_{21}(t_f,0)z_2(0) + \phi_{22}(t_f,0)\lambda_2(0) + p_2(t_f) \tag{64}$$

where $p_1(t_f)$ and $p_2(t_f)$ are the evaluation of the integrals in Eqs. (62a) and (62b) at the final time. The resulting expressions for $p_1(t_f)$ and $p_2(t_f)$ are functions of the target acceleration model. Since $\lambda_2(t_f)$ is known from Eq. (51), and the line-of-sight is known at the initial time, $\lambda_2(0)$ can be found using Eqs. (63) and (64).

$$\lambda_2(0) = \frac{[S_{f_0}\phi_{11}(t_f,0) - \phi_{21}(t_f,0)]}{[\phi_{22}(t_f,0) - S_{f_0}\phi_{12}(t_f,0)]}z_2(0) + \frac{[S_{f_0}p_1(t_f) - p_2(t_f)]}{[\phi_{22}(t_f,0) - S_{f_0}\phi_{12}(t_f,0)]} \tag{65}$$

The resulting solution to the differential equation in Eq. (60) is

$$z_2(t) = (1 - \frac{t}{t_f})^{\frac{1}{2}(D-1)} z_2(0) + p_1(t) \tag{66}$$

$$\lambda_2(t) = \frac{(D+3)}{2} \gamma_2 t_f \dot{r}_0^2 (1 - \frac{t}{t_f})^{\frac{1}{2}(D+1)} z_2(0) + p_2(t) \tag{67}$$

The minimizing control in the transverse direction for a maneuvering target can now be expressed as a function of time as

$$a_{M_\theta}(t) = -\frac{(D+3)}{2} \dot{r}_0 \dot{\theta}_0 (1 - \frac{t}{t_f})^{\frac{1}{2}(D-1)} + \frac{p_2(t)}{\gamma_2 r_0 (1 - \frac{t}{t_f})} \tag{68}$$

where $p_2(t)$ is a function of $(1 - \frac{t}{t_f})$, D, and $a_{T_\theta}(t)$. If $t = 0$ is assumed to be the current time, the minimizing control in the transverse direction with a maneuvering target becomes

$$a_{M_\theta} = -\frac{(D+3)}{2} \dot{r}_0 \dot{\theta}_0 + \frac{p_2(0)}{\gamma_2 r_0} \tag{69}$$

IV. APPROXIMATION FOR THE COEFFICIENT D

In this section the coefficient D will be evaluated for various typical intercept scenarios. Two methods for solving the two-point boundary value problem, for a maneuvering target, will be evaluated using a 6-DOF missile-target simulation. The two methods that will be used are the state transition matrix (STM) solution that has been presented above, and an iterative method (ITR).

By substituting $F = \frac{1}{\dot{r}_0^2 \gamma_2}$ into Eq. (39), D can be expressed as

$$D = \sqrt{9 + \frac{4}{\dot{r}_0^2} \frac{\gamma_1}{\gamma_2}} \tag{70}$$

For many typical intercept scenarios, D can be approximated as 3. The reason that this approximation can be made

comes from the ratio of $\frac{\gamma_1}{\gamma_2}$ in Eq. (70). If the weight on the line-of-sight rate, γ_1, is two orders of magnitude larger than the weight on the control effort, γ_2, (ratio of $\frac{\gamma_1}{\gamma_2}$ is 1000) then the above approximation holds for intercept scenarios with initial ranges of 3000 ft. to 7000 ft. and any aspect angle or boresight angle. The smallest value D can have, for any scenario, is 3 since the second term in Eq. (70) will always be positive no matter what the initial condition of the range rate($\dot{r}_0 < 0$ or $\dot{r}_0 > 0$).

A 6-DOF missile-target simulation was used to compare two methods for solving the two-point boundary value problem with a maneuvering target. The state transition solution was evaluated using the complete expression for D and the approximation that $D = 3$. These methods were compared to an iterative method, which has an initial value specified for the lagrangian multiplier, λ_2, and then iterates to find the optimal solution. In the simulation, the target performs a 9-g maneuver up and to the right, relative to its reference, until the time-to-go reaches 1 second when it rolls 180° and pulls 9-g's until conclusion. The results from the simulation are shown in Table 1.

Method	D	Range (ft.)	Aspect Angle (deg.)	Boresight Angle (deg.)	Miss Distance (ft.)	Flight Time (Sec.)
STM	3	7000	60	0	0.236	3.97
ITR *	----	7000	60	0	9.345	3.97
STM	3	3000	60	0	1.76	2.37
ITR *	----	3000	60	0	122.62	2.36
STM	≠3	7000	60	0	0.06	3.95
ITR	----	7000	60	0	0.71	3.95
STM	≠3	3000	60	0	0.67	2.37
ITR	----	3000	60	0	2.4	2.38
STM	≠3	3000	120	40	1.31	1.77
ITR	----	3000	120	40	2.14	1.77

Table 1

The two runs made with the iterative method that are marked with the * had difficulty converging to an optimal solution. The result of this difficulty shows up in the large miss distances. The STM solution directly provides

the optimal solution which results in much smaller miss distances for the same two scenarios. Table 1 shows that the state transition matrix (STM) solution resulted in a smaller miss distances compared with the iterative solution for all scenarios. The run time for the simulation was also greatly reduced when the STM solution was used as apposed to the ITR method.

V. OPTIMAL GUIDANCE LAW COMPARISON WITH FORMS OF PROPORTIONAL NAVIGATION

In this section a comparison of the optimal guidance law that has been developed above will be compared to two forms of proportional navigation. The two forms of proportional navigation are Ideal Proportional Navigation (IPN) and True Proportional Navigation (TPN). The comparison will be done for a non-maneuvering and maneuvering target.

In Ideal Proportional Navigation [5], the commanded acceleration, a_c, is applied normal to the relative velocity, v, and its magnitude is proportional to the line-of-sight rate. For a non-maneuvering target the equations of motion for the target-intercept problem are

$$\ddot{r} - r\dot{\theta}^2 = -\lambda r\dot{\theta}^2 \tag{71}$$

$$r\ddot{\theta} + 2\dot{r}\dot{\theta} = \lambda\dot{r}\dot{\theta} \tag{72}$$

where λ is the effective proportional navigation constant. The line-of-sight rate is found from Eq. (72) to be

$$\dot{\theta} = \dot{\theta}_0\left(\frac{r}{r_0}\right)^{\lambda-2} \tag{73}$$

where $\dot{\theta}$ goes to ∞ if $\lambda < 2$ and to 0 if $\lambda > 2$. The resulting commanded acceleration in the transverse direction is

$$a_{M_\theta} = \lambda v_0\dot{\theta}_0\left(\frac{r}{r_0}\right)^{\lambda-2} \tag{74}$$

where the relative velocity is a constant. To avoid a_{M_θ} going to ∞, λ must be chosen to be > 2. We can compare Eqs. (73) and (74) with Eqs. (55) and (57) from the STM solution for a non-maneuvering target. The assumption in Eq. (23) produces the following substitutions, $(1 - \frac{t}{t_f}) = \frac{r}{r_0}$ and $-\dot{r}_0 = v_0$. Using these substitutions in Eqs. (55) and (57) produces

$$\dot{\theta}(t) = \dot{\theta}_0\left(\frac{r}{r_0}\right)^{\frac{1}{2}(D-1)} \tag{75}$$

$$a_{M_\theta}(t) = \frac{(D+3)}{2} v_0 \dot{\theta}_0 (\frac{r}{r_0})^{\frac{1}{2}(D-1)} \tag{76}$$

The equations for $\dot{\theta}$ and a_{M_θ} for the two guidance law solutions, for a non-maneuvering target, are similar . One difference that can be seen in Eqs. (75) and (76) is that $\dot{\theta}$ and a_{M_θ} will always go to 0 since the minimum value of D is 3. The reason that there is no restriction to keep $\dot{\theta}$ and a_{M_θ} from going to ∞, as is the case for λ in the IPN solution, is due to the fact that Eqs. (75) and (76) are the optimal solutions.

For a maneuvering target the equations of motion of the target-intercept problem are

$$\ddot{r} - r\dot{\theta}^2 = -\lambda r\dot{\theta}^2 + a_T \frac{r\dot{\theta}}{v} \tag{77}$$

$$r\ddot{\theta} + 2\dot{r}\dot{\theta} = \lambda \dot{r}\dot{\theta} - a_T \frac{\dot{r}}{v} \tag{78}$$

where the target maneuver is always normal to the relative velocity. The line-of-sight rate is found from Eq. (78) to be

$$\dot{\theta} = \dot{\theta}_0 (\frac{r}{r_0})^{\lambda-2} + \frac{a_T}{v_0(\lambda - 2)} [1 - (\frac{r}{r_0})^{\lambda-2}] \qquad \lambda \neq 2 \tag{79}$$

where $\dot{\theta}$ goes to ∞ if $\lambda \leq 2$ and to $\frac{a_T}{v_0(\lambda-2)}$ if $\lambda > 2$. The first term of the line-of-sight rate is induced by the initial line of sight rate and the second term is induced by the maneuver of the target. The resulting commanded acceleration in the transverse direction is

$$a_{M_\theta} = \lambda v_0 \dot{\theta}_0 (\frac{r}{r_0})^{\lambda-2} + \frac{\lambda a_T}{(\lambda-2)} [1 - (\frac{r}{r_0})^{\lambda-2}] \qquad \lambda \neq 2 \tag{80}$$

where the relative velocity is constant. The second term in Eq. (80) is due to the target maneuver. To avoid a_{M_θ} going to ∞, λ must be chosen to be > 2. With $\lambda > 2$, the first term in Eq. (80) will go to zero, which results in a_{M_θ} going to $\frac{\lambda a_T}{(\lambda-2)}$. We can compare Eqs. (79) and (80) with Eqs. (66) and (68) from the STM solution for

a maneuvering target. Using the same substitutions in Eqs. (66) and (68) that were used in the non-maneuvering solution produces

$$\dot{\theta}(t) = \dot{\theta}_0\left(\frac{r}{r_0}\right)^{\frac{1}{2}(D-1)} + p_1(t) \tag{81}$$

$$a_{M_\theta}(t) = \frac{(D+3)}{2} v_0 \dot{\theta}_0\left(\frac{r}{r_0}\right)^{\frac{1}{2}(D-1)} + \frac{p_2(t)}{\gamma_2 r} \tag{82}$$

where the second terms in Eqs. (81) and (82) are due to the target maneuver. The equations for $\dot{\theta}$ and a_{M_θ} for the two guidance law solutions, for a maneuvering target, are also similar . One difference that can be seen is that since the minimum value of D is 3, the first terms in Eqs. (81) and (82) will go to zero, which results in $\dot{\theta}$ and a_{M_θ} always going to a function of the target maneuver, a_{T_θ}. There is again no restriction to keep $\dot{\theta}$ and a_{M_θ} from going to ∞, as is the case for λ in the IPN solution, since Eqs. (81) and (82) are the optimal solutions.

In True Proportional Navigation [6], the commanded acceleration, a_c, is applied normal to the missile-target line-of-sight and its magnitude is proportional to the line-of-sight rate. For a non-maneuvering target the equations of motion for the target-intercept problem are

$$\ddot{r} - r\dot{\theta}^2 = 0 \tag{83}$$

$$r\ddot{\theta} + 2\dot{r}\dot{\theta} = \lambda\dot{r}\dot{\theta} \tag{84}$$

where λ is the effective proportional navigation constant. The line-of-sight rate is found to be the same as the line-of-sight rate for the IPN non-maneuvering target solution in Eq. (73), where $\dot{\theta}$ goes to ∞ if $\lambda < 2$ and to 0 if $\lambda > 2$. The resulting commanded acceleration in the transverse direction is

$$a_{M_\theta} = \lambda\dot{r}_0\dot{\theta}_0\left(\frac{r}{r_0}\right)^{\lambda-2}\sqrt{1 - \frac{r_0^2\dot{\theta}_0^2}{(\lambda-1)\dot{r}_0^2}\left[1 - \left(\frac{r}{r_0}\right)^{2\lambda-2}\right]} \tag{85}$$

To avoid a_{M_θ} going to ∞, λ must be chosen to be > 2. We can compare Eq. (85) with Eq. (57) from the STM solution for a non-maneuvering target. Using the substitution, $\left(1 - \frac{t}{t_f}\right) = \frac{r}{r_0}$ in Eq. (57) produces

$$a_{M_\theta}(t) = -\frac{(D+3)}{2}\dot{r}_0\dot{\theta}_0\left(\frac{r}{r_0}\right)^{\frac{1}{2}(D-1)} \tag{86}$$

The equations for $\dot{\theta}$ and a_{M_θ} for the two guidance law solutions, for a non-maneuvering target, are similar. In Eqs. (75) and (86), $\dot{\theta}$ and a_{M_θ} will always go to 0 since the minimum value of D is 3. There is again no restriction to keep $\dot{\theta}$ and a_{M_θ} from going to ∞, as is the case for λ in the TPN solution, since Eqs. (75) and (86) are the optimal solutions. The sign difference between the commanded acceleration in Eqs. (85) and (86) is because the origin of the reference frame for the TPN solution is located at the target where in the STM solution the origin is located at the missile.

The comparison of the optimal guidance law and TPN for a maneuvering target is currently being developed. The comparison of the performance, in a missile-target simulation, of the optimal guidance law with IPN and TPN is currently being investigated. The optimal guidance law should be able to achieve the same performance as IPN and TPN and should also produce smaller miss distances for many intercept scenarios.

VI. CONCLUSIONS

An optimal control law in polar coordinates has been developed by introducing a pseudo-control to decouple the intercept dynamics. The optimal guidance law was developed for a maneuvering and a non-maneuvering target using modern control techniques. The closed form solution for the commanded acceleration in the radial direction was determined through the use of the pseudo-control. The closed form solutions for the commanded acceleration in the transverse direction was derived through the use of the state transition matrix of the intercept dynamics. Approximations for the STM solution were evaluated for typical intercept scenarios and it was found that D can be approximated as 3 for a wide range of intercept scenarios. A 6-DOF missile-target simulation was used to compare the state transition matrix (STM) solution with an iterative (ITR) method for determining the commanded acceleration in the transverse direction. The STM solution resulted in smaller miss distances and shorter computation time. The optimal guidance law that was developed in polar coordinates was compared to the closed form solutions for IPN and TPN.

REFERENCES

1. Balakrishnan, S. N., "Decoupled Dynamics for Control and Estimation," *Proc. NAECON*, 1991.
2. Stansbery, D. T., Balakrishnan, S. N., Evers, J. H., and Cloutier, J. R., "Analytical Guidance Laws and Integrated Guidance/Autopilot for Homing Missiles," *IEEE Conference on Control Applications*, Vancouver, Canada, Sept. 1993..
3. Bryson, A. E. and Ho, Y. C., *Applied Optimal Control*, Waltham, MA.: Blaisdell, 1969.
4. Cloutier, J. R., Evers, J. H., and Feeley, J. J., "Assessment of Air-to-Air Missile Guidance and Control Technology," *IEEE Control Systems Magazine*, pp. 27-34, Oct., 1986.
5. Yuan, J. P., and Chern, J. S., "Ideal Proportional Navigation," *Journal of Guidance, Control and Dynamics*, Vol. 15, No. 5, pp. 1161-1165, Sept.-Oct. 1992.
6. Yuan, J. P., and Chern, J. S., "Solutions of True Proportional Navigation for Maneuvering and Non-Maneuvering Targets," *Journal of Guidance, Control and Dynamics*, Vol. 15, No. 1, pp. 268-271, Jan.-Feb. 1992.
7. Lin, C. F., *Modern Navigation, Guidance, and Control Processing*, Englewood Cliffs, NJ: Prentice Hall, 1991.
8. Guelman, M., "The Closed-Form Solution of True Proportional Navigation."*IEEE Trans. on Aerospace and Electronic Systems*, Vol. AES-12, No. 4, pp. 472-482, July 1976.
9. Shukla, U. S., "The Proportional Navigation Dilemma - Pure or True?." *IEEE Trans. on Aerospace and Electronic Systems*, Vol. 26, No. 2, pp. 382-392, March 1990.

A Comparison of Biasing Options in the Laser Multiphoton Ionization Detection of Methyl Radicals in a Filament-Assisted Chemical Vapor Deposition Reactor

Craig A. Bartell
Graduate Student
Department of Chemistry

Wright State University
3640 Col. Glen Highway
Dayton, OH 45435

Final Report for:

Graduate Student Research Program
Wright Laboratory
Aero-Propulsion and Power Directorate
Wright-Patterson Air Force Base

Sponsored by:

Air Force Office of Scientific Research
Bolling Air Force Base, Washington, D.C.

September, 1993

A Comparison of Biasing Options in the Laser Multiphoton Ionization Detection of Methyl Radicals in a Filament-Assisted Chemical Vapor Deposition Reactor

Craig Bartell
Graduate Student
Department of Chemistry
Wright State University

Abstract

An apparatus and procedures were developed for the detection of methyl radicals in a filament assisted chemical vapor deposition reactor operating with methane/hydrogen gas mixtures similar to those used in the generation of diamond-like carbon films. The apparatus was designed to detect small transient currents as the focussed output of a tunable dye laser ionizes methyl radicals between a hot filament and a deposition substrate. The current design incorporates the use of an electrode pair for ion collection, that may be translated between the filament and substrate. Results from two circuit designs with different bias geometries for ion collection are presented.

A Comparison of Biasing Options in the Laser Multiphoton Ionization Detection of Methyl Radicals in a Filament-Assisted Chemical Vapor Deposition Reactor

Craig A. Bartell

INTRODUCTION

There is general agreement from modeling results and from experiments that the methyl radical ($CH_3\cdot$) is one of the "growth species" linked to the transport of carbon to the substrate where diamond growth occurs in filament assisted chemical vapor deposition (CVD) of diamond-like carbon films.[1] Quantitative measurements of [$CH_3\cdot$] using resonance enhanced multiphoton ionization (REMPI) allows for a degree of spatial resolution because ions are only created in a small focal volume. Celii and Butler[2] have used the REMPI[3] technique to measure the relative $CH_3\cdot$ concentration in a filament-assisted diamond CVD reactor as a function of several process parameters. In their application an ion collector wire was fixed 4 mm above the substrate surface, the laser focus was approximately midway between the wire and the substrate, and the filament position was varied in order to probe the spatial [$CH_3\cdot$] profile.

This report describes the development of a REMPI detection experiment for methyl radicals that is designed for spatial profiling of [$CH_3\cdot$] in a fixed gap between the filament and substrate. This design avoids changing the filament-to-substrate gap as the spatial profiling is accomplished. Preliminary results are presented, and suggestions are made for continuing efforts.

APPARATUS and PROCEDURES

The filament-assisted CVD reactor was constructed from heavy-walled 4.5 inch O.D. glass pipe. The reactor was constructed in two sections, connected with an o-ring seal. Its overall length was ~18". Kovar rods, sealed through the top section of the reactor, were used to power the filament and give it support. A short section of glass rod held the tips of the kovar rods apart by ~25 mm and provided an anchor for supporting the center of the filaments. A 1" dia. port centered in this section allowed for the introduction of mixed gas flows through a 0.5" dia. pyrex tube at selected distances from the filament.

The length of the kovar rods was such that the filament was located ~5 cm inside the other section when the reactor was assembled. This section (the main body of the reactor) held the windows for passing the laser, the pressure measurement and vacuum ports, and the introduction port for a linear translator for the biasing and collection electrodes. The vacuum port was mounted to an aluminum plate for connection to a pressure control throttle valve. Flexible tubing connected this valve to the 400 m^3 hr^{-1} booster pump, which was backed by a 60 m^3 hr^{-1} two-stage rotary pump.

Typical coiled filaments were constructed using nine turns (~5 mm dia coils) of a 0.010" dia. tungsten (G.E. "218") wire which was attached to the Kovar rods by winding the free ends of the wire around the rod a few times and securing it with an alligator clip. Some filaments were more simply made from a straight length (~25 mm) of wire. The center of each filament was supported from the glass connecting rod by the use of a loop of the tungsten wire. The filament was heated by adjusting the current slowly to approximately 8 amperes, and the filament temperature was monitored with a hot filament pyrometer. A 200 sccm gas flow of 2% CH_4 in H_2 was caused to flow over the filament toward the substrate 7-14 mm away and on to the pumping port at the far end of the reactor. Gas flow rates were measured with electronic mass flow controllers, and total pressure was measured with a capacitance manometer with a 10 torr full scale rating. The substrate was a 1" dia x 0.1" thick molybdenum disc in the current work. The substrate was not connected electrically in the first circuit design (Fig. 1) to be described in this report. In the second design (Fig. 7) the substrate was electrically grounded.

In a previous circuit design using only a filament and substrate, it appeared that the collection efficiency for laser-generated ions was a function of the bias voltage used to control the discharge current. In an attempt to overcome this undesirable effect, a pair of kovar rod (0.060" dia) electrodes were mounted on a linear translator for movement between the filament and the substrate. In the first circuit design (Fig. 1), one rod was biased and the other was connected through a load resistor (1820 or 4090 ohms) to electrical ground. In the second circuit design (Fig. 7), both electrodes were tied together and connected to ground through the load resistor. Transient REMPI signals were detected as a voltage generated across the load resistor and passed through a capacitor to a digital oscilloscope (1 MΩ AC input impedance) for summed averaging over 100-1000 laser shots. Most often, peak REMPI signal levels were recorded and plotted; however, the time duration of the signals decreased at higher bias

New Circuit with Double Probes

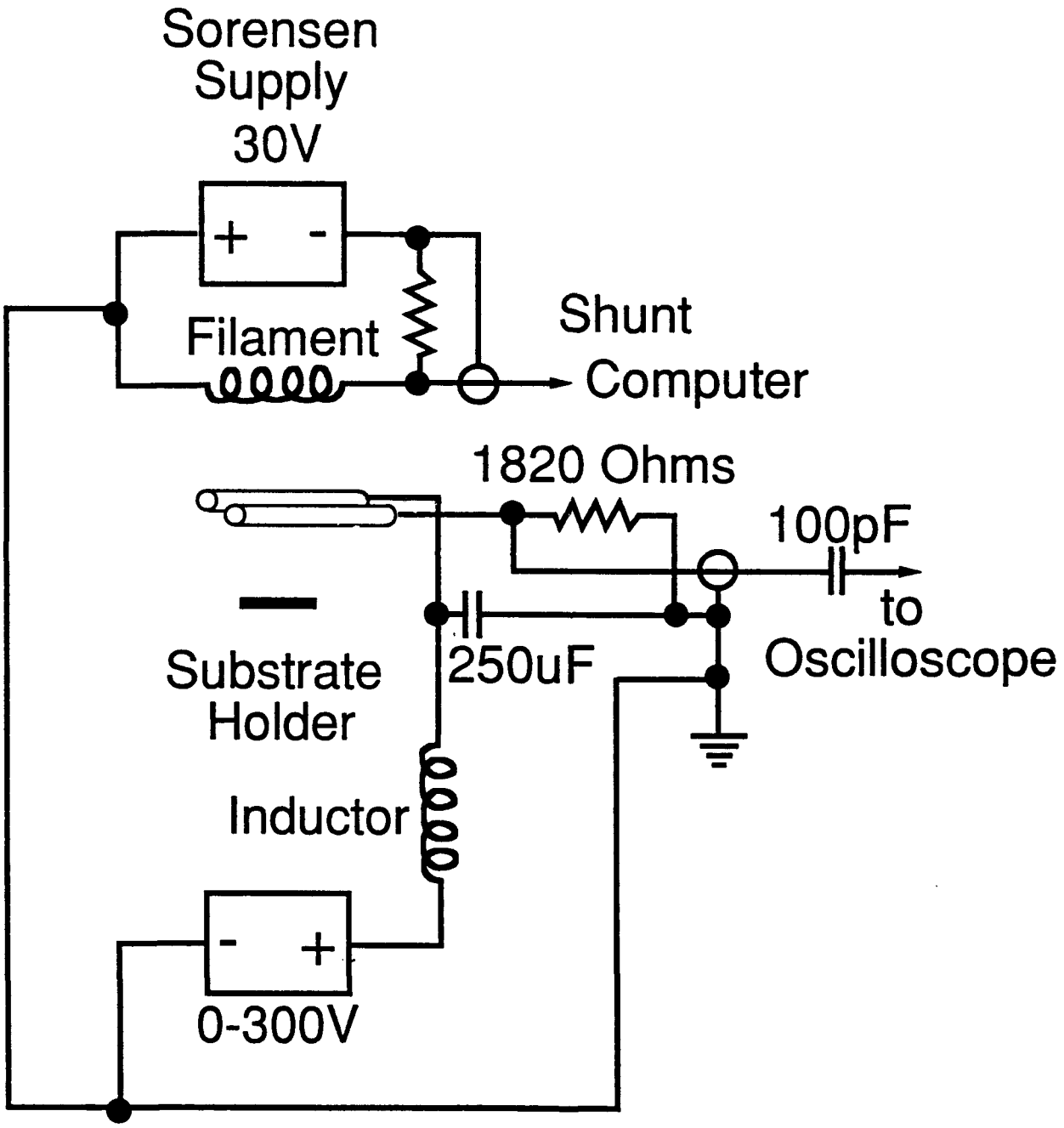

FIG. 1. Circuit design with bias and collector electrodes.

voltages and lower pressures. Consequently, a somewhat different view of the data (larger signals at lower voltages and higher pressures) is obtained by using integrated REMPI signal intensities (see Fig. 10). Unfortunately, the large amplitude electromagnetic interference generated at the time of the excimer laser firing overlapped the expected time for collection of photoelectron current. Consequently, the REMPI signals observed in this study are attributed to the movement of molecular ions.

REMPI signals were obtained by scanning the tunable output of an excimer-pumped dye laser (Lambda Physik EMG-103MSC/FL2002) near the 333.5 nm transition for methyl radicals and near 339.4 nm for methyl iodide. The dye laser delivered up to 8mJ/pulse at 333.5nm using a p-terphenyl/p-dioxane dye solution pumped at 248 nm with a KrF excimer laser. It was common for the laser power to decrease significantly by 1-2 mJ/pulse over the course of some of the longer experiments. No power correction has been made for any of the data presented here. Most of the current work was done with the laser operating at 10Hz. The laser was focussed between the electrodes with a 20 cm focal length lens. The vertical and horizontal positions of the laser could be adjusted externally with turning prisms mounted on linear tranlation stages. Filament, substrate, and electrode positions were determined by moving the laser beam until contact was determined visually by the spark generated.

RESULTS and DISCUSSION

The first evaluation of the circuit design with bias and collector electrodes (Fig. 1) was made using a 2% methyl iodide/hydrogen gas mixture at 10 Torr because of the ability to generate uniform concentrations with a stable species. The filament was cold for these evaluations. Fig. 2 presents a time-resolved REMPI signal observed for methyl iodide with a +150 volt bias on the one electrode and the filament biased at +27 volts to simulate the potential of a hot filament. This observation is the difference of 200 laser shots "on resonance" (at the peak near 339.4 nm) and 200 laser shots "off-resonance" (at 338.0 nm). The time-scale for observations such as this ranged from ~25 μs at 300 volt bias to ~200 μs with no bias.

The results for various combinations of filament and bias potentials are presented in Fig. 3. The results are qualitatively as expected. The positive potential sends positive ions to the (grounded) collector and attracts electrons (and/or negative ions, if present) to the biased electrode. The current generates a positive voltage drop across the

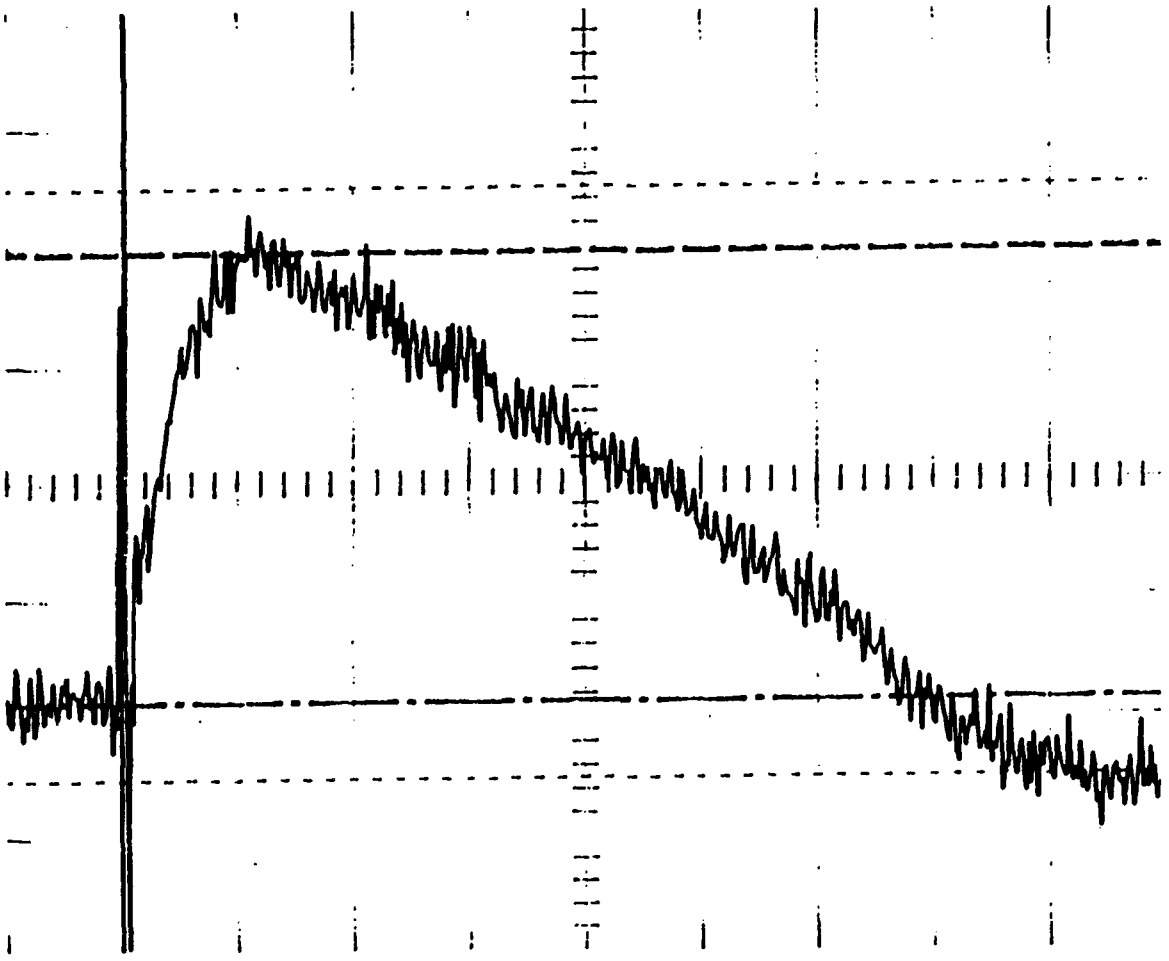

FIG. 2. Time-resolved REMPI signal from methyl iodide excited at 339.4 nm.

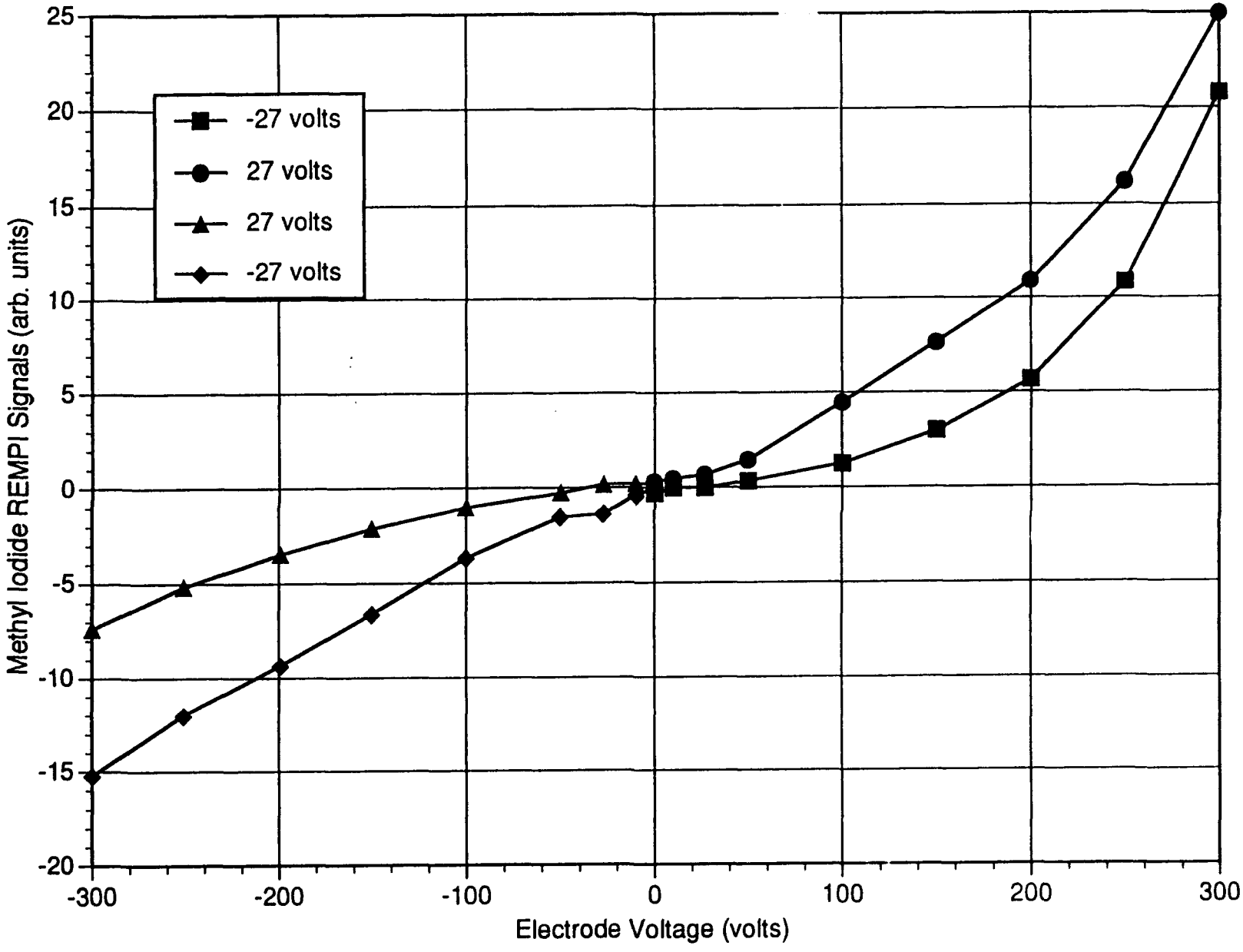

FIG. 3. Methyl Iodide REMPI signals as a function of bias voltage.

load resistor. Negative potentials generate negative polarity signals due to the reversed current direction. The increasing magnitudes of the slopes of the curves at the higher potentials is consistent with secondary ionization by accelerated photoelectrons. The actual collection of electrons is estimated to occur within 2 μs of the laser pulse[4], the drift time of the ions being much longer. The electron collection period is obscured by the electromagnetic interference (EMI) caused by the excimer laser pulse. Thus, most of the signals collected during this study are attributed to ion currents. Methyl radicals were generated in a 2% methane/hydrogen gas mixture using tungsten filaments operated at typical temperatures of 1800-2000°C. The methyl radical REMPI signals are presented in Fig. 4 as a function of bias voltage and electrode micrometer readings. True distances from the filament are 2 mm greater than the stated micrometer readings. The filament potential ranges from ground at one side to -31 volts at the other side, and the filament temperature was 1970°C. The laser energy was 3 mJ/pulse, and the on- and off-resonance wavelengths were 333.5 nm and 333.0 nm, respectively.

The contrasting behavior (compared to Fig. 3) of the methyl radical REMPI signals is immediately apparent. Near the filament the peak REMPI signals are quite strong when no potential is applied to the collection electrodes, and the maximum signal occurs at -10 volts potential. The signal falls off rapidly as the potential is made increasingly negative. At +10 volt potential there is still a net negative signal, although it is of interest to note that the off-resonance signal was entirely positive. REMPI signals are more difficult to detect at more positive potentials. There is no opposite polarity similarity for the methyl radical REMPI signals as there was in Fig. 3 for methyl iodide. The same qualitative behavior with respect to potential was observed at 5mm and 9mm micrometer readings but with reduced intensity in keeping with the expected reduction in methyl radical concentration away from the filament.

Further investigation of methyl radical REMPI signals as a function of distance from the filament gave results similar to those depicted in Fig. 5. Peak signals were always greater (negative polarity) near the filament, falling off as the laser focus and collection electrodes were translated toward the substrate (14 mm filament-to-substrate gap). This behavior is in agreement with the expectation of [$CH_3\cdot$] reduction away from the filament confirmed in other studies[1,5]. The occurrence of larger REMPI signals at lower collection potentials is demonstrated again in this figure.

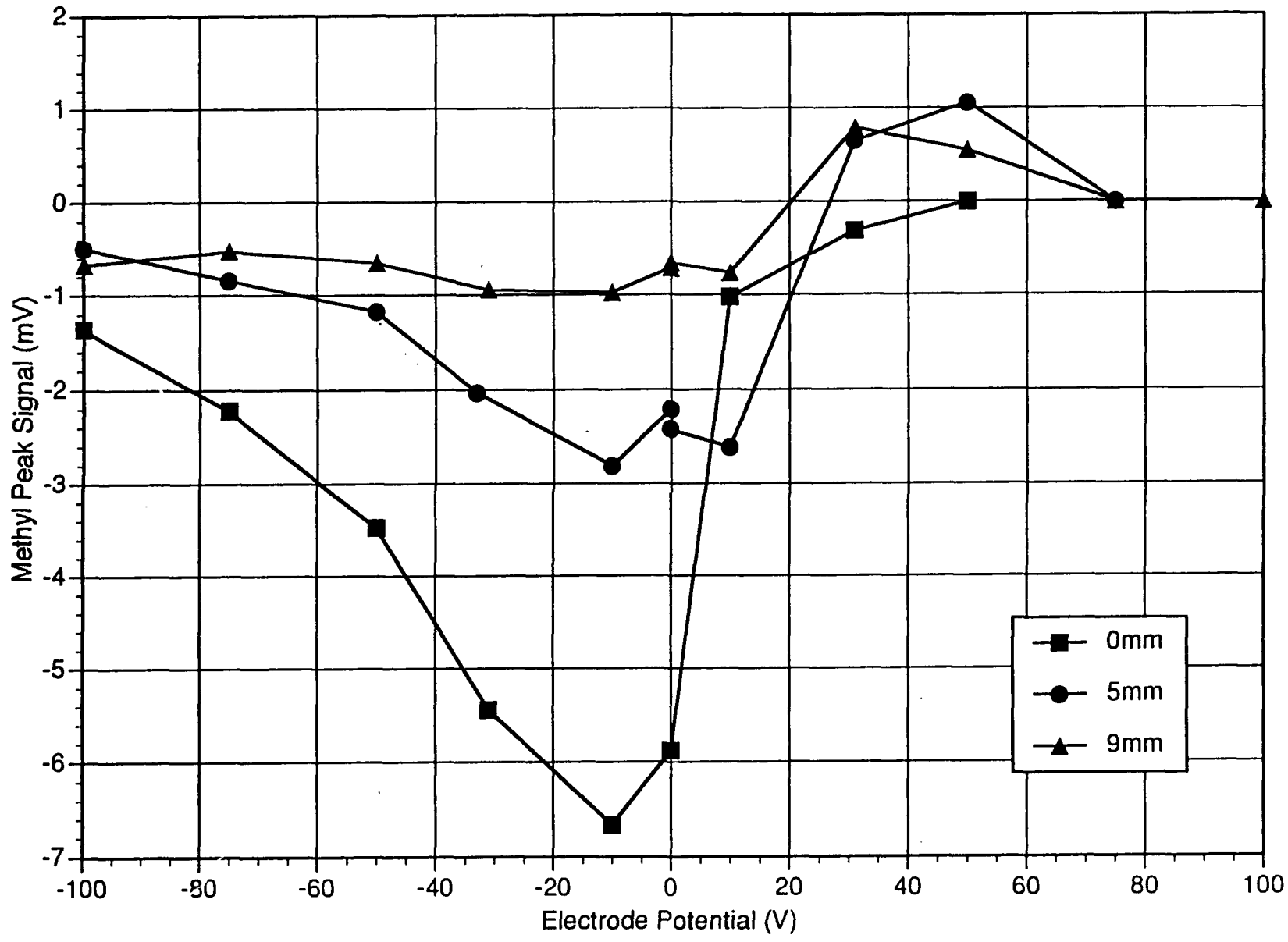

FIG. 4. Methyl radical REMPI signals as a function of bias voltage.

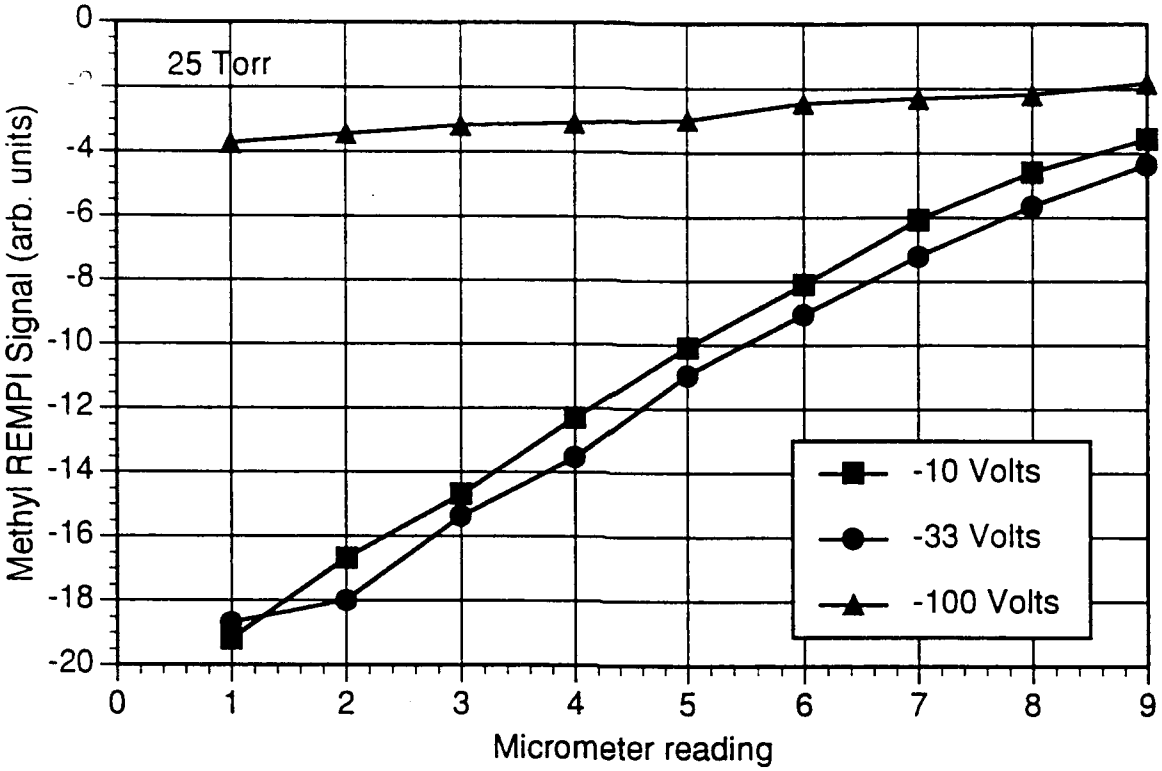

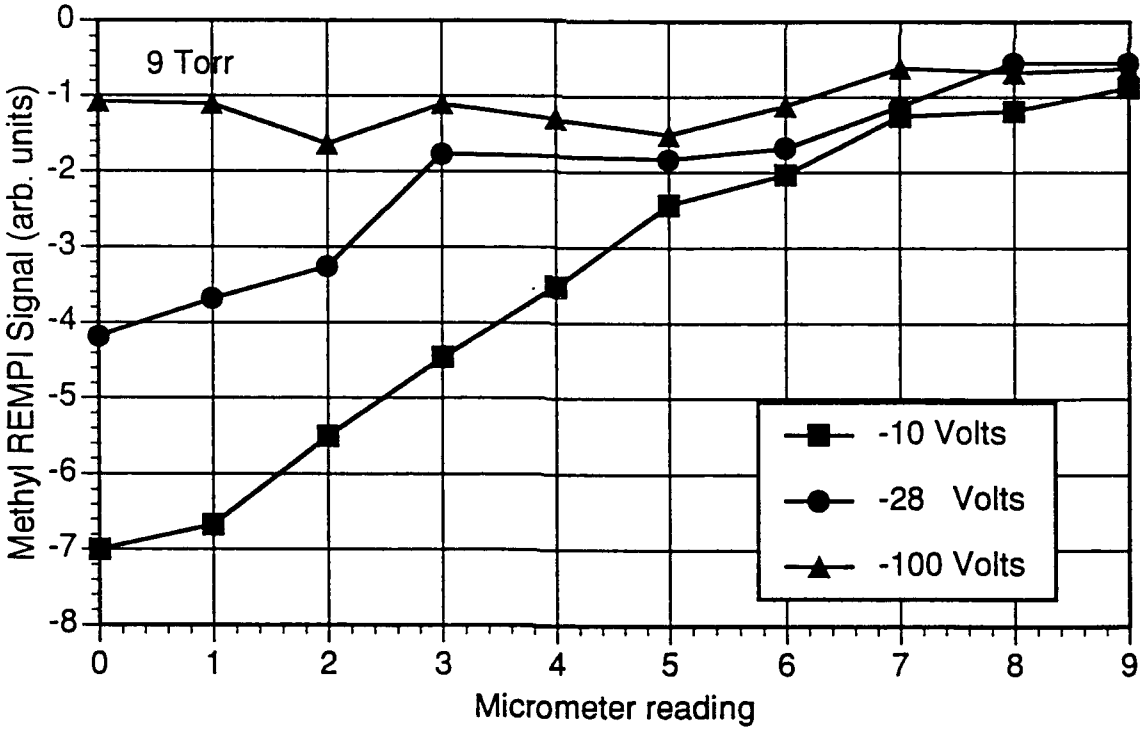

FIG. 5. Methyl radical REMPI signals as a function of distance from the filament. True distance is obtained by adding 2 mm to the micrometer reading.

During the course of this work, it was observed that the DC current through the load resistor increased, under certain biasing conditions, with increasing temperature and decreasing filament-to-electrode distance. Large DC current levels proved to suppress the REMPI signals, as shown in Fig. 6A, where peak REMPI signals and DC current are plotted versus electrode distance from filament. When the electrodes were within 4 mm of the 2020°C filament, the DC current was in excess of 0.5 mA, and the peak REMPI signals jumped to lower values. At the lower 1940°C filament temperature the DC current was not excessive, and the REMPI signal levels increase nearer to the filament (in agreement with the expectations of Fig. 5).

A further demonstration of this effect is demonstrated in Fig. 6B, where the REMPI signals (mV) and the resistor voltages (V) are plotted versus filament temperature for the 2mm electrode position. The equivalent DC current is 0.5 mA at -2 volts across the load resistor. Here, again, the peak REMPI signal suffers reduction when the filament temperature reaches a point where large currents are picked up by the collector electrode. This behavior was not noted in other studies[1,5] where the methyl radical REMPI signals (electron current) increased with temperature up to a nearly constant value between 2200°C and 2500°C.

Near the end of this study we modified the circuit design of the apparatus to closely reproduce that reported by Corat and Goodwin[5] in a recent publication. This design, presented in Fig. 7, grounds the substrate and incorporates an additional power supply to maintain a constant potential difference between the filament and the paired collection electrodes (20 volts more positive than the low side of the filament). The filament-to-substrate gap was 7-9 mm, depending upon the filament placement, for all of this work. Corat and Goodwin[5] showed increasing REMPI signals from 0-50 volts electrode bias, and they were able to obtain saturated electron collection conditions over the range of 50-150 volts electrode bias (their figure 3). REMPI signals were obtained as a function of bias voltage (Fig. 8), distance from the filament (Fig. 9), and total pressure (Fig. 10) in the present study.

REMPI signals as a function of electrode bias voltage were obtained with the collection electrodes and the laser focus positioned 4 mm above the grounded substrate (~3 mm from the filament). The laser beam was parallel to the electrode rods in this study whereas the beam traveled perpendicular to the single collection electrode in the apparatus of Corat and Goodwin[5]. The squares in Fig. 8 were obtained with a (coiled) filament temperature of

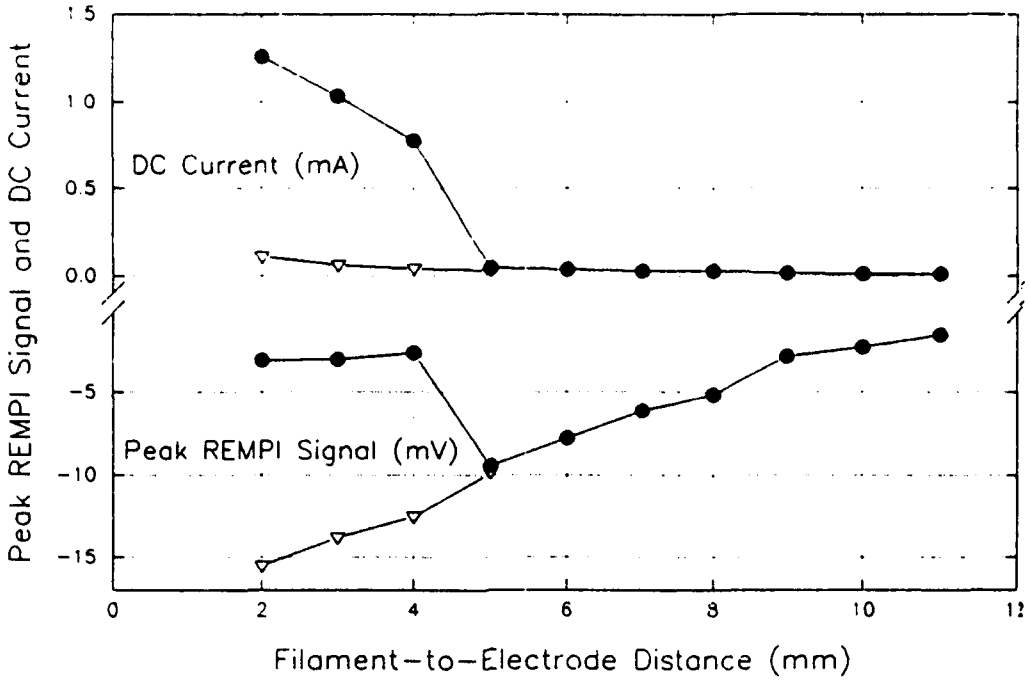

Fig. 6A Methyl radical REMPI signal and DC current as a function of electrode position.
● points were obtained with T_{fil}=2020°C (32.6 V @ 8.0 A) first.
▽ points were obtained with T_{fil}=1940°C (30.7 V @ 8.0 A) after the first set.
Laser pulse energy was 4.8–4.9 mJ, and the collection potential was −32 V.

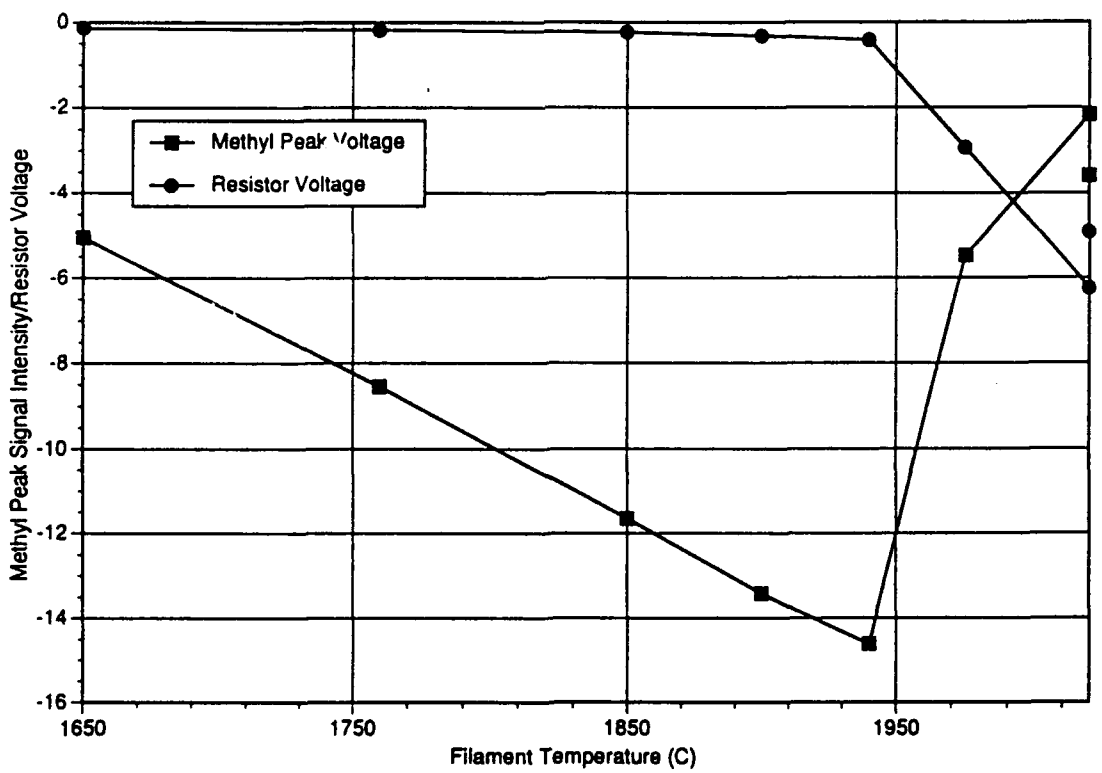

FIG. 6B Methyl radical REMPI signal and D.C. voltage across load resistor as a function of filament temperature.

Fig.7 Circuit design with constant potential between filament and collection electrodes (similar to Goodwin's design)

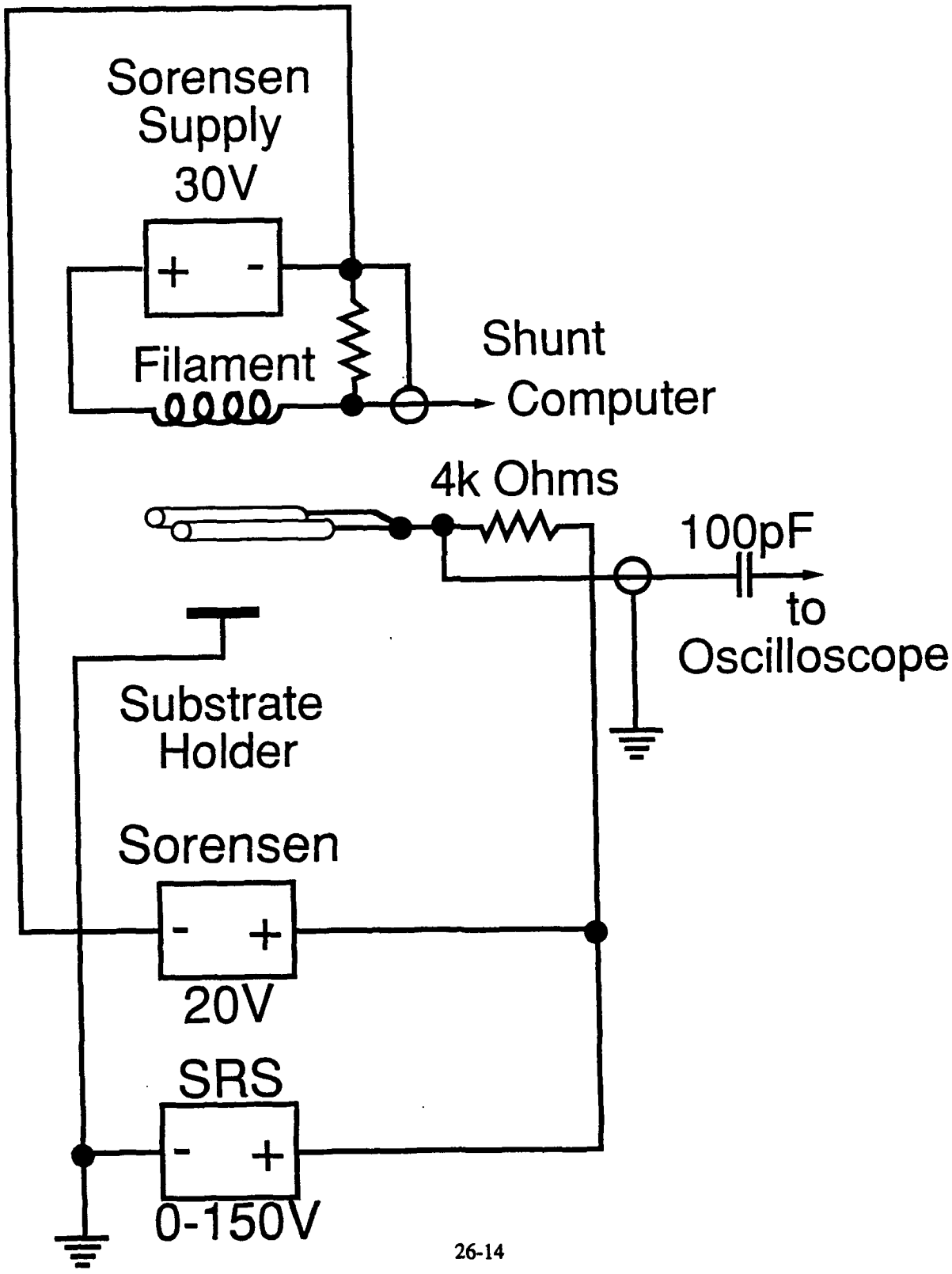

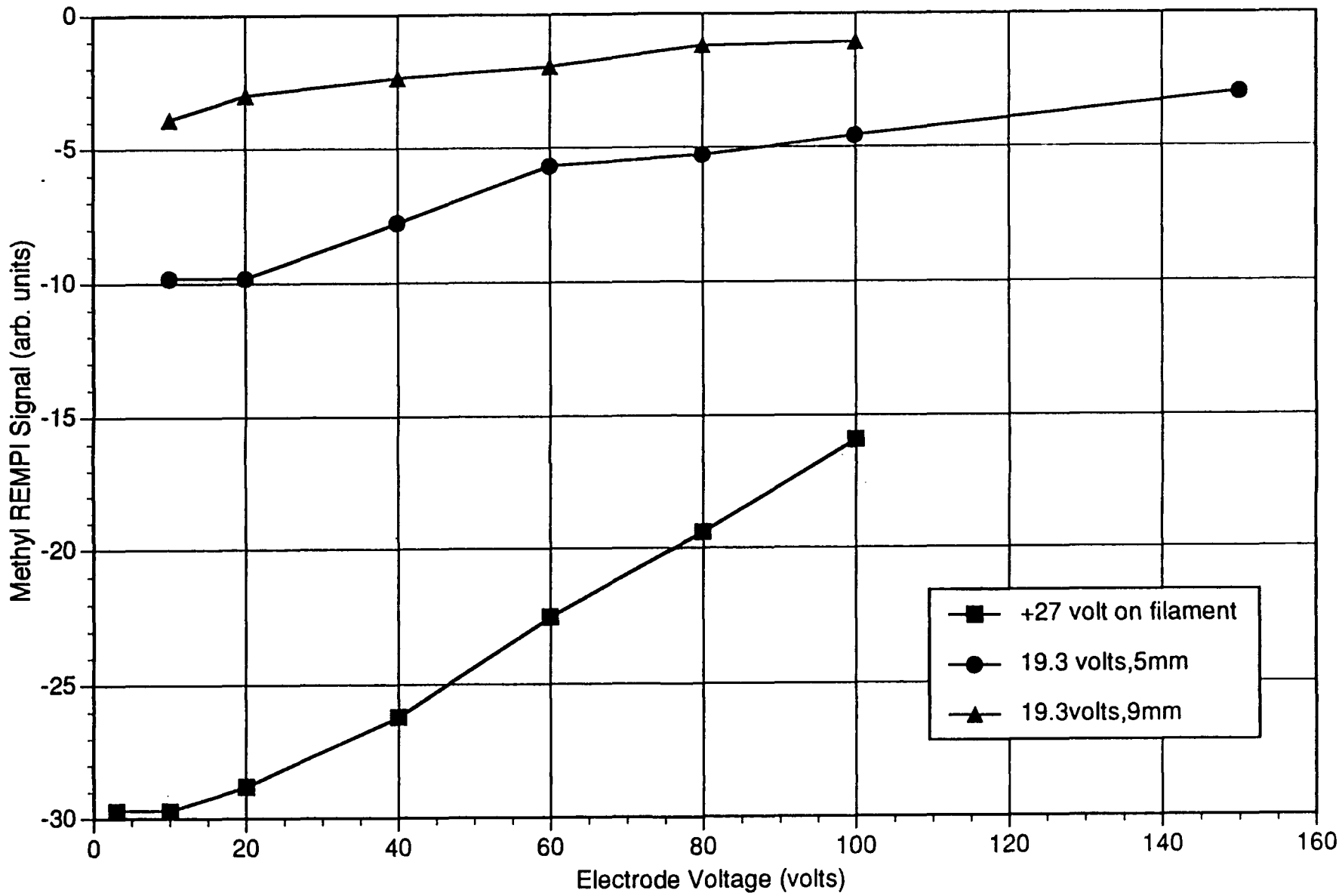

FIG. 8. Methyl REMPI Signals as a function of bias voltage.

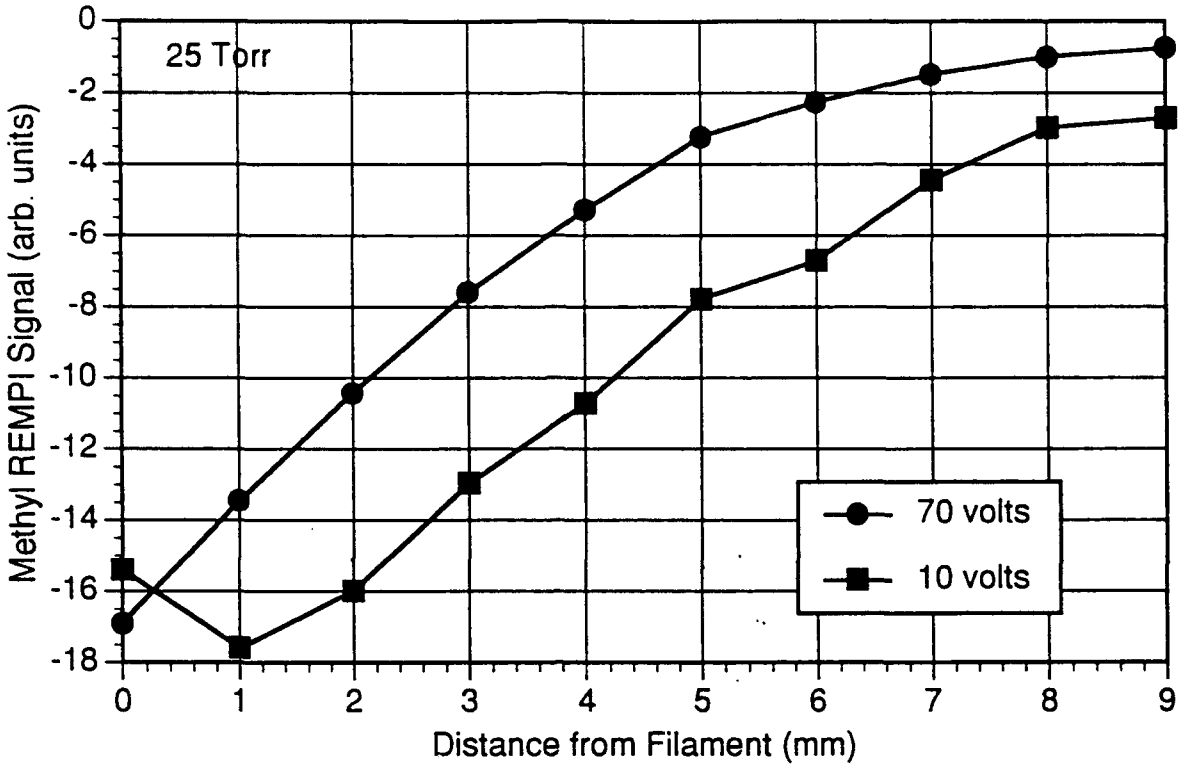

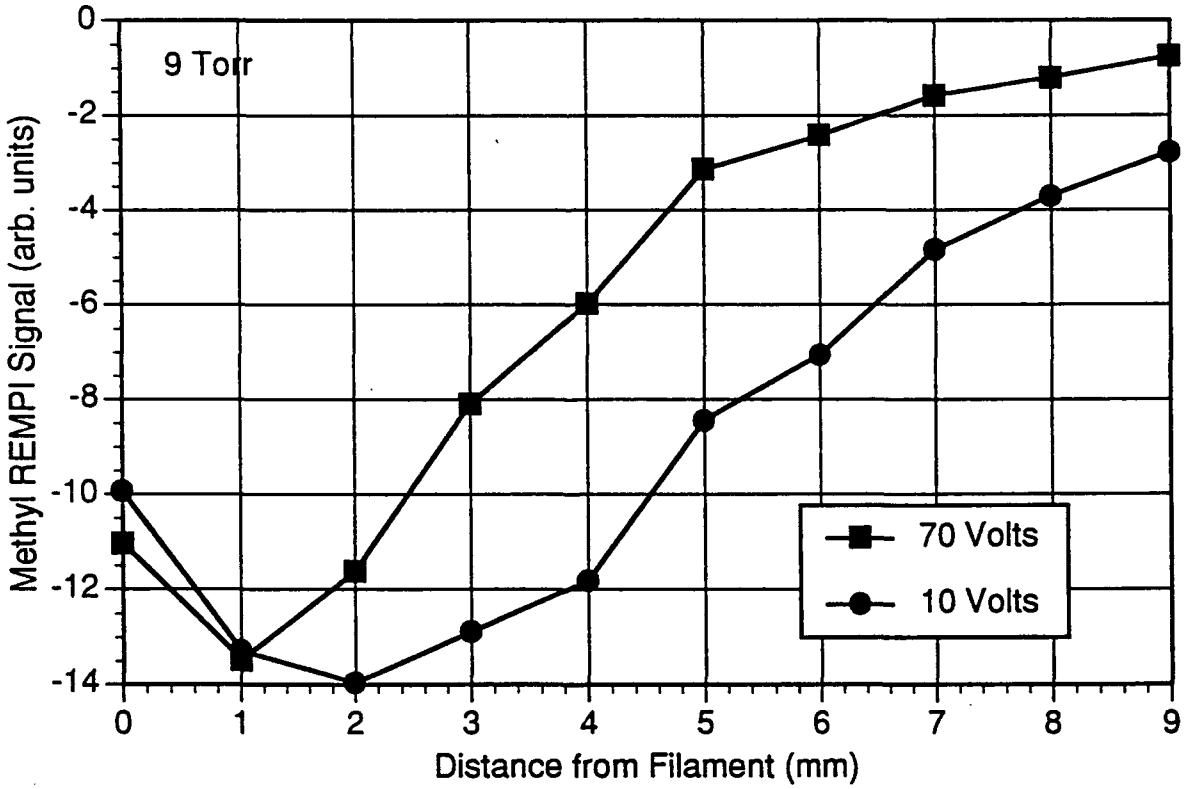

FIG. 9. Methyl radical REMPI signals as a function of distance from the filament. True distance is obtained by adding 2 mm to the micrometer reading.

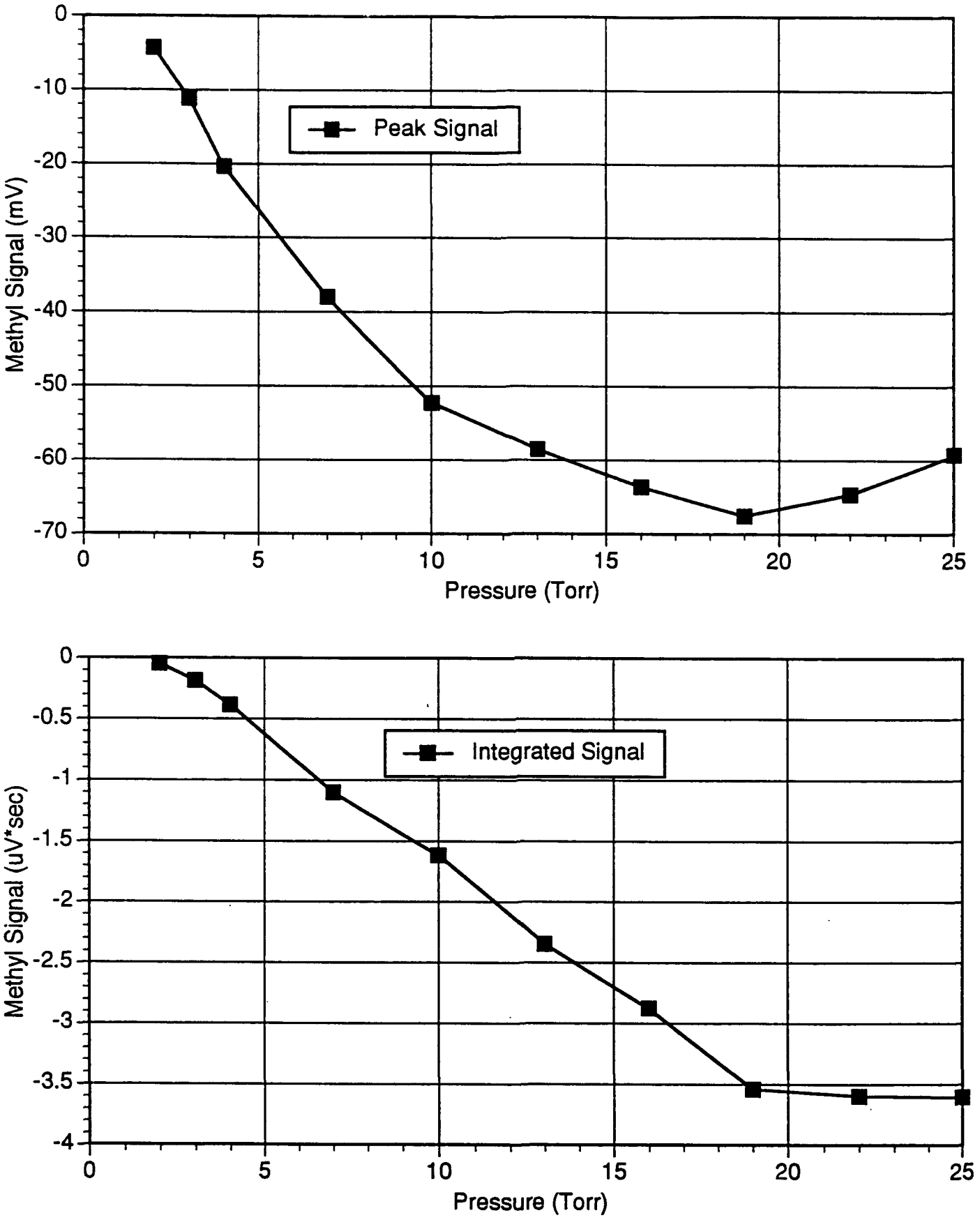

FIG. 10. Methyl radical REMPI signals as a function of total pressures.

~1900°C and 6.5 mJ/pulse laser energy. REMPI signals were reduced by a factor of two or more when the laser focus was located midway between the collection electrodes and the substrate (Corat and Goodwin's arrangement[5]). The circles and triangles in Fig. 8 were obtained on a different day with a single strand electrode, T_{fil}=1850°C, and 5.2 mJ/pulse laser energy. The 5 mm and 9 mm labels of Fig. 8 are micrometer readings that correspond to 4 mm and 8 mm distances from the filament. The DC current was less than 0.1 mA for all of the data of Fig. 8. The REMPI (ion current) signals were not observed to saturate with bias voltage in the manner observed by Corat and Goodwin[5] for electron current.

REMPI signals as a function of distance from the filament are more completely presented in Fig. 9. These data were obtained on two different days using single strand tungsten filaments at 2030°C (top) and 1880°C (bottom) and two bias voltages (10 and 70 volts) at 9 and 25 Torr total pressures. The laser pulse energies were 5.2 mJ for the 25 Torr data (top) and 4.3 mJ for the 9 Torr data (bottom). Peak REMPI signals were greater at the lower bias voltage, and they decayed as the detection point was moved away from the filament. The small decreases close to the filament are related to the larger DC currents observed at those positions (as in Fig. 6A). The observations of Figs. 8 and 9, greater REMPI signals at lower bias voltages and decreasing signal away from the filament, are qualitatively the same as those presented in Figs. 4 and 5 for the previous circuit design.

The observation of larger REMPI signals at lower collection potentials is quite puzzling. It has been suggested by one author (MDK) that the behavior is suggestive of the presence of negative ions, presumably produced by attachment of the electrons generated by the REMPI laser pulse. The electron attachment hypothesis is consistent with smaller cross-sections for the higher collection potentials that yield more energetic electrons. In fact, calculations[6] have shown that dissociative attachment ($e^- + H_2(v) \rightarrow H\cdot + H\cdot^-$) involving vibrationally excited H_2 can be efficient. Detection of $H\cdot^-$ produced in pure hydrogen gas flowing over a hot tungsten filament suggests that the process is more efficient at lower pressures where vibrational deactivation of the $H_2(v)$ reactant is reduced[7]. In our experiments, however, higher pressures are expected to yield greater methyl concentrations, the source of the electrons to be attached. Thus, there are competitive processes at work that make it difficult to predict the pressure dependence of the REMPI signals. Results from an investigation of REMPI signal versus total pressure of the 2% CH_4/H_2 gas mixture are presented in Fig. 10. Peak signals and integrated signals are presented. The

integration limits were from ~2 μs to the point where the signal crossed zero as it underwent damped oscillation. For this experiment the filament was maintained at 1960-1990°C, the electrode bias was 15 volts, and the laser energy was 6.1 mJ/pulse. The longer time duration of the signals at lower pressure tend to increase the relative level of the integrated signals at lower pressures. The result is an approximately linear dependence of integrated REMPI signals with pressure over the range 2-20 Torr, at which point the signal seems to saturate. The DC current collected by the probe ranged from 0.27 mA at 25 Torr to 0.64 mA at 2 Torr. We do not expect that any significant reduction of signal occurred at these current levels. While the negative ion hypothesis has some support, there is one remaining observation that it still does not answer. The almost complete lack of REMPI signal with the positive collection potentials (Fig. 4) in the first circuit design is yet a mystery. The potentials modeled for the experiments indicate that ions generated between the electrodes should be detected, and the number of $CH_3\cdot^+$ ions should equal or exceed that of $H\cdot^-$; but little or no signal is detected.

SUMMARY and CONCLUSIONS

Methyl radical REMPI signals, with temporal and spatial resolution, were obtained from 2% methane/hydrogen gas mixtures in a filament-assisted CVD reactor using different collection geometries and biasing options. Observations were attributed to photo-generated ion currents because detection of transient electron currents was blocked by laser noise. While the observations of REMPI ion currents in 300K methyl iodide was in qualitative agreement with expectations, the REMPI signals generated from methyl radicals at 333.5 nm exhibited unconventional behavior with respect to collection potentials. A hypothesis involving the production of negative ions by dissociative attachment to vibrationally excited H_2 was considered because it was consistent with the occurrence of larger REMPI signals at lower potentials. The suggestion has been made[8] that using a photodetachment laser pulse delayed after the REMPI laser might provide a further test of the negative ion hypothesis.

Because of the uncertainty of the source of the observed REMPI signals with the present detection methods, we cannot recommend using the present procedures even as a relative measure of methyl radical concentrations in a CVD reactor. We are confident, however, that quantitative measurements could be obtained by observing the

electron current generated in the MPI event. This would require efforts at laser EMI noise reduction so that the early time signals could be obtained with much less interference.

ACKNOWLEDGEMENTS

Ideas and assistance from Dr. Peter Bletzinger were invaluable as were conversations with Drs. Bish Ganguly and Alan Garscadden. I appreciate the calculation of electron mobilities by Rajish Nagpal and the mapping of potentials by Peter Bletzinger. The technical expertise and cheerful assistance of Mike Ray and Bob Knight made this work possible. I acknowledge the assistance of David Dolson and Michelle Klingshirn in collecting a significant portion of the data.

REFERENCES

1. Two reviews of the diamond CVD processes are: P. K. Bachmann; R. Messier *Chem. Eng. News*, pp 24-38, May 15, 1989. and F. G. Celii; J. E. Butler *Ann. Rev. Phys. Chem.* **(1991)**, *42*, 643-84.
2. F. G. Celii; J. E. Butler *J. Appl. Phys.* **(1992)**, *71*, 2877-83.
3. J. W. Hudgens; T. G. DiGuiseppe; M. C. Lin *J. Chem. Phys.* **(1983)**, *79*, 571.
4. R. Nagpal, private communication.
5. E. J. Corat; D. G. Goodwin *J. Appl. Phys.* **(1993)**, *74*, 2021-9.
6. A. Garscadden; W. F. Bailey *Prog. Astronaut. Aeronaut.* **(1981)**, *74(Rarefied Gas Dyn., Pt. 2)*, 1125-37. and W. F. Bailey; A. Garscadden *Brookhaven Natl. Lab., [Rep.] BNL* **(1980)**, BNL-51304, Proc. Int. Symp. Prod. Neutralization Negat. Hydrogen Ion Beams, 2nd, 33-41.
7. P. Bletzinger, private communication.

Design of an Apparatus to Measure Particle Size and Carbon Deposition in Thermally Stressed Hydrocarbon Fuels

Robert T. Foster

Department of Mechanical Engineering
The University of Iowa
Iowa City, IA

Final Report for :
Graduate Student Research Program
Wright Laboratory

Sponsored by:
Air Force Office of Scientific Research
Bolling Air Force Base, Washington D.C.

August 1993

Design of an Apparatus to Measure Particle Size and Carbon Deposition in Thermally Stressed Hydrocarbon Fuels

Robert T. Foster
Department of Mechanical Engineering
The University of Iowa

Abstract

WL/POSF has a need to improve current generation jet fuels, and to conduct research that will result in future fuels. This research consists of fundamental experimentation to generate global fuel properties, as well as research to determine specific properties of fuels currently in use. One area of fuel property research concerns the deposition process. This study looks at the design of an experimental apparatus to combine photon correlation spectroscopy and the quartz crystal microbalance to analyze the deposition process. Research with this unit will be conducted to determine if there is a correlation between particle size of molecular chains suspended in the fuel and the rate of surface deposition.

Design of an Apparatus to Measure Particle Size and Carbon Deposition in Thermally Stressed Hydrocarbon Fuels

Introduction

The heat load requirements that current military jet aircraft place on fuels has been increasing dramatically and will continue to do so in the foreseeable future due to increasing levels of performance. As a fuel is thermally stressed to higher levels, it breaks down chemically, creating deposits which can cause degradation of the performance of the system. JP-8 can be operated to a maximum temperature of 325°F, according to Gray and Shayeson. To combat the problem of thermally induced fuel deposition, the Air Force has issued requirements for two future fuels, JP-8+100 and JP-900. The goal of JP-8+100 is to increase the current level of fuel operating temperatures by 100°F. JP-900 is a concept for a future fuel which will be thermally stable to 900°F.

In order to create JP-8+100 and JP-900, it is necessary to understand the deposition process that goes on in the current generation of fuels. Two avenues that have been pursued in researching these characteristics are studies using photon correlation spectroscopy (PCS) and the quartz crystal microbalance (QCM). PCS has been used by Sandia National Labs, as well as the QCM technique. They have used these techniques to study the deposition process to determine such kinetic fuel factors as the global activation energy.

This study was done to allow PCS to be mated with a QCM to allow

both of these sensors to function at the same time. This ability will allow researchers to gather data on correlation's that can be inferred between the increase in particulate size in the fuel and the subsequent deposition on the QCM. This interaction is not yet completely understood, hence this data will give new insight into the fundamental process involved in surface deposition.

Design

It was proposed by Dr. V. Vilimpoc that the QCM be mated with the PCS to allow evaluation and correlation of increases in particle size with increased surface deposition. The QCM is ideally suited for use in situations were the surface deposition may be varying with time, because it allows time dependent measurements to be made of the deposition. This way of measuring is in contrast with Leco Carbon Burnoff analysis, which tests the total mass of deposition at the end of an experiment. This mass then must be assumed to be constantly deposited with time, which may not be a completely valid assumption, according to preliminary work done at WL/POSF. Therefore, using the QCM in low flow situations will enable the researcher to take data concerning the time rate of deposition that has not been previously available.

The PCS is the other important aspect of this experimental design. With funding and research support from Wright Laboratory, research has been conducted at Sandia National Laboratories which attempted to correlate both time dependent deposition with the QCM, and then to examine that

same fuel to analyze the particle size, in order to discover how the oxygen was moving into deposits according to O'Hern et al. The PCS allows small particle size measurement as well as verification of concentrations of different sized particles.

The design of this apparatus will allow for the PCS laser to take data simultaneously with the QCM measurements. The system was designed around a maximum external diameter of 1.5" for the flow tube. This diameter was chosen because it was a standard size for the Watlow heaters that were available, and also because it was a standard size of 302 Stainless Stock (302 SS), which would result in reduced fabrication time. It was desired to have a rapid transition to high, steady state temperatures, in contrast to the Parr bom calorimeter. The calorimeter has been used for many of the QCM experiments and takes 40 minutes to heat to steady state conditions. 302 SS has a marginal thermal conductivity for metals, but the trade off in heating time with copper is balanced by the fact that copper has been shown to affect deposition readings. Additionally, 302 SS will withstand temperatures that will burn off any carbon that deposits in the system. This is important because it addressed concerns with the ability to completely clean the system that were raised during the design process. These concerns centered around the unknown, but highly probable interactions between a system with old deposits on the QCM and PCS readings. An added bonus of 302 SS is that it has a low thermal expansion coefficient, which results in an added assurance that seals will remain intact throughout the entire temperature regime.

The components of the measuring system from top to bottom, as per figure 1, are inlet/manifold, main heating section, lower manifold, lazing section, lower heating section and QCM holder with ceramic insert.

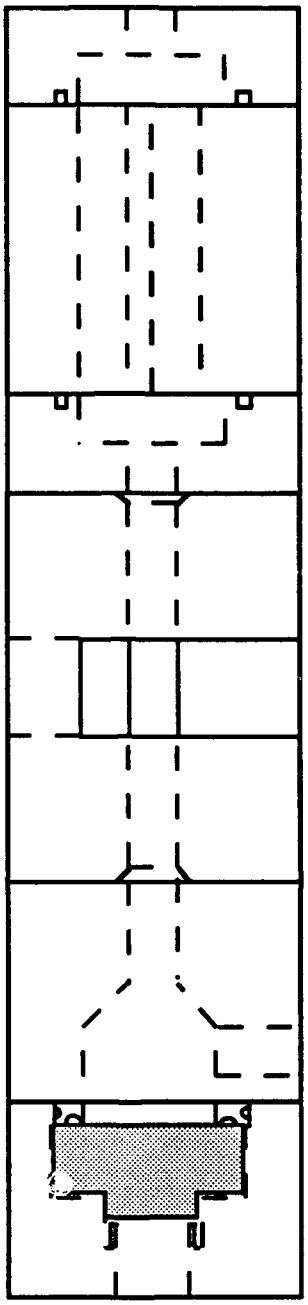

Figure 1: Overall of view of test cell.

The inlet/manifold of figure 2 has a 1/16 tap swage lock connector in the top, and mid way into the piece the 1/4" stream is allowed to manifold, and then flow into a 3/4" manifold.

The inlet/manifold is o-ring sealed to the main heating section using Viton o-rings. These o-rings are capable of withstanding temperatures of up to 600 °F, but normally are operated between -20 and 500 °F. When the experimental setup of this system has been verified, Kelress o-rings will be purchased which will allow system temperatures to be increased.

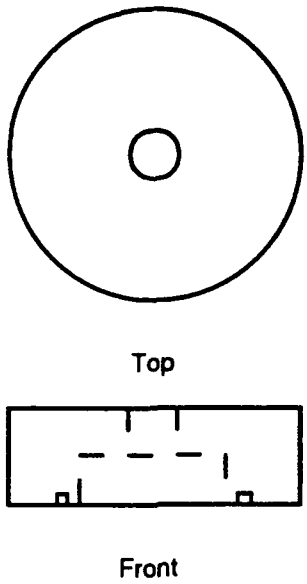

Figure 2: Inlet/Manifold.

The main heating section is the primary heating zone for this system, and can be viewed in figure 3. The fuel will flow through three 1/4" tubes through the main 2" heating section. This will cause the fuel in this section to have a higher residence time here then in other portions of the system. The heating jacket that is to be placed around this portion of the system completely encompasses the heating area. The heat jacket is a Watlow type B heater, capable of an advertised Watt density of 41, based on 240 Volts and 500

Watts of power. The heater will be controlled by a heat control unit, which will allow the heated section to produce an outlet flow into the lazing section with constant temperature.

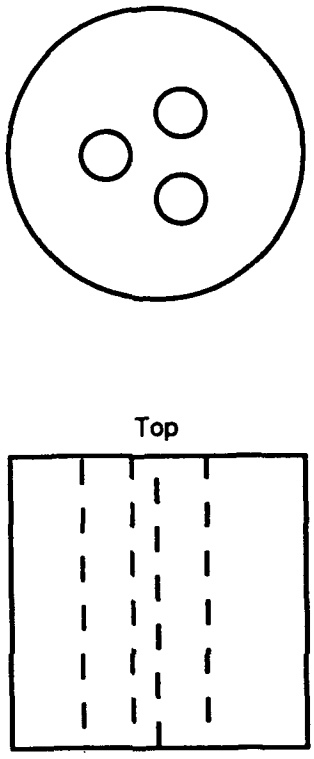

Figure 3: Main heating section.

The flow will exit the main heating section and flow into the lower manifold, which is also viewed in figure 4, were it will be collected and directed into the lazing section. This lower manifold has a .0625" relief area to allow for the insertion of the glass, to prevent breakage of that portion of the system during heating and cooling. The lower manifold also provides the flat surface to seal the upper o-ring on the glass tube in the lazing section.

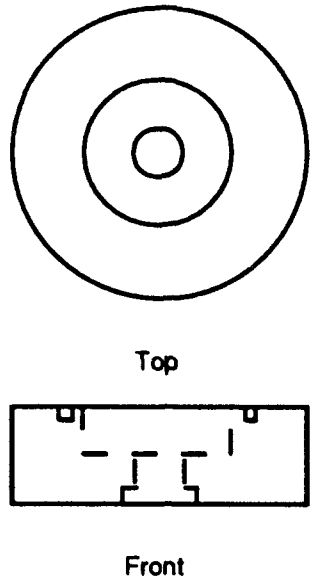

Figure 4: Lower manifold schematic.

The lazing, or PCS, section in figure 5, will have a 1/2" OD glass tube o-ring sealed into it. This tube is heavy walled clear fused silica. The lazing section has 2, 1/2" long slots machined into it's mid section. One of these slots is .15" wide, and will be facing the laser as it emits into the system. On the other side, the slot is machined into the cylinder to cover 120°. This 120° will allow for complete PCS correlation based on different viewing angles.

The lower heating section provides a stable temperature for the fluid from the time that it leaves the lazing section until the time that is contacts the QCM and then exits the system as viewed in figure 6. This heating is performed by a 1 1/2" long Watlow heating jacket rated at a Watt density of 77, based on 240 Volts and 450 Watts. This is a higher rating than the upper jacket, which should allow this section to be able to quickly respond to necessary changes in the heat input to maintain a stable temperature in this

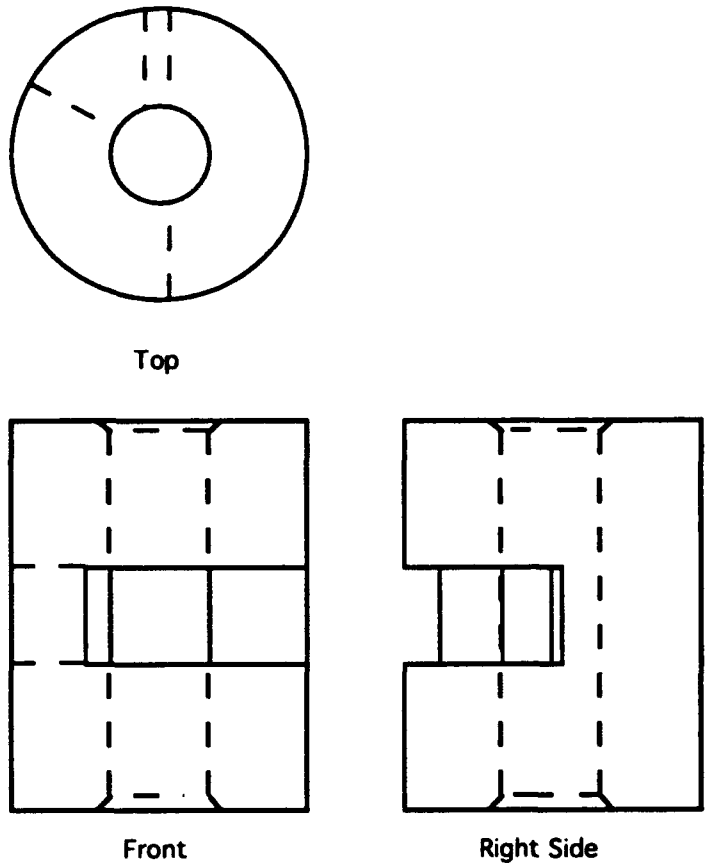

Figure 5: Lazing section.

region. It is critical that the temperature be maintained constant in this region due to the fact that the QCM frequency changes are dependent on the viscosity of the fluid. The viscosity is temperature dependent. Therefore it is necessary to keep the fluid in as isothermal state as possible. This section also provides the o-ring sealing for the Quartz Crystal (QC) and also the safety o-ring. This section has a .125" protrusion into the QC holder that has two o-rings on it. One of these rings face down, and seals the top face of the QC. The other ring faces outwards, and seal against the inner face of the QCM

holder. Additionally, the outlet port for the fuel is in this section.

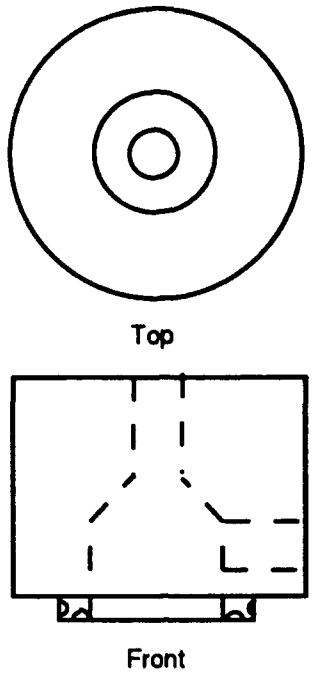

Figure 6: Lower heating section.

Finally, the lowest portion is the QCM holder with the ceramic insert from figure 7. The QCM holder was designed to accept a 1" diameter polished QC. The stainless portion has a grounded shield SMA connector heliarc welded into the bottom to allow for an information out port to go to the QC reader. Attaching to this port is a ceramic plug, which allows electrical connections to be made which run from the lower QC face to the outlet. Marcor machinable ceramic was used to make this plug. It was chosen based on the fact that it's thermal expansion coefficient is relatively close to that of 302 stainless, which should keep the o-ring seal in tact to the 300 psi that the system should see. In addition, it was necessary to electrically isolate the QC

from the surrounding surface. The ceramics perform this function.

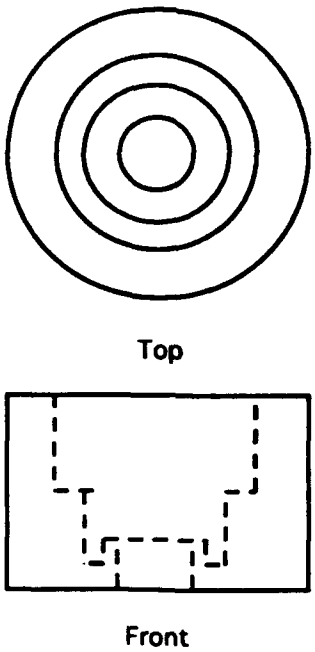

Figure 7: QCM holder with ceramic insert.

Use

At the conclusion of my summer posting to Wright Labs, the test cell had not been completely fabricated. The proposed use address' some difficulties that were envisioned in the systems use, and ways to overcome them.

Dr. Larry Goss is currently using a PCS system for SRL to determine correlation's between particle size and oxygen content for certain fuels. This experience demonstrated the viability of the PCS system to this experiment.

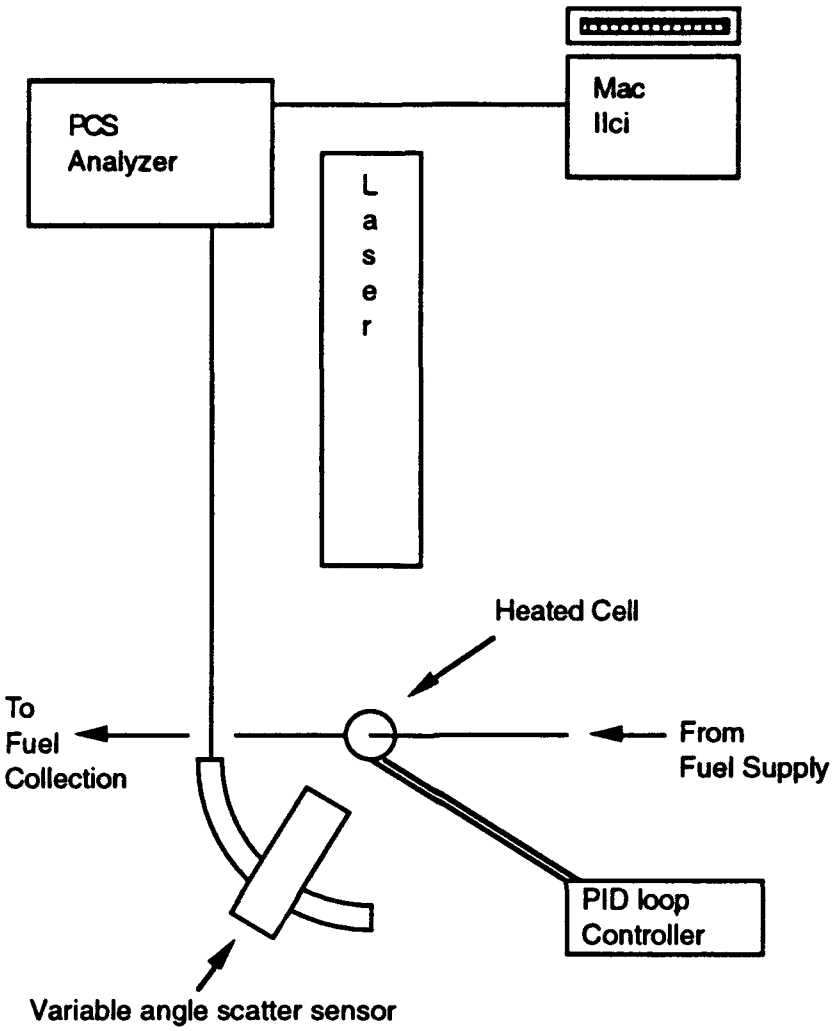

Figure 8: Schematic for proposed experimental setup for use of test cell.

Using a Mac IIci, a photon scattering sensing device is used to monitor scattering caused by particles in the fuel. This scattering, and the use of different angles relative to the sample, allow the PCS analyzer to transfer data to the Mac which can be used to determine particle size and density. A sample of the proposed experimental setup is given in figure 8.

Concerns were raised that the test cell would have some difficulty

accurately controlling temperature during testing. To relieve these concerns, the fuel line leading into the cell can be heated with heating tape to raise the fuel temperature from ambient to a level that does not prestress the fuel before the heating section of the experiment. This will relieve the heating units placed around the cell from all of the load of heating the fuel from ambient. The upper heating jacket will be used to heat the fuel to the desired temperature. A thermocouple will be mounted either in the fuel stream as the fuel leaves the upper (heated) section and enters the lazing section, or possibly mounted on a hole drilled into the stainless at that same point. The hole drill into the stainless has been proven to be an easy way to obtain an accurate measure of the wetted wall temperature and is a modification envisioned after the cell has been verified experimentally.

The temperature recorded as the fuel enters the lazing section will be fed into a PID loop. This loop will take an outlet temperature for the system as well. This can be obtained by placing a T swagelock piece at the exit, or possibly taking a wetted wall temperature as described earlier. With these two temperatures, the PID loop should be able to use the lower heater to maintain a constant temperature in the lower section. This will ensure that the fuel is kept at a constant temperature as it is analyzed with the PCS as well as with the QCM.

Additional concerns were raised that a large temperature gradient across the QCM would allow it to not accurately detect changes in surface deposition. According to Kanazawa and Gordon, the equation controlling surface deposition with changes in the resonance frequency are related by equation [1].

$$\Delta f = -f_o^{\frac{3}{2}} \left(\frac{\eta_L \rho_L}{\pi \mu_Q \rho_Q} \right)^{\frac{1}{2}} \qquad [1]$$

In equation 1, f_o is the oscillating frequency of the free (dry) crystal, η_L is the absolute viscosity of the fluid, ρ_L is the absolute density of the liquid, μ_Q is the elastic modulus of the QC and ρ_Q is the density of the QC. In the case of this system, f_o=4.9 MHz.

To evaluate this equation, it is necessary to know the fluid viscosity exactly. This means that the viscosity, and hence temperature, should not be allowed to vary with time. A solution to this is to heavily insulate the section holding the ceramic plug. With this insulation, the heat loss will be minimized. With a negligible heat loss, the lower section should heat to a steady state temperature that is the same as the rest of the test section.

Discussion and Conclusions

The design of the test cell to allow for simultaneous PCS and QCM measurements to be taken utilized much of the time provided for in the AFOSR grant. Through continued discussion with the lab, confidence is high that the test cell will function as designed, with only slight modifications. At this time, the test cell is running and the heating characteristics appear to be stable. The current system requires in the order of ten minutes to reach steady state. It also appears that the possibility of unstable temperature across the QC can be accounted for.

The system has been slow to achieve operational status due to unforeseen inaccuracies in QC readings, and those are being dealt with presently.

It is hoped that this system will allow simultaneous determination of particle size and surface deposition. This will verify claims that these techniques can be done separately and still yield data as accurately as if the two components were done at the same time. When operational, this system will allow accurate data to be taken by two different measuring systems with measure both particles suspended in the fuel, along with surface deposition. This knowledge will allow researchers to further understand the fuel degradation process.

The knowledge gained from this project will be used to further understand the interactions causing deposition. With this knowledge, further advances can be made towards achieving Air Force goals of producing JP-8+100 and JP-900.

References

1. Gray, C.N. and Shayeson, M.W., "Aircraft Fuel Heat Sink Utilization," Report No. AFAPL-TR-73-51. General Electric Co., July, 1973.

2. O'Hern, T.J., Trott, W.M., Martin, S.J. and Klavetter, E.A., "Advanced Diagnostics for In Situ Measurement of Particle Formation and Deposition in Thermally Stressed Jet Fuels,", AIAA Paper 93-0363.

3. Kanazawa, K.K., and Gordon II, J.G., "The Oscillation Frequency of a Quartz Resonator in Contact with a Liquid," Analytica Chimica Acta, 175 (1985) 99.

A NOVEL APPROACH TO TWO-COLOR PARTICLE-IMAGING VELOCIMETRY

Jonathan H. Frank
Graduate Student
Department of Mechanical Engineering
Center for Laser Diagnostics

Yale University
P.O. Box 2157 Yale Station
New Haven, CT 06520

Final Report for:
Graduate Student Research Program
Wright Laboratory

Sponsored by:
Air Force Office of Scientific Research
Bolling Air Force Base, Washington, D.C.

September 1993

A NOVEL APPROACH TO TWO-COLOR PARTICLE-IMAGING VELOCIMETRY

Jonathan H. Frank
Graduate Student
Department of Mechanical Engineering
Center for Laser Diagnostics
Yale University

Abstract

A method of two-color particle-imaging velocimetry (PIV) was developed and demonstrated in a gas phase flow. The technique enables instantaneous imaging of two components of the velocity field using two diffferent-wavelength (i.e. color) lasers and a single two-dimensional detector. The problem of directional ambiguity is resolved by shifting the particle images generated by the two lasers. This shift is introduced in the collection optics by a dichroic mirror and is subtracted off from the computed velocity vectors to obtain actual velocities.

A NOVEL APPROACH TO TWO-COLOR PARTICLE-IMAGING VELOCIMETRY

Jonathan H. Frank

Introduction

Particle-imaging velocimetry is a technique for simultaneously measuring instantaneous velocity at multiple points in a flow field. Seed particles, which follow the flow, are illuminated by two pulses of laser light with a known time delay between them. Mie scattering from the particles are then imaged onto a two-dimensional detector. Each particle is imaged twice, once from each laser pulse. The separation of the particle images provides a measurement of the distance the particle travels between laser pulses. A velocity can be calculated since the time between laser pulses is known.

There are a variety of implementations of PIV. The method described here uses two lasers of different colors, green and red, in order to resolve directional ambiguity. Previously, this has been accomplished by recording particle images on color film and subsequently digitizing the color negative with a CCD array. The red and green particle images were first digitized onto two separate frames which were then used to calculate velocities. By separating the red and green images, directional ambiguity is alleviated. However, in the present work the detector need not distinguish between the two different colored particle images. The illuminated particles are imaged directly onto a CCD array. In order to resolve directional ambiguity, two different laser colors and a dichroic mirror in the collection optics are employed. The dichroic mirror separates the red and green particle images by a known distance on the CCD array.

Experimental Setup

Two pulsed lasers were used to illuminate the flow field for two-color PIV (Fig. 1.) Green light ($l = 532$ nm) was produced by a Q-switched Nd:YAG laser with a doubling crystal. A second Nd:YAG laser was used to pump a broadband dye laser (maximum energy output at $l \sim 605$ nm). The red and green beams were combined via a dichroic beamsplitter. After passing through sheet-forming optics, the overlapping beams were directed through the flow field. In the imaged region of the flow the beam height was ~ 8 cm with a waist of ~ 1mm . The delay time between the red and green lasers was adjusted by electronics that vary the phase of the 10 Hz electronic oscillator driving each Nd:YAG laser. A photodiode was used to measure the time between laser pulses.

Mie scattering from the seed particles was collected by a camera lens and imaged onto a 1024 x 1024 pixel Thompson CCD array. A separation of the red and green particle images was created by a dichroic mirror placed between the flow field and the imaging lens. Therefore, for particles having zero velocity, the red and green images are separated by a known distance determined by the magnification of the collection optics and the thickness of the dichroic mirror. The particle image separation that is actually measured in a flow depends on this imposed, "zero velocity," image separation, the flow velocity, and the time delay between laser pulses. In order to resolve the directional ambiguity, it is necessary to know the order in which the particle images are produced. For a given flow field and zero velocity separation, the time delay is adjusted such that every red particle image is to the right of its corresponding green image. Since the red laser pulse occurs after the green

laser pulse, every measured vector must have a component along the positive x-axis. To determine the actual particle velocity, the imposed zero velocity vector is subtracted from the measured vectors. The direction that the red image is shifted with respect to the green image depends on the orientation of the dichroic mirror relative to the detector. The actual direction of the shift is not significant as long as it is measured.

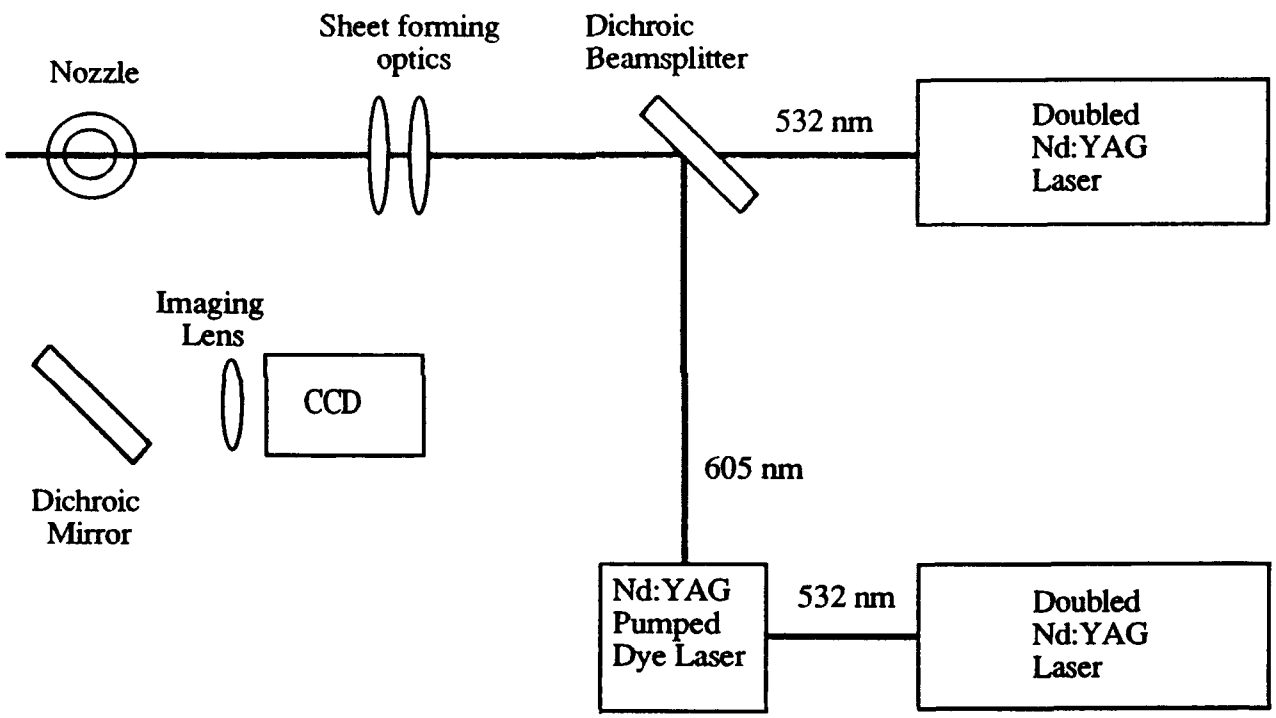

Fig. 1 Experimental setup used for two-color PIV. Mie scattering from seed particles is imaged directly onto a two-dimensional CCD array. The dichroic mirror in the collection optics shifts the red and green particle images so that directional ambiguity can be resolved.

Image Processing

The procedure for deriving a velocity field measurement from the raw data which contains both the red and green particle images is as follows. Within a 128 x 128 subregion of the digitized image, the average separation of the green and red particle images is determined. This process is repeated throughout the 1024 x 1024 image with overlapping subregions to produce a raw vector field. The zero velocity vector field is then subtracted from the raw vector field to obtain the actual particle displacements.

The average separation of red and green particle images in a subregion is automated by an auto-correlation technique performed on a computer. The resulting auto-correlation of the particle images has a central peak and two secondary peaks. The secondary peaks are at a distance from the central peak that is equal to the characteristic spacing of red and green particle image pairs. The auto-correlation is symmetric about the central peak, and therefore the two secondary peaks are 180 degrees apart. The direction of the imposed zero velocity shift determines which peak is chosen, thus resolving the directional ambiguity. This procedure is applicable as long as the red-green particle image separation is less than half the dimension of the subregion (i.e. 64 pixels).

In order to measure smaller scale flows, the magnification of the imaging lens is increased and, as a result the imposed zero velocity shift is increased to greater than 64 pixels. One solution is to use a thinner dichroic mirror to reduced this shift. Otherwise, the auto-correlation technique requires that a subregion larger than 128 x 128 pixels be used which reduces the resolution of the velocity measurement. However, at the time of this project an alternate dichroic mirror was not available. In order to increase

the resolution for smaller scale flows, an alternative method of processing is used. A cross-correlation technique is employed by making two copies of the image in computer memory. The first copy is the original image and the second is a shifted version of the original. The shift is chosen such that the computed red-green particle image separation is less than 64 pixels thus allowing a 128 x 128 subregion to be used for calculating each vector.

Results

The PIV technique described above has been demonstrated with a stagnation point flow. An air jet, seeded with ~5mm diameter alumina micro-balloons, issues form a circular 8 cm diameter nozzle into ambient air. The average exit velocity is ~ 1 m/s. One nozzle diameter down stream of the exit the jet impinges on a flat plate producing a stagnation flow.

The raw vectors obtained directly from the images are shown in Fig. 2. The time delay between laser pulses is 1.5 ms. To obtain the imposed zero velocity shift throughout the imaged region, a piece of sandpaper is illuminated by scattering both the red and green laser light off a diffuse reflector. Processing the sandpaper images yields a zero velocity vector field (Fig. 3) which is then subtracted from the raw vectors to give the actual flow velocities in Fig. 4. The flow is from top to bottom and the splitting of the flow direction near the plate can be seen.

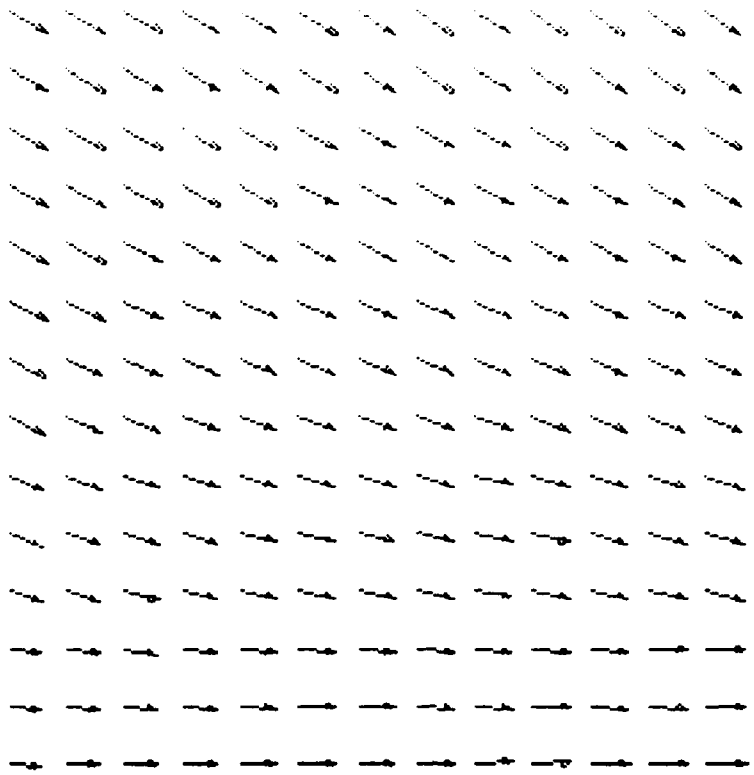

Fig. 2 Vector field of stagnation point flow before zero velocity field is subtracted. Directional ambiguity is resolved because the imposed shift gives all vectors a positive x-axis component.

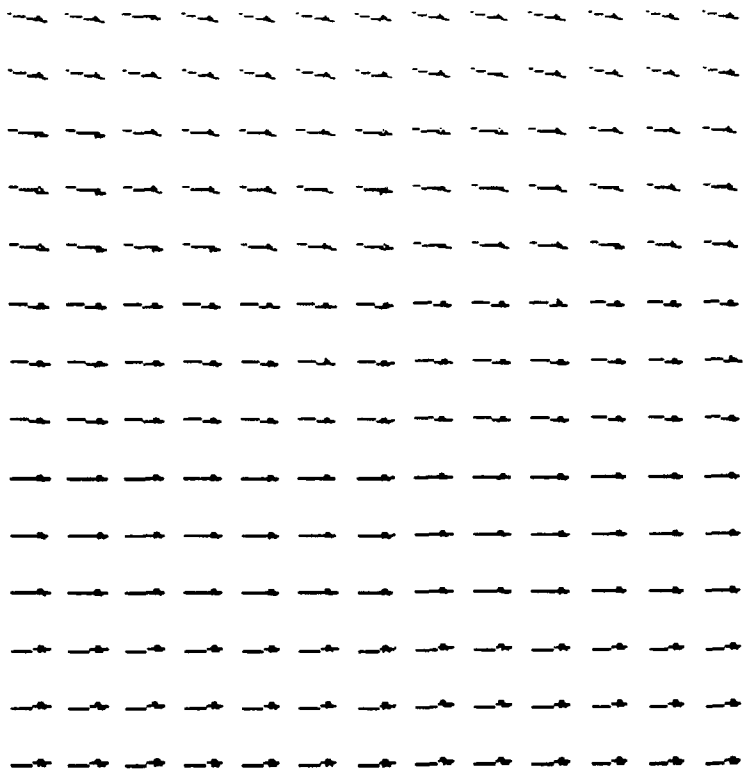

Fig. 3 Zero velocity field obtained by imaging sandpaper.

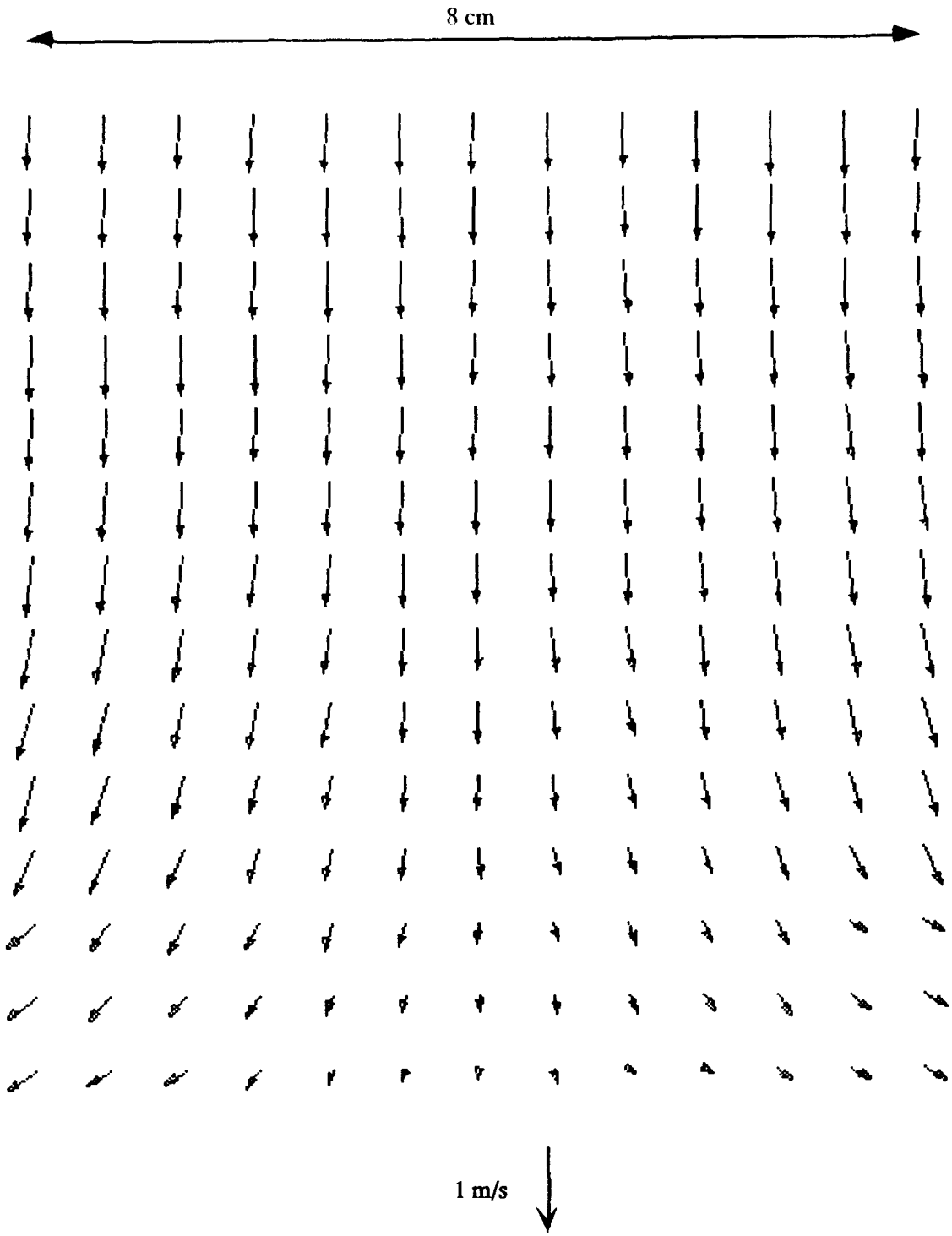

Fig. 4 Velocity field of stagnation point flow measured by two-color PIV technique. These vectors are the result of subtracting fig. 3 vectors from fig. 2 vectors.

Precision of the velocity measurements was determined by the following technique. A piece of illuminated sandpaper was attached to a translation stage with a digital position readout. A uniform flow was simulated by first illuminating the sandpaper with green light and acquiring a green image. Then, the sandpaper was translated a known distance and a red image was acquired. After superimposing the red and green images, the displacement is measured using the PIV processing described above. The measurement is compared with the actual displacement of the translation stage. Ideally, all of the displacement vectors throughout the image should be exactly the same. However, there exists a finite distribution of measured displacements. The width of this distribution provides an indication of the precision with which a single vector can be measured. The distribution width is found to be less than one pixel.

Although the precision of the measurement is less than the size of a pixel, the accuracy of an actual velocity measurement depends on a variety of factors including seeding density, particle size distribution, background signal, and the ability of particles to follow the flow. Furthermore, it must be kept in mind that each measured velocity vector is an average of particle velocities within a finite subregion of the flow. Significant velocity gradients within a subregion adds noise to the velocity measurement.

Conclusion

A new implementation of two-color PIV has been demonstrated. The resolution of directional ambiguity has been achieved by separating red and green images with a dichroic mirror in the collection optics. As a test case, the velocity field in a stagnation point flow was successfully measured. In this

method of PIV. Mie scattering from seed particles can be imaged directly onto a two-dimensional CCD array. Film is not required. However, use of a CCD is limited by the number of pixels on the detector. The ongoing development of larger format CCD arrays will expand the usefulness of this particular PIV technique. Extending the capabilities of PIV will permit further study of more complex flows. Of particular interest is the ability to compare instantaneous and time averaged velocity fields to understand the importance of transient flow phenomena. These types of investigations may provide useful insight in such research areas as combustor design.

Chandra Nagaraja's report not available at time of publication.

A STUDY OF MOS CONTROLLED THYRISTOR (MCT) DRIVER

Sonny T. Nguyen
Graduate Student
Department of Electrical Engineering

Wright State University
3640 Colonel Glenn Hwy
Dayton, Ohio 45435

Final Report for:
Summer Research Program
Wright Laboratory

Sponsored by:
Research and Development Laboratory
5800 Uplander Way
Culver City, CA 90230-6608

Abstract

The MOS Controlled Thyristor (MCT) driver II Integrated circuit, originally designed to gate P-MCT's is also able to gate other MOS devices, both N and P types. It is a single monolithic multi-function circuit designed to drive large capacitive loads at high slew rates. The device is optimized for driving several parallel connected MOS gates, with a total capacitance of $60nF$. At this load level the Gate Driver II achieves rise time of $< 200nS$ and fall time of $< 300nS$. The output provides $+/-$ voltage on the power device gate up to a total voltage swing of 35V.

This experiment is to design an external circuit for MOS Controlled Thyristor (MCT) driver II. The $24VDC$ power supply will be use as a input voltage. The test result will be the output squarewave of the $+12V$ for turn-ON and the $-12V$ for turn-OFF.

Introduction

The MOS Controlled Thyristor (MCT) is very promising switch device which combines the high power capability of thyristors and the low energy gate control of a MOS device. The MOS Controlled Thyristor (MCT) has high voltage and high current capabilities and its power dissipation depends on the losses due to turn-on. turn-off and conduction.

The search for the perfect driver to turn the power switch MOS Controlled Thyristor (MCT) ON and OFF. The new MOS Controlled Thyristor (MCT) driver II has introduce. The MOS Controlled Thyristor (MCT) driver II has been developed which is not yet available commercially. This Integrated Circuit (IC) has been designed to provide the power circuit designer with many usefull functions. The figure (1) shows a simplified diagram of this integrated circuit. The circuit contains three major blocks. power circuit, main MCT ON/OFF channel and auxiliary comparators.

The IC can be powered from a negative supply (7V - 12V), internally clamped at 12V, or from center tapped supply (P- to PA to P+) or from a single ended supply (P- to P+). When using a negative supply an internal charge pump energizes the P+ terminal. A $-4.7V$ reference voltage can sink up to $30mA$ and can be used to directly energize opto receivers or other control circuits. Standby current is less than $5mA$ for the IC.

All control signals enter the IC through comparators which require only a few mV of input signal. The common mode range includes the PA terminal and $-4.7V$ REF terminal allowing several volts of noise rejection. The main ON channel controls the gate output which is capable of driving 4 MCT gates connected in parallel. The ON channel includes Minimum-ON-Time and Minimum-OFF-Time functions which are user programmable by adding external capacitance. These functions can be used to provide adequate snubber reset time for example.

The IC contains both undervoltage inhibit and a latch which when set will force the ON channel to the MCT OFF state. The latch is set by the L comparator and is reset by the R comparator. When the latch is set the LO output will sink current (20mA max) for driving LED. With these inputs the user can implement over current or over temperature lockout functions for example.

The IC also contains two uncommitted comparator channels. The "A" channel has a

totem pole output, "AO", capable of driving $20mA$. The "B" channel has two comparator inputs which are OR'ed together and drive the "BO" output which will source current (20mA max) for driving an LED. These uncommitted channels can be used for detection, timing, and logic functions for example.

External circuit design for an MCT driver II

The circuit was powered by a 1 KHz squarewave frequency to provide isolated gate drive power. The 5 volt reference can directly power associated signal conditioning circuit. Using opto-receiver as a comparator input to accommodate a variety of signal source. The circuit require a few external components to implement a wide variety of MOS gating circuit.

Figure (2) is a schematic to show how this integrated circuit can be used in its simplest configuration to drive an P-MCT. The REF terminal is used to power an opto-receiver and provide reference voltage for the comparator input. In the arrangement shown resistor R_1 and R_2 establish the division of bus voltage between positive and negative voltage applied to the MCT gate. Capacitors C_2 and C_3 provide bus filtering and the peak current required to switch the MCT gate capacitance. Resistor R_3 provide current to energize the internal logic and external circuit which are powered by voltage across the internal 12 volt zener diode. Resistor R_4 provides damping the gate voltage waveform.

Figure (2) also shows the test circuit for measuring the output voltage of MCT driver II without resistive load condition. It consits of a dc power supply, opto-receiver, resistors, capacitors. The circuit had the following parameters:

1. Opto-receiver (T-1521 / R-2521)
2. Frequency (f=1 KHz); 5V Amplitute; 2.5V offset
3. $R_a = 50\ \Omega$
4. $R_b = 1K\ \Omega$
5. $C_b = .1\ \mu$F
6. MCT driver II
7. $R_1 = 1K\ \Omega$
8. $R_2 = 1K\ \Omega$
9. $R_3 = 820\ \Omega$
10. $R_4 = 4\ \Omega$

11. $R_5 = 1K\ \Omega$

12. $C_1 = 100\ \mu F$

13. $C_2 = 100\ \mu F$

14. $V_s = 24VDC$

Experimental Result

The waveforms were observed in the circuit designed in figure (2). The waveform (1) is shown the output squarewave of the $+12V$ for turn-ON and the $-12V$ for turn-OFF. The waveform (2) is shown the rise time and the waveform (3) is shown the fall time.

The experimental result of testing the MCT driver II was successfully demonstrated. The external circuit of an MCT driver was designed and test to meet the specification with the input voltage $24VDC$ and the result were positive and negative $12V$ squarewave for turn-ON and turn-OFF respectively. The rise time was $16nS$ and the fall time was $27nS$.

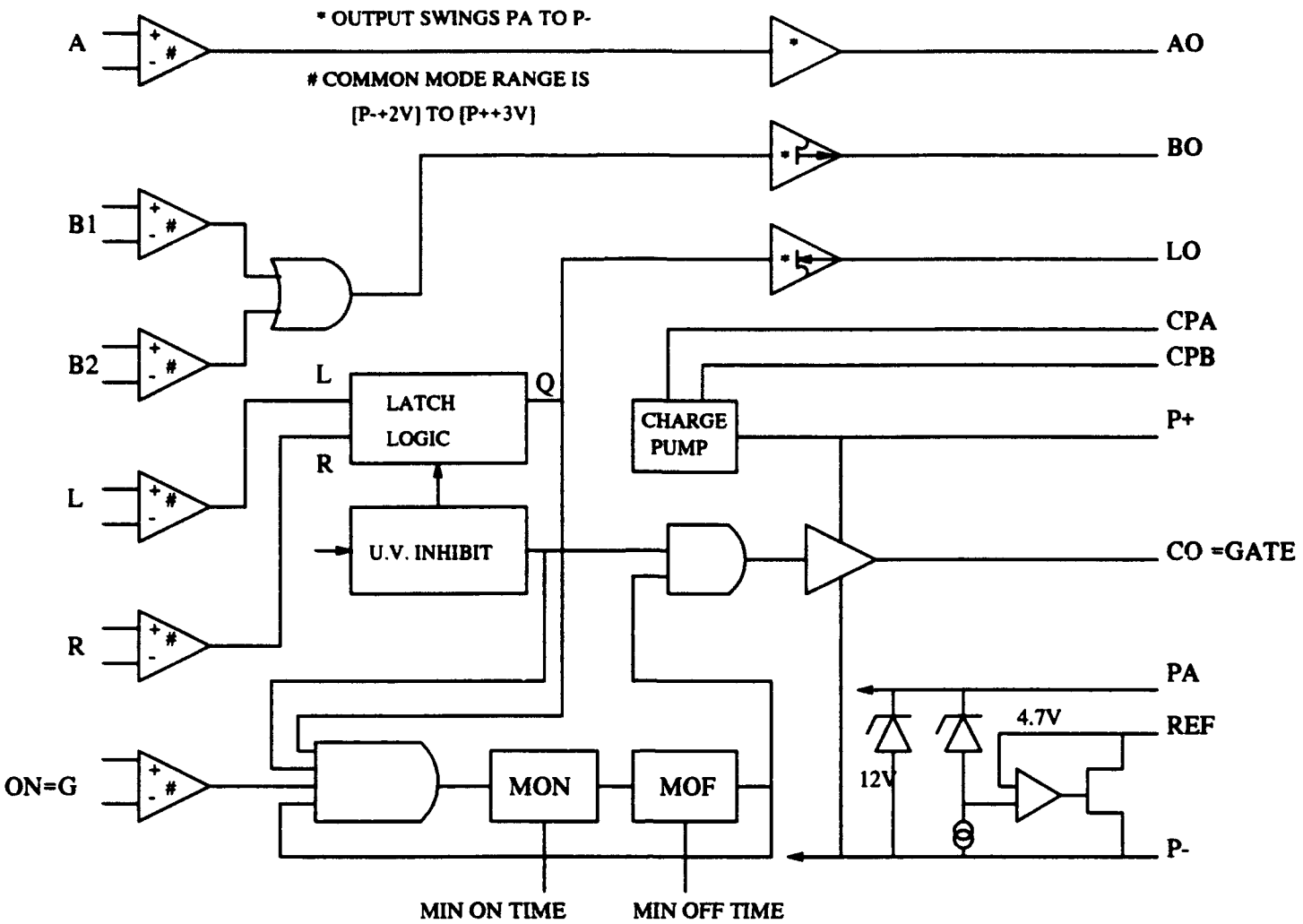

FUNCTIONAL BLOCK DIAGRAM MCT DRIVER II

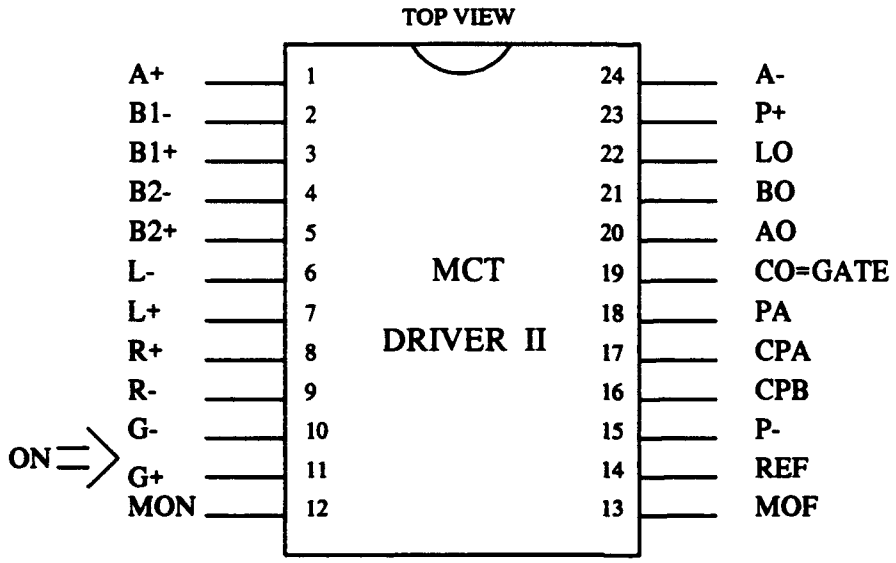

PINOUTS

Figure 1

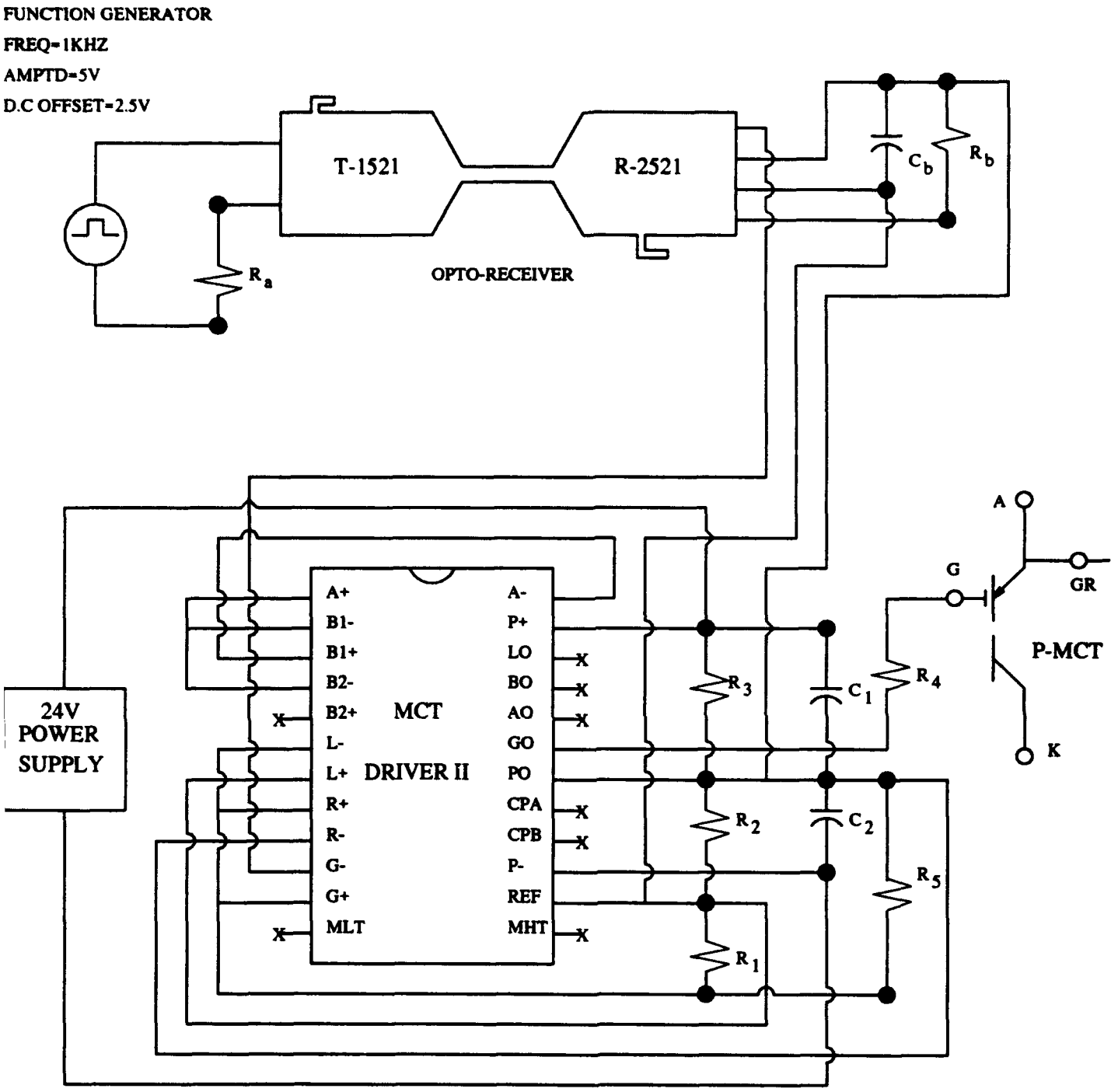

SCHEMATIC OF AN EXTERNAL CIRCUIT DESIGNED FOR AN MCT DRIVER II

Figure 2

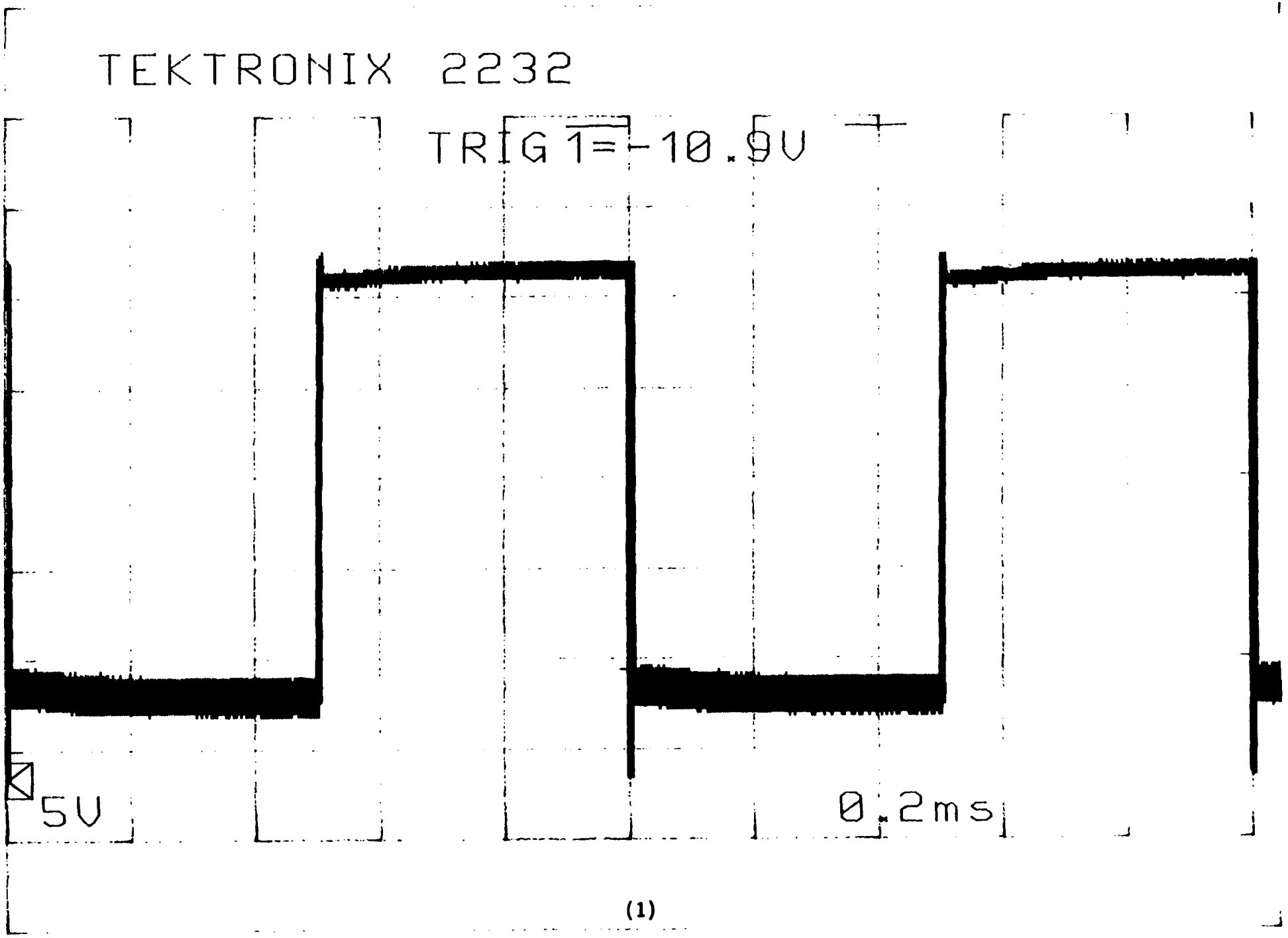

(1)

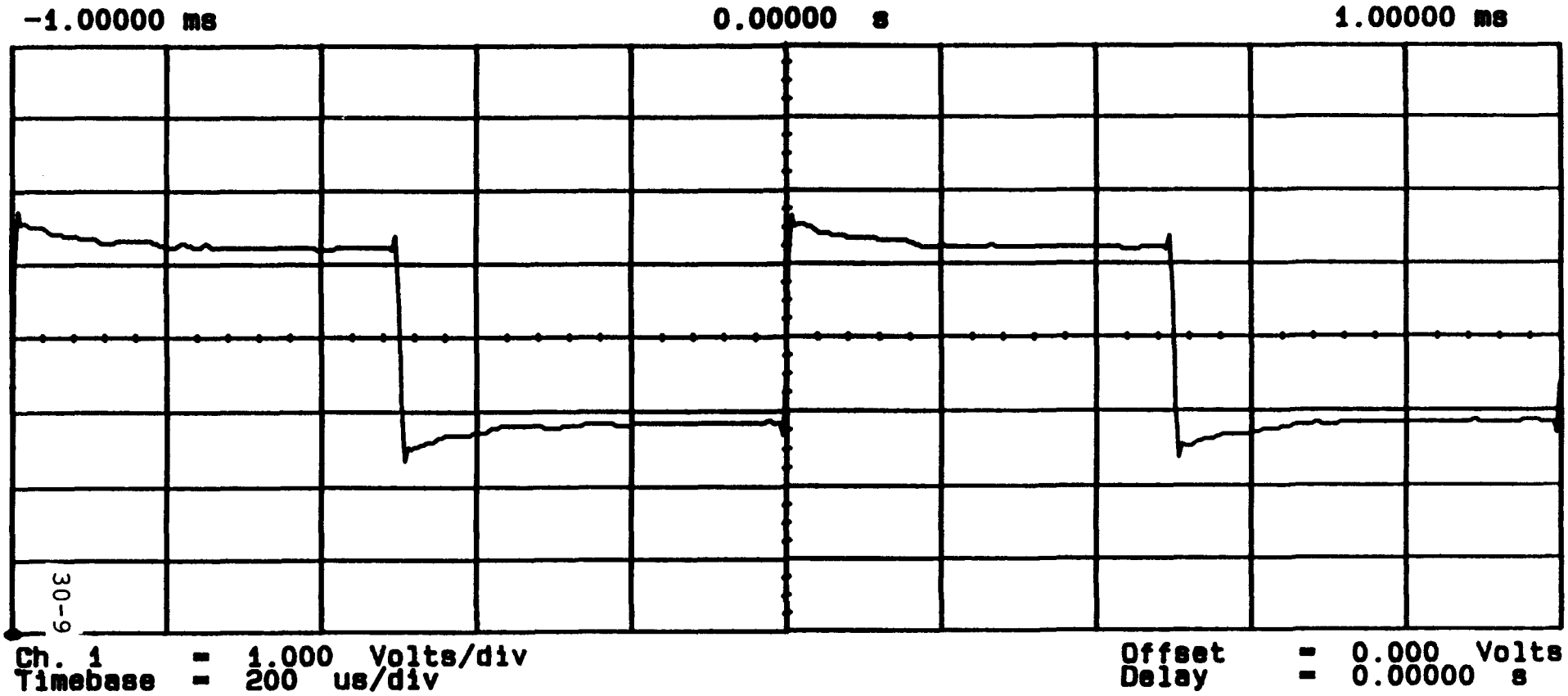
-1.00000 ms
0.00000 s
1.00000 ms
30-9
Ch. 1 = 1.000 Volts/div
Timebase = 200 us/div
Offset = 0.000 Volts
Delay = 0.00000 s

(1)

-1.98106 ms -981.056 us 18.9440 us

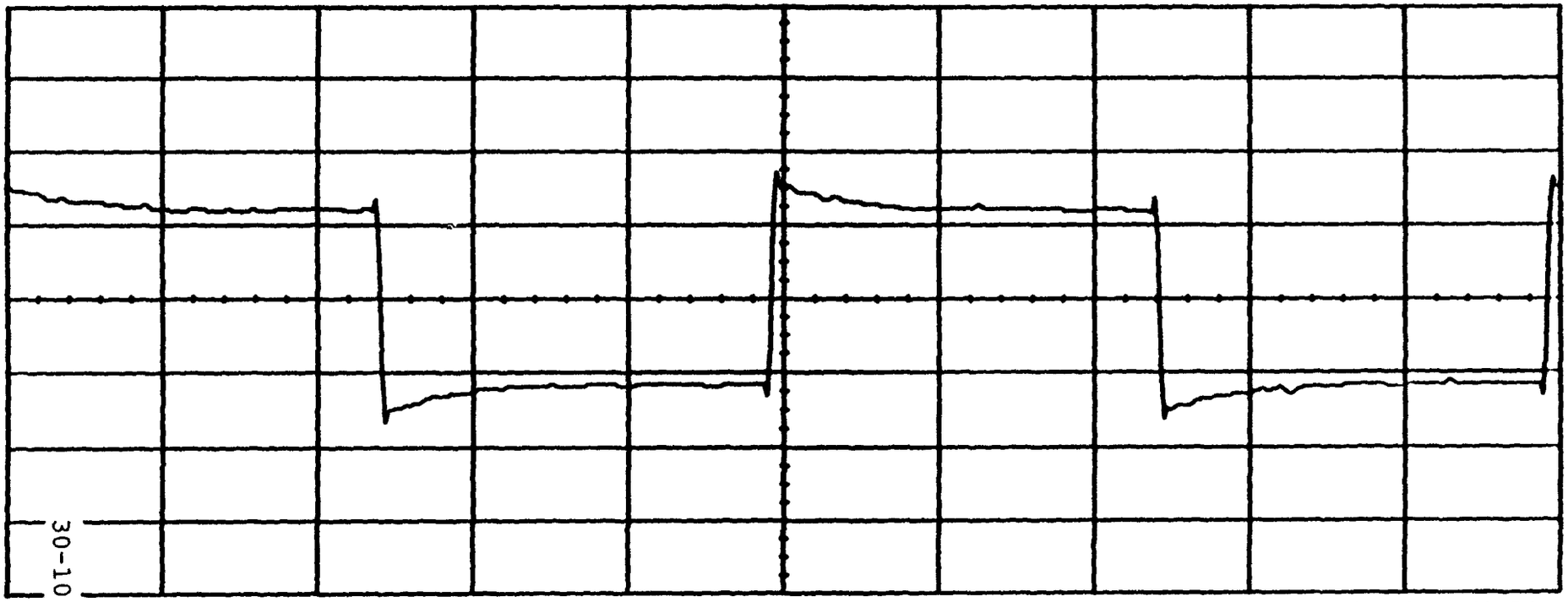

Ch. 1 = 1.000 Volts/div
Timebase = 200 us/div

Offset = 0.000 Volts
Delay = 18.9440 us

-981.056 us 18.9440 us 1.01894 ms

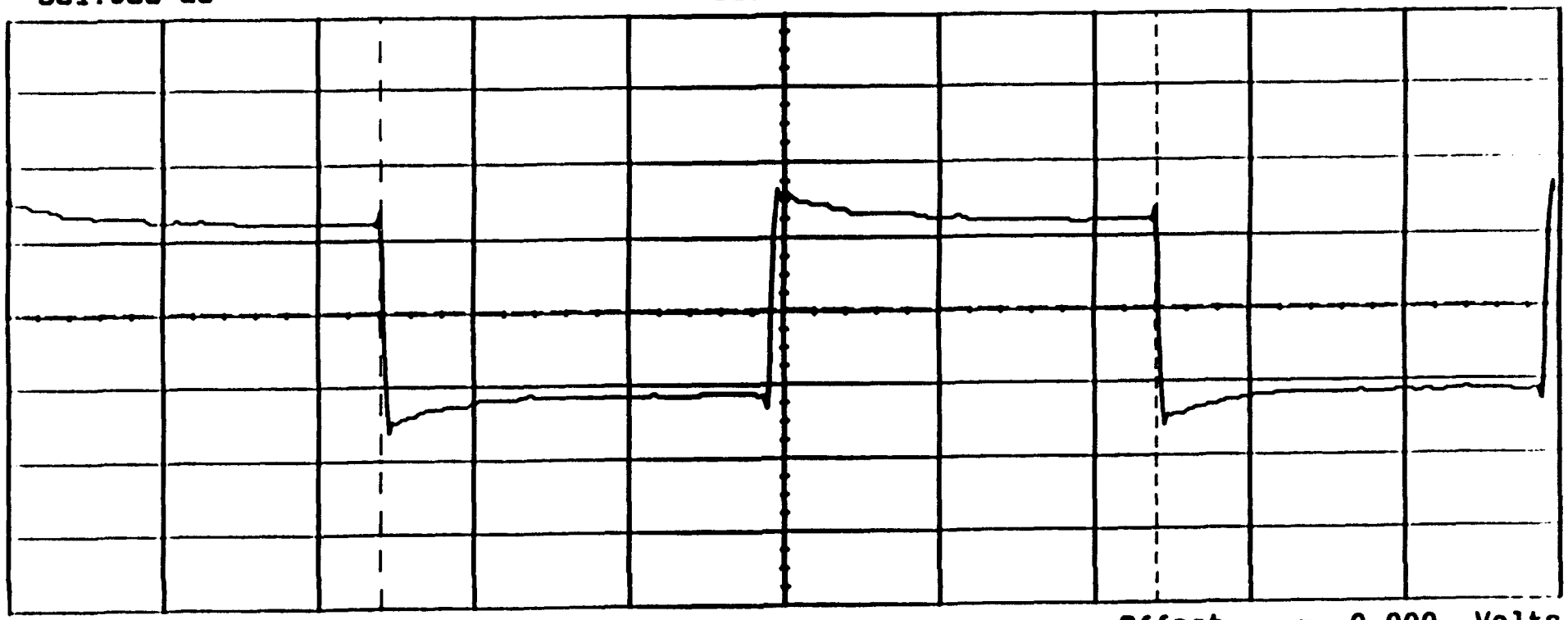

Ch. 1 = 1.000 Volts/div
Timebase = 200 us/div
Channel 1 Parameters
Rise Time = 5.38491 us
Fall Time = 5.45010 us
P-P Volts = 3.380 Volts
Dutycycle = 50.00 %
Start = -499.824 us
Vmarker1 = 40.00 mVolts

Freq. = 1.00111 kHz
+Width = 499.690 us
Preshoot = 500.0 mVolts
Avg Volts = 43.70 mVolts

Stop = 499.068 us
Vmarker2 = 40.00 mVolts

Offset = 0.000 Volts
Delay = 18.9440 us
Period = 999.183 us
-Width = 499.493 us
Overshoot = 500.0 mVolts
RMS Volts = 1.245 Volts

Delta T = 998.892 us
Delta V = 0.000 Volts

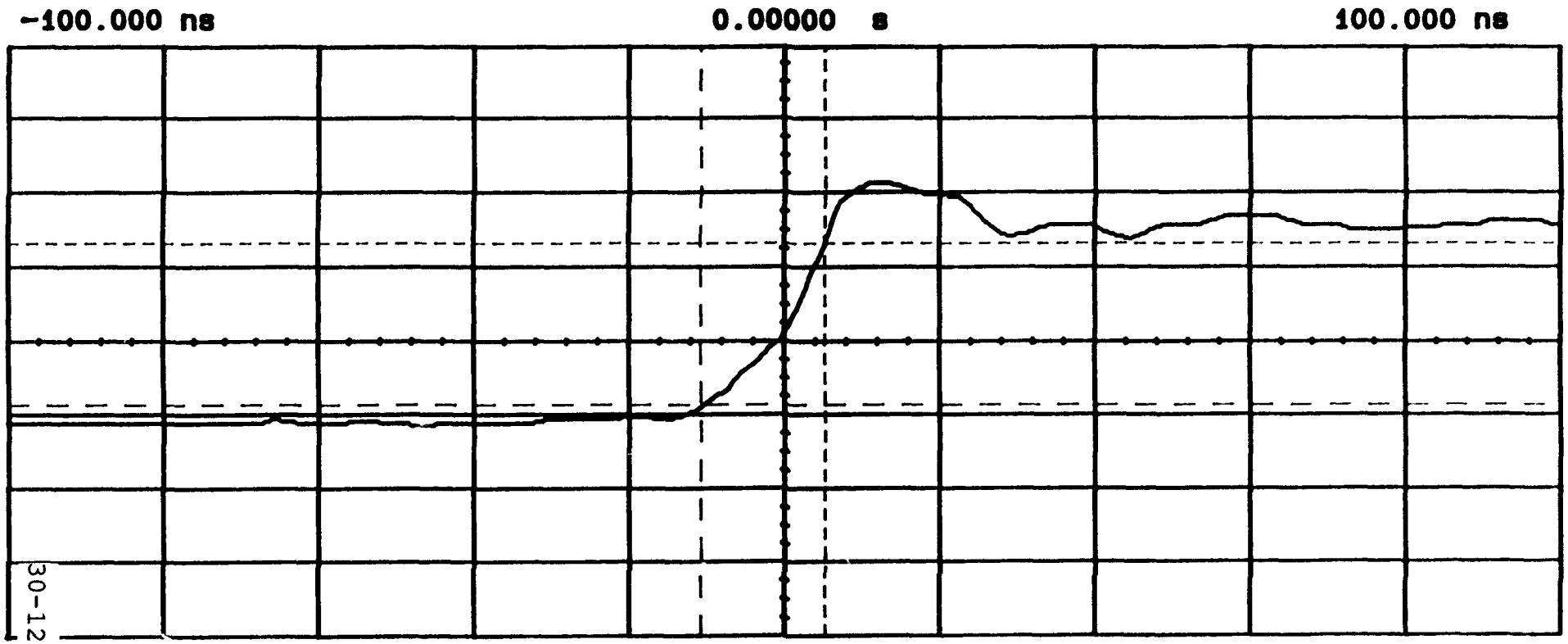

Ch. 1 = 1.000 Volts/div
Timebase = 20.0 ns/div
Start = -10.800 ns
Vmarker1 = -860.0 mVolts
Stop = 5.150 ns
Vmarker2 = 1.300 Volts
Offset = 0.000 Volts
Delay = 0.00000 s
Delta T = 15.950 ns
Delta V = 2.160 Volts

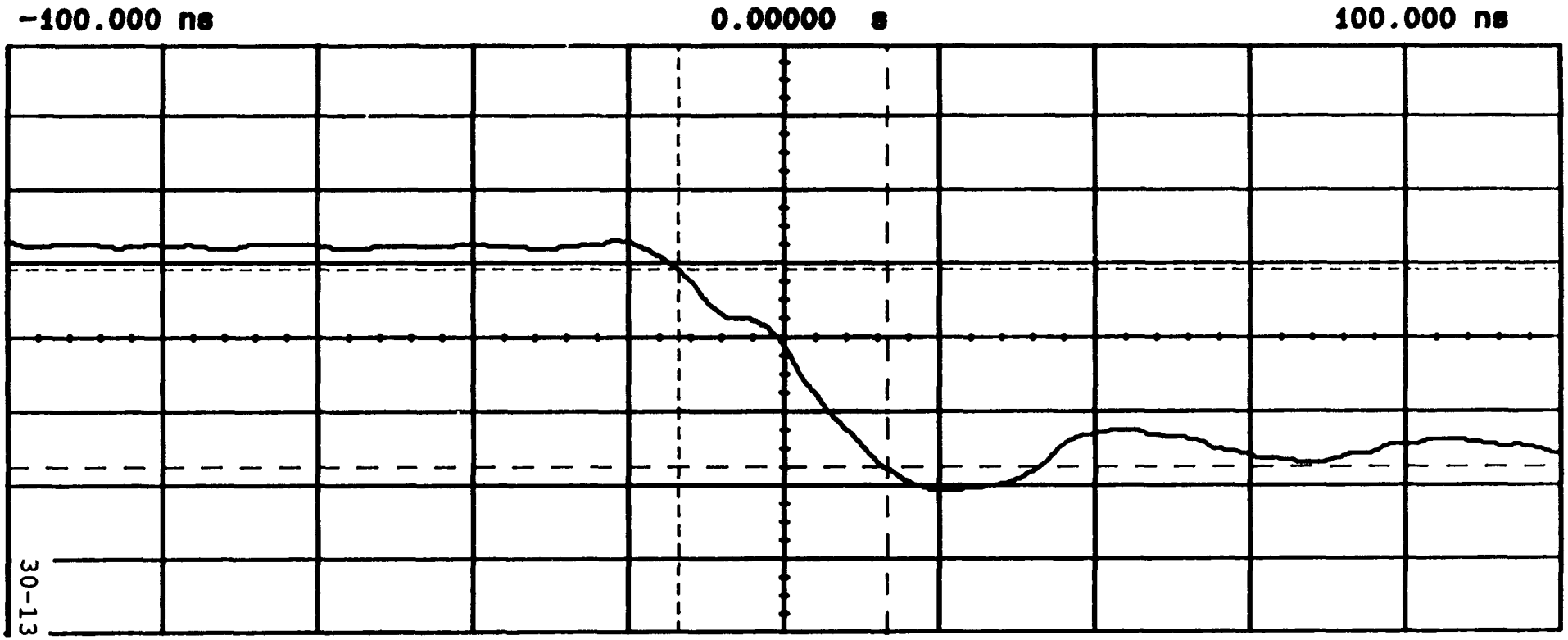

Ch. 1 = 1.000 Volts/div
Timebase = 20.0 ns/div
Start = 13.200 ns
Vmarker1 = -1.740 Volts
Stop = -13.800 ns
Vmarker2 = 900.0 mVolts
Offset = 0.000 Volts
Delay = 0.00000 s
Delta T = -27.000 ns
Delta V = 2.640 Volts

HEAT TRANSFER ASPECTS OF SUPERCRITICAL FUELS

Ronald W. Schwing

Department of Mechanical Engineering
University of Iowa
Iowa City, IA

Final Report for:
Summer Research Program
Wright Laboratory

Sponsored by:
Air Force Office of Scientific Research
Wright Pattterson AFB, OH

August 1993

HEAT TRANSFER ASPECTS OF SUPERCRITICAL FUELS

Ronald W. Schwing
Department of Mechanical Engineering
University of Iowa

Abstract

Approximately twenty years ago military aircraft began using fuel as a coolant. Today, fuel is the primary coolant for many aircraft subsystems such as engine, hydraulics, and environmental control. Fuels for then next generation of high speed aircraft will need to absorb a significantly increased heat load. Increasing heat loads will eventually push the fuel into the supercritical range. The supercritical heat transfer mechanism is not fully understood. The Air Force has a long term goal of obtaining a feasible fuel which can be heated into the supercritical range. This study looks into that possibility.

Table of Contents

I. Introduction 4

II. Methodology and Experimental Set-Up 7

III. Results and Discussion 12

IV. Conclusions and Recommendations 16

V. References 17

Introduction

Modern military aircraft use fuel not only as an energy source but also as the main coolant for several aircraft subsystems (such as engine, hydraulics, and environmental control units). As the technology of these subsystems improves so does the amount of heat which these subsystems produce. The Integrated High Performance Turbine Engine Technology (IHPTET) program has a goal to double the thrust-to-weight ratio of aircraft turbine engines [1]. This will more than triple the heat load of this future aircraft over an F-4 or F-15 (see figure below).

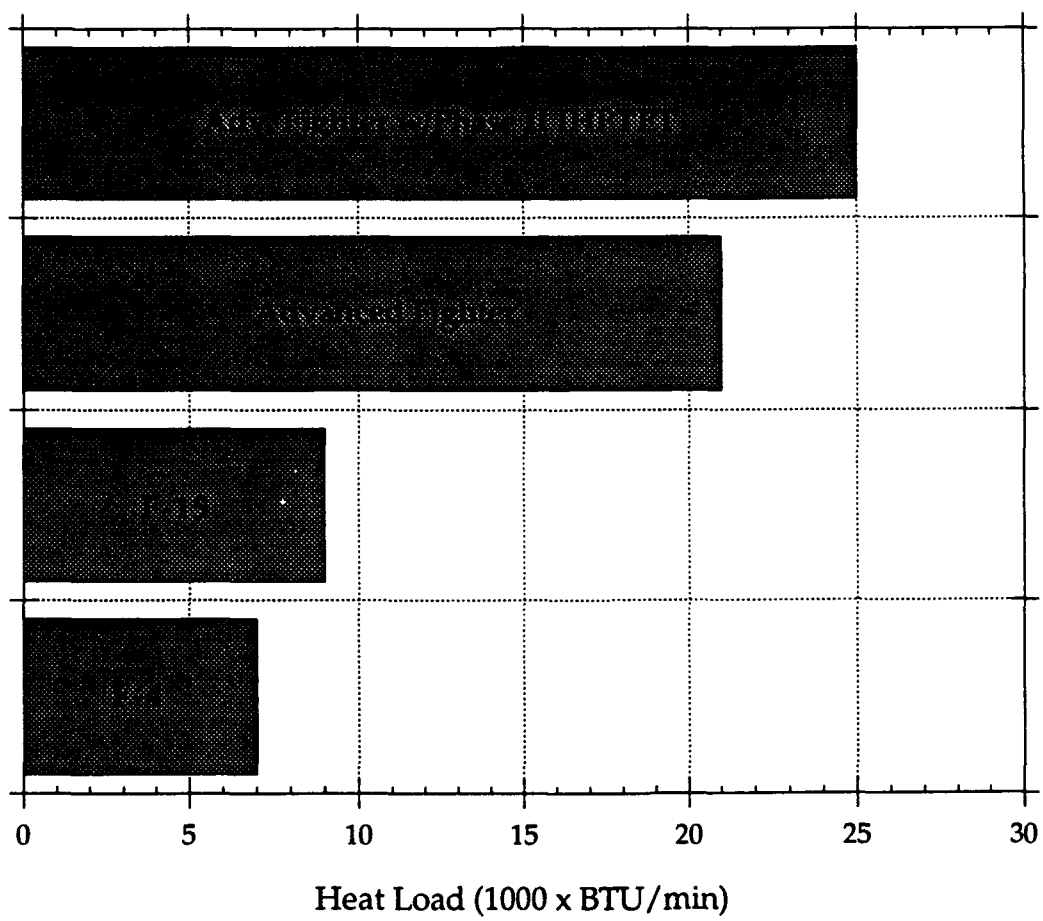

Figure 1.0: Heat loads produced by various aircraft.

Current aircraft fuels such as JP-4 and JP-8 are thermally stable below a temperature of 325 F [2]. Detrimental problems develop if the fuel is stressed beyond this point. The fuel begins to decompose chemically leaving large deposits that cause control valves to stick and heat exchangers and nozzles to foul. For some current aircraft this 325 F limit is not enough of a heat sink and some of the fuel is recirculated through a heat exchanger and back to the main tank. Recirculation can be inefficient because of the additional weight of the recirculation system and it forces the aircraft to carry more fuel than is required [1]. Fuel that is only passed through the system once would be considerably more efficient. This would require the fuel to be thermally stable at significantly higher temperatures.

The Air Force has started a program to develop high temperature thermally stable (HiTTS) fuels. The HiTTS program has two goals. A short term goal to develop JP-8+100, a JP-8 based fuel that will be able to be heated an additional 100 F and still be thermally stable. A long term goal to develop JP-900, a hydrocarbon fuel that will be thermally stable up to 900 F. JP-900 would increase the heat sink by 500% [2]. This is the future of hydrocarbon fuels. Figure 2.0 shows the cooling loads of several hydrocarbon fuels.

At 900 F all hydrocarbons are well above the critical point and into the supercritical region. The critical point is where gas and liquid both exist in equilibrium. Any rise in temperature will push the substance into the supercritical region. The problem in studying heat transfer has been regarded as one in which the variation of physical properties with temperature becomes extremely important. Both specific heat and thermal conductivity go towards infinity at the critical point [3]. Because of these property variations the supercritical heat transfer mechanism is not fully understood.

Another important concern of using a supercritical fuel is that there have been a few studies that have seen severe pressure oscillations with peak-to-peak magnitudes of up to 380 psi during experiments with supercritical fuel, enough to rupture .350 in. tubing. This oscillation phenomenon must also be understood in order to avoid its' occurrence during actual flight operation. This study had two major goals, one to determine the conditions under which these

supercritical oscillations occur and secondly try to determine the effectiveness of using a supercritical fluid as a heat sink.

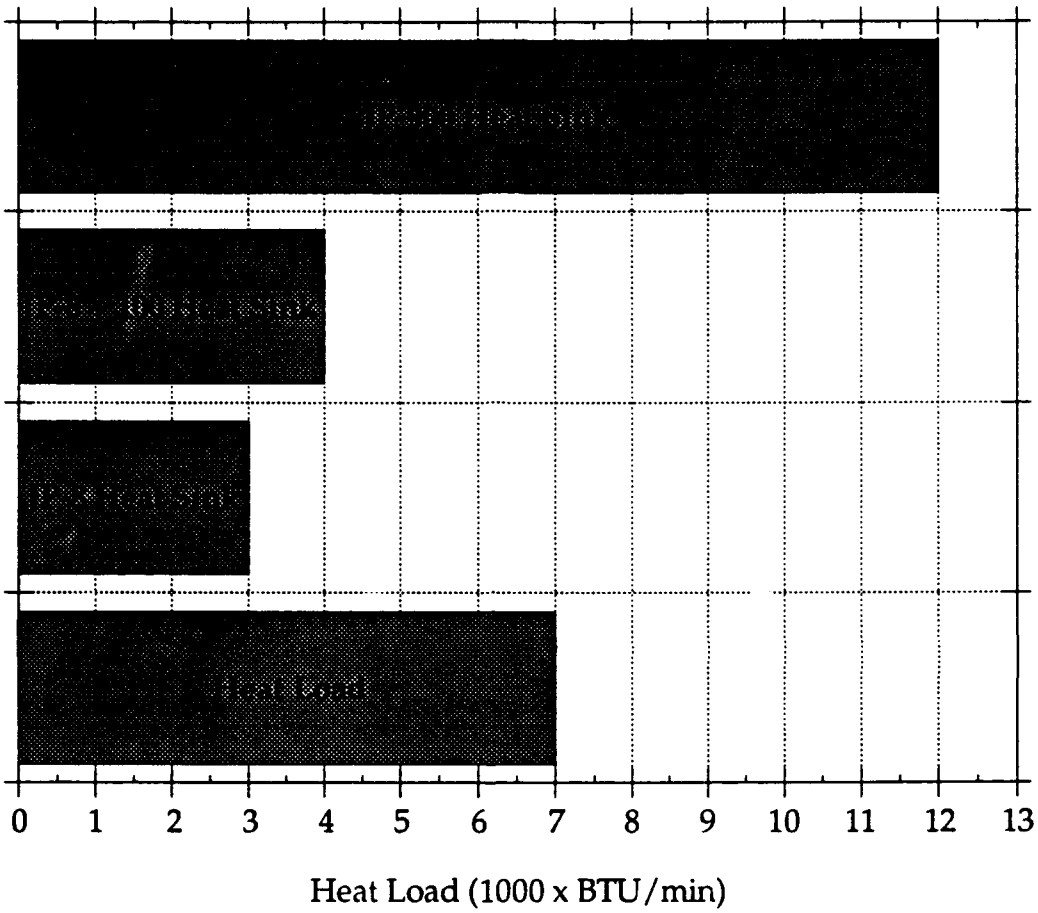

Figure 2.0: Cooling loads available for the idle descent for a IHPTET Phase II aircraft.

Methodology and Experimental Set-Up

The first part of this study deals with understanding the supercritical pressure oscillation phenomenon seen when heating hydrocarbon fuels and determining the conditions under which they exist. W. S. Hines and H. Wolf ran some supercritical experiments using hydrocarbon fuels RP-1 and diethylcyclohexane (DECH). The test section was heated through means of electrical resistance with heat fluxes ranging from 2 to 9 BTU/in^2-sec. Reynolds numbers ranged from 90,000 to 900,000 along the length of the test section. At a reduced pressure of approximately two with the wetted-wall temperature reaching the critical temperature a vibration was observed which produced audible noise, increased heat transfer, and resulted in tube splits and pinhole leaks. The vibrations observed had a frequency ranging between 1200 and 7500 Hz with amplitudes ranging from 60 and 380 psi [4].

The Shell Development Company also observed some pressure oscillations during some experiments with supercritical Jet A fuel. The test section was also heated through means of electrical resistance with heat fluxes between 1 and 4 BTU/in^2-sec. Reynolds numbers reached over 40,000 towards the end of the test section with a reduced pressure maintained throughout the test section of about two. Again, audible noise was detected which had pressure oscillations with frequencies ranging between 1500 and 3000 Hz with amplitudes ranging from 100 to 350 psi [5]. No damage to the tubes was observed.

Using the experimental set-up shown in figure 3.0, an attempt to reproduce the supercritical pressure oscillation was made. Jet A (2926) fuel is fed by gravity from an air sparred tank to a high pressure liquid chromatography pump (HPLC). From the pump the fuel passes through a 0.45μm filter to remove any small particles present in the fuel. After passing through the filter the fuel then enters the Lindberg high temperature furnace. A PCB piezoelectric pressure transducer is mounted three inches from the inlet of the Furnace. Ideally, it would be better to have the pressure transducer at the outlet. The outlet temperature however far exceeds the maximum temperature rating for the transducer. If the oscillations are so pronounced that

they become audible they should transmit throughout the length of the test section. Nineteen thermocouples are spot welded along the outside of the test section. The test section is 48 in. long, .125 in. OD, 0.055 in. ID 316 stainless steel tubing.

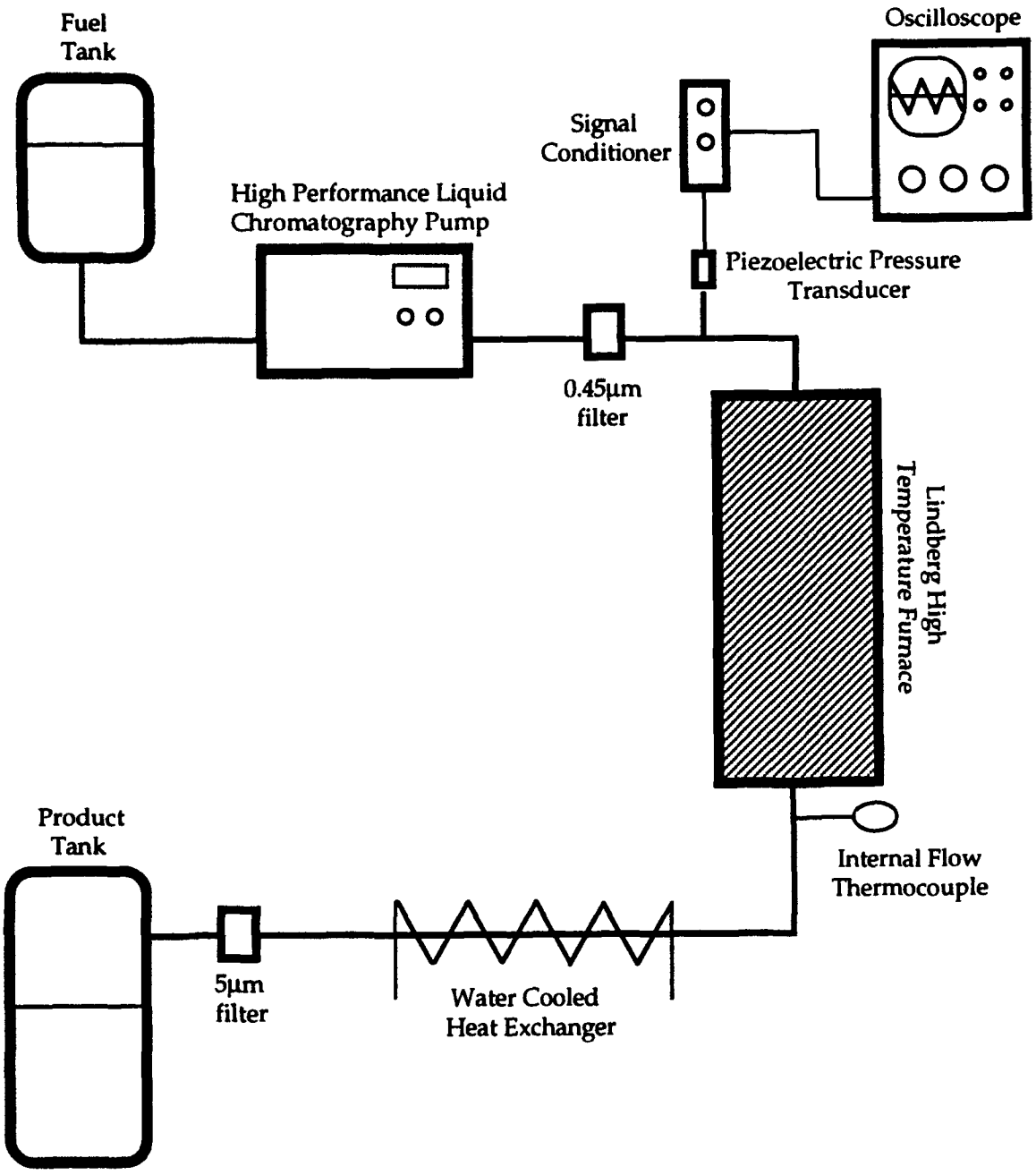

Figure 3.0: Test Rig Set-Up for Measuring Supercritical Pressure Oscillations

After exiting the furnace, an internal bulk flow fuel temperature is taken. The fuel is then passed through a concentric tube parallel-flow water heat exchanger. This is done to bring the temperature of the fuel below the flash temperature prior to entering the storage tank. Again, the fuel is passed through another 5μm filter before finally resting in the storage tank.

It was desired to have near the same operating conditions as those of the Hines & Wolf and the Shell Development Company's experiments. This was not possible with our experimental set-up. The furnace even operating at its maximum operating temperature (1200 C) only resulted in a maximum heat flux of around .35 BTU/in^2-sec. The HPLC pump was also pushed to it's maximum (100 ml/min) which only resulted in Reynolds numbers ranging from 3,000 to 26,000. Two 10 hour tests were run with a constant pressure of 700 psi while operating the furnace and the pump at maximum capacity.

The second part of this study dealt with trying to determine the rate of heat transfer of a supercritical fluid and to visualize the thermal boundary layer of a supercritical fluid along a heated surface. This was accomplished using a holographic interferometer. The experimental set-up can be seen in figure 4.0. The optical test cell consists of a large stainless-steel rectangular block with four window slots. One of the slots contains an aluminum block with heating elements embedded within the block. The slot opposite to that is a stainless steel block and the other two slots contain sapphire windows. Flow enters from the bottom and exits out the top. Initially the cell was designed to operate with hydrocarbon fuels, but the high temperatures and pressures developed sealing problems and cracking of the expensive sapphire windows.

Experimentation with the cell is now done using sulfur-hexafluoride (SF_6), a non-toxic, non-reactive, stable compound. SF_6 has a critical temperature of only 45.4 C and a critical pressure of 545 psi. At these conditions there are no sealing problems associated with the cell. SF_6 is pressurized and pushed through the system with helium. The flowrate is controlled with a fine metering valve and flowrate is measured with a flowmeter down stream. The interferometry is done using a helium-neon laser. The laser is split with a variable beam splitter. Approximately 33% of the beam passes through the optical cell and onto the holographic plate.

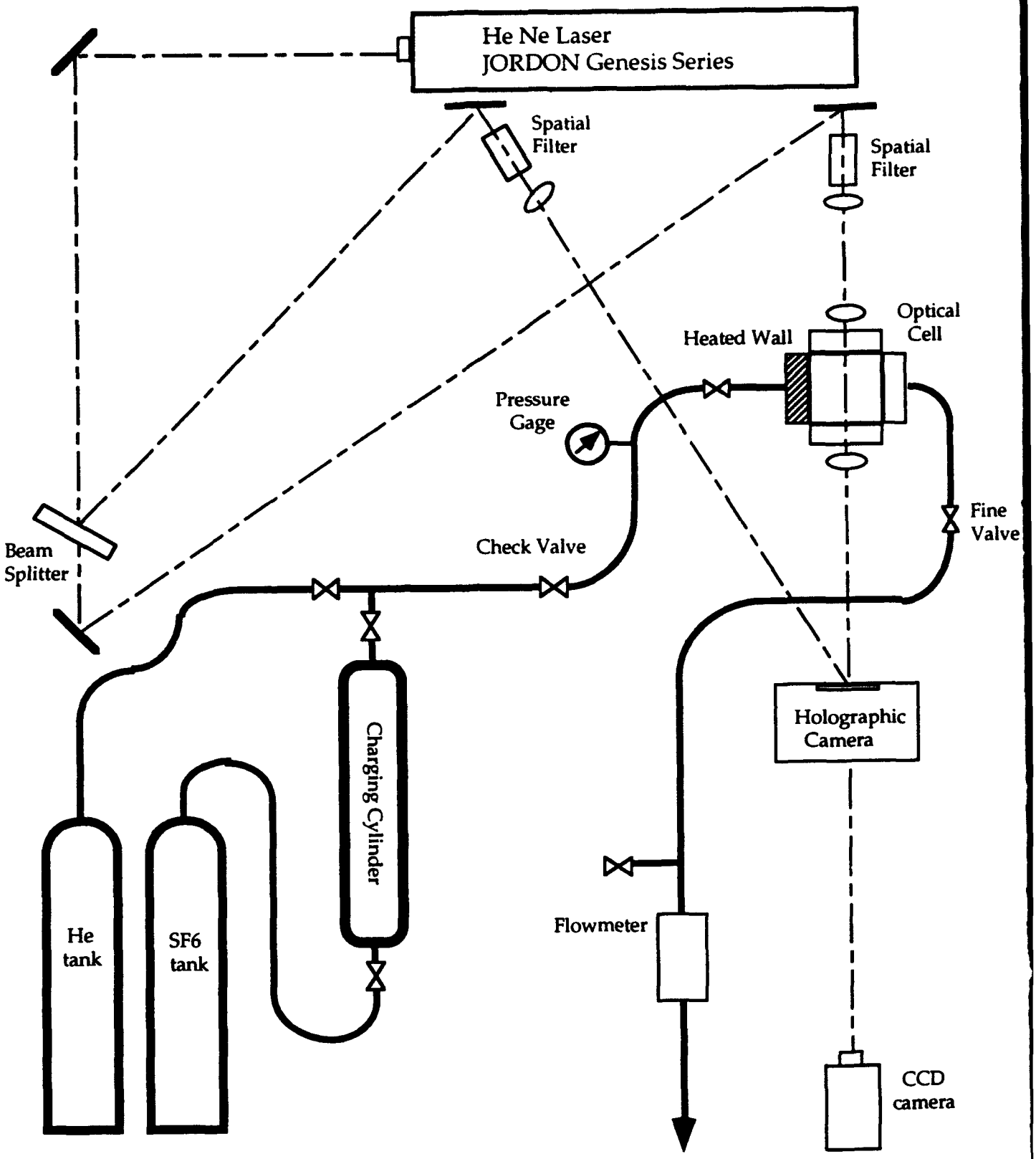

Figure 4.0: SF_6 Holographic Interferometer Set-Up

This is the object beam. The other portion of the beam (the reference beam) goes directly to the holographic plate forming a 31 degree angle with the object beam. Both beams traverse the same distance from the beam splitter to the holographic plate.

Newport has developed the HC-300 Thermoplastic Recorder. The hologram is produced on a thermoplastic plate which is developed electrically is just a few minutes, eliminating the delay and inconvenience of chemical photographic processing. After both beams pass through the thermoplastic plate the resulting fringe pattern is recorded using a CCD camera.

Results and Discussion

From the experimental set-up shown in figure 3.0 no pressure oscillations in the 1 to 8 kHz range were observed. The HPLC pump set at its' maximum flowrate of 100 ml/min produced a very large amount of noise associated with a pressure oscillation of +/- 80 psi. This oscillation however was only in the .1 kHz range. For the two runs, both ten hours each, running the pump and the furnace at maximum operating conditions nothing other than the pump driven oscillations were observed. The fuel went well into the supercritical range with the pressure oscillating around 700 psi and outside wall temperatures reaching over 1000 F. The temperature profile can be seen in figure 5.0 below.

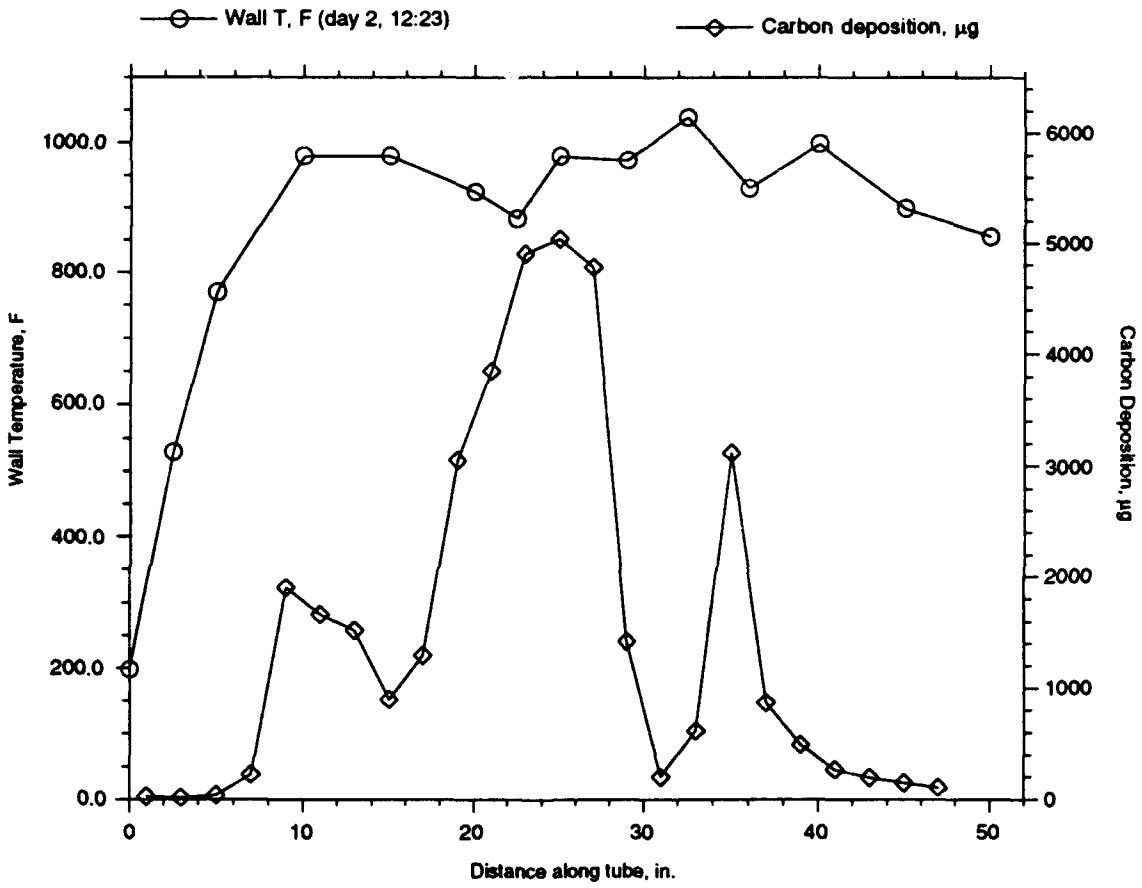

Figure 5.0: Temperature and Carbon Deposition Profile along tube.

It is thought that these pressure oscillations are flow instabilities which are caused by rapid changes in fluid properties during heat transfer near the critical point. As heat was transferred to the fuel there were rapid changes in the physical properties. The viscosity would decrease rapidly causing a thinning in the thermal boundary layer and an increase in the heat transfer coefficient. This would then cause a decrease in the film temperature of the fuel which would increase the viscosity. The thermal boundary layer would increase again and the cycle could repeat itself [5]. At a high rate of heat transfer the cycles would repeat themselves at a faster rate causing the instabilities to be greater and produce significant pressure oscillations. At lower heat fluxes these rapid changes may not occur and the cycle would never begin. The Hines & Wolf and Shell Development Company experiments with their electrically heated tubes had heat fluxes 3 to 30 times that of what Hindberg furnace could produce even operating at its maximum capacity.

The results from the holographic interferometer also proved to be disappointing. There were many problems with the initial experimental set-up. The fine meter-valve would stick due to the large temperature and pressure drop across the valve that made controlling the flowrate impossible. Flowrate was later stabilized by using an ISCO syringe pump to push the SF_6 through the system. The problem with using this pump is that you can control the flowrate but not the pressure. Pressure would be controlled moderately by a check valve to within 30 psi of a desired setting.

Another problem using holographic interferometry in a flowing system is that the flow must be uniform in order to achieve nice, steady, straight, and definitive fringe patterns. With only one heated surface in a large, wide channel, non-uniform flow became a problem. This creates a large temperature gradient between the heated wall and the bulk flow. This large temperature gradient causes a circular recirculation pattern to develop. This recirculation will diminish the quality of the fringes and also causes them to move rapidly. This problem can be seen with the image taken with a CCD camera in figure 6.0.

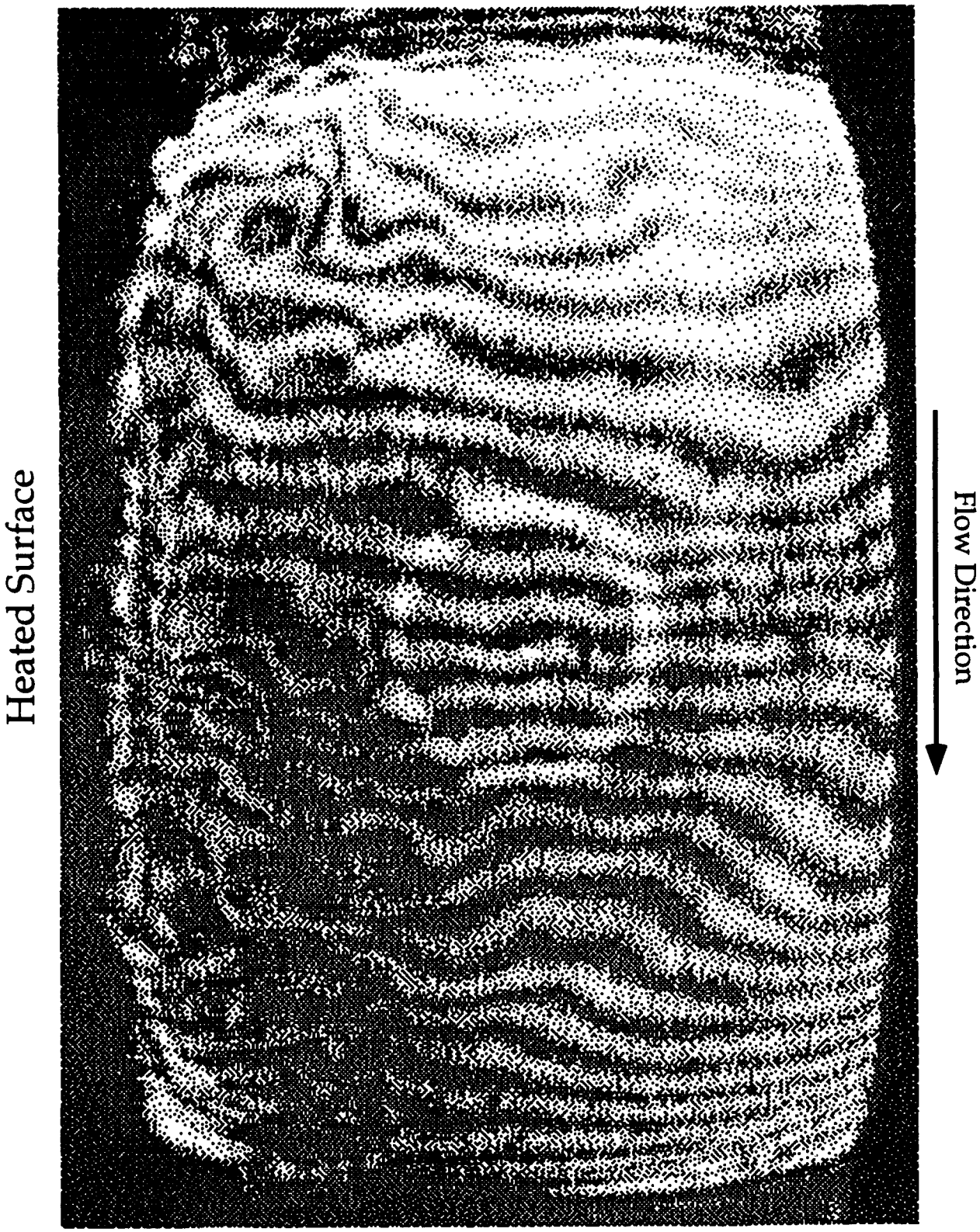

Figure 6.0: Unsteady Fringe Pattern from Holographic Interferometry Set-up.

The optical cell was then changed so that both sides of the cell were heated in order to reduce the temperature gradient across the cell, but because the channel was so wide the bulk flow temperatures were still significantly less than the heated surfaces. The heated surfaces were then extended on both sides so that there was only a 3 mm gap between the heated surfaces. This would increase the velocity, reduce the temperature gradient, and the recirculation effects. This latest modification also did not produce fringe patterns at supercritical temperatures. When the fluid in the cell reached about 38 C the index of refraction was changing so rapidly that one could see the changes optically with the human eye. The object beam had become distorted which destroyed the fringe pattern behind the holographic plate. It was determined at this point that holographic interferometry would not be a good method to obtain temperature measurements with supercritical sulfur-hexafluoride.

Conclusions and Recommendations

The future of high performance aircraft is dependent on developing a fuel that will be able to handle an increased heat load. This fuel will almost definitely be a supercritical fluid. Many aspects of supercritical fluids must be understood before moving down this path. Other studies have seen pressure oscillations with supercritical fuels severe enough to rupture tubing at high heat fluxes. Fuel lines running past or near the combustor nozzle could experience high enough heat fluxes to possibly cause these detrimental pressure oscillations. A high temperature furnace can not obtain a high enough heat flux required to observe these oscillations. Experiments with electrically heated tubes need to be performed in order to observe and understand this phenomenon.

Accurate means of measuring near wall temperatures are also needed in order to determine the effectiveness of a supercritical fluid as a heat sink. Holographic interferometry is not feasible with supercritical sulfur-hexafluoride. The index of refraction changes so rapidly that the object beam becomes distorted and fringe patterns can not be formed. Other temperature measuring devices are being looked into to obtain these near wall temperature, such as liquid crystal temperature tape and infrared thermometers.

References

1. Edwards, T. "High Temperature, Thermally Stable JP Fuels -- An Overview", AIAA Paper 92-0807.

2. Edwards, T. "USAF Supercritical Hydrocarbon Fuel Interests", AIAA 93-0807.

3. Hall, W. B. "Heat Transfer Near the Critical Point", Advances in Heat Transfer, pp. 1-86; 1971.

4. Hines, W. S., Wolf, H. "Pressure Oscillations Associated with Heat Transfer to Hydrocarbon Fluids at Supercritical Pressures and Temperatures", ASR Journal, Vol. 32, March 1962.

5. Faith, L. E., Ackerman, G. H., Henderson, H.T. "Heat Sink Capability of Jet A Fuel: Heat Transfer and Coking Studies", NASA CR-72951, July 1971.

Local Environment Effects on Evaporation Rates of Flowing Droplets

J. Christian Swindal

Department of Applied Physics

and

Center for Laser Diagnostics

Yale University

P.O. Box 208284

New Haven, CT 06520-8284

Final Report for:

Graduate Student Research Program

Wright Laboratory

Sponsored by:

Air Force Office of Scientific Research

Bolling Air Force Base, Washington, D.C.

and

WL/POSF, Fuels and Lubrication Laboratory

Wright-Patterson Air Force Base, Dayton, OH

September 1993

Local Environment Effects on Evaporation Rates of Flowing Droplets

J. Christian Swindal
Department of Applied Physics and Center for Laser Diagnostics
Yale University

Abstract

The local environment is observed to have an effect on the evaporation rates of flowing micrometer-sized droplets. A 9-orifice droplet generator is used to produce 9 droplet streams arranged in a 3 x 3 square array. Droplet evaporation rates are deduced from spectroscopic droplet size change measurements. Ethanol and ethanol/acetone droplets are doped to a concentration of 5×10^{-5} M Rhodamine 6-G laser dye. With illumination by the 532 nm second harmonic Nd:YAG laser pulse, the droplets can reach the lasing threshold because the droplets act as optical cavities, supporting discrete wavelengths which corresponding to Morphology-Dependent Resonances (MDR's) of the droplets. The difference in size among the droplets can be deduced by measuring the wavelength-shift of a particular MDR for successive droplets in the flowing streams. The rate of size change for droplets within a given droplet stream is observed to depend on the stream position within the 3 x 3 array. The center droplet stream exhibits the lowest evaporation rate, the edge droplet stream exhibits more evaporation, and the corner droplet streams exhibit the highest evaporation rate.

Local Environment Effects on Evaporation Rates of Flowing Droplets

J. Christian Swindal

Introduction

When a liquid droplet is injected into a gaseous environment, its hydro- and thermodynamic behavior is described by a coupled set of heat, mass, and momentum transfer equations. For an isolated droplet, heat transfer within the droplet is governed principally by diffusion. If the droplet is flowing through a gaseous environment, a shear stress develops at the liquid interface, pulling the sides upward, causing an internal circulation of material up the outside of the droplet and down through its center, as has been visualized[1] with two-dimensional imaging of fluorescence quenching by O_2. The heat transfer within the droplet is then governed principally by convection. As heat is transferred to the droplet from the environment, the droplet undergoes evaporation with a concomitant decrease in size. As evaporation take place, mass and temperature gradients are formed by the vapor which trails behind the flowing droplet. In a segmented stream of droplets, these gradients formed by the lead droplet will alter the environment of the trailing droplet with respect to its own environment. Consequently, the behaviors of the lead and successive trailing droplets are expected to exhibit different behaviors. Similarly, for continuous streams of droplets, the high vapor concentration surrounding the stream must diffuse into the surrounding environment, producing mass and temperature gradients in directions lateral to the stream. A group of droplet streams situated in close proximity, such that different streams experience different environments, should influence the hydrodynamics of one another.

Many techniques have been devised to provide information on droplet sizes and evaporation rates. Size measurements on large droplets have been made by using shadowgraphy[2] and ray tracing[3] techniques. Transmittance measurements[4] have been used to size small droplets, with radius 3 μm < a < 15 μm, to an accuracy of 10% by making use of the known relationship between droplet diameter and extinction. Two-color transmission techniques[5] have improved the measurement accuracy and extended the measurable size range to a > 0.1 μm. Laser Doppler anemometry (LDA) is a commercially available technique for measuring droplet size and velocity distributions for droplets which pass through a fixed probe volume. Relative evaporation rates of droplets in a single segmented stream have been determined[6] by shifts in the droplet-cavity fluorescence peaks.

The spherical morphology of droplets provides several features which are well suited to light scattering measurements. First, the curved interface between the liquid and its surroundings acts like a lens to concentrate the incident radiation to a small region near the droplet surface of the shadow side of the droplet [see Fig. 1]. This focusing effect can increase the intensity just within the shadow side by a factor of more than 100 relative to the incident radiation. This helps to lower the input intensity threshold required to achieve nonlinear optical processes in droplets such as lasing, stimulated Raman scattering (SRS), and stimulated Brillouin scattering (SBS).

Second, the droplet acts as a high-Q optical cavity, providing feedback for nonlinear optical processes. Classically, light that is emitted or generated within the droplet may strike the liquid-air interface at an angle above the critical angle to achieve near-total internal reflection. This reflection process may occur many times as the light travels around the circumference of the droplet. If the light wave returns to its initial starting point with its initial phase, the droplet acts as an optical cavity for that particular wavelength.

Third, the presence of the spherical optical cavity can lead to cavity quantum electrodynamic (QED) effects. In contrast to bulk liquid in a cell, where the final radiation states are a continuum of modes, the final radiation states of a droplet are the discrete cavity modes.[7] For a molecule undergoing a radiative transition, this leads to an increased probability of emission at wavelengths corresponding to the droplet MDR's, and a decreased probability of emission at other wavelengths.[8] The enhancement of emission at MDR wavelengths subsequently increases the efficiency of stimulated processes, e.g., increases the fluorescence or Raman gain coefficient. Each of these effects contributes to reducing the thresholds for stimulated emission in droplets.

The spectral positions of spherical resonance modes (referred to as morphology-dependent resonances, or MDR's) are described by a set of vector-spherical harmonics, and can be calculated mathematically from Lorenz-Mie theory.[9,10] Each MDR can be labeled by three indices: n is the angular mode number, l is the radial mode order, and m is the azimuthal mode number. For a perfect sphere, each mode is (2n+1)-fold degenerate in m. For a sphere with radius a, the droplet modes occur at discrete size parameters $x_{n,\ell} = 2\pi a/\lambda_{n,\ell}$, where λ is the wavelength in the surrounding medium. A quality factor (Q-value) associated with each mode describes the amount of radiation stored divided by the radiation leakage from the cavity mode during one optical cycle. MDR's with higher Q-values therefore provide more feedback for stimulated emission processes than MDR's with lower Q-values. These high Q-value modes are located radially closer to the droplet interface. The threshold for stimulated emission is reached first by the highest Q-value

MDR's which have significant spatial overlap with the high input intensity region inside the droplet.

Because the trapped light within a droplet MDR is very sensitive to small phase changes that accumulate after traveling many times around the droplet circumference, a small change in droplet size is manifest as a shift in the spectral location of the MDR's [see Fig. 2]. For a given MDR, a change in droplet radius of Δa will cause the MDR to shift by $\Delta\lambda = (\lambda/a)\Delta a$. By measuring the spectral shift of the MDR, the change in droplet radius Δa can be determined, as can the change in droplet volume $\Delta V = 4\pi a^2 \Delta a$. Determination of Δa for several consecutive droplets in a flowing stream permits the deduction of the mean droplet evaporation rate provided the droplet flow velocity is known.

If a droplet is distorted, such that its shape is spheroidal, the previously degenerate m-modes will split into n+1 non-degenerate modes [see Fig. 3]. If the distortion is small, so that $|e| << 1$ where $e = (r_e - r_p)/a$, r_e is the equatorial radius, r_p is the polar radius, and a is the radius of the droplet in the absence of any distortion, then the frequency of each m-mode MDR (for a MDR of a given n) is given by[11]

$$\omega(m) = \omega_o\left\{1 - \frac{e}{6}\left[1 - \frac{3m^2}{n(n+1)}\right]\right\} \qquad (1)$$

where ω_o is the frequency of the degenerate MDR (at $\lambda_{n,\ell}$) for a perfect sphere. The frequency shifts of several MDR-related elastic scattering peaks[12] and lasing peaks[13] have been observed for droplets undergoing quadrupolar shape oscillations. Several m-mode MDR-related SRS peaks from flowing droplets have been spectrally resolved with a Fabry-Perot interferometer.[14] Temporal precession of the degeneracy-split m-modes has been observed in stream of flowing droplets.[15]

Experimental Details

The droplets are produced by a custom droplet generator, made by Fluid Jet Associates. Liquid from an external reservoir is forced through a particle filter to the body of the droplet generator and through an orifice plate at a pressure of 27.3 psi. The orifice plate, which is patterned by a photolithographic technique, contains nine 34 μm-diameter orifices, arranged in a 3 x 3 square array. The spacing between nearest-neighbor orifices is nominally 500 μm measured center-to-center. The body of the droplet generator incorporates a piezo-electric transducer element. The transducer is driven at a frequency of 128.6 kHz by a modified Denon POA-280 stereo power amplifier. As the liquid is forced through the body of the droplet generator and the orifice plate, the piezoelectric transducer

produces pressure undulations, which cause the emerging liquid column the break-up into streams of monodispersed droplets with radius $a \approx 30\ \mu m$ and a velocity of ≈ 10 m/s.

The droplets are subsequently illuminated by the second-harmonic output of a Nd:YAG laser (532 nm) which has a pulse duration of 10 ns and a pulse repetition rate of 10 Hz. The laser beam is focused into a sheet by a converging cylindrical lens. The droplets are placed near the focus of the laser sheet so that only the 3 droplet streams which are in the plane of the sheet are illuminated, as shown in Fig. 4. A segment of droplets from one of the illuminated streams is imaged through a red color filter to the entrance slit of a 0.5 m spectrograph. The spectrograph houses a 1200 groove/mm grating. Collection of the droplet lasing emission at 90° with respect to the input-laser propagation direction minimizes the elastically scattered light, while the red filter serves to block residual elastically scattered light and pass the wavelength-shifted lasing emission from the droplets. The spectrograph is equipped with a two-dimensional charge-coupled device (CCD) at its output to provide for the recording of spectral information as well as spatial information along the length of the input slit. A portion of a particular droplet stream can be imaged onto the spectrograph slit by translating the entire droplet generator to bring the desired stream into the illuminating laser sheet and into the field of view of the collection lens.

Discussion

Figure 5 shows a portion of a typical CCD recording. The wavelength-dispersed lasing spectra of six droplets in a continuous stream is measured along the x axis, while the spatial distance below the orifice plate is measured along the y-axis. There are three things to note in this image.

First, for each droplet, a series of nearly equally spaced emission lines is observed, corresponding to adjacent n- mode MDR's of the droplets. Three distinctive peaks are observed for each droplet, corresponding to three successive n-mode MDR's. The spectral separation of these n-modes can be used to calculate the droplet size in Lorenz-Mie theory[10]. Although the solution in computationally intensive, approximations[16,17] to the exact theory greatly simplify the calculations and still yield results accurate to 1% or better. A convenient expression that approximates (for large size parameter and large n), the droplet size is:[18]

$$a \approx \frac{\arctan\sqrt{(m^2 - 1)}}{2\pi\sqrt{(m^2 - 1)}} \left(\frac{1}{\lambda_1} - \frac{1}{\lambda_2}\right)^{-1} \qquad (2)$$

where m is the relative index of refraction, λ_1 is the wavelength of shorter wavelength n-mode, and λ_2 is the wavelength of the longer wavelength n-mode. For the spectra in Fig. 5, equation (2) yields $a \approx 32.5$ μm, which is within 10% of the 30.0 μm radius deduced from flow rate and droplet frequency measurements.

Second, the wavelength of the emission corresponding to each MDR is not the same for all points along the droplet rim, but varies with position, producing distinctive ⊃-shapes on the CCD image. This shape results from two effects. The predominant cause is the splitting of the m-mode MDR's. As the droplets flow through the surrounding air, hydrodynamic forces act to distort the droplets. The resulting spheroidal shape of the droplet splits the m-mode MDR's into n+1 non-degenerate modes in accordance with equation (1). The m = ± n mode is mainly confined to the region around the equator [see Fig. 3(b)]. For an oblate droplet, the m = ±n mode senses a larger circumference and is upshifted in wavelength. The m = 0 mode, which is mainly confined to the polar regions, senses a shorter circumference and is downshifted in wavelength. The wavelength range between the m = ± n and m = 0 modes is spanned by the other m-modes as depicted in Fig. 3(b). Since each m-mode is mainly confined to a particular region along the droplet rim, when the droplet rim of a sufficiently distorted droplet is imaged onto the entrance slit of a spectrometer, the variation in wavelength of the various m-modes may be determined. The region near the equator is red-shifted, while the regions toward both poles are blue-shifted, resulting in the ⊃-shape seen in the CCD data of Fig. 5, and as depicted in Fig. 6. Secondly, since the spectrograph we used is not an imaging spectrograph, and the image at the entrance slit of the spectrograph is itself a semi-circular image, and the spectral output at the CCD should exhibit a ⊃-shaped aberration. Depending on whether the left side or right side of the droplet is imaged to the spectrometer, the ⊃-shaped imaging aberration will subtract or add to the ⊃-shaped spectral dispersion of the light emanating from the distorted droplet rim. Measurements of ⊃-shaped image can permit the determination of the shape distortion amplitude.[19]

Third, the emission from any n-mode MDR is progressively shifted to shorter wavelengths as the droplets travel further downstream from the orifice plate. The laser emission shift to shorter wavelengths corresponds to a decrease in droplet size. We attribute the decrease in size to evaporation. Fig. 7 shows a plot of the wavelength for a particular MDR as a function of distance below the orifice plate for the center stream and one of the corner streams, with ethanol as the liquid. Each data point represents the m = ± n mode for one droplet (the vertex of the ⊃-shape on the CCD image). The entire set of data points for each stream is pieced together from 6 overlapping CCD images, with each image centered on different spatial regions. The data covers the region from

0.9375 cm to 1.6875 cm below the droplet generator orifice. The oscillatory behavior of the MDR wavelengths for droplets closer to the orifice plate is a result of the droplet shape oscillations (because of droplet break-up from the jet column) causing the wavelength of the measured m-modes to oscillate with it. Figure 8 shows a CCD image for droplets closer to the orifice plate. A small but perceptible difference is observed in the rate of size change between the center droplet stream of the 3 x 3 array and a corner droplet stream. In fact, the center droplet stream shows no droplet size change over the measurement region, within the error limits of the measurements. Figure 7 yields an evaporation rate of -6.4×10^{-4} cm^2/s for the corner droplet stream.

In addition to the droplet size change, the spectral oscillations exhibited by droplets closer to the orifice plate can be used to deduce the surface tension of the liquid. It must be assumed that the droplets are oscillating in a purely quadrupole mode (higher order oscillation modes damp out much more quickly, and, empirically, the five complete oscillation periods in the spectral measurement region of Fig. 7 are identical). The measured oscillation period can be used to calculate[20] the surface tension. The lasing spectra of Fig. 7 yields a surface tension for ethanol of 24.5 dynes/cm. This is to be compared to the published value[21] of 22.8 dynes/cm at 20° C.

In an attempt to increase the evaporation rate of the droplets, a mixture of acetone and ethanol was used in a 2:9 volumetric ratio. Acetone has a lower boiling point at 56° C, than that of ethanol, which has a boiling point of 79° C. Figure 9 shows a plot of the wavelength for a particular MDR as a function of distance below the orifice plate for the center droplet stream, an edge droplet stream, and a corner droplet stream in the 3 x 3 array for the acetone/ethanol mixture. The corner stream of the 2:9 acetone:ethanol droplets now exhibits a larger rate of size change relative to the stream of ethanol droplets. The mixture droplets located in an edge stream are also observed to decrease in size but at a slower rate. The center stream exhibits the lowest rate of size change. The drop-to-drop size fluctuations of the center stream are markedly greater than the other streams, but the trend to decreasing size is unmistakable. The size fluctuation among the acetone/ethanol mixture droplets was greater than that for ethanol droplets. These fluctuations prevented the measurement of droplet MDR's closer to the orifice plate, where the droplets undergo shape oscillations produced by break-up. The calculated evaporation rates for the corner, edge, and center droplet streams are -13×10^{-4} cm^2/s, -8.1×10^{-4} cm^2/s, and -2.24×10^{-4} cm^2/s , respectively.

Conclusions

The lasing emission corresponding to droplet cavity modes has been used to deduce the evaporation rates of ethanol and ethanol/acetone droplets in a 3 x 3 array of droplet streams. An influence on the droplet evaporation rates is observed, due to the vapor produced by the neighboring droplet streams. For ethanol, the center stream of the 3 x 3 is not observed to exhibit significant evaporation within the detectability of the instruments. The corner stream had a detectable amount of evaporation.

Using a mixture of acetone and ethanol, each of the droplet streams in the 3 x 3 array exhibited evaporation. The evaporation rate is different depending upon the location of the stream within the array. The center droplet stream is observed to possess the lowest evaporation rate. The edge droplet stream exhibits a greater evaporation rate, with the corner droplet stream exhibiting the largest evaporation rate.

The flowing droplets exhibit a shape distortion which splits the degenerate m-modes of the spherical MDR's. As the liquid exits the orifice plate and breaks apart into droplets, the oscillating the droplets cause the spectral position of the m-mode MDR's to oscillate with the same period. Measurement of the oscillation frequency allows the determination of the liquid surface tension.

Acknowledgments

I would like to thank Drs. Thomas Jackson and Mel Roquemore for their help and support of this work. Dr. John Dressler is gratefully acknowledged for his help in obtaining and using the 9-hole droplet generator. I would also like to thank Prof. Richard K. Chang for many helpful discussions.

References

1. M. Winter, L.A. Melton, "Measurement of Internal Circulation in Droplets Using Laser-Induced Fluorescence," Appl. Opt. 29, 4574 (1990).

2. T. Kamimoto, S.K. Ahn, Y.J. Chang, H. Kobayashi, and S. Matsuoka, "Measurement of Droplet Diameter and Fuel Concentration in Non-Evaporating Diesel Spray by Means of an Image Analysis of Shadow Photographs," SAE Paper 840276 (Society of Automotive Engineers), 1984.

3. K.-I. Hayashi, and T. Karakama, "Droplet Size Measurements with Linear Charge Coupled Device Camera," J. of Nuclear Sci. Tech 27, 295 - 306 (1990).

4. H.R. Carlon, M.E. Milham, and R.H. Frickel, "Determination of Aerosol Droplet Size and Concentration from Simple Transmittance Measurements," Appl. Opt. 15, 2454 - 2456 (1976).

5. P.C. Ariesohn, S.A. Self, and R.H. Eustis, "Two-Wavelength Laser Transmissometer for Measurements of the Mean Size and Concentration of Coal Ash Droplets in Combustion Flows," Appl. Opt. 19, 3775 - 3781 (1980).

6. G. Chen, A. Serpenguzel, R.K. Chang, and W.P. Acker, "Relatice Evaporation Rates of Droplets in a Segmented Stream Determined by Droplet Cavity Fluorescence Peak Shifts," SPIE Proceedings Series, vol. 1862, pp. 200 - 208 (1993).

7. E.M. Purcell, "Spontaneous Emission Probabilities at Radio Frequencies," Phys. Rev. 69, 681 (1946).

8. S.C. Ching, H.M. Lai, and K. Young, "Dielectric Microspheres as Optical Cavities: Thermal Spectrum and Density of States," J. Opt. Sci. Am. B 4, 1995 - 2003 (1987).

9. C.F. Bohren and D.R. Huffman, *Aborption and Scattering of Light by Small Particles* (Wiley, New York, 1983), pp. 93 - 104.

10. S.C. Hill and R.E. Benner, "Morphology-Dependent Resonances," in *Optical Effects Associated with Small Particles*, P.W. Barber and R.K. Chang, eds. (World Scientific, Singapore, 1988), pp. 3 - 61.

11. H.M. Lai, P.T. Leung, K. Young, P.W. Barber, and S.C. Hill, Phys Rev. A 41, 5187 (1990).

12. S. Arnold, D.E. Spock, and L.M. Folan, "Electric Field Modulated Light Scattering Near a Morphological Resonance of a Trapped Aerosol Particle," Opt. Lett. 15, 1111 - 1113 (1990).

13. H.-M. Tzeng, M.B. Long, R.K. Chang, and P.W. Barber, "Laser-Induced Shape Oscillations of Flowing Droplets Deduced from Morphology-Dependent Resonances in Fluorescence Spectra," Opt. Lett. 10, 201 - 211 (1985).

14. G. Chen, R.K. Chang, S.C. Hill, and P.W. Barber, Opt. Lett. 16, 1269 (1991).

15. J.C. Swindal, D.H.Leach, R.K. Chang, and K. Young, "Precession of Morphology-Dependent Resonances in Nonspherical Droplets," Opt. Lett. 18, 191 - 193 (1993).

16. P. Chylek, "Resonance Structure of Mie Scattering: Distance Between Resonances," J. Opt. Sci. Am. A 7, 1609 - 1613 (1990).

17. C.C. Lam, P.T. Leung, and K. Young, "Explicit Asymptotic Formulas for the Positions, Widths, and Strengths of Resonances in Mie Scattering," J. Opt. Soc. Am. B 9, 1585 - 1592 (1992).

18. P. Chylek, J. Opt. Soc. Am. 66, 285 (1976).

19. G. Chen, Md.M. Mazumder, Y.R.Chemla, A. Serpenguzel, R.K. Chang, and S.C. Hill, "Wavelength Variation of Laser Emission Along the Entire Rim of Slightly Deformed Microdroplets," Opt. Lett. (to be published).

20. Trinh, Zwern, Wang, J. Fluid Mech. 115, 453 (1982).

21. *CRC Handbook of Chemistry and Physics*, 59th edition, (CRC Press, Inc., 1979) pp. F-46.

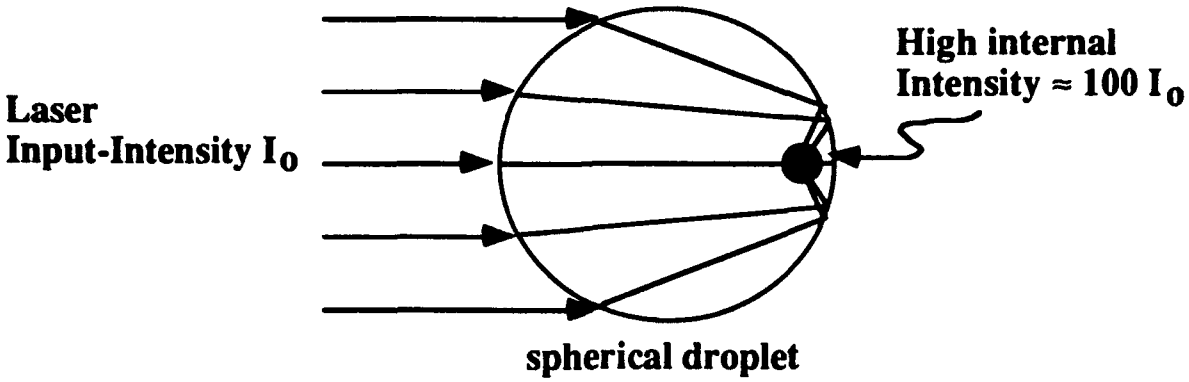

Fig. 1: The curved surface of the droplet intercepts incident radiation of Intensity I_0 and concentrates it near the shadowside of the droplet with an increase in intensity of approximately 100 I_0.

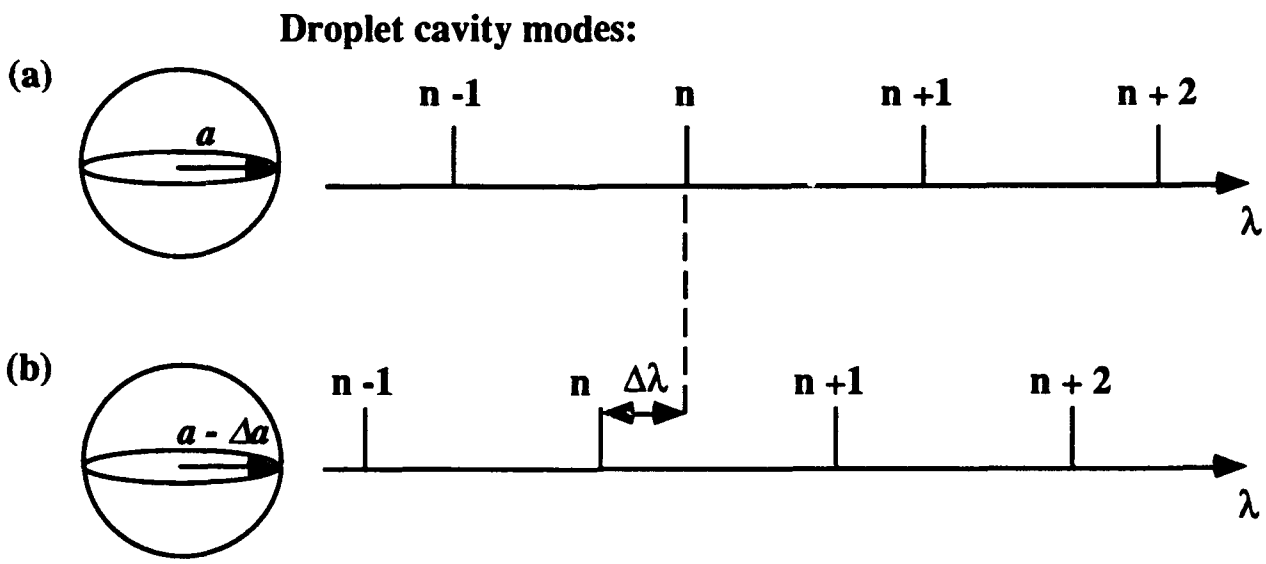

Fig. 2: (a) For a spherical droplet with radius a, the spectral separations between adjacent n-mode MDR's have nearly equal spacing for large values of n. (b) A decrease in droplet radius by Δa causes the MDR's to shift to shorter wavelengths by $\Delta\lambda$, where $\Delta\lambda = (\lambda/a)\Delta a$.

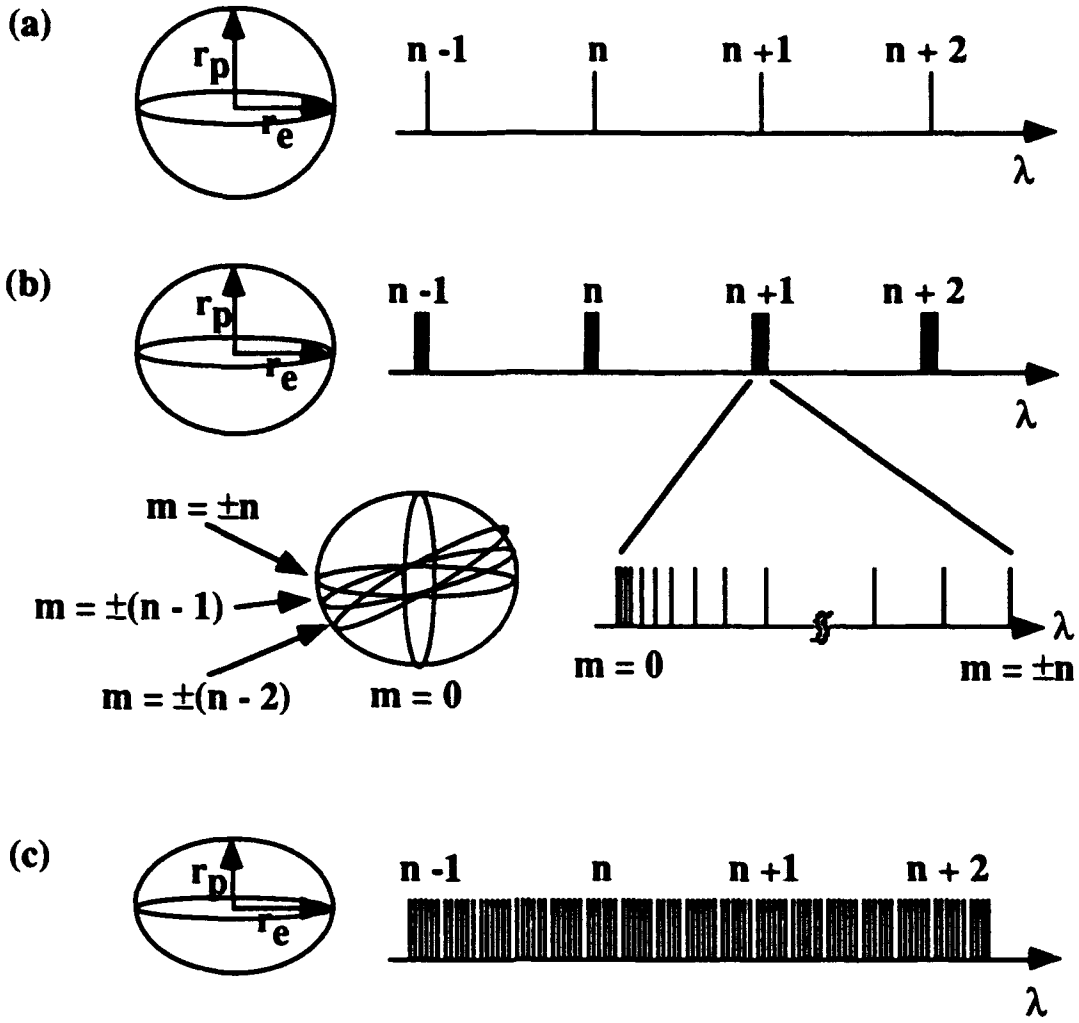

Fig. 3: Each MDR of a spherical droplet (a) is (2n+1)-fold degenerate in the azimuthal mode order m. A slightly distorted droplet (b) causes the m-modes to split, and if unresolved will appear to be spectrally broadened. For a severely distorted droplet (c) the splitting can become so large that the spectra appears as a continuum.

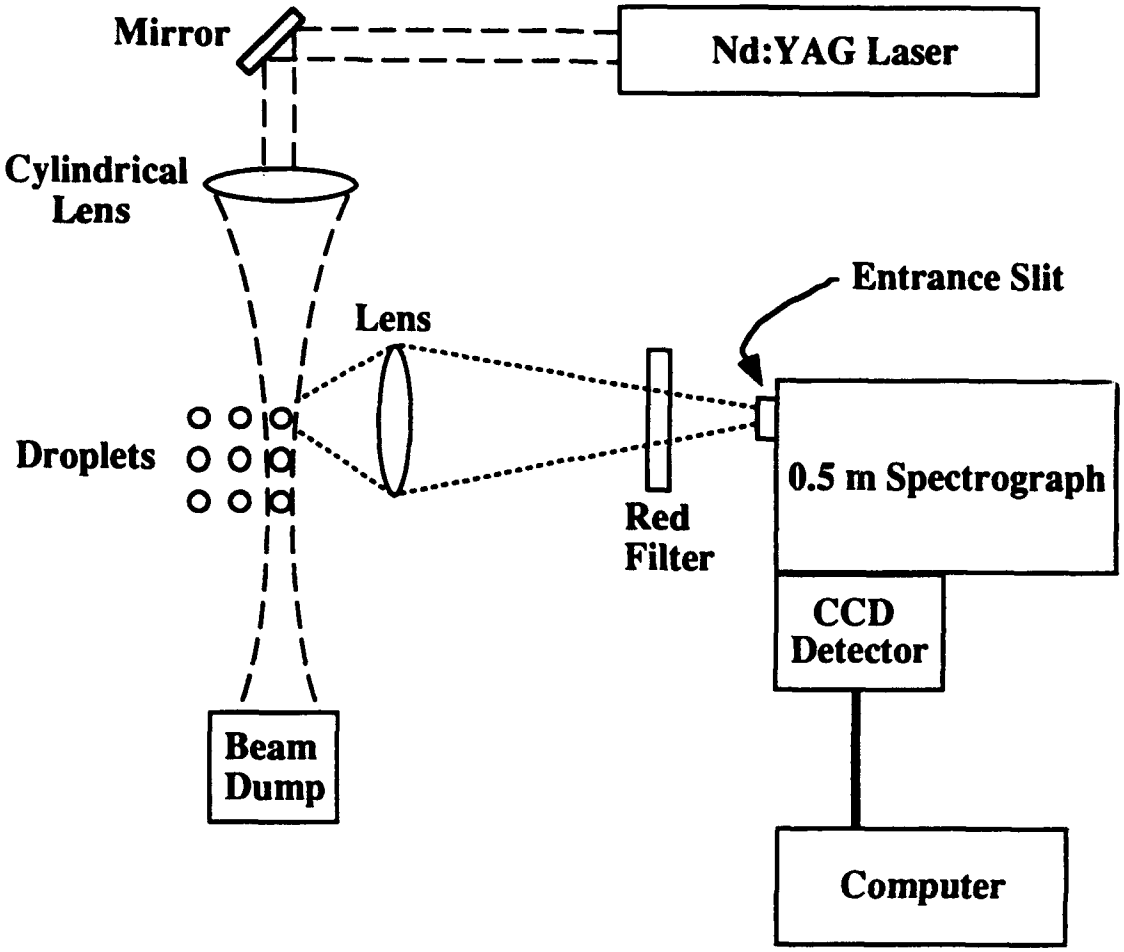

Fig. 4: Experimental set-up showing the input-laser illumination of three droplet streams. One of the droplet streams is imaged onto the entrance slit of the spectrograph. The red filter blocks the elastically scattered 532 nm input-laser and passes the wavelength shifted red lasing emission from the droplets.

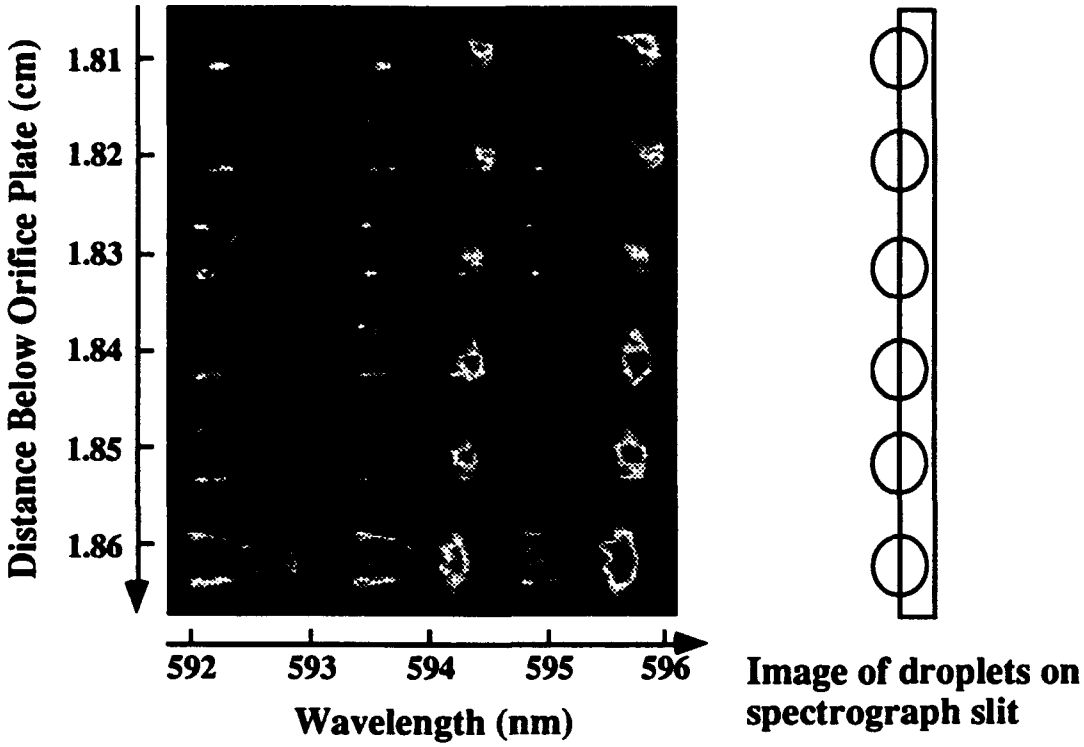

Fig. 5: CCD image of a portion of the lasing spectra from six droplets in an ethanol/acteone droplet stream located at the edge of the 3 x 3 square array. The image of the droplets at the entrance slit of the spectrograph is also shown. Three adjacent n-modes are shown. The ⊃-shape of each n-mode corresponds to the splitting of the m-modes due to shape distortion. The wavelengths of each n-mode decrease with distance from the orifice plate, indicating a size decrease of the successive droplets from the orifice plate.

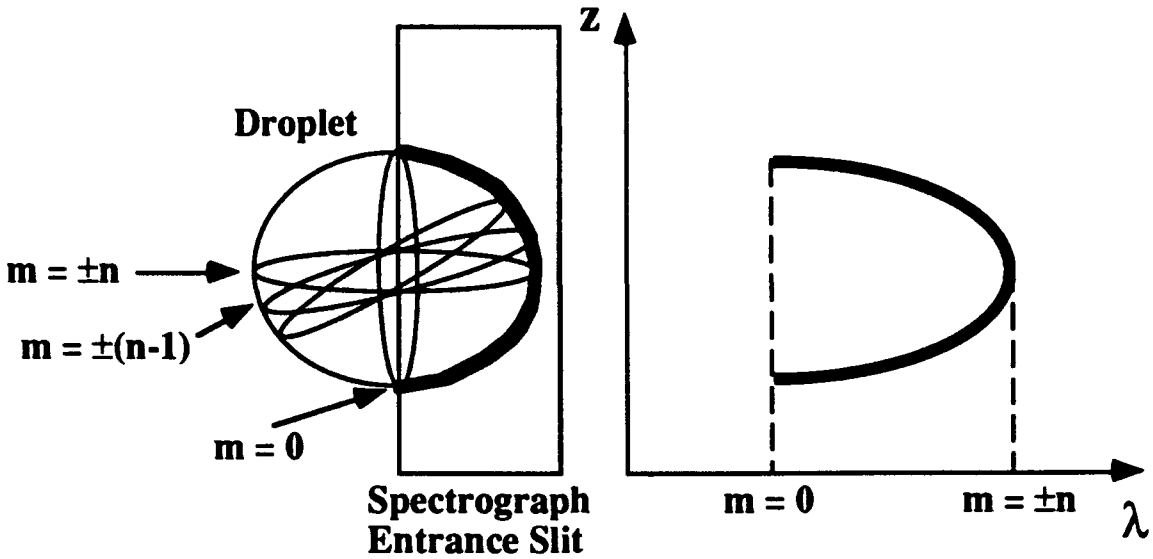

Fig. 6: The degeneracy-split m-mode MDR's of a spheroidal droplet are mainly confined to different regions around the droplet rim. Each of the non-degenerate m-modes corresponds to unique wavelengths, so that when a portion of the droplet rim is imaged onto the entrance slit of a spectrograph, the dispersed wavelengths produce a u-shaped image at the spectrograph output plane.

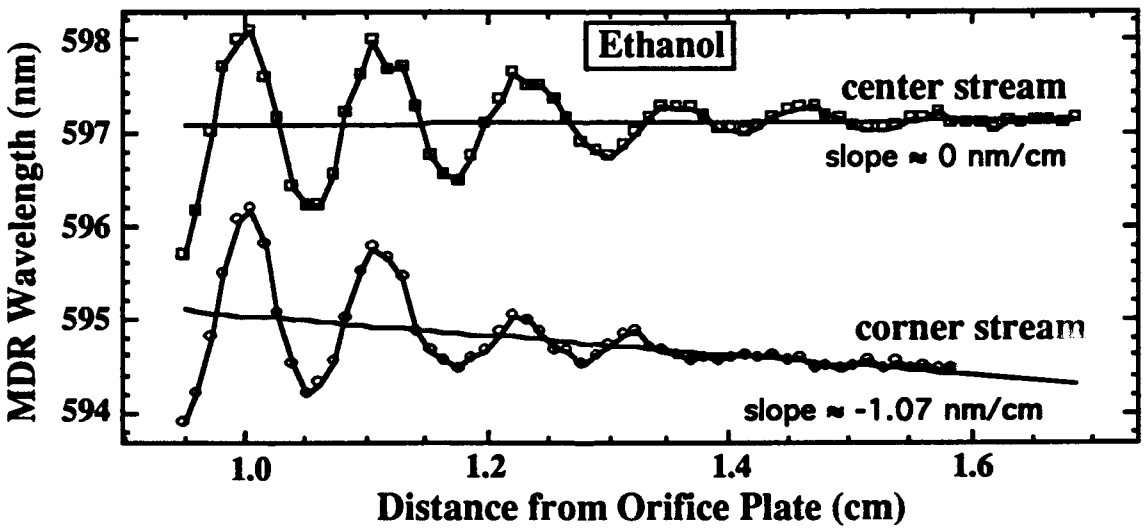

Fig. 7: Plot of the wavelength associated with the degeneracy-split m=±n MDR for ethanol droplets as a function of droplet distance from the orifice plate. The droplets in the corner stream are seen to decrease in sizewith distance from orifice plate. The center droplet stream exhibits no measurable size change. The oscillatory behavior of the spectra from droplets nearer to orifice plate is associated with droplet shape oscillations.

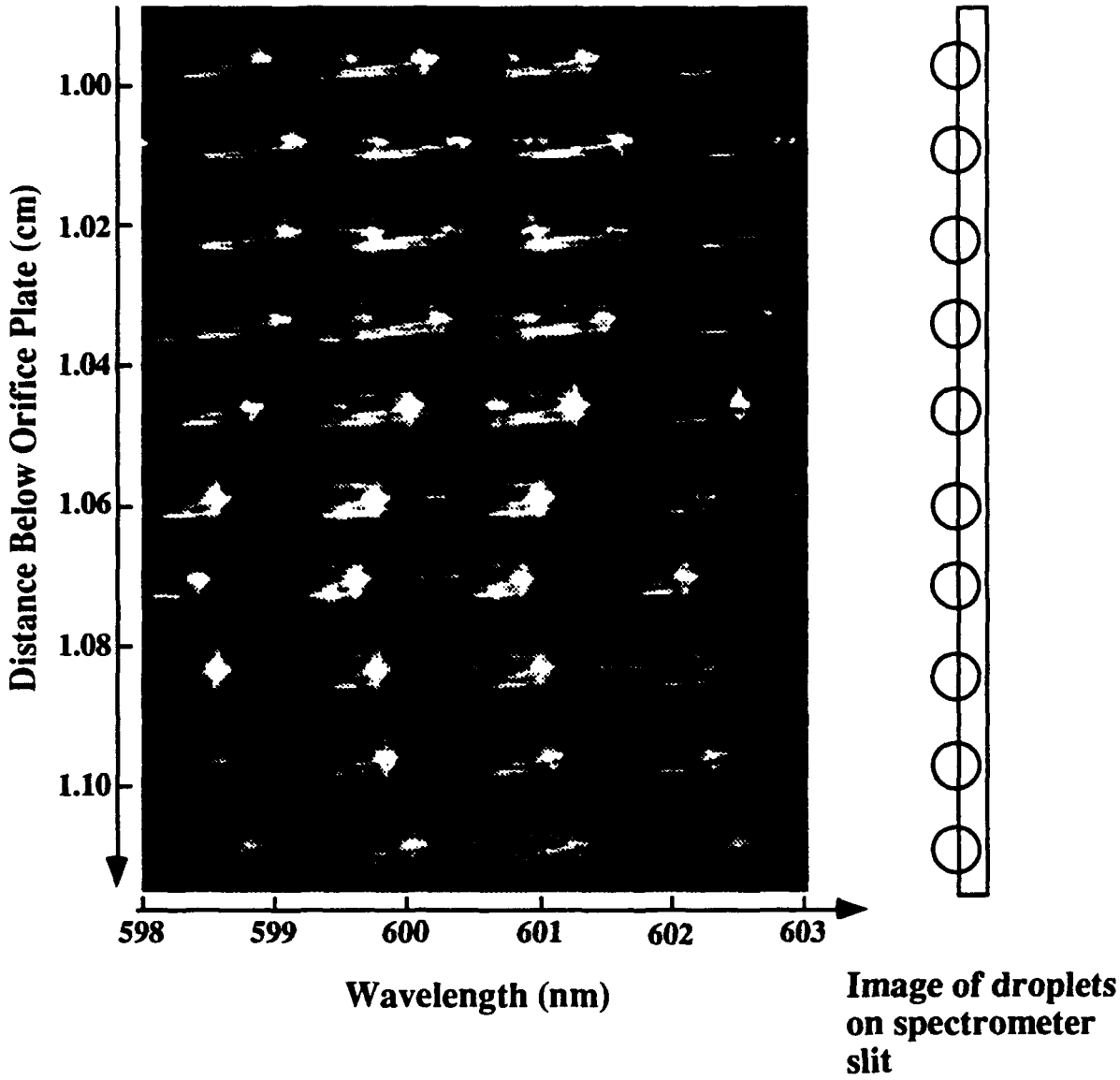

Fig. 8: CCD image of a portion of the lasing spectrum from 10 droplets in an ethanol droplet stream. The droplets are located near the orifice plate and are still oscillating soon after the break-up from the liquid column jet. The lasing emission corresponding to the four adjacent n-modes is shown. The length of the ⊃-shape of the degeneracy-split m-modes also exhibits oscillations as the droplet shape changes for successive droplets downstream.

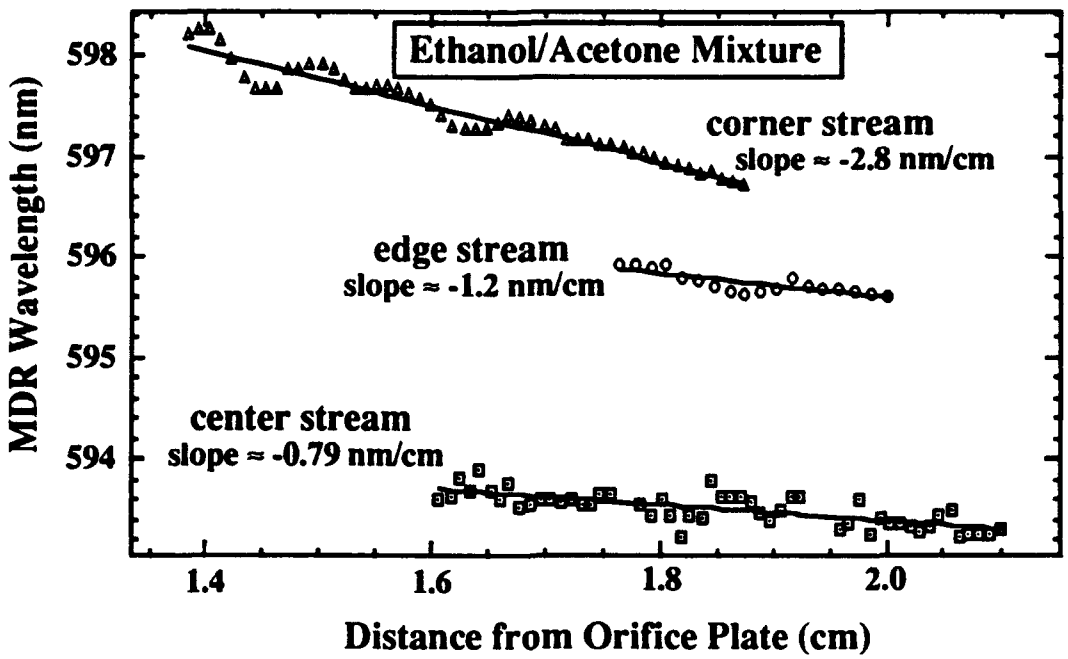

Fig. 9: Plot of the wavelength associated with the degeneracy-split m = ±n MDR for ehtanol/acetone mixture droplets as a function of droplet distance from the orifice plate. The droplets in all the streams are observed to decrease in size with distance from the orifice plate. The droplets in the corner stream exhibit the greatest evaporation rate. The edge droplet stream exhibits a lower evaporation rate. And the center stream has the lowest evaporation rate.